UNIVERSITÉ D'ORLÉANS

ÉCOLE DOCTORALE
ENERGIE, MATERIAUX, SCIENCES DE LA TERRE ET DE L'UNIVERS

ICARE-CNRS ORLEANS

THÈSE présentée par :

Lisa MICHELAT

soutenue le : **8 décembre 2023**

pour obtenir le grade de : **Docteur de l'Université d'Orléans**

Discipline/ Spécialité : Chimie. Chimie de l'atmosphère et computationnelle

---

"Measuring and predicting the atmospheric oxidation kinetics of unsaturated volatile organic compounds, with a focus on biomass burning and industrial species."

THÈSE dirigée par :
Abdelwahid MELLOUKI   Directeur de recherche, ICARE-CNRS/UM6P-MAROC
A.R. RAVISHANKARA   Professeur, Colorado State University, Fort Collins, USA

RAPPORTEURS :
Bénédicte PICQUET-VARRAULT   Professeure, LISA-UPEC
John WENGER   Professeur, University College Cork

JURY :
Abdelwahid MELLOUKI   Directeur de recherche, ICARE-CNRS/UM6P   Directeur
A.R. RAVISHANKARA   Professeur, Colorado State University   Co-directeur
Max MCGILLEN   Chargé de recherche (HDR), ICARE-CNRS   Co-encadrant
Anne MONOD   Professeure, LCE AMU, Présidente du Jury   Examinateur
Bénédicte PICQUET-VARRAULT Professeure, LISA-UPEC   Rapporteur
John WENGER   Professeur, University College Cork   Rapporteur
Bernard AUMONT   Professeur, LISA-UPEC   Examinateur
Alexandre KUKUI   Chargé de recherche, LPC2E-CNRS   Examinateur

Table of contents

Publications and research activity

Publications, proposal, and other research experiences conducted during this PhD are listed below:

Scientific publications

 • **Michelat, L.**, Mellouki, M., Ravishankara, A., El Othmani, H., V., Papadimitriou, V., Daële, V, and McGillen, M. R. (2022). Temperature-Dependent Structure-Activity Relationship of OH + Haloalkene Rate Coefficients under Atmospheric Conditions and Supporting Measurements. ACS Earth and Space Chem. doi.org/10.1021/acsearthspacechem.2c00296

• Newland, M. J., Ren, Y., McGillen, M. R., **Michelat, L.**, Daële, V., and Mellouki, A. (2022). NO_3 chemistry of wildfire emissions: a kinetic study of the gas-phase reactions of furans with the NO_3 radical. Atmos. Chem. Phys. doi.org/10.5194/acp-22-1761-2022

• McGillen, M. R., **Michelat, L.**, Orlando, J. J., & Carter, W. P. (2023). The use of the electrotopological state as a basis for predicting hydrogen abstraction rate coefficients: a proof of principle for the reactions of alkanes and haloalkanes with OH. Env. Sci. Atm. doi.org/10.1039/D3EA00147D

• **Michelat, L.**, Mellouki, A., Ravishankara, A.R., Paton, R. and McGillen, M. R. (2024) A fully automated tool for estimating gas-phase electrophilic addition reaction rate coefficients of OH, NO_3, O_3 and Cl to unsaturated organic compounds. [in prep.]

Conference presentations

- **Michelat, L.,** Mellouki, A., Ravishankara, A.R., McGillen, M. R. (2023). A fully automated tool for estimating atmospheric oxidation reaction rate coefficients of unsaturated volatile organic compounds with OH, NO_3, O_3 and Cl. *Goldschmidt conference, Lyon, France,* doi.org/10.7185/gold2023.15836 – Oral

- **Michelat, L.,** Mellouki, A., Ravishankara, A.R., McGillen, M.R. 2023. A fully automated tool for estimating atmospheric oxidation reaction rate coefficients of unsaturated volatile organic compounds with OH, NO_3, O_3 and Cl. *Quantum Science and Technology workshop, Beijing, China*, 1, https://www.wyss.org.cn/2022/en/quantum2022/ – Oral

- **Michelat, L.,** Mellouki, A., Ravishankara, A.R., McGillen, M. R. (2023). A fully automated tool for estimating atmospheric oxidation reaction rate coefficients of unsaturated volatile organic compounds with OH, NO_3, O_3 and Cl *Journées des Jeunes Chercheurs* , 2, https://j2c.sciencesconf.org/ – Oral

- **Michelat, L.,** Mellouki, A., Ravishankara, A.R., McGillen, M. R. (2021). Atmospheric degradation of 3,3,3-trifluoropropene. *Journées des Jeunes Chercheurs* , 1, https://j2c.sciencesconf.org/ – Oral

- **Michelat, L.,** Mellouki, A., Ravishankara, A.R., McGillen, M. R. (2022). Structure-activity relationship to predict Arrhenius parameters of OH addition to unsaturated volatile organic compounds under atmospheric conditions. *Atmospheric Chemical Mechanisms Conference, UC Davis, CA, US* , 2, https://acm.aqrc.ucdavis.edu/2022-technical-program-committee – Poster

- **Michelat, L.,** Mellouki, A., Ravishankara, A. R., McGillen, M. R. (2022). Gas-phase kinetics and theoretical calculations to investigate the effect of substitution on the reactivity of unsaturated volatile organic compounds. *26th International Symposium on Gas Kinetics and Related Phenomena, Rennes, France* , 26, https://gk2022.sciencesconf.org/ – Poster

- **Funded proposal for scientific exchange "Theoretical calculations to investigate the effects of substitution on the reactivity of unsaturated Volatile Organic Compounds from biomass burning emissions."** In collaboration with Profs. A. R. Ravishankara and Robert Paton – Department of Chemistry, Colorado State University, US. 3 months-financial support ($5,886 USD) from LABEX Voltaire, 2022-2023.

Research experiences

Keywords : Physical chemistry, thermochemistry, general chemistry, and methodology

Teaching practical classes and tutorial classes – University of Orléans, France

- Practical Chemistry Methodology (L1 Chemistry, 20h)
- Physical Chemistry - Atomistics (L2 Chemistry, 28h)
- General Chemistry (L1 Chemistry, 16h)
- Thermochemistry (L1 Chemistry, 12h)

Training

- 26th *International Symposium on Gas Kinetics and Related Phenomena* (2022), Rennes (France) 32h

- *CHEM 651C: Computational Organic Chemistry* (2022) Prof. R. Paton, Colorado State University, Fort Collins (USA) 20h

- *Biostatistics in R programming* (2022) Faculté de Médecine, Tours (France) 18h

- MOOC *Scientific integrity in the research profession* (2021), online 2h

- MOOC *Spectroscopy: fundamentals and applications* (2021), online 20h

- MOOC *Spectroscopy: fundamentals and applications Part 2* (2021), online 45h

Abstract

Air pollution is one of the leading causes of premature mortality worldwide, and a major public health issue directly linked to atmospheric chemistry. A fraction of this pollution originates from the oxidation of volatile organic compounds (VOCs), and studying their reaction rate coefficients and the products formed from these reactions is crucial. Unsaturated volatile organic compounds account for a large fraction of the organic carbon present in the atmosphere. Their degradation is mainly initiated by their reactions with tropospheric oxidants OH, Cl, NO_3, and O_3. My thesis focuses on measuring and predicting the rate coefficients of tropospheric gas-phase oxidation of unsaturated VOCs. The reaction rate coefficients of OH and NO_3 reactions with compounds emitted from biomass burning and of two hydrofluoroolefins produced by industry were measured experimentally using different techniques at room temperature k_{298} and as a function of temperature k(T).

Manyunsaturated VOCs are present in the atmosphere, and it is difficult to study all these reactions experimentally. This has led to the development of structure-activity relationships (SARs) to predict these reaction rate coefficients to provide input to atmospheric models when no experimental data are available. Two SARs have been developed: the first predicts room temperature rate coefficients, k_{298}, for reactions of halogenated alkenes with tropospheric oxidants and k(T) for reactions with OH and NO_3; the second predicts the total and site-specific k_{298} values of OH, NO_3, O_3 and Cl reactions with a large variety of unsaturated VOCs. This SAR uses information on the electronic and steric structure of VOCs and provides an automated, fast, and easy-to-use tool for predicting the rate coefficients of large lists of VOCs. This work aims to guide decision-making by industry and policy-makers in choosing chemicals that are less harmful to the planet.

Keywords: *Biomass burning, Unsaturated Volatile Organic Compounds, Kinetics, Structure Activity Relationship (SAR), Oxidation, Furans*

Résumé

La pollution de l'air est l'une des principales causes de mortalité prématurée dans le monde, et un problème majeur de santé publique directement lié à la chimie atmosphérique. Une fraction de cette pollution provient de l'oxydation des composés organiques volatils (COVs), et l'étude de leurs vitesses de réaction et des produits formés par ces réactions est d'une importance cruciale. Les COVs insaturés représentent une grande partie du carbone organique présent dans l'atmosphère. Leur dégradation est principalement initiée par leurs réactions avec les oxydants troposphériques OH, Cl, NO_3 et O_3. Ma thèse porte sur la mesure et la prévision de la cinétique de l'oxydation des COVs insaturés en phase gazeuse dans la troposphère. Les coefficients de vitesse de réaction de OH et NO_3 avec les composés émis par la combustion de la biomasse, et de deux hydrofluorooléfines produites par l'industrie ont été mesurés expérimentalement en utilisant différentes techniques à la température ambiante k_{298} et en fonction de la température $k(T)$.

Un grand nombre de COVs insaturés sont présents dans l'atmosphère et il est difficile d'étudier toutes ces réactions de manière expérimentale. Cela a conduit au développement de relations structure-activité (SARs) pour prédire les k_{298} et $k(T)$, afin d'alimenter les modèles atmosphériques en l'absence de données expérimentales. Deux SARs ont été développées : la première prédit k_{298} pour les réactions des alcènes halogénés avec les oxydants troposphériques et $k(T)$ pour les réactions avec OH et NO_3 ; la seconde prédit les valeurs totales et spécifiques au site de k_{298} pour les réactions OH, NO_3, O_3 et Cl avec une grande variété de COVs insaturés. Cette SAR utilise des informations sur la structure électronique et stérique des COVs et fournit un outil automatisé, rapide et facile d'utilisation pour prédire les coefficients de vitesses de nombreux COVs. Ce travail vise à guider la prise de décision de l'industrie et des décideurs politiques vers des substances chimiques moins nocives pour la planète.

Mots clés*: Feux de biomasse, Composés organiques volatiles insaturés, Cinétique, Relation structure à activité (SAR), Oxydation, Furanes*

General introduction

The atmosphere has long been a source of wonder, belief, and questioning. It was studied by the very first scientists. Yet, as discoveries and knowledge progressed, the world is still full of unknowns. Thinking of the Earth as an apple, the atmosphere would be its skin. Despite its small thickness compared to the Earth it surrounds, the impact of the atmosphere on the ecosystem at the surface is tremendous. One of the major points is that without the atmosphere, there would be no life on Earth. The atmosphere screens the Earth's surface from harmful radiation and provides the oxygen and water vapor essential to life and the development of biodiversity and microorganisms. Moreover, the air that living species breathe contains trace gases and particles that are emitted into the atmosphere and the products formed degrade, which, depending on their toxicity, can directly impact human health. Another aspect is the essential role those atmospheric gases play in the balance of the climate, as a small change in its composition can have a major impact on all the other components of the climate system. For example, an increase in the concentration of a trace gas such as CO_2, currently about 421 ppm (representing just 421 molecules of CO_2 among 1 million molecules of air) strongly perturbs the radiative balance of the atmosphere. This imbalance warms the Earth's surface temperature, affecting oceans, glaciers, the biosphere, soils, and the evolution of living organisms.

"Things are what they are because they have been what they have been..." said Hubert Reeves in *Patience dans l'azur*, published in 1981, in reference to certain principles of astrophysics. This quote perfectly encapsulates the study of atmospheric composition and the chemical reactions that lead to it. Nature and human activities are responsible for the emission of a multitude of molecules into the atmosphere, which react with each other, with free radicals, or are destroyed by reactions with sunlight or different surfaces. Thus, the reactivity of a compound can lead to the formation of one or more molecules, which in turn undergo multiple reactions to form numerous new compounds. These processes lead to the formation of a multitude of species, with varying lifetimes in the atmosphere. A compound that degrades slowly in the troposphere can be transported a long way from its emission site and even into the upper layers of the atmosphere for the lesser reactive compounds. It is therefore essential to understand and characterize these reactions so that, to paraphrase Hubert Reeves, we can understand why atmospheric molecules are what they are, to be able to assess the role of the atmosphere on our planet and our future.

Atmospheric chemistry and physics and their relation to the climate have been studied for at least 200 years. Some of the most crucial discoveries were made in the 19th century. An article of Joseph Fourier published in 1827 in the *Memoirs* of the French Academy is considered as the first literature to mention atmospheric "greenhouse effect" (Fourier, 1827). Nowadays, climate change caused by anthropogenic greenhouse gases remains a major unresolved challenge, impacting various societal needs. Another

growing problem, recognized for over 2,400 years, is air pollution. It has been discussed since ca 400 BC that air quality is related to human health issues (Fowler et al., 2020). This phenomenon has been observed ever since, and has accelerated since the industrial revolution, with major events such as the London fog and Los Angeles smog of the early 1950s confirming the significant contribution that anthropogenic emissions can make to air pollution (Fowler et al., 2020; Haagen-Smit, 1952; Wilkins, 1954). In this context, it is evident that understanding the atmospheric reactivity of the gases and particles emitted into the atmosphere, their lifetimes, and what products they may form throughout their degradation is crucial. This helps to understand how these chemicals alter atmospheric composition and properties. However, the number and diversity of compounds in the atmosphere is vast. Studying that many reactions is challenging but can be partially tackled by combining different scientific methods.

To study atmospheric chemistry, laboratory measurements, modelling, and validation through field observations are essential. Atmospheric chemical models allow the prediction of future climate, evolution of air pollution, and can help to guide more environmentally-friendly policy measures. However, these models require a large amount of kinetic data and mechanistic understanding, if possible as a function of temperature and pressure, to adequately describe the behavior of the atmosphere under various conditions. Gas-phase atmospheric chemical mechanisms are an essential component of these models, which, for the more explicit models, can become very large and complex. It is, therefore, necessary to reach for a simplified mechanism, which necessitates a comprehensive understanding of the chemistry of trace gases, and mostly, VOCs which represent a large part of the reactive atmospheric gases. This is why estimation techniques are developed, when experimental findings can be correlated to some structural patterns, and thus, allow the estimation of more reaction kinetic data used as input in the models. This thesis combines experimental work, theoretical calculations, and the development of new estimation methods to help fill the gaps in the kinetic database and provide new inputs for models. The focus has been placed on industrial and biomass burning related species, especially on nighttime chemistry because it is less well-understood.

New laboratory measurements of the atmospheric oxidation rate coefficients of unsaturated volatile organic compounds, UVOCs, conducted using various experimental set-ups, such as atmospheric simulation chambers, spectroscopic techniques, and discharge flow reactors are presented. These experiments include measurements of the room temperature reaction rate coefficients, k_{298}, for the NO_3 reaction with 14 furans and two pyrroles, and the OH reaction with four furans. This work also presents new temperature-dependent measurements of the OH reaction rate coefficients k(T) of biacetyl and two hydrofluoroolefins.

Two new structure-activity relationships (SARs) have been developed to estimate the rate coefficients of the addition reactions of the four primary tropospheric oxidants, OH, Cl, NO_3 and O_3, to UVOCs. Based on a clear trend between substitution and reactivity for a group of halogenated alkenes, CHX where X=F, Cl, Br, a SAR applicable to these CHX unsaturated compounds has been developed based on a diagonal-substitution approach. It provides estimations of k_{298} for reactions with the four oxidants and derives k(T) for the reactions with OH and NO_3. This is the first work reported to provide estimations of k(T) for these reactions. This tool provides estimates in excellent agreement with experiments, but is limited to CHX alkenes (containing F, Cl, and/or Br atoms). These CHX alkenes represent a group of industrial species and do not include other compound types more representative of atmospheric species (containing O, N, S or P atoms). This SAR is also limited to monoalkenes.

A more general tool has been developed, based on a parametrization that uses *a priori* information on the electronic and steric structure of the molecule studied, which are calculated using quantum chemical approaches, either density functional theory (DFT) or a semi-empirical method (PM6). This new SAR has been applied to a broader range of compounds, similar to the variety of compounds encountered in the atmosphere, including CHNOSPX substitutions, where X=F, Cl, Br, I, alkenes, polyalkenes, cyclic, aromatic, benzenoids, furans, and pyridines compounds, and that for OH, Cl, NO_3 and O_3. This tool is based on a new methodology. Compared with other techniques, it requires fewer fitting parameters, is more general and, is based on *a priori* calculated information. Therefore, it has a better potential for extrapolation to new species. More specifically, the prediction of new compounds relies on calculating their chemical properties using our software, not solely on existing experimental data. Consequently, it can be successfully extended to predict reactions that remain less well-known or difficult to measure in the laboratory, such as the nighttime oxidation of VOCs from biomass combustion (e.g., the oxidation of furans and pyrroles by NO_3). This SAR provides k_{298} for the addition reaction with the four tropospheric oxidants and total and site-specific reaction rate coefficients. It is implemented in a fully automated, easy-to-use, and rapid tool that can be applied to a large number of reaction rate coefficients.

This work helps estimate rate coefficients for reactions that remain less well-known or difficult to measure in the laboratory. These results can be used as input data for atmospheric chemical models, and by industry and policy-makers to take a step towards more environmentally-friendly policies.

Introduction générale

L'atmosphère est depuis longtemps une source d'émerveillement, de croyances et d'interrogations. Elle a été étudiée par les premiers scientifiques. Néanmoins, au fur et à mesure que les découvertes et les connaissances progressent, le monde demeure plein d'inconnues. Si l'on considère la Terre comme une orange, l'atmosphère serait sa peau. Malgré sa petite épaisseur par rapport à la Terre qu'elle entoure, l'impact de l'atmosphère sur l'écosystème de la surface terrestre est énorme. L'un des points majeurs est que sans l'atmosphère, il n'y aurait pas de vie sur Terre. L'atmosphère protège la surface de la Terre de rayonnements UV nocifs et fournit l'oxygène et la vapeur d'eau indispensables à la vie et au développement de la biodiversité et des micro-organismes. De plus, l'air que les espèces vivantes respirent est composé des gaz et des particules émis dans l'atmosphère et des produits formés lors de leur dégradation, qui impactent directement la santé humaine s'ils sont nocifs. Un autre aspect crucial est le rôle essentiel que jouent ces gaz atmosphériques dans l'équilibre du climat, puisqu'une petite modification de la concentration atmosphérique de certains gaz à effet de serre peut avoir un impact majeur sur toutes les autres composantes du système climatique. Ainsi, l'augmentation de la concentration d'un gaz à l'état de trace comme le CO_2, de l'ordre de 421 ppm actuellement (représentant seulement 421 molécules de CO_2 parmi 1 million de molécules d'air) peut déséquilibrer l'équilibre radiatif de l'atmosphère. Ce déséquilibre réchauffe la température de surface sur terre, affectant les océans, les glaciers, la biosphère, les sols, et l'évolution des organismes vivants.

"Les choses sont ce qu'elles sont parce qu'elles étaient ce qu'elles étaient…" a dit Hubert Reeves dans *Patience dans l'azur* publié en 1981, en faisant référence à certains principes de l'astrophysique. Cette citation reflète parfaitement l'étude de la composition de l'atmosphère et les réactions chimiques qui y conduisent. La nature ainsi que les activités humaines sont responsables de l'émissions d'une multitude de molécules dans l'atmosphère, qui vont réagir entre elles, avec des radicaux libres, ou être détruits par des réactions avec la lumière solaire ou différentes surfaces. Ainsi, la réactivité d'un composé peut engendrer la formation d'une ou plusieurs molécules, qui elles-mêmes subiront de multiples réactions formant de multiples nouveaux composés. Ces processus vont conduire à la formation d'une multitude d'espèces, aux temps de vie plus ou moins long dans l'atmosphère. Un composé qui se dégrade lentement dans la troposphère pourra être transporté à distance de son lieu d'émission, voir pour les composés les moins réactifs, jusqu'à des couches plus hautes de l'atmosphère. Il est donc essentiel de comprendre et caractériser ces réactions qui font de "ce que [les composés atmosphériques] ont été ce qu'ils sont", comme le dirait Hubert Reeves, si l'on veut pouvoir évaluer le rôle de l'atmosphère sur notre planète et notre avenir.

Depuis au moins 200 ans, la physique et la chimie de l'atmosphère ainsi que leurs relations avec le climat sont étudiées. Certaines des découvertes les plus cruciales ont été faites au 19e siècle. Un article de Joseph Fourier publié en 1827 dans les *Mémoires de l'Académie française* est considéré comme la première mention dans la littérature d'un "effet de serre" atmosphérique (Fourier, 1827). De nos jours, le changement climatique causé par les gaz à effet de serre anthropiques reste un défi majeur non résolu, avec des incidences sur divers besoins sociétaux. Un autre problème croissant, reconnu depuis plus de 2 400 ans, est la pollution de l'air. Depuis environ 400 ans avant J.-C., il est admis que la qualité de l'air est liée à des problèmes de santé humaine (Fowler et al., 2020). Ce phénomène a été observé depuis lors et s'est accéléré après la révolution industrielle, des événements majeurs tels que les brouillards de Londres et de Los Angeles au début des années 1950 confirmant la contribution significative des émissions anthropiques à la pollution de l'air (Fowler et al., 2020 ; Häagen-Smit, 1952 ; Wilkins, 1954). Dans ce contexte, il est évident qu'il est essentiel de comprendre la réactivité atmosphérique des gaz et des particules émis dans l'atmosphère, leur durée de vie et les produits qu'ils peuvent former tout au long de leur dégradation. Cela permet de comprendre comment ces produits chimiques modifient la composition et les propriétés de l'atmosphère. Cependant, le nombre et la diversité des composés présents dans l'atmosphère sont considérables. L'étude d'un tel nombre de réactions est un défi, mais il peut être partiellement relevé en combinant différentes méthodes scientifiques.

L'étude de la chimie atmosphérique passe par des mesures en laboratoire, la modélisation et la validation par des observations sur le terrain. Les modèles chimiques atmosphériques permettent de prédire le climat futur, l'évolution de la pollution atmosphérique et peuvent aider à orienter des mesures politiques plus respectueuses de l'environnement. Toutefois, ces modèles nécessitent une grande quantité de données cinétiques et une bonne compréhension des mécanismes, si possible en fonction de la température et de la pression, afin de décrire correctement le comportement de l'atmosphère dans diverses conditions. Les mécanismes chimiques atmosphériques en phase gazeuse sont une composante essentielle de ces modèles, qui, pour les modèles les plus explicites, peuvent devenir très vastes et complexes. Il est donc nécessaire de parvenir à des mécanismes simplifiés, ce qui nécessite une compréhension globale de la chimie des gaz à l'état de traces, et surtout des COVs qui représentent une grande partie des gaz atmosphériques réactifs. C'est pourquoi des techniques d'estimation sont développées, lorsque les résultats expérimentaux peuvent être corrélés à certains modèles structurels, et permettent ainsi l'estimation de plus de cinétiques de réaction utilisées comme données d'entrée dans les modèles. Cette thèse combine donc des travaux expérimentaux, des calculs théoriques et le développement de nouvelles méthodes d'estimation pour aider à combler les lacunes de la base de données cinétiques et fournir de nouvelles données pour les modèles. L'accent a été mis sur les espèces liées à l'industrie et à la combustion de la biomasse, en particulier sur leur chimie nocturne parce qu'elle est moins connue.

De nouvelles mesures en laboratoire des coefficients de vitesses d'oxydation atmosphérique des composés organiques volatils (COVs) insaturés, réalisées à l'aide de divers dispositifs expérimentaux, tels que des chambres de simulation atmosphérique, des techniques spectroscopiques et des réacteurs à flux de décharge, sont présentées. Ces expériences comprennent des mesures des coefficients de vitesse de réaction à température ambiante, k_{298}, pour la réaction NO_3 avec 14 furannes et deux pyrroles, et pour la réaction OH avec quatre furannes. Ce travail présente également de nouvelles mesures dépendantes de la température des coefficients de vitesse de réaction OH $k(T)$ du biacétyle et de deux hydrofluorooléfines.

Deux nouvelles relations structure-activité (SARs) ont été développées pour estimer les coefficients de vitesse des réactions d'addition des quatre oxydants troposphériques primaires, OH, Cl, NO_3 et O_3, aux COVs insaturés. Sur la base d'une tendance claire entre la substitution et la réactivité pour un groupe d'alcènes halogénés, CHX où X=F, Cl, Br, une SAR applicable à ces composés insaturés CHX a été développé sur la base d'une approche de substitution diagonale. Il fournit des estimations de k_{298} pour les réactions avec les quatre oxydants et déduit $k(T)$ pour les réactions avec OH et NO_3. Il s'agit du premier travail rapporté à fournir des estimations de $k(T)$ pour ces réactions. Cet outil fournit des estimations en excellent accord avec les expériences, mais se limite aux alcènes CHX (contenant des atomes F, Cl, et/ou Br). Ces alcènes CHX représentent un groupe d'espèces industrielles, qui n'inclut pas d'autres types de composés plus représentatifs des espèces atmosphériques (contenant des atomes O, N, S ou P). Cette SAR est également limitée aux monoalcènes.

Un outil plus général a été développé, basé sur une paramétrisation qui utilise des informations *a priori* sur la structure électronique et stérique de la molécule étudiée, qui sont calculées par des approches de chimie quantique, soit la théorie de la fonctionnelle de la densité (DFT), soit une méthode semi-empirique (PM6). Cette nouvelle SAR a été appliquée à une gamme plus large de composés, similaire à la variété de composés rencontrés dans l'atmosphère, y compris les substitutions CHNOSPX, où X=F, Cl, Br, I, alcènes, polyalcènes, composés cycliques, aromatiques, benzénoïdes, furannes et pyrroles, et celui pour OH, Cl, NO_3 et O_3. Cette SAR est basée sur une nouvelle méthodologie. Comparé à d'autres techniques, elle nécessite moins de paramètres d'ajustement, est plus générale et est basée sur des informations calculées *a priori*. Par conséquent, elle a un meilleur potentiel d'extrapolation à de nouvelles espèces. Plus précisément, la prédiction de nouveaux composés repose sur le calcul de leurs propriétés chimiques à l'aide de notre outil, et pas uniquement sur les données expérimentales existantes. Cette SAR peut donc être étendue avec succès pour prédire des réactions qui restent moins bien connues ou difficiles à mesurer en laboratoire, telles que l'oxydation nocturne des COVs provenant de la combustion de la biomasse (par exemple, l'oxydation des furanes et des pyrroles par le NO_3). Cette SAR fournit k_{298} pour la réaction d'addition avec les quatre oxydants troposphériques, et les coefficients de vitesse de réaction totaux et spécifiques au site.

Elle est mise en œuvre dans un outil entièrement automatisé, facile à utiliser et rapide qui peut être appliqué à un grand nombre de constantes de vitesses de réactions.

Ce travail permet de prévoir les constantes de vitesses de réactions qui restent moins bien connues ou difficiles à mesurer en laboratoire. Ces résultats peuvent être utilisés comme données d'entrée pour les modèles chimiques atmosphériques, et par l'industrie et les décideurs politiques pour faire un pas vers des politiques plus respectueuses de l'environnement.

References

Fourier, J., 1827. Mémoire sur les températures du globe terrestre et des espaces planétaires. Mémoires de l'Académie Royale des Sciences de l'Institut de France 7, 570–604.

Fowler, D., Brimblecombe, P., Burrows, J., Heal, M.R., Grennfelt, P., Stevenson, D.S., Jowett, A., Nemitz, E., Coyle, M., Liu, X., Chang, Y., Fuller, G.W., Sutton, M.A., Klimont, Z., Unsworth, M.H., Vieno, M., 2020. A chronology of global air quality. Philosophical Transactions of the Royal Society A: Mathematical, Physical and Engineering Sciences 378, 20190314.

Haagen-Smit, A.J., 1952. Chemistry and physiology of Los Angeles smog. Industrial & Engineering Chemistry 44, 1342–1346.

Wilkins, E.T., 1954. Air pollution and the London fog of December, 1952. Journal of the Royal Sanitary Institute 74, 1–21.

Chapter I : Introduction

Summary of the chapter I

In the Chapter I, the intricate nature of atmospheric oxidation of volatile organic compounds (VOCs) and the associated scientific challenges will be presented and discussed. The first section is addressing the health, environmental, and climatic issues related to atmospheric species. Atmospheric chemical reactivity and kinetics are linked to various crucial challenges, such as air pollution affecting public health, ozone layer depletion or climate change. Among the atmospheric compounds of interest, the focus is placed on the unsaturated volatile organic compounds (UVOCs), which are an important class of species emitted from both industrial and biogenic sources. These olefins react by electrophilic addition of the atmospheric radicals.

The second section explains what is influencing the concentration of these UVOCs in the atmosphere, by presenting their emission sources and the sinks through which they are degraded forming new products. There are transport and mixing in the atmosphere. The atmospheric chemistry of the troposphere is emphasized, noting its complexity and diversity due to the involvement of a multitude of compounds and multiplicity of possible degradation pathways, including gas-phase free radical reactions, photolysis, and multiphase/heterogeneous processes. There is a large variety of UVOCs present in the atmosphere, both from direct emission and formation.

The third and last section covers the advances and challenges encountered by atmospheric scientists when studying the reactivity of these organic compounds in the atmosphere. The classes of compounds that remain under-represented both in the experimental kinetic database and in the estimation techniques available are also presented. The atmospheric chemical models can be complex and the amount of data needed due to the large number of atmospheric compounds necessitates adequate predictive tools to fill the gaps in experimental database.

This chapter acknowledges the complexity of atmospheric chemistry with its numerous reactions and emphasizes the vastness of what is both known and unknown, especially regarding UVOCs. While ample data exists for certain compounds like CHOX substituted UVOCs, there is a scarcity of information for the multifunctional, less reactive, or low volatility compounds. The reactions associated with these compounds can represents an experimental challenge. This is also the case in terms of rate coefficients for the oxidation-initiation reactions, especially their temperature dependence. The OH radical chemistry is generally better characterized than that of the other oxidants Cl, NO_3 and O_3. The need for new measurements and theoretical/predictive methods is underscored. This endeavor will be the focus of the following chapters of this thesis.

Résumé du chapitre I

Dans le chapitre I, la nature complexe de l'oxydation atmosphérique des composés organiques volatils (COVs) et les défis scientifiques associés seront présentés et discutés. La première section aborde les questions sanitaires, environnementales et climatiques liées aux espèces atmosphériques. La réactivité et la cinétique chimiques atmosphériques sont liées à divers défis cruciaux, tels que la pollution de l'air affectant la santé publique, l'appauvrissement de la couche d'ozone ou le changement climatique. Parmi les composés atmosphériques d'intérêt, l'accent est mis sur les COVs insaturés, qui constituent une classe importante d'espèces émises par des sources industrielles et biogéniques. Ces oléfines réagissent par addition électrophile des radicaux atmosphériques.

La deuxième section explique ce qui influence la concentration de ces COVs insaturés dans l'atmosphère, en présentant leurs sources d'émission et les puits par lesquels ils sont dégradés pour former de nouveaux produits. La chimie atmosphérique de la troposphère est mise en évidence, en notant sa complexité et sa diversité dues à l'implication d'une multitude de composés et à la multiplicité des voies de dégradation possibles, y compris les réactions radicalaires en phase gazeuse, la photolyse et les processus multiphasiques/hétérogènes. La variété des COVs insaturés présents dans l'atmosphère, provenant à la fois de l'émission directe et de la formation au cours des processus d'oxydation, est renforcée.

La troisième et dernière section couvre les progrès et les défis rencontrés par les scientifiques atmosphériques lors de l'étude de la réactivité de ces composés organiques dans l'atmosphère. Les classes de composés qui restent sous-représentées à la fois dans la base de données cinétiques expérimentales et dans le champ d'application des techniques d'estimation sont également présentées. La complexité croissante des modèles chimiques atmosphériques et la quantité de données nécessaires en raison du grand nombre de composés atmosphériques requièrent des outils prédictifs adéquats pour combler les lacunes de la base de données expérimentale.

Ce chapitre reconnaît la complexité de la chimie atmosphérique avec ses nombreuses réactions et souligne l'immensité de ce qui est à la fois connu et inconnu, en particulier en ce qui concerne les COVs insaturés. Alors que de nombreuses données existent pour certains composés tels que les COVs insaturés substitués par du CHOX, les informations sont rares pour les composés multifonctionnels, moins réactifs ou à faible volatilité. Les réactions associées à ces composés peuvent représenter un défi expérimental. C'est également le cas en termes de coefficients de vitesse pour les réactions d'initiation de l'oxydation, en particulier en ce qui concerne leur dépendance à la température. La chimie du radical OH est généralement mieux caractérisée que celle des autres oxydants Cl, NO_3 et O_3. Le besoin de nouvelles mesures et de méthodes théoriques/prédictives est souligné. Cet effort sera au centre des chapitres suivants de cette thèse.

Introduction

Some of the most crucial challenges for humanity relate to health and environmental issues, such as air pollution, climate change, and ozone layer depletion, each of which are closely connected to atmospheric chemistry (Finlayson-Pitts, 2010). Each year, 8 million deaths are attributed to the direct and indirect impact of air pollution (Lelieveld et al., 2019). Air quality is determined by the complex mixture of various chemicals released into the atmosphere by human activities and natural sources, together with the large variety of species formed from the degradation pathways of the latter into the oxidizing environment that is the atmosphere (Goldstein and Galbally, 2007). These pollutants can have severe health implications, leading to cardio-vascular, cerebral and respiratory diseases (Brunekreef and Holgate, 2002; Pope III and Dockery, 2006; Pöschl, 2005).

Among the diversity of gases identified in the atmosphere, volatile organic compounds (VOCs), and especially unsaturated ones (UVOCs), constitute a significant portion of the trace carbon component in the atmosphere (Fehsenfeld et al., 1992; Monks et al., 2009; Piccot et al., 1992). These compounds can be natural, like isoprene, in origin. Others come from industrial activities, and some are manufactured, like hydrofluoroolefins (HFOs). Quantifying the rate coefficients of these UVOCs in the atmosphere is crucial for improving atmospheric models and addressing health and environmental challenges related to air pollution, climate change, and ozone layer depletion.

Climate change is another pressing issue, which directly impacts public health due to the changes it causes to the biosphere and the various components of the climate system: ocean, plants, soils, glaciers, atmosphere (IPCC, 2023; IPCC, 2022a, 2022b). Some outcomes of the climate crisis and global warming include the enhancement of extreme weather events such as wildfires (IPCC, 2023; IPCC, 2022a, 2022b). This affect air quality since wildfires release large quantities of gases and particles, among which a variety of UVOCs, such as furans, pyrroles or dialdehydes (Coggon et al., 2019; Decker et al., 2021, 2019; Gilman et al., 2015).

The rise of the global surface temperature over the past century has been attributed to the increase of the emission of greenhouse gases since industrial revolution in the 1900s (IPCC, 2023; IPCC, 2022a, 2022b). Many of these greenhouse gases have very long lifetimes because of low loss rates from the atmosphere, and high radiative efficiency. It is thus crucial to improve our understanding of the reactivity of gases present in the atmosphere in order to adequately determine their climatic impact and that of the stable end-products they may form throughout their atmospheric degradation.

However, understanding atmospheric chemistry, especially in the troposphere, is complex since the atmosphere contains a wide variety of compounds, and multiple degradation pathways, including reactions

with different gas-phase, photolysis, and heterogeneous processes (Atkinson, 1997; Atkinson and Arey, 2003a). The understanding of these processes relies on the combination of field measurements, laboratory work, and modelling. Since the number of reactions to study is extremely high, estimations techniques can also be used in place of experimental data when none is available. Also, theoretical calculations can be computed to study the thermodynamics of reactions or predict their rate coefficients. However, the advances in the understanding of atmospheric chemistry showed that many compounds are involved and that they can undergo a variety of different pathways, generating a large number of degradation products. As a result, atmospheric chemical models have become increasingly complex. They often require software tools and extensive number of new kinetic and mechanistic data (Vereecken et al., 2018). Estimation techniques can thus play an important role in providing rapid estimates to fill the gaps of the experimental database.

I-1. Atmospheric chemistry: impacts on human health and environment

Atmospheric trace chemical composition is governed by the complex balance between sources of chemicals emitted into the atmosphere, both from natural and anthropogenic causes, and their removal through gas-phase and multiphase processes. The sources of atmospheric gases are described in more details in the section I-2.2. Most organic pollutants are destroyed through oxidation reactions in the lower layer of the atmosphere, including the reactions with OH, O_3, NO_3 and Cl. Secondary pollutants are also formed throughout these degradation reactions, as detailed in section I-2.3. (Atkinson, 1986, 1997, 2000; Atkinson and Arey, 2003a; Aumont et al., 2005; McGillen et al., 2011). Atmospheric chemical reactions play a vital role in both destroying and producing organic pollutants in the air, which definitely affects air quality and climate, as discussed in this section.

I-1.1. Air quality

Air pollution, via breathing toxic gases and particles, is one of the primary causes of death worldwide nowadays, with more than millions of premature deaths a year (World Health Organization, 2008). Some historical events have illustrated the link between atmospheric chemistry and air pollution. For example, the emission of organic compounds, NO_x and SO_2 from increased coal combustion in London in the early 50s, combined with natural light, led to the photochemical production of particles and secondary pollutants in the gas phase, generating a smog that directly harmed the health of the population (Wilkins, 1954). Breathing $PM_{2.5}$ or PM_{10} particles of diameter less than 2.5 and 10 μm diameter is harmful for human health through increased the risk of respiratory issues, and premature mortality. When considering all anthropogenic and natural sources of air pollution, the annual premature mortality is estimated at 8.8 million deaths (Lelieveld et al., 2019; Pope et al., 2006).

The primary controlled pollutants are ozone, nitrogen oxides, SO_2, CO, and PM. Among these trace gases affecting air quality, tropospheric ozone, O_3, is also related to adverse effects on human health and the biosphere, when present at elevated levels, e.g., (Anenberg et al., 2010; Crutzen, 1988; Jerrett et al., 2009; Lim et al., 2012). The relation between NO_x, O_3 and VOCs is crucial in tropospheric chemistry (see details in section I-2.3.1.), since tropospheric O_3 can be controlled by decreasing the level of ozone precursors (e.g., hydrocarbons and NO_x) through adequate air quality policies. Primary particles are directly emitted into the atmosphere as sea spray aerosols, from dust and soil erosion, wildfires, volcanoes, or as biological airborne material. They are also produced by human activities such as fossil fuel combustion, construction, agriculture, transportation, or waste disposal. Secondary particles can also be formed from the chemistry of the organic matter present in the atmosphere, such as the nucleation and accumulation to form secondary organic aerosols (SOA) (Valorso et al., 2011). Some of the processes by which SOAs are formed remains not well understood, and this is directly correlated to the complexity and variety of the gas-phase aerosol precursors (Hallquist et al., 2009).

I-1.2. Ozone layer depletion

Emissions of some trace gases that are not destroyed in the troposphere can impact beyond this region, since they can survive transport to the stratosphere (Crutzen et al., 1979; Molina and Rowland, 1974; Rowland and Molina, 1975; Forster et al., 2007; Hansen et al., 1997). For example, the depletion of the stratospheric ozone layer has been directly linked to the emission of ozone depleting substances (ODSs) such as chlorofluorocarbons (CFCs). They have very long lifetimes due to poor chemical reactivity with tropospheric oxidants. Thus, they are transported to the stratosphere where they release chlorine that can take part in catalytic cycles that destroy stratospheric ozone (Molina and Rowland, 1974; Rowland and Molina, 1975). Stratospheric O_3 screens harmful ultraviolet radiation from reaching the surface thanks to its strong absorption in the UV, and consequently allows living organisms to survive on the Earth's surface. These ODSs are another example of gases whose harmful effects on human health are linked to their atmospheric reactivity – in this case, the absence of major removal pathways in the troposphere and transport of chlorine- and bromine-containing chemicals that participate in ozone destruction cycle in the stratosphere. These ODSs have been phased out (or being phased out) following the Montreal Protocol in 1987 and have been replaced by substitutes such as hydrofluorocarbons (HFCs) (WMO and NASA, 1990). HFCs, in turn, are to be phased out because of their climate impact (Kigali Amendment to the Montreal Protocol in 2019) (WMO and NASA, 1990; WMO, 2018). Therefore, more reactive hydrofluoroolefins (HFOs) are being phased in. These HFOs are studied in this thesis (Chapter II). They contain hydrogen atoms and unsaturated bonds, allowing them to be more reactive towards tropospheric oxidants and consequently be more rapidly degraded in the troposphere. Additionally, the example of ODSs illustrate the need to quantify the lifetime and understand the reactivity of gases when emitted into the atmosphere. Due to

their long lifetime, and high radiative efficiency, these ODSs also contribute to another crucial issue for climate: global warming (see section I-1.3).

I-1.3. Global warming and climate change

This year [2023], the month of July reached the highest average global surface temperature measured since global records began in 1850, 173 years ago (NOAA, 2023). For four consecutive months, from April to July, the global ocean surface temperature also reached a record high, with a July sea surface temperature anomaly 0.07°C (0.12°F) higher than the previous anomaly in June 2023, which was already an all-time record in itself (NOAA, 2023). There are climate changes due to global warming, which is caused by greenhouse gases (GHG). GHG have the potential to absorb strongly in the infrared range (7 to 13 μm), decrease the outgoing radiation flux, and increase of global surface temperature (Lenoble, 1993). These affect different parts of the climate, e.g., sea level rise, melting of glaciers, or ocean warming. There is also an increase in extreme weather events observed, like wildfires, tropical cyclones, heatwaves, floods, and droughts (IPCC, 2023; IPCC, 2022a, 2022b).

The increase in severity, spread and frequency of wildfires and wild land fires has been observed especially in recent years (Jones et al., 2020; Richardson et al., 2022; Running, 2006; Zou et al., 2021) in multiple regions of the world, for example in California (Abatzoglou et al., 2020; Goss et al., 2020; Keeley and Syphard, 2021), Australia (Borchers Arriagada et al., 2020; Liu et al., 2021; Shi et al., 2021; Tran et al., 2020), and Europe (Dupuy et al., 2020). Biomass burning releases large quantities of organic species, NO_x and particles, such as black and brown carbon, which impact air quality locally, and regionally, and contribute to global warming by emitting and forming greenhouse gases, such as CO_2 (emitted and formed), CH_4, and N_2O (only emitted by combustion) (Crutzen et al., 1979). The unsaturated compounds emitted from biomass burning will thus be studied in this thesis (Chapter III).

All of these processes highlight the intricate and multiple links between atmospheric chemistry, public health and climate. Mostly, the significant impact of carbon matter, organic compounds and other trace gases on various facets of climate and living species, despite their overall low concentrations. The multiple consequences for the environment, public health and the biosphere demonstrate the urgent need to reduce greenhouse gas emissions and other contributions to global warming, by implementing appropriate policies and limiting harmful industrial emissions. To do so, it is required to identify the sources of these compounds (section I-2.2) and their degradation in the atmosphere (section I-2.3) in order to assess whether or not some of these compounds should be restricted. This is the motivation of this work, that further provides new kinetic data (Chapter III) and new tools to efficiently assess the impact of large dataset of compounds on air quality and climate (Chapter II and IV).

I-2. The chemistry of the atmosphere: the complexity and diversity of the reactions

In order to characterize atmospheric chemical composition, it is essential to identify the source by which the compounds are emitted, the kinetics of the reactions by which they are degraded, and the products that will be formed. Their lifetimes will define if they will survive transport away from their source, and if they will impact air quality and public health on a local, regional, or global scale. A wide range of reactivities is observed in atmospheric compounds: some very reactive species, such as some hydrocarbons and unsaturated compounds, have short lifetimes (seconds/minutes to days), while others, such as the perfluoro alkanes, are less reactive and can persist for thousands of years in the atmosphere. In this section, the variety of emission sources (section I-2.2) and the different sinks through which they are degraded into the atmosphere (section I-2.3) will be detailed.

I-2.1. The structure of the atmosphere

The atmosphere is divided into a lower and an upper atmosphere. The pressure decreases with altitude according to (Eq. I-1), and the temperature varies according to a succession of temperature inversions, which define the portioning between different layers of the atmosphere (Figure I-1).

The atmospheric pressure gradient with altitude is described by an exponential function:

$$P(z) = P(z_0)\exp((z-z_0)/H) \text{ (Eq. I-1)}$$

where $H=RT/(M_{air}g)$ is the scale height, z the altitude, z_0 the initial altitude (both z and z_0 in kilometers), $R=8.314472$ J K^{-1} mol^{-1}, the gas constant, T the temperature in K, M_{air} the molecular weight of air (dry/wet) in g mol^{-1}, and $g=9.80665$ m s^{-2} the gravitational constant (Seinfeld and Pandis, 2016).
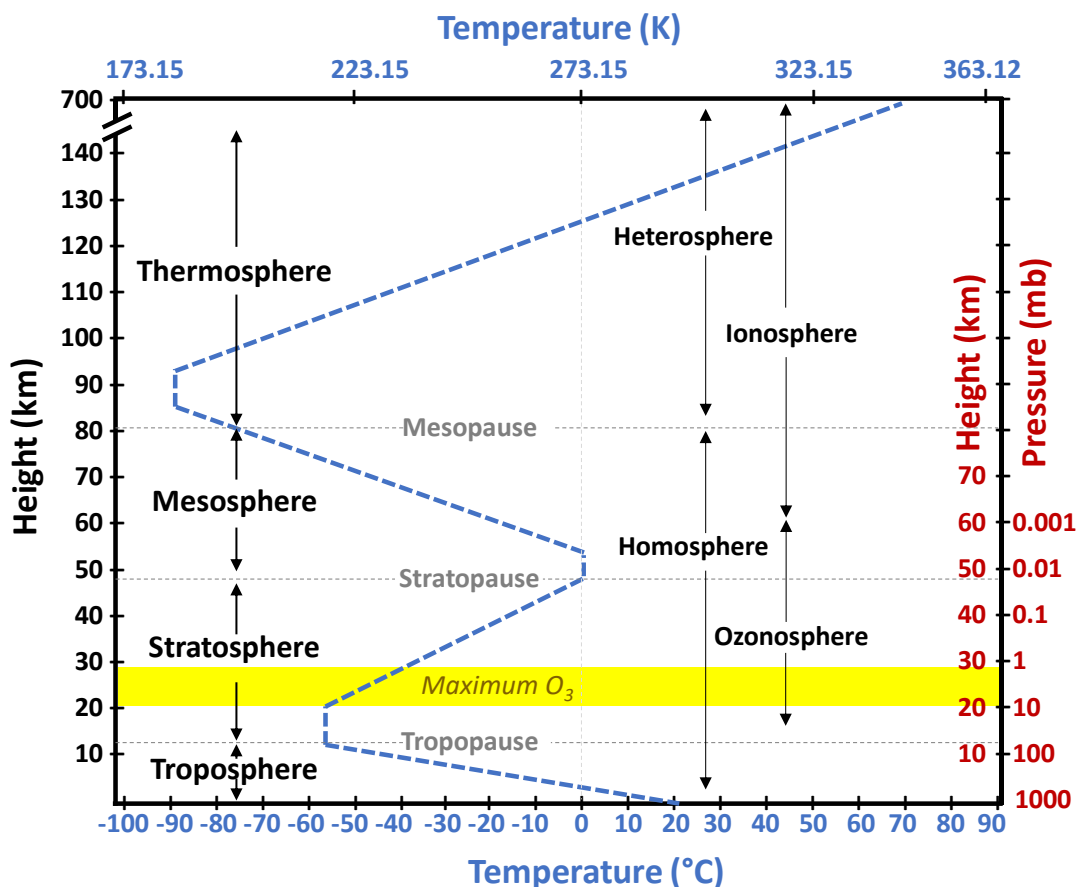
Figure I-1 : Temperature and pressure profile of the atmosphere, with the upper and lower atmosphere layers: troposphere, stratosphere, mesosphere, and thermosphere in order, as a function of altitude. The figure has been developed using the pressure gradient defined in (Eq. I-1), and the atmospheric temperature gradient both obtained from (Seinfeld and Pandis, 2016). It is noted that the pressure and temperature gradients are different in the tropics.

The troposphere is the lowest layer which extends up to ~10–15 km in altitude depending on the latitude and time of the year and into which most gases and particles are emitted. This layer is characterized by decreasing temperatures with height (around 288 K (15°C) at the surface up to ~200 K (-73°C) at the tropopause), and a rapid vertical mixing. Almost all of the water vapor of the atmosphere is contained in the troposphere. Despite the fact that it represents only a small fraction (less than 3% considering the outermost region of the atmosphere up to 500 km) of the atmosphere's vertical extent, the troposphere contains 80% of its total mass (Figure I-1). Air masses in the troposphere undergo temperature and pressure variation. They also can be subject to variation of relative humidity (from dry, <40%, to humid, above 40%). These parameters will thus affect the chemistry of the organic compounds emitted and formed in the troposphere (Atkinson, 2000; Finlayson-Pitts and Pitts, 1999; McIlveen, 1998).

The next layer above the troposphere is stratosphere, from the tropopause to the stratopause (~45 to 55 km altitude), identified by the temperature increase with altitude (up to 271 K at 50 km), which leads to a layer that has slow vertical mixing (Figure I-1). The water vapor content is much smaller compared to the

troposphere, making the stratosphere a dry region of the atmosphere with distinctly different chemistry. Also, the solar ultraviolet radiation reaching the stratopause is more energetic ($hv\sim280–320$ nm). The thermal structure of the stratosphere is mostly due to the absorption in the Chapuis band in the visible range. The stratospheric chemistry is thus different than that of the troposphere and is not detailed in this thesis since it focuses on gas-phase tropospheric oxidation chemistry (Finlayson-Pitts and Pitts, 1999).

The troposphere and stratosphere represent the lower and middle layers of the atmosphere. Above these lower layers is the upper atmosphere: the mesosphere, the thermosphere, and the exosphere. The temperature decreases in the mesosphere (80–90 km), up to the coldest point in the atmosphere, and is thus undergoing a rapid vertical mixing (Figure I-1). The thermosphere is characterized by higher temperatures due to the absorption of short-wavelength radiation by N_2 and O_2 and by a rapid vertical mixing (Heintzenberg, 1989). In between the thermosphere and the mesosphere, the ionosphere is a region characterized by ions produced by photoionization. Organic species under study are not reaching these upper layers of the atmosphere, and thus, gas-phase oxidation chemistry will not be studied for these layers (Ratcliffe, 1960).

The fate of species emitted at the ground level will depend on their chemistry and their transport into the different layers of the atmosphere. Their transport to the stratosphere depends on how fast they react in the troposphere and the fraction exchanged from the troposphere to the stratosphere. This transport is expected to be very small transport for short lived species. Such species include the unsaturated VOCs (e.g., HFOs, furans) that react rapidly with tropospheric oxidants (Atkinson, 1997; Atkinson and Arey, 2003a; Burkholder et al., 2015). Since these organic species represent the main focus of this thesis, effort will be made to understand and quantify their oxidation chemistry in the troposphere only. When air masses are adiabatically transported vertically through the atmosphere, their temperature changes. The troposphere undergo mixing, and the temperature and pressure vary with location and altitude. The concentrations also depend on the extent of mixing. Therefore, one needs to consider atmospheric dynamics and meteorology for assessing air quality impacts of emissions. These are some of the challenges faced when studying atmospheric chemistry. Each reaction must be investigated under various conditions to be adequately described in atmospheric models.

I-2.2. The variety of unsaturated volatile organic compounds emitted into the atmosphere

The atmosphere contains a large number and variety of compounds, including an important class of species, the volatile organic compounds (VOCs). VOCs are emitted from various anthropogenic and biogenic sources detailed in this section. Some of the VOCs are yet to be identified (Goldstein and Galbally, 2007). Natural emissions of non-methane volatile organic compounds (VOCs) into the atmosphere (billion

tons of carbon per year worldwide, (National Research Council, 1991; World Meteorological Organization, 1995)) exceed those from anthropogenic sources (140 million tons per year world-wide, (National Research Council, 1991; World Meteorological Organization, 1995)), except in urban areas, with their primary anthropogenic sources being biomass burning and transportation (National Research Council, 1991; Placet et al., 2000; Sawyer et al., 2000; World Meteorological Organization, 1995). Unsaturated VOCs (UVOCs) are an important class of compounds that are emitted largely from both natural and anthropogenic sources. Natural and anthropogenic UVOCs possess a variety of structures and functional groups, i.e., alkene, polyalkenes, cycloalkene, aromatic, benzenoid, furan, pyridine structures. They can have different types of substitution containing C, H, N, O, P, S, X=(F, Cl, Br, I) atoms, and thus contain a variety of functional groups, such as esters, alcohols, aldehydes, ketones, carboxylic acids, amines, nitrates (Monks et al., 2009). These UVOCs will be the sole focus of this section and thesis.

The biosphere is the primary source of VOCs (90% of the total emissions (Fall, 1999; Fehsenfeld et al., 1992; Guenther et al., 1995)) and emit large quantities of UVOCs including isoprene (500-750 Tg per year, (Guenther et al., 2006)) and other terpenes (e.g., α-pinene). Biogenic emissions also include aromatic compounds, benzenoids, and oxygenated species such as aldehydes. Terpenes are the main species of NMVOCs which are emitted from plants as a protection mechanism against heat stress and the damaging effects of insects and pests (Kansal, 2009). Isoprene can also be emitted from anthropogenic sources such as the burning of crop residues, or industrial production of solvents, coatings, and adhesives; but these sources are minor compared to biogenic emissions.

Anthropogenic emissions of unsaturated VOCs include a variety of straight-chain and cyclic alkenes, polyalkenes, and aromatics. Anthropogenic emissions originate mostly from transportation, energy production, agriculture, waste disposal, solvent utilization, and domestic sources (Friedrich and Obermeier, 1999). Alkenes and polyalkenes (apart from isoprene and terpenes) like ethene, propene, or butene, are emitted from human activities, including the industry of petroleum and fuel production, production of plastics, polymers, and solvents. Natural sources of polyalkenes are rare, unlike anthropogenic sources, which release large quantities of these volatile organic compounds every day.

Halogenated unsaturated VOCs can be emitted naturally from the marine environment (Br and Cl), or anthropogenically from industrial uses as refrigerants, solvents, or propellants (e.g., hydrofluoroolefins). Among these, chlorinated alkenes (e.g., vinyl chloride, vinylidene Chloride or trichloroethylene) can be used in various industrial processes such as the production of plastics, polymers, resins, or solvents. Brominated alkenes are used for their resistance to fire as flame retardants. Iodinated alkenes can be used in synthetic chemistry. Fluorinated alkenes, such as hydrofluoroolefins (HFOs), are widely used as refrigerants and

propellants, replacing ozone-depleting substances such as CFCs, hydrochlorofluorocarbons (HCFCs) and hydrofluorocarbons (HFCs).

Sulphur (e.g., thiophenes) containing UVOCs can be emitted from plants. Nitrogen containing UVOCs like amines (e.g., amines like trimethylamine (TMA) and dimethylamine (DMA)) can be emitted from marine organisms (Rinnan et al., 2005). Some alkaloids, containing azote in their structure, are unsaturated and can be produced naturally from various organisms (e.g., nicotine and morphine), and anthropogenically from pharmaceutical processes. Phosphorus containing UVOCs can be present in insecticides and thus be released into the atmosphere (e.g., dichlorvos, COP(=O)(OC=C(Cl)Cl)OC, containing phosphorus and chlorine).

Cyclic UVOCs include aromatics and non-aromatics compounds. Cycloalkenes can be emitted from plants and microorganisms, but they are mostly issued from anthropogenic sources as the production of certain chemicals, emissions from vehicles, solvent use and waste incineration. Benzenes are emitted from human activity including transportation, industrial production of plastics and chemicals, gasoline, tobacco smoke, solvent sued and waste incineration. Natural sources of benzenoids include biogenic emissions as well as forest fires or volcanic eruptions. Pyridines are heterocyclic aromatic compounds containing nitrogen, resulting from natural sources (e.g., oils, coal tar, and some plants) and anthropogenic sources (e.g., tobacco smoke, industrial use as solvent or precursor for some pharmaceutical chemicals, herbicides or dyes). Pyrroles are five-membered ring structure containing nitrogen that are both issued from natural sources (i.e., plants, organisms, chlorophyll, proteins and bacteria) as well as industrial sources such as organic synthesis, polymers, or other pharmaceuticals uses. Furans can be naturally emitted from combustion processes including cooking, food processing, and biomass burning. They are also produced in various industrial processes as those of pyrroles. Furan aldehydes, i.e., furfurals, can be emitted from fruits and wheat, and they contain oxygenated groups. It is noted as mentioned previously that wildfires and biomass burning release a complex mixture of volatile compounds, e.g., furans, pyrroles, oxygenated compounds, aromatics, heteroaromatics and polycyclic aromatic compounds, as well as particles. Many of such species remain unidentified (Coggon et al., 2019; Decker et al., 2021, 2019; Gilman et al., 2015). Other polycyclic aromatic hydrocarbons (PAHs) (e.g., naphthalene and anthracene) are anthropogenically produced from manufacturing of fossil fuel, combustion processes and pharmaceutical synthesis (Kesselmeier and Staudt, 1999; Koppmann, 2008; Stotzky et al., 1976).

I-2.3. Oxidation of unsaturated organic volatile compounds in the troposphere

The atmosphere is an oxidizing environment. Organic compounds can be oxidized via gas-phase reactions or photolyzed or photo isomerized; they can undergo various heterogeneous or multiphase processes

(Blacet, 1952; Kley, 1997). In this work, only the gas-phase reactions will be investigated in detail, and additional information on photolysis (section App-I-1), decomposition (section App-I-2), and multiphase processes (section App-I-3) are given in Appendices of the Chapter I. The organic molecules are oxidized through chain-reactions that are initiated by an oxidant, such as the hydroxyl radical, OH, the nitrate radical, NO_3, the chlorine atom, Cl, and ozone, O_3, depending on the molecule's structure, and functional groups. The contribution of each reaction will vary with environmental conditions, location, and time. As discussed in the section I-1., the kinetics of these reaction(s) through which the compound is destroyed will determine its lifetime in the atmosphere, the products formed, and thus the potential of the VOC and its degradation products to eventually persist in the environment. Other oxidants exist in the troposphere, such as Criegee intermediates, CIs, that are formed during the 1,3-cycladdition of O_3 to alkenes (see subsection I-2.3.3.), $O(^3P)$, $O(^1D)$, or Br, and others in the aqueous phase, but represent minor mechanisms. Thus, they will not be detailed here. This thesis focuses on the gas-phase oxidation reactions of UVOCs with OH, Cl, NO_3 and O_3.

During its atmospheric degradation, carbon matter is oxidized from lower oxidation states up to higher ones to achieve greater stability in the oxidizing environment that is the atmosphere. The oxidation of organic compounds eventually leads to the formation of carbon dioxide, CO_2, in the atmosphere (Kroll et al., 2011). Through most tropospheric degradation, the carbon chain becomes smaller as a result of fragmentation, which is mostly governed $RO^\bullet$ chemistry, and photofragmentation (Orlando et al., 2003). On the other hand, molecules can undergo heterogenous or multiphase processes through which they can be metabolized by the biosphere or transformed into other phases (e.g., dissolved in water, uptake on aerosols particles). As mentioned in the previous section, organic molecules can exist in different phases in the atmosphere, and that phase will affect the processes through which it is degraded and its lifetime (Bidleman, 1988).

I-2.3.1. Photochemical cycle of NO_x, HO_x, O_3 and VOCs

To discuss the oxidation of VOCs in the troposphere, it is essential to describe the VOCs/NO_x/O_3 cycle (Figure I-2), which is a crucial mechanism that forms OH radical, degrade trace gases, and governs the formation/destruction of NO_x and O_3 (Atkinson, 2000). As illustrated in Figure I-2, the oxidation of carbon monoxide, CO, methane, CH_4, or any NMVOC by OH is the dominant initiating step for the production of O_3 in the troposphere (Chameides and Walker, 1973; Crutzen, 1973; Fishman and Crutzen, 1978). The contribution of NMVOC to the net photochemical ozone production is up to 40% and result in a 17% increase of the tropospheric ozone column under low NO_x conditions (Houweling et al., 1998). The stratosphere-troposphere exchange is also a source of ozone in the troposphere and was long considered the most important source of tropospheric ozone (Brewer, 1949) until the work of (Chameides and Walker,

1973; Crutzen, 1973; Fishman and Crutzen, 1978) showed that most of tropospheric ozone is made in the troposphere. Ozone can also be transferred from the stratosphere (Fabian and Pruchniewicz, 1977; Gidel and Shapiro, 1980; Mahlman et al., 1980; Tarasick and Slater, 2008).

The photolysis of O_3 leads to OH radicals, which will react with most hydrocarbons, and induce their degradation (see section I-2.3.2.). From these interactions, it is observed that OH, NO_x, and O_3 are generated in catalytic cycles in the troposphere, by reacting with atmospheric trace gases. Additional pathways contribute to the RO_x chemistry, such as ozone that can react with some unsaturated NMVOCs and form HO_2. In the lower troposphere, HO_2 itself can also react with ozone to form OH or with another HO_2 molecule to form hydrogen peroxide, H_2O_2, which can react with OH through (R1–2) :

$$HO_2 + HO_2 \longrightarrow H_2O_2 + O_2 \text{ (R1)}$$

$$H_2O_2 + OH \longrightarrow HO_2 + H_2O \text{ (R2)}$$
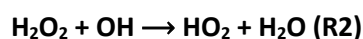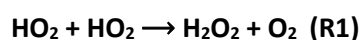
Hydroxyl radical can also react with NO_2 to form nitric acid, HNO_3. H_2O_2 and HNO_3 are mostly removed by rainout, dry deposition, or uptake by aerosols/cloud drops.
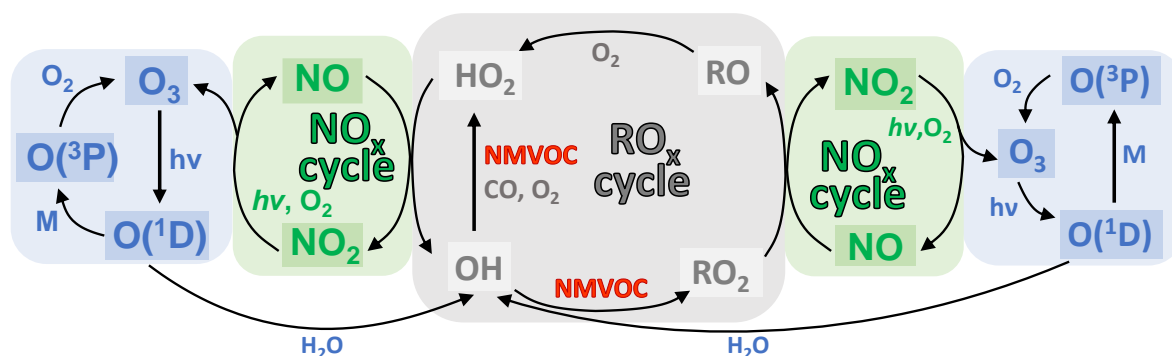

Figure I-2 : Daytime gas-phase photochemical NMVOCs/NO_x/O_3 cycle, including ozone photolysis (blue), NO_x cycle (green), RO_x cycle (gray) and NMVOC contribution (red). This schematic focuses on the HO_x chemistry and its interactions with the NO_x cycle, and O_3 photolysis. However, other pathways exist, and are detailed in the text of this section (additional reactions involving HO_x, NO_x and O_3), and in the subsequent subsections (reactions with other oxidants). M, the collision partner, is N_2 or O_2. Schematic built based on the reactions described in the previous work of (Atkinson, 2000; Ehhalt et al., 1990; Logan et al., 1981).

The next subsection will investigate the different oxidation processes initiated by OH, as partly described in the RO_x cycle in Figure I-2, and that initiated with other oxidants, as O_3, Cl, and NO_3. Additional degradation processes of importance for tropospheric chemistry will be briefly described. The mechanistic insights will focus mostly on pathways that unsaturated VOCs and carbonyls can undergo, as they represent the group of species studied in this thesis.

I-2.3.2. Hydroxyl radical (OH)

I-2.3.2.1. General tropospheric chemistry

In the troposphere, many oxidants initiate the degradation of VOCs. The highly reactive hydroxyl radical, OH, is considered the major oxidizing species in the troposphere, and is ubiquitous during the day. Even though the most abundant oxidants in the troposphere are O_2 and O_3, they are generally less reactive , making of OH the primary tropospheric oxidizing agent (Levy, 1972). The OH radicals have a short lifetime ~1 s under clean conditions, and <1 s under polluted conditions, which results in very low concentrations in the troposphere (Ehhalt et al., 1990). The daytime OH concentration can be up to ~1 × 10^7 molecule cm^{-3} (~0.4 pptv at sea the surface), (Crutzen and Fishman, 1977; Ehhalt et al., 1990) and depends on the local chemical conditions, i.e., solar flux, O_3, and water vapor. For comparison, the HO_2 radical formed during the OH formation cycle (described in Figure I-2) has a longer lifetime than OH and thus reaches an approximate daytime peak concentration of ~10^8 molecule cm^{-3} (~4 pptv).

As briefly discussed in the previous section and illustrated in Figure I-2, the primary source of OH radicals in the troposphere is considered to be the reaction of excited-state oxygen atoms $O(^1D)$, with H_2O, (Levy, 1972) as a result of the photolysis of ozone (first-order photolysis rate coefficient at the Earth's surface at solar zenith angle 0° is 6 × 10^{-5} s^{-1}, (Bahe and Schurath, 1978; Bahe et al., 1979)). Ozone photolysis at wavelength <330 nm (Ravishankara et al., 1998) in the troposphere (and the stratosphere) produces ground state oxygen, $O(^3P)$, and excited singlet oxygen atoms, $O(^1D)$, following reactions (R3–4):

$$O_3 + h\nu \longrightarrow O_2 + O(^3P) \qquad \textbf{(R3)}$$

$$\longrightarrow O_2 + O(^1D) \qquad \textbf{(R4)}$$

$$O(^3P) + O_2 + M \longrightarrow O_3 + M \quad \textbf{(R5)}$$

$$O(^1D) + M \longrightarrow O(^3P) + M \quad \textbf{(R6)}$$

$$O(^1D) + H_2O \longrightarrow 2OH \qquad \textbf{(R7)}$$
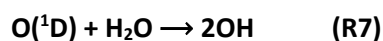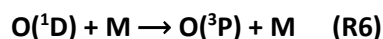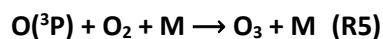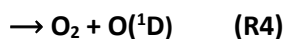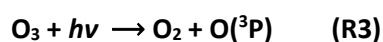
The ground state $O(^3P)$ rapidly combines with O_2 to reform O_3 in the presence of a collision partner M, e.g., O_2 or N_2 (R5). Overall, the cycle of (R3) and (R5) does not lead to ozone loss. Yet, the singlet oxygen $O(^1D)$ formed through (R4) react with atmospheric species, is often quenched to its ground state by collision with N_2 or O_2 (R6), and up to 10% of the $O(^1D)$ can also react with water vapor, H_2O, to form two hydroxyl radicals (R7) (Demore et al., 1985; Ehhalt et al., 1990; Kley, 1997).

However, OH radicals can also be formed by other processes such as the photolysis of acetone in the upper troposphere, (McKeen et al., 1997; Singh et al., 1995) and may exceed the contribution of $O(^1D)$ + H_2O at altitude of about >10km up to the tropopause where the atmosphere is drier (see Figure 3 from the work of (Wennberg et al., 1998)). This is also the case for the photolysis of formaldehyde, (Calvert et al., 1972) hydrogen peroxide (H_2O_2), (Chatfield and Crutzen, 1984) and methyl hydrogen peroxide (CH_3OOH) (Jaeglé

et al., 1997; Prather and Jacob, 1997) which can represent a significant source of HO_x in the upper troposphere when transported from the lower troposphere.

During daytime, OH reactions are the primary removal processes for most tropospheric compounds, such as CO, CH_4 and higher hydrocarbons, H_2, NO_2, H_2S, $(CH_3)_2S$, NH_3, the hydrochlorofluorocarbons (HCFCs) and hydrofluorocarbons (HFCs), and consequently governs the lifetime of many species. It reacts through two main mechanisms, hydrogen abstraction, and electrophilic addition reactions. The H-abstraction mechanism (R8) occurs for many molecules containing an H atom, as follows:

$$^\bullet OH \ + \ R-H \longrightarrow R^\bullet \ + \ H_2O \quad (R8)$$

It will form H_2O and the associated radical, that can further react with O_2 and subsequent chain-reactions. The electrophilic addition mechanism occurs via addition of OH to the carbon-carbon double bond of the unsaturated VOC, a process through which the electron of the hydroxyl radical interacts with the π-orbital of the double-bond. This initial interaction forms an adduct in a reversible reaction. This adduct can be stabilized to form the carbon-centered radical product, a β-hydroxyalkyl radical, with the hydroxyl group attached to either side of the double-bond or decompose back to the reactant. The mechanism is as follows:
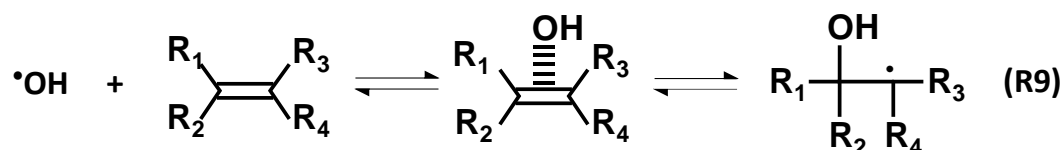
This addition mechanism (R9) occurs in any compound containing a carbon-carbon double-bond, either with a straight-chain or cyclic structure, e.g., furans and benzenoids. The radical formed can also compose back to the middle radical, depending on the bond strength. The C–OH bond formed must be sufficiently strong to stay intact or the radical must react with O_2 before it decomposes.

This mechanism is influenced by many factors due to the structure and the substitutions across the reactive double-bond, such as the importance of electron density in the π-orbital, which governs the attraction of the electrophilic radical towards the reactive sites (Went, 1986). Additionally, steric effects can play a major role via non-bonded repulsion between substituents, bond angle strain, stretch/compression of bonds in the structure, and steric shielding (hindrance), which results in an increase in the energy barrier height between the reactants and the transition states formed (Pinter et al., 2012; Taft, 1956). Also, the electron delocalization observed in conjugated systems impacts the electron density on the double-bond when it is conjugated to another π-system, whose orbitals will overlap and thus these electrons will be shared (Went, 1986). This can either increase or decrease the reactivity on a given site compared to its non-conjugated

analogous compound depending on the type and structure of the compound (Calvert et al., 2000; Vereecken et al., 2018).

The H-abstraction pathways and the electrophilic addition reaction of OH are competitive, but for most alkenes the addition will be dominant at low temperatures relevant to the atmosphere. For larger/more reactive saturated substituents, containing more C–H bonds, hydrogen abstraction can be significant, as discussed in (McGillen et al., 2007).

I-2.3.2.2. Detailed mechanism for industrial and biomass burning related species

This thesis focuses on industrial and biomass burning related species, especially unsaturated VOCs. Specifically, halogenated alkenes emitted by industrial processes are studied, together with compounds measured in high concentration in biomass burning plumes, such as furans and dicarbonyls (Chapter III). In order to investigate the mechanistic pathways, an hydrofluoroolefin, HFO, is used as the detailed case studies 1, 3, 5 and 7 for two main reasons. First, these HFOs react with the four major tropospheric oxidants, OH, Cl, NO_3 and O_3. This is not the case of biacetyl, a dicarbonyl, which reacts through H-abstraction and photolysis. Second, the mechanism for the degradation of these compounds is mostly well-known with the four tropospheric oxidants studied. This is not the case for all oxidation processes of furans, whose chemistry with NO_3 or Cl, for example, remains less well-quantified. The case studies 2, 4, 6 and 8 will thus briefly investigate the differences in mechanism and the main stable end products of furans and related biomass burning related compounds using literature values.

Case study 1: OH-initiated degradation of CH$_2$=CHCF$_3$

The mechanism and detailed pathways of the atmospheric oxidation of CH_2=$CHCF_3$ initiated by OH is presented in Figure I-3. The proposed mechanism has been developed based on mechanistic insights from (Atkinson, 1997, 2000, 2007; Atkinson and Arey, 2003a; Aumont et al., 2005; Burkholder et al., 2015; Calvert et al., 2000; Orlando et al., 2003).

The initiation step of the OH-addition mechanism leads to formation of the alkyl radicals $CF_3CH(X)$-$CH^•$ and $CF_3CH^•$-$CH(X)$, with a greater yield of the more stable secondary radical. The regioselectivity of this addition reaction will determine the structure of the products subsequently produced. The addition of O_2 occurs rapidly (room temperature rate constant of $k_{298} > 10^{-12}$ cm^3 molecule^{-1} s^{-1} at atmospheric pressure) to the center carbon atom of the halo-alkyl radical, R$^•$, leading to the formation of a hydroxy-haloperoxy radical, $RO_2^•$. The $RO_2^•$ radicals are important intermediates in the RO_x/HO_x radical cycle (see Figure I-2) as a source of OH radicals.

Under tropospheric conditions, the alkyl peroxy radical, $RO_2^\bullet$, can be reduced by NO to form an alkoxy radical $RO^\bullet$ and NO_2 ($k_{NO} \sim 1.3 \times 10^{-11}$ $cm^3molecule^{-1}s^{-1}$), which is favored at higher pressure and lower temperatures. $RO_2^\bullet$ may also react with $HO_2^\bullet$ ($k_{HO2} = 4 \times 10^{-12}$ $cm^3molecule^{-1}s^{-1}$), or another $RO_2^\bullet$ to form an hydroperoxide (ROOH) that will photolyzed to form $RO^\bullet$ radicals or halo-acids that may undergo multiphase loss processes. Additionally, $RO_2^\bullet$ can react with NO and NO_2 to generate halo-peroxynitrate ($RONO_2$ or $ROONO_2$) that constitute temporary halogen and NO_x reservoir species, although they thermally decompose back to reactants very rapidly ($k_{dec} \sim 3 \times 10^{-11}$ $cm^3molecule^{-1}s^{-1}$, P=760Torr and T=298K). Reactions with NO are expected to dominate in urban environment under high NO_x conditions, and reaction with other alkyl peroxy radicals under low NO_x conditions. Finally, halo-alkoxy radicals, $RO^\bullet$, undergo either thermal decomposition, i.e., C–C bond scission or halogen elimination, unimolecular isomerization (for carbon length >C_5), or reacts with O_2 to form stable halo-aldehyde (Orlando et al., 2003).

A variety of products can be formed through this degradation, including oxygenated species, such as aldehydes, and nitrated species. The 1st generation stable end-products expected from the OH-initiated chemistry of $CH_2=CHCF_3$ are formaldehyde, HCHO, trifluoro acetaldehyde, $CF_3C(O)H$, fluorinated nitrates, and fluorinated carbonyls. Depending on the structure of the starting compound, and the length of the initial carbon chain, the products formed can possess a large range of functional groups, which enhance the complexity and large variety of compounds that can be formed in the atmosphere as a result of the oxidation of VOCs.
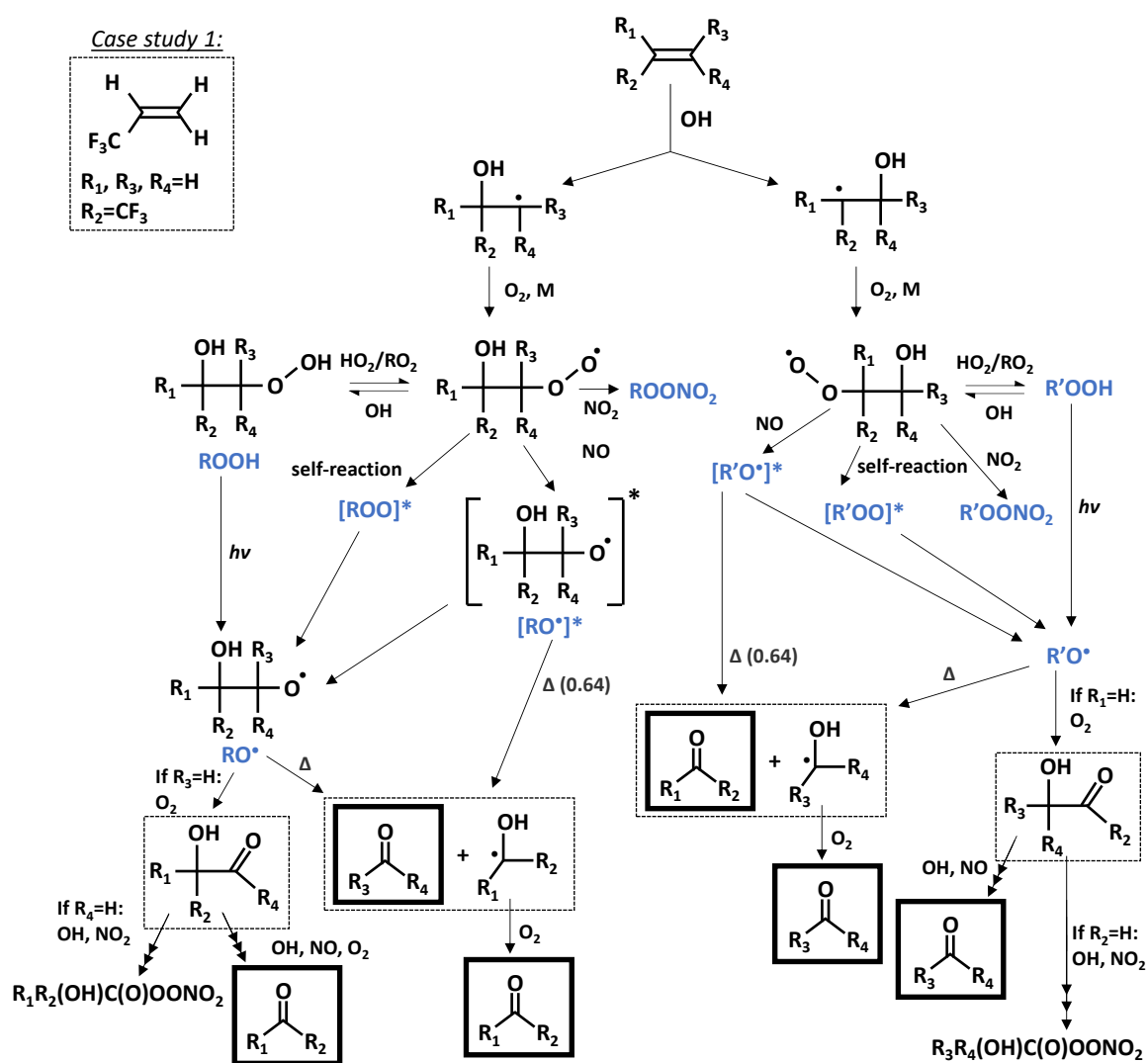
Figure I-3 : Scheme of the atmospheric gas-phase degradation of CH₂=CHCF₃ (HFO-1243zf) initiated by the OH radical. Mechanism proposed has been developed based on the literature for alkenes and haloalkenes (Atkinson, 2000, 2007; Atkinson and Arey, 2003a; Aumont et al., 2005; Burkholder et al., 2015; Calvert et al., 2000; Orlando et al., 2003). The mechanism is described in the main text, and the main stable-end products expected are formaldehyde (HCHO), 2,2,2-trifluoroacetaldehyde $CF_3C(O)H$, fluorinated nitrates and fluorinated carbonyls. Multiphase processes are not included in this degradation scheme since this thesis focuses on gas-phase processes.

Case study 2: OH-initiated degradation of aromatics and furans

The previous mechanism for the OH-initiated oxidation of the fluorinated alkene can be developed for other unsaturated volatile organic compounds that are found in high concentrations in biomass burning plumes, the other focus of this thesis. By analogy to the previous mechanism (Figure I-3), the reaction of OH with aromatics, and other types of cyclic alkenes is similar to that of straight-chain alkenes described above, involving H-abstraction and OH addition as initiation steps, and following reactions of the radical with O_2, forming an $RO_2^•$ radical reacting with NO to form $RO^•$ reacting further. However, for the cyclic compounds, additional pathways for the bicyclic oxy radical formed from the peroxy radical reaction with

NO can be observed, as fragmentation via favorable β-scission reactions, with further decomposition of the subsequent RO• radical formed (Calvert et al., 2002). For the example of toluene, the ring opening pathways of the mechanism (R10), initiated via OH addition to the aromatic ring, will lead to the formation of different aldehydes, i.e., glyoxal, methylglyoxal, methyl butenedial and 1,4-butenedial (Calvert et al., 2002).
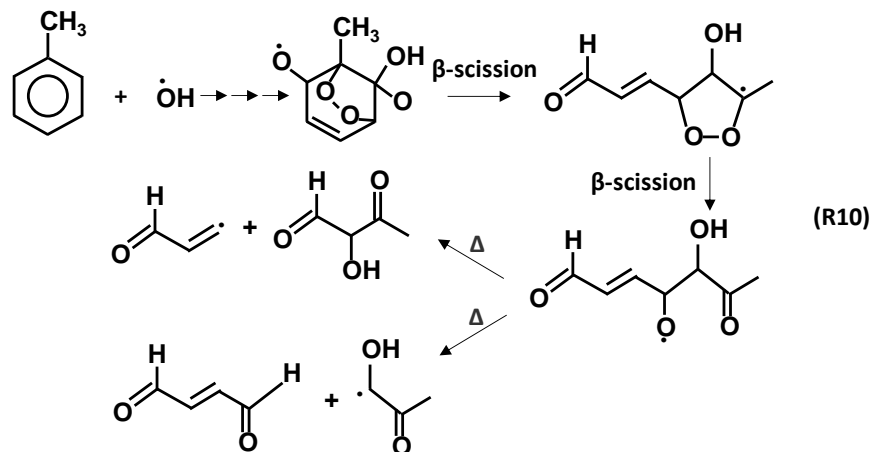

Additionally, the products observed for the reaction of furans with OH are mostly dicarbonyls, hydroxy furanone, maleic anhydride, glyoxal, and their related species (Aschmann et al., 2014; Coggon et al., 2019; Jiang et al., 2020; Tapia et al., 2011).

I-2.3.3. Ozone (O$_3$)
I-2.3.3.1. General tropospheric chemistry

As discussed in the previous section I-2.3.1, O$_3$ is an important tropospheric compound. Ozone is a less reactive and more selective oxidant than OH, but its concentration in the troposphere is nearly a million times higher than that of the OH radical, which allows it to play an important role in atmospheric chemical reactions even with its lower reaction rate coefficient.

As discussed previously, stratospheric O$_3$ plays a critical role in absorbing ultraviolet radiation to screen the surface from shortwave UV radiation that damages living organisms, and it represents around 90% of the column ozone present in the atmosphere. However, ozone is a greenhouse gas contributing to climate change and is an air pollutant at the surface. Since the preindustrial revolution, the amount of surface tropospheric O$_3$ has more than doubled due to anthropogenic emissions (Figure I-2) (Atkinson, 2000). The peaks of surface ozone are observed around the mid-day. Ozone mostly reacts with olefins, through 1,3-cycloaddition (R11), as follows:
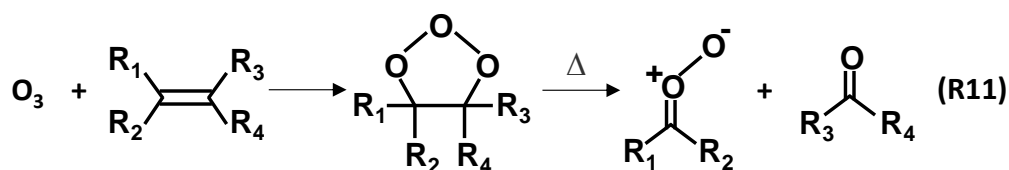
From (R11), it appears that the ozonolysis mechanism leads to the formation of a geometrically strained adduct, compared to the mechanism of the OH addition, and suggest that additional influences that were not affecting OH addition reaction could play a role in the O_3 mechanism.

Compared to the OH mechanism of electrophilic addition described in the previous section I-2.3.2., the steric effects may play a more important role in the O_3 addition mechanism. The approach of the O_3 electrophilic oxidant to the nucleophilic carbon-carbon double-bond may be hindered resulting in reduced reactivity in the 1,3-cycloaddition reactions (Leather et al., 2010; McGillen et al., 2008; Taft, 1956). It can be envisioned that the channel (R11) may be governed by additional energetic and steric parameters compared to the OH reaction of addition (R9), since (R11) due to the geometrical reorganization required by the formation of the primary ozonide that fragment into Criegee Intermediates. By analogy to hydrocarbons as discussed in (Wiberg, 1986), the specific bond angles of -O-O-O- leads to additional ring strain compared to the radical formed in (R9).

I-2.3.3.2. Detailed mechanism for industrial and biomass burning related species

Case study 3: O_3-initiated degradation of $CH_2=CHCF_3$

An example of the mechanism and detailed pathways of the atmospheric oxidation of the hydrofluoroolefin $CH_2=CHCF_3$ initiated by O_3 is presented in Figure I-4, based on literature information from (Atkinson, 1997, 2000, 2007; Atkinson and Arey, 2003a; Atkinson and Carter, 1984; Aumont et al., 2005; Burkholder et al., 2015; Calvert et al., 2000, 2015; McGillen et al., 2008). The ozonolysis mechanism starts with the formation of an unstable primary ozonide that will decompose by O–O and C–C bond breaking to form excited Criegee Intermediates (CIs) and a halo-carbonyl. The energy-rich Criegee intermediates formed are very unstable and have multiple fates under atmospheric conditions: stabilization, unimolecular decomposition, rearrangement to form radicals, and/or stable product (see Figure I-4).

The stabilized CI will react with atmospheric molecules (e.g., H-abstraction by H_2O, SO_2/H_2O in urban polluted environment, NO_x or carbonyls) leading mainly to formation of (halo-)aldehydes and ketones. The main products expected are formaldehyde, $CF_3C(O)H$, formic acid, trifluoroacetic acid (TFA), $CF_3C(O)OH$, and secondary ozonides.

This ozonolysis mechanism highlights the multiplicity of reactions and products formed through the oxidation mechanism of one molecule. The products formed can play important roles in the oxidation of other VOCs. For example, many oxygenated species and acids (e.g., TFA) formed can affect air quality and the environment, e.g., contribution to acid rain (Boutonnet et al., 1999).
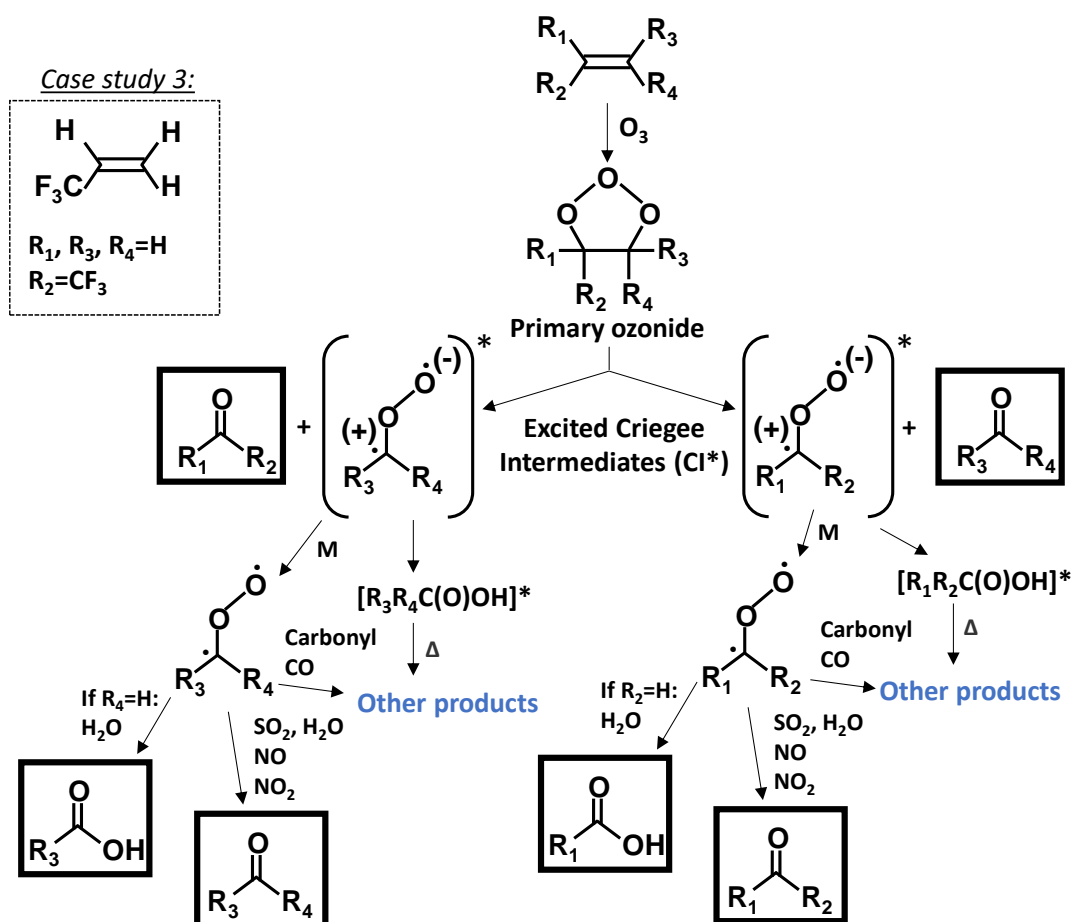
Figure I-4: Scheme of the atmospheric gas-phase degradation of $CH_2=CHCF_3$ (HFO-1243zf) initiated by its ozonolysis. Mechanism proposed has been developed based on the literature for alkenes and haloalkenes (Atkinson, 2000, 2007; Atkinson and Arey, 2003a; Aumont et al., 2005; Burkholder et al., 2015; Calvert et al., 2000, 2015; McGillen et al., 2008). The ozonolysis mechanism forms excited Criegee Intermediates (CIs) and halocarbonyls, that reacts to eventually form formaldehyde, $CF_3C(O)H$, formic acid, trifluoroacetic acid (TFA) $CF_3C(O)OH$, and secondary ozonides. The chemistry of CIs is not detailed since it is not the focus of this thesis, but the end-products that can be formed throughout the ozonolysis mechanism are presented. Multiphase processes are not included in this degradation scheme since this thesis focuses on gas-phase processes.

I-2.3.4. Nitrate radical (NO₃)
I-2.3.4.1. General tropospheric chemistry

The nitrate radical, NO_3, is the major oxidant at night, (Noxon et al., 1980; Platt et al., 1980) since it photolyzes rapidly during daytime via two pathways (Figure I-5):

$$NO_3 + h\nu \ (\lambda < 700 \ nm) \rightarrow NO + O_2 \ \ (R12)$$

$$NO_3 + h\nu \ (\lambda < 580 \ nm) \rightarrow NO_2 + O \ \ (R13)$$

NO_3 is rapidly destroyed during daytime due to its photolysis (R12–13) and reaction with NO (Figure I-5). This results in a short midday lifetime of NO_3 of around 15 s under tropospheric conditions ([NO]= 2.5×10^9 molecule cm^{-3}) (Brown and Stutz, 2012; Sander et al., 2006)).

The dominant source of nitrate radicals is the reaction of ozone with NO_2 (Brown and Stutz, 2012) and the photolysis of some organic nitrates (Flowers et al., 2005; Mazely et al., 1997) (Figure I-5). NO_3 in presence of NO_2 is removed to form N_2O_5 (R14) and the thermal decomposition of N_2O_5 leads to NO_3 formation (R15):

$$NO_2 + NO_3 + M \rightarrow N_2O_5 + M \textbf{ (R14)}$$

$$N_2O_5 + M \rightarrow NO_2 + NO_3 + M \textbf{ (R15)}$$
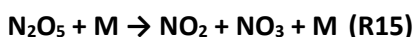
In the troposphere, NO_3 radicals are in thermal equilibrium with N_2O_5 (Figure I-5) (Brown et al., 2003). This results in nighttime mixing ratio of around 5×10^8 molecule cm^{-3} (Atkinson, 1991).
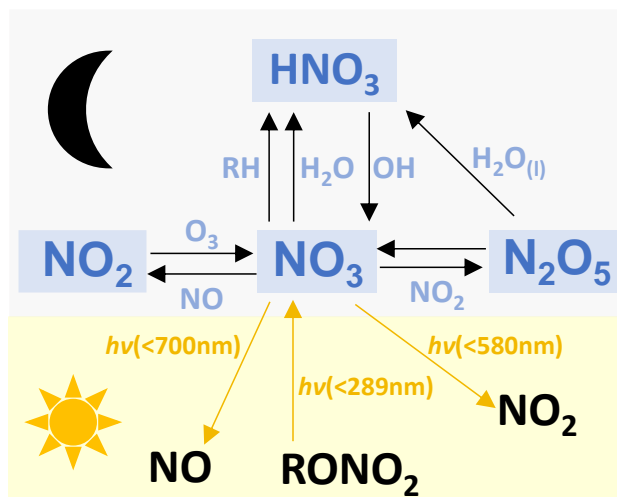

Figure I-5 : The sources and sinks of NO_3 in the troposphere, including its equilibrium with NO_2 and N_2O_5, and degradation under daytime and nighttime. A source of NO_x from the soils is also contributing to the NO_3 cycle, but not represented in the figure. This schematic has been build using reaction pathways from previous work (Brown and Stutz, 2012; Ng et al., 2017; Noxon et al., 1980; Wayne et al., 1991).

The reactions of NO_3 with organic compounds are similar to those of the OH radicals and include hydrogen abstraction and electrophilic addition. NO_3 abstracts H atoms from aldehydes only (R16), as follows:
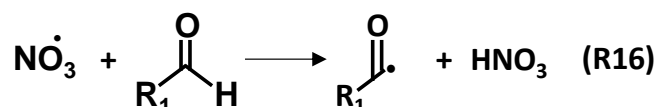
The electrophilic addition reaction (R17) of NO_3 to alkenes and furans is usually very efficient, and forms a β-nitrooxy alkyl radical, as follows:
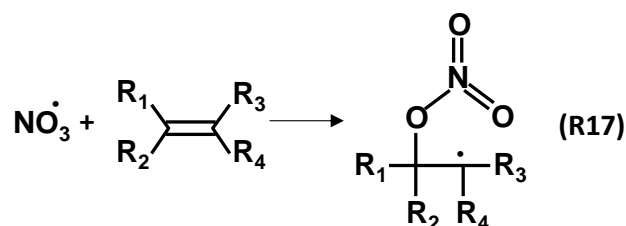
It has also been observed that epoxidation (R18) occurs during the reaction of NO_3 with alkenes (Benter et al., 1994; Oizmann et al., 1994; Skov et al., 1994):

$$NO_3^\bullet + \ \underset{R_2}{\overset{R_1}{>}}{=}\underset{R_4}{\overset{R_3}{<}} \longrightarrow \left[R_1 - \underset{R_2 \quad R_4}{\overset{ONO_2}{|}}\overset{\bullet}{|} - R_3 \right]^* \longrightarrow R_1 - \underset{R_2 \quad R_4}{\overset{O}{\triangle}} - R_3 + \ NO_2 \quad (R18)$$
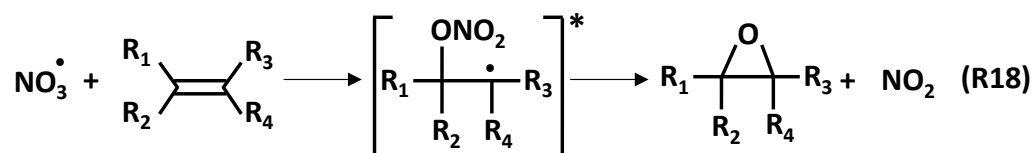
NO$_3$ displays a high reactivity towards unsaturated species, e.g., alkenes (Atkinson, 1991, 1997; Atkinson and Arey, 2003a; Calvert et al., 2000), furans (Al Ali et al., 2022; Colmenar et al., 2012; Newland et al., 2022), terpenes (Atkinson and Arey, 2003a), and typically a slow reactivity with saturated VOCs (Atkinson, 1997; Atkinson et al., 2004; Sander et al., 2006).

Nitrate chemistry has a particular importance for the oxidation of biomass burning volatile organic compounds (BBVOCs), e.g., as discussed in (Brown and Stutz, 2012; Coggon et al., 2019; Decker et al., 2021, 2019; Newland et al., 2022; Urbanski et al., 2008), since it can represent the primary removal for BBVOCs, such as furans, in the wildfire plumes under high NO$_x$ and dark conditions. During nighttime, NO$_3$ and O$_3$ reaction with alkenes (section 2.3.3. and 2.3.4.) forms radicals, OH, HO$_2$ and RO$_2$. The homogeneous and heterogenous reactions of nocturnal chemistry are leading to a loss of O$_3$ and NO$_x$ (Dentener and Crutzen, 1993; Warneke et al., 2004; Wong and Stutz, 2010). These are thus controlling the availability of radicals, O$_3$, HO$_x$ and NO$_x$ compounds the next day and consequently impacting the photochemistry of the following day. The reactions of NO$_3$ with alkenes and terpenes also contribute significantly to the formation of secondary organic aerosol (SOA) (Hoyle et al., 2011). Additionally, the uptake of NO$_3$ and N$_2$O$_5$ on heterogeneous surfaces is efficient, for example, the hydrolysis of N$_2$O$_5$ forming nitric acid (Figure I-5) (Nenes et al., 1998; Sander et al., 2006). By analogy to the work of (Boodaghians et al., 1988), in the NO$_3$ addition reaction, it can be expected that additional steric effects are playing a role compared to the OH addition reaction, due to the orientational requirement needed for the formation of the radical in channel (R17). This can be easily rationalized due to the difference in the size and the dipole moment between the NO$_3$ and OH radicals, and thus, the geometrical differences in the mechanisms.

I-2.3.4.2. Detailed mechanism for industrial and biomass burning related species

Case study 5: NO$_3$-initiated degradation of CH$_2$=CHCF$_3$

An example of the mechanism and detailed pathways of the atmospheric oxidation of CH$_2$=CHCF$_3$ initiated by NO$_3$ is presented in Figure I-6 and has been developed based on previous work on alkenes and haloalkenes from literature, i.e., (Atkinson, 1991, 1997; Atkinson and Arey, 2003a; Aumont et al., 2005; Burkholder et al., 2015; Calvert et al., 2000). The addition of NO$_3$ to the HFO lead to the formation of a β-nitrooxy alkyl radical via formation of an adduct radical that stabilizes, or forms an epoxide (Benter et al., 1994; Oizmann et al., 1994; Skov et al., 1994). The β-nitrooxy alkyl radical, R$^\bullet$, subsequently adds rapidly to O$_2$ under atmospheric conditions and forms an β-nitratoalkyl peroxy radical RO$_2^\bullet$. The alkyl peroxy radical

RO$_2^{\bullet}$ will then react with NO to form a β-nitratoalkoxy radical RO$^{\bullet}$ and NO$_2$ or the corresponding alkyl nitrate RONO$_2$. The NO$_3$-initiated chemistry leads to the formation of organic nitrates, which is an important mechanism of NO$_x$ removal for analogous alkanes, and is of particular interest during nighttime as the reversible thermal decomposition channel is slowed down.
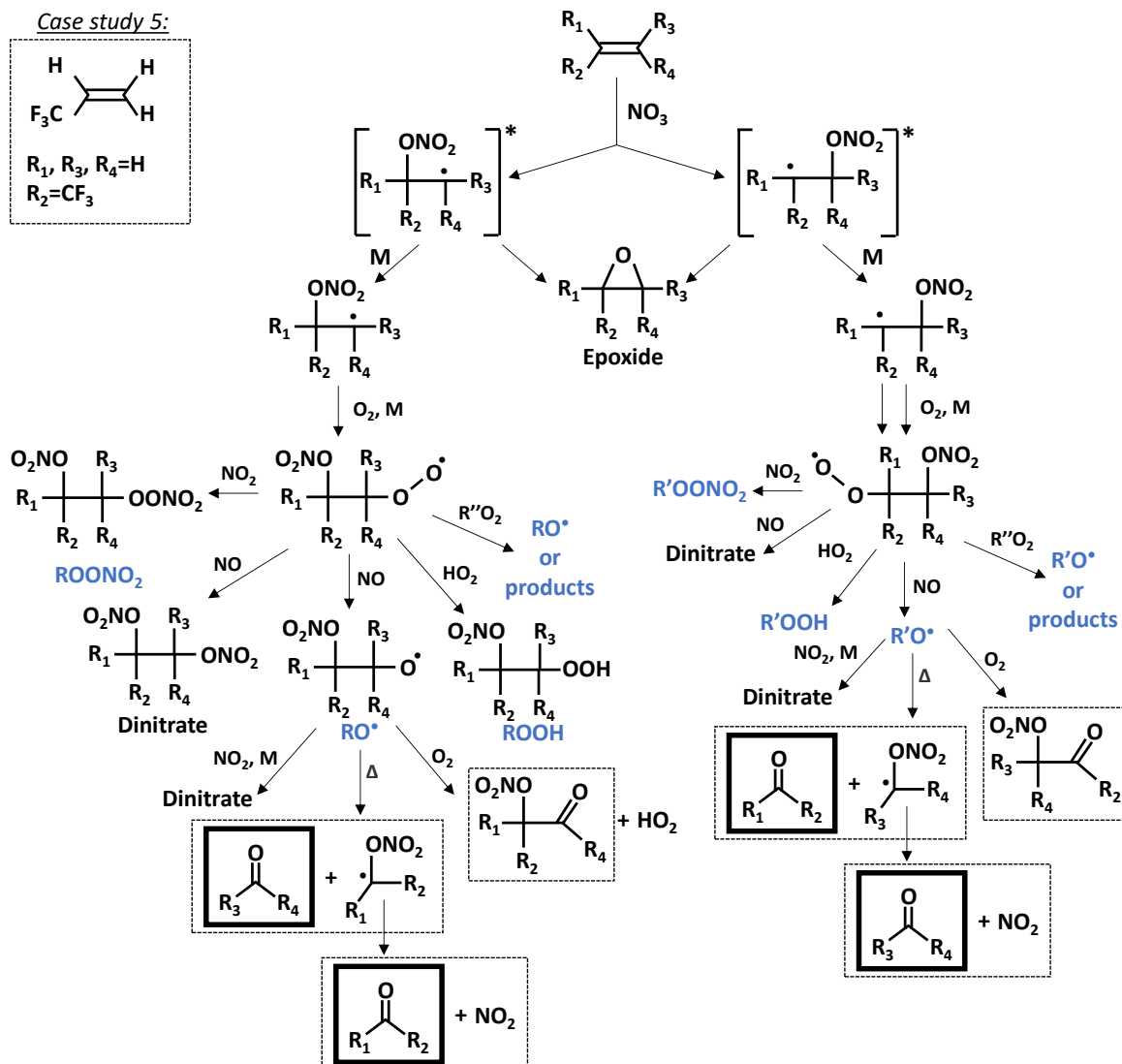
Figure I-6 : Scheme of the atmospheric gas-phase degradation of CH$_2$=CHCF$_3$ (HFO-1243zf) initiated by the addition reaction of NO$_3$. The mechanism proposed has been developed based on previous work on alkenes and haloalkenes from literature (Atkinson, 1991, 1997; Atkinson and Arey, 2003a; Aumont et al., 2005; Burkholder et al., 2015; Calvert et al., 2000). The mechanism of the NO$_3$ initiated oxidation differs from that of OH by the subsequent formation of epoxides, halo-nitrates, although it follows similar oxidation steps as described before, although similar end-products are also formed (HCHO, CF$_3$C(O)H). Multiphase processes are not included in this degradation scheme since this thesis focuses on gas-phase processes.

Case study 6: NO$_3$-initiated degradation of furans

A mechanism analogous to that in Figure I-6 occurs for NO$_3$ addition to the cyclic compound followed by formation of an adduct radical NO$_3$/furan that stabilize to form a 3*H*-furan-2-one or by ring cleavage to form *cis*-butenedial (Berndt et al., 1997; Joo et al., 2019; Tapia et al., 2011). These are the main

products observed in the NO_3 + furan oxidation mechanism, with sometimes organic nitrates formed for, e.g., in the case of 3-methylfuran (Joo et al., 2019; Tapia et al., 2011).

I-2.3.5. Chlorine atom (Cl)
I-2.3.5.1. General tropospheric chemistry

The chlorine atom, Cl, is a highly reactive oxidant, usually more reactive than the OH radical. It has been observed in high concentrations in coastal and marine environments, (Khalil et al., 1999) but its major precursor, nitril chloride, $ClNO_2$, has more recently been also measured away from the oceans, suggesting that a significant production of chlorine atoms could arise from anthropogenic sources (Thornton et al., 2010). Other sources include Cl_2, ClBr, and other species that photolyze to give Cl. Due to its high reactivity, Cl atom has a low globally averaged daytime concentration compared to other oxidants, of about 1×10^4 atoms cm^{-3} (Wingenter et al., 1996). Reactive halogen species emitted from the oceans are contributing to increase the oxidative capacity of the troposphere in coastal and marine environments (Khalil et al., 1999; Spicer et al., 1998).
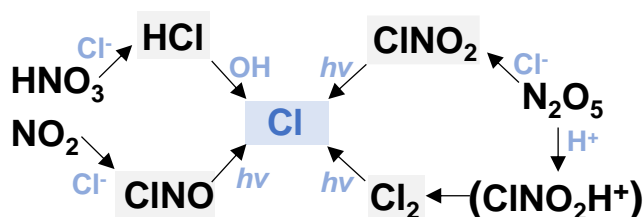

Figure I-7 : Pathways of conversion of chloride ions, from sea salts to photochemically active chlorine atom, Cl, as observed in the troposphere (Finlayson-Pitts, 2010b). More pathways are discussed in more details in the work of (Graedel and Keene, 1995; Wang et al., 2019) but are not included here for simplicity. This schematic includes multiple multiphase reactions.

The Cl reactions, similar to those of OH and NO_3, occur through hydrogen abstraction and electrophilic addition. Contrary to NO_3, the hydrogen abstraction (R19) by Cl is usually very efficient, and leads to the formation of HCl and alkyl radical as follows:

$$^{\bullet}Cl \ + \ R–H \longrightarrow R^{\bullet} \ + \ HCl \quad (R19)$$
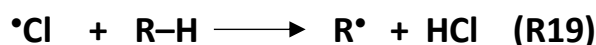
The electrophilic addition reaction (R20) is also rapid and forms a β-chloro alkyl radical:
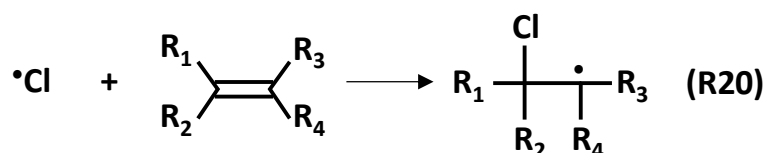
Contrary to NO_3, the H-abstraction reaction can compete with the addition reactions in the case of olefins. For the electrophilic addition reactions of Cl, the steric effects are expected to be similar than those of the OH reaction, since no major difference in mechanism exist between both oxidants (Atkinson, 1991, 1997; Atkinson and Arey, 2003a; Calvert et al., 2000).

I-2.3.5.2. Detailed mechanism for industrial and biomass burning related species

Case study 7: Cl-initiated degradation of CH$_2$=CHCF$_3$

The mechanism of the atmospheric gas-phase degradation initiated by addition of Cl to CH$_2$=CHCF$_3$ is presented in Figure I-8. This scheme highlights the variety of compounds formed throughout this oxidation pathway, including Cl-containing end products and oxygenated species. These can be of importance since they can form Cl-containing stable end-products such as trifluoro acetyl chloride, CF$_3$C(O)Cl, from the parent non-chlorinated compound (Burkholder et al., 2015).
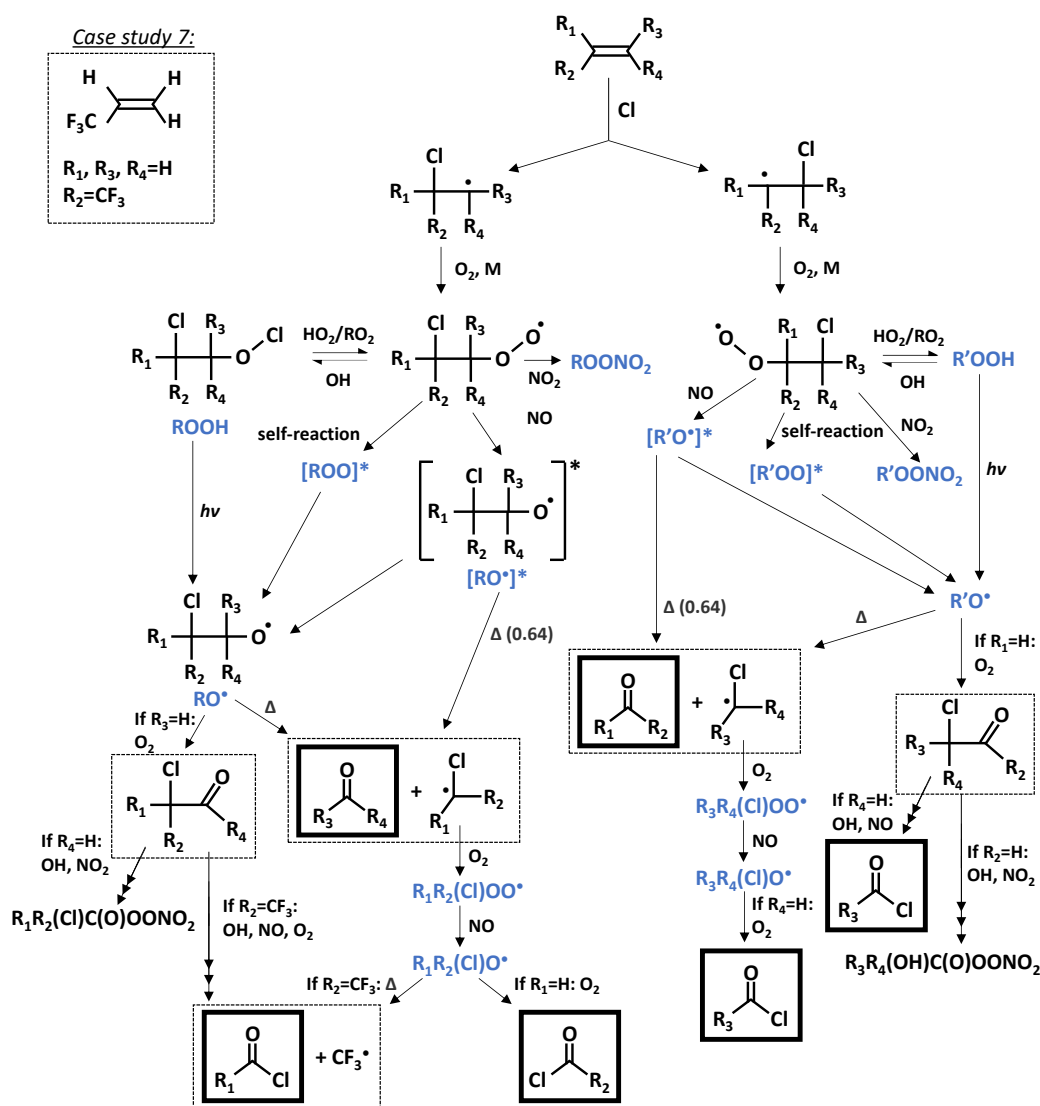
Figure I-8 : Scheme of the gas-phase atmospheric degradation of CH$_2$=CHCF$_3$ (HFO-1243zf) initiated by the addition reaction of Cl atom. The mechanism proposed has been developed based on previous work on alkenes and haloalkenes from literature, e.g., (Atkinson and Arey, 2003a, 2003b; Burkholder et al., 2015; Calvert et al., 2000; Wang et al., 2019). The mechanism of the Cl initiated oxidation forms mostly the same products as OH, with the additional possibility of some Cl-containing end-products such as trifluoro acetyl chloride, CF$_3$C(O)Cl. Multiphase processes are not included in this degradation scheme since this thesis focuses on gas-phase processes.

Case study 8: Cl-initiated degradation of furans

The reaction of chlorine atom with furans has been measured to be very fast, compared to that of OH (Cabanas et al., 2005). Product studies for the reaction of Cl with furans have reported chlorinated methyl furanones and hydroxy-methyl furanones as stable end-products, (Tapia et al., 2011) similar to what has been observed between the analogy of OH and Cl mechanisms with the HFO.

I-2.4. Conclusions

A variety of sources and degradation pathways for organic compounds in the atmosphere have been described. It appeared that a large range of compounds can be encountered, and these can possess different structure and functionalities. The products of the oxidation mechanisms that organic compounds can undergo highlight the diversity of compounds formed, with a variety of functional groups and structures, during atmospheric degradation. It appears crucial to quantify the kinetics of the different reactions in each mechanism to define which pathway(s) will predominate and which major products will be formed through the degradation of an unsaturated VOC. As discussed in section I-2., since the atmosphere encounters various temperatures and pressures, it is necessary to define this kinetics as a function of these parameters to better model the atmosphere and the impacts linked to its composition, i.e., air pollution and climate change.

I-3. Approaches to measure and estimate the kinetics of atmospheric oxidation processes – The known unknowns we have to study and the need for estimation techniques

This section aims at investigating the different methods and tools used by atmospheric scientists to study, quantify and characterize the chemistry of such a large range of compounds and reactions. The development, challenges and limits of each of these methods to date are also discussed. In order to study these atmospheric chemical reactions, the combination of five main approaches is usually employed: field measurements, laboratory measurements, theoretical calculations, estimation techniques, and modeling. Field measurements provide direct data on the ambient mixing ratios of gases in the atmosphere, emission factors from various sources, rate of processes and elementary reactions. Laboratory measurements include kinetic studies and product studies to understand the mechanism of the reactions and the products formed, together with other properties (e.g., vapor pressure, etc.). This allows us, for instance, to determine the relative contribution of different gas degradation pathways in the atmosphere. Theoretical calculations provide insights on the thermochemistry of reactions, and its kinetics. Atmospheric modelling using information from measurements predict the changes in mixing ratios over time and help to simulate complex chemical evolutions. Estimation techniques provide the magnitudes for a large panel of

compounds when no experimental data is available, based on relation between the structure of some class of molecules and their reactivities.

I-3.1. Laboratory measurements

Measurements of the kinetics of the reactions of VOCs with tropospheric oxidants, together with products quantification, can be conducted in the laboratory using various approaches and instrumentation, such as those presented in Chapter II and III, i.e., spectroscopic techniques and atmospheric simulation chambers. Laboratory approach allows one to control the pressure, temperature, and relative humidity under which the measurements are conducted, as well as the specific reaction under study, since the concentration of the compounds in the reactor or the simulation chamber can be quantified and varied. Advances in analytical techniques are providing new methods enabling the detection of a wider range of analytes, and high-resolution mass spectrometry and sensitive optical methods provide enhanced detection abilities.

However, laboratory measurements can be challenging for some reactions, and are often limited to room temperature and atmospheric pressure (Vereecken et al., 2018). They are also very time consuming and require significant efforts. Therefore, they are limited. For example, from the most up-to-date database from (McGillen et al., 2020), it can be observed that 1366 kinetic data for reactions at room temperature have been measured for OH, while only 552 temperature-dependent rate coefficients have been derived. It has to be noted that these numbers are lower for O_3, NO_3 and Cl rate coefficients that remain less well studied than that of OH. As highlighted in the previous section, temperature and pressure dependence are of major importance to describe the atmospheric reactivity of the VOCs and other trace gases emitted into the atmosphere. There is a need to extend the available kinetic data to include more measurements of temperature-dependent rate coefficients, in order to take account of variations in atmospheric temperature and to better understand the effect of substitution and functional groups on temperature-dependent reactivities (Vereecken et al., 2018). Measuring temperature- and pressure- dependent kinetics, k(T) and k(P), can be challenging in atmospheric simulation chambers where the temperature and pressure cannot be controlled easily. In smaller reactors, e.g., flow tubes, these parameters can be controlled, allowing one to investigate pressure and temperature dependencies, but the smaller volume of the reaction cell also leads to increased interaction with surfaces; such interactions can be enhanced at lower temperatures, thus also limiting the ability to measure k(T) and k(P) within certain ranges of temperature and pressure. This shows the challenges that can be encountered to study one reaction using different set-ups, but also the advantage of combining different techniques to measure the rate coefficients under different conditions.

The kinetic database also lack data for compounds beyond simple hydrocarbons or mono-functional species (Goldstein and Galbally, 2007). Measuring the rate coefficients of multifunctional species can

represent a challenge due to their low volatility or high surface affinity (Vereecken et al., 2018). There is a need for obtaining new kinetic data for functionalized oxidation products, such as those observed as products in the oxidation mechanisms in the previous section. There is a real need for data concerning some multifunctional species, low volatility species, larger carbon-chain compounds ($>C_5$), and some specific structures or types of compounds, such as furans, or oxygenated species (Vereecken et al., 2018). Some of these can be slow reactions that are consequently challenging to measure using some techniques, e.g., using "absolute" methods.

Additionally, there is a need for new kinetic and mechanistic data of biomass burning compounds, some of which may have been recently identified by new field studies, e.g., (Andreae, 2019; Decker et al., 2021, 2019). The composition of biomass burning plumes is complex and the reactions occurring within the plume remain not completely characterized. Many of the species measured as wildfires emissions have yet to have their rate coefficients measured, and some compounds measured have still not been identified (Coggon et al., 2019; Decker et al., 2021, 2019; Koss et al., 2018). Among these, nighttime chemistry remains not well described, with poor coverage of kinetic measurements of the NO_3 radical, such as the variety of furans measured the field measurements of biomass burning emissions, or the organic nitrates formed during the oxidation of biomass burning volatile organic compounds, BBVOCs (Decker et al., 2021, 2019).

I-3.2. Theoretical calculations

Theory can be used to evaluate the thermochemistry of the reactions studied, and further investigate the dominant mechanistic pathways and their kinetics. These rely on experimental data to benchmark the calculations and benchmark the different level of theory employed. The computational advancements allow to improve kinetic predictions and thermodynamics understanding of reactions, which can be very useful to elucidate reaction mechanisms and major pathways. However, quantum chemical studies require significant workload and comprehensive description of the reactions, together with experimental data to calibrate the theoretical results and benchmark the various methods of calculations. Challenges remain in calculations for pressure dependent reactivities, and there is a lack of systematic efforts to compile evaluated theoretical data for atmospheric modeling needs (Vereecken et al., 2018). The description of the thermochemistry of a reaction can also be challenging when the reaction occurs via the formation of many transition states and intermediates (Schatz, 1989).

I-3.3. Estimation techniques

Due to the large variety of organic compounds in the atmosphere (Goldstein and Galbally, 2007) it is necessary to provide data for such a large number of reactions by using other means than laboratory and

theoretical results. Since these require expertise, significant workload, and computational time. Also, as discussed previously, some experimental measurements can be challenging, leading to a need for an estimated value, when no measurement is available. In the past 30 years, less than 1500 rate coefficients for the oxidation reactions of organic and inorganic compounds have been measured, based on the most recent collection of data provided by (McGillen et al., 2020). Thus, estimation techniques, such as structure-activity relationship, SAR, were developed to help in estimating a large number of values in a short amount of time based on accurate parametrizations built upon relation between structure and reactivity.

Some conflicts can arise among the existing SARs, some of which may not easily and/or reliably apply to new compounds, and may be difficult to employ (Vereecken et al., 2018). A well-known method, that of Atkinson and co-workers, (Atkinson, 1988, 1988, 1987; Kwok and Atkinson, 1995) is commonly used for rate coefficient estimation based on functional groups. This method works well for mono-functional compounds but may not extend well to multi-functional ones (Vereecken et al., 2018). Additionally, this method has the great advantage to be implemented as an easy-to-use and rapid tool, Estimation Programs Interface (EPI) Suite, developed by the US EPA, which allows its application to large database of compounds in an easy and efficient way (US EPA, 2015). This is not the case for most SARs, limiting the scope of their applicability. Also, there is a need for SARs that predict the site-specific rate coefficients and branching ratios of products formed, in order to refine atmospheric chemical modelling (see following section I-3.6). Yet, predicting site-specific reactivity requires complex data analysis and has been a challenge for most SARs to date (Vereecken et al., 2018).

I-3.4. Atmospheric chemical modelling

Atmospheric chemical modelling is used to model the evolution of atmospheric chemical composition under various conditions (e.g., regional/global scale, meteorological conditions, urban polluted or remote environment, etc.). Atmospheric models are crucial to help understanding and predicting the chemistry of the atmosphere under various conditions and the impact on crucial challenges such as air pollution or climate change. For example, they help to characterize the production of air pollution (Stockwell et al., 2011) and how pollutants are degraded in the atmosphere. Chemical mechanisms (e.g., GECKO-A (Aumont et al., 2005), MCM (Jenkin et al., 1997), SAPRC (Carter, 2010)) can be employed and provide input in larger chemical transport and earth system models (e.g., GEOS-Chem (Eastham et al., 2014) or UKCA (Hewitt et al., 2010)). These mechanisms require extensive data on the rate coefficients, the branching ratios and the products formed during the degradation of atmospheric compounds. Thus, they rely strongly on laboratory measurements as well as estimation techniques when no experimental data is available.

I-4. Conclusion

Large varieties of gas-phase organic compounds are emitted into the atmosphere or formed as a result of secondary production, with an important class of compounds being the unsaturated volatile organic compounds, UVOCs (Aumont et al., 2005; Goldstein and Galbally, 2007; Valorso et al., 2011). UVOCs can possess a variety of structures and substituent types which result in a diversity of reactivities. Their tropospheric oxidation is primarily initiated by the electrophilic addition reactions with the four primary oxidants, OH, NO_3, O_3 and Cl. They also occur via H-abstraction pathway in certain cases, e.g., important pathway for the OH and Cl reaction of long chain UVOCs and in some cases via addition, e.g., OH, NO_3, and O_3. These different mechanisms presented in section I-2 lead to the formation of important products such as carbonyls and nitrates, resulting from their oxidation in the presence of O_2 and NO_x. These products can add the functional group of the oxidant that initiated their degradation, e.g., chlorine atoms from Cl reactions, hydroxyl group from OH reactions, or nitrated group from NO_3 reactions. These differences in the structure of the UVOCs are associated with different reactivities and with different physico-chemical properties that eventually have an impact on air quality (section I-1). They can contribute to O_3 pollution and SOA formation. In order to assess these effects, it is necessary to quantify the rate coefficients of the associated reactions and to characterize the mechanism of the degradation.

To do address the above issue, one often turns to experimental measurements. However, the number of rate coefficients that have been experimentally measured is significantly lower than the number of compounds expected to be found in the atmosphere, (McGillen et al., 2020) despite continued effort. Thus, it is useful to combine these experimental determinations with other tools such as structure-activity relationships, SARs, to estimate the rate coefficients of a broader range of reactions, in a fast and efficient way (Vereecken et al., 2018). Efforts on measuring rate coefficients of reactions that are challenging or that remain less studied (see section I-3) have to be made, including low vapor pressure compounds, slow reactions, and multifunctional species, as well as reaction with NO_3, O_3 and Cl that remain less studied than OH. This highlights the importance of new measurements, as those presented in Chapter II and Chapter III, and the need for use of theoretical and predictive methods when no kinetic data is available or measurements remain too challenging to obtain, as discussed in Chapter II and IV. Combining multiple experimental measurements with theoretical calculations and estimation methods allows one to obtain a more comprehensive understanding of some atmospheric chemical reactions and mechanisms, to enhance a complete database available as input for atmospheric chemical models, and to evaluate the impact of UVOCs on air quality and climate.

References

Abatzoglou, J.T., Smith, C.M., Swain, D.L., Ptak, T., Kolden, C.A., 2020. Population exposure to pre-emptive de-energization aimed at averting wildfires in Northern California. Environ. Res. Lett. 15, 094046.

Al Ali, F., Coeur, C., Houzel, N., Bouya, H., Tomas, A., Romanias, M.N., 2022. Rate Coefficients for the Gas-Phase Reactions of Nitrate Radicals with a Series of Furan Compounds. J. Phys. Chem. A 126, 8674–8681.

Andreae, M.O., 2019. Emission of trace gases and aerosols from biomass burning – an updated assessment. Atmospheric Chem. Phys. 19, 8523–8546. https://doi.org/10.5194/acp-19-8523-2019

Anenberg, S.C., Horowitz, L.W., Tong, D.Q., West, J.J., 2010. An estimate of the global burden of anthropogenic ozone and fine particulate matter on premature human mortality using atmospheric modeling. Environ. Health Perspect. 118, 1189–1195.

Aschmann, S.M., Nishino, N., Arey, J., Atkinson, R., 2014. Products of the OH Radical-Initiated Reactions of Furan, 2-and 3-Methylfuran, and 2, 3-and 2, 5-Dimethylfuran in the Presence of NO. J. Phys. Chem. A 118, 457–466.

Atkinson, R., 2007. Rate constants for the atmospheric reactions of alkoxy radicals: An updated estimation method. Atmos. Environ. 41, 8468–8485. https://doi.org/10.1016/j.atmosenv.2007.07.002

Atkinson, R., 2000. Atmospheric chemistry of VOCs and NOx. Atmos. Environ.

Atkinson, R., 1997. Gas-Phase Tropospheric Chemistry of Volatile Organic Compounds: 1. Alkanes and Alkenes. J. Phys. Chem. Ref. Data 26, 215–290. https://doi.org/10.1063/1.556012

Atkinson, R., 1991. Kinetics and mechanisms of the gas-phase reactions of the NO3 radical with organic compounds. J. Phys. Chem. Ref. Data 20, 459–507.

Atkinson, R., 1988. Estimation of gas-phase hydroxyl radical rate constants for organic chemicals. Environ. Toxicol. Chem. 7, 435–442. https://doi.org/10.1002/etc.5620070604

Atkinson, R., 1986. Kinetics and mechanisms of the gas-phase reactions of the hydroxyl radical with organic compounds under atmospheric conditions. Chem. Rev. 86, 69–201. https://doi.org/10.1021/cr00071a004

Atkinson, R., Arey, J., 2003a. Gas-phase tropospheric chemistry of biogenic volatile organic compounds: a review. Atmos. Environ. 37, 197–219. https://doi.org/10.1016/S1352-2310(03)00391-1

Atkinson, R., Arey, J., 2003b. Atmospheric Degradation of Volatile Organic Compounds. Chem. Rev. 103, 4605–4638. https://doi.org/10.1021/cr0206420

Atkinson, R., Baulch, D.L., Cox, R.A., Crowley, J.N., Hampson, R.F., Hynes, R.G., Jenkin, M.E., Rossi, M.J., Troe, J., 2004. Evaluated kinetic and photochemical data for atmospheric chemistry: Volume I - gas phase reactions of Ox, HOx, NOx and SOx species. Atmospheric Chem. Phys. 4, 1461–1738. https://doi.org/10.5194/acp-4-1461-2004

Atkinson, R., Carter, W.P.L., 1984. Kinetics and mechanisms of the gas-phase reactions of ozone with organic compounds under atmospheric conditions. Chem. Rev. 84, 437–470. https://doi.org/10.1021/cr00063a002

Atkinson, Roger., 1987. Estimation of OH radical reaction rate constants and atmospheric lifetimes for polychlorobiphenyls, dibenzo-p-dioxins, and dibenzofurans. Environ. Sci. Technol. 21, 305–307. https://doi.org/10.1021/es00157a013

Aumont, B., Szopa, S., Madronich, S., 2005. Modelling the evolution of organic carbon during its gas-phase tropospheric oxidation: development of an explicit model based on a self-generating approach. Atmospheric Chem. Phys. 5, 2497–2517. https://doi.org/10.5194/acp-5-2497-2005

Bahe, F., Schurath, U., 1978. Measurement of O(1D) formation by ozone photolysis in the troposphere. Pure Appl. Geophys. PAGEOPH 116, 537–544. https://doi.org/10.1007/BF01636906

Bahe, F.C., Marx, W.N., Schurath, U., Röth, E.P., 1979. Determination of the absolute photolysis rate of ozone by sunlight, O3+ hv→ O (1D)+ O2 (1Δg), at ground level. Atmospheric Environ. 1967 13, 1515–1522.

Benter, Th., Liesner, M., Schindler, R.N., Skov, H., Hjorth, J., Restelli, G., 1994. REMPI-MS and FTIR Study of NO2 and Oxirane Formation in the Reactions of Unsaturated Hydrocarbons with NO3 Radicals. J. Phys. Chem. 98, 10492–10496. https://doi.org/10.1021/j100092a018

Berndt, T., Böge, O., Rolle, W., 1997. Products of the gas-phase reactions of NO3 radicals with furan and tetramethylfuran. Environ. Sci. Technol. 31, 1157–1162.

Bidleman, T.F., 1988. Atmospheric processes. Environ. Sci. Technol. 22, 361–367.

Blacet, F.E., 1952. Photochemistry in the Lower Atmosphere. Ind. Eng. Chem. 44, 1339–1342. https://doi.org/10.1021/ie50510a044

Boodaghians, R.B., Canosa-Mas, C.E., Carpenter, P.J., Wayne, R.P., 1988. The reactions of NO3 with OH and H. J. Chem. Soc. Faraday Trans. 2 84, 931. https://doi.org/10.1039/f29888400931

Borchers Arriagada, N., Bowman, D.M., Palmer, A.J., Johnston, F.H., 2020. Climate change, wildfires, heatwaves and health impacts in Australia. Extreme Weather Events Hum. Health Int. Case Stud. 99–116.

Boutonnet, J.C., Bingham, P., Calamari, D., Rooij, C. de, Franklin, J., Kawano, T., Libre, J.-M., McCul-Loch, A., Malinverno, G., Odom, J.M., 1999. Environmental risk assessment of trifluoroacetic acid. Hum. Ecol. Risk Assess. Int. J. 5, 59–124.

Brewer, A.W., 1949. Evidence for a world circulation provided by the measurements of helium and water vapour distribution in the stratosphere. Q. J. R. Meteorol. Soc. 75, 351–363. https://doi.org/10.1002/qj.49707532603

Brown, S.S., Stark, H., Ravishankara, A.R., 2003. Applicability of the steady state approximation to the interpretation of atmospheric observations of NO $_3$ and N $_2$ O $_5$. J. Geophys. Res. Atmospheres 108, 2003JD003407. https://doi.org/10.1029/2003JD003407

Brown, S.S., Stutz, J., 2012. Nighttime radical observations and chemistry. Chem. Soc. Rev. 41, 6405–6447.

Brunekreef, B., Holgate, S.T., 2002. Air pollution and health. The Lancet 360, 1233–1242. https://doi.org/10.1016/S0140-6736(02)11274-8

Burkholder, J.B., Cox, R.A., Ravishankara, A.R., 2015. Atmospheric Degradation of Ozone Depleting Substances, Their Substitutes, and Related Species. Chem. Rev. 115, 3704–3759. https://doi.org/10.1021/cr5006759

Cabanas, B., Villanueva, F., Martin, P., Baeza, M., Salgado, S., Jimenez, E., 2005. Study of reaction processes of furan and some furan derivatives initiated by Cl atoms. Atmos. Environ. 39, 1935–1944. https://doi.org/10.1016/j.atmosenv.2004.12.013

Calvert, J.G., Atkinson, R., Becker, K.H., Kamens, R.M., Seinfeld, J.H., Wallington, T.H., Yarwood, G., 2002. The Mechanisms of Atmospheric Oxidation of the Aromatic Hydrocarbons. Oxford University Press.

Calvert, J.G., Atkinson, R., Kerr, J.A., Madronich, S., Moortgat, G.K., Wallington, T.J., Yarwood, J.G., 2000. The Mechanisms of Atmospheric Oxidation of the Alkenes, New York Oxford. ed. Oxford University Press.

Calvert, J.G., Kerr, J.A., Demerjian, K.L., McQuigg, R.D., 1972. Photolysis of Formaldehyde as a Hydrogen Atom Source in the Lower Atmosphere. Science 175, 751–752. https://doi.org/10.1126/science.175.4023.751

Calvert, J.G., Orlando, J.J., Stockwell, W.R., Wallington, T.J., 2015. The Mechanisms of Reactions Influencing Atmospheric Ozone. Oxford University Press.

Carter, W.P.L., 2010. Development of the SAPRC-07 chemical mechanism. Atmos. Environ., Atmospheric Chemical Mechanisms: Selected Papers from the 2008 Conference 44, 5324–5335. https://doi.org/10.1016/j.atmosenv.2010.01.026

Chameides, W., Walker, J.C.G., 1973. A photochemical theory of tropospheric ozone. J. Geophys. Res. 1896-1977 78, 8751–8760. https://doi.org/10.1029/JC078i036p08751

Chatfield, R.B., Crutzen, P.J., 1984. Sulfur dioxide in remote oceanic air: Cloud transport of reactive precursors. J. Geophys. Res. Atmospheres 89, 7111–7132.

Coggon, M.M., Lim, C.Y., Koss, A.R., Sekimoto, K., Yuan, B., Gilman, J.B., Hagan, D.H., Selimovic, V., Zarzana, K.J., Brown, S.S., 2019. OH chemistry of non-methane organic gases (NMOGs) emitted from laboratory and ambient biomass burning smoke: evaluating the influence of furans and oxygenated aromatics on ozone and secondary NMOG formation. Atmospheric Chem. Phys. 19, 14875–14899.

Colmenar, I., Cabañas, B., Martínez, E., Salgado, M.S., Martín, P., 2012. Atmospheric fate of a series of furanaldehydes by their NO3 reactions. Atmos. Environ. 54, 177–184. https://doi.org/10.1016/j.atmosenv.2012.02.087

Crutzen, P., 1973. A discussion of the chemistry of some minor constituents in the stratosphere and troposphere. Pure Appl. Geophys. 106, 1385–1399.

Crutzen, P.J., 1988. Tropospheric Ozone: An Overview, in: Isaksen, I.S.A. (Ed.), Tropospheric Ozone: Regional and Global Scale Interactions, NATO ASI Series. Springer Netherlands, Dordrecht, pp. 3–32. https://doi.org/10.1007/978-94-009-2913-5_1

Crutzen, P.J., Fishman, J., 1977. Average concentrations of OH in the troposphere, and the budgets of CH 4, CO, H 2 and CH 3CCl 3. Geophys. Res. Lett. 4, 321–324. https://doi.org/10.1029/GL004i008p00321

Crutzen, P.J., Heidt, L.E., Krasnec, J.P., Pollock, W.H., Seiler, W., 1979. Biomass burning as a source of atmospheric gases CO, H2, N2O, NO, CH3Cl and COS. Nature 282, 253–256.

Decker, Z.C.J., Robinson, M.A., Barsanti, K.C., Bourgeois, I., Coggon, M.M., DiGangi, J.P., Diskin, G.S., Flocke, F.M., Franchin, A., Fredrickson, C.D., Gkatzelis, G.I., Hall, S.R., Halliday, H., Holmes, C.D., Huey, L.G., Lee, Y.R., Lindaas, J., Middlebrook, A.M., Montzka, D.D., Moore, R., Neuman, J.A., Nowak, J.B., Palm, B.B., Peischl, J., Piel, F., Rickly, P.S., Rollins, A.W., Ryerson, T.B., Schwantes, R.H., Sekimoto, K., Thornhill, L., Thornton, J.A., Tyndall, G.S., Ullmann, K., Van Rooy, P., Veres, P.R., Warneke, C., Washenfelder, R.A., Weinheimer, A.J., Wiggins, E., Winstead, E., Wisthaler, A., Womack, C., Brown, S.S., 2021. Nighttime and daytime dark oxidation chemistry in wildfire plumes: an observation and model analysis of FIREX-AQ aircraft data. Atmospheric Chem. Phys. 21, 16293–16317. https://doi.org/10.5194/acp-21-16293-2021

Decker, Z.C.J., Zarzana, K.J., Coggon, M., Min, K.-E., Pollack, I., Ryerson, T.B., Peischl, J., Edwards, P., Dubé, W.P., Markovic, M.Z., Roberts, J.M., Veres, P.R., Graus, M., Warneke, C., de Gouw, J., Hatch, L.E., Barsanti, K.C., Brown, S.S., 2019. Nighttime Chemical Transformation in Biomass Burning Plumes: A Box Model Analysis Initialized with Aircraft Observations. Environ. Sci. Technol. 53, 2529–2538. https://doi.org/10.1021/acs.est.8b05359

Demore, W.B., Margitan, J.J., Molina, M.J., Watson, R.T., Golden, D.M., Hampson, R.F., Kurylo, M.J., Howard, C.J., Ravishankara, A.R., 1985. Tables of rate constants extracted from chemical kinetics and photochemical data for use in stratospheric modeling. Evaluation number 7. Int. J. Chem. Kinet. 17, 1135–1151. https://doi.org/10.1002/kin.550171010

Dentener, F.J., Crutzen, P.J., 1993. Reaction of N2O5 on tropospheric aerosols: Impact on the global distributions of NO x , O3, and OH. J. Geophys. Res. Atmospheres 98, 7149–7163. https://doi.org/10.1029/92JD02979

Dupuy, J., Fargeon, H., Martin-StPaul, N., Pimont, F., Ruffault, J., Guijarro, M., Hernando, C., Madrigal, J., Fernandes, P., 2020. Climate change impact on future wildfire danger and activity in southern Europe: a review. Ann. For. Sci. 77, 1–24.

Eastham, S.D., Weisenstein, D.K., Barrett, S.R., 2014. Development and evaluation of the unified tropospheric–stratospheric chemistry extension (UCX) for the global chemistry-transport model GEOS-Chem. Atmos. Environ. 89, 52–63.

Ehhalt, D.H., Dorn, H.-P., Poppe, D., 1990. The chemistry of the hydroxyl radical in the troposphere. Proc. R. Soc. Edinb. Sect. B Biol. Sci. 97, 17–34. https://doi.org/10.1017/S0269727000005273

Fabian, P., Pruchniewicz, P.G., 1977. Meridional distribution of ozone in the troposphere and its seasonal variations. J. Geophys. Res. 1896-1977 82, 2063–2073. https://doi.org/10.1029/JC082i015p02063

Fall, R., 1999. Biogenic emissions of volatile organic compounds from higher plants, in: Reactive Hydrocarbons in the Atmosphere. Elsevier, pp. 41–96.

Fehsenfeld, F., Calvert, J., Fall, R., Goldan, P., Guenther, A.B., Hewitt, C.N., Lamb, B., Liu, S., Trainer, M., Westberg, H., 1992. Emissions of volatile organic compounds from vegetation and the implications for atmospheric chemistry. Glob. Biogeochem. Cycles 6, 389–430.

Finlayson-Pitts, B.J., 2010. Atmospheric Chemistry. Proc. Natl. Acad. Sci. 107, 6566–6567. https://doi.org/10.1073/pnas.1003038107

Finlayson-Pitts, B.J., 2010b. Halogens in the Troposphere. Anal. Chem. 82, 770–776. https://doi.org/10.1021/ac901478p

Finlayson-Pitts, B.J., Pitts, J.N., 1999. Chemistry of the Upper and Lower Atmosphere: Theory, Experiments, and Applications. Elsevier Science.

Fishman, J., Crutzen, P.J., 1978. The origin of ozone in the troposphere. Nature 274, 855–858. https://doi.org/10.1038/274855a0

Flowers, B.A., Angerhofer, M.E., Simpson, W.R., Nakayama, T., Matsumi, Y., 2005. Nitrate Radical Quantum Yield from Peroxyacetyl Nitrate Photolysis. J. Phys. Chem. A 109, 2552–2558. https://doi.org/10.1021/jp045529n

Forster, P., Ramaswamy, V., Artaxo, P., Berntsen, T., Betts, R., Fahey, D.W., Haywood, J., Lean, J., Lowe, D.C., Myhre, G., 2007. Changes in atmospheric constituents and in radiative forcing. Clim. Change 2007 Phys. Sci. Basis Contrib. Work. Group 4th Assess. Rep. Intergov. Panel Clim. Change.

Friedrich, R., Obermeier, A., 1999. Anthropogenic emissions of volatile organic compounds, in: Reactive Hydrocarbons in the Atmosphere. Elsevier, pp. 1–39.

Gidel, L.T., Shapiro, M.A., 1980. General circulation model estimates of the net vertical flux of ozone in the lower stratosphere and the implications for the tropospheric ozone budget. J. Geophys. Res. Oceans 85, 4049–4058. https://doi.org/10.1029/JC085iC07p04049

Gilman, J.B., Lerner, B.M., Kuster, W.C., Goldan, P.D., Warneke, C., Veres, P.R., Roberts, J.M., de Gouw, J.A., Burling, I.R., Yokelson, R.J., 2015. Biomass burning emissions and potential air quality impacts of volatile organic compounds and other trace gases from fuels common in the US. Atmospheric Chem. Phys. 15, 13915–13938. https://doi.org/10.5194/acp-15-13915-2015

Goldstein, A.H., Galbally, I.E., 2007. Known and Unexplored Organic Constituents in the Earth's Atmosphere. Environ. Sci. Technol. 41, 1514–1521. https://doi.org/10.1021/es072476p

Goss, M., Swain, D.L., Abatzoglou, J.T., Sarhadi, A., Kolden, C.A., Williams, A.P., Diffenbaugh, N.S., 2020. Climate change is increasing the likelihood of extreme autumn wildfire conditions across California. Environ. Res. Lett. 15, 094016.

Graedel, T.E., Keene, W.C., 1995. Tropospheric budget of reactive chlorine. Glob. Biogeochem. Cycles 9, 47–77. https://doi.org/10.1029/94GB03103

Guenther, A., Hewitt, C.N., Erickson, D., Fall, R., Geron, C., Graedel, T., Harley, P., Klinger, L., Lerdau, M., McKay, W.A., 1995. A global model of natural volatile organic compound emissions. J. Geophys. Res. Atmospheres 100, 8873–8892.

Guenther, A., Karl, T., Harley, P., Wiedinmyer, C., Palmer, P.I., Geron, C., 2006. Estimates of global terrestrial isoprene emissions using MEGAN (Model of Emissions of Gases and Aerosols from Nature). Atmospheric Chem. Phys. 6, 3181–3210.

Hallquist, M., Wenger, J.C., Baltensperger, U., Rudich, Y., Simpson, D., Claeys, M., Dommen, J., Donahue, N.M., George, C., Goldstein, A.H., 2009. The formation, properties and impact of secondary organic aerosol: current and emerging issues. Atmospheric Chem. Phys. 9, 5155–5236.

Hansen, J., Sato, M., Ruedy, R., 1997. Radiative forcing and climate response. J. Geophys. Res. Atmospheres 102, 6831–6864. https://doi.org/10.1029/96JD03436

Heintzenberg, J., 1989. Fine particles in the global troposphere A review. Tellus B 41B, 149–160. https://doi.org/10.1111/j.1600-0889.1989.tb00132.x

Hewitt, H.T., Copsey, D., Culverwell, I.D., Harris, C.M., Hill, R.S.R., Keen, A.B., McLaren, A.J., Hunke, E.C., 2010. Design and implementation of the infrastructure of HadGEM3: The next-generation Met Office climate modelling system. Geosci. Model Dev. Discuss. 3, 1861–1937.

Houweling, S., Dentener, F., Lelieveld, J., 1998. The impact of nonmethane hydrocarbon compounds on tropospheric photochemistry. J. Geophys. Res. Atmospheres 103, 10673–10696. https://doi.org/10.1029/97JD03582

Hoyle, C.R., Boy, M., Donahue, N.M., Fry, J.L., Glasius, M., Guenther, A., Hallar, A.G., Huff Hartz, K., Petters, M.D., Petäjä, T., Rosenoern, T., Sullivan, A.P., 2011. A review of the anthropogenic influence on biogenic secondary organic aerosol. Atmospheric Chem. Phys. 11, 321–343. https://doi.org/10.5194/acp-11-321-2011

Intergovernmental Panel on Climate Change (IPCC) (Ed.), 2023. The Earth's Energy Budget, Climate Feedbacks and Climate Sensitivity, in: Climate Change 2021 – The Physical Science Basis: Working Group I Contribution to the Sixth Assessment Report of the Intergovernmental Panel on Climate Change. Cambridge University Press, Cambridge, pp. 923–1054. https://doi.org/10.1017/9781009157896.009

IPCC, 2022a. Summary for Policymakers. Clim. Change 2022 Impacts Adapt. Vulnerability Contrib. Work. Group II Sixth Assess. Rep. Intergov. Panel Clim. Change.

IPCC, 2022b. Climate Change 2022: Impacts, Adaptation and Vulnerability. Summary for Policymakers.

Jaeglé, L., Jacob, D.J., Wennberg, P.O., Spivakovsky, C.M., Hanisco, T.F., Lanzendorf, E.J., Hintsa, E.J., Fahey, D.W., Keim, E.R., Proffitt, M.H., Atlas, E.L., Flocke, F., Schauffler, S., McElroy, C.T., Midwinter, C., Pfister, L., Wilson, J.C., 1997. Observed OH and HO2 in the upper troposphere suggest a major source from convective injection of peroxides. Geophys. Res. Lett. 24, 3181–3184. https://doi.org/10.1029/97GL03004

Jenkin, M.E., Saunders, S.M., Pilling, M.J., 1997. The tropospheric degradation of volatile organic compounds: a protocol for mechanism development. Atmos. Environ. 31, 81–104. https://doi.org/10.1016/S1352-2310(96)00105-7

Jerrett, M., Burnett, R.T., Pope, C.A., Ito, K., Thurston, G., Krewski, D., Shi, Y., Calle, E., Thun, M., 2009. Long-Term Ozone Exposure and Mortality. N. Engl. J. Med. 360, 1085–1095. https://doi.org/10.1056/NEJMoa0803894

Jiang, J., Carter, W.P.L., Cocker, D.R., Barsanti, K.C., 2020. Development and Evaluation of a Detailed Mechanism for Gas-Phase Atmospheric Reactions of Furans. ACS Earth Space Chem. 4, 1254–1268. https://doi.org/10.1021/acsearthspacechem.0c00058

Jones, M.W., Smith, A., Betts, R., Canadell, J.G., Prentice, I.C., Le Quéré, C., 2020. Climate change increases the risk of wildfires. Sci. Rev. 116, 117.

Joo, T., Rivera-Rios, J.C., Takeuchi, M., Alvarado, M.J., Ng, N.L., 2019. Secondary organic aerosol formation from reaction of 3-methylfuran with nitrate radicals. ACS Earth Space Chem. 3, 922–934.

Kampa, M., Castanas, E., 2008. Human health effects of air pollution. Environ. Pollut. 151, 362–367.

Kansal, A., 2009. Sources and reactivity of NMHCs and VOCs in the atmosphere: A review. J. Hazard. Mater. 166, 17–26.

Keeley, J.E., Syphard, A.D., 2021. Large California wildfires: 2020 fires in historical context. Fire Ecol. 17, 1–11.

Kesselmeier, J., Staudt, M., 1999. Biogenic Volatile Organic Compounds (VOC): An Overview on Emission, Physiology and Ecology. J. Atmospheric Chem. 33, 23–88. https://doi.org/10.1023/A:1006127516791

Khalil, M. a. K., Moore, R.M., Harper, D.B., Lobert, J.M., Erickson, D.J., Koropalov, V., Sturges, W.T., Keene, W.C., 1999. Natural emissions of chlorine-containing gases: Reactive Chlorine Emissions Inventory. J. Geophys. Res. Atmospheres 104, 8333–8346. https://doi.org/10.1029/1998JD100079

Kley, D., 1997. Tropospheric chemistry and transport. Science 276, 1043–1044.

Koppmann, R., 2008. Volatile Organic Compounds in the Atmosphere. John Wiley & Sons.

Koss, A.R., Sekimoto, K., Gilman, J.B., Selimovic, V., Coggon, M.M., Zarzana, K.J., Yuan, B., Lerner, B.M., Brown, S.S., Jimenez, J.L., Krechmer, J., Roberts, J.M., Warneke, C., Yokelson, R.J., de Gouw, J., 2018. Non-methane organic gas emissions from biomass burning: identification, quantification, and emission factors from PTR-ToF during the FIREX 2016 laboratory experiment. Atmospheric Chem. Phys. 18, 3299–3319. https://doi.org/10.5194/acp-18-3299-2018

Kroll, J.H., Donahue, N.M., Jimenez, J.L., Kessler, S.H., Canagaratna, M.R., Wilson, K.R., Altieri, K.E., Mazzoleni, L.R., Wozniak, A.S., Bluhm, H., Mysak, E.R., Smith, J.D., Kolb, C.E., Worsnop, D.R., 2011.

Carbon oxidation state as a metric for describing the chemistry of atmospheric organic aerosol. Nat. Chem. 3, 133–139. https://doi.org/10.1038/nchem.948

Kwok, E.S.C., Atkinson, R., 1995. Estimation of hydroxyl radical reaction rate constants for gas-phase organic compounds using a structure-reactivity relationship: An update. Atmospheric Environment 29, 1685–1695.

Leather, K.E., McGillen, M.R., Percival, C.J., 2010. Temperature-dependent ozonolysis kinetics of selected alkenes in the gas phase: an experimental and structure–activity relationship (SAR) study. Phys. Chem. Chem. Phys. 12, 2935. https://doi.org/10.1039/b919731a

Lelieveld, J., Klingmüller, K., Pozzer, A., Burnett, R.T., Haines, A., Ramanathan, V., 2019. Effects of fossil fuel and total anthropogenic emission removal on public health and climate. Proc. Natl. Acad. Sci. 116, 7192–7197.

Lenoble, J., 1993. Atmospheric radiative transfer. A. Deepak Pub.

Levy II, H., 1972. Photochemistry of the lower troposphere. Planet. Space Sci. 20, 919–935.

Lim, S.S., Vos, T., Flaxman, A.D., Danaei, G., Shibuya, K., Adair-Rohani, H., AlMazroa, M.A., Amann, M., Anderson, H.R., Andrews, K.G., 2012. A comparative risk assessment of burden of disease and injury attributable to 67 risk factors and risk factor clusters in 21 regions, 1990–2010: a systematic analysis for the Global Burden of Disease Study 2010. The lancet 380, 2224–2260.

Liu, Y., Williams, E., Li, Z., Guha, A., LaPierre, J., Stock, M., Heckman, S., Zhang, Y., DiGangi, E., 2021. Lightning enhancement in moist convection with smoke-laden air advected from Australian wildfires. Geophys. Res. Lett. 48, e2020GL092355.

Logan, J.A., Prather, M.J., Wofsy, S.C., McElroy, M.B., 1981. Tropospheric chemistry: A global perspective. J. Geophys. Res. Oceans 86, 7210–7254.

Mahlman, J.D., Levy, H., Moxim, W.J., 1980. Three-Dimensional Tracer Structure and Behavior as Simulated in Two Ozone Precursor Experiments. J. Atmospheric Sci. 37, 655–685. https://doi.org/10.1175/1520-0469(1980)037<0655:TDTSAB>2.0.CO;2

Mazely, T.L., Friedl, R.R., Sander, S.P., 1997. Quantum Yield of NO3 from Peroxyacetyl Nitrate Photolysis. J. Phys. Chem. A 101, 7090–7097. https://doi.org/10.1021/jp971298r

McGillen, M.R., Archibald, A.T., Carey, T., Leather, K.E., Shallcross, D.E., Wenger, J.C., Percival, C.J., 2011. Structure–activity relationship (SAR) for the prediction of gas-phase ozonolysis rate coefficients: an extension towards heteroatomic unsaturated species. Phys. Chem. Chem. Phys. 13, 2842–2849. https://doi.org/10.1039/C0CP01732A

McGillen, M.R., Carey, T.J., Archibald, A.T., Wenger, J.C., Shallcross, D.E., Percival, C.J., 2008. Structure–activity relationship (SAR) for the gas-phase ozonolysis of aliphatic alkenes and dialkenes. Phys. Chem. Chem. Phys. 10, 1757. https://doi.org/10.1039/b715394e

McGillen, M.R., Carter, W.P.L., Mellouki, A., Orlando, J.J., Picquet-Varrault, B., Wallington, T.J., 2020. Database for the kinetics of the gas-phase atmospheric reactions of organic compounds. Earth Syst. Sci. Data 12, 1203–1216. https://doi.org/10.5194/essd-12-1203-2020

McGillen, M.R., Percival, C.J., Shallcross, D.E., Harvey, J.N., 2007. Is hydrogen abstraction an important pathway in the reaction of alkenes with the OH radical? Phys. Chem. Chem. Phys. 9, 4349–4356. https://doi.org/10.1039/B703035E

McIlveen, R., 1998. Fundamentals of weather and climate. Psychology Press.

McKeen, S.A., Gierczak, T., Burkholder, J.B., Wennberg, P.O., Hanisco, T.F., Keim, E.R., Gao, R.-S., Liu, S.C., Ravishankara, A.R., Fahey, D.W., 1997. The photochemistry of acetone in the upper troposphere: A source of odd-hydrogen radicals. Geophys. Res. Lett. 24, 3177–3180. https://doi.org/10.1029/97GL03349

Molina, M.J., Rowland, F.S., 1974. Stratospheric sink for chlorofluoromethanes: chlorine atom-catalysed destruction of ozone. Nature 249, 810–812.

Monks, P.S., Granier, C., Fuzzi, S., Stohl, A., Williams, M.L., Akimoto, H., Amann, M., Baklanov, A., Baltensperger, U., Bey, I., Blake, N., Blake, R.S., Carslaw, K., Cooper, O.R., Dentener, F., Fowler, D., Fragkou, E., Frost, G.J., Generoso, S., Ginoux, P., Grewe, V., Guenther, A., Hansson, H.C., Henne, S., Hjorth, J., Hofzumahaus, A., Huntrieser, H., Isaksen, I.S.A., Jenkin, M.E., Kaiser, J., Kanakidou, M., Klimont, Z., Kulmala, M., Laj, P., Lawrence, M.G., Lee, J.D., Liousse, C., Maione, M., McFiggans,

G., Metzger, A., Mieville, A., Moussiopoulos, N., Orlando, J.J., O'Dowd, C.D., Palmer, P.I., Parrish, D.D., Petzold, A., Platt, U., Pöschl, U., Prévôt, A.S.H., Reeves, C.E., Reimann, S., Rudich, Y., Sellegri, K., Steinbrecher, R., Simpson, D., Ten Brink, H., Theloke, J., Van Der Werf, G.R., Vautard, R., Vestreng, V., Vlachokostas, Ch., Von Glasow, R., 2009. Atmospheric composition change – global and regional air quality. Atmos. Environ. 43, 5268–5350. https://doi.org/10.1016/j.atmosenv.2009.08.021

National Research Council, 1991. Rethinking the ozone problem in urban and regional air pollution. National Academies Press, Washington, DC.

Nenes, A., Pandis, S.N., Pilinis, C., 1998. ISORROPIA: A New Thermodynamic Equilibrium Model for Multiphase Multicomponent Inorganic Aerosols. Aquat. Geochem. 4, 123–152. https://doi.org/10.1023/A:1009604003981

Newland, M.J., Ren, Y., McGillen, M.R., Michelat, L., Daële, V., Mellouki, A., 2022. NO 3 chemistry of wildfire emissions: A kinetic study of the gas-phase reactions of furans with the NO 3 radical. Atmospheric Chem. Phys. 22, 1761–1772.

Ng, N.L., Brown, S.S., Archibald, A.T., Atlas, E., Cohen, R.C., Crowley, J.N., Day, D.A., Donahue, N.M., Fry, J.L., Fuchs, H., Griffin, R.J., Guzman, M.I., Herrmann, H., Hodzic, A., Iinuma, Y., Jimenez, J.L., Kiendler-Scharr, A., Lee, B.H., Luecken, D.J., Mao, J., McLaren, R., Mutzel, A., Osthoff, H.D., Ouyang, B., Picquet-Varrault, B., Platt, U., Pye, H.O.T., Rudich, Y., Schwantes, R.H., Shiraiwa, M., Stutz, J., Thornton, J.A., Tilgner, A., Williams, B.J., Zaveri, R.A., 2017. Nitrate radicals and biogenic volatile organic compounds: oxidation, mechanisms, and organic aerosol. Atmospheric Chem. Phys. 17, 2103–2162. https://doi.org/10.5194/acp-17-2103-2017

NOAA National Centers for Environmental Information, n.d. Monthly Global Climate Report for July 2023 (No. published online August 2023, retrieved on August 15, 2023).

Noxon, J.F., Norton, R.B., Marovich, E., 1980. NO3 in the troposphere. Geophys. Res. Lett. 7, 125–128. https://doi.org/10.1029/GL007i002p00125

Oizmann, M., Benter, Th., Liesner, M., Schindler, R.N., 1994. On the pressure dependence of the NO2 product yield in the reaction of NO3 radicals with selected alkenes. Atmos. Environ. 28, 2677–2683. https://doi.org/10.1016/1352-2310(94)90440-5

Orlando, J.J., Tyndall, G.S., Wallington, T.J., 2003. The atmospheric chemistry of alkoxy radicals. Chem. Rev. 103, 4657–4690.

Piccot, S.D., Watson, J.J., Jones, J.W., 1992. A global inventory of volatile organic compound emissions from anthropogenic sources. Journal of Geophysical Research: Atmospheres 97: 9897-9912.

Pinter, B., Fievez, T., Bickelhaupt, F.M., Geerlings, P., Proft, F.D., 2012. On the origin of the steric effect. Phys. Chem. Chem. Phys. 14, 9846–9854. https://doi.org/10.1039/C2CP41090G

Placet, M., Mann, C.O., Gilbert, R.O., Niefer, M.J., 2000. Emissions of ozone precursors from stationary sources: a critical review. Atmos. Environ. 34, 2183–2204.

Platt, U., Perner, D., Winer, A.M., Harris, G.W., Pitts Jr., J.N., 1980. Detection of NO3 in the polluted troposphere by differential optical absorption. Geophys. Res. Lett. 7, 89–92. https://doi.org/10.1029/GL007i001p00089

Pope III, C.A., Dockery, D.W., 2006. Health effects of fine particulate air pollution: lines that connect. J. Air Waste Manag. Assoc. 56, 709–742.

Pöschl, U., 2005. Atmospheric aerosols: composition, transformation, climate and health effects. Angew. Chem. Int. Ed. 44, 7520–7540.

Prather, M.J., Jacob, D.J., 1997. A persistent imbalance in HOx and NOx photochemistry of the upper troposphere driven by deep tropical convection. Geophys. Res. Lett. 24, 3189–3192.

Ratcliffe, J.A., 1960. Physics of the upper atmosphere. Phys. Up. Atmosphere.

Ravishankara, A.R., Hancock, G., Kawasaki, M., Matsumi, Y., 1998. Photochemistry of Ozone: Surprises and Recent Lessons. Science 280, 60–61. https://doi.org/10.1126/science.280.5360.60

Richardson, D., Black, A.S., Irving, D., Matear, R.J., Monselesan, D.P., Risbey, J.S., Squire, D.T., Tozer, C.R., 2022. Global increase in wildfire potential from compound fire weather and drought. NPJ Clim. Atmospheric Sci. 5, 23.

Rinnan, R., Rinnan, Å., Holopainen, T., Holopainen, J.K., Pasanen, P., 2005. Emission of non-methane volatile organic compounds (VOCs) from boreal peatland microcosms—effects of ozone exposure. Atmos. Environ. 39, 921–930.

Rowland, F.S., Molina, M.J., 1975. Chlorofluoromethanes in the environment. Rev. Geophys. 13, 1–35.

Running, S.W., 2006. Is global warming causing more, larger wildfires? Science 313, 927–928.

Sander, S.P., Friedl, R.R., Golden, D.M., Kurylo, M.J., Moortgat, G.K., Wine, P.H., Ravishankara, A.R., Kolb, C.E., Molina, M.J., Finlayson-Pitts, B.J., Huie, R.E., Orkin, V.L., Keller-Rudek, H., 2006. Chemical Kinetics and Photochemical Data for Use in Atmospheric Studies Evaluation Number 15.

Sawyer, R.F., Harley, R.A., Cadle, S.H., Norbeck, J.M., Slott, R., Bravo, H.A., 2000. Mobile sources critical review: 1998 NARSTO assessment. Atmos. Environ. 34, 2161–2181.

Schatz, G.C., 1989. The analytical representation of electronic potential-energy surfaces. Rev. Mod. Phys. 61, 669.

Schraufnagel, D.E., Balmes, J.R., Cowl, C.T., De Matteis, S., Jung, S.-H., Mortimer, K., Perez-Padilla, R., Rice, M.B., Riojas-Rodriguez, H., Sood, A., 2019. Air pollution and noncommunicable diseases: A review by the Forum of International Respiratory Societies' Environmental Committee, Part 2: Air pollution and organ systems. Chest 155, 417–426.

Seinfeld, J.H., Pandis, S.N., 2016. Atmospheric Chemistry and Physics: From Air Pollution to Climate Change. Wiley.

Shi, G., Yan, H., Zhang, W., Dodson, J., Heijnis, H., Burrows, M., 2021. Rapid warming has resulted in more wildfires in northeastern Australia. Sci. Total Environ. 771, 144888.

Singh, H.B., Kanakidou, M., Crutzen, P.J., Jacob, D.J., 1995. High concentrations and photochemical fate of oxygenated hydrocarbons in the global troposphere. Nature 378, 50–54.

Skov, H., Benter, Th., Schindler, R.N., Hjorth, J., Restelli, G., 1994. Epoxide formation in the reactions of the nitrate radical with 2,3-dimethyl-2-butene, cis- and trans-2-butene and isoprene. Atmos. Environ. 28, 1583–1592. https://doi.org/10.1016/1352-2310(94)90304-2

Spicer, C.W., Chapman, E.G., Finlayson-Pitts, B.J., Plastridge, R.A., Hubbe, J.M., Fast, J.D., Berkowitz, C.M., 1998. Unexpectedly high concentrations of molecular chlorine in coastal air. Nature 394, 353–356. https://doi.org/10.1038/28584

Stockwell, W.R., Lawson, C.V., Saunders, E., Goliff, W.S., 2011. A review of tropospheric atmospheric chemistry and gas-phase chemical mechanisms for air quality modeling. Atmosphere 3, 1–32.

Stotzky, G., Schenck, S., Papavizas, G.C., 1976. Volatile Organic Compounds and Microorganisms. CRC Crit. Rev. Microbiol. 4, 333–382. https://doi.org/10.3109/10408417609102303

Taft, R.W., 1956. Steric effects in organic chemistry, MS Newman, John Wiley&Sons, New York. ed.

Tapia, A., Villanueva, F., Salgado, M.S., Cabañas, B., Martínez, E., Martín, P., 2011. Atmospheric degradation of 3-methylfuran: kinetic and products study. Atmospheric Chem. Phys. 11, 3227–3241.

Tarasick, D.W., Slater, R., 2008. Ozone in the troposphere: Measurements, climatology, budget, and trends. Atmosphere-Ocean 46, 93–115. https://doi.org/10.3137/ao.460105

Thornton, J.A., Kercher, J.P., Riedel, T.P., Wagner, N.L., Cozic, J., Holloway, J.S., Dubé, W.P., Wolfe, G.M., Quinn, P.K., Middlebrook, A.M., 2010. A large atomic chlorine source inferred from mid-continental reactive nitrogen chemistry. Nature 464, 271–274.

Tran, B.N., Tanase, M.A., Bennett, L.T., Aponte, C., 2020. High-severity wildfires in temperate Australian forests have increased in extent and aggregation in recent decades. PLoS One 15, e0242484.

Urbanski, S.P., Hao, W.M., Baker, S., 2008. Chapter 4 Chemical Composition of Wildland Fire Emissions, in: Developments in Environmental Science. Elsevier, pp. 79–107. https://doi.org/10.1016/S1474-8177(08)00004-1

US EPA, O., 2015. EPI Suite™-Estimation Program Interface. URL: https://www.epa.gov/tsca-screening-tools/epi-suitetm-estimation-program-interface (accessed 7.6.22).

Valorso, R., Aumont, B., Camredon, M., Raventos-Duran, T., Mouchel-Vallon, C., Ng, N.L., Seinfeld, J.H., Lee-Taylor, J., Madronich, S., 2011. Explicit modelling of SOA formation from α-pinene photooxidation: sensitivity to vapour pressure estimation. Atmospheric Chem. Phys. 11, 6895–6910. https://doi.org/10.5194/acp-11-6895-2011

Vereecken, L., Aumont, B., Barnes, I., Bozzelli, J.W., Goldman, M.J., Green, W.H., Madronich, S., Mcgillen, M.R., Mellouki, A., Orlando, J.J., Picquet-Varrault, B., Rickard, A.R., Stockwell, W.R., Wallington, T.J., Carter, W.P.L., 2018. Perspective on Mechanism Development and Structure-Activity Relationships for Gas-Phase Atmospheric Chemistry: Perspective On Gas-Phase Atmospheric Chemical Kinetic Mechanism. Int. J. Chem. Kinet. 50, 435–469. https://doi.org/10.1002/kin.21172

Wang, X., Jacob, D.J., Eastham, S.D., Sulprizio, M.P., Zhu, L., Chen, Q., Alexander, B., Sherwen, T., Evans, M.J., Lee, B.H., Haskins, J.D., Lopez-Hilfiker, F.D., Thornton, J.A., Huey, G.L., Liao, H., 2019. The role of chlorine in global tropospheric chemistry. Atmospheric Chem. Phys. 19, 3981–4003. https://doi.org/10.5194/acp-19-3981-2019

Warneke, C., Gouw, J.A. de, Goldan, P.D., Kuster, W.C., Williams, E.J., Lerner, B.M., Jakoubek, R., Brown, S.S., Stark, H., Aldener, M., Ravishankara, A.R., Roberts, J.M., Marchewka, M., Bertman, S., Sueper, D.T., McKeen, S.A., Meagher, J.F., Fehsenfeld, F.C., 2004. Comparison of daytime and nighttime oxidation of biogenic and anthropogenic VOCs along the New England coast in summer during New England Air Quality Study 2002. J. Geophys. Res. Atmospheres 109. https://doi.org/10.1029/2003JD004424

Wayne, R.P., Barnes, I., Biggs, P., Burrows, J.P., Canosa-Mas, C.E., Hjorth, J., Bras, G.L., Moortgat, G.K., Perner, D., Poulet, G., Restelli, G., Sidebottom, H., 1991. The nitrate radical: Physics, chemistry, and the atmosphere. Atmospheric Environ. Part Gen. Top. 25, 1–203. https://doi.org/10.1016/0960-1686(91)90192-A

Wennberg, P.O., Hanisco, T.F., Jaegle, L., Jacob, D.J., Hintsa, E.J., Lanzendorf, E.J., Anderson, J.G., Gao, R.-S., Keim, E.R., Donnelly, S.G., 1998. Hydrogen radicals, nitrogen radicals, and the production of O3 in the upper troposphere. science 279, 49–53.

Went, C., 1986. Electrophilic Addition Reactions of Alkenes and Alkynes, in: Went, C. (Ed.), Ionic Organic Mechanisms, Dimensions of Science. Macmillan Education UK, London, pp. 193–219. https://doi.org/10.1007/978-1-349-07964-3_9

Wiberg, K.B., 1986. The Concept of Strain in Organic Chemistry. Angew. Chem. Int. Ed. Engl. 25, 312–322. https://doi.org/10.1002/anie.198603121

Wilkins, E.T., 1954. Air pollution and the London fog of December, 1952. J. R. Sanit. Inst. 74, 1–21.

Wingenter, O.W., Kubo, M.K., Blake, N.J., Smith Jr, T.W., Blake, D.R., Rowland, F.S., 1996. Hydrocarbon and halocarbon measurements as photochemical and dynamical indicators of atmospheric hydroxyl, atomic chlorine, and vertical mixing obtained during Lagrangian flights. J. Geophys. Res. Atmospheres 101, 4331–4340.

Wong, K.W., Stutz, J., 2010. Influence of nocturnal vertical stability on daytime chemistry: A one-dimensional model study. Atmos. Environ. 44, 3753–3760. https://doi.org/10.1016/j.atmosenv.2010.06.057

World Health Organization, 2008. The global burden of disease : 2004 update 146.

World Meteorological Organization, 2018. Scientific Assessment of Ozone Depletion: 2018, Global Ozone Research and Monitoring Project–Report No. 58, Geneva, Switzerland. page 588.

World Meteorological Organization, 1995. Scientific Assessment of Ozone Depletion: 1994. World Meteorological Organization Global Ozone Research and Monitoring Project – Report No. 37, Geneva, Switzerland, February.

World Meteorological Organization and National Aeronautics and Space Administration, 1990. Scientific assessment of stratospheric ozone: 1989. Scientific assessment of stratospheric ozone, National Aeronautics and Space Administration.

Zou, Y., Rasch, P.J., Wang, H., Xie, Z., Zhang, R., 2021. Increasing large wildfires over the western United States linked to diminishing sea ice in the Arctic. Nat. Commun. 12, 6048.

Appendices : Chapter I

App-I-1. Photolysis

The main source of energy in the atmosphere is the sunlight. This solar radiation provides energy to break chemical bonds in molecules, and lead to their fragmentation into radicals and molecules. By definition, the wavelength of the radiation is directly correlated to the energy, by :

$$E = h\nu = hc/\lambda \text{ (Eq. App-I-1)}$$

where E is the energy in J, h=6,63 10^{-34} J s the Planck constant, ν the frequency in s^{-1}, c=3.10^8 m s^{-1} the speed of light, and λ the wavelength in m. Hence, stronger a bond will be, the smaller the wavelength of the radiation must be to provide enough energy to break it. Photolysis is responsible for the fragmentation of molecules and can form radicals that will further react with O_2, NO_x and other radicals, as already discussed in the section about oxidation processes (section I-2.3)).

App-I-2. Thermal decomposition

Another pathway is thermal decomposition, through which molecules are converted back to their precursors due to thermal instability, for example, peroxynitrates and peroxy acyl nitrates. These species act as NO_x reservoirs that can be converted to peroxy radical and NO_2 (R21) and (R22) :
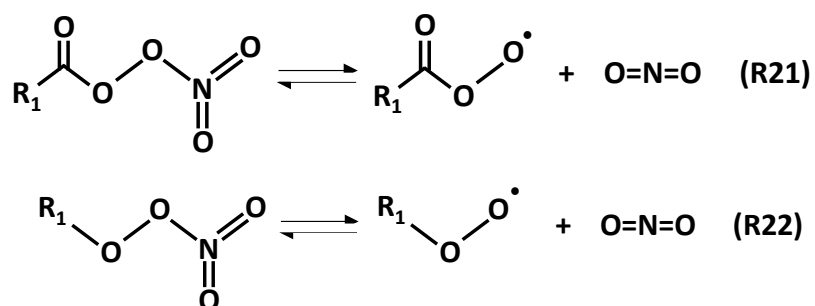
Again, these pathways lead to the formation of radicals that will further be reduced by NO or react with HO_x/RO_x species, as discussed in the section I-2.3 about the tropospheric oxidation processes.

App-I-3. Multiphase and heterogenous processes

Other processes occurring in the aqueous phase or multiphase are briefly discussed in this subsection, but not detailed, since this thesis only focuses on the gas-phase oxidation processes. These other processes include wet deposition and hydrolysis. Wet deposition is effective to remove gas-phase molecules with high Henry's law coefficients, e.g., oxygenated products formed throughout atmospheric oxidation reactions, with polar oxygenated groups that enhance their ability to dissolve into the liquid phase. The largest wet deposition occurs onto cloud droplets, and represent a lifetime of about 10 days similar to water (Brasseur et al., 1999). VOCs can also partition into the organic condensed phase of aerosols. The

SOA uptake will depend in the nature of the aerosol coating, e.g., most aerosols are coated with water and VOC uptake will require a high proton affinity with H_2O (Atkinson, 1997; Brown et al., 2013).

References

Atkinson, R., 1997. Gas-Phase Tropospheric Chemistry of Volatile Organic Compounds: 1. Alkanes and Alkenes. J. Phys. Chem. Ref. Data 26, 215–290. https://doi.org/10.1063/1.556012

Brasseur, G.P., Orlando, J.J., Tyndall, G.S., 1999. Atmospheric chemistry and global change Oxford University Press, New York. 654. pp.

Brown, S.S., Dubé, W.P., Bahreini, R., Middlebrook, A.M., Brock, C.A., Warneke, C., de Gouw, J.A., Washenfelder, R.A., Atlas, E., Peischl, J., Ryerson, T.B., Holloway, J.S., Schwarz, J.P., Spackman, R., Trainer, M., Parrish, D.D., Fehshenfeld, F.C., Ravishankara, A.R., 2013. Biogenic VOC oxidation and organic aerosol formation in an urban nocturnal boundary layer: aircraft vertical profiles in Houston, TX. Atmospheric Chem. Phys. 13, 11317–11337. https://doi.org/10.5194/acp-13-11317-2013

Keller-Rudek, H., Moortgat, G.K., Sander, R., Sörensen, R., 2013. The MPI-Mainz UV/VIS spectral atlas of gaseous molecules of atmospheric interest. Earth Syst. Sci. Data 5, 365–373.

Chapter II :
Measuring and estimating OH reaction rate coefficients with a set of industrial compounds (halogenated alkenes)*

Summary of the chapter II

The Chapter II focuses on the measurement and estimation of the kinetics of OH reactions with a set of industrial compounds, specifically halogenated alkenes. The experimental section describes the pulsed-laser photolysis – laser-induced fluorescence, PLP–LIF, technique employed to measure the temperature-dependent rate coefficients of the OH reactions of two hydrofluoroolefins, $CH_2=CHCF_3$ and $CF_2HCH=CF$.

The next section presents a new predictive method developed for addition reactions of OH radical to haloalkenes, CHX, which differs in its principles from the most commonly used and updated approach from Atkinson and co-workers (Kwok and Atkinson, 1995). This method is an update of the method presented by (Tokuhashi et al., 2021), which has been adapted to include temperature dependence and additional substitutions. The extension to other oxidation reactions, i.e., Cl, O_3, and NO_3 reactions, is also presented. The applicability of the SAR to Cl and O_3 reactions is discussed. This new structure-activity relationship, SAR, represents the first approach to estimating the temperature-dependent rate coefficient for the addition reactions of OH, and NO_3 with CHX alkenes.

In the results and discussion section, the performance of the SAR at room temperature, compared to the other existing literature methods, and as a function of temperature are presented. New experimental measurements are presented for the reactions of $CH_2=CHCF_3$ and $CF_2HCH=CF$ with OH, the latter representing the first reported measurement to date. The application of the SAR is tested on these new measurements, and the validity and limitations of this approach are discussed.

This chapter concludes with the good prediction ability of this new SAR for these CHX alkenes and the innovation of deriving temperature-dependent predictions for CHX (halogenated alkenes) reactions with OH and NO_3. However, the differences in the mechanism for Cl and O_3 compared to OH and NO_3 are found to inhibit the applicability of this SAR for temperature-dependence predictions. Also, the method applies to a restricted range of compounds, CHX alkenes, which are mostly emitted from industrial processes, and it would be useful to derive a method that applies to a more diverse selection of natural compounds, such as those emitted from biomass burning, e.g., furans, oxygenated compounds, and oxidation products. This will be the focus of the following chapters.

Résumé du chapitre II

Le chapitre II se concentre sur la mesure et l'estimation des coefficients de vitesses des réactions OH avec un ensemble de composés industriels, en particulier les alcènes halogénés. La section expérimentale décrit la technique de photolyse laser pulsée – fluorescence induite par laser, PLP–LIF, employée pour mesurer la cinétique des réactions OH en fonction de la température de deux hydrofluorooléfines, $CH_2=CHCF_3$ et $CF_2HCH=CF$.

La section suivante présente une nouvelle méthode prédictive développée pour les réactions d'addition du radical OH aux haloalcènes, CHX, qui diffère dans ses principes de l'approche la plus couramment utilisée et mise à jour par Atkinson et ses collaborateurs (Kwok and Atkinson, 1995). Cette méthode est une mise à jour de la méthode présentée par (Tokuhashi et al., 2021), qui a été adaptée pour inclure la dépendance de la température et des substitutions supplémentaires. L'extension à d'autres réactions d'oxydation, à savoir les réactions Cl, NO_3 et O_3, est également présentée. Cette nouvelle relation structure-activité, SAR, représente la première approche pour estimer le coefficient de vitesse en fonction de la température pour les réactions d'addition de OH, Cl, NO_3 et O_3 avec les alcènes CHX.

La section *résultats et discussion* présente les performances de la SAR à température ambiante, comparées aux autres méthodes existantes dans la littérature, et en fonction de la température. De nouvelles mesures expérimentales sont présentées pour les réactions de $CH_2=CHCF_3$ et $CF_2HCH=CF$ avec OH, cette dernière représentant la première mesure rapportée à ce jour. L'application de la SAR est testée sur ces nouvelles mesures, et la validité et les limites de cette approche sont discutées.

Ce chapitre conclut sur la bonne capacité de prédiction de cette nouvelle SAR pour ces alcènes CHX et sur l'innovation que représente le fait de dériver des prédictions en fonction de la température pour les réactions CHX (alcènes halogénés) avec OH et NO_3. Cependant, les différences dans le mécanisme pour Cl et O_3 par rapport à OH et NO_3 s'avèrent empêcher l'applicabilité de cette SAR pour les prédictions en fonction de la température. En outre, la méthode s'applique à une gamme restreinte de composés, les alcènes CHX, qui sont principalement émis par les processus industriels, et il serait utile de dériver une méthode qui s'applique à une sélection plus diversifiée de composés naturels, tels que ceux émis par la combustion de la biomasse, par exemple les furannes, les composés oxygénés et les produits d'oxydation. Les chapitres suivants seront consacrés à cette question.

Introduction

The implementation of substitutes to ozone-depleting substances (ODSs) has attempted to mitigate stratospheric ozone depletion, minimize harmful impacts on climate, and environment (Burkholder et al., 2015). For this purpose, long-lived substances with high global warming potential (GWP) and high ODP, e.g., dichlorodifluoromethane CCl_2F_2, have been replaced by reactive compounds, e.g., species containing abstractable H atoms or reactive carbon-carbon double-bonds, with lower GWP and shorter lifetimes (Hodnebrog et al., 2013). Among these ODSs substitutes, hydrofluoroolefins (HFOs) are gaining popularity (Hashimoto et al., 2019).

HFOs are now produced in large quantities for various industrial applications as refrigerants, propellants, and foam-blowing agents for their specific thermal properties and stability, e.g. (Hu et al., 2020; Nair, 2020), and many new species are patented each year. Composed of hydrogen, fluorine, carbon and an olefinic carbon double-bond, they constitute a subset of the broader class of haloalkenes, which contain any combination of an olefinic bond and halogen substitutions. These olefins have many other uses as solvents, cleaning fluids and raw materials for polymers. As a result of their widespread use, the emissions of HFOs into the atmosphere are increasing and some atmospheric monitoring programs are now able to detect them (Rust et al., 2022).

In the atmosphere, they are a source of perfluorocarboxylic acids, PFCAs, such as trifluoroacetic acid, TFA, which may have an immediate or long-term harmful effect on the biosphere (e.g. (Wang et al., 2014)), the environment (e.g., (Ahrens et al., 2014; Land et al., 2018)) or human health (e.g., on fetal and childhood growth (Land et al., 2018; Wang et al., 2016)). Longer-chain PFCAs, such as perfluorooctanoic acid, have been found to be toxic for people, animals, and aquatic environments (Gilliland et al., 1993; Kudo et al., 2003; Post et al., 2012; Steenland et al., 2010).

The primary removal of HFOs and related haloalkenes from the troposphere is the electrophilic addition of the OH radical to their double bonds. Given that a wide variety of haloalkenes are already in use, and that global demand for efficient and environmentally-friendly refrigeration technologies is increasing (Mota-Babiloni et al., 2021), it is likely that the OH reaction rate coefficients of many new haloalkenes proposed as replacements have not yet been measured. Yet, it is useful to know accurately the OH reaction rate coefficient in order to inform the atmospheric models that assess their contribution to air pollution, stratospheric ozone depletion, and global warming (Burkholder et al., 2015). In order to examine the impact of these compounds when they are emitted into the atmosphere before considering their implementation, it is therefore desirable to have reliable estimates of these rate coefficients, which is the main objective of this work.

Structure-activity relationships (SARs) are widely used to estimate reaction rate coefficients by correlating between the chemical structure of a molecule and its reactivity (Vereecken et al., 2018). Based on trends observed in the available kinetic data, the SARs can derive satisfactory estimations that can be applied to a broader set of compounds for which kinetic data are not available. Similarly, as atmospheric chemical models become more explicit and comprehensive, SARs need to be developed and refined (Vereecken et al., 2018). In addition, as the development of this SAR involves parameterizing the chemical reactivity, this work also aims to improve our understanding of the chemical mechanism of the electrophilic addition reaction of the OH radical to substituted alkenes.

In the literature, the rate coefficients of 77 halogenated alkenes have already been determined, especially for the molecules containing ˗CHX, where X=F, Cl, Br substitution patterns, and temperature dependence are also available for 64 cases (McGillen et al., 2020). Halogenated substitutions have a high capacity to modify the reactivities of molecules. As a result, the haloalkenes dataset can be a useful training set for investigating the reactivity of unsaturated organic volatile compounds, UVOCs, in a systematic way. This Chapter focuses on developing, based on previous work by Tokuhashi and co-workers, (Tokuhashi et al., 2021) a new structure-activity relationship (SAR) to predict temperature dependent (200˗400K) rate coefficients of similar reactions (˗$C_nH_mX_p$ alkenes + OH where X=F, Cl, Br and m+p=2n+1) for atmospherically relevant temperature ranges (Michelat et al., 2022). To date, there are no other SAR estimates the temperature dependence of these reaction rate coefficients. Room temperature OH reaction rate coefficients of haloalkenes, k_{298}, was estimated using the AOPWIN v1.92 module of the estimation programs interface EPI Suite, (Meylan et al., 1993; US EPA, 2015) which uses the approach of Kwok and Atkinson (Kwok et al., 1995). The more recent method of Tokuhashi et al. to predict k_{298} was applied (Tokuhashi et al., 2021, 2019, 2018a, 2018c, 2018b). The addition reactions studied in this chapter are assumed to be at their high-pressure limit at atmospheric pressure, and is therefore not a parameter that influences the kinetics in this case.

These calculations were compared with new laboratory measurements of the absolute OH reaction rate coefficients as a function of the temperature of two HFOs, HFO-1243zf ($CH_2=CHCF_3$, 3,3,3-trifluoropropene) (212–367 K) and HFO-1234zc ($CF_2HCH=CF_2$, 1,1,3,3-tetrafluoropropene) (223–373 K), obtained using the pulsed-laser photolysis–laser-induced fluorescence (PLP–LIF) technique (Michelat et al., 2022). Studies have reported kinetic data for OH, Cl, and O_3 chemistry (temperature and pressure dependency), (Andersen et al., 2005; Ballesteros et al., 2017; Calvert et al., 2015; González et al., 2015; Nakayama et al., 2007; Orkin et al., 1997; Tokuhashi et al., 2018a), with some product analyses for OH and Cl chemistry, (Ballesteros et al., 2017; Nakayama et al., 2007). To the best of our knowledge, the rate coefficients on the HFO-1243zf reaction with NO_3 has not been reported, and the reactions of $CF_2HCH=CF_2$ with any of the four oxidants noted

here are not studied. $CF_3CH=CH_2$ is expected to form TFA through atmospheric degradation, while $CF_2HCH=CF_2$ is not. Additionally, many compounds containing the $-CF_3$ group (such as HFO-1243zf) have been studied, while compounds containing the $-CF_2H$ substitution (such as HFO-1234zc) are much less well-characterized, which is useful for providing estimation tools with new structural patterns.

II-1. Experimental

II-1.1. Pulsed-laser photolysis – laser-induced fluorescence (PLP–LIF) set-up

The temperature-dependent OH reaction rate coefficients of two HFOs, $CF_3CH=CH_2$ (T=212–367K) and $CF_2HCH=CF_2$ (T=223–373K) were measured using a pulsed-laser photolysis–laser-induced fluorescence (PLP–LIF) apparatus (Figure II-9) described elsewhere (Mellouki et al., 1995; El Othmani et al., 2021). The PLP–LIF employs lasers to generate free radicals, excite them to generate induced fluorescence emission, and follow their emitted fluorescence signal intensity evolution over time (e.g., Hollas, 2004; Le Calvé et al., 1998; Mellouki et al., 1995). For this purpose, an excimer laser emitting at 248nm induces the photolysis of the radical precursors, to form OH radicals, (pulsed-laser photolysis) and a Nd:YAG laser coupled with a dye laser and a doubling crystal emits a beam at 282nm (laser-induced fluorescence) that generates fluorescence of the OH radicals. The two lasers are triggered to the center of the reaction cell containing the mixture of bath gas (He or Ar), reactants ($CF_3CH=CH_2$ or $CF_2HCH=CF_2$), and radical precursors (hydrogen peroxide (H_2O_2) or nitric acid (HNO_3)). By varying the delay, Aτ, between both laser pulses, i.e., between the formation of radicals t=0 and the induction of fluorescence at reaction time t=Aτ, fluorescence signal intensity can be evaluated at different reaction times to retrieve its decay over time.

Set-up

The reaction cell is a 200 cm^3 Pyrex vessel inside which OH radicals are produced by photolysis of hydrogen peroxide (H_2O_2) or nitric acid (HNO_3) using a pulsed KrF excimer laser (PLP) (λ = 248 nm, 25–85 mJ pulse^{-1} cm^{-2} in the reaction cell):

$$H_2O_2 + h\nu \rightarrow 2OH \qquad \text{(Eq. II-1)}$$

$$HNO_3 + h\nu \rightarrow OH + NO_2 \quad \text{(Eq. II-2)}$$

The initial concentration of hydroxyl radicals in the PLP–LIF reaction cell is estimated from:

$$[OH]_0 = F_{248nm}\ \varphi_{OH}\ \sigma_{248nm}\ [\text{precursor}]_0 \qquad \text{(Eq. II-3)}$$

where σ_{248nm} are the absorption cross sections of H_2O_2 and HNO_3 at 248 nm (9×10^{-20} cm^2 molecule^{-1} and 2×10^{-20} cm^2 molecule^{-1}, respectively), (Burkholder et al., 2020) φ_{OH} the OH quantum yields of the precursors ($\varphi_{OH/H2O2}$ =0.97 and $\varphi_{OH/HNO3}$ =0.88), (Atkinson et al., 2004), F_{248nm} is the photolysis laser fluence at the photolysis wavelength (in photon cm^{-2} s^{-1}), and [precursor]$_0$ the concentration of the precursors (H_2O_2 or HNO_3) in molecule cm^{-3}.

In the case of HNO$_3$, the concentration of the precursor is measured directly by Fourier-transform infrared spectroscopy (FTIR). In the case of H$_2$O$_2$, the concentration is estimated using the following relationship:

$$[precursor]_0 = k'/rate, \text{ with rate} = 2.9\times10^{-12}\exp(-160/T) \quad \text{(Eq. II-4)}$$

where T the temperature in K, k' the pseudo-first-order rate coefficient for OH loss in s^{-1}, *rate* the temperature-dependent rate coefficient of the reaction of OH with the precursor H$_2$O$_2$ in s^{-1} (Burkholder et al., 2020).
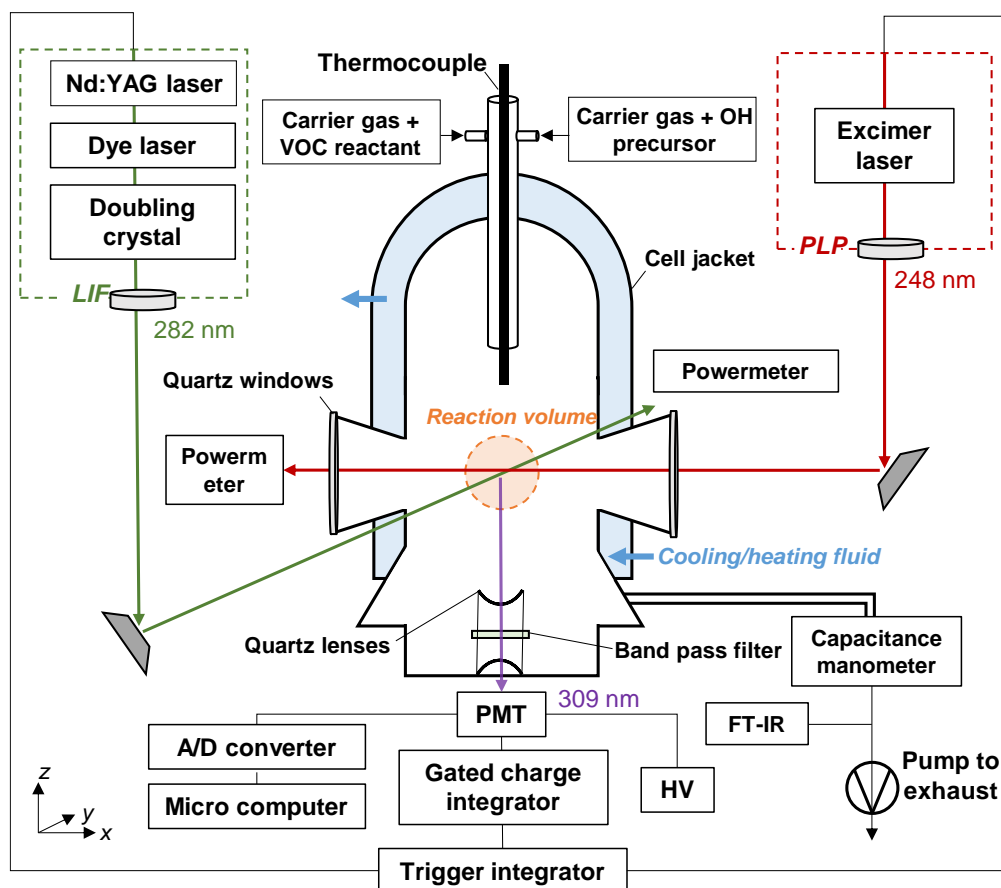
Figure II-9 : Schematic diagram of the pulsed laser photolysis-laser induced fluorescence experimental set-up.

During these experiments, the initial hydroxyl radical concentrations, [OH]$_0$, were varied in the ranges (1.7–30.6) $\times$ 10^{10} molecule cm^{-3} and (6.7–279.0) $\times$ 10^{10} molecule cm^{-3} for the reaction with CF$_3$CH=CH$_2$ and CF$_2$HCH=CF$_2$, respectively (see (Eq. II-4), Table App-II-1 and Table App-II-2 in Appendices section App-II-1 for the experimental conditions). The concentration of the HFOs, [HFO], are presented for each experiment in Table App-II-1 and Table App-II-2. The output of the Nd:YAG pumped dye laser (Rhodamine 590) is doubled and subsequently employed to excite the Q$_1$1 line in the (1,0) band of the (A$^2\Sigma^+$,v'=1) $\leftarrow$ (X$^2\Pi$,v''=0) transition of OH radicals near 282 nm. Resulting OH fluorescence signals emitted from the (A$^2\Sigma^+$, v'=1) $\rightarrow$ (X$^2\Pi$, v''=1) and (A$^2\Sigma^+$, v'=0) $\rightarrow$ (X$^2\Pi$, v'=0) transitions (308–316 nm) are detected by a photomultiplier tube, equipped with a narrow band pass filter centered at 309 nm (FWHM = 7.6 nm) to minimize the detection

of scattered light by the probe laser, (Le Calvé et al., 1998; Mellouki et al., 1995) and are integrated using a gated charge integrator over a fixed period. Collisional quenching of the OH($^2\Sigma_1^+$) is minimized by using a bath gas that reduces energy transfer, such as helium or argon (Curme et al., 1952). The energies of both laser beams are measured at the exit of the reaction cell with a power meter. The resulting OH fluorescence signal is detected by the PMT.

Absolute-rate method

The delay Aτ between the photolysis (PLP) and probe laser (LIF) pulses is varied from 10 μs to 10 ms, and the fluorescence signal (S_t) from 100 probe laser pulses at 10 Hz was averaged for each delay time to obtain the temporal profiles of the OH radical signal, which is proportional to its concentration, [OH]$_t$, see (Eq. II-6). Usually, 10 delay times are used to construct an OH-decay profile. Under pseudo-first-order conditions in [OH] ([HFO] ≫ [OH]), the following relationship is obeyed:

$$\ln\left(\frac{[OH]_t}{[OH]_0}\right) = \ln\left(\frac{S_t}{S_0}\right) = -(k\times[HFO] + k_d)t = -k't \qquad \textbf{(Eq. II-5)}$$

The pseudo-first-order OH decay rate coefficients in the presence (k') and absence (k_d) of the HFO reactant are directly measured (Eq. II-6). OH radicals are lost through reaction with the HFO, by reaction with the OH precursor (H$_2$O$_2$ or HNO$_3$) and by diffusion out of the detection zone. These last two losses were taken into account in the background removal rate coefficient, k_d, including the reaction of OH with H$_2$O$_2$ and diffusion (Mellouki et al., 1995). CF$_3$CH=CH$_2$ and CF$_2$HCH=CF$_2$ concentrations were varied over (0.19–65) and (2.8–47) × 10^{13} molecule cm^{-3}, respectively. The absolute second-order rate coefficients, k (in cm^3 molecule^{-1} s^{-1}), at a given pressure and temperature were derived from the slope of the (k'-k_d) as a function of [HFO] using a linear regression. They are presented for certain temperatures for CF$_3$CH=CH$_2$ and CF$_2$HCH=CF$_2$ with the experimental conditions in Table App-II-1 and Table App-II-2 in Appendices section App-II-1.

The mixture of the OH precursor, HFO, and bath gas was flowed through the reaction cell in order to avoid the accumulation of products in the reaction cell. Calibrated mass flow controllers were used to quantify gases flowing into the system. The temperature of the bath gas was regulated by circulating a cooling (ethanol) or heating fluid (ethanol/monopropylene glycol) through the outer jacket that surrounds the reactor and measured using a retractable thermocouple (212–373 K to within ± 0.1 K). The pressure in the reaction cell was continuously measured with two calibrated pressure gauges (1000 Torr). Concentrations of the reactants, CF$_3$CH=CH$_2$ and CF$_2$HCH=CF$_2$, were both monitored online at 298 K using a 1000 cm path length Fourier-transform infrared (FTIR) spectrometer (1 cm^{-1} resolution, 500–4000 cm^{-1} range) located downstream of the LIF reactor. The integrated band strengths were measured in the PLP–LIF set-up (see *Absolute IR absorption cross sections* below) and corrected for pressure and temperature differences

between the LIF reactor and the FTIR cell. They were then used to calculate the concentrations of the HFOs in the reactor.

Absolute IR absorption cross sections

The integrated IR absorption cross sections, S_{int}, which represents the absolute IR cross section $\sigma(\tilde{v})$ integrated over a specific wavenumber range $d\tilde{v}$, can be determined through the Beer–Lambert law as follows:

$$S_{int} = \int\sigma(\tilde{v})d\tilde{v} = \int(A(\tilde{v})/l)[HFO]d\tilde{v} \quad \text{(Eq. II-6)}$$

where $A(\tilde{v})$ (in base e) is the absorbance at a given wavenumber $\tilde{v}$, l is the optical path length in cm, and [HFO] is the concentration of $CF_3CH=CH_2$ or $CF_2HCH=CF_2$ inside the gas cell in molecule cm^{-3}. The absolute IR cross section $\sigma(\tilde{v})$ can be evaluated from the slope of the linear regression of $A(\tilde{v})/l$ versus [HFO], as presented in Figure II-10. The integrated IR absorption cross sections, S_{int}, defined as the integrated $\sigma(\tilde{v})$ over a specific wavenumber range, are obtained by applying the Beer–Lambert law as in (Eq. II-7) in terms of integrated absorbances (A_{int}).

Table II-1 : $CHF_2CH=CF_2$ integrated band strengths, $S_{int,}$ measured at wavenumber ranges relevant to the atmospheric window using manometrically prepared mixtures in He, ideal gas, and Beer-Lambert laws. Individual IR spectra were measured at 1 cm^{-1} resolution with 128 co-added scans.

CHF$_2$CH=CF$_2$	
Wavenumber Range (cm^{-1})	$(S_{int} \pm 2\sigma)^a$ (10^{-17} cm molecule^{-1})
760 – 846	0.48 ± 0.05
848 – 998	1.79 ± 0.04
998 – 1480	12.4 ± 0.02
1689 – 1827	5.16 ± 0.07
760 – 2000	20.0 ± 0.02

^{a} Uncertainties are the precision of linear least-square analysis at 95 % level of confidence (2σ).

Table II-2 : $CF_3CH=CH_2$ integrated band strengths, $S_{int,}$ measured at wavenumber ranges relevant to the atmospheric window using manometrically prepared mixtures in He, ideal gas, and Beer-Lambert laws. Individual IR spectra were measured at 0.5 cm^{-1} resolution with 100 co-added scans.

CF$_3$CH=CH$_2$	
Wavenumber Range (cm^{-1})	$(S_{int} \pm 2\sigma)^a$ (10^{-17} cm molecule^{-1})
1120-1220	7.69 ± 0.30
1255-1340	2.33 ± 0.06
1400-1700	1.00 ± 0.28

^{a} Uncertainties are the precision of linear least-square analysis at 95 % level of confidence (2σ).
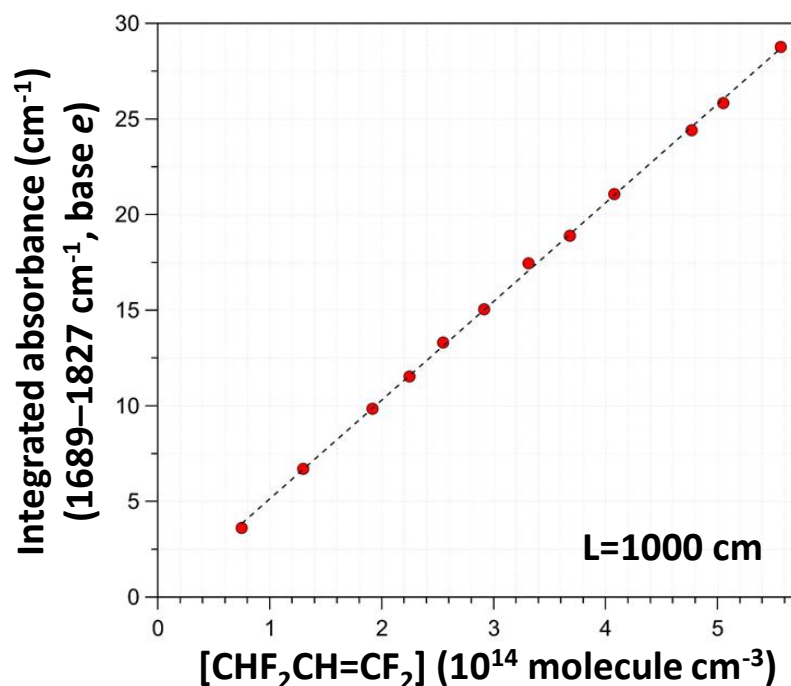
Figure II-10 : Typical Beer-Lambert plot showing the integrated band strength determination at the wavenumber range used to obtain [$CHF_2CH=CF_2$] in OH kinetic analysis, S_{int}(1689-1827 cm^{-1}) = (5.16 $\pm$ 0.07) cm molecule^{-1}. The quoted uncertainties are obtained from the 2σ precision of the linear least-squares fit of the measured integrated absorption versus concentration (Michelat et al., 2022).

II-1.2. Chemicals

All the gases used were UHP certified to be >99.9995 % (Air Liquide) pure. $CF_3CH=CH_2$ (3,3,3-trifluoropropene) and $CF_2HCH=CF_2$ (1,1,3,3-tetrafluoropropene) were purchased from SynQuest Labs (CAS: 677-21-4, purity 99%) and (CAS: 4556-24-5, purity 98%), respectively. Two mixtures were prepared (1% and 10% in He). A 50% by weight solution of H_2O_2 was obtained from Sigma Aldrich and purified air was bubbled through it for several days to concentrate it. Purified nitric acid in the gas phase was obtained by dehydrating high-purity nitric acid HNO_3 (70% in H_2O) in solution by adding concentrated sulphuric acid H_2SO_4 (>95%) dropwise in a 1:2 ratio. Precautions have been taken to prevent the formation of NO_2 in this sample over time by maintaining it at a temperature ≤0°C and preventing the entry of ambient air; the purity was confirmed by IR analysis.

II-2. SAR techniques for estimating rate coefficient of OH + haloalkenes, and extension to Cl, NO_3 and O_3

II-2.1. Literature methods

In this section, the existing methods to predict k_{298} from the structure of an olefin are briefly described. The Tokuhashi method (Tokuhashi et al., 2021, 2019, 2018a, 2018c, 2018b) and the automated implementation

of Atkinson's SAR (Kwok et al., 1995) in the EPI Suite tool (Meylan and Howard, 1993) are both limited to room temperature (298 K).
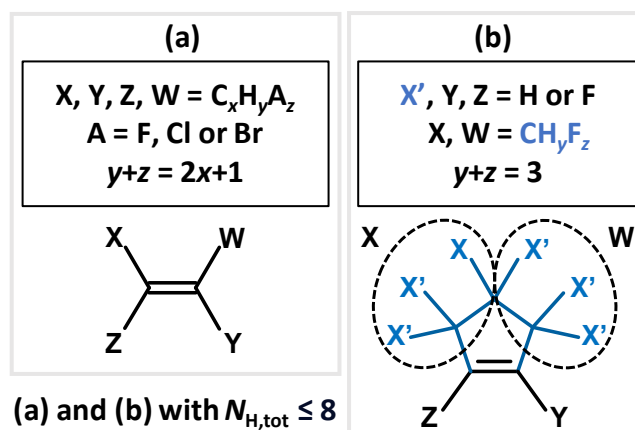
Figure II-11 : Schematic of the structure of the alkenes used in the models, with (a) being the description applied for acyclic alkenes where X, Y, Z, W substituents are defined by $C_xH_yA_z$ where A = F, Cl or Br and where y + z = 2x+1, where x ≥ 0 and (b) referring specifically to the cyclic olefins containing H and F substitutions only, both (a) and (b) defined for molecules with a total hydrogen count, $N_{H,tot}$, of ≤8. In structure (b), X', Z, and Y substituents can be either H or F atoms. The two groupings X and W are defined by splitting the cycle into two symmetrical chains, each possessing three X' atoms in the case of a cyclopentyl group. In Tokuhashi et al.'s recent work (Tokuhashi et al., 2021) only linear olefins, as in structure (a), are described, excluding Br substitutions and limited to values of x ≤ 2.

II-2.1.1. Atkinson approach

The approach of Kwok and Atkinson is implemented in the EPI Suite software that outputs estimations of the gas-phase hydroxyl radical and ozone reaction rate coefficients at 298 K (Meylan and Howard, 1993). Additionally, based on Kwok and Atkinson, 1995, it is possible to derive temperature-dependent rate coefficient from this approach, but this has not so far been implemented in the current version of EPI Suite. The work of Atkinson and co-workers, with the most recent update described in Kwok and Atkinson's paper, (Kwok and Atkinson, 1995) estimates the reactivity of a large variety of volatile organic compounds (VOCs). For halogenated alkenes, the total OH reaction rate coefficient is predicted using the reactivity of the C=C bond towards OH radical electrophilic addition with negligible contributions from H-abstraction.

The reactivity of the alkenes is expected to be affected by the substituents' types, their electron-withdrawing inductive effects, their electronegativity, their interaction with neighboring groups and their respective positions. For a haloalkene of formula X(Z)C=C(W)Y (see structure (a) in Figure II-11), the room temperature rate coefficient towards the OH reaction is calculated as follows:

$$k_{298,Atkinson}X(Z)C=C(W)Y = k_{base} \times F(X) \times F(Y) \times F(Z) \times F(W) \qquad \text{(Eq. II-7)}$$

where k_{base} is the base rate coefficient of the associated generic alkene, -C=C, -C=C-, >C=C, >C=C- or >C=C<, and its stereoisomer (*cis* or *trans*), and F(X), F(Y), F(Z), F(W) are multiplicative constants that are specific to

70

a functional group (X, Y, Z, W being halogens or alkyl groups) (Kwok et al., 1995). Further details on the method can be found in the original work of Atkinson, (Atkinson, 1988, 1987, 1986) and (Kwok and Atkinson, 1995) or the website of the EPI Suite tool (Meylan and Howard, 1993).

For halogenated alkyl groups, i.e., allylic halogen substitutions, "F(–Halogen)" is set at a constant value of 0.76 in the Atkinson approach in order to describe the substitution effect (Kwok et al., 1995). If halogen substitutions of the alkenes are more distant than the allylic position with respect to the olefinic bond, these compounds are treated as regular alkenes. Consequently, different structures (e.g., compounds with alkyl substituents of various chain length) are estimated to a unique value and not distinguished, which we can be defined as a degeneracy effect.

II-2.1.2 Tokuhashi's method - Diagonal substituent factors:

Tokuhashi and co-workers recently developed a method for estimating OH reaction rate coefficients of halogenated alkenes by considering the haloalkene's reactivity to be related to the types and the position of the substituents around the double bond (Tokuhashi et al., 2021, 2019, 2018a, 2018c, 2018b). The diagonal substitution pattern across the olefinic bond was found to be a critical parameter that alters the rate coefficient.

In their previous work, (Tokuhashi et al., 2018c) Tokuhashi and co-workers observed that the experimental rate coefficients of halogenated ethenes are determined by the type of substituents attached to the olefinic bond but also by that of the substituent on the opposite side of the double bond. By considering the diagonal position of the substituents, Tokuhashi et al. have developed a method that reproduces most of the available kinetic data within a factor of two (Tokuhashi et al., 2021, 2019, 2018a, 2018c, 2018b).

Substituent factors are designed to account for the changes in the electron density in the π-orbitals, which are expected to be of primary importance in describing the reactivity of the double bond towards an electrophilic addition of OH. The calculated OH rate coefficient at room temperature is obtained by:

$$k_{298,Tokuhashi}X(Z)C=C(W)Y = k_{base} \times F(X\text{-}C=C\text{-}Y) \times F(Z\text{-}C=C\text{-}W) \qquad \text{(Eq. II-8)}$$

The base rate coefficient, k_{base} = 1.0 × 10^{-12} cm^3 molecule^{-1} s^{-1}, (Tokuhashi et al., 2021, 2019) is that of the unsubstituted case. The terms F(X-C=C-Y) and F(Z-C=C-W) are the substituent factors for the structures shown in parentheses. The X-C=C-Y and Z-C=C-W represent diagonal positions (see structure (a) in Figure II-11), as defined by Tokuhashi et al.

II-2.2. This work (modified Tokuhashi approach)

In this section, an updated and extended version of the Tokuhashi method is presented (Michelat et al., 2022). This SAR estimates temperature-dependent rate coefficients for the CHX alkenes dataset, for an

extended range of compounds. This method was then extended to apply to more tropospheric oxidants, including Cl, NO_3 and O_3, by following the same method as described in the following sections II-2.2.2.2 and II-2.2.2.3.

II-2.2.1. Estimating k_{OH} at T=298K

In the original work of Kwok and Atkinson (1995), and that of Tokuhashi et al. (2021), the OH-addition rate coefficient for cycloalkenes is not estimated. In the EPI Suite tool, in contrast, k_{298} are predicted for cyclic compounds by treating them as linear alkenes with a structure separated into two symmetrical chains on both sides of the olefinic bond. Based on (Eq. II-8), the OH-reaction rate coefficient of $CF_3CF=CFCF_3$ (structure #54, see Figure II-16) estimated by EPI Suite is equal that of the cyclic perfluorocyclopentene (#63). However, the acyclic compound in this case has a much larger experimental rate coefficient than the cyclic compound. Hence, the ring strain, and/or the supplementary steric effects encountered in cyclic structures compared to linear geometries may be the reason for the difference in reactivities (Atkinson et al., 1983). To account for this, a single additional factor F_{cycle} was added in our approach, although it remains uncertain, given that experimental data are sparse for cyclic haloalkenes. As new data become available, this factor may be expanded as a function of ring size.

Hence, the model built in the present work estimates k_{298} for the electrophilic addition reaction of OH with molecule X(Z)C=C(W)Y from the following formula:

$$k_{298,calc} = k_{base} \times F(X\text{-}C=C\text{-}Y) \times F(Z\text{-}C=C\text{-}W) \times F_{cycle} \qquad \textbf{(Eq. II-9)}$$

where $k_{base} = 1.0 \times 10^{-12}$ cm^3 molecule^{-1} s^{-1}, which is intended to represent the base-level reaction rate coefficient of electrophilic addition to the >C=C< bond. The F-factors in (Eq. II-10) are the substituent factors, $F(X\text{-}C=C\text{-}Y)$ and $F(Z\text{-}C=C\text{-}W)$ that account for the diagonal structure around the olefinic bond (see structures (a) and (b), Figure II-11) and the F_{cycle} that accounts for an olefin's cyclic structure. If alkenes are acyclic, F_{cycle} is 1. Because it is necessary to distinguish each diagonal substitution across the double bond in this method, the rate coefficients reported for undefined stereoisomers or a mixture of E and Z isomers have been excluded from the training set.

The calculated k_{298} values were optimized using a numerical solver that optimized the F-factor values in order to minimize the relative difference between estimated and experimental results, defined as $RE(\%)=100\times(k_{298,calc}-k_{298,meas})/k_{298,meas}$. The resulting optimized F-factors are presented in section II-3.2.1. Additionally, our SAR provides a method to estimate the temperature-dependent reaction rate coefficient, $k(T)$, based on the values of the calculated k_{298}, and the Arrhenius equation, as presented in section II-3.2.2.

II-2.2.2. The relationship between k_{298} and E_a/R for OH, Cl, NO$_3$ and O$_3$

The experimental values of E_a/R can be correlated with the logarithm of the experimental rate coefficients at room temperature, $\ln(k_{298})$, for the reaction with OH, Cl, NO$_3$ and O$_3$. It is obvious that the availability of temperature-dependent kinetic data varies for these oxidants, with 64 Arrhenius parameters measured for OH, 6 for Cl, 16 for O$_3$ and 9 for NO$_3$. Thus, the parametrization is expected to be less reliable when less data was available, i.e., for Cl, O$_3$ and NO$_3$. However, in order to present the method that can be improved later when more data are available, additional details on the methods described in this section II-2.2.2 are provided in section App-II-2 of the Appendices together with all the Arrhenius parameters and rate coefficients measured and predicted, when available, for the 64 reactions in the section App-II-3 of the Appendices. The approach to predict the Arrhenius parameters of the Cl reaction rate coefficients was not found to be effective; the associated parameterization (section App-II-2) and results (section App-II-3.2) are presented in the appendices as a preliminary study only.

II-2.2.2.1. OH reaction

Next, the effect of temperature on alkene and haloalkene reaction rate coefficients was investigated by correlating room temperature rate coefficients to activation energy, and it is clear that the experimental temperature dependence factor (E_a/R) switches from a positive to a negative value as the rate coefficient at 298 K becomes larger (Michelat et al., 2022). The experimental E_a/R was correlated to the reactivity at 298K (see Figure II-12) and this correlation was fitted adequately by an inverse sigmoidal function for E_a/R ranging from -784 K to +920 K, as:

$$\ln\left(\frac{k_{298}}{2.7\times10^{-10}}\right) = \frac{-8.6}{\left[1+\exp\left(\frac{-300\text{ K}-\frac{E_a}{R}}{363\text{ K}}\right)\right]} \qquad \textbf{(Eq. II-10)}$$

where $\ln(k_{298})$ is the natural logarithm of the room temperature rate coefficient k_{298} in cm^3 molecule^{-1} s^{-1}, and E_a/R is the Arrhenius activation energy in Kelvin, both of which are measured properties, and remaining values being optimized fitting parameters. (Eq. II-11) is a parametrization function and does not provide physical meanings for the parameters. The reactions with the lowest activation energies have a rate coefficient close to their collision limits, which results in the lower limit in the activation energies, E_a/R. Although the exact size of the collision rate coefficient will vary depending on several parameters such as the size or the polarizability of the molecules involved, it is unlikely that the probability of collision between the OH radical and the olefinic bond would change drastically within the training set.

It is hypothesized that halogenated substitutions can withdraw electrons from the olefinic bond, e.g., in perfluoro olefins, and that there is a limit to the extent of this withdrawal. Indeed, the less reactive

molecules in this study display similar E_a/R values. Hence, the lower bound of the fit is assumed to be equal to the lowest measured value of E_a/R present in this training set.

As presented in Figure II-12, the upper and lower bounds (($E_a/R)_{min}$ = -784 K and ($E_a/R)_{max}$ = +920 K) bracket the range of values that we encountered in this training set and limit the parametrization of this SAR. In the following steps of the calculation, for k_{298} larger than 7.3×10^{-11} cm^3 molecule^{-1} s^{-1} and smaller than 2.3×10^{-14} cm^3 molecule^{-1} s^{-1}, the calculated E_a/R factors were forced to be equal to the upper and lower limits. The variation of $k_{298,OH}$ with the A-factor are presented in Figure App-II-1 in Appendices.
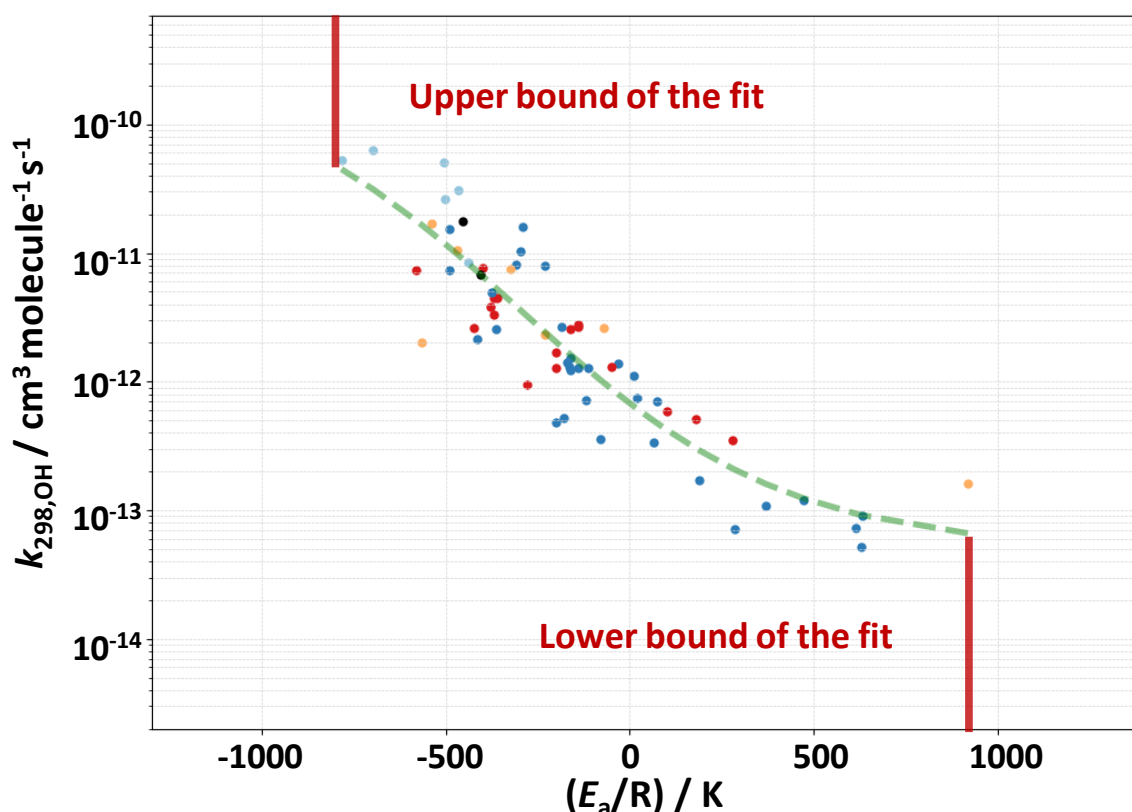
Figure II-12 : Inverse sigmoidal fit of k_{298} vs. E_a/R for all the 77 molecules included in this study.

II-2.2.2.2. O$_3$ reaction

From Figure II-13, the rate coefficients for O$_3$ are correlated to the activation energy, E_a/R. It can be observed from Figure II-13 that tetrachloroethene and trichloroethene (red square) have the largest values of E_a/R over the available dataset, and their Arrhenius parameters are unusual, with the A-factors being surprisingly high, i.e., a few orders of magnitude larger than collision frequency calculated using reasonable molecular sizes (e.g., E_a/R=14060K, A=6×10^{-4} cm^{3}molecule^{-1}s^{-1}). For that reason, these values have been excluded from this analysis.

The sigmoidal fit obtained from the relationship between the experimental $\ln k_{298,O3}$ and E_a/R for the O$_3$ reaction presented in Figure II-14 is as follows:

$$k_{298,O3} = \exp\left(-33.442 - \frac{16.514}{1+\exp\left(\frac{-(E_a/R-2320.8)}{889}\right)}\right) \quad \text{(Eq. II-11)}$$

From the (Eq. II-12), the value of the E_a/R can be estimated using the predicted values of $k_{298,O3}$. The limits of the fit are defined by the limits in the available E_a/R dataset as follows:

$$(E_a/R)_{O3,max} = 3704K \text{ if } k_{298,O3} < 1.46\times10^{-21} \text{ cm}^3\text{molecule}^{-1}\text{s}^{-1}$$

$$(E_a/R)_{O3,min} = 345K \text{ if } k_{298,O3} > 5.60\times10^{-16} \text{ cm}^3\text{molecule}^{-1}\text{s}^{-1}$$

These limits can be updated when more data become available. The fit in (Eq. II-12) can be used to obtain an estimation of the E_a/R value of a reaction from the value of the O_3 reaction rate coefficient at room temperature $k_{O3,298K}$. The correlation between $k_{298,O3}$ and $k_{298,OH}$ is presented in Figure App-II-2 in Appendices.
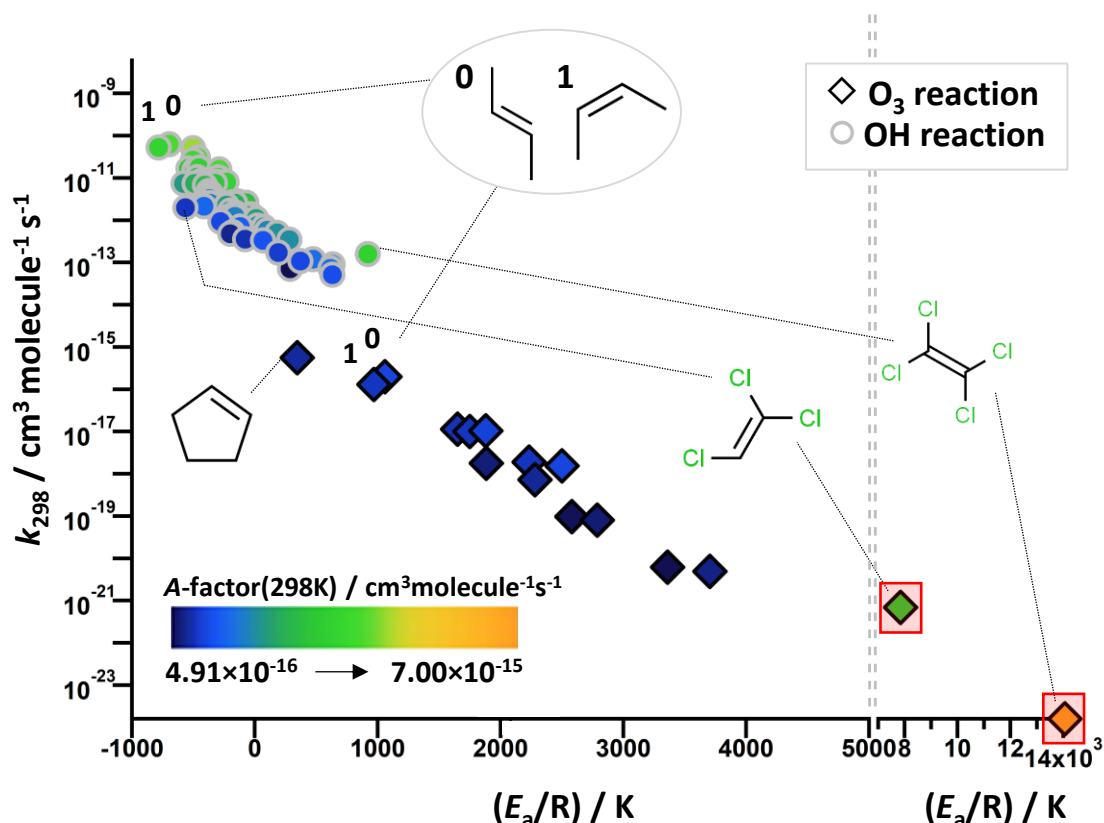
Figure II-13 : Rate coefficient for the O_3 (diamond) and OH (circle) reactions at room temperature as a function of the activation energy, E_a/R, of the temperature-dependent rate coefficients, k(T). The colors vary with the value of the A-factor defined by k(T)=Aexp(-E_a/(RT)). For the O_3 reaction, the relationship between E_a/R and $k_{298,O3}$ is strong, as can be observed with the slope in the plot, and it seems that it may be the case for the A-factor as well, since the smallest value is that of tetrachloroethene which also displays the bigger value of A-factor. However, it should be noted that this compound may be an exception, and the value of the A-factor and E_a/R parameters are very specific to that reaction. Red squares identify the datapoints excluded from the rest of the analysis in this section.
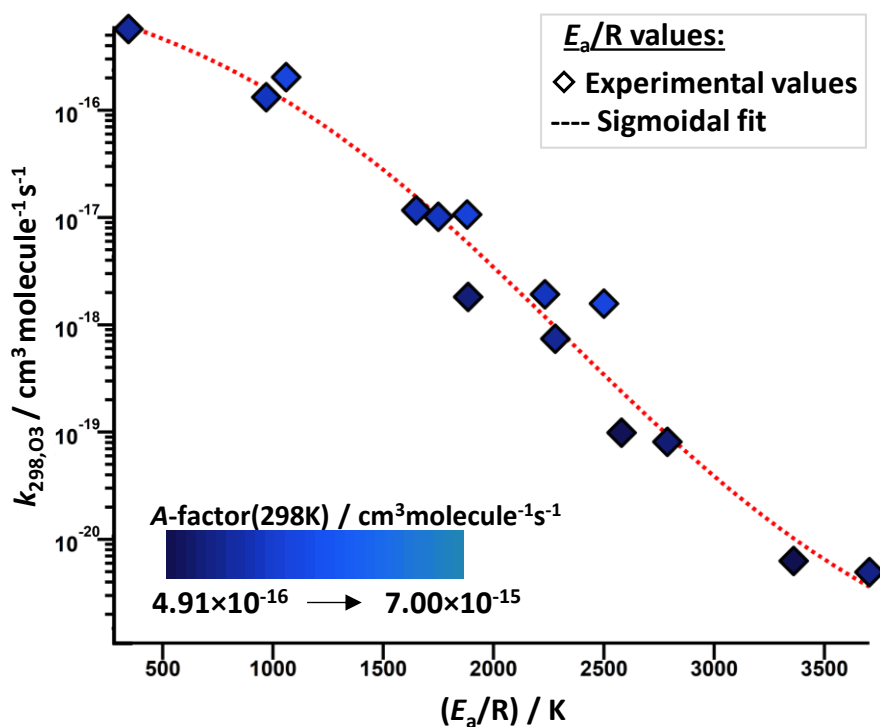
<u>Figure II-14 :</u> Sigmoidal fit of the relationship between the experimental $\ln k_{298,O3}$ and E_a/R, for the O_3 reaction (red). The relationship is strong, and the values are limited to the extremes by the mathematical limits from the logarithm function.

II-2.2.2.3. NO₃ reaction

In the Figure II-15, the relationship between $k_{298,NO3}$ and E_a/R for the NO_3 reaction is compared with that of the other oxidants, OH, and NO_3. The reactivity at room temperature decreases with increasing activation energy for the three oxidants. It is interesting to note that the slope of the correlation of the room temperature rate coefficient with E_a/R is similar between OH, NO_3 and O_3, but seems shifted to lower values of rate coefficients at room temperature, which suggests that these differences are attributed to the A-factor. It is observed that OH and NO_3 reactivity are described by a similar range of A-factors (7.17×10^{-12} to 9.40×10^{-12} $cm^3 molecule^{-1} s^{-1}$). This is not the case for the O_3 reaction whose temperature dependence is governed by smaller A-factors (4.91×10^{-16} to 7.00×10^{-15} $cm^3 molecule^{-1} s^{-1}$). This seems to be due to a difference in the O_3 reaction mechanism compared to the two other oxidants, since O_3 adds to both carbons of the double-bond to form an ozonide.

From the Figure II-15, it appears that the values for $k_{NO3}(T)$ are limited (9 determination of the Arrhenius parameters), but a trend is observed, for that range of available kinetic data. When fitting the $k_{NO3,298K}$ data as a function of E_a/R, the following equation can be obtained:

$$(E_a/R)_{NO3} = -11911-405.84 \times \ln k_{298,NO3} \qquad \text{(Eq. II-12)}$$

From that, the activation energy can be estimated for the NO$_3$ reaction. In order to respect the range of applicability conferred by the kinetic data available, and extrapolate below the collision limits, the E_a/R values have been restricted to:

$$(E_a/R)_{NO3,min} = -2444K \text{ if } k_{298,NO3} > 7.40\times10^{-11} \text{ cm}^3\text{molecule}^{-1}\text{s}^{-1}$$

$$(E_a/R)_{NO3,max} = 3000K \text{ if } k_{298,NO3} < 1.00\times10^{-16} \text{ cm}^3\text{molecule}^{-1}\text{s}^{-1}$$

However, future work to measure more kinetic data of k_{NO3} may allow a better definition of that relationship and its limits.
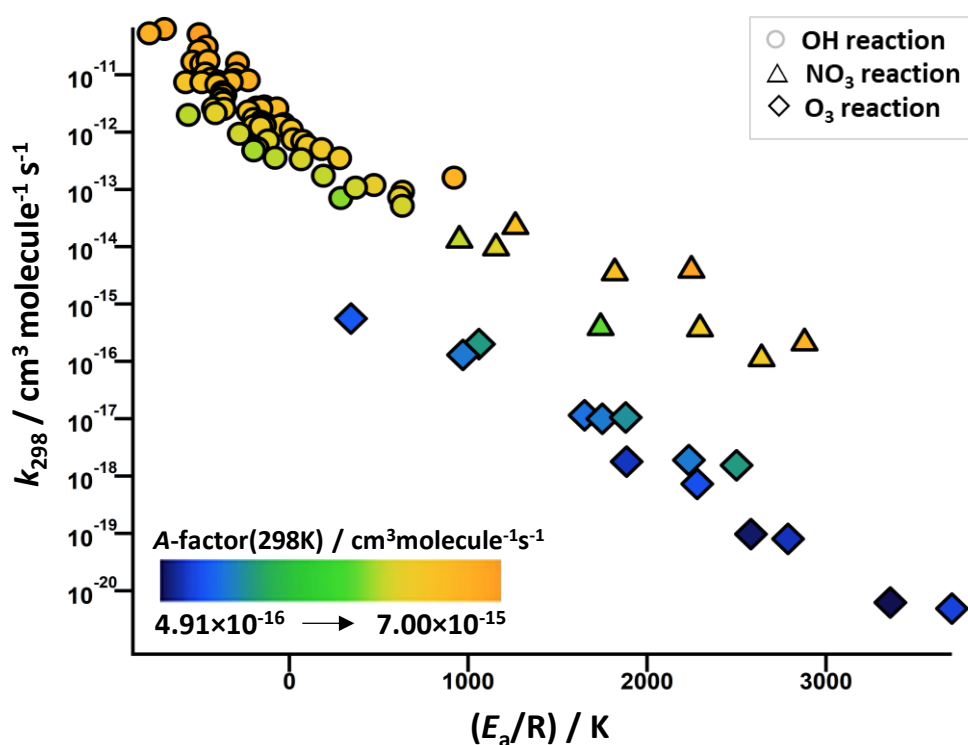
Figure II-15 : Experimental rate coefficient for the NO$_3$ (triangle) reaction, $k_{298,NO3}$, together with those of OH reaction (circle), Cl reaction (square), and O$_3$ reaction (diamond) as a function of their associated activation energy, E_a/R. The colors vary with the value of the A-factor defined by $k(T)=A\times\exp(-E_a/(RT))$. For the NO$_3$ reaction, he relationship between E_a/R and $k_{298,O3}$ is similar to that for OH, but the data are limited, so the fit may be valid only for that range of reactivities.

II-3. Results and discussion

II-3.1. SAR training set

In this and the subsequent sections, the species for which kinetic data included in our multilinear regression analysis to derive the F-factors is defined as the training set. The F-factors were optimized using a numerical solver to minimize the difference between experimental, k_{EXP}, and calculated rate coefficients, k_{pred}, the latter of which was derived using (Eq. II-10) in section II-2.2.2.1.

A comprehensive list of 77 reaction rate coefficients at 298K for OH radical reactions with CHX alkenes where X=F, Cl, Br, were compiled into a training set using data from the most up-to-date database (McGillen et al., 2020). As presented in the list of compounds Figure II-15 and the Arrhenius plots in Figure II-16, among this training set, 64 compounds have been measured as a function of temperature (structures 1–64) and the remaining 13 were only determined at room temperature, ~298K, (structures A-M).

All the kinetic data are assumed to be in their high-pressure limit for an addition reaction. In the literature, pressure dependence in the OH reaction has been observed for only a small number of alkenes, at pressures <100 Torr, and these are molecules with fewer heavy atoms such as ethene (IUPAC, 2022). However, if a rate coefficient included in the SAR was not at its high-pressure limit, it is expected that it would be an outlier in the correlation plots. Additionally, in order to exclude a large contribution from H-abstraction to the total rate coefficient, the alkenes with large alkyl substituents containing numerous abstractable H atoms have been excluded from the dataset (McGillen et al., 2007).

In the training set, the temperature-dependent rate coefficients of (E)-$(CF_3)_2CFCH=CHF$ (T=214 to 380K), (Z)-1,1,1,2,3,4,4,4-octafluorobut-2-ene (T=230-370K), and (E)-1,1,1,2,3,4,4,4-octafluorobut-2-ene (T=230-370K) were better described by a non-Arrhenius behavior, $k(T)=A\exp(-B/T)(T/300)^n$, and these have been refitted to a simple Arrhenius equation in this work within the experimental temperature range. The worst discrepancy between an individual k_{EXP} and its values from the refitted Arrhenius equation differs by at most 13% for (E)-1,1,1,2,3,4,4,4-octafluorobut-2-ene at T=370 K. Hence, it has been observed that this results in a minor impact on the temperature-dependent behavior for the aims of this study. The structures for each of the molecules of the training set presented in Figure II-16 are listed in order of reactivity and divided into three groups as:

1. compounds with known Arrhenius parameters (numbers 1–64)

2. compounds with only room temperature measurements (letters A–M)

3. compounds not included in the training set (grey background, see details in section II-3.2.2.)

The SAR of Kwok and Atkinson implemented in EPI Suite has not been extended, since almost all organic structures are included (Kwok and Atkinson, 1995). This work extends the approach of Tokuhashi and co-workers (2021) further since it is applied to a limited range of haloalkene structures. Here, additional alkenes and haloalkenes were included, with more substitution patterns and longer carbonyl chains for haloalkenes. In this sense, this SAR is rather a quantification of the electrophilic addition reaction to the olefinic bond within a molecule than its total reaction rate coefficient. However, it is possible to extend this SAR to include hydrogen abstraction, similar to the SAR of Kwok and Atkinson (1995).
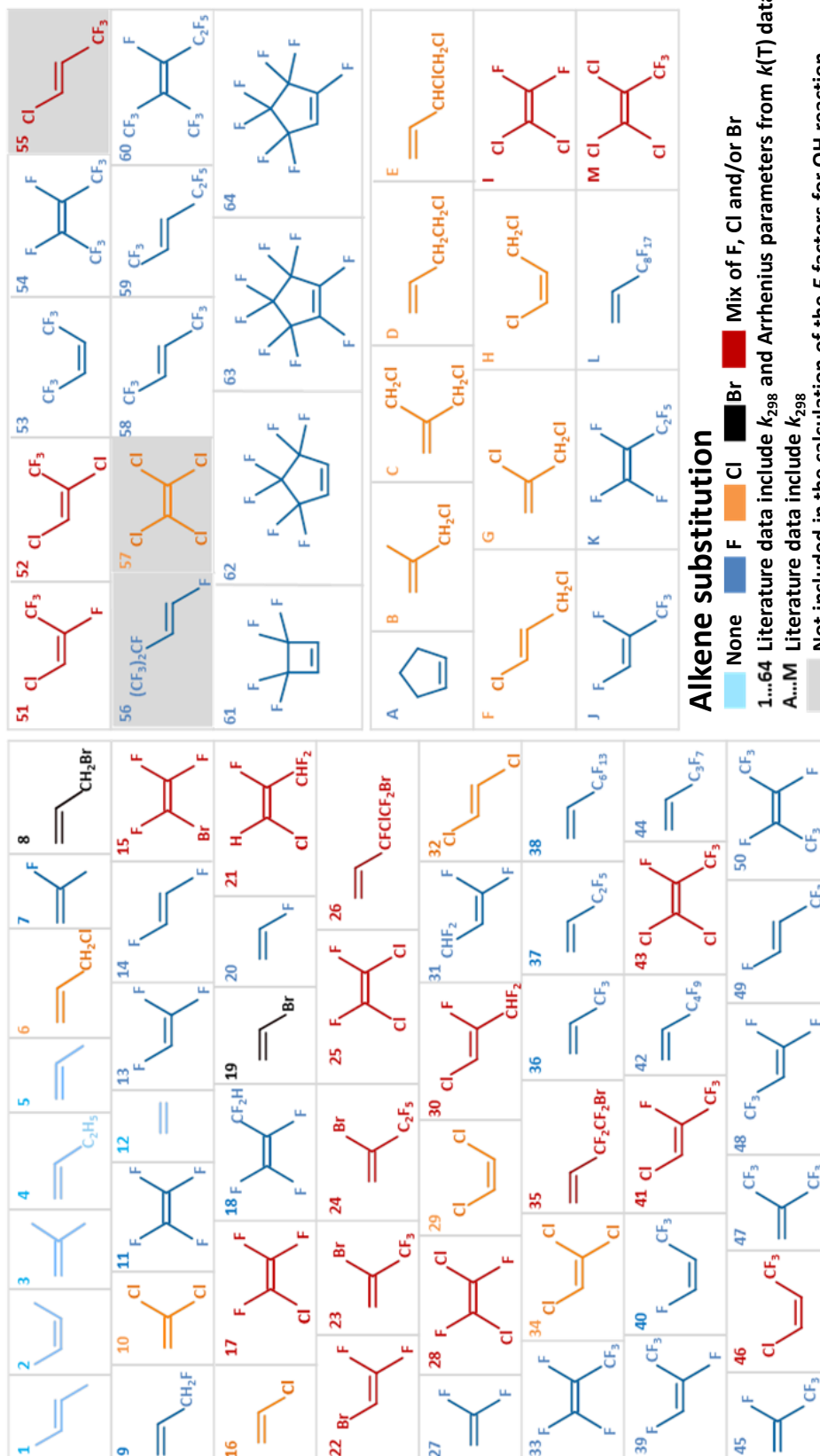
Figure II-16 : Training set composed of 77 molecules included in this study. Molecules with k(T) data (1–64) and with only k_{298} data (A–M) are ordered by reactivity at 298 K.
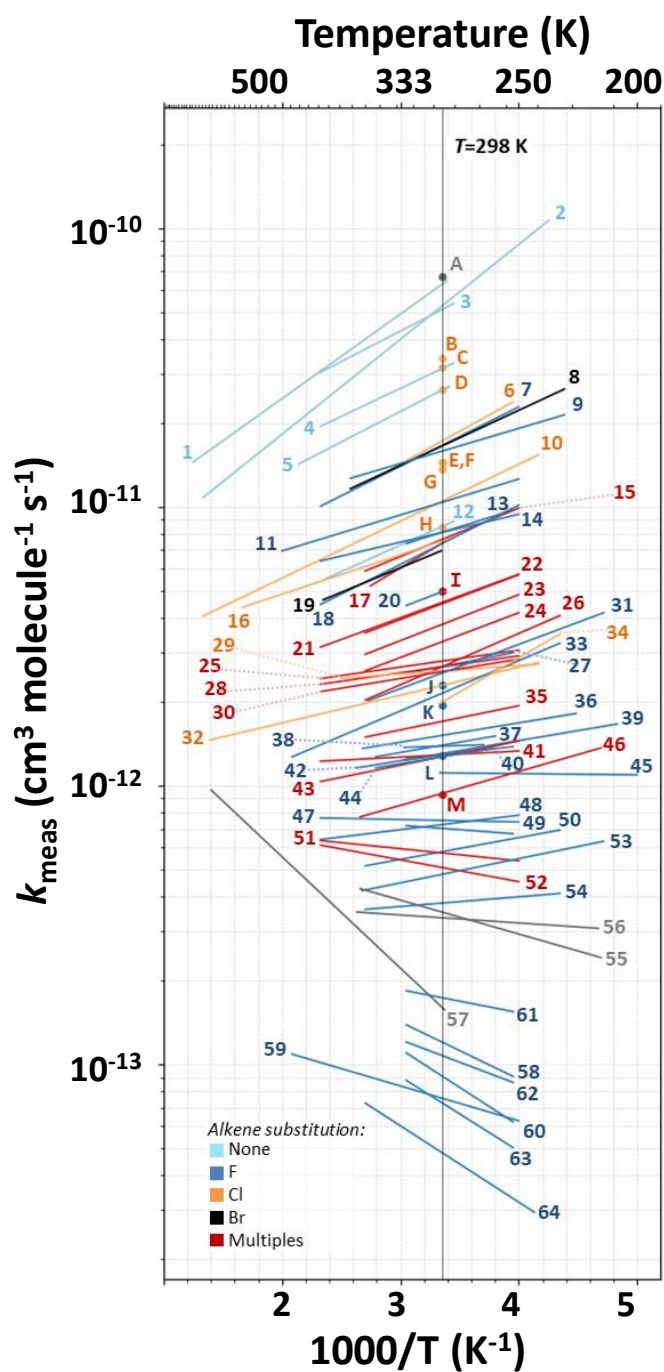
<u>Figure II-17</u> : Arrhenius plots of the OH reaction rate coefficients of the 77 alkenes and haloalkenes included in this study. Data were taken from the recent database of (McGillen et al., 2020). Dots represent measurements at room temperature only, and lines represent temperature-dependent determinations.

II-3.2. Performance of SARs to predict room temperature and temperature-dependent k_{OH} of haloalkenes

Given that the kinetic data available for the OH reaction with haloalkenes includes more data than the other oxidants for room temperature and temperature-dependent rate coefficients, and that it is a generally well-characterized reaction, the SAR method was initially tested against the k_{OH}(T=200–400K) experimental values for OH.

II-3.2.1. Estimations of $k_{298, OH}$ and comparison with existing techniques

The optimized *F*-factors of (Eq. II-10) included in the model are presented in Table II-3. More fitting parameters are required to apply the Tokuhashi et al. approach compared to that of Kwok and Atkinson. Therefore, this approach requires a large amount of data with similar structures to train the corresponding *F*-factor. Since new diagonal substituent factors are added in this approach, the rate coefficients of more species can be estimated, especially for longer perfluoroalkyl substitution patterns.

Table II-3 : Substituent *F*-factors optimized for the diagonal structure around the olefinic bond from this work and that of Model 1 of Tokuhashi et al. (2021) The *F*-factors for this SAR are presented as defined in (Eq. II-10).

Diagonal substitutions across the double bond	Substituent factors (*F*)	
	This work	Tokuhashi et al. (2021)
H-C=C-H	2.39	2.348
H-C=C-F	1.87	2.041
H-C=C-Cl	2.21	2.218
H-C=C-Br	5.57	Not included
H-C=C-CH$_2$Cl	5.62	4.971
H-C=C-CH$_2$Br	7.32[a]	Not included
H-C=C-CH$_2$F	6.69[a]	5.395[a]
H-C=C-CHF$_2$	2.54[a]	1.121[a]
H-C=C-C$_x$H$_y$ ($x \le 2$)	9.14	7.561 for $x=1$
H-C=C-C$_x$F$_y$	5.93×10^{-1}	8.43×10^{-1} for $x=1$
H-C=C-C$_x$F$_y$X$_z$	8.57×10^{-1}	Not included
C$_x$H$_y$-C=C-C$_z$H$_w$ ($x=z=1$)	2.64×10^{10a}	Not included
F-C=C-F	3.50	3.453
F-C=C-Cl	1.76	2.261
F-C=C-Br	2.28	Not included
F-C=C-CHF$_2$	1.69	2.109[a]
F-C=C-C$_x$F$_y$	5.54×10^{-1}	3.84×10^{-1} for $x=1$
Cl-C=C-Cl	9.04×10^{-1}	5.79×10^{-1}
Cl-C=C-CHF$_2$	1.36	2.194[a]
Cl-C=C-C$_x$F$_y$	7.20×10^{-1}	2.94×10^{-1} for $x=1$
C$_x$F$_y$-C=C-C$_x$F$_y$	7.78×10^{-2}	Not included
Cl-C=C-CH$_2$Cl	6.02[a]	6.132[a]
F_{cycle}[b]	3.07×10^{-1}	Not included

[a] Factors were optimized only from one experimental k_{298} data. [b] The F_{cycle} factor value is 1 for acyclic compounds by definition.

The performance of the SARs of Kwok and Atkinson (1995), the SAR of Tokuhashi et al. (2021), and our extension of the SAR of Tokuhashi et al. have been tested at 298K. Calculated and experimental rate coefficients have been compared (see Figure II-18) for each of these methods. The SAR of Kwok and Atkinson, in its original form, was found to be significantly less accurate than the other methods, with 64% of the predictions from the training set underestimated or overestimated by more than 50%, with many outliers being up to two orders of magnitude larger or smaller than the measured values. For example, the estimated rate coefficient for (*E*)-CF$_3$CH=CHCF$_2$CF$_3$ is 400 larger than the measured value, with k_{meas} = 9.10 $\times$ 10^{-14} cm^3 molecule^{-1} s^{-1} and k_{calc} = 3.70 $\times$ 10^{-11} cm^3 molecule^{-1} s^{-1}. Several reasons may explain this

discrepancy. It may be a limitation of the algorithm itself, demonstrating a high degree of degeneracy with respect to certain structural features. This degeneracy is defined as various substitution patterns yielding identical rate coefficients (see Figure II-18). In addition, the method predicts equally measured rate coefficients within two orders of magnitude of each other, *cf.* $CF_2=CF_2$ ($k_{meas} = 1.04 \times 10^{-11}$ cm^3 molecule^{-1} s^{-1}) versus $CCl_2=CCl_2$ ($k_{meas} = 1.60 \times 10^{-13}$ cm^3 molecule^{-1} s^{-1}), which are both estimated to have a rate coefficient of $k_{calc} = 2.14 \times 10^{-13}$ cm^3 molecule^{-1} s^{-1}. The predictions and measured values agree well in our approach. The extended version of the Tokuhashi approach developed in this chapter provides individual prediction of rate coefficients for specific isomeric structures, which is one of the reasons why the degeneracy in these approaches is reduced compared to the Atkinson method (Atkinson, 1988, 1987, 1986; Kwok et al., 1995).

The difficulties with multiple substituted haloalkenes in the Atkinson approach have been recognized since its introduction, (Kwok et al., 1995) and can be correlated to a limited database available at the time of writing, compared to the Tokuhashi approach presented here. The room temperature rate coefficients, k_{298}, were well-predicted using the modified Tokuhashi approach, as illustrated in Figure II-18. Only minor differences were observed between the original Tokuhashi method and our extended version, with 80% and 77% of cases being reproducible to within a factor of 2 respectively. The extension of the SAR to include more haloalkenes and alkenes does not appear to be at the cost of a reduction in its overall performance.
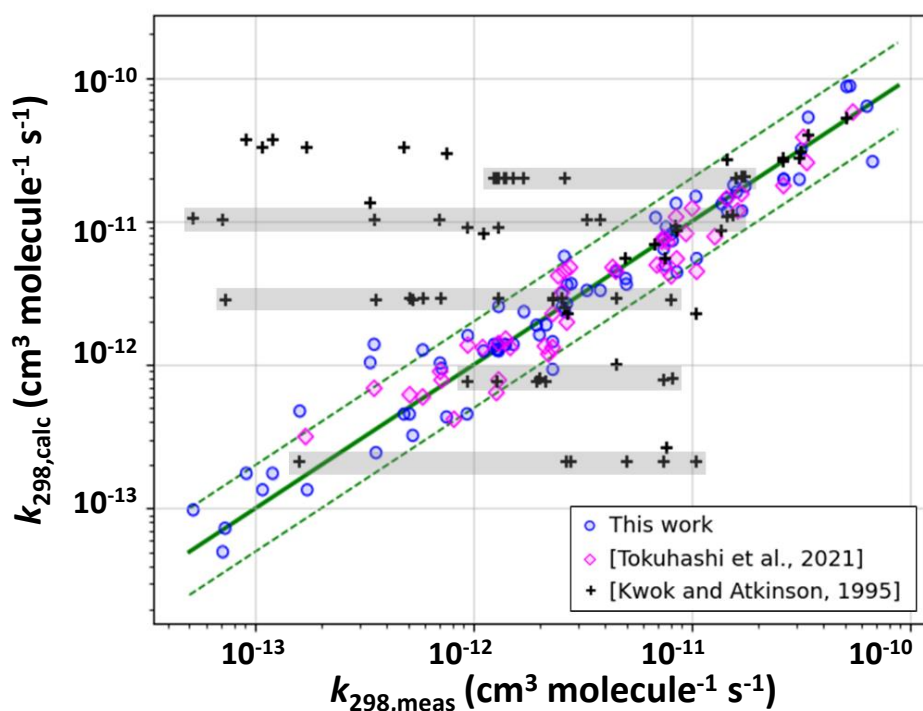
Figure II-18 : SAR results and comparison with Tokuhashi et al. (2021) predictions (magenta diamond) and EPI Suite tool calculations based on Kwok and Atkinson approach (1995) (black plus) at 298 K. Blue circles are predictions using our SAR model ($k_{298,calc}$). Green dashed and bold lines show the interval in which data calculated agree within a factor of 2 with measured data. The grey areas indicate identical predictions from EPI Suite as a consequence of the degeneracy in the SAR algorithm.

II-3.2.2. Performance for temperature-dependent rate coefficients k(T=200-400K)

To extend the SAR to predict temperature-dependent rate coefficients, the A-factor (in cm^3 molecule^{-1} s^{-1}) has been calculated. As seen in the Appendices section App-II-3.1 (Table App-II-3), the A-factor in our training set can range from 1.98×10^{-13} cm^3 molecule^{-1} s^{-1} to 9.42×10^{-12} cm^3 molecule^{-1} s^{-1}. Hence, the A-factor variation can be retrieved using the estimated k_{298} (Eq. II-10) and the estimated E_a/R factor (Eq. II-11) using the simple Arrhenius relationship:

$$A = k_{298} \exp(E_a/(R \times 298K)) \qquad \textbf{(Eq. II-13)}$$

Then, the Arrhenius parameters and $k(T)$ can be calculated over the temperature range of this study (200–400 K) for every value of k_{298} that the SAR can estimate. The predicted values of k(T) are presented in Figure II-19. To quantify the agreement between measurements and calculations $k_{calc}(T)$, the ratio relative to the measured values $k_{meas}(T)$, defined as k_{calc}/k_{meas} when $k_{calc} > k_{meas}$ and k_{meas}/k_{calc} when $k_{meas} > k_{calc}$, is calculated and presented in Figure II-20. Generally, the temperature dependence is well-predicted using this approach, since 84% of the predicted rate coefficients are within a factor of two of the experimental values throughout the studied temperature range, as presented in the Figure II-14 where calculated $k_{SAR,OH}$(T) are plotted against experimental $k_{EXP,OH}$(T).

The predicted rate coefficients of the compounds $CCl_2=CCl_2$, (*E*)-CHCl=CHCF$_3$, and (*E*)-(CF$_3$)$_2$CFCH=CHF are bigger than those measured and were excluded from the fitting procedure as they showed no apparent improvement when the *F*-factors were optimized. These three molecules exhibit a high degree of halogenation, and two of them contain chlorine. Tokuhashi et al. (2021) observed previously that chlorination can result in worse predictions using this method. This may be due either to a mechanistic difference whereby this SAR does not correctly describe chlorinated molecules, or to significant uncertainties and disagreements in the experimental data. The exact reason for this behavior is not yet known.

For highly halogenated compounds, the number of halogen substituents and the bulkiness of chlorine substitutions near the reactive bond may contribute to the steric strain and steric shielding that is encountered in the electrophilic addition (Pinter et al., 2012). In addition, as these are electrophilic addition reactions, the removal of electrons in π-orbitals is expected to have a significant effect on the overall rate coefficients. The reactivity can also be influenced by specific combinations of halogen substitutions within a side chain. In the case of (*E*)-(CF$_3$)$_2$CFCH=CHF, for example, the (CF$_3$)$_2$CF- substitution may have a stronger electron-withdrawal effect than the generic CF$_2$X- to which we have attributed it. The resonance and field parameters, which are significantly different from those of straight-chain perhalogen substitutions, (Hansch, 1991) and which could be responsible for the low reactivity of (*E*)-(CF$_3$)$_2$CFCH=CHF towards OH, are evidence of such an influence. However, to better explain the mechanisms of these reactions, further

theoretical work and measurements are needed. It is also possible that there are mechanistic differences for some of the reactions in our data set. This could explain why some rate coefficients are not well predicted using this SAR approach, since one of the main assumptions of this work is that all reactions considered here are governed by the same structural attributes.
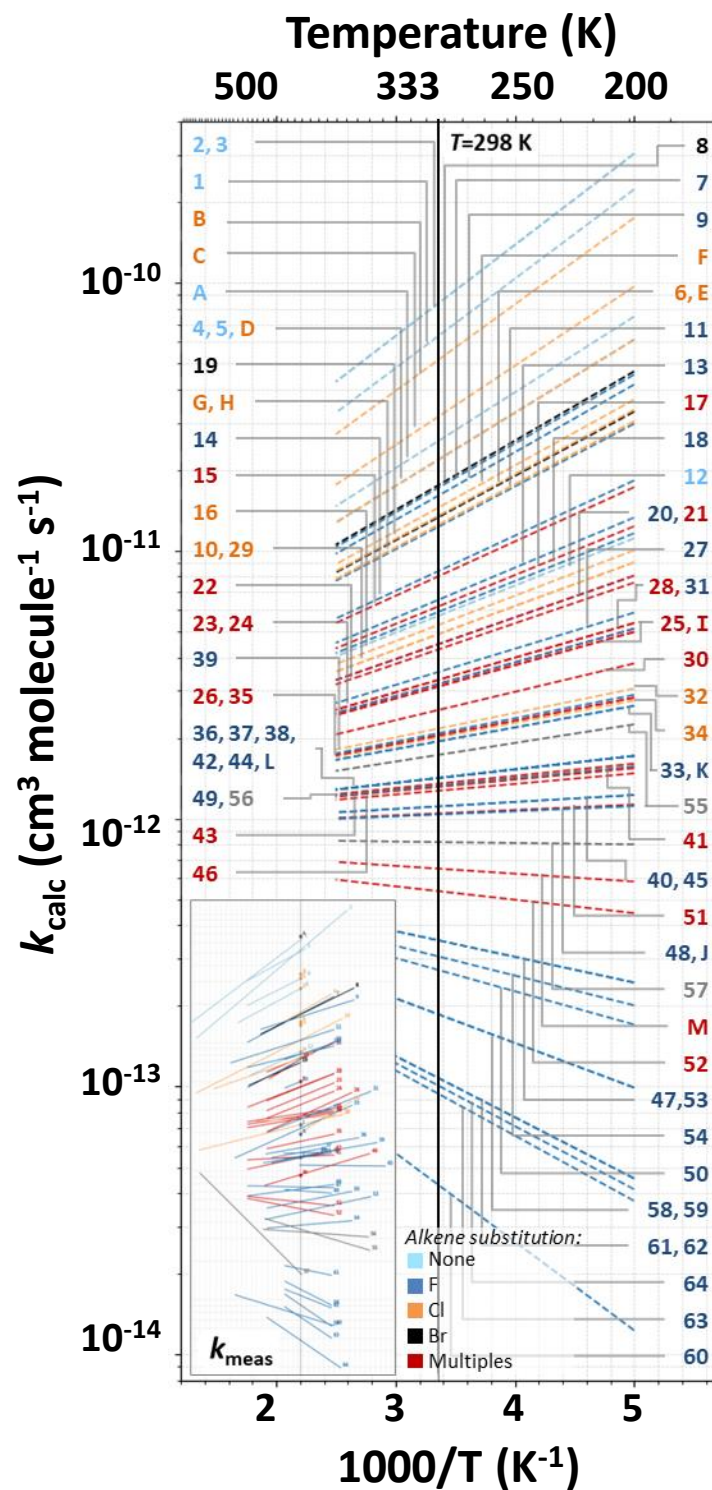
Figure II-19 : Experimental data (inset) and predictions of k_{calc}(T) over the studied temperature range (200–400 K) in dashed lines using our SAR model. Experimental values are plotted in bold lines using the Arrhenius parameters taken from (McGillen et al., 2020).
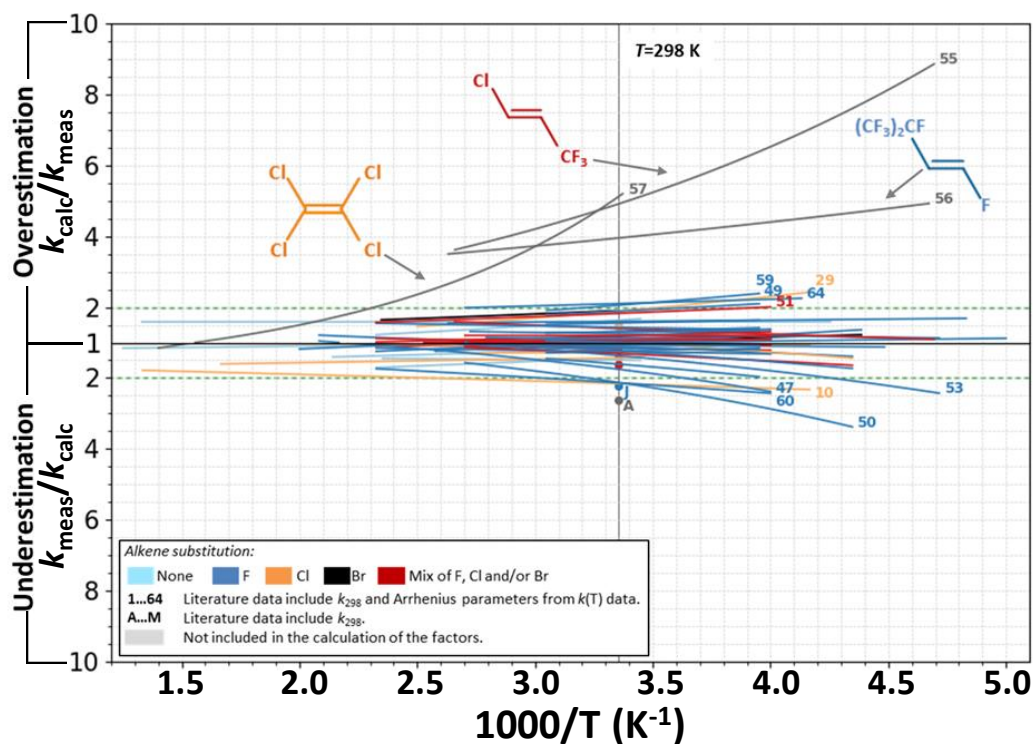
Figure II-20 : Ratio between measured and calculated rate coefficients over the temperature range of this study, is defined as k_{calc}/k_{meas} when $k_{calc} > k_{meas}$ and k_{meas}/k_{calc} when $k_{meas} > k_{calc}$. Green dashed and bold lines showing the interval in which data calculated agree within a factor 2 with measured data.
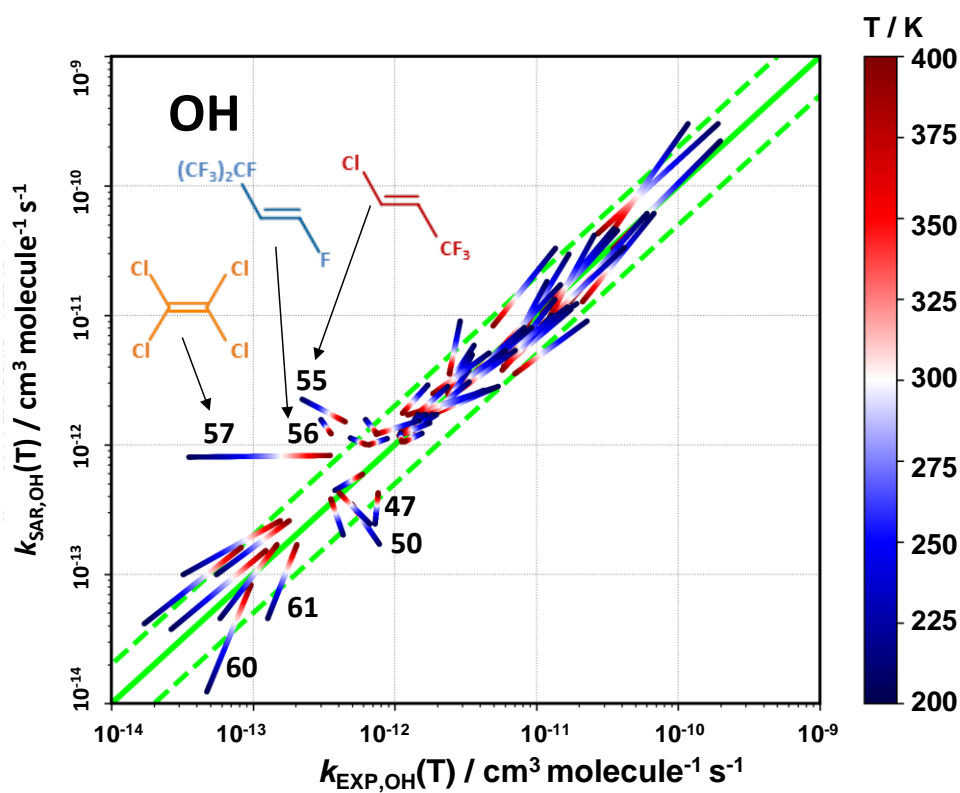
Figure II-21 : Calculated OH rate coefficients versus measured OH reaction rate coefficients as a function of temperature over 200–400K. The bold green line represents the perfect agreement between prediction and measurements. The dashed lines identify the range within which calculations and measurements agree within a factor of 2 on either side.

II-3.3. Extension to other oxidants, Cl, NO$_3$, and O$_3$

The SAR has been extended to the other oxidants, Cl, NO$_3$, and O$_3$ using the same approach presented in section II-2.2.1. for estimating k_{298}, and the extension presented in section II-2.2.2. to derive temperature-dependent rate coefficient, by estimating E_a/R using its relationship with k_{298} and the Arrhenius equation.

II-3.3.1. Room temperature k_{298}

The CHX dataset of kinetic data available in the literature is more limited, and thus the applicability of the method can be reduced depending on the availability of the data. The optimized values of the F-factors to estimate the total reaction rate coefficient at 298K for each oxidant are presented in the Table II-4 below. The substituent factors show large significant figures to ensure that the fit is reproduced and it is noted that no physical meaning is associated to the significant figures. When only one rate coefficient is used to optimize the value of diagonal substitution factor, it is labelled in the Table II-4. It can be observed that this number increases for the NO$_3$ and O$_3$ reactions, which highlights the patterns that may be lacking in the experimental database to extend and improve this method. This can be solved by conducting new measurements in the laboratory.

Table II-4 : Substituent factors optimized for the diagonal structure around the olefinic bond from this work and that of Model 1 of (Tokuhashi et al., 2021). The F-factors from this work are presented as defined in (Eq. II-10).

Diagonal substitutions across the double bond	Substituent factors (F)		
	Cl reaction	NO$_3$ reaction	O$_3$ reaction
k_{base}(C=C)	1.00×10^{-12}	1.00×10^{-16}	1.00×10^{-19}
H-C=C-H	14.86	1.45	18.03
H-C=C-F	12.25	1.14	0.79
H-C=C-Cl	10.32	2.55	0.74
H-C=C-Br	15.71	Not included	Not included
H-C=C-CH$_2$Cl	12.41	3.80	6.24
H-C=C-CH$_2$Br	8.28^a	24.15^a	10.54^a
H-C=C-CH$_2$F	3.31^a	26.91^a	Not included
H-C=C-CHF$_2$	Not included	Not included	Not included
H-C=C-C$_x$H$_y$ ($x\leq2$)	18.17	59.16	55.45
H-C=C-C$_x$F$_y$	6.07	0.23^a	1.11
H-C=C-C$_x$F$_y$X$_z$	Not included	Not included	Not included
C$_x$H$_y$-C=C-C$_z$H$_w$ ($x=z=1$)	23.55^a	2691.26^a	1108.95^a
F-C=C-F	7.48	1.75^a	12.37^a
F-C=C-Cl	8.19^a	Not included	Not included
F-C=C-Br	Not included	Not included	Not included
F-C=C-CHF$_2$	Not included	Not included	Not included
F-C=C-C$_x$F$_y$	2.95	Not included	0.02^a
Cl-C=C-Cl	7.46	1.00	0.44^a
Cl-C=C-CHF$_2$	Not included	Not included	Not included
Cl-C=C-C$_x$F$_y$	3.51^a	Not included	0.01^a
C$_x$F$_y$-C=C-C$_x$F$_y$	0.98	Not included	Not included
Cl-C=C-CH$_2$Cl	Not included	65.56^a	03.71^a
$F_{cycle}{}^b$	1.12	1.37	182.14

^{a} Factors were optimized only from one experimental k_{298} data. ^{b} The F_{cycle} factor value is 1 for acyclic compounds by definition.

The relationship between these *F*-factors between the oxidants has been investigated (Figure II-22). From Figure II-22, it appears that the diagonal substituents *F*-factors of the three oxidants Cl, NO$_3$ and O$_3$ are correlated with those of OH. The fits of these relationships are presented on the plots. It can be observed that there are relationships between these oxidants' reactions. There are some differences in the Cl reaction that can be expected from the different trend of the F_{Cl} with F_{OH} compared to that of F_{O3} and F_{NO3}. The correlations between the *F* substituent factors of the 4 oxidants suggest that there is a physical meaning behind these factors and that they do describe the reactivity of the structures regarding the electrophilic addition of these oxidants.

Furthermore, there are many examples of *F*-factors that are derived from only one experimental datapoint (dotted red circle in Figure II-22). It would be anticipated that in such cases, the exact values of these *F*-factors would be highly uncertain. However, in fact, these singly derived values do not appear to represent major outliers in Figure II-22. This is reassuring and it indicates not only that these *F*-factors appear to possess some physical meaning about the reactivity of haloalkenes towards these oxidants, but it also shows the commonality between the rate coefficients of the electrophilic addition of oxidants towards alkenes in general. Nevertheless, some scatter would be expected since there are some clear differences between these mechanisms, such as the importance of steric effects in ozonolysis (cf. Chapter I-2).
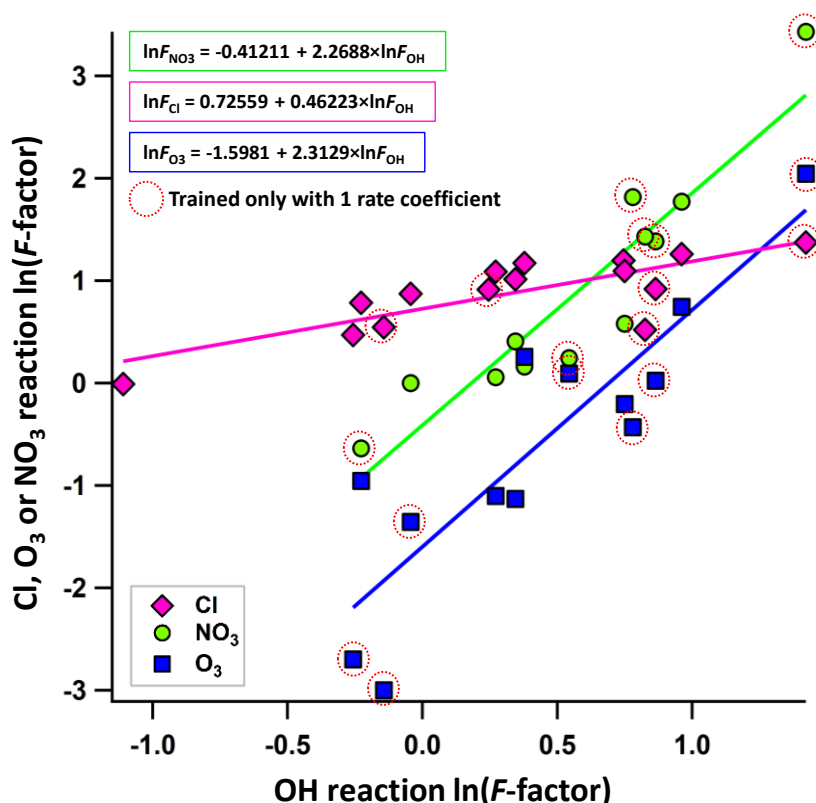
Figure II-22 : Correlation between the logarithm values of the diagonal substituents *F*-factors (Table II-3 and Table II-4) of the four oxidants, OH, Cl, NO$_3$, O$_3$. *F*-cycle factors are not included in the fits. It appears that linear relationships exist between the *F*-factors of the 3 oxidants and those of OH.

II-3.3.2. Predictions of temperature-dependent rate coefficients

As presented for the OH reaction in section II-2.2.2.1, the temperature-dependent rate coefficients are estimated using their Arrhenius relationship with the activation energy, E_a/R, and the A-factor. The estimation of E_a/R for each oxidant is presented in section II-2.2.2, and the A-factor is derived using the Arrhenius relationship as for OH (see details in section II-2.2.2.1). In this section, the temperature-dependent rate coefficients for the Cl reaction are not presented, as Cl reactions do not possess a significant temperature dependence with regard to existing experimental data.. These preliminary results can however be found in Appendices section App-II-3.2 (Figure App-II-7 and Table App-II-4).

II-3.3.2.1. NO$_3$ reaction

Next, the method has been extended to the NO$_3$ reaction. The activation energy is estimated for NO$_3$ using the (Eq. II-13) and the A-factor (in cm^3 molecule^{-1} s^{-1}) is calculated using (Eq. II-14). The A-factor in the NO$_3$ training set ranges from 1.40×10^{-13} cm^3 molecule^{-1} s^{-1} to 7.17×10^{-12} cm^3 molecule^{-1} s^{-1} and the E_a/R from -399K to 3000K. The predicted k_{NO3}(T=200–400K) are estimated over the temperature range of this study (200–400 K) and are compared to available measurements in Figure II-23. The Arrhenius plots and data of the experimental and predicted rate coefficients are provided in Appendices section App-II-3.3 (Figure App-II-8 and Table App-II-5).

The temperature-dependent predictions of k_{NO3} are in excellent agreement with measurements, within the range of temperature studied (T=200–400K), although estimates for a few species are more than a factor of 2 different compared to measurements for lower temperatures (T<250K). However, the discrepancy in this case remains small enough to be considered in good agreement with the measurements (<5%). The main outliers are 1,1-dichloroethene, vinyl fluoride, and (Z)-1,2-dichloroethene, and two of them contain allylic chlorine substituents, which, as discussed in the previous section, may be less well described by this parametrization.

Similar to the Cl reaction, the experimental k_{NO3}(T) data remain limited (9 values). However, in the case of the NO$_3$ reaction, as discussed in section II-2.2.2., the temperature dependence is stronger, and thus, the relationship between $(E_a$/R$)_{NO3}$ and $k_{298,NO3}$ is described better by its parametrization function (Eq. II-13). This may explain why predictions are better compared to the Cl reaction despite a similar amount of k(T) data. This also represents the first SAR to predict temperature-dependent rate coefficients for the NO$_3$ addition to CHX alkenes, where X=F, Cl, Br, to our knowledge. As new measurements become available, this approach can be extended and refined.
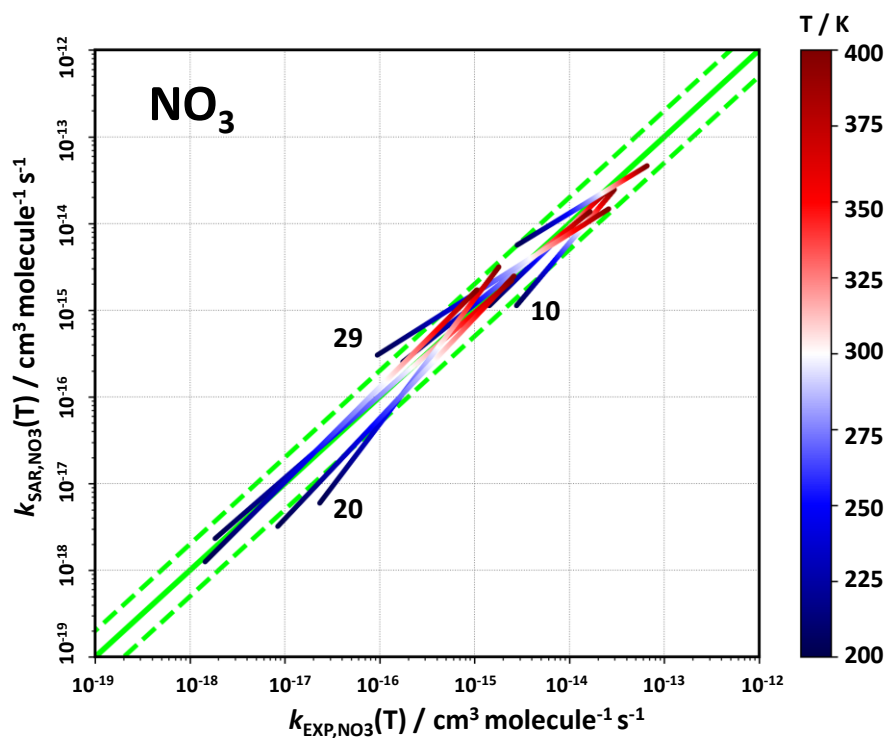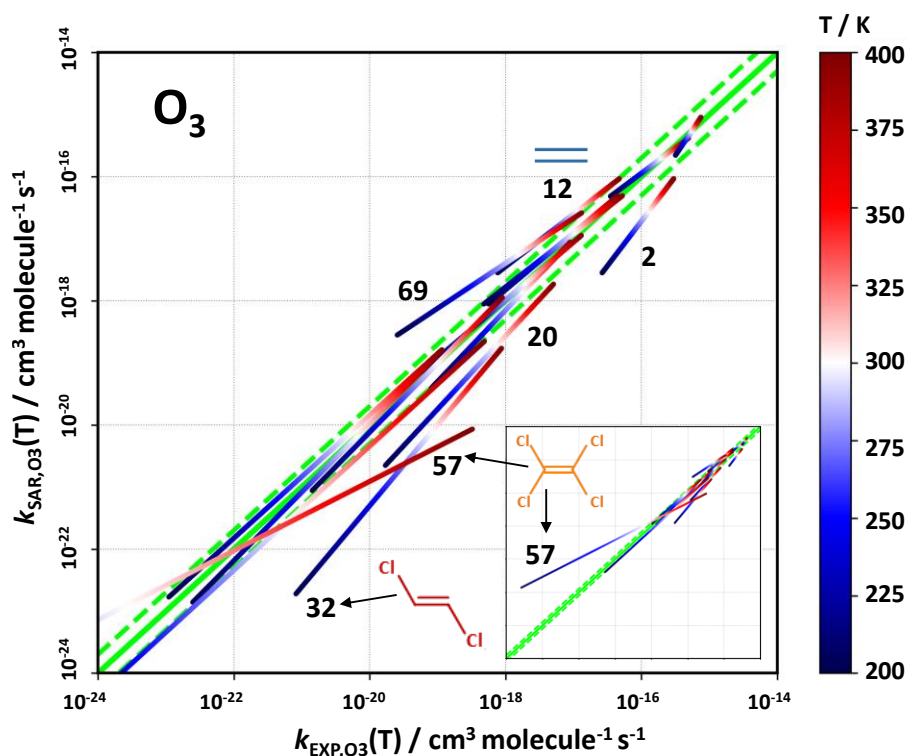
<u>Figure II-23</u> : Calculated NO₃ rate coefficients versus measured NO₃ reaction rate coefficients as a function of temperature over 200–400K. The bold green line represents the perfect agreement between prediction and measurements. The dashed lines identify the range within which calculations and measurements agree within a factor of 2 on either side.

II-3.3.2.2. O₃ reaction

The method is then applied to the O_3 reaction, with the activation energy estimated using the (Eq. II-12) and the *A*-factor (in cm^3 molecule^{-1} s^{-1}) calculated using (Eq. II-12). The *A*-factor in the O_3 training set ranges from 4.91×10^{-16} cm^3 molecule^{-1} s^{-1} to 6.00×10^{-14} cm^3 molecule^{-1} s^{-1} and the E_a/R from 345K to 3704K. The predicted k_{O3}(T=200–400K) are estimated over the temperature range of this study (200–400 K) and compared to available measurements (see Figure II-24). The Arrhenius plots and data for the experimental and predicted rate coefficients are provided in Appendices section App-II-3.4 (Figure App-II-9 and Table App-II-6).

In general, the compounds are well predicted, and most estimations are within a factor of 2 of $k_{EXP,O3}$, with a few exceptions. As for OH, the biggest outlier is tetrachloroethene, together with other chlorinated species (#32, #69) and this might be due to the same reasons discussed previously. Some normal and fluorinated alkenes tend to have poorer predictions at lower temperatures (#69, #20, #2); the reasons for this are not clear.

However, the range of reactivities for the O_3 reaction is larger, since $k_{298,O3}$ ranges from 1.60×10^{-24} to 5.60×10^{-16} cm^3 molecule^{-1} s^{-1}, which includes 8 order of magnitude compared to that of OH, which extends between 5.20×10^{-14} and 6.70×10^{-11} cm^3 molecule^{-1} s^{-1}. This can be a challenge for an SAR, whose simple

parameterization must describe a large range of behaviors. It is noted that many fitting factors are trained only on one kinetic measurement, which can result in overfitting. However, from the Figure II-22, it appears that most of these *F*-factors are reasonably well predicted and are not always outliers despite the fact that they are optimized with one experimental value only. Hence, new data are needed to test the SAR further and refine it. This represents the first SAR to predict temperature-dependent rate coefficient for the O_3 addition to CHX alkenes, where X=F, Cl, Br, to the best of our knowledge.

Figure II-24 : Calculated O_3 rate coefficients versus measured O_3 reaction rate coefficients as a function of temperature over 200–400K. The bold green line represents the perfect agreement between prediction and measurements. The dashed lines identify the range within which calculations and measurements agree within a factor of 2 on either side.

II-3.4. Measurements of the temperature dependence for the reaction rate coefficients of OH with CF₃CH=CH₂ and CF₂HCH=CF₂ and application of the SAR

In order to test the performance of the SAR in predicting temperature dependence, $k_{OH,CF2HCH=CF2}$(T=223–373 K) has been measured using the PLP–LIF set-up for the reaction of OH with CF₂HCH=CF₂, for which no experimental data is available, and the $k_{OH,CF3CH=CH2}$(T=212–367K) for the OH reaction of CF₃CH=CH₂. The predictions of the SAR and the experimental measurements for both reactions are presented in Figure II-26, together with the available literature data for the reaction of CF₃CH=CH₂. The fitting parameters are summarized in Table II-5. The measured values of the OH reaction rate coefficient as a function of temperature for the two selected HFOs, CF₃CH=CH₂ and CF₂HCH=CF₂, are provided in Appendices section App-II-1, Tables App-II-1 and App-II-2, respectively, together with the experimental conditions. The second-order plots of the pseudo-first-order decay rate coefficients of the OH fluorescence signal *k'* (s⁻¹),

as a function of $CF_3CH=CH_2$ concentration (in molecule cm^{-3}) are presented in Figure II-25. The slopes of these linear scatter plots yield the OH reaction rate coefficients k (cm^3 $molecule^{-1}$ s^{-1}) based on (Eq. II-6). The uncertainties reported on the rate coefficients are the statistical uncertainties (2σ at 95% CI) from the uncertainty-weighted linear least squares fit of the data. The overall systematic errors of the measurements were estimated to be <15%, and include statistical error in k' (<6%) and temperature (1%), in addition to estimated uncertainty in the concentration of the HFO (~10%) and pressure (~6%). To test the reproducibility of the measurements, the flow rates and concentrations of gases were varied between each experiment. Either nitric acid or hydrogen peroxide were used as precursors for OH radicals and no difference in the measured rate coefficients was observed. The linear correlations in the second-order plots suggests that the pseudo-first-order assumption is valid under these experimental conditions.
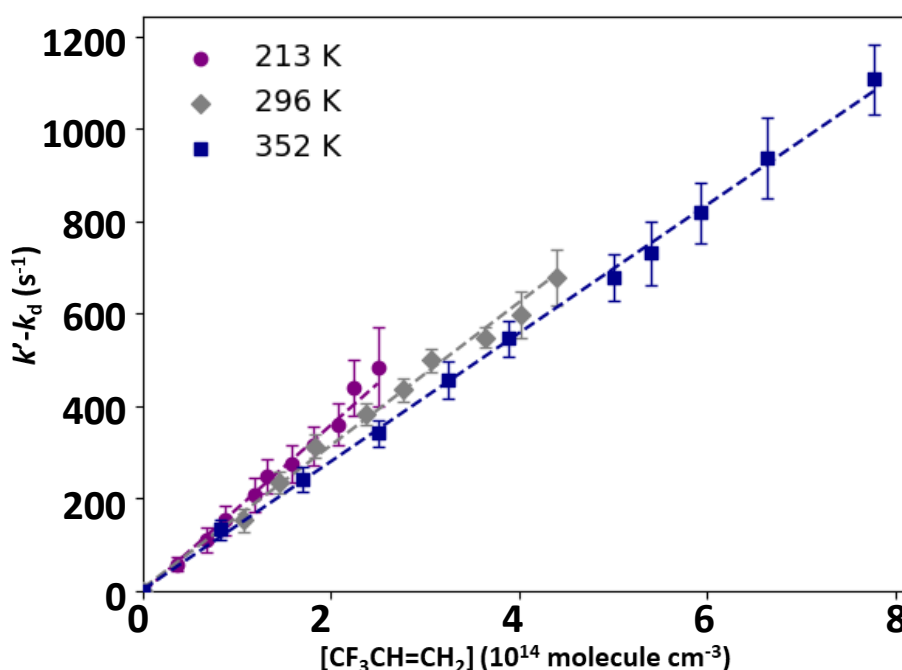
Figure II-25 : Representative plots of the dependence of the pseudo-first-order rate coefficient (k') on [$CF_3CH=CH_2$] at three temperatures measured using the PLP–LIF apparatus. Plotted uncertainties represent statistical errors (2σ at 95% CI).

The measured temperature dependence of the reaction rate coefficients $k_{OH,CF3CH=CH2}$(T=212–367K) and $k_{OH,CF2HCH=CF2}$(T=223–373 K) were well described by a simple Arrhenius expression, with a negative temperature dependency, as illustrated in Figure II-26. An uncertainty-weighted linear least squares curve-fitting method was applied to the logarithm of the temperature-dependent rate coefficient data, $\ln(k_{298})$, as a function of inverse temperature, using the reported statistical uncertainties of the experimental data. These fits render the Arrhenius parameters presented in Figure II-26 and Table II-5. The parameters from this work and the literature are presented together in Table II-5. The fits of the experimental rate coefficients are defined as:

$$k_{OH+CF_3CH=CH_2}(T)=(8.4\pm1.3)\times10^{-13} \exp\left(\frac{161\pm12}{T}\right) \qquad \text{(Eq. II-14)}$$

and

$$k_{OH+CF_2HCH=CF_2}(T)=(7.6\pm1.2)\times10^{-13}\exp\left(\frac{365\pm6}{T}\right) \qquad \textbf{(Eq. II-15)}$$

where the uncertainties reported are the combination of absolute and statistical errors (2σ at 95% CI) of the measurements. Our measurements and the associated uncertainties for the OH reaction with $CF_3CH=CH_2$ were compared with those of (Tokuhashi et al., 2018a), (Orkin et al., 1997) and (González et al., 2015) in Figure II-26. The plotted uncertainties of $k(T)$ for the literature data are only statistical errors. Our measurements are in excellent agreement with the data from (Orkin et al., 1997), and slightly different at lower temperatures from those of (Tokuhashi et al., 2018a) and (González et al., 2015). To the best of our knowledge, our measurements of the rate coefficients for the OH reaction with $CF_2HCH=CF_2$ are the first reported. The reactivity of $CF_2HCH=CF_2$ is higher, with a larger negative temperature dependence ($A=(7.46 \pm 0.34)\times10^{-13}$ cm^3molecule^{-1} s^{-1}, E_a/R= (365 $\pm$ 13)K, k_{298}= (2.55 $\pm$ 0.18)$\times10^{-12}$ cm^3 molecule^{-1} s^{-1}), than that of $CF_3CH=CH_2$ ($A=(8.86 \pm 0.71)\times10^{-13}$ cm^3molecule^{-1} s^{-1}, E_a/R= (160 $\pm$ 24)K, k_{298}= (1.40 $\pm$ 0.67)$\times10^{-12}$ cm^3 molecule^{-1} s^{-1}). This was expected from the relationship between k_{298} and E_a/R presented in Figure II-14.

Using the SAR presented in this chapter, the Arrhenius parameters have been predicted and are shown in Figure II-26 and Table II-5 (bold lines). The measured values are well predicted by the SAR, with the k_{298} values for $CF_3CH=CH_2$ underpredicted by at most 7% and those of $CF_2HCH=CF_2$ overpredicted by 24%. In the plots, the red lines represent the SAR predictions without adding the new temperature-dependent data measured in this work. Thus, as can be expected, the previously well-studied $CF_3CH=CH_2$ was well predicted by the SAR, since data were already constraining the model for the diagonal substituents of this compound (F(H-C=C-CF$_3$) and F(H-C=C-H)). On the contrary, the F(F-C=C-CF$_2$H) feature of $CF_2HCH=CF_2$ was poorly constrained in the SAR (only 1 rate coefficient), and no kinetic data was available. When including these new data in the SAR, and reoptimizing the F-factors, it can be observed (dark lines) that notable improvement in the predictions of $CF_2HCH=CF_2$ rate coefficients are obtained, since the diagonal factors are better constrained with additional data, while that of $CF_3CH=CH_2$ does not change much, which suggests that the F-factors were already well parametrized for these substitution types (Figure II-26).

Literature data are available to 250K for the lowest temperature, but since the upper layers of the troposphere and stratosphere encounter lower temperature up to ~200K, this range was extended in this work up to the temperature of 212K for the OH reaction rate coefficient with $CF_3CH=CH_2$ (Tokuhashi et al., 2018a). This can help provide atmospheric chemical models with new data for the altitudes at colder temperatures.

Table II-5 : Arrhenius parameters for reactions of OH with $CF_3CH=CH_2$ and $CF_2HCH=CF_2$ compiled from this work and previous studies (see reference column in table). For $CF_3CH=CH_2$, the recommendation of Arrhenius parameters results from the fit including

data of this work and that of Orkin et al. (1997), while k_{298} is a weighted average of all the rate coefficients reported in the literature. P is the total pressure of the carrier gas (He or Ar) and reactive compound. The quoted error bars are those of the authors.

Molecule	A (10^{-13} cm^3 molecule^{-1} s^{-1})	E_a/R (K)	k_{298} (10^{-12} cm^3 molecule^{-1} s^{-1})	T (K)	P (Torr)	Technique[a]	Reference
CF$_3$CH=CH$_2$	9.60	116	1.42	200–400		Calculations[b]	This work
			1.51	298		Calculations	(Tokuhashi et al., 2021)
	8.86 ± 0.82	159 ± 26	1.47 ± 0.25	212–367	100	PLP–LIF	This work
	8.28 ± 0.7	183 ± 26	1.52 ± 0.02	252–370	100	FP–RF	(Orkin et al., 1997)
	7.65 ± 0.26	165 ± 10	1.31 ± 0.14	263–358	50–650	PLP–LIF	(González et al., 2015)
	10.6 ± 0.20	80 ± 10	1.40 ± 0.01	250–430	20–200	FP, PLP–LIF	(Tokuhashi et al., 2018a)
			1.36 ± 0.25	296	700	RR	(Andersen et al., 2005)
	8.86 ± 0.71	160 ± 24	1.40 ± 0.67				Recommendation
CF$_2$HCH=CF$_2$	12.0	290	3.17	200–400		Calculations[b]	This work
	7.46 ± 0.34	365 ± 13	2.55 ± 0.18	223–373	100	PLP–LIF	This work – Recommendation

[a] FP: flash photolysis, RF: resonance fluorescence, RR: relative rate methods. [b] Reported values for A, E_a/R, and k_{298} in the table are the SAR predictions when including new measurements for CF$_3$CH=CH$_2$ and CF$_2$HCH=CF$_2$. For comparison, the values of (A, E_a/R, k_{298}) predicted from the SAR before adding the new measurements are (1.32×10^{-12} cm^3 molecule^{-1} s^{-1}, 351K, 4.28×10^{-12} cm^3 molecule^{-1} s^{-1}) for CF$_2$HCH=CF$_2$ and (9.61×10^{-13} cm^3 molecule^{-1} s^{-1}, 117 K, 1.43×10^{-12} cm^3 molecule^{-1} s^{-1}) for CF$_3$CH=CH$_2$.
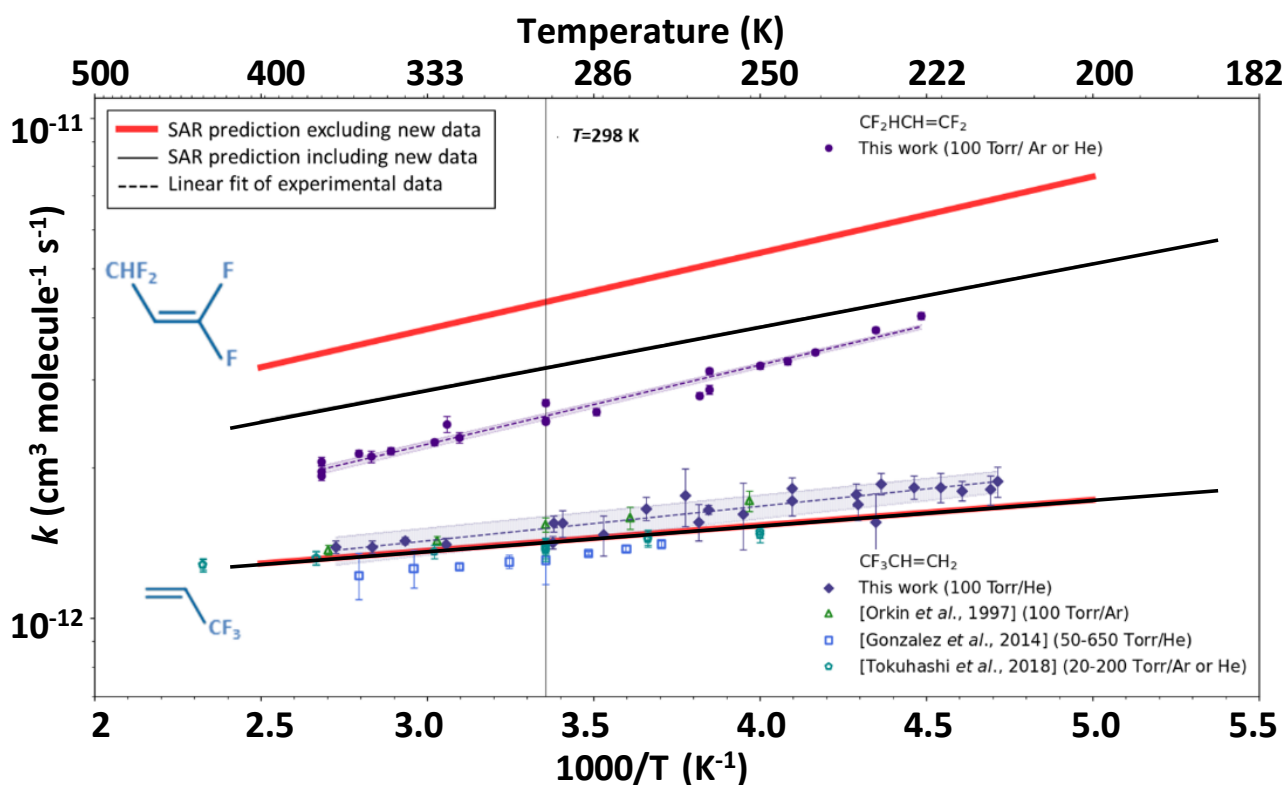
Figure II-26 : Arrhenius plots showing the experimental measurements of the k(T) as a function of inverse temperature, 1000/T, for the reaction of OH radicals with CF$_3$CH=CH$_2$ and CF$_2$HCH=CF$_2$ measured in this work, compared to the literature. SAR predictions from the model without including the new measurements presented in this work are plotted in red, while the updated version that

includes the new data is plotted in black. A notable improvement in the prediction of OH rate coefficient for the reaction with $CF_2HCH=CF_2$ is observed, whose diagonal factors were constrained by only one previous measurement.

II-3.5. Discussion of the SAR for OH reactions with olefins

In this section, the degeneracy of our SAR and other existing methods is discussed and compared for all the possible isomers between C_2 and C_4. All isomers of alkenes and haloalkenes containing C, H, F, Cl and Br up to a carbon number of 4, N_{tot}, are listed. N_{tot} was enumerated using a set of Markush structures generated in MarvinSketch version 22.5.0, ChemAxon (https://www.chemaxon.com). The EPI Suite tool estimates individual H-abstraction rate coefficient, k_{abs}, and addition rate coefficient, k_{add}, together with total rate coefficient, $k_{tot}=k_{abs}+k_{add}$, which allows to test the degeneracy of the Atkinson approach towards the OH electrophilic addition reaction by selecting only $k_{add,EPI}$. Similarly, the SAR of this chapter is applied to obtain k_{add} for all possible isomers. The predictions $k_{pred,EPI}$ and $k_{pred,SAR}$ were enumerated and duplicates were eliminated in order to obtain the number of unique predictions for each approach, N_{pred}. The comparison between the number of existing isomers and the number of unique predictions from each approach is presented in Figure II-27. In these counts, optical isomers are present, but this form of isomerization is not expected to make a change to the rate coefficient, which consequently does not affect the total number of unique predictions.

Numerous structures are possible with all combinations of halogens and alkenes (Figure II-27). So far, the substituted ethene category represents 76 isomers. As the number of carbons increases, the number of isomers increases exponentially, and many of them are of potential interest for a variety of applications. It would be impractical to measure the rate coefficients of every one of these reactions, or to calculate them all theoretically. The advantage of SARs is to provide a rapid and efficient way of estimating all these possibilities. However, as this is a simplification, uncertainties in these predictions are to be expected (Figure II-27, panel a). Significant degeneracy has been observed in the predictions of EPI Suite (see highlighted similar k-value trends in Figure II-18). It should be noted that in this case (Figure II-18) the k-values include both OH addition and H-abstraction pathways, k_{tot}, even though the latter is expected to be negligible. In this section, only the values of the OH electrophilic addition rate coefficient is compared, k_{add}. Significant degeneracy in the EPI Suite estimates is also observed for k_{add} (Figure II-28, panel 3). For example, for a carbon number of 2, there are 76 isomers, and, in the best case, 36 unique predictions are obtained from this SAR. But as the number of carbons increases, the number of unique predictions slowly increases relative to the number of possible isomers (Figure II-27, panel b). In the interests of clarity, only our SAR predictions are shown with those of EPI Suite, as our algorithm is only an extension of the (Tokuhashi et al., 2021) approach and, consequently, the level of degeneracy and the distribution of predictions are similar.

An important concern when developing SARs is that the need for simplicity in the approach, which may be connected with uncertainty in the predictions. This can be accepted up to a certain limit, the question being where that limit lies. When looking at the distribution of the experimental rate coefficients from the available literature dataset, it can be observed that the range of reactivities is evenly distributed (Figure II-28, panel 1). No mode (i.e., sub-range of reactivities) is dominant, and it is almost continuous. This is also the case for the predictions from our SAR for this dataset (Figure II-28, panel 2), while the predictions of EPI Suite have several degenerate modes, with a large number of identical estimations (Figure II-28, panel 3), and these dominant modes are not representative of the experimental values. For example, clusters 56 and 82 (x-axis) out of the 100 data clusters in Figure II-28 contain the highest frequencies of predictions for the EPI Suite (panel 3), meaning that many estimates have the same rate coefficient, even though there is little or no experimental data in this range (panel 1). Thus, our approach is more representative of the experimental database that EPI Suite, from this point of view. This highlights the problem of degeneracy and inaccuracy when using a SAR. This work improves on previous methods since it appears to reproduce and uniformly cover the whole distribution, in line with the pattern of experimental data.
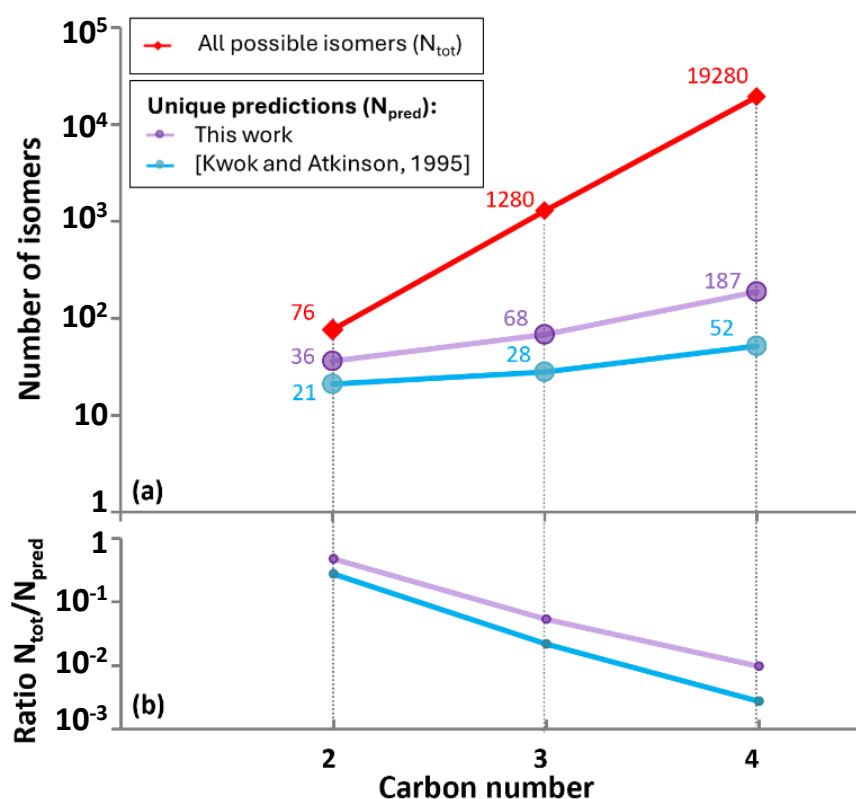
Figure II-27 : Panel a: Number of possible olefinic isomers from the combination of H, F, Cl, and Br substitutions at carbon numbers between 2 and 4, N_{tot}, in relation to the number of unique predictions, N_{pred}, obtained with the approaches of Kwok and Atkinson (1995) obtained from EPI Suite and this work. Panel b: Ratio between N_{tot} and N_{pred}.
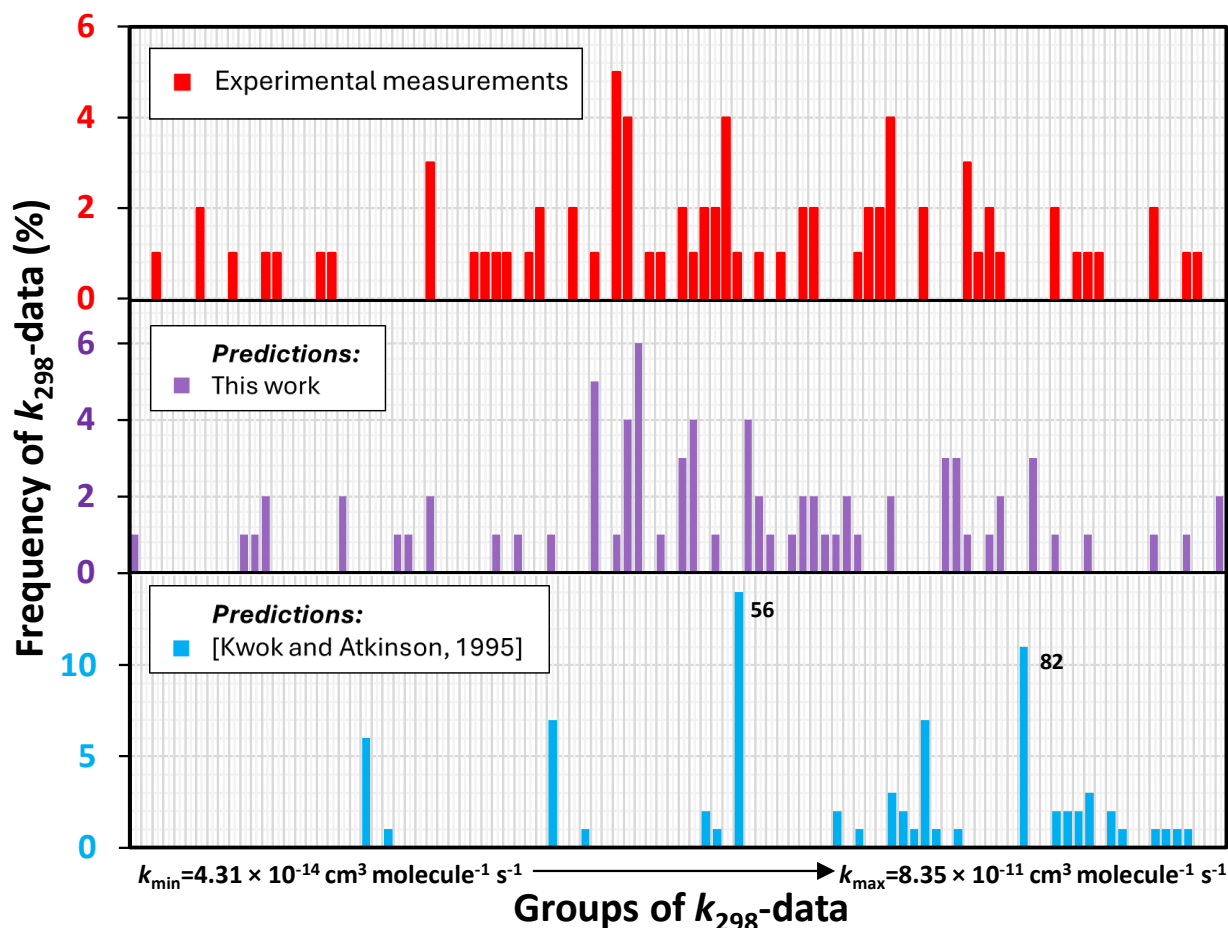
Figure II-28 : Histograms of the available kinetic data for the OH reaction with alkenes of interest. Upper panel: the measured rate coefficients, Middle panel: values calculated from this work, Lower panel: values calculated with the approach of Kwok and Atkinson (1995) outputted from EPI Suite. Rate coefficients are binned into 100 groups of evenly distributed k_{298}-rate coefficients ranging from the minimum k_{298} through to the maximum.

II-3.6. Discussion of the SAR for the four main tropospheric oxidants

The SAR at room temperature, k_{298}, performs well for the four oxidants under study, OH, Cl, NO₃, and O₃. When extending to temperature-dependent estimations, $k(T)$, the correlation between k_{298} and the activation energy E_a/R of the temperature-dependent rate coefficients allowed to derive a parametrization to estimate E_a/R. This SAR for $k(T)$ works well for OH and NO₃. This can be explained by the large amount of data for the OH reaction and the strong dependence of the rate coefficient with the activation energy (Figure II-12). A similar trend is observed for NO₃, which may explain why the SAR works well and may be governed by a similar mechanism (Figure II-15). However, concerning the O₃ reaction, it appeared that the SAR performs worse. This can be explained by possible differences between the O₃ electrophilic addition reaction with haloalkenes compared to those of OH and NO₃. An attempt has been made to derive $k(T)$ for the Cl reaction, but this was not successful because the available $k(T)$ data for Cl displayed no energy barrier (i.e., no variation in E_a/R). In addition, there is a lack of temperature-dependent data (only 6 Arrhenius parameter determinations) for Cl reaction. The SAR doesn't appear to work with this oxidant, which can be

explained by a difference in the mechanism. It may be due to the fact that Cl is an atom and not a radical, which thus possesses no dipole moment and no sufficient energy barrier. From that, only the k(T) estimation for OH and NO_3 are recommended. Overall, it is also noted that there is a scarcity of temperature-dependent kinetic data for Cl, NO_3 and O_3.

II-3.7. Atmospheric implications

The majority of the haloalkenes in this training set are short-lived and are therefore not well mixed in the troposphere. Their lifetime strongly depends on the location and time of their emission, (Brioude et al., 2010; Wuebbles et al., 2001) thus a calculation of the average tropospheric lifetime would not be accurate in all cases. The tropospheric lifetime of a species of interest can be estimated using the approach of (Brioude et al., 2010) and the temperature-dependent rate coefficients estimated using this SAR for the studied conditions (T, OH concentration).

Therefore, instead of focusing on the lifetime of each compound in the troposphere, the potential of this SAR as a screening tool was explored. This approach enables the rate coefficient of the OH reaction to be estimated simply and rapidly for a large number of haloalkenes, providing scientists, industry and decision-makers with an easy way of selecting more environmentally friendly candidate products.

This SAR provides the temperature-dependent estimation of the rate coefficients of the four main tropospheric oxidants, OH, and NO_3 with halogenated alkenes. This represents the first estimation of these values to the best of our knowledge. These predictions can be made for any compounds whose diagonal substitution patterns are included in the SAR, i.e., if at least one kinetic determination of k_{EXP} exists for a compound that possesses the same substitution pattern. There is a great improvement in the estimation accuracy of these CHX alkenes for OH and NO_3 reactions and this can help improve the atmospheric chemical modelling of these species, and their impact on climate and air quality.

II-4. Conclusions

In this chapter, a new method for predicting the Arrhenius parameters of the rate coefficients for the OH addition reaction of haloalkenes and related compounds has been developed (Michelat et al., 2022). Literature data for the OH rate coefficients of hydrofluoroolefins (HFOs) and related haloalkenes were gathered in a training set of 77 molecules to which this SAR was applied. The application of this SAR to the OH rate coefficients of this training set allowed us to observe a trend between reactivity, structure and activation energy, that could thus be parametrized. The more reactive compounds (k_{298} ~ 10^{-12}–10^{-10} cm^3 molecule^{-1} s^{-1}) show a predominantly negative temperature dependence, while the less reactive compounds (k_{298} ~ 10^{-12}–10^{-14} cm^3 molecule^{-1} s^{-1}) show a predominantly positive temperature dependence. This is expected from the thermochemistry of the electrophilic addition reaction since the energy barrier

for a reaction hinders reactivity for many compounds. Our method to calculate room temperature OH reaction rate coefficients, $k_{298,OH}$, was in good agreement with measurements as well as previous approaches developed by Tokuhashi et al. (2021) and Kwok and Atkinson (1995), as implemented in the EPI Suite tool, (US EPA, 2015) and was consequently extended to estimate temperature-dependent $k(T)$ over the temperature range 200–400 K. This is the first temperature-dependent calculation method to predict the rate coefficients of OH-addition to haloalkenes. The general performance of this new approach has proved to be satisfactory, with 90% of the estimated Arrhenius parameters agreeing within a factor of 2 for the 77 compounds examined. This SAR constitutes an excellent starting point for estimating the OH electrophilic addition rate coefficient as a function of temperature for a wide range of halogenated alkenes using a simple multiplication of three F-factors, including 2 diagonal substitution factors and 1 F_{cycle}.

Since the approach was demonstrated to perform well for the OH reaction, it was extended to three other main tropospheric oxidants, Cl, O_3 and NO_3. The SAR at room temperature works well for the four oxidants, however, the extension to temperature-dependent rate coefficient estimation only performs well for NO_3, and not for Cl and O_3. This is due to the sparsity of data and the potential differences in the mechanism of reaction, and the behavior of the reaction rate coefficients as a function of temperature. Similar to OH, the NO_3 estimations agree reasonably well with the available data, despite a sparsity of temperature-dependent kinetic data. No other technique provides temperature-dependent estimations of the electrophilic addition rate coefficient $k_{NO3}(T)$ for this class of compounds to the best of our knowledge, and thus, this represents a preliminary approach in order to help provide atmospheric chemical models with missing data. It is noted that this method may be overfitted when kinetic data are sparse, but this can be improved with reoptimizing the SAR using new measurements when they become available.

The F-factors used in this parametrization are probably proportional to the reactivity of the double bond. The multiplicative substitution factors, F(X-C=C-Y) and F(Z-C=C-W), can be related to, among other possible influences, the electron density of the π orbital of the double bond in the compounds. The lower the diagonal substitution factor value, the lower the electron density, and the higher the diagonal substitution factor, the greater the reactivity. Additional steric effects could occur for cyclic structures compared with linear structures, which could modify their reactivity. These effects are taken into account by the additional multiplicative factor F_{cycle}. There is a commonality between all the alkenes in our study, suggesting that the mechanism is essentially the same without drastic changes within the training set, with potential exceptions for some chlorinated compounds. This commonality is interpreted as a similar mechanism for the electrophilic addition reaction.

In addition, measurements of the OH reaction rate coefficient as a function of temperature are presented for two HFOs, $CF_3CH=CH_2$ (212–367 K) and $CF_2HCH=CF_2$ (223–373 K), using the PLP–LIF technique. These

measurements of $k(T)$ for $CF_3CH=CH_2$ are in good agreement with those reported in the literature, the temperature range being extended in this study up to 212K. This is expected to be relevant for the upper layer of the troposphere, and the stratosphere, although, due to their short lifetime, these HFOs are not expected to be transported to the stratosphere in most cases. The measurements of the rate coefficients of $CF_2HCH=CF_2$ are the first available to date to our knowledge and are in good agreement with the rate coefficients predicted using this new SAR. Measurements of the latter compound have made it possible to refine the parameterization of the CF_2H functionality, which had previously been poorly constrained with one unique value.

The predictions of this SAR constitute an improvement in our ability to predict the rate coefficients of haloalkene degradation with the OH radical, Cl atom, NO_3 radical, and O_3 molecule. The main benefit of this work is the improvement in our ability to estimate the rate coefficient easily and quickly for OH reactions with at least 291 haloalkenes, including 214 compounds for which no experimental data has been reported to date. A significant improvement was observed in reducing the degeneracy of estimates and increasing the variety of predictable structures compared with other existing methods. Furthermore, this SAR is different in its principle from the commonly used and updated Atkinson method that is based on a group additivity approach. It is notable that improvements in the prediction of the haloalkenes compounds (CHX) is especially useful because (1) other existing methods such as (Jenkin et al., 2018) do not apply to these species and (2) the Atkinson approach implementation in the EPI Suite tool estimate CHX rate coefficients with OH and O_3 with large uncertainties and high degeneracy. Thus, this method provides a tool that industrialists and decision-makers can easily employ to select the most reactive molecules among the various possible compounds that could be implemented as new substitutes in order to avoid persistent emissions into the atmosphere and estimate their local ozone production potential.

References

Ahrens, L., Bundschuh, M., 2014. Fate and effects of poly- and perfluoroalkyl substances in the aquatic environment: A review. Environmental Toxicology and Chemistry 33, 1921–1929. https://doi.org/10.1002/etc.2663

Andersen, M.S., Nielsen, O.J., Toft, A., Nakayama, T., Matsumi, Y., Waterland, R.L., Buck, R.C., Hurley, M.D., Wallington, T.J., 2005. Atmospheric chemistry of CxF2x+ 1CHCH2 (x= 1, 2, 4, 6, and 8): Kinetics of gas-phase reactions with Cl atoms, OH radicals, and O3. Journal of Photochemistry and Photobiology A: Chemistry 176, 124–128.

Atkinson, R., 1988. Estimation of gas-phase hydroxyl radical rate constants for organic chemicals. Environ Toxicol Chem 7, 435–442. https://doi.org/10.1002/etc.5620070604

Atkinson, R., 1987. A structure-activity relationship for the estimation of rate constants for the gas-phase reactions of OH radicals with organic compounds. Int. J. Chem. Kinet. 19, 799–828. https://doi.org/10.1002/kin.550190903

Atkinson, R., 1986. Kinetics and mechanisms of the gas-phase reactions of the hydroxyl radical with organic compounds under atmospheric conditions. Chem. Rev. 86, 69–201. https://doi.org/10.1021/cr00071a004

Atkinson, R., Aschmann, S.M., Carter, W.P., 1983. Effects of ring strain on gas-phase rate constants. 2. OH radical reactions with cycloalkenes. International journal of chemical kinetics 15, 1161–1177.

Atkinson, R., Baulch, D.L., Cox, R.A., Crowley, J.N., Hampson, R.F., Hynes, R.G., Jenkin, M.E., Rossi, M.J., Troe, J., 2004. Evaluated kinetic and photochemical data for atmospheric chemistry: Volume I - gas phase reactions of Ox, HOx, NOx and SOx species. Atmos. Chem. Phys. 4, 1461–1738. https://doi.org/10.5194/acp-4-1461-2004

Ballesteros, B., Jiménez, E., Moreno, A., Soto, A., Antiñolo, M., Albaladejo, J., 2017. Atmospheric fate of hydrofluoroolefins, CxF2x+1CHCH2 (x = 1,2,3,4 and 6): Kinetics with Cl atoms and products. Chemosphere 167, 330–343. https://doi.org/10.1016/j.chemosphere.2016.09.156

Brioude, J., Portmann, R.W., Daniel, J.S., Cooper, O.R., Frost, G.J., Rosenlof, K.H., Granier, C., Ravishankara, A., Montzka, S.A., Stohl, A., 2010. Variations in ozone depletion potentials of very short-lived substances with season and emission region. Geophysical Research Letters 37.

Burkholder, J.B., Cox, R.A., Ravishankara, A.R., 2015. Atmospheric Degradation of Ozone Depleting Substances, Their Substitutes, and Related Species. Chem. Rev. 115, 3704–3759. https://doi.org/10.1021/cr5006759

Burkholder, J.B., Sander, S.P., Abbatt, J.P.D., Barker, J.R., Cappa, C., Crounse, J.D., Dibble, T.S., Huie, R.E., Kolb, C.E., Kurylo, M.J., Orkin, V.L., Percival, C.J., Wilmouth, D.M., Wine, P.H., 2020. Chemical kinetics and photochemical data for use in atmospheric studies; evaluation number 19 (Technical Report). Pasadena, CA: Jet Propulsion Laboratory, National Aeronautics and Space Administration, 2020.

Calvert, J.G., Orlando, J.J., Stockwell, W.R., Wallington, T.J., 2015. The Mechanisms of Reactions Influencing Atmospheric Ozone. Oxford University Press.

Curme, H.G., Rollefson, G.K., 1952. The Effect of Inert Gases on the Quenching of Fluorescence in the Gaseous State1a,b [WWW Document]. ACS Publications. https://doi.org/10.1021/ja01121a007

Gilliland, F.D., Mandel, J.S., 1993. Mortality among employees of a perfluorooctanoic acid production plant. Journal of Occupational Medicine 950–954.

González, S., Jiménez, E., Ballesteros, B., Martínez, E., Albaladejo, J., 2015. Hydroxyl radical reaction rate coefficients as a function of temperature and IR absorption cross sections for CF3CH=CH2 (HFO-1243zf), potential replacement of CF3CH2F (HFC-134a). Environ Sci Pollut Res 22, 4793–4805. https://doi.org/10.1007/s11356-014-3426-2

Hansch, Corwin., Leo, A., Taft, R.W., 1991. A survey of Hammett substituent constants and resonance and field parameters. Chem. Rev. 91, 165–195. https://doi.org/10.1021/cr00002a004

Hashimoto, M., Otsuka, T., Fukushima, M., Okamoto, H., Hayamizu, H., Ueno, K., Akasaka, R., 2019. Development of New Low-GWP Refrigerants–Refrigerant Mixtures Including HFO-1123. Science and Technology for the Built Environment 25, 776–783. https://doi.org/10.1080/23744731.2019.1603779

Hodnebrog, Ø., Etminan, M., Fuglestvedt, J.S., Marston, G., Myhre, G., Nielsen, C.J., Shine, K.P., Wallington, T.J., 2013. Global warming potentials and radiative efficiencies of halocarbons and

related compounds: A comprehensive review: Halocarbon Review. Rev. Geophys. 51, 300–378. https://doi.org/10.1002/rog.20013

Hollas, J.M., 2004. Modern Spectroscopy, John Wiley&Sons. ed.

Hu, S., Li, J., Yang, F., Yang, Z., Duan, Y., 2020. Multi-objective optimization of organic Rankine cycle using hydrofluoroolefins (HFOs) based on different target preferences. Energy 203, 117848. https://doi.org/10.1016/j.energy.2020.117848

Kudo, N., Kawashima, Y., 2003. Toxicity and toxicokinetics of perfluorooctanoic acid in humans and animals. The Journal of toxicological sciences 28, 49–57.

Kwok, E.S.C., Atkinson, R., 1995. Estimation of hydroxyl radical reaction rate constants for gas-phase organic compounds using a structure-reactivity relationship: An update. Atmospheric Environment 29, 1685–1695.

Land, M., de Wit, C.A., Bignert, A., Cousins, I.T., Herzke, D., Johansson, J.H., Martin, J.W., 2018. What is the effect of phasing out long-chain per- and polyfluoroalkyl substances on the concentrations of perfluoroalkyl acids and their precursors in the environment? A systematic review. Environ Evid 7, 4. https://doi.org/10.1186/s13750-017-0114-y

Le Calvé, S., Hitier, D., Le Bras, G., Mellouki, A., 1998. Kinetic studies of OH reactions with a series of ketones. The Journal of Physical Chemistry A 102, 4579–4584.

McGillen, M.R., Carter, W.P.L., Mellouki, A., Orlando, J.J., Picquet-Varrault, B., Wallington, T.J., 2020. Database for the kinetics of the gas-phase atmospheric reactions of organic compounds. Earth System Science Data 12, 1203–1216. https://doi.org/10.5194/essd-12-1203-2020

McGillen, M.R., Percival, C.J., Shallcross, D.E., Harvey, J.N., 2007. Is hydrogen abstraction an important pathway in the reaction of alkenes with the OH radical? Phys. Chem. Chem. Phys. 9, 4349–4356. https://doi.org/10.1039/B703035E

Mellouki, A., Teton, S., Le Bras, G., 1995. Kinetics of OH radical reactions with a series of ethers. International journal of chemical kinetics 27, 791–805.

Meylan, W.M., Howard, P.H., 1993. Computer estimation of the Atmospheric gas-phase reaction rate of organic compounds with hydroxyl radicals and ozone. Chemosphere 26, 2293–2299. https://doi.org/10.1016/0045-6535(93)90355-9

Michelat, L., Mellouki, A., Ravishankara, A.R., El Othmani, H., Papadimitriou, V.C., Daële, V., McGillen, M.R., 2022. Temperature-Dependent Structure–Activity Relationship of OH + Haloalkene Rate Coefficients under Atmospheric Conditions and Supporting Measurements. ACS Earth Space Chem. 6, 3101–3114. https://doi.org/10.1021/acsearthspacechem.2c00296

Mota-Babiloni, A., Makhnatch, P., 2021. Predictions of European refrigerants place on the market following F-gas regulation restrictions. International Journal of Refrigeration 127, 101–110. https://doi.org/10.1016/j.ijrefrig.2021.03.005

Nair, V., 2020. HFO refrigerants: A review of present status and future prospects. International Journal of Refrigeration. https://doi.org/10.1016/j.ijrefrig.2020.10.039

Nakayama, T., Takahashi, K., Matsumi, Y., Toft, A., Sulbaek Andersen, M.P., Nielsen, O.J., Waterland, R.L., Buck, R.C., Hurley, M.D., Wallington, T.J., 2007. Atmospheric chemistry of CF3CH=CH2 and

C4F9CH=CH2: Products of the gas-phase reactions with Cl atoms and OH radicals. The Journal of Physical Chemistry A 111, 909–915.

Orkin, V.L., Huie, R.E., Kurylo, M.J., 1997. Rate constants for the reactions of OH with HFC-245cb (CH3CF2CF3) and some fluoroalkenes (CH2=CHCF3, CH2=CFCF3, CF2=CFCF3, and CF2=CF2). The Journal of Physical Chemistry A 101, 9118–9124.

Othmani, H.E., Ren, Y., Mellouki, A., Daële, V., McGillen, M.R., 2021. Gas-phase rate coefficient of OH + cyclohexene oxide measured from 251 to 373 K. Chemical Physics Letters 783, 139056. https://doi.org/10.1016/j.cplett.2021.139056

Pinter, B., Fievez, T., Bickelhaupt, F.M., Geerlings, P., Proft, F.D., 2012. On the origin of the steric effect. Phys. Chem. Chem. Phys. 14, 9846–9854. https://doi.org/10.1039/C2CP41090G

Post, G.B., Cohn, P.D., Cooper, K.R., 2012. Perfluorooctanoic acid (PFOA), an emerging drinking water contaminant: a critical review of recent literature. Environmental research 116, 93–117.

Rust, D., Katharopoulos, I., Vollmer, M.K., Henne, S., O'Doherty, S., Say, D., Emmenegger, L., Zenobi, R., Reimann, S., 2022. Swiss halocarbon emissions for 2019 to 2020 assessed from regional atmospheric observations. Atmospheric Chemistry and Physics 22, 2447–2466. https://doi.org/10.5194/acp-22-2447-2022

Steenland, K., Fletcher, T., Savitz, D.A., 2010. Epidemiologic evidence on the health effects of perfluorooctanoic acid (PFOA). Environmental health perspectives 118, 1100–1108.

Task Group on Atmospheric Chemical Kinetic Data Evaluation – Data Sheet II.A2.5 HOx_VOC3, n.d. 4.

Tokuhashi, K., Takizawa, K., Kondo, S., 2021. Rate constants for reactions of OH radicals with (Z)-CF3CCl=CHCl, CHF2CF=CF2, (E)-CF3CH=CHF, (Z)-CF3CH=CHF, CH3CF=CH2, and CH2FCH=CH2. Atmospheric Environment 255, 118428. https://doi.org/10.1016/j.atmosenv.2021.118428

Tokuhashi, K., Takizawa, K., Kondo, S., 2018a. Rate constants for the reactions of OH radicals with CF3CX=CY2 (X= H, F, CF3, Y= H, F, Cl). Environmental Science and Pollution Research 25, 15204–15215.

Tokuhashi, K., Takizawa, K., Kondo, S., 2018b. Rate constants for the reactions of OH radicals with fluorinated ethenes: Kinetic measurements and correlation between structure and reactivity. The Journal of Physical Chemistry A 122, 4593–4600.

Tokuhashi, K., Uchimaru, T., Takizawa, K., Kondo, S., 2019. Rate Constants for the Reactions of OH Radicals with the (E)/(Z) Isomers of CFCl=CFCl and (E)-CHF=CHF. The Journal of Physical Chemistry A 123, 4834–4843.

Tokuhashi, K., Uchimaru, T., Takizawa, K., Kondo, S., 2018c. Rate Constants for the Reactions of OH Radical with the (E)/(Z) Isomers of CF3CF=CHCl and CHF2CF=CHCl. The Journal of Physical Chemistry A 122, 3120–3127.

US EPA, O., 2015. EPI Suite™-Estimation Program Interface. URL https://www.epa.gov/tsca-screening-tools/epi-suitetm-estimation-program-interface (accessed 7.6.22).

Vereecken, L., Aumont, B., Barnes, I., Bozzelli, J.W., Goldman, M.J., Green, W.H., Madronich, S., Mcgillen, M.R., Mellouki, A., Orlando, J.J., Picquet-Varrault, B., Rickard, A.R., Stockwell, W.R., Wallington, T.J., Carter, W.P.L., 2018. Perspective on Mechanism Development and Structure-Activity

Relationships for Gas-Phase Atmospheric Chemistry: Perspective On Gas-Phase Atmospheric Chemical Kinetic Mechanism. Int. J. Chem. Kinet. 50, 435–469. https://doi.org/10.1002/kin.21172

Wang, Y., Adgent, M., Su, P.-H., Chen, H.-Y., Chen, P.-C., Hsiung, C.A., Wang, S.-L., 2016. Prenatal Exposure to Perfluorocarboxylic Acids (PFCAs) and Fetal and Postnatal Growth in the Taiwan Maternal and Infant Cohort Study. Environ Health Perspect 124, 1794–1800. https://doi.org/10.1289/ehp.1509998

Wang, Y., Niu, J., Zhang, L., Shi, J., 2014. Toxicity assessment of perfluorinated carboxylic acids (PFCAs) towards the rotifer Brachionus calyciflorus. Science of The Total Environment, Halogenated Persistent Organic Pollutants (Dioxin2013, Daegu/Korea) 491–492, 266–270. ttps://doi.org/10.1016/j.scitotenv.2014.02.028

Wuebbles, D.J., Patten, K.O., Johnson, M.T., Kotamarthi, R., 2001. New methodology for Ozone Depletion Potentials of short-lived compounds: n-Propyl bromide as an example. Journal of Geophysical Research: Atmospheres 106, 14551–14571.

Appendices : Chapter II

App-II-1. Experimental conditions for the measurements in the PLP–LIF set-up of the rate coefficients of $CF_2HCH=CF_2$ and $CF_3CH=CH_2$

Table App-II-1 : Experimental conditions and parameters of the absolute rate measurements of the reaction of OH radicals with $CF_2HCH=CF_2$ using the pulsed-laser photolysis–laser-induced fluorescence (PLP–LIF) set-up.

T (K)	P (Torr)	Bath gas	OH source	E_{248nm} (mJ pulse^{-1} cm^{-2})	$[OH]_0$ (10^{10} molecule cm^{-3})	$[CF_2HCH=CF_2]_0$ (10^{13} molecule cm^{-3})	k' range (s^{-1})	$k(T)$ (10^{-12} cm^3 molecule^{-1}s^{-1})
223	101	He	HNO$_3$	11.9	10.1	4.96–46.56	286–1877	4.03 ± 0.07
230	101	He	HNO$_3$	11.9	13.1	5.14–43.98	292–1731	3.77 ± 0.05
240	101	He	HNO$_3$	11.9	12.3	3.33–32.99	183–952	3.41 ± 0.04
245	100	He	HNO$_3$	16.9	7.8	5.52–41.25	199–1390	3.27 ± 0.06
250	101	He	HNO$_3$	9.9	14.2	5.98–41.10	266–1441	3.20 ± 0.05
260	100	He	HNO$_3$	9.9	11.6	4.30–38.97	237–1278	3.12 ± 0.04
260	100	He	HNO$_3$	16.9	5.4	4.39–40.15	172–1164	2.87 ± 0.05
262	100	Ar	H$_2$O$_2$	8.0	3.2	4.27–39.03	162–1131	2.79 ± 0.04
285	101	Ar	H$_2$O$_2$	7.0	4.0	2.61–34.31	156–942	2.59 ± 0.04
298	101	He	H$_2$O$_2$	17.9	23.8	3.92–35.52	195–983	2.48 ± 0.03
298	100	He	HNO$_3$	11.9	13.5	3.91–35.14	197–965	2.49 ± 0.03
298	101	He	HNO$_3$	11.9	19.1	4.77–43.28	290–1573	2.70 ± 0.04
323	101	Ar	HNO$_3$	4.0	1.9	4.17–31.90	124–738	2.30 ± 0.05
327	101	Ar	H$_2$O$_2$	4.4	30.6	7.51–25.33	737–1205	2.45 ± 0.09
331	101	He	H$_2$O$_2$	17.9	20.6	3.25–30.95	165–805	2.25 ± 0.03
346	100	He	H$_2$O$_2$	17.9	16.4	4.07–30.27	156–717	2.16 ± 0.03
353	101	Ar	HNO$_3$	4.0	1.7	3.53–29.10	108–667	2.11 ± 0.06
358	100	He	H$_2$O$_2$	17.9	17.6	3.67–28.24	146–707	2.14 ± 0.03
373	100	He	H$_2$O$_2$	17.9	15.8	2.84–27.67	130–633	2.06 ± 0.04
373	101	He	HNO$_3$	9.0	23.4	3.70–27.94	159–665	1.93 ± 0.04
373	101	Ar	H$_2$O$_2$	7.0	1.7	3.23–27.74	82–558	1.97 ± 0.05

Table App-II-2 : Experimental conditions and parameters of the absolute rate measurements of the reaction of OH radicals with $CF_3CH=CH_2$ using pulsed-laser photolysis–laser-induced fluorescence (PLP–LIF) set-up.

T (K)	P (Torr)	Bath gas	OH source	E_{248nm} (mJ pulse^{-1}cm^{-2})	$[OH]_0$ (10^{10} molecule cm^{-3})	$[CF_3CH=CH_2]_0$ (10^{14} molecule cm^{-3})	k' range (s^{-1})	$k(T)$ (10^{-12} cm^3 molecule^{-1}s^{-1})
212	104	He	HNO$_3$	27.9	6.7	2.52–21.30	518–4114	1.88 ± 0.13
213	104	He	HNO$_3$	27.9	7.5	0.37–2.50	118–543	1.81 ± 0.12
217	105	He	HNO$_3$	28.8	6.8	4.64–34.20	895–6708	1.80 ± 0.08
220	104	He	HNO$_3$	29.8	10.6	0.49–3.21	137–528	1.83 ± 0.12
224	104	He	HNO$_3$	27.9	14.5	2.54–19.80	533–4076	1.83 ± 0.09
229	111	He	HNO$_3$	34.8	18.0	0.35–2.68	160–590	1.86 ± 0.09
230	96	He	HNO$_3$	67.6	36.6	0.19–1.51	124–292	1.56 ± 0.22
233	111	He	HNO$_3$	71.6	47.9	1.36–8.69	270–1717	1.69 ± 0.12
233	104	He	HNO$_3$	27.9	15.8	2.36–18.90	516–3512	1.77 ± 0.09
244	103	He	HNO$_3$	34.8	35.1	0.37–2.39	178–532	1.72 ± 0.12
244	103	He	HNO$_3$	67.6	68.3	0.99–6.55	310–1325	1.82 ± 0.09
253	101	He	HNO$_3$	35.8	45.0	0.23–1.34	151–338	1.62 ± 0.25
260	101	He	H$_2$O$_2$	85.5	179.0	0.60–4.91	250–998	1.65 ± 0.03
262	106	He	H$_2$O$_2$	25.9	13.1	0.31–2.65	81–418	1.56 ± 0.13
265	100	He	HNO$_3$	35.8	48.1	0.20–1.21	152–309	1.76 ± 0.23

273	102	He	HNO$_3$	71.6	207.0	0.69–5.85	343–1183	1.66 ± 0.09
283	106	He	H$_2$O$_2$	27.9	41.5	0.34–2.07	156–402	1.47 ± 0.14
294	103	He	HNO$_3$	75.6	279.0	0.62–5.27	322–1054	1.55 ± 0.10
296	101	He	H$_2$O$_2$	85.5	195.0	1.21–4.55	323–848	1.55 ± 0.06
296	109	He	H$_2$O$_2$	67.6	254.0	13.90–64.60	2527–12272	1.42 ± 0.04
327	101	He	H$_2$O$_2$	85.5	194.0	0.45–4.18	240–742	1.41 ± 0.04
341	101	He	H$_2$O$_2$	51.7	96.0	0.63–5.51	246–1069	1.43 ± 0.02
353	103	He	H$_2$O$_2$	37.8	45.7	0.83–7.78	231–1206	1.39 ± 0.04
367	103	He	H$_2$O$_2$	37.8	55.7	0.88–6.31	248–1030	1.39 ± 0.04

App-II-2. Temperature dependence using SAR from (Michelat et al., 2022)

OH reaction
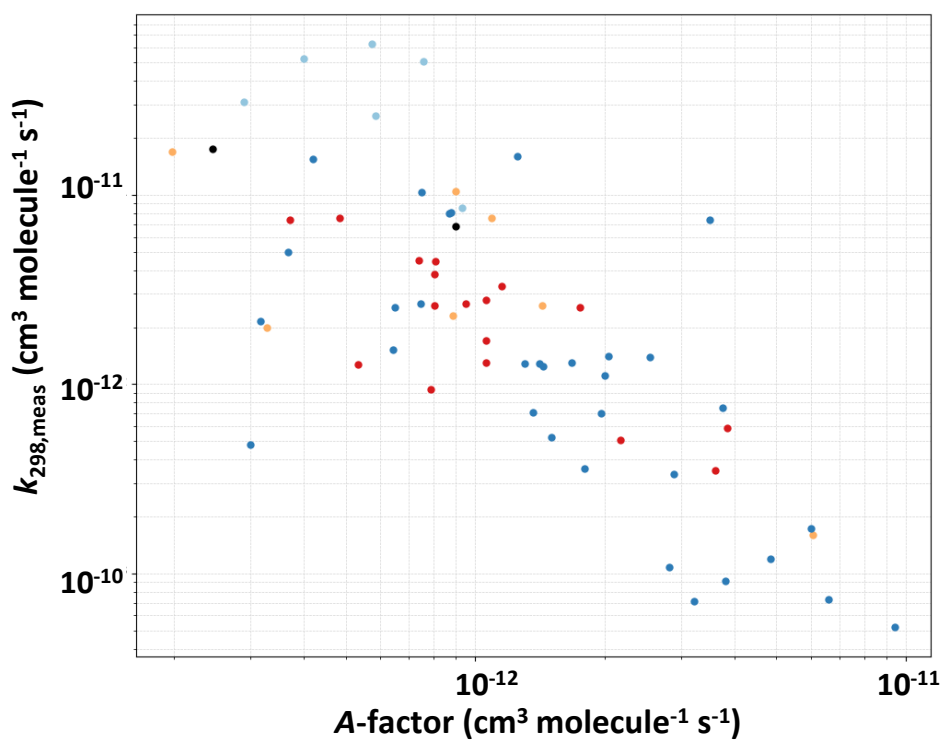
Figure App-II-1: Reaction rate constant at room temperature k_{298} as a function of the Arrhenius A-factor, expressed in logarithmic scale in cm^3 molecule^{-1} s^{-1}.

O$_3$ reaction
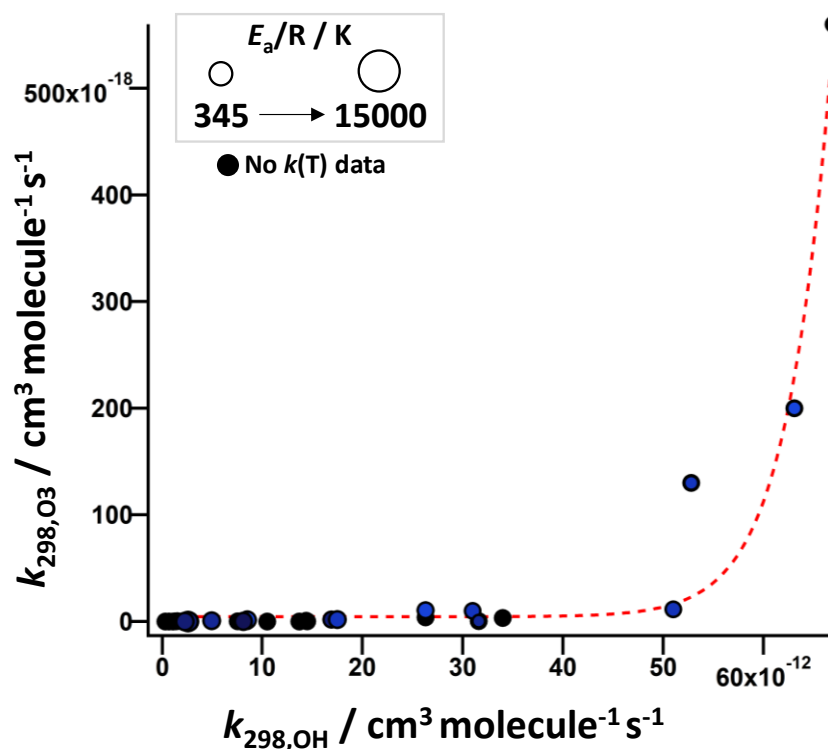
Cl reaction

Caveat: An attempt has been made to derive Arrhenius parameters for the Cl reaction, as described below. However, due to the very small amount of data and the lack of the barrier for the Cl reaction with CHX UVOCs, it has been concluded that it was unsuccessful, as could be expected from the difference in mechanism.

From Figure App-II-3, the rate coefficients for Cl are correlated to the activation energy, E_a/R, of their temperature dependence relationship, together with that of the OH reaction. Since the data are too limited to derive a reliable correlation and the reactivity of Cl is correlated to that of OH, as presented in the Figure App-II-4, it is possible to approximate the relationship between k_{298} and E_a/R for the Cl reaction from its correlation with that of OH. However, as illustrated by the example of some molecules in Figure App-II-3, it is not certain that the trends are similar. For example, ethene has one of the highest activation energies for Cl, while it is one of the smallest for OH reaction. Similarly, (E)-1,2-dichloroethene has the smallest E_a/R value for Cl reaction, around -1000K while it is in the middle of the range of values for OH reaction. It is possible that ethene represents an exception, and that the trend is similar, but due to the lack of data, it is not possible to conclude on this yet. The orange data point is that of ethene, and the literature data available in the database from (McGillen et al., 2020) recommend a value for the A-factor of 1×10^{-10} $cm^3molecule^{-1}s^{-1}$, with E_a/R=0K. This suggests that k_{Cl}(T) does not vary with temperature. From the Figure App-II-3, it appears that substitution is affecting this, by decreasing the value of the activation energy, and thus, the rate coefficient varies with temperature, as follows $k(T)=A\times exp(-E_a/(RT))$.
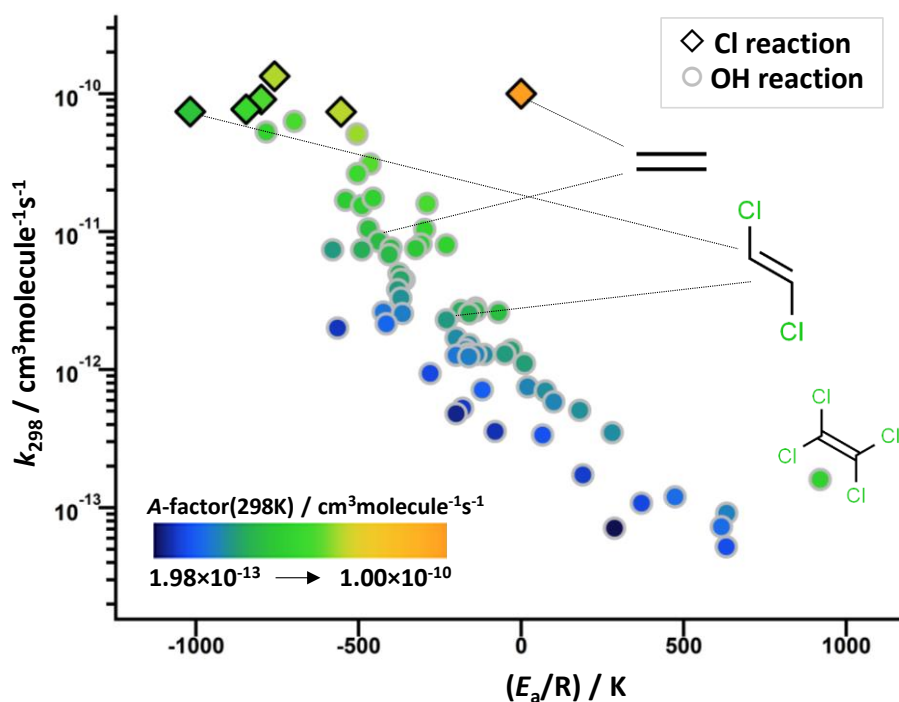
Figure App-II-3 : Rate coefficient for the Cl (diamond) and OH (circle) reactions at room temperature as a function of the activation energy, E_a/R, of the temperature dependent rate coefficients, k(T). The colors vary with the value of the A-factor defined by k(T)=A×exp(-E_a/(RT)). Smaller values of E_a/R and larger values of A-factor are correlated with faster rate coefficients, for the OH reaction. For the Cl reaction, the relationship is not clear, due to the lack of data. The A-factor seems correlated with the E_a/R values.
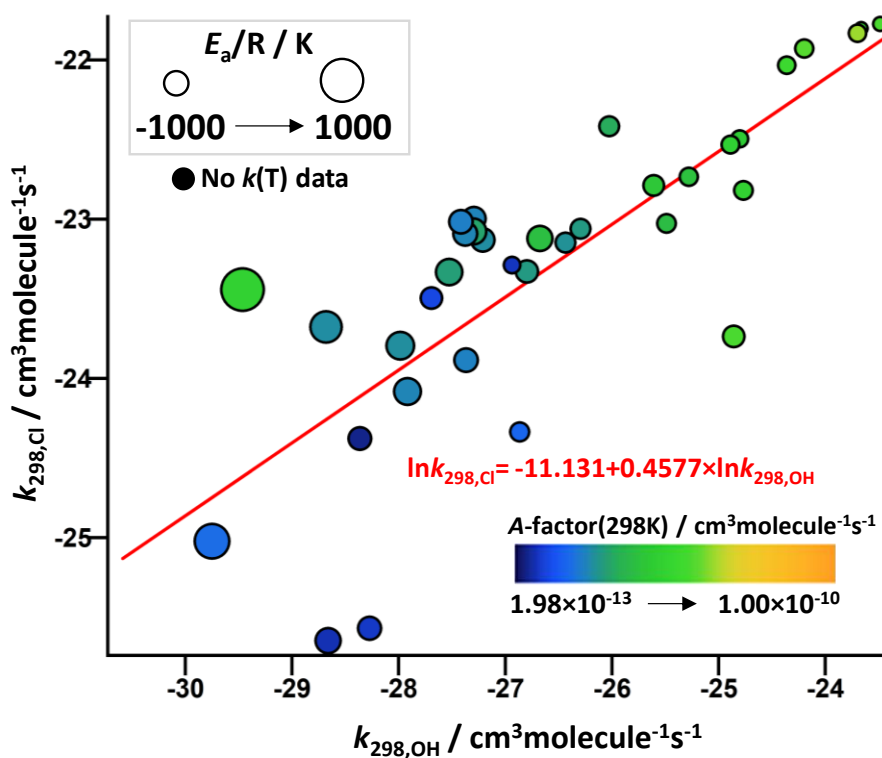
Figure App-II-4 : Rate coefficient for the Cl (y-axis) and OH (x-axis) reactions at room temperature, with size of the datapoints scaled on the value of the activation energy, E_a/R, of the temperature dependent rate coefficients, k_{OH}(T). When no k(T) is available, the data are plotted as a dark circle. All datapoints are included in the fit. The colors vary with the value of the A-factor defined by

$k(T)=A\times\exp(-E_a/(RT))$. There is a linear correlation between the Cl and the OH reactivity at room temperature and the relationship is written in red.

Taking this into account, a suggested method to obtain $(E_a/R)_{Cl}$ from the previous relationship is proposed. The calculation to obtain the relationships presented here are developed in detail in appendices. From the relationship in (Eq. II-10) from section II-3.2. in chapter II, $(E_a/R)_{OH}$ is obtained as a function of $k_{298,OH}$ as:

$$(E_a/R)_{OH} = -363K \times \ln(-8.6 / \ln(k_{298,OH} / 2.7\times10^{-10}) - 1) - 300K \qquad \text{(Eq. App-II-1)}$$

From the fit in Figure App-II-4, $k_{298,Cl}$ can be obtained as a function of $k_{298,OH}$, as follows:

$$k_{298,OH} = \exp((\ln k_{298,Cl} + 11.131)/0.4577) \quad \text{(Eq. App-II-2)}$$

Thus, by combining (Eq. App-II-1) and (Eq. App-II-2), $(E_a/R)_{Cl}$ can be obtained as a function of $k_{298,Cl}$:

$$(E_a/R)_{Cl} = -363K \times \ln([-8.6 / (2.1848 \times \ln(k_{298,Cl}) + 46.352) - 1]) - 300K \text{ (Eq. App-II-3)}$$

The relationship for OH has been extended to bigger values of E_a/R and larger rate coefficients, thus, the limits of the relationship for OH are updated to obtain those for Cl, as follows:

$$(E_a/R)_{Cl,max} = 920K \text{ if } k_{298,Cl} < 2.30\times10^{-14} \text{ cm}^3\text{molecule}^{-1}\text{s}^{-1}$$

$$(E_a/R)_{Cl,min} = -246K \text{ if } k_{298,Cl} > 7.40\times10^{-11} \text{ cm}^3\text{molecule}^{-1}\text{s}^{-1}$$

The predicted values of $(E_a/R)_{Cl}$ are plotted with the experimental Cl reaction rate coefficient in Figure App-II-5, together with those of OH in the inset, for comparison. Since the Cl reaction is faster than that of OH, it can be observed in Figure App-II-5 that the value of the activation energy is mostly estimated to be that of the limit, -246K, for the available kinetic dataset. From the previous Figure App-II-3, it was suggested that the reactivity does not vary significantly with the activation energy but mostly with the A-factor value, which is highlighted when comparing to the stronger temperature dependence for OH. Hence, the approximation on the limits of the sigmoid for Cl is reasonable.
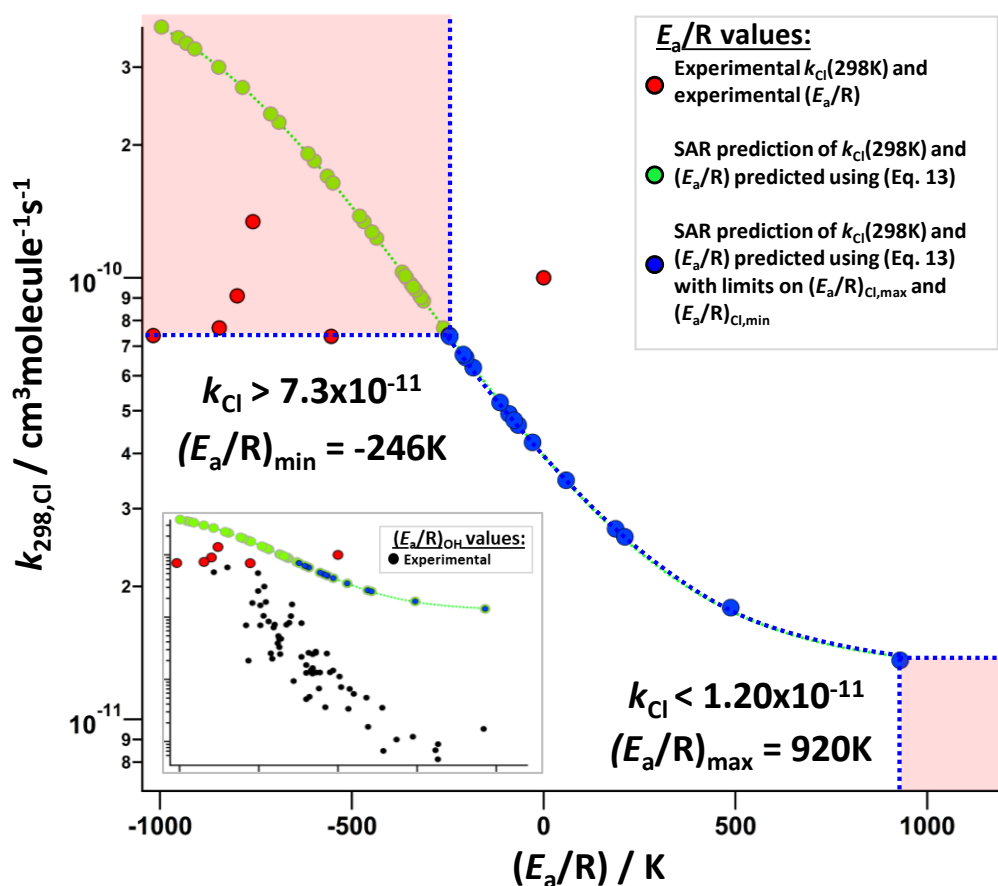
Figure App-II-5 : Sigmoidal fit of $k_{298,Cl}$ as a function of $(E_a/R)_{Cl}$, with limits in rate coefficients and activation energy. See the comparison between the relationships between $k(298K)$ and (E_a/R) for OH and Cl reactions in Figure App-II-3. The experimental values for $k_{Cl}(298K)$ and the activation energy are taken from (McGillen et al., 2020). The SAR predictions are obtained from the method described in this section. The activation energies are estimated based on the relationship between $k_{Cl}(298K)$ and $(E_a/R)_{Cl}$ expressed in (Eq. App-II-3). *Inset:* The $k_{298,OH}$ as a function of $(E_a/R)_{OH}$ are plotted together with the $k_{298,Cl}$ as a function n of $(E_a/R)_{Cl}$ from this plot to show the differences between Cl and OH correlations.

App-II-3. Additional data on results in section II-3

App-II-3.1. Predicting k(T) for the OH reaction of CHX alkenes

Experimental and predicted values of temperature-dependent rate coefficients, together with Arrhenius parameters, for the OH reaction are presented in Table App-II-3.

Table App-II-3: Results of the predictions using the model with factors in Table II-3. OH reaction rate constant at room temperature and Arrhenius parameters are retrieved. Calculated data are presented in the first column, and measurement data taken from (McGillen et al., 2020) database are displayed in the second main column, with temperature range associated. Unit of k_{298} and A-factor is cm³ molecule⁻¹ s⁻¹; E_a/R, T_{min} and T_{max} are expressed in K.

Index	Molecule	SAR predictions			Measurements			T-range^a (K)	
		k_{298} (10^{-12} cm^3 molecule^{-1} s^{-1})	A (10^{-13} cm^3 molecule^{-1} s^{-1})	E_a/R (K)	k_{298} (10^{-12} cm^3 molecule^{-1} s^{-1})	A (10^{-13} cm^3 molecule^{-1} s^{-1})	E_a/R (K)	T_{min}	T_{max}
1	(E)-CH$_3$CH$_2$=CH$_2$CH$_3$	6.31E-11	4.79E-12	-768	6.31E-11	6.06E-12	-698	295	800
2	(Z)-CH$_3$CH$_2$=CH$_2$CH$_3$	8.35E-11	6.01E-12	-784	5.28E-11	3.80E-12	-784	235	750
3	CH$_2$=C(CH$_3$)$_2$	8.35E-11	6.01E-12	-784	5.10E-11	9.40E-12	-505	290	430
4	CH$_2$=CHCH$_2$CH$_3$	2.19E-11	2.64E-12	-629	3.10E-11	6.60E-12	-465	290	430
5	CH$_2$=CHCH$_3$	2.19E-11	2.64E-12	-629	2.63E-11	4.85E-12	-504	293	467
6	CH$_2$=CHCH$_2$Cl	1.34E-11	2.09E-12	-555	1.69E-11	2.82E-12	-540	253	371
7	CH$_2$=CFCH$_3$	1.71E-11	2.34E-12	-593	1.55E-11	3.22E-12	-490	250	430
8	CH$_2$=CHCH$_2$Br	1.75E-11	2.37E-12	-596	1.75E-11	3.60E-12	-455	228	388
9	CH$_2$=CHCH$_2$F	1.60E-11	2.27E-12	-582	1.60E-11	6.00E-12	-290	228	388
10	CH$_2$=CCl$_2$	4.89E-12	1.38E-12	-376	1.05E-11	2.17E-12	-470	240	750
11	CF$_2$=CF$_2$	1.23E-11	2.00E-12	-540	1.04E-11	3.84E-12	-297	250	500
12	CH$_2$=CH$_2$	5.72E-12	1.46E-12	-406	8.52E-12	1.96E-12	-438	290	425
13	CF$_2$=CHF	6.56E-12	1.54E-12	-431	8.13E-12	2.89E-12	-308	253	328
14	(E)-CHF=CHF	8.38E-12	1.70E-12	-475	8.02E-12	3.75E-12	-230	250	430
15	CF$_2$=CFBr	8.00E-12	1.67E-12	-467	7.60E-12	2.00E-12	-400	250	370
16	CH$_2$=CHCl	5.29E-12	1.42E-12	-391	7.55E-12	2.54E-12	-325	289	600
17	CF$_2$=CFCl	6.18E-12	1.51E-12	-420	7.40E-12	1.06E-12	-580	297	364
18	CF$_2$=CFCHF$_2$	5.92E-12	1.48E-12	-412	7.40E-12	1.43E-12	-490	250	430
19	CH$_2$=CHBr	1.33E-11	2.08E-12	-553	6.81E-12	1.79E-12	-406	299	426
20	CH$_2$=CHF	4.48E-12	1.34E-12	-359	4.97E-12	1.41E-12	-376	299	328
21	(Z)-CHCl=CFCHF$_2$	4.48E-12	1.34E-12	-359	4.48E-12	1.36E-12	-360	250	430
22	CF$_2$=CHBr	4.28E-12	1.32E-12	-350	4.50E-12	1.30E-12	-370	250	370
23	CH$_2$=CBrCF$_3$	3.30E-12	1.21E-12	-298	3.80E-12	1.06E-12	-380	250	370
24	CH$_2$=CBrCF$_2$CF$_3$	3.30E-12	1.21E-12	-298	3.30E-12	9.50E-13	-370	250	370
25	(Z)-CFCl=CFCl	3.11E-12	1.19E-12	-286	2.80E-12	1.75E-12	-140	250	430
26	CH$_2$=CHCFClCF$_2$Br	2.05E-12	1.05E-12	-198	2.62E-12	6.45E-13	-424	230	370
27	CH$_2$=CF$_2$	3.50E-12	1.24E-12	-311	2.68E-12	1.44E-12	-185	253	328
28	(E)-CFCl=CFCl	3.17E-12	1.20E-12	-290	2.67E-12	1.67E-12	-140	250	430
29	(Z)-CHCl=CHCl	4.89E-12	1.38E-12	-376	2.60E-12	2.04E-12	-70	240	400
30	(E)-CHCl=CFCHF$_2$	2.54E-12	1.12E-12	-244	2.54E-12	1.50E-12	-160	250	430
31	CF$_2$HCH=CF$_2$	3.17E-12	1.20E-12	-290	2.55E-12	7.46E-13	-365	212	367
32	(E)-CHCl=CHCl	2.16E-12	1.07E-12	-210	2.30E-12	1.06E-12	-230	240	720
33	CF$_2$=CFCF$_3$	1.94E-12	1.04E-12	-186	2.15E-12	5.34E-13	-415	230	480
34	CHCl=CCl$_2$	2.00E-12	1.05E-12	-193	2.00E-12	3.00E-13	-565	230	300
35	CH$_2$=CHCF$_2$CF$_2$Br	2.05E-12	1.05E-12	-198	1.70E-12	8.70E-13	-200	250	370
36	CH$_2$=CHCF$_3$	1.42E-12	9.60E-13	-116	1.52E-12	8.86E-13	-160	223	373
37	CH$_2$=CHCF$_2$CF$_3$	1.42E-12	9.60E-13	-116	1.40E-12	7.90E-13	-170	263	358
38	CH$_2$=CHCF$_2$CF$_2$CF$_2$CF$_2$CF$_3$	1.42E-12	9.60E-13	-116	1.39E-12	1.25E-12	-31	270	330
39	(Z)-CHF=CFCF$_3$	2.08E-12	1.06E-12	-201	1.30E-12	7.50E-13	-165	207	380
40	(Z)-CHF=CHCF$_3$	1.11E-12	9.08E-13	-60	1.29E-12	8.80E-13	-114	253	328
41	(E)-CHCl=CFCF$_3$	1.35E-12	9.49E-13	-105	1.30E-12	1.09E-12	-50	250	430
42	CH$_2$=CHCF$_2$CF$_2$CF$_2$CF$_3$	1.42E-12	9.60E-13	-116	1.29E-12	8.09E-13	-139	270	330

111

43	CCl$_2$=CFCF$_3$	1.27E-12	9.36E-13	-91	1.27E-12	6.50E-13	-200	250	430
44	CH$_2$=CHCF$_2$CF$_3$	1.42E-12	9.60E-13	-116	1.24E-12	7.40E-13	-161	263	358
45	CH$_2$=CFCF$_3$	1.11E-12	9.08E-13	-60	1.11E-12	1.15E-12	10	200	300
46	(Z)-CHCl=CHCF$_3$	1.31E-12	9.43E-13	-98	9.40E-13	3.67E-13	-280	213	376
47	CH$_2$=C(CF$_3$)$_2$	3.52E-13	7.38E-13	221	7.51E-13	8.03E-13	20	250	430
48	CF$_2$=CHCF$_3$	1.04E-12	8.95E-13	-44	7.14E-13	4.85E-13	-120	250	430
49	(E)-CHF=CHCF$_3$	1.32E-12	9.45E-13	-101	7.02E-13	9.01E-13	74	253	328
50	(E)-CF$_3$CF=CFCF$_3$	2.73E-13	7.12E-13	286	5.26E-13	3.17E-13	-180	230	370
51	(Z)-CHCl=CFCF$_3$	1.05E-12	8.96E-13	-46	5.84E-13	8.02E-13	100	250	430
52	(Z)-CF$_3$CCl=CHCl	5.36E-13	7.89E-13	115	5.08E-13	9.30E-13	180	250	430
53	(Z)-CF$_3$CH=CHCF$_3$	3.52E-13	7.38E-13	221	4.80E-13	2.46E-13	-200	212	374
54	(Z)-CF$_3$CF=CFCF$_3$	3.07E-13	7.23E-13	256	3.57E-13	2.90E-13	-80	230	370
55	(E)-CHCl=CHCF$_3$	1.72E-12	1.01E-12	-160	3.50E-13	9.00E-13	280	213	376
56	(E)-(CF$_3$)$_2$CFCH=CHF	1.32E-12	9.45E-13	-101	3.36E-13	4.19E-13	66	214	380
57	CCl$_2$=CCl$_2$	8.18E-13	8.52E-13	12	1.60E-13	3.50E-12	920	296.5	714
58	(E)-CF$_3$CH=CHCF$_3$	1.86E-13	6.76E-13	384	1.20E-13	5.87E-13	473	253	328
59	(E)-CF$_3$CH=CHCF$_2$CF$_3$	1.86E-13	6.76E-13	384	9.10E-14	7.56E-13	632	253	328
60	(CF$_3$)$_2$C=CFCF$_2$CF$_3$	4.31E-14	5.56E-13	762	7.10E-14	1.98E-13	287	250	480
61	c-C$_4$H$_2$F$_4$	1.08E-13	6.30E-13	526	1.73E-13	3.28E-13	190	253	328
62	c-C$_5$H$_2$F$_6$	1.08E-13	6.30E-13	526	1.08E-13	3.72E-13	370	253	328
63	c-C$_5$F$_8$	9.42E-14	6.19E-13	561	7.27E-14	5.74E-13	616	253	328
64	c-C$_5$HF$_7$	1.01E-13	6.25E-13	543	5.20E-14	4.00E-13	631	242	370
A	c-C$_5$H$_8$	2.56E-11	2.87E-12	-652	6.70E-11			200	400
B	CH$_2$=C(CH$_3$)CH$_2$Cl	5.14E-11	4.23E-12	-744	3.40E-11			200	400
C	CH$_2$=C(CH$_2$Cl)$_2$	3.16E-11	3.21E-12	-681	3.16E-11			200	400
D	CH$_2$=CHCH$_2$CH$_2$Cl	2.19E-11	2.64E-12	-629	2.63E-11			200	400
E	CH$_2$=CHCHClCH$_2$Cl	1.34E-11	2.09E-12	-555	1.45E-11			200	400
F	(E)-CHCl=CHCH$_2$Cl	1.44E-11	2.16E-12	-566	1.44E-11			200	400
G	CH$_2$=CClCH$_2$Cl	1.24E-11	2.02E-12	-542	1.37E-11			200	400
H	(Z)-CHCl=CHCH$_2$Cl	1.24E-11	2.02E-12	-542	8.45E-12			200	400
I	CCl$_2$=CF$_2$	3.11E-12	1.19E-12	-286	5.00E-12			200	400
J	(E)-CHF=CFCF$_3$	1.04E-12	8.95E-13	-44	2.30E-12			200	400
K	CF$_2$=CFCF$_2$CF$_3$	1.94E-12	1.04E-12	-186	1.94E-12			200	400
L	CH$_2$=CH(CF$_2$)$_7$CF$_3$	1.42E-12	9.60E-13	-116	1.28E-12			200	400
M	CCl$_2$=CClCF$_3$	6.51E-13	8.16E-13	68	9.32E-13			200	400

^{a} Temperature ranges indicated are that of the experimental data when available; otherwise, the range T=200–400K is mentioned,

as the one over which prediction has been made.

App-II-3.2. Predicting k(T) for the Cl reaction of CHX alkenes

The activation energy is estimated for Cl using the (Eq. App-II-2) and the *A*-factor (in cm^3 molecule^{-1} s^{-1}) is calculated using (Eq. App-II-3). The *A*-factor in the Cl training set ranges from 2.40×10^{-12} cm^3 molecule^{-1} s^{-1} to 1.00×10^{-10} cm^3 molecule^{-1} s^{-1} and the E_a/R from -1018K to 0K. The predicted k_{Cl}(T=200–400K) are estimated over the temperature range of this study (200–400 K) and compared to available measurements (see Figure App-II-6). The Arrhenius plots for the experimental and predicted rate coefficients are provided below.

It is observed in the Figure App-II-6 that the $k_{SAR,Cl}$ have the tendency to be underpredicted at lower temperatures and overpredicted at higher temperature. Given the small amount of data on the temperature dependence of the Cl reaction, there may be some uncertainty in the determinations. Most of the alkenes are likely to react around a value of 1×10^{-10} cm^3 molecule^{-1} s^{-1}, which result in a similar value of E_a/R predicted using the (Eq. App-II-3). From the Figure App-II-5, it appears clear that the experimental values of the available dataset of E_a/R are lower than the values that can be predicted using the sigmoidal fit. There is room for improvement in the method to predict E_a/R of the Cl reaction but this would require new kinetic data to improve the parametrization of the Arrhenius parameters.

Despite these uncertainties, most of the rate coefficients $k_{SAR,Cl}$ are predicted within a factor of 2 of agreement with $k_{EXP,Cl}$ over the temperature range T=250–375K. The largest discrepancies are mostly for the lower temperatures. The main outlier is ethene, since no temperature dependence was obtained from the recommended value of the temperature-dependent rate coefficients in (McGillen et al., 2020) database. Here, the SAR predicts the following Arrhenius expression: k_{Cl}(T) = 9.22×10^{-11} exp(246/T)).
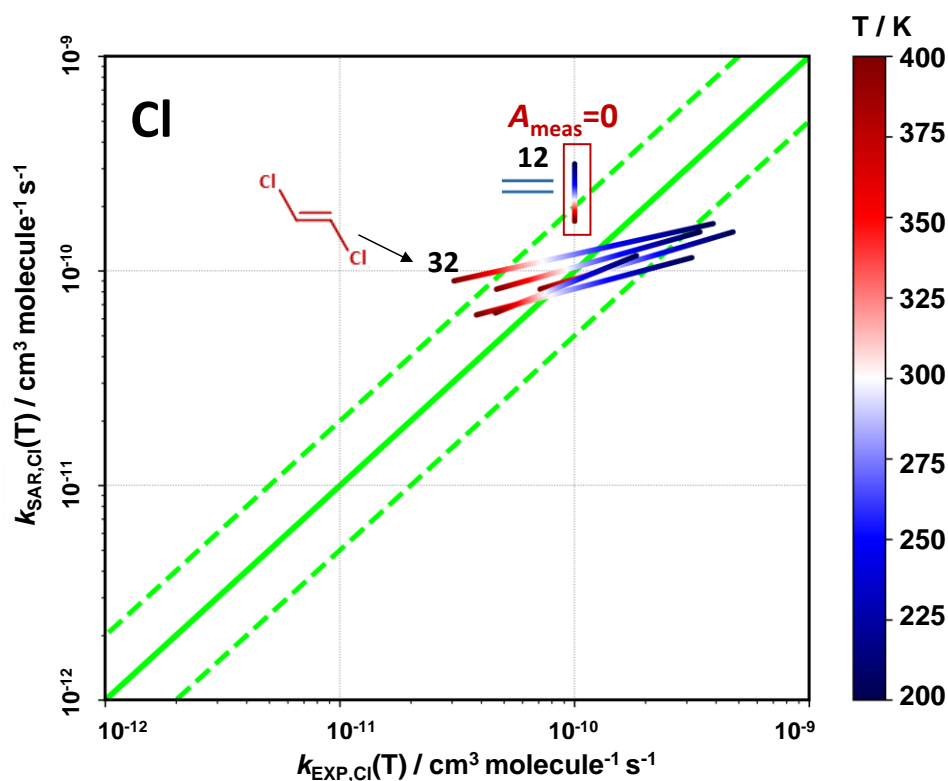
Figure App-II-6 : Calculated Cl rate coefficients versus measured Cl reaction rate coefficients as a function of temperature over 200–400K. The bold green line represents the perfect agreement between prediction and measurements. The dashed lines identify the range within which calculations and measurements agree within a factor of 2 on either side.

With the limited availability of temperature-dependent data for the Cl dataset, this parameterization of the Cl temperature dependence remains speculative. However, based on the reduced reactivity of some of the more electron-withdrawn molecules in the k_{298} data, it can be anticipated that some of this variation can be explained by the presence of a measurable activation energy. New temperature-dependent measurements for some of these less reactive compounds in the chlorine dataset would be useful in this regard.

Experimental and predicted values of temperature-dependent rate coefficients, together with Arrhenius parameters, for the Cl reaction are presented in Figure App-II-7 and Table App-II-4.
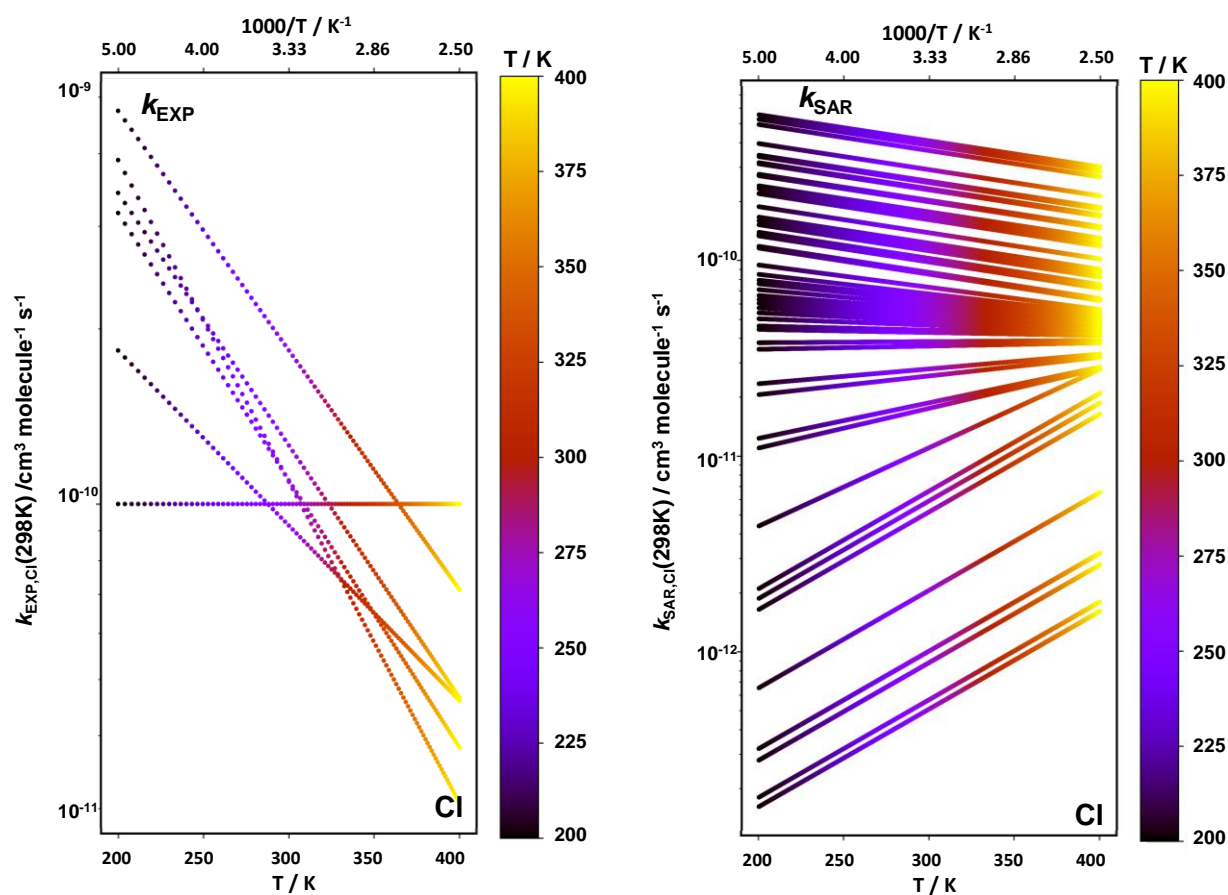
Figure App-II-7 : Arrhenius plots of the Cl reaction rate coefficients of the 77 alkenes and haloalkenes included in this study. Data were taken from the recent database of (McGillen et al., 2020). Left panel: lines represent temperature-dependent measurements. Right panel: lines represent temperature-dependent predictions.

Table App-II-4 : Results of the predictions for Cl using the model with factors in Table II-4. Cl reaction rate constant at room temperature and Arrhenius parameters are retrieved. Calculated data are presented in the first column, and measurement data taken from (McGillen et al., 2020) database are displayed in the second main column, with temperature range associated. Unit of k_{298} and A-factor is cm^3 molecule^{-1} s^{-1}; E_a/R, T_{min} and T_{max} are expressed in K.

		SAR predictions (Cl)			Measurements (Cl)			T-range^a (K)	
Index	Molecule	k_{298} (cm³ molecule⁻¹ s⁻¹)	A (cm³ molecule⁻¹ s⁻¹)	E_a/R (K)	k_{298} (cm³ molecule⁻¹ s⁻¹)	A (cm³ molecule⁻¹ s⁻¹)	E_a/R (K)	T_{min}	T_{max}
1	(E)-CH₃CH₂=CH₂CH₃	3.51E-10	1.54E-10	-246	3.50E-10				
2	(Z)-CH₃CH₂=CH₂CH₃	3.30E-10	1.44E-10	-246	3.40E-10				
3	CH₂=C(CH₃)₂	3.30E-10	1.44E-10	-246	3.30E-10				
4	CH₂=CHCH₂CH₃	2.64E-10	1.15E-10	-246	3.00E-10				
5	CH₂=CHCH₃	2.64E-10	1.15E-10	-246	2.70E-10				
6	CH₂=CHCH₂Cl	1.81E-10	7.91E-11	-246	1.70E-10				
7	CH₂=CFCH₃	2.30E-10	1.01E-10	-246	1.64E-10				
8	CH₂=CHCH₂Br	1.47E-10	6.42E-11	-246	1.23E-10				
9	CH₂=CHCH₂F	4.92E-11	3.63E-11	-90.95	4.92E-11				
10	CH₂=CCl₂	1.01E-10	4.44E-11	-246	1.34E-10	1.07E-11	-758	298	348
11	CF₂=CF₂	5.37E-11	3.52E-11	-125.89					
12	CH₂=CH₂	2.11E-10	9.22E-11	-246	1.00E-10	1.00E-10	0	250	300
13	CF₂=CHF	9.28E-11	4.07E-11	-246					
14	(E)-CHF=CHF	1.06E-10	4.66E-11	-246					
15	CF₂=CFBr	7.33E-13	1.61E-11	920					
16	CH₂=CHCl	1.46E-10	6.40E-11	-246	1.27E-10				
17	CF₂=CFCl	6.00E-11	3.41E-11	-168.38					
18	CF₂=CFCHF₂	7.33E-13	1.61E-11	920					
19	CH₂=CHBr	2.08E-10	9.10E-11	-246					
20	CH₂=CHF	1.84E-10	8.05E-11	-246	1.84E-10				
21	(Z)-CHCl=CFCHF₂	8.18E-13	1.79E-11	920					
22	CF₂=CHBr	1.27E-12	2.78E-11	920					
23	CH₂=CBrCF₃	8.89E-11	3.89E-11	-246	9.67E-11				
24	CH₂=CBrCF₂CF₃	8.89E-11	3.89E-11	-246	8.87E-11				
25	(Z)-CFCl=CFCl	6.70E-11	3.31E-11	-209.99					
26	CH₂=CHCFClCF₂Br	1.45E-12	3.18E-11	920					
27	CH₂=CF₂	1.60E-10	7.02E-11	-246					
28	(E)-CFCl=CFCl	5.60E-11	3.48E-11	-142.24					
29	(Z)-CHCl=CHCl	1.01E-10	4.44E-11	-246	9.10E-11	6.30E-12	-799	298	348
30	(E)-CHCl=CFCHF₂	1.27E-12	2.78E-11	920					
31	CF₂HCH=CF₂	1.27E-12	2.78E-11	920					
32	(E)-CHCl=CHCl	1.11E-10	4.86E-11	-246	7.40E-11	2.40E-12	-1018	298	348
33	CF₂=CFCF₃	2.14E-11	6.58E-11	335.29	2.70E-11				
34	CHCl=CCl₂	7.70E-11	3.37E-11	-246	7.70E-11	4.60E-12	-846	298	348
35	CH₂=CHCF₂CF₂Br	1.45E-12	3.18E-11	920					
36	CH₂=CHCF₃	9.01E-11	3.95E-11	-246	9.02E-11				
37	CH₂=CHCF₂CF₃	9.01E-11	3.95E-11	-246	1.03E-10				
38	CH₂=CHCF₂CF₂CF₂CF₂CF₃	9.01E-11	3.95E-11	-246	9.51E-11				
39	(Z)-CHF=CFCF₃	4.55E-11	3.73E-11	-59.69	4.24E-11				
40	(Z)-CHF=CHCF₃	7.87E-11	3.45E-11	-246					
41	(E)-CHCl=CFCF₃	4.56E-11	3.73E-11	-59.86					
42	CH₂=CHCF₂CF₂CF₃	9.01E-11	3.95E-11	-246	9.38E-11				
43	CCl₂=CFCF₃	2.94E-11	4.70E-11	139.59					

44	CH$_2$=CHCF$_2$CF$_2$CF$_3$	**9.01E-11**	**3.95E-11**	-246	**1.01E-10**				
45	CH$_2$=CFCF$_3$	**7.87E-11**	**3.45E-11**	-246	**7.37E-11**	1.15E-11	-554	300	462
46	(Z)-CHCl=CHCF$_3$	**6.26E-11**	**3.37E-11**	-184.39	**6.26E-11**				
47	CH$_2$=C(CF$_3$)$_2$	**3.86E-11**	**4.00E-11**	10.61	**3.48E-11**				
48	CF$_2$=CHCF$_3$	**3.69E-11**	**4.09E-11**	30.51					
49	(E)-CHF=CHCF$_3$	**4.23E-11**	**3.84E-11**	-28.86	**4.64E-11**				
50	(E)-CF$_3$CF=CFCF$_3$	**7.46E-12**	**1.63E-10**	920	**7.87E-12**				
51	(Z)-CHCl=CFCF$_3$	**5.08E-11**	**3.58E-11**	-104.13					
52	(Z)-CF$_3$CCl=CHCl	**4.75E-11**	**3.67E-11**	-76.86					
53	(Z)-CF$_3$CH=CHCF$_3$	**3.86E-11**	**4.00E-11**	10.61	**2.59E-11**				
54	(Z)-CF$_3$CF=CFCF$_3$	**8.50E-12**	**1.86E-10**	920	**7.28E-12**				
55	(E)-CHCl=CHCF$_3$	**5.22E-11**	**3.55E-11**	-114.54	**5.22E-11**				
56	(E)-(CF$_3$)$_2$CFCH=CHF	**4.23E-11**	**3.84E-11**	-28.86					
57	CCl$_2$=CCl$_2$	**5.85E-11**	**3.43E-11**	-158.44	**6.60E-11**				
58	(E)-CF$_3$CH=CHCF$_3$	**1.48E-11**	**1.76E-10**	738.13	**1.36E-11**				
59	(E)-CF$_3$CH=CHCF$_2$CF$_3$	**1.48E-11**	**1.76E-10**	738.13					
60	(CF$_3$)$_2$C=CFCF$_2$CF$_3$	**2.97E-12**	**6.50E-11**	920					
61	c-C$_4$H$_2$F$_4$	**4.33E-11**	**3.80E-11**	-38.81					
62	c-C$_5$H$_2$F$_6$	**4.33E-11**	**3.80E-11**	-38.81					
63	c-C$_5$F$_8$	**9.53E-12**	**2.09E-10**	920					
64	c-C$_5$HF$_7$	**2.03E-11**	**7.12E-11**	373.51					
A	c-C$_5$H$_8$	**3.70E-10**	**1.62E-10**	-246	**3.70E-10**				
B	CH$_2$=C(CH$_3$)CH$_2$Cl	**2.26E-10**	**9.90E-11**	-246	**2.25E-10**				
C	CH$_2$=C(CH$_2$Cl)$_2$	**1.55E-10**	**6.79E-11**	-246					
D	CH$_2$=CHCH$_2$CH$_2$Cl	**2.64E-10**	**1.15E-10**	-246	**2.35E-10**				
E	CH$_2$=CHCHClCH$_2$Cl	**1.81E-10**	**7.91E-11**	-246	**1.91E-10**				
F	(E)-CHCl=CHCH$_2$Cl	**1.45E-12**	**3.18E-11**	920					
G	CH$_2$=CClCH$_2$Cl	**1.25E-10**	**5.49E-11**	-246	**1.38E-10**				
H	(Z)-CHCl=CHCH$_2$Cl	**1.25E-10**	**5.49E-11**	-246					
I	CCl$_2$=CF$_2$	**6.70E-11**	**3.31E-11**	-209.99	**6.70E-11**				
J	(E)-CHF=CFCF$_3$	**3.69E-11**	**4.09E-11**	30.51	**4.76E-11**				
K	CF$_2$=CFCF$_2$CF$_3$	**2.14E-11**	**6.58E-11**	335.29	**1.79E-11**				
L	CH$_2$=CH(CF$_2$)$_7$CF$_3$	**9.01E-11**	**3.95E-11**	-246	**9.54E-11**				
M	CCl$_2$=CClCF$_3$	**2.75E-11**	**4.97E-11**	176.1					

[a] Temperature ranges indicated are that of the experimental data when available; otherwise, the range T=200–400K is mentioned, as the one over which prediction has been made.

App-II-3.3. Predicting *k*(T) for the NO₃ reaction of CHX alkenes

Experimental and predicted values of temperature-dependent rate coefficients, together with Arrhenius parameters, for the NO₃ reaction are presented in Figure App-II-8 and Table App-II-5.
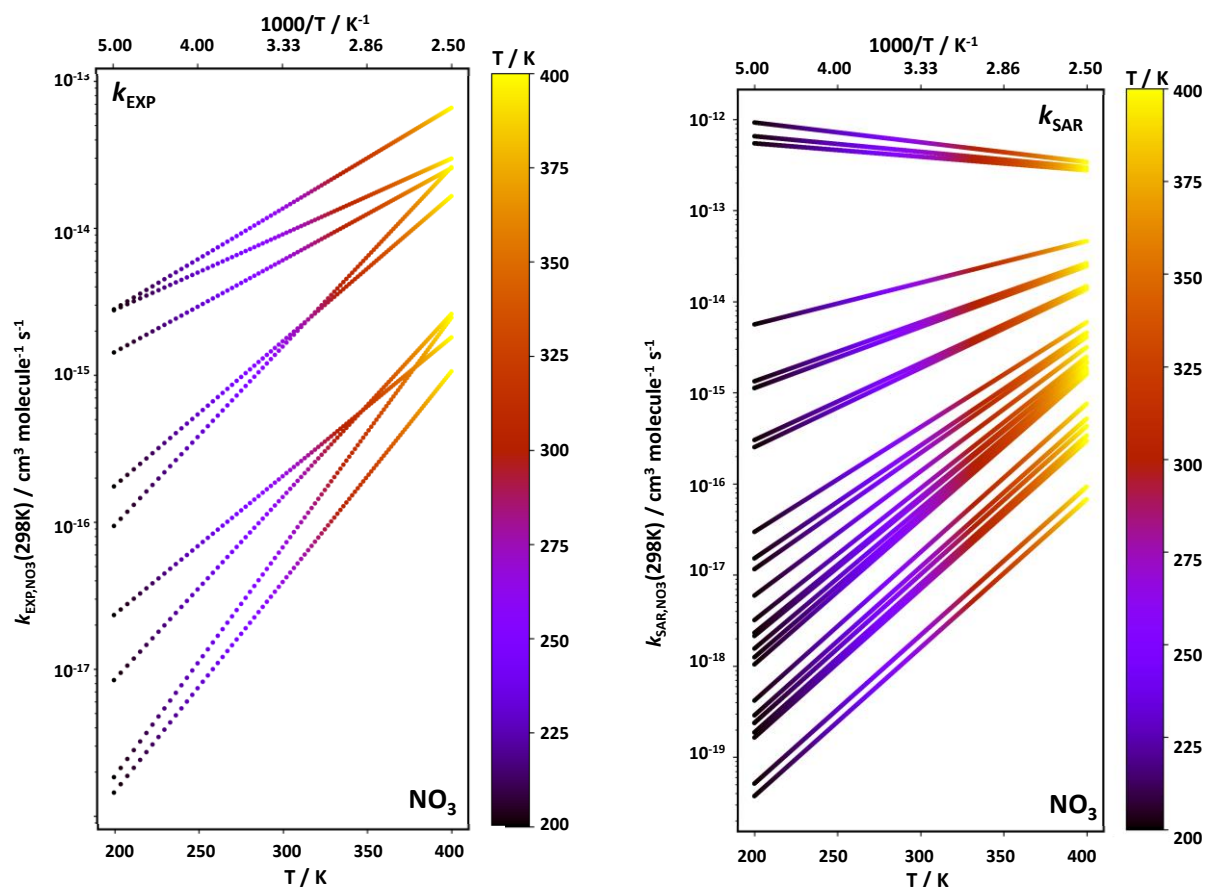
<u>Figure App-II-8</u> : Arrhenius plots of the NO₃ reaction rate coefficients of the 77 alkenes and haloalkenes included in this study. Data were taken from the recent database of (McGillen et al., 2020). Left panel: lines represent temperature-dependent measurements. Right panel: lines represent temperature-dependent predictions.

<u>Table App-II-5 :</u> Results of the predictions for NO₃ using the model with factors in Table II-4. NO₃ reaction rate constant at room temperature and Arrhenius parameters are retrieved. Calculated data are presented in the first column, and measurement data taken from (McGillen et al., 2020)) database are displayed in the second main column, with temperature range associated. Unit of k_{298} and A-factor is cm³ molecule⁻¹ s⁻¹; E_a/R, T_{min} and T_{max} are expressed in K.

		SAR predictions (NO₃)			Measurements (NO₃)			T-range^a (K)	
Index	Molecule	k_{298} (cm³ molecule⁻¹ s⁻¹)	A (cm³ molecule⁻¹ s⁻¹)	E_a/R (K)	k_{298} (cm³ molecule⁻¹ s⁻¹)	A (cm³ molecule⁻¹ s⁻¹)	E_a/R (K)	T_{min}	T_{max}
1	(E)-CH₃CH₂=CH₂CH₃	3.90E-13	1.35E-13	-315	3.90E-13				
2	(Z)-CH₃CH₂=CH₂CH₃	3.50E-13	1.41E-13	-271	3.50E-13				
3	CH₂=C(CH₃)₂	3.50E-13	1.41E-13	-271	3.40E-13				
4	CH₂=CHCH₂CH₃	8.57E-15	5.39E-13	1234	1.30E-14	3.20E-13	950	230	480
5	CH₂=CHCH₃	8.57E-15	5.39E-13	1234	9.50E-15	4.60E-13	1155	290	430
6	CH₂=CHCH₂Cl	5.51E-16	1.46E-12	2348	5.52E-16				
7	CH₂=CFCH₃	6.75E-15							
8	CH₂=CHCH₂Br	3.50E-15	7.46E-13	1598	3.50E-15	1.56E-12	1819	296	428
9	CH₂=CHCH₂F	3.90E-15	7.17E-13	1554	3.90E-15	7.17E-12	2248	296	430
10	CH₂=CCl₂	6.49E-16	1.37E-12	2282	1.53E-15				
11	CF₂=CF₂	3.08E-16							
12	CH₂=CH₂	2.10E-16	2.06E-12	2740	2.10E-16	3.30E-12	2880	270	340
13	CF₂=CHF	2.00E-16	2.10E-12	2759	2.00E-16				
14	(E)-CHF=CHF	2.54E-16							
15	CF₂=CFBr								
16	CH₂=CHCl	3.69E-16	1.68E-12	2511	3.90E-16	1.40E-13	1740	266	367
17	CF₂=CFCl								
18	CF₂=CFCHF₂								
19	CH₂=CHBr								
20	CH₂=CHF	1.65E-16	2.25E-12	2837	1.90E-16				
21	(Z)-CHCl=CFCHF₂								
22	CF₂=CHBr								
23	CH₂=CBrCF₃								
24	CH₂=CBrCF₂CF₃								
25	(Z)-CFCl=CFCl								
26	CH₂=CHCFClCF₂Br								
27	CH₂=CF₂	1.30E-16	2.46E-12	2934	1.30E-16				
28	(E)-CFCl=CFCl	1.75E-16							
29	(Z)-CHCl=CHCl	6.49E-16	1.37E-12	2282	1.50E-16				
30	(E)-CHCl=CFCHF₂								
31	CF₂HCH=CF₂								
32	(E)-CHCl=CHCl	1.45E-16	2.36E-12	2890	1.11E-16	7.80E-13	2640	293	373
33	CF₂=CFCF₃								
34	CHCl=CCl₂	2.55E-16	1.93E-12	2661	3.70E-16	8.10E-13	2295	278	367
35	CH₂=CHCF₂CF₂Br								
36	CH₂=CHCF₃	3.30E-17	7.78E-13	3000					
37	CH₂=CHCF₂CF₃	3.30E-17	7.78E-13	3000					
38	CH₂=CHCF₂CF₂CF₂CF₂CF₃	3.30E-17	7.78E-13	3000					
39	(Z)-CHF=CFCF₃	4.00E-17	9.42E-13	3000					
40	(Z)-CHF=CHCF₃	2.60E-17	6.12E-13	3000					
41	(E)-CHCl=CFCF₃								
42	CH₂=CHCF₂CF₂CF₂CF₃	3.30E-17	7.78E-13	3000					
43	CCl₂=CFCF₃								

#									
44	$CH_2=CHCF_2CF_2CF_3$	3.30E-17	7.78E-13	3000					
45	$CH_2=CFCF_3$	2.60E-17	6.12E-13	3000	2.60E-17				
46	$(Z)-CHCl=CHCF_3$	5.81E-17	1.37E-12	3000					
47	$CH_2=C(CF_3)_2$	5.20E-18	1.22E-13	3000					
48	$CF_2=CHCF_3$								
49	$(E)-CHF=CHCF_3$								
50	$(E)-CF_3CF=CFCF_3$								
51	$(Z)-CHCl=CFCF_3$								
52	$(Z)-CF_3CCl=CHCl$	2.28E-17	5.37E-13	3000					
53	$(Z)-CF_3CH=CHCF_3$	5.20E-18	1.22E-13	3000					
54	$(Z)-CF_3CF=CFCF_3$								
55	$(E)-CHCl=CHCF_3$								
56	$(E)-(CF_3)_2CFCH=CHF$								
57	$CCl_2=CCl_2$	1.00E-16							
58	$(E)-CF_3CH=CHCF_3$								
59	$(E)-CF_3CH=CHCF_2CF_3$								
60	$(CF_3)_2C=CFCF_2CF_3$								
61	$c-C_4H_2F_4$	7.13E-18	1.68E-13	3000					
62	$c-C_5H_2F_6$	7.13E-18	1.68E-13	3000					
63	$c-C_5F_8$								
64	$c-C_5HF_7$								
A	$c-C_5H_8$	4.80E-13	1.26E-13	-399	4.80E-13				
B	$CH_2=C(CH_3)CH_2Cl$	2.25E-14	3.80E-13	843	2.25E-14	1.55E-12	1262.86	298	473
C	$CH_2=C(CH_2Cl)_2$	1.45E-15							
D	$CH_2=CHCH_2Cl$	8.57E-15	5.39E-13	1234	4.48E-15				
E	$CH_2=CHCHClCH_2Cl$	5.51E-16	1.46E-12	2348	3.00E-16				
F	$(E)-CHCl=CHCH_2Cl$	9.50E-15	5.20E-13	1193	9.50E-15				
G	$CH_2=CClCH_2Cl$	9.69E-16	1.19E-12	2119	1.45E-15				
H	$(Z)-CHCl=CHCH_2Cl$	9.69E-16							
I	$CCl_2=CF_2$								
J	$(E)-CHF=CFCF_3$								
K	$CF_2=CFCF_2CF_3$								
L	$CH_2=CH(CF_2)_7CF_3$	3.30E-17	7.78E-13	3000					
M	$CCl_2=CClCF_3$								

[a] Temperature ranges indicated are that of the experimental data when available; otherwise, the range T=200–400K is mentioned, as the one over which prediction has been made.

App-II-3.4. Predicting *k*(T) for the NO₃ reaction of CHX alkenes

Experimental and predicted values of temperature-dependent rate coefficients, together with Arrhenius parameters, for the O₃ reaction are presented in Figure App-II-9 and Table App-II-6.
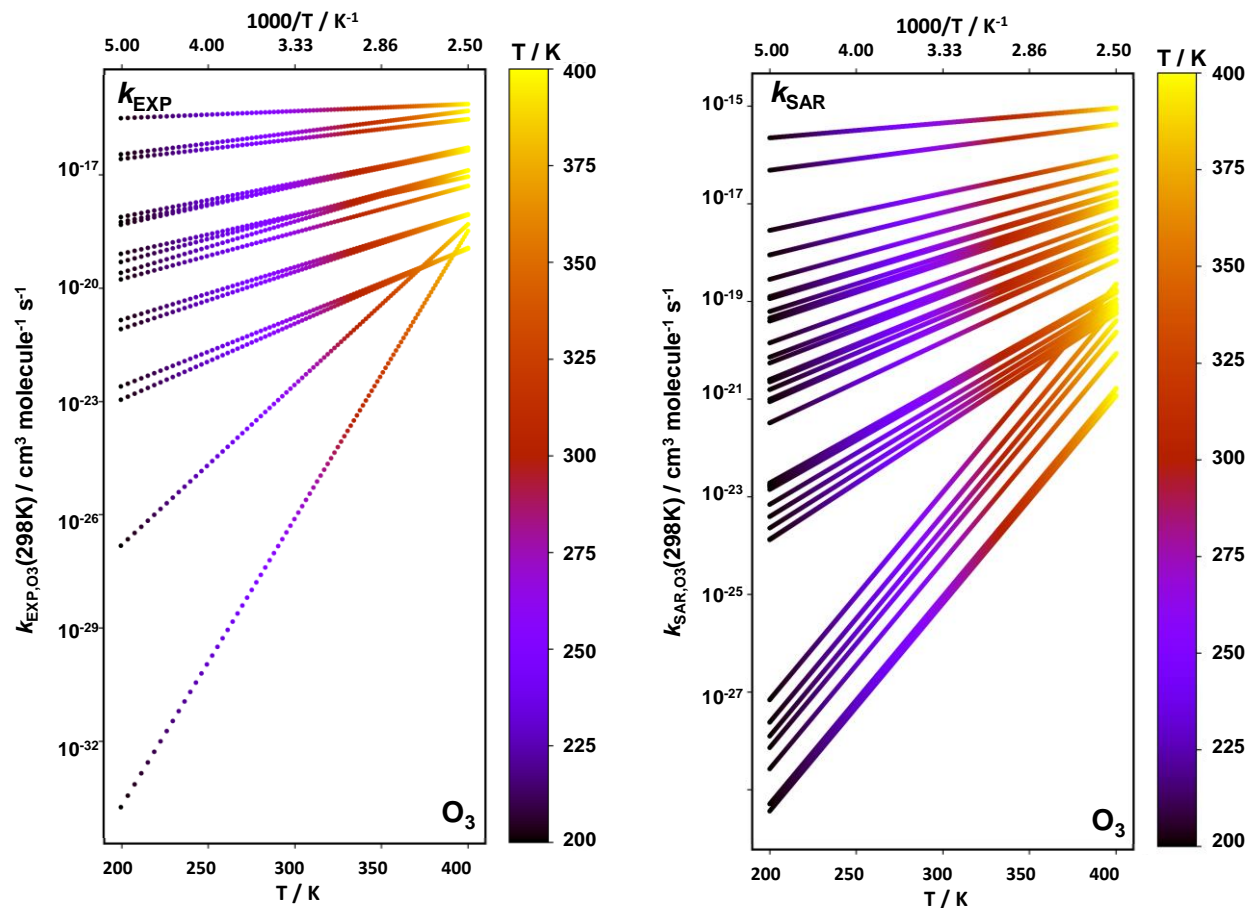
Figure App-II-9 : Arrhenius plots of the O₃ reaction rate coefficients of the 77 alkenes and haloalkenes included in this study. Data were taken from the recent database of (McGillen et al., 2020). Left panel: lines represent temperature-dependent measurements. Right panel: lines represent temperature-dependent predictions.

Table App-II-6 : Results of the predictions for O₃ using the model with factors in Table II-4. O₃ reaction rate constant at room temperature and Arrhenius parameters are retrieved. Calculated data are presented in the first column, and measurement data taken from (McGillen et al., 2020) database are displayed in the second main column, with temperature range associated. Unit of k_{298} and *A*-factor is cm³ molecule⁻¹ s⁻¹; E_a/R, T_{min} and T_{max} are expressed in K.

Index	Molecule	SAR predictions (O₃)			Measurements (O₃)			T-range^a (K)	
		k_{298} (cm³ molecule⁻¹ s⁻¹)	A (cm³ molecule⁻¹ s⁻¹)	E_a/R (K)	k_{298} (cm³ molecule⁻¹ s⁻¹)	A (cm³ molecule⁻¹ s⁻¹)	E_a/R (K)	T_{min}	T_{max}
1	(E)-CH₃CH₂=CH₂CH₃	2.00E-16	3.65E-15	865.39	2.00E-16	7.00E-15	1060	220	370
2	(Z)-CH₃CH₂=CH₂CH₃	2.81E-17	3.05E-15	1397.03	1.30E-16	3.37E-15	970	220	370
3	CH₂=C(CH₃)₂	2.81E-17	3.05E-15	1397.03	1.15E-17	2.92E-15	1650	220	370
4	CH₂=CHCH₂CH₃	1.25E-17	2.74E-15	1606.87	1.00E-17	3.55E-15	1750	220	370
5	CH₂=CHCH₃	1.25E-17	2.74E-15	1606.87	1.05E-17	5.77E-15	1880	230	370
6	CH₂=CHCH₂Cl	1.38E-18	1.98E-15	2166.37	1.79E-18	1.00E-15	1885	278	353
7	CH₂=CFCH₃	4.18E-19	1.69E-15	2475.00					
8	CH₂=CHCH₂Br	1.90E-18	2.08E-15	2085.19	1.90E-18	3.47E-15	2233	288	328
9	CH₂=CHCH₂F								
10	CH₂=CCl₂	7.05E-21	1.58E-15	3671.35	4.90E-21				
11	CF₂=CF₂	1.53E-18	2.01E-15	2140.53					
12	CH₂=CH₂	5.53E-18	2.43E-15	1813.94	1.55E-18	6.82E-15	2500	180	360
13	CF₂=CHF	9.76E-20	1.47E-15	2866.98	9.76E-20	5.70E-16	2580	236	308
14	(E)-CHF=CHF	2.91E-18	2.21E-15	1977.06					
15	CF₂=CFBr								
16	CH₂=CHCl	1.97E-19	1.56E-15	2674.27	2.45E-19				
17	CF₂=CFCl								
18	CF₂=CFCHF₂								
19	CH₂=CHBr								
20	CH₂=CHF	1.86E-19	1.55E-15	2690.88	7.31E-19	1.52E-15	2280	236	308
21	(Z)-CHCl=CFCHF₂								
22	CF₂=CHBr								
23	CH₂=CBrCF₃								
24	CH₂=CBrCF₂CF₃								
25	(Z)-CFCl=CFCl								
26	CH₂=CHCFClCF₂Br								
27	CH₂=CF₂	6.23E-21	1.61E-15	3714.05	6.23E-21	4.91E-16	3360	236	308
28	(E)-CFCl=CFCl	4.00E-21	1.76E-15	3873.20					
29	(Z)-CHCl=CHCl	7.05E-21	1.58E-15	3671.35	4.90E-21	1.22E-15	3704	315	382
30	(E)-CHCl=CFCHF₂								
31	CF₂HCH=CF₂								
32	(E)-CHCl=CHCl	7.60E-21	1.56E-15	3645.33	8.00E-20	9.30E-16	2788	301	394
33	CF₂=CFCF₃	1.48E-21	2.46E-15	4268.63					
34	CHCl=CCl₂	2.71E-22	7.28E-11	7842.00	6.90E-22	1.60E-10	7842	334	388
35	CH₂=CHCF₂CF₂Br								
36	CH₂=CHCF₃	2.00E-19	1.56E-15	2670.77	3.50E-19				
37	CH₂=CHCF₂CF₃	2.00E-19	1.56E-15	2670.77	2.00E-19				
38	CH₂=CHCF₂CF₂CF₂CF₂CF₃	2.00E-19	1.56E-15	2670.77	2.00E-19				
39	(Z)-CHF=CFCF₃	1.05E-19	1.48E-15	2846.25					
40	(Z)-CHF=CHCF₃	6.71E-21	1.59E-15	3688.12					
41	(E)-CHCl=CFCF₃	4.90E-23	1.31E-11	7842.00					
42	CH₂=CHCF₂CF₂CF₂CF₃	2.00E-19	1.56E-15	2670.77	2.00E-19				
43	CCl₂=CFCF₃								

44	$CH_2=CHCF_2CF_2CF_3$	2.00E-19	1.56E-15	2670.77					
45	$CH_2=CFCF_3$	6.71E-21	1.59E-15	3688.12	2.77E-21				
46	$(Z)-CHCl=CHCF_3$	7.14E-21	1.58E-15	3666.88					
47	$CH_2=C(CF_3)_2$	7.23E-21	1.57E-15	3662.41					
48	$CF_2=CHCF_3$	9.43E-23	2.53E-11	7842.00					
49	$(E)-CHF=CHCF_3$	2.81E-21	1.94E-15	4006.49	2.81E-21				
50	$(E)-CF_3CF=CFCF_3$								
51	$(Z)-CHCl=CFCF_3$								
52	$(Z)-CF_3CCl=CHCl$	2.75E-22	7.38E-11	7842.00					
53	$(Z)-CF_3CH=CHCF_3$	7.23E-21	1.57E-15	3662.41					
54	$(Z)-CF_3CF=CFCF_3$	1.43E-24	3.83E-13	7842.00					
55	$(E)-CHCl=CHCF_3$	1.46E-21	2.47E-15	4273.76	1.46E-21				
56	$(E)-(CF_3)_2CFCH=CHF$	2.81E-21	1.94E-15	4006.49					
57	$CCl_2=CCl_2$	1.05E-23	2.80E-12	7842.00	1.60E-24	0.0006	14059.84	369	409
58	$(E)-CF_3CH=CHCF_3$								
59	$(E)-CF_3CH=CHCF_2CF_3$								
60	$(CF_3)_2C=CFCF_2CF_3$								
61	$c-C_4H_2F_4$	1.44E-19	1.52E-15	2759.30					
62	$c-C_5H_2F_6$	1.44E-19	1.52E-15	2759.30					
63	$c-C_5F_8$	2.85E-23	7.64E-12	7842.00					
64	$c-C_5HF_7$	2.03E-21	2.16E-15	4136.32					
A	$c-C_5H_8$	5.60E-16	3.70E-15	562.89	5.60E-16	1.78E-15	345	270	330
B	$CH_2=C(CH_3)CH_2Cl$	3.11E-18	2.24E-15	1959.73	3.37E-18				
C	$CH_2=C(CH_2Cl)_2$	3.45E-19	1.65E-15	2525.42	3.90E-19				
D	$CH_2=CHCH_2CH_2Cl$	1.25E-17	2.74E-15	1606.87	3.96E-18				
E	$CH_2=CHCHClCH_2Cl$	1.38E-18	1.98E-15	2166.37	2.09E-19				
F	$(E)-CHCl=CHCH_2Cl$	6.70E-19	1.80E-15	2352.33	6.70E-19				
G	$CH_2=CClCH_2Cl$	4.93E-20	1.42E-15	3060.71	4.62E-20				
H	$(Z)-CHCl=CHCH_2Cl$	4.93E-20	1.42E-15	3060.71	1.50E-19				
I	$CCl_2=CF_2$								
J	$(E)-CHF=CFCF_3$	9.43E-23	2.53E-11	7842.00					
K	$CF_2=CFCF_2CF_3$	1.48E-21	2.46E-15	4268.63					
L	$CH_2=CH(CF_2)_7CF_3$	2.00E-19	1.56E-15	2670.77	2.00E-19				
M	$CCl_2=CClCF_3$	2.01E-24	5.39E-13	7842.00					

[a] Temperature ranges indicated are that of the experimental data when available; otherwise, the range T=200–400K is mentioned, as the one over which prediction has been made.

References

Finlayson-Pitts, B.J., Pitts, J.N., 1999. Chemistry of the Upper and Lower Atmosphere: Theory, Experiments, and Applications. Elsevier Science.

Griffiths, P.R., de Haseth, J.A., 1986. Fourier Transform Infrared Spectrometry John Wiley & Sons. New York 340.

McGillen, M.R., Carter, W.P.L., Mellouki, A., Orlando, J.J., Picquet-Varrault, B., Wallington, T.J., 2020. Database for the kinetics of the gas-phase atmospheric reactions of organic compounds. Earth System Science Data 12, 1203–1216.

Michelat, L., Mellouki, A., Ravishankara, A.R., El Othmani, H., Papadimitriou, V.C., Daële, V., McGillen, M.R., 2022. Temperature-Dependent Structure–Activity Relationship of OH + Haloalkene Rate Coefficients under Atmospheric Conditions and Supporting Measurements. ACS Earth Space Chem. 6, 3101–3114.

Skoog, D.A., Holler, F.J., Crouch, S.R., 2019. Textbook "Principles of Instrumental Analysis". Cengage Learning; 6 edition.

Skoog, D.A., West, D.M., Holler, F.J., Crouch, S.R., 2013. Fundamentals of analytical chemistry. Cengage learning.

Chapter III :

Measuring the NO$_3$ and OH reaction rate coefficients for a selection of biomass burning organic compounds*

Summary of the chapter III

Chapter III provides new experimental measurement of the rate coefficients of the oxidation of biomass burning volatile organic compounds, BBVOCs, and the associated challenges encountered. Due to the high concentration of compounds like furans and biacetyl measured in biomass burning plumes, and the lack of kinetic data for modeling their oxidation reactions, further measurements have been conducted, and insights in the substitution effect on their reactivities is discussed, as well as challenges to conduct such experiments.

The experimental section presents the multiple set-ups employed to measure the OH and/or NO_3 reaction rate coefficients of multiple furans and biacetyl: the 7.3m^3 indoor atmospheric simulation chamber, CSA, and the tube reactor LARKIN, for OH and NO_3 relative rate measurements, in addition to the discharge flow reactor, DFT, used for absolute measurements of OH reactivity. Additional measurements have been conducted in the PLP–LIF set-up presented in the previous Chapter II.

The results section includes the new measurements conducted for compounds related to biomass burning, including 16 reaction rate coefficients at room temperature of furans + NO_3 reactions, 4 reaction rate coefficients at room temperature of furans + OH reactions, and temperature-dependent rate coefficients of the biacetyl + OH reaction. The impact of substitution on the reactivity of furans and related BBVOCs is investigated. Also, the limitation and the challenges encountered when studying these reactions, and the need for a combination of experimental techniques are discussed.

Atmospheric implications for the various oxidation reactions of BBVOCs under study are discussed. This chapter reflects on the importance of the new measurements in addressing gaps in the literature related to biomass burning emissions, specifically in the case of furans and nighttime chemistry. For biacetyl measurements, it appears that challenges persist despite the use of various measurement techniques.

In view of the amount of work required and certain limitations to measuring reaction rate coefficient of certain reactions, as seen in this chapter, it appears obviously useful to develop predictive tools to provide data for the large number of species present in the atmosphere when no experimental data are available. Furthermore, links between substitution and reactivity are emerging and may therefore enable the development of SAR techniques covering a larger number of compounds than that presented in Chapter I.

Résumé du chapitre III

Le chapitre III présente de nouvelles mesures expérimentales de la cinétique de l'oxydation des composés organiques volatils issus de la combustion de la biomasse (BCOVs), ainsi que les difficultés rencontrées. En raison de la concentration élevée de composés tels que les furanes et le biacétyle mesurée dans les panaches de combustion de la biomasse, et du manque de données cinétiques pour modéliser leurs réactions d'oxydation, des mesures supplémentaires ont été effectuées, et des aperçus de l'effet de substitution sur leurs réactivités sont discutés, ainsi que les défis à relever pour mener de telles expériences.

La section expérimentale présente les multiples installations utilisées pour mesurer les coefficients de vitesse de réaction OH et/ou NO_3 de plusieurs furanes et biacétyle : la chambre de simulation atmosphérique intérieure de 7,3 m^3, CSA, et le réacteur tubulaire LARKIN, pour les mesures de vitesse relative OH et NO_3, en plus du réacteur à flux de décharge, DFT, utilisé pour les mesures absolues de la réactivité OH. Des mesures supplémentaires ont été effectuées dans l'installation PLP–LIF présentée au chapitre II.

La section des résultats comprend les nouvelles mesures effectuées pour les composés liés à la combustion de la biomasse, y compris 16 coefficients de vitesse de réaction à température ambiante des réactions furanes + NO_3, 4 coefficients de vitesse de réaction à température ambiante des réactions furanes + OH, et les coefficients de vitesses de la réaction biacétyle + OH en fonction de la température. L'impact de la substitution sur la réactivité des furanes et des BCOVs apparentés est étudié. Les limites et les défis rencontrés lors de l'étude de ces réactions, ainsi que la nécessité d'une combinaison de techniques expérimentales, sont également discutés.

Les implications atmosphériques des différents groupes de réactions d'oxydation des BCOVs étudiés sont discutées. Ce chapitre souligne l'importance des nouvelles mesures pour combler les lacunes de la littérature concernant les émissions dues à la combustion de la biomasse, en particulier dans le cas des furannes et de la chimie nocturne. En ce qui concerne les mesures des biacétyle, il semble que des difficultés persistent malgré l'utilisation de diverses techniques de mesure.

Compte tenu de la quantité de travail nécessaire et de certaines limitations à la mesure du coefficient de vitesse de certaines réactions, comme ce qui a été vu dans ce chapitre, il apparaît évidemment utile de développer des outils prédictifs pour fournir des données pour le grand nombre d'espèces présentes dans l'atmosphère lorsqu'aucune donnée expérimentale n'est disponible. De plus, des liens entre substitution et réactivité émergent et peuvent donc permettre le développement de techniques SARs couvrant un plus grand nombre de composés que celui présenté dans le chapitre I.

Introduction

As discussed in Chapter I, it is crucial to understand the chemistry of biomass burning emissions since the frequency and intensity of wildfires is predicted to increase under future warming scenarios (IPCC, 2022). Biomass burning, which includes natural and anthropogenic sources such as forest, savannas, crop residues and peatlands fires, as well as waste incineration, or biofuel combustion, (Akagi et al., 2011) is a significant source of particles and the second largest source of trace gases in the atmosphere (Andreae et al., 2001; Forster et al., 2007; Guenther et al., 2006, 1995). Among the trace gases emitted during biomass combustion, a large fraction consists of non-methane volatile organic compounds (NMVOCs), such as furans, furfurals, phenols, terpenes, aromatics, carbonyls, alkanes and alkenes, (Greenberg et al., 2006) that arise from the pyrolysis of the main components of biomass, i.e. cellulose, hemicellulose and lignin (Collard et al., 2014; Greenberg et al., 2006; Lu et al., 2011; Paine et al., 2008; Patwardhan et al., 2009).

The particles emitted and formed in biomass burning plumes (Yokelson et al., 2008) impact climate directly and indirectly (Hobbs et al., 2003; Rosenfeld, 1999) and can lead to bad air quality (Andreae et al., 1988; Heintzenberg, 1989; Reid et al., 1998). The NMVOCs emitted can also affect air quality by contributing to the formation of tropospheric O_3 (Akagi et al., 2013; Alvarado et al., 2015; Bein et al., 2008; Coggon et al., 2019; Hobbs et al., 2003; Morris et al., 2006; Oltmans et al., 2010; Pfister et al., 2008; Real et al., 2007; Singh et al., 2012; Yokelson et al., 2009). For example, as a result of the wildfires in California in 2007, (Pfister et al., 2008) observed that these intense biomass burning events can increase the occurrence of ozone concentration peaks beyond health standards. In the study of (Sudo et al., 2007), the authors observed that O_3 emitted by biomass-burning regions of the world (i.e., South America, Africa and Australia) impacts the southern hemisphere by increasing ozone levels in this region. It is essential to quantify the lifetime of the NMVOC and identify the compounds it may form during its degradation in order to assess the contribution to each of these processes.

The OH oxidation chemistry is a source of secondary organic compounds in biomass burning plumes that are involved in O_3 and SOA formation. Even though the OH reactions are better studied than that of the other oxidants, as discussed in Chapter I, such studies are lacking for a large fraction (22%–56%, (Hatch et al., 2017)) of the NMVOCs identified in biomass burning plumes (Hatch et al., 2017); they are not included in models, e.g., Figure 4 and 5 in (Decker et al., 2021). The detailed chemical mechanisms for the formation of secondary NMVOCs have been investigated only in a few studies, e.g., (Alvarado et al., 2015; Jiang et al., 2020; Liu et al., 2016; Mason et al., 2001; Müller et al., 2016), and still lack many kinetic and mechanistic data. The role of NO_3 as a nighttime removal path for of BBVOCs has been highlighted in recent field studies (Decker et al., 2021). There is thus an important need to study the rate coefficients and the mechanisms of the degradation of not only OH but also NO_3 reactions of these compounds.

Furan and various substituted furans are emitted from biomass burning and other combustion processes such as cooking that emits, for example, furanones, dihydrofurans, and 2-pentylfuran (Coggon et al., 2019; Lipari et al., 1984; Rogge et al., 1991). Some furans are also used as solvents for resins and in the manufacture of lacquers, agricultural chemicals and stabilizers (Cheremisinoff, 2003). Furans and their derivative have gained interest since they have been recently measured in high concentration in biomass burning plumes, during the FIREX-AQ field campaign in the US in 2019 (Decker et al., 2021; Gkatzelis et al., 2023). They are generally identified as emissions from biomass and forest fires (e.g., (Ciccioli et al., 2001; Greenberg et al., 1984; Koss et al., 2018)). They were observed in large concentrations from the US western wildfires in 2013 (Liu et al., 2017) and 2011 (Akagi et al., 2014). During the COALA campaign on the 2019-2020 Australian wildfires, furans were also measured in the plumes (Mouat et al., 2022, 2021).

Additionally, the photooxidation of conjugated dienes, such as isoprene, 1,3-butadiene, and 1,3-pentadiene, also produces furan and substituted furans, (e.g., 3-methylfuran formed from the oxidation of isoprene by OH (Atkinson et al., 1989; Paulson et al., 1992; Tuazon et al., 1990). Since these alkenes can be emitted in large amounts as discussed in the Chapter I, they can represent an important source of furans in the atmosphere. It is thus important to improve the knowledge on the atmospheric chemistry of furans.

Previous studies have suggested that furans could act as SOA precursors and participate in the tropospheric ozone pollution, especially in the high NO_x environment that constitute biomass burning plumes (Alvarado et al., 2015; Bruns et al., 2017; Gilman et al., 2015; Gómez Alvarez et al., 2009; Hatch et al., 2015; Hennigan et al., 2011; Joo et al., 2019). However, the yields of SOA formation remain poorly characterized as discussed in (Hatch et al., 2017, 2015; Jiang et al., 2018). Specific impacts of NMVOCs on O_3 are not well defined as it has been observed to increase ((e.g., (Andreae et al., 1988; Mauzerall et al., 1998), decrease (e.g., (Alvarado et al., 2010)) or remain unaffected (Jaffe et al., 2012). This suggest that further work is required to describe the impact of BBVOCs on air quality.

Despite its importance, the atmospheric chemistry of biomass burning smoke remains poorly understood due to the complexity of smoke processing. As discussed in Chapter I, the oxidation of furans remains not fully understood, especially concerning the NO_3, Cl and O_3 rate coefficients. Furan, alkyl substituted furans, and furfurals are degraded rapidly in the troposphere, within minutes to hours, through their reaction with OH that is thought to be their major removal during daytime (lifetime within 3h if the OH daytime concentration of $2.5×10^6$ radicals cm^{-3}, (McGillen et al., 2020)) and through their reaction with NO_3 which is their most important nighttime removal process (lifetime of few minutes to 0.5 hour depending on the conditions, (McGillen et al., 2020)). Reaction with ozone is usually a minor loss process during day and night. At room temperature, kinetic studies are available for the reaction of OH radicals with furan (Atkinson et al., 1983; Bierbach et al., 1995, 1992; Lee et al., 1982; Tuazon et al., 1984), alkyl substituted

furans (Aschmann et al., 2011; Atkinson et al., 1989; Bierbach et al., 1995, 1992; Tapia et al., 2011), furfurals (Bierbach et al., 1995), and unsaturated dihydrofurans (Adeniji et al., 1981; Alwe et al., 2014; Calogirou et al., 1999). As a function of temperature, only a few kinetic studies on the OH reaction with furan and alkyl substituted furans are available (Eble et al., 2015; Elwardany et al., 2016; Liljegren et al., 2013; Whelan et al., 2020; Wine et al., 1984). Laboratory (Aschmann et al., 2014, 2011; Bierbach et al., 1995; Gómez Alvarez et al., 2009; Strollo et al., 2013) and theoretical (Anglada, 2008; Yuan et al., 2017; Zhang et al., 2008a, 2008b) studies investigating the product formation from the OH-initiated oxidation of furan, methylfurans, and furfurals are available.

For the NO_3 reaction, kinetic data for substituted furans have been reported by (Ali et al., 2022; Alvarado et al., 1996; Atkinson et al., 1985; Calogirou et al., 1999; Colmenar et al., 2012; Kind et al., 1996; Newland et al., 2022; Tapia et al., 2011) at room temperature, and by (Cabañas et al., 2004) as a function of temperature. NO_3 reaction has been found to be the primary removal for furfurals at nighttime, compared to the OH and Cl reaction (Colmenar et al., 2012; Huang et al., 2019). One study from Berndt et al. (1997) investigates the mechanism of NO_3-initiated oxidation of furan and tetra methyl furan. No kinetic data has been reported, to the best of our knowledge, for the reaction of NO_3 with unsaturated dihydrofurans.

Concerning the other oxidants, very few data are available. Kinetic measurements and mechanistic considerations on the Cl reaction with furan, alkyl substituted furans, and furfurals are presented in the work of (Cabanas et al., 2005), (Villanueva et al., 2007), and (Christensen et al., 1998). Data on the ozonolysis of furan and substituted furans are sparse (Andersen et al., 2016; Atkinson et al., 1992, 1983; Calogirou et al., 1999; Matsumoto, 2011). A theoretical study on the ozonolysis of furans and derivatives has been published by (Liu et al., 2018).

Biacetyl, 2,3-butanedione is another compound of interest which has been measured in biomass-burning plumes (Akagi et al., 2011; Andreae, 2019; Andreae et al., 2001; Koss et al., 2018; Stockwell et al., 2015; Yokelson et al., 2008). It is also formed during the photo-oxidation of aromatic hydrocarbons in the presence of NO_x (Arey et al., 2009; Obermeyer et al., 2009) and during the oxidation of α,β-unsaturated ketones initiated by OH (Illmann et al., 2021). Kinetic data on this important component of wildfire chemistry are very few, e.g., the OH kinetic as a function of temperature by (Dagaut et al., 1988), and at room temperature by (Darnall et al., 1979). No direct product study on the OH + biacetyl reaction has been reported, with only the study of (Christensen et al., 1998) which reports the mechanism of the Cl + biacetyl reaction, and discuss by analogy the OH mechanism. This suggest that the rate coefficients must be re-evaluated and that additional loss pathways such as photolysis must be investigated and quantified.

Hence, the rate coefficients of the NO_3 and OH reactions with a list of substituted furans (16 k_{NO3} and 4 k_{OH}) have been measured at room temperature using different techniques (atmospheric simulation chambers,

spectroscopic methods, flow tube apparatus) (Newland et al., 2022). The photolysis and the rate coefficients of the reaction of OH + biacetyl as a function of temperature have been studied in order to investigate further the photochemistry of biacetyl and the mechanistic pathways of its OH-initiated degradation. This aims at filling gaps in the knowledge on the atmospheric chemistry of a selection of BBVOCs, with a particular focus on their radical chemistry with NO_3 and OH. The mechanisms by which they are degraded and the effect of substitution of their reactivity are investigated. Atmospheric implications of the results and limits in available measurement techniques are also discussed. These results provide new data for atmospheric chemical models and predictive SAR methods.

III-1. <u>Experimental techniques</u>

In this work, different techniques have been used to measure the same rate coefficients. This approach allows to generate more accurate kinetic data. Measurements of the absolute rate coefficients of the reaction of OH + biacetyl have been conducted in the DF/MS set-up as a function of temperature (230–770K), and in the PLP–LIF set-up at room temperature. Relative rate coefficients for the reaction of OH + biacetyl have been measured in the CSA at room temperature and in the LARKIN set-up as a function of temperature (273–403K). Additionally, investigation of the biacetyl photolysis has been conducted in the PLP–LIF setup.

Relative-rate measurements of the NO_3 + furans reaction rate coefficients have been measured in the CSA at room temperature for 14 furans (furan, 2-methylfuran, 2,5-dimethylfuran, furfural, α-Angelica lactone (5-methyl-2(3H)-Furanone), γ-crotonolactone (2(5H)-Furanone), 2-furoic acid, 2,5-dimethoxy-2,5-dihydrofuran, furfuryl alcohol, 5-methylfurfural, furfuryl acetate, 2,3-dihydrofuran, 2,5-dihydrofuran, 2-ethylfuran) and 2 pyrroles (pyrrole, 2,5-dimethylpyrrole). Relative-rate measurements of the OH + furans rate coefficients have been carried out in the LARKIN set-up at room temperature for 4 furans (furfuryl alcohol, 2,3-dihydrofuran, 5-methylfurfural, 2-ethylfuran).

III-1.1. <u>Atmospheric simulation chamber (CSA)</u>

<u>Set-up</u>
The gas-phase rate coefficient of the reaction of a volatile organic compound (VOC) towards an oxidant (Ox) is measured in a large cubic indoor atmospheric simulation chamber (CSA, V=7.3m^3) under tropospheric conditions. The chamber (CSA) is made of Teflon foil and operates at room temperature (T=298±5K for the experiments presented here) and atmospheric pressure (760 Torr) of purified dry air (RH<2%), as illustrated in Figure III-29. The CSA is surrounded by protection panels to perform dark reactions (e.g., for NO_3 chemistry) and a set of 14 germicidal lamps (UV-A T-40 L, 40 W, Viber Lourmat) centered on 254 nm, 24 black lamps (UV-A T-40 L, Viber Lourmat) centered on 365 and 12 daylight

lamps (Orsam Ultra-Vitalux) with wavelengths >300 nm placed around the chamber to simulate UV irradiation and to drive photochemical production of OH.

To ensure reactants are well mixed, two fans made of Teflon are installed in the CSA and operated continuously throughout the experiment. A flow of purified air (5 L min^{-1}) was continuously added during the experiment to maintain a slight overpressure inside of the chamber, avoiding contamination from outside air, and compensating for air withdrawn for sample analysis and leaks (Ren et al., 2017). The ventilation is performed by two electronic valves on opposite ends of the chamber. Sensors are continuously measuring the temperature (Thermocouple PT-100) and relative humidity (Vaisala HMT330 series transmitters) in the chamber. Known volumes of liquid species are introduced into a three-path glass tube (e.g., furans and biacetyl) and known concentrations of gaseous species (e.g., SF_6) are introduced into a calibrated cylinder (V=0.9 L) equipped with two pressure gauges of 0–10 Torr and 0–100 Torr (MKS Baratron). The contents of the cylinder are carried into the chamber by a stream of purified air. Concentrations of the reactants in the chamber are retrieved using the ideal gas law (generally, VOC concentration is ∼ 3–6 ppmv).

To quantify the dilution of the compounds inside the chamber, SF_6 is introduced before reactants are added (∼ 200 ppb in the chamber). Prior to the start of an experiment, air flowed through the chamber for at least 30 min to measure the dilution rate. The compounds of interest are introduced and irradiated for another 30 min if the experiment will be conducted under UV illumination, to assess whether or not the VOCs are potentially subject to significant photolysis. If the loss of the VOC under illumination is greater than the dilution, it is possible that there is a contribution from its photolysis or from its reaction with OH, which would have been produced by photolysis of trace amounts of HONO present on the surface of the chamber walls. In the experiments reported here, the photolysis of the compounds of interest were small compared to their loss in the presence of NO_3 radicals. This was not the case for the reaction of biacetyl with OH radicals, as discussed in section III-2.1.2.1.

Since the oxidants under study are free radicals, they must be produced *in situ* either using a species in an equilibrium with the desired radical (e.g., N_2O_5 in thermal equilibrium with NO_3 and NO_2) or by photolysis of a precursor that generates the radicals of interest (e.g., HONO, see (Cox, 1975), or methyl nitrite, CH_3ONO, in air and presence of NO, see (Atkinson et al., 1981)).

Production of NO$_3$ radicals:
To produce NO_3 radicals, one method is to introduce N_2O_5 under dark conditions, which is thermally converted to NO_2 and NO_3 following (R23):

$$N_2O_5 + M \rightleftharpoons NO_2 + NO_3 + M \quad \text{(R23)}$$
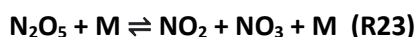
Experiments must be conducted under dark conditions, since NO_3 photolyzes rapidly under visible light (between 420–640nm), as discussed in Chapter I.

Production of OH radicals:

To form OH radicals in the CSA, the favored method here is to introduce methyl nitrite, CH_3ONO, and photolyze it at 365nm (R23–26) as:

$$CH_3ONO + h\nu(365nm) \rightarrow CH_3O + NO \text{ (R24)}$$

$$CH_3O^{\bullet} + O_2 \rightarrow HCHO + HO_2^{\bullet} \text{ (R25)}$$

$$HO_2^{\bullet} + NO \rightarrow OH + NO_2 \text{ (R26)}$$
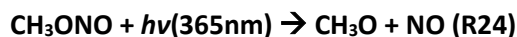
After introduction of all the reactants and SF_6, the reaction is initiated by introducing the oxidant precursor. For NO_3 chemistry, the N_2O_5 sample is kept in a cold trap at $\sim$ 235 K and introduced continuously by flowing a small flow of purified air through the two-path glass tube throughout the experiment. For the OH chemistry, the CH_3ONO precursor is introduced several times, as needed, either by using a similar approach to that of N_2O_5 or by injecting a previously prepared mixture of CH_3ONO in an inert gas.

The experiment is conducted until most ($\sim$ 50%) of the VOC studied has been consumed, while taking care not to run the experiment for too long, to avoid product build-up that could interfere with sample analyses, and to avoid large wall-loss and dilution contributions.

The concentration of the VOC was determined by in-situ Fourier transform infrared (FTIR) spectroscopy using a Nicolet 5700 coupled to a White-type multipass cell with a pathlength of 143 m. Each IR spectrum scan is made of 30 or 100 co-additions (2–6 min) at a spectral resolution of 0.25 cm^{-1}. The number of co-additions is chosen depending on the rate of the reactions in order to obtain at least 10 scans evenly distributed during the reaction part. For example, if the reaction was fast (e.g., $k_{NO3} \sim 10^{-11} - 10^{-10}$ cm^3 $molecule^{-1}s^{-1}$), 30 co-additions (2 min) was chosen, to obtain enough scans to derive the decay of the reaction with 10 datapoints before reaction was complete or too much product had accumulated.

After each experiment, the chamber was flushed with purified air (flow$\sim$250 L min^{-1}) to remove the remaining compounds inside and, potentially, on the walls. The chamber was manually cleaned when accumulation of dirt was observed inside the chamber, a procedure that is usually not required more than once a year, depending on the compounds (and their concentrations) that were introduced (e.g., low volatility species).
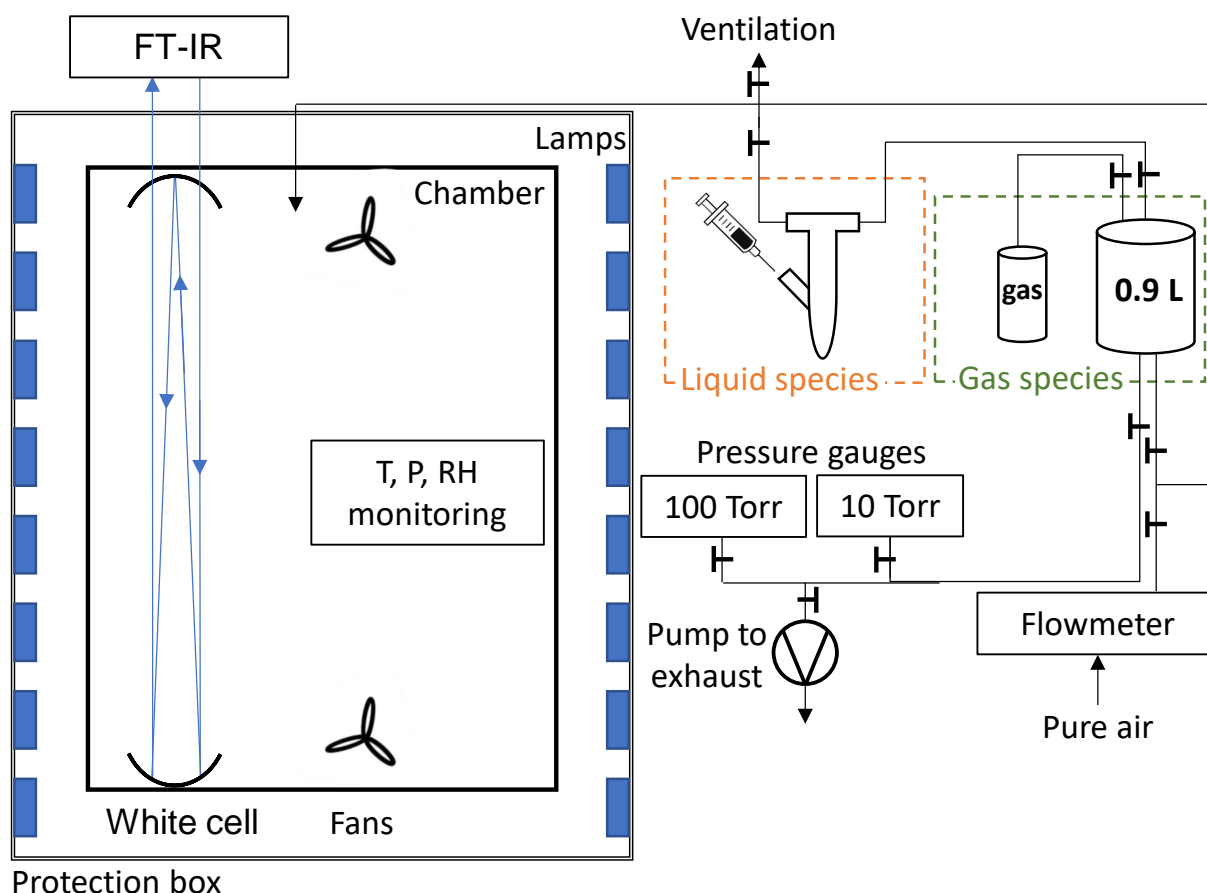
Figure III-29 : Schematic representation of the CSA chamber facility (V=7.3 m³).

Relative-rate method

In order to determine the rate coefficient of the studied reaction, VOC + oxidant, in the atmospheric simulation chamber, the relative-rate method was used. A reference compound whose rate coefficient with OH or NO_3 was well-known was chosen. In addition, the criteria for this choice are: First, its reference rate coefficient with the oxidant under study, k_{ref}, should be of same order of magnitude as that of the studied compound, k_{VOC}, to ensure that the reference compound changes are comparable to those of the VOC of interest (Finlayson-Pitts and Pitts, 1999). In our experiments, all k_{ref} were within a factor of 5 of the k_{VOC} value, and both compounds were introduced in similar concentrations to obtain comparable first-order loss rates. Second, the IR spectrum of the VOC is distinctly different and separable from those of reference and product(s) produced from both the reference and VOC of interest. If a product build-up was identified on an absorption band under study, it can be subtracted from the IR spectrum using its reference spectrum, if it is possible to quantify the product by another band or another method. Finally, the reference compound must not react with the VOC under study or the oxidant precursor and must not be a product of the VOC + oxidant reaction.

In addition to the studied reaction with OH, the VOC and reference can undergo other removal processes (k'_{loss}), such as loss on the walls of the chamber, and dilution. Considering all the mentioned processes, and assuming the rate coefficients are governed by a pseudo-first-order rate constant, it can be shown that:

$$\ln\left(\frac{[HFO]_0}{[HFO]_t}\right) - k_{d,HFO} = \frac{k_{HFO}}{k_{ref}} \times \ln\left(\frac{[ref]_0}{[ref]_t}\right) - k_{d,ref} \quad \text{(Eq. III-16)}$$

where $[VOC]_0$, $[VOC]_t$ are the initial concentrations of VOC and reference, and $[ref]_0$, $[ref]_t$ those at the reaction time t. Hence, the slope b= k_{HFO}/k_{ref} of the linear second-order plots of $\ln([HFO]_0/[HFO]_t)$-$k_{d,HFO}$t against $\ln([ref]_0/[ref]_t)$-$k_{d,ref}$t render the k_{HFO} value by multiplying its slope b with the known k_{ref}.

III-1.2. Long Axis Reactor for KINetic studies (LARKIN)

The Long Axis Reactor for KINetic studies (LARKIN) cell is a cylindrical tube of 1 m length and volume ~4680 cm^3, see schematic in Figure III-30. The reaction cell is jacketed and connected to a cryostat which circulates a cooled/heated fluid, i.e., ethanol to achieve temperatures below 0°C, and monopropylene glycol to heat above room temperature up to ~130°C. Temperature was controlled using a Thermocouple PT-100 and maintained usually at ±2K throughout the experiment (unless otherwise specified in the experimental conditions).

The injection system was composed of a glass bulb (V=596 cm^3) into which liquid or gaseous samples are injected, monitored using pressure gauges (MKS Baratron) of 1000 mbar, 1 Torr and 10 Torr, depending on the pressure required. Liquid compounds were directly injected into the glass bulb and introduced using a fast flow of purified air or O_2 to the reaction cell. Oxygen, O_2, was employed to maximize the production of OH radicals by driving the reaction (R25). A pressure gauge (MKS Baratron) of 1000 Torr was connected to the inside of the cell, to monitor the total pressure in the reaction volume. The compounds concentration into the cell were monitored using an FTIR (pathlength = 10 m) connected to the cell, after circulating the reaction volume with a diaphragm pump to achieve homogeneous mixing.

To initiate the reaction, OH radicals were produced by photolysis of CH_3ONO precursor (10% in N_2) using a 355nm-laser beam aligned using mirrors to the center of the cell and produced by the third-harmonic of a Nd:YAG laser triggering at 10Hz (fluence P=250mW). The Nd:YAG laser produces a 1064 nm laser beam that is then directed through a nonlinear crystal which converts the 1064 nm light into its second harmonic, 532 nm. Both 1064 nm and 532 nm beams are mixed in a nonlinear crystal to produce 355nm (UV light). The laser beam was not expanded to fill the volume of the cell. Thus, there is a possibility of radical-radical reactions in this small volume. The beam fluence was not decreasing drastically between the entry and the exit of the cell which suggests that the gradient in laser fluence along the length was not significant. Since the mixture was not flowed continuously, a given reaction volume may be subject to multiple laser pulses.

Thus, there is the possibility of radical interactions. However, due to the need to keep the gas mixture where the reaction occurs at a constant temperature throughout the experiment, it was helpful to work under a stopped-flow condition. No test was conducted at different fluences since the value employed was optimal for this laser system. Such tests, together with the inclusion of a beam-expander could be done in future developments of the LARKIN system.

During a typical experiment, the FTIR background (co-addition of 250 scans at resolution 0.5 cm^{-1}) was measured at atmospheric pressure and at the temperature of interest. The cell was filled with the bath gas (purified air or O_2). Then, the cell was flushed and filled with the reactants and radical precursor. IR reference spectra were measured under the same conditions of pressure and temperature prior to the experiment. The laser was triggered for various timescales depending on the rate coefficient of the reaction (~3–5 min for initial steps, when reaction is faster, to 10 min for last steps when reaction gets slower). After each photolysis step, the gases in the reaction volume were mixed for 1 min using the circulating pump, and IR spectrum were measured by co-addition of 50 scans at resolution 0.5 cm^{-1}. The time steps for the photolysis of the precursor were chosen in order to obtain at least 10 data points for a final consumption of the reactant of ~50% of the initial concentration. When the experiment was completed, the cell was cleaned by introducing bath gas at atmospheric pressure, circulating it for several minutes (~3-5 min), and pumping the reaction volume for several minutes (~15 min). This process was repeated at least 3 times between experiments, and the pumping was conducted for a longer time at the end of the day (~30 min to few hours). In between experiments, if the cell was not evacuated, the cell was filled with bath gas to atmospheric pressure and the valves were closed to isolate it and avoid any leaks of exterior air. The cell was flushed and cleaned with bath gas as described before any experiment. IR backgrounds can be measured again if the time between experiments exceeded 3 hours, in order to ensure that the cell was cleaned by comparing with the previous spectrum.

The rate of loss of the reference compound and VOC in the absence of light was measured by conducting the same experiment without OH precursor and laser light. For photolysis test, the same procedure was applied under 355nm illumination, and by introducing an excess concentration of CO (~9.27×10^{17} molecule cm^{-3} in the LARKIN cell) in the cell in order to scavenge OH radicals which may be generated during the experiments. This would yield HO_2, which in the absence of NO, will be lost through self-reaction to form H_2O_2. No detectable levels of NO were observed (<ppb), but it is possible that small quantities could result in small amounts of OH recycling, that could result in some sample loss.
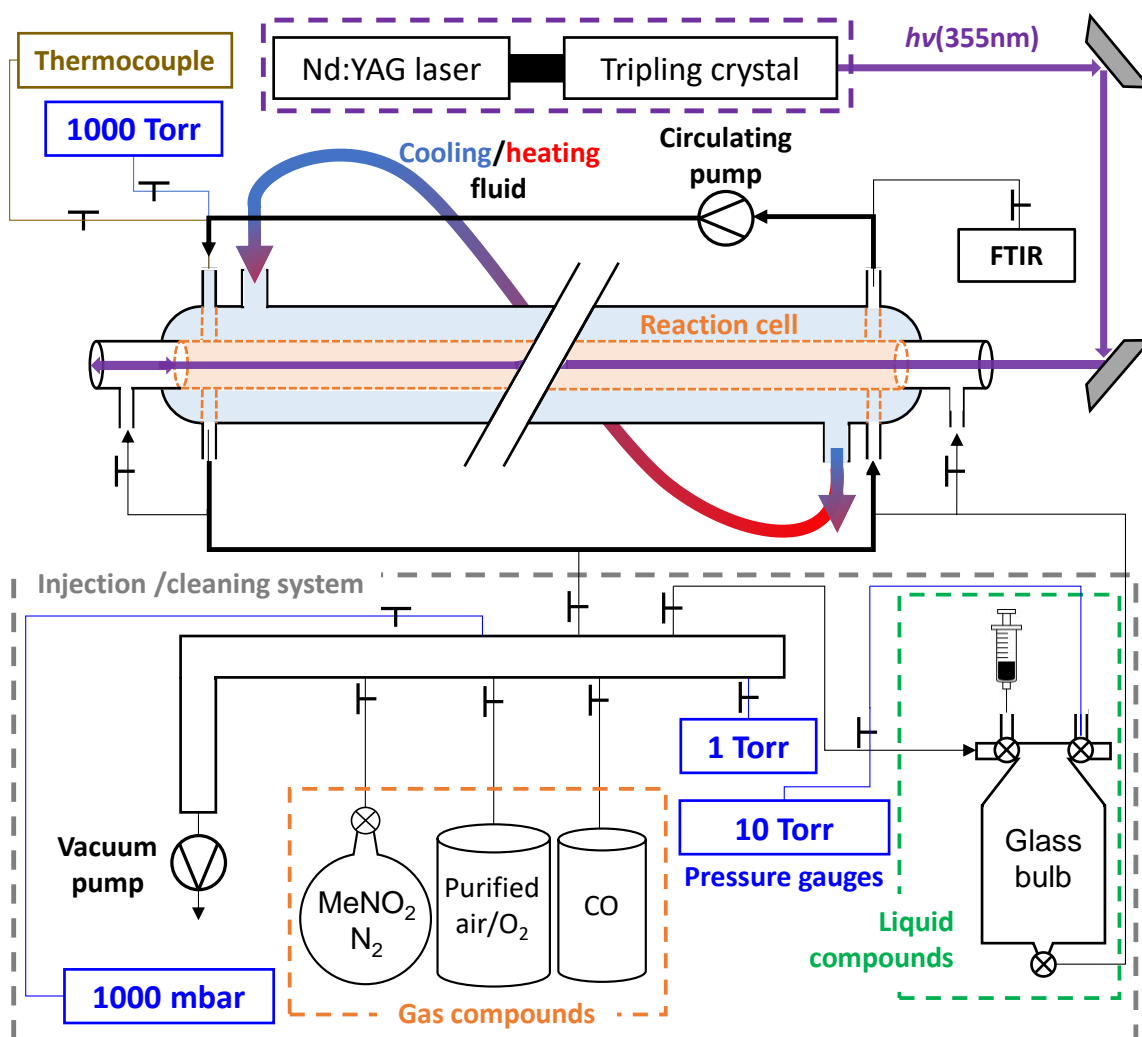
III-1.3. Discharge flow reactor*

These experiments were conducted together with Dr. Yuri Bedjanian (ICARE-CNRS, Orleans) as part of a common project on the study of the rate coefficients of biacetyl + OH reaction.

The reaction studied in a discharge-flow system in this chapter is that of OH + biacetyl ($CH_3C(O)C(O)CH_3$), which was conducted using a modulated molecular beam mass spectrometry with electron impact ionization (25–30 eV energy) to monitor the species involved (see Figures App-III-1 and App-III-2 in Appendices section App-III-1) (Bedjanian et al., 1999; Morin et al., 2015). In this work, two flow reactors were employed. The first reactor was made of Pyrex tube (45 cm length and 2.4 cm i.d.) and coated with halocarbon wax. It was used at the lower temperatures (T=220–320K) The reactor was jacketed to circulate temperature-regulated ethanol (see Figure App-III-1 in Appendices section App-III-1). The second reactor was employed at the higher temperatures (T=305–770 K), as illustrated in Figure App-III-2 in Appendices section App-III-1), and was composed of an electrically heated uncoated Quartz tube (45 cm length and 2.5

cm i.d.) (Morin et al., 2015). The OH radicals were produced using two methods. In the first approach, they were produced in a rapid reaction of fluorine atoms, F, with excess H_2O (see Figure App-III-1 in Appendices section App-III-1):

$$F + H_2O \rightarrow OH + HF \qquad \text{(R27)}$$
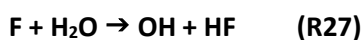
The rate coefficient of the reaction (R27) has been reported to be $k_2 = (1.40\pm0.15) \times 10^{-11}$ cm^3 molecule^{-1} s^{-1} (T=240–380K) by (Atkinson et al., 2007). F atoms were produced in the microwave discharge of trace amounts of F_2 in He in an alumina tube. Using mass spectrometry, it was measured that more than 90% of F_2 was dissociated.

The second method used was the fast reaction of hydrogen atoms with excess NO_2, where H atoms were generated by dissociation of H_2, diluted in He, in a microwave discharge (see Figure App-III-2 in Appendices section App-III-1):

$$H + NO_2 \rightarrow OH + NO \qquad \text{(R28)}$$
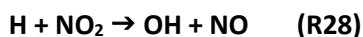
The rate coefficient of the reaction (R28) has been reported to be $k_3 = (1.47\pm0.26) \times 10^{-10}$ cm^3 molecule^{-1} s^{-1} (T=195–2000K) by (Su et al., 2002). An excess of Br_2 ([Br_2] = (3–5)×10^{13} molecule cm^{-3}) was added at the end of the reactor 5 cm upstream of the sampling cone, to scavenge OH radicals, as illustrated in Figures App-III-1 and App-III-2 in Appendices section App-III-1. The OH radicals were converted to HOBr (R29) and HOBr was detected using mass spectrometry at m/z = 96/98 (HOBr$^+$) :

$$OH + Br_2 \rightarrow HOBr + Br \qquad \text{(R29)}$$

The rate coefficient of the reaction (R29) has been reported to be $k_4 = 2.16\times10^{-11}$ exp(207/T) cm^3 molecule^{-1} s^{-1} (T=220–950K) by (Bedjanian, 2019). This reaction also allowed the determination of the absolute concentrations of OH through their chemical conversion to HOBr in excess of Br_2: [OH] = [HOBr] = Δ[Br_2], i.e., the concentration of OH (HOBr) was determined from measuring the consumed fraction of [Br_2]. The possible influence of secondary chemistry on this method to detect OH radicals and quantifying their absolute concentrations has been discussed in another article (Bedjanian et al., 1999).

Biacetyl was introduced in the reactor by flowing an inert bath gas (He) over a liquid biacetyl sample and was monitored by mass spectrometry at its parent peak at m/z = 86. Absolute calibration of biacetyl in the mass spectrometer was carried out using two methods. In the first, absolute biacetyl concentrations were calculated from the flow rates obtained from pressure drop measurements of the biacetyl mixture in He prepared by manometry and stored in a calibrated volume vial. In the second method, a known volume of

biacetyl (0.6–6.0 µL) was injected into a He stream in the reactor under experimental kinetic measurement conditions (pressure, temperature, total bath gas flow) and the mass peak at m/z = 86 was recorded. To determine the calibration factor, the integrated area of the mass spectrometric signal that corresponds to the known total number of biacetyl molecules injected into the reactor was calculated. Absolute biacetyl concentrations calibrated by flow rates and determined with the two methods employed agreed to within 10%.

III-1.4. <u>Synthesis and chemicals</u>

Chemicals

The gases used for the discharge-flow experiments have purities as follows: He (>99.9995%, Alphagaz), passed through a liquid nitrogen trap; H_2 (>99.998%, Alphagaz); F_2, 5% in helium (Alphagaz); Br_2 (>99.99%, Aldrich); NO_2 (> 9%, Alphagaz), 2,3-butanedione (biacetyl, >99% , Sigma-Aldrich). For the PLP–LIF experiments, the gases were as specified in Chapter II, section II-2.2., and the 2,3-butanedione was as previously mentioned.

For the other experiments, in CSA and LARKIN, the VOCs of interest were used as supplied without further purification, and their purities were as follows: furan (>99%, Sigma-Aldrich), 2-methylfuran (>98%, TCI), 2,5-dimethylfuran (>98%, TCI), pyrrole (>99%, TCI), α-angelicalactone (>98%, TCI), furfural (>99%, TCI), γ -crotonolactone (>93%, TCI), 2-ethylfuran (>98.0%, TCI), 2,3-duhydrofuran (>98.0%, TCI), 2,5-dihydrofuran (>98.0%, TCI), 5-methylfurfural (>99% , Sigma-Aldrich), 2-furoic acid (>98.0%, TCI), 2,5-dimethoxy-2,5-dihydrofuran (>98.0%, TCI), furfuryl alcohol (>98.0%, TCI), furfuryl acetate (99%, Sigma-Aldrich), 2,5-dimethylpyrrole (>98.0%, TCI)**,** 2,3-butanedione (≥99 %, Sigma-Aldrich).

The reference compounds were: 2,3-dimethyl-but-2-ene (98%, Sigma-Aldrich), 2-carene (97%, Sigma-Aldrich), camphene (95%, Sigma-Aldrich), α-pinene (98%, Sigma-Aldrich), cyclohexene (≥99%, Sigma-Aldrich), 3-methyl-3-buten-1-ol (97%, Sigma-Aldrich), and cyclohexane (99.5%,Sigma-Aldrich)**,** α-terpinene (97%, Sigma-Aldrich), 1,3-cyclohexadiene (97%, Sigma-Aldrich)

The gases were of purities: CO (≥ 99,997%, Alphagaz), purified air (≥ 99,9999%, Alphagaz), O_2 (≥ 99,9995%, Alphagaz), N_2 (≥ 99,9999%, Alphagaz). The cooling fluid used are ethanol (96%, Carlo Erba) and monopropylene glycol (Lubrisolve).

Synthesis of CH$_3$ONO

CH_3ONO was synthesized by dropwise addition of 50% H_2SO_4 in water to a saturated solution of $NaNO_2$ in methanol. This mixture was stirred and maintained at T=0°C. The gaseous CH_3ONO formed was subsequently carried by a slow flow of N_2 through a water bubbler and a Teflon U-tube containing P_2O_5 and

glass beads, and cold trapped at -196°C. For the CH_3ONO synthesis, the gases were: N_2 (≥ 99,9999%, Alphagaz), H_2SO_4 (>95%, Normapur), $NaNO_2$ (≥97.0%, Sigma-Aldrich), methanol (95%, Carlo Erba), P_2O_5 (>98%, Fluka).

Synthesis of N_2O_5

N_2O_5 was synthesized by reacting NO_2 with an excess of O_3, (Johnston et al., 1974) as follows:

$$NO + O_3 \rightarrow NO_2 + O_2 \quad \text{(R30)}$$

$$NO_2 + O_3 \rightarrow NO_3 + O_2 \quad \text{(R31)}$$

$$NO_2 + NO_3 \rightarrow N_2O_5 \quad \text{(R32)}$$

where O_3 was produced *in situ* using an ozone generator which applied an electrical charge to O_2 molecules, splitting them apart into oxygen atoms (O) that could then form ozone by reaction with O_2 as: $O_2 + O + M \rightarrow O_3 + M$. Following reaction (R30), NO and O_3 were first mixed to form NO_2. The resulting NO_2/O_3 mixture was then flushed into a bulb in which NO_3 and subsequently N_2O_5 were generated through reactions (R31) and (R32). N_2O_5 crystals were collected in a cold trap at T=190K. The N_2O_5 sample was purified by trap-to-trap distillation under a flow of O_2/O_3. The final sample was stored at 190 K and used within a week.

III-1.5. **Error analysis**

In this section, the uncertainties from the measurements in the different set-ups are discussed in detail, and the formulae applied to calculate the uncertainties on the rate coefficient determination are provided. For the absolute measurements in the DF/MS set-up, the uncertainties include the statistical error of linear least squares fit of the measured first order rate coefficient with reactant concentration, error on the pressure and on the temperature measurements. These were estimated to be 15% of the total rate coefficient determination, as explained in previous work from the group (El Othmani et al., 2021).

For relative rate studies in CSA and LARKIN (see Eq. III-17), the uncertainty in the measured rate coefficient (Δk_{VOC}) was calculated by accounting for the uncertainties on the slope (b= k_{VOC}/k_{ref} see Eq. III-17) and the known reference rate coefficient (k_{ref}). The standard deviation, σ, obtained from the least squares linear regression of the relative rate plots divided by the square root of the number of data points is the uncertainty associated with the slope b. The uncertainty on the reference rate coefficient k_{ref} is the recommended uncertainty Δk_{ref}(%) provided in the database of McGillen et al. (2020). In the case of the LARKIN experiments, the uncertainties in the photolysis rate coefficient, $k_{photolysis}$, that is used to correct the actual value of the rate coefficient was also included. The uncertainties were added in quadrature. The uncertainty on the slope of the relative rate plot (Eq. III-17) is:

$$\Delta b = \sqrt{\left(\frac{std(b)}{\sqrt{n}}\right)^2 + (\Delta k photolysis)^2} \qquad \textbf{(Eq. III-17)}$$

where std(b) is the standard deviation of the linear regression (Eq. III-17) and n the number of datapoints, and $k_{photolysis} = (1.98 \pm 0.07) \times 10^{-5}$ s^{-1} the correction on the values of the Y-axis of the relative rate plot (Eq. III-17), so $\Delta k_{photolysis} = 0.07 \times 10^{-5}$ s^{-1} is the uncertainty on the first-order photolysis rate coefficient that was used to correct the value of Y.

Then, since $k_{VOC} = b \times k_{ref}$, the uncertainty on k_{VOC} is as follows :

$$\Delta k_{VOC} = k_{VOC} \times \sqrt{\left(\frac{unc(b)}{b}\right)^2 + \left(\frac{unc(k_{REF})}{k_{REF}}\right)^2} \qquad \textbf{(Eq. III-18)}$$

where $\Delta k_{ref}(\%)$ was obtained from the database as a percentage of the k_{ref}, so unc(k_{ref}) / k_{ref} = ($\Delta k_{ref}(\%) \times k_{ref}$) / k_{ref} = $\Delta k_{ref}(\%)$. If n measurements of the rate coefficient have been conducted, the uncertainty on the final average value of k_{VOC} was calculated by considering the uncertainty Δk_i on each individual measurement k_i by adding these uncertainties in quadrature as follows:

$$\Delta k_{average} = \sqrt{\frac{\sum_{i=1}^{n} (\Delta k_i)^2}{n}} \qquad \textbf{(Eq. III-19)}$$

The final rate coefficient provided in the results sections are the $k_{recommendation} = k_{average} \pm \Delta k_{average}$. This was also the case for the reported rate coefficient for multiple references which were averaged the same way (Eq. III-20) over the multiple experiments using different references. The uncertainties were added in quadrature with the assumptions that the variables are uncorrelated.

III-2. Results and discussion

III-2.1. Biacetyl chemistry : reaction with OH, photolysis and fluorescence

The UV absorption cross section spectrum of biacetyl has been determined; however, improvements remain to be made on the set-up and will be the aim of future work. Thus, cross section measurements were included in Appendices section App-III-3. Additionally, the kinetics of OH + biacetyl were studied in the PLP–LIF set-up; however, experimental difficulties were encountered, due to the photolysis of biacetyl under 248 nm illumination that led to the production of OH radicals. It is concluded that OH is produced from the photolysis of biacetyl which forms an acetyl radical that reacts with trace impurities of O_2 to form OH radical. Further work is required to measure the rate coefficient of OH + biacetyl from this set-up (see results, discussion and future directions provided in Appendices section App-III-4). The following sections present the kinetics study conducted in the discharge flow reactor (absolute measurements), in the atmospheric simulation chamber CSA and in the LARKIN set-up (relative rate measurements). These results, challenges encountered and future work needed are discussed.

III-2.1.1.   Rate coefficient of OH + biacetyl : Absolute method - Discharge flow reactor

The temperature-dependent reaction rate coefficient of OH + biacetyl (BA) was measured in a discharge-flow system. The absolute measurements were conducted at a total pressure of 2–8 Torr, in He, under pseudo-first order conditions in OH concentration, i.e., the OH consumption is monitored in an excess of biacetyl (see Table III-6 for the range of biacetyl concentrations used). The flow velocity in the reactor was between (650–2160) cm s^{-1}. The OH decays follow the equation $[OH]_t = [OH]_0 \times \exp(-k' \times t)$, where $[OH]_0$ and $[OH]_t$ are the initial concentration of OH radicals and that at a reaction time t, respectively, and $k' = k_{BA,DFMS} \times [BA] + k_w$ is the pseudo-first-order rate coefficient with k_w representing the heterogeneous pseudo-first-order loss rate coefficient of OH. Some typical temporal profiles of OH radicals were measured with various concentrations of biacetyl at T=475K and are presented in Figure App-III-3 in Appendices section App-III-1. The values of k' obtained from the slopes of the linear correlation in these profiles were corrected for axial and radial diffusion of OH in the carrier gas (Kaufman, 1984), He, with these corrections being less than 13%.

In Figure III-31, the pseudo-first-order rate coefficient, k', measured at different temperatures in the reactor are plotted against the concentration of biacetyl, [BA], and the slopes of the linear fits render the values of the absolute second-order rate coefficient of the OH radical reaction with biacetyl, $k_{BA,DFMS}$, at each temperature. The results of the absolute measurements of k_1 at various temperatures in the range T=230–770K are presented in Table III-6. The limit in the temperature for these experiments (T$_{max}$=770 K) was determined by the thermal decomposition of biacetyl. This was observed due to the formation of CH$_3$ radicals converted to CH$_3$Br in the presence of Br$_2$ and identified by mass spectrometry at m/z = 94/96 (CH$_3$Br$^+$). The reported uncertainty on the measured rate coefficients is estimated to be about 15 %, and are the addition in quadrature of the statistical error (within a few percent, Table III-6), the uncertainties on the measurements of the flow (5%), the pressure (3%), the temperature (1%) and the absolute concentration of biacetyl (< 10%).
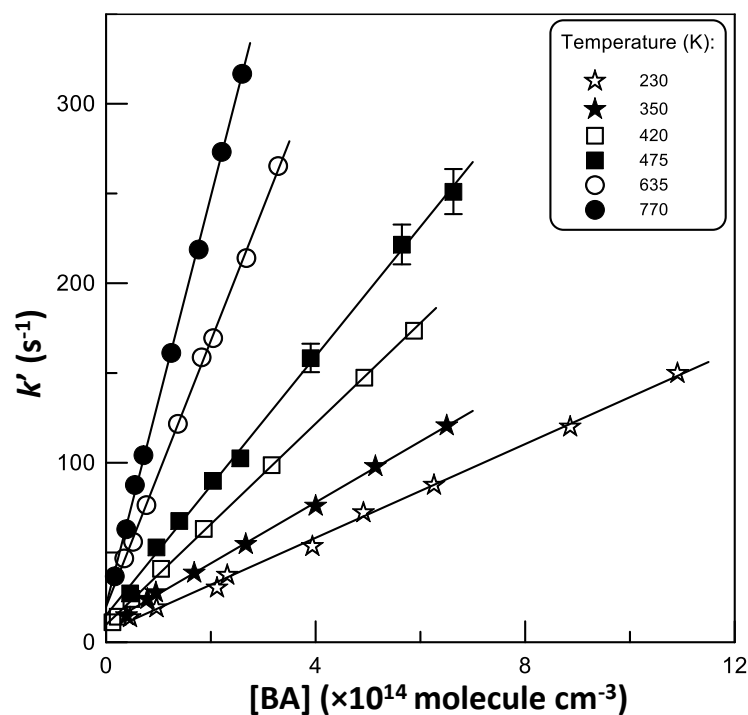
<u>Figure III-31</u> : Pseudo-first-order rate constant (k') as a function of biacetyl concentration at different temperatures obtained in the DF/MS system. Partially shown error bars represent typical uncertainties (of ≤ 5%) on the determination of k'. For clarity, the data at T =230K have been offset by -20 s^{-1}.

<u>Table III-6</u> : Summary of the absolute measurements of $k_{BA,DFMS}$ using DF/MS apparatus

T (K)	Number of measurements	[BA][a]	$k_{BA,DFMS}$[b]	Reactor[c] / OH source / Pressure
230	9	0.46-10.9	1.31±0.03	HW / F+H_2O / 8 Torr
240	15	0.60-11.6	1.31±0.02	HW / F+H_2O / 8 Torr
250	9	0.35-4.59	1.38±0.02	HW / F+H_2O / 2 Torr
252	6	1.06-12.4	1.31±0.04	HW / F+H_2O / 8 Torr
260	9	0.58-7.73	1.38±0.02	HW / F+H_2O / 2 Torr
270	9	0.65-7.28	1.38±0.02	HW / F+H_2O / 2 Torr
281	16	0.39-17.5	1.36±0.02	HW / F+H_2O / 2 - 8 Torr
298	9	0.43-9.00	1.38±0.02	HW / H+NO_2 / 2 Torr
305	9	0.15-7.78	1.44±0.03	Q / H+NO_2 / 2 Torr
320	10	0.24-9.68	1.52±0.03	HW / H+NO_2 / 2 Torr
330	8	0.32-3.67	1.58±0.02	Q / H+NO_2 / 2 Torr
350	9	0.39-6.50	1.70±0.03	Q / H+NO_2 / 2 Torr
370	8	0.10-4.95	1.81±0.02	Q / H+NO_2 / 2 Torr
390	8	0.25-5.17	1.98±0.03	Q / H+NO_2 / 2 Torr
420	8	0.12-5.88	2.80±0.03	Q / H+NO_2 / 2 Torr
475	8	0.46-6.63	3.61±0.06	Q / H+NO_2 / 2 Torr
540	8	0.10-2.36	4.87±0.05	Q / H+NO_2 / 2 Torr
635	8	0.35-3.29	7.41±0.10	Q / H+NO_2 / 2 Torr
770	8	0.17-2.60	11.4±0.20	Q / H+NO_2 / 2 Torr

[a] Units of 10^{14} molecule cm^{-3} [b] Uncertainties on k_1 are 2σ statistical errors, total estimated uncertainty is nearly 15%, units of 10^{-13} cm^3molecule$^{-1}s^{-1}$ [c] HW: Halocarbon wax coated reactor, Q: uncoated Quartz reactor.

The y-intercepts of the linear fits, k_w, as those presented in Figure III-31, are in the range of (7–20) s^{-1}, and are in good agreement with the value of k_w measured in the absence of biacetyl in the reactor. This is the case at all temperatures, with the exception of the lowest temperatures, T=230 and 240K, where k_w was found to be higher, around 30 s^{-1}. The reason for this could be the effect of a drastic increase of the wall loss of OH radicals in the presence of biacetyl in the reactor, which was observed at low temperatures (below 0°C) when using the H+NO$_2$ reaction to produce the OH radicals (reaction (3) in section III-1.3). When the reaction F+H$_2$O was used as a source of OH radicals (reaction (2) in section III-1.3), the value of k_w was found to be less strong. Thus, this reaction was used to generate OH radicals at low temperatures. The measured values of $k_{BA,DFMS}$ in both reactors (low and high temperatures) are similar for different surfaces (Quartz and Halocarbon wax coating, T = 298–330 K) and different total pressures (P= 2 and 8 Torr, T = 250–281 K), as presented in Table III-6.

In the Figure III-32, the results of the DF/MS measurements of the temperature-dependent OH reaction with biacetyl are presented against inverse temperature. The fit of the $k_{BA,DFMS}$(T) data is described by the sum of two exponential functions (solid line) as follows:

$$k_{BA,DFMS} = 9.3 \times 10^{-12} \exp(-1672/T) + 5.2 \times 10^{-14} \exp(213/T) \text{ cm}^3\text{molecule}^{-1}\text{s}^{-1} \text{ (T = 240-770 K) (Eq. III-20)}$$

The measured rate coefficients are lower than those previously reported by (Dagaut et al., 1988), by a factor 1.5. The possible reasons are the following. First, the absolute concentrations of biacetyl measured in two studies can have larger uncertainties in the study from Dagaut et al. (1988). In our study, the values were confirmed by employing two quantification methods, using a calibrated mixture and a direct injection with consistent results between both methods (within 10%). Second, it is possible that the sample used in the previous study contained impurities. However, such impurities would have to be very reactive. Dagaut et al. stated a sample of 98% purity, while in the present study, the sample is >99% purity. The distillation of the biacetyl samples with use of the middle fraction had no impact on the kinetic measurements. It has also been observed that the biacetyl sample can easily change its color (from a yellow to orange) and become more viscous, if exposed to air and light. The light and air may induce photolysis and potentially isomerize it. This might be another reason for the discrepancies between both studies depending on the condition under which the sample was stored and employed. However, in the present study, the sample has been stored under adequate conditions and IR analysis have ensured that it was not degraded. The rate coefficient at room temperature is $k_{BA,DFMS}$=(1.38±0.21)×10^{-13} cm^{3}molecule^{-1}s^{-1}. At low temperatures, the OH rate coefficients of biacetyl were found to be close to that of acetone. From the Figure III-32, it appears that at the low pressures, it is very clear that biacetyl displays a non-Arrhenius behavior. This could be expected from the presence of hydrogen-bonded pre-reactive complexes similar to the reaction of OH + acetone, e.g., (Smith et al., 2002; Talukdar et al., 2003), or the reaction of OH + HNO$_3$ which is pressure

and temperature dependent, most likely due to the competition between direct abstraction and pre-reaction complex formation (Brown et al., 1999). The high-pressure limit could be of a few hundred Torr and it is possible that the reaction is pressure dependent.
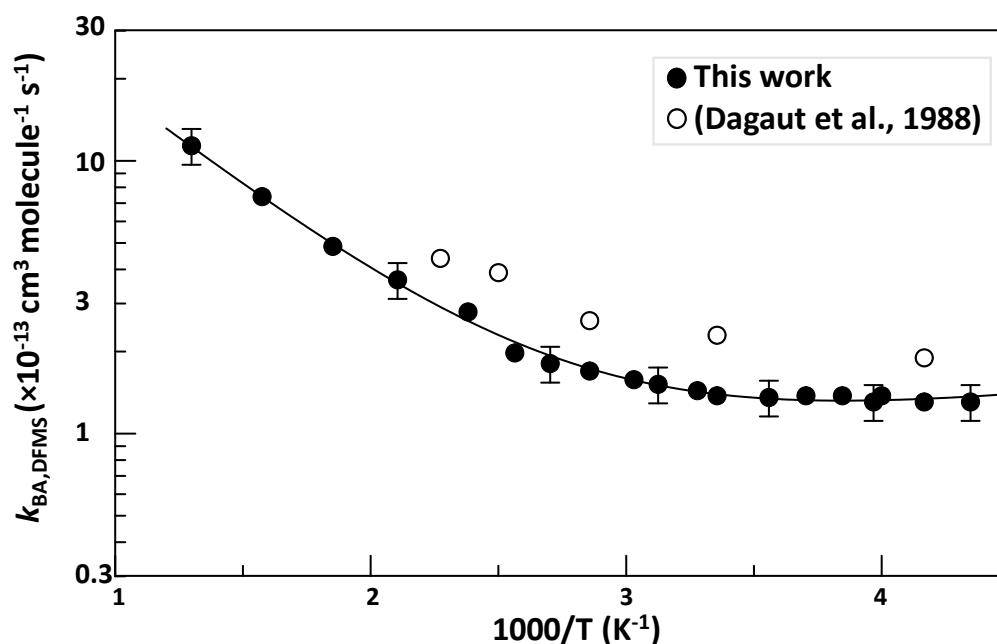
Figure III-32 : Summary of the measurements of k_1. Partially shown error bars represent estimated 15% uncertainties on the present measurements of k_1'.

III-2.1.2.   Rate coefficient of OH + biacetyl : Relative rate measurements
III-2.1.2.1. Atmospheric simulation chamber, CSA

The experimental conditions, together with the rate coefficients determinations, are presented in Table III-7 for 3 experiments conducted in the CSA for the OH reaction with biacetyl, using two different references (acetone and methyl formate). Additional experimental details are provided in Appendices section App-III-2. Second-order plots for the rate coefficients determination at room temperature are presented in Figure III-33. In order to obtain the subtraction factors, some isolated absorption bands of each compound of interest have been subtracted in the following wavenumber ranges: 1074–1151 cm^{-1} for biacetyl; 1280–1180cm^{-1} for acetone; 1175–1225cm^{-1} for methyl formate. The dilution/photolysis rate are calculated as the decay over time during dark/illumination conditions, and the reaction rate coefficient were calculated from the decay of the compound corrected for dilution over time. The total pressure in all of these experiments was atmospheric pressure 760±10 Torr.

Table III-7 : Experimental conditions and rate coefficient determination for the OH reaction relative-rate measurements in the CSA for biacetyl with two references, acetone and methyl formate. Literature data from (Dagaut et al., 1988) and (Darnall et al., 1979).

Date	Technique	Reference	Product subtraction	Pressure and temperature		Compounds concentrations			Dilution	Reaction with OH	
				P (Torr)	T (K)	$P_{SF6}{}^a$	$[ref]^b$	$[BA]^c$	$k_{dilution,SF6}{}^d$	$k_{ref}{}^e$	$k_{BA}{}^e$
26/04/2021		Acetone	-	760±10	295	1.114	4.814	4.652	3.44×10^{-5}	1.83	1.93
27/04/2021		Acetone	-	760±10	296	0.96	4.478	4.814	5.13×10^{-5}	1.83	2.49
29/04/2021		Methyl formate	-	760±10	295	1.13	4.26	6.61	2.96×10^{-5}	1.76	2.08
29/04/2021		Methyl formate	Formic acid, AFA^f	760±10	295	1.130	4.260	6.610	2.96×10^{-5}	1.76	1.84
Average of above measurements				**295±1**							**2.085**
(Dagaut et al., 1988)	FP-RF^g	-	-	25–50	298	-	-	$(2–454)\times10^3$ molecule cm^{-3}	-	-	2.3±0.2
(Darnall et al., 1979)	FP-RF^g	-	-	25–50^h	298	-	-	0.065 ppm	-	-	2.4±0.3

^{a} All pressures are in Torr. ^{b} [ref] refers to the concentration of the reference compound (see column Reference), in ppmv. ^{c} [BA] refers to the concentration of biacetyl in ppmv unless other specified. ^{d} $k_{dilution,SF6}$: dilution rate under dark conditions, in $\times10^{-5}$ s^{-1}. ^{e} Reaction rate coefficients are at room temperature, in $\times10^{-13}$ cm^{3}molecule^{-1}s^{-1}. ^{f} AFA: Acetic formic anhydride. ^{g} FP-RF: Flash photolysis – resonance fluorescence. ^{h} No value is provided in the original paper, but they refer to previous work where they describe the set-up and employ it at pressures between 25 to 50 Torr. Thus, this is a reasonable range for these experiments. More details are presented in Table App-III-I and Table App-III-2 in Appendices section App-III-2.
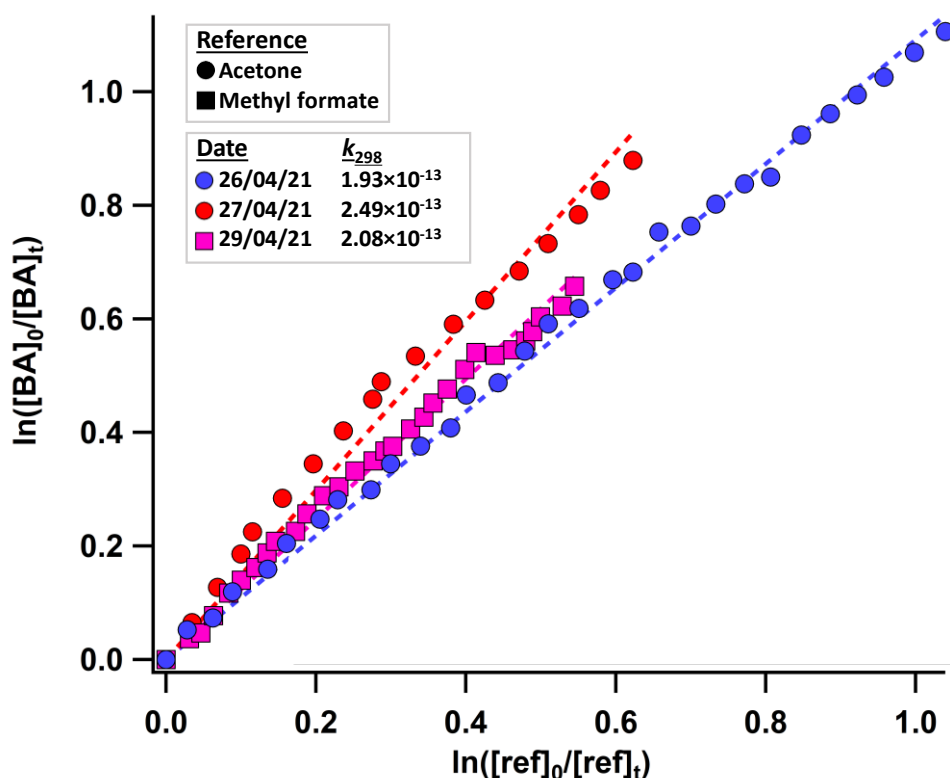
Figure III-33 : Second-order plots for the relative-rate measurements of the biacetyl (BA) reaction with OH radicals conducted in the CSA, using two references, acetone (circles) and methyl formate (square), whose respective reference rate coefficients with OH are 1.83×10^{-13} and 1.76×10^{-13} cm^{3}molecule^{-1}s^{-1}. k_{298} refers to the room temperature rate coefficient evaluated for the experiment associated, in cm^{3}molecule^{-1}s^{-1}.
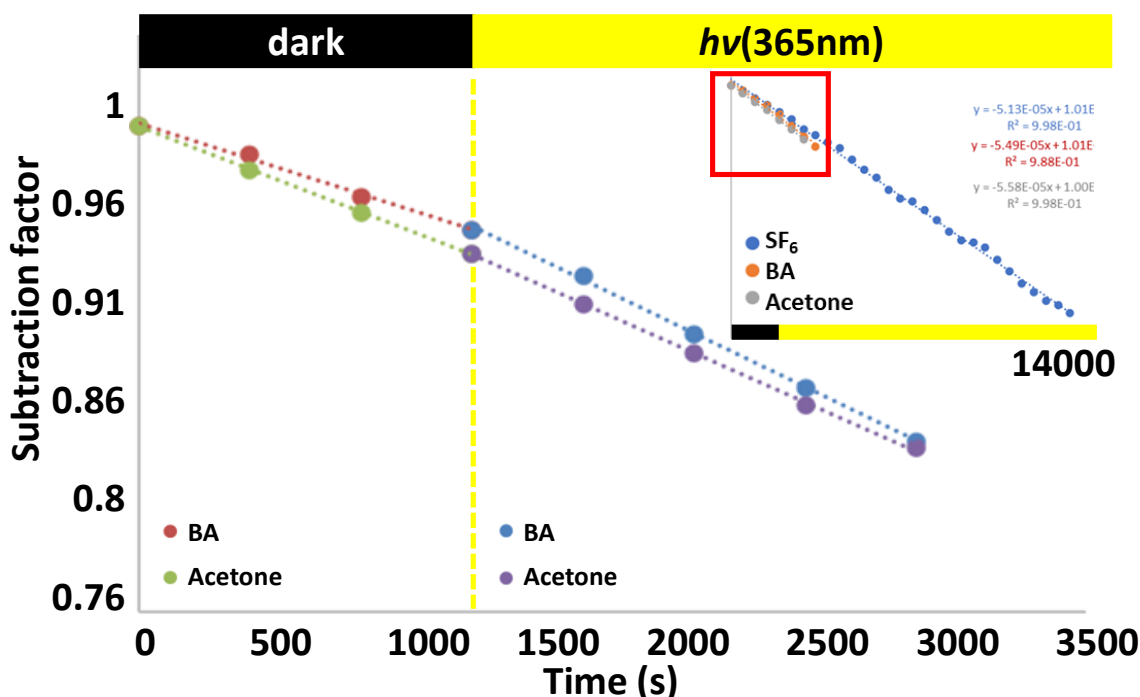
Figure III-34 : Dilution rates with and without illumination of the 14 lamps at 365nm. SF_6 is only subject to dilution, and it shows the decay due to dilution only. It can be observed that when lights are on, the removal of BA and acetone is slightly faster than dilution only. For BA, this decay under illumination was distinctively faster compared to dark conditions, which suggests that BA was photolyzed. For acetone, the difference was found to be negligible between dark and photolysis conditions. The inset represents the dilution during the whole experiment, to observe the decay of SF_6 with time, and the main plot represents the zoomed in section of the inset (red square box), for a more detailed overview of BA and acetone decay during dilution process, before the reaction is initiated.

The decay rate of biacetyl under dark conditions is equal to that of SF_6 within experimental errors (Figure III-34), which shows that wall deposition is not an important sink for biacetyl in these experiments. From these data, it can be observed that BA is photolyzed at 365nm ($\sigma_{365nm}=1.2\times10^{-20}$ cm^{2}molecule^{-1}, Figure App-III-7 in Appendices section App-III-2), as illustrated by the Figure III-34. However, this contribution is reasonably negligible if compared to the dilution rate itself and can be corrected for in the total rate coefficient (<10% of the dilution rate). This would require further investigation, and photolysis is discussed in the Appendices section App-III-4 about PLP–LIF measurements.

To avoid photolysis of biacetyl, another source of OH radicals could be tried instead, such as photolysis of H_2O_2 at 254nm, but this is unpractical since biacetyl has a larger absorption cross-section at this wavelength (see Figure App-III-7, σ_{254nm} = 3.8×10^{-20} cm^{2}molecule^{-1}), and would thus photolyze more under the same experimental conditions. Another option would be to decrease the intensity of UV-light in the chamber, by reducing the number of lamps on. However, since the reaction is slow, this would be unpractical because it would decrease the rate of the reaction and thus make the value even closer to that of the dilution rate.

Apart from the photolysis contribution, it is notable that the loss rate was very close to the dilution rate (e.g., for k_{BA} = 2.49×10^{-13} cm^{3}molecule^{-1}s^{-1} on 27/04/2023, the dilution rate accounts for more than 86% of the total loss rate, see Table App-III-1). Consequently, the reaction rate coefficient determination remained highly uncertain, highlighting the challenge of making these measurements in this set-up under the present conditions. Additionally, the formation of products on the peak analyzed was investigated. For the experiments with acetone, it was observed that a small amount of acetone may be produced during the experiment. This can be corrected for by subtracting the IR spectrum of acetone. During the experiment with the reference compound methyl formate, formic acid, and acetic formic anhydride (AFA) have been identified as products. These compounds were synthetized in the laboratory and identified using IR spectroscopy. Then, their reference spectra were subtracted from the experimental spectra, and rate coefficient was recalculated. Lastly, formaldehyde can be formed and subtracted from the spectrum. Yet, the values of the reaction rate coefficient remain similar to that of the dilution/photolysis rate, after correction, which suggests that these additional losses contribute significantly to the total rate coefficient under these experimental conditions. It can also be observed that these analyses have large uncertainties due to low concentrations, slow decay rates, and interferences. Even after stripping the spectrum from products formed, the determination of the decay rates varied greatly (see k_{ref} and k_{BA} for experiment 29/01/2021), which was due to the fact that the reaction is too slow, and dilution induces a large variability in the decays.

Also, it was not possible to increase the concentration of OH precursor in the chamber in order to increase OH reactivity since this leads to build-up of CH_3ONO, NO_2 and HNO_3. As the reaction rate coefficient of CH_3ONO is close to that of biacetyl ($k_{CH3ONO+OH}$= 2.7×10^{-13} cm^{3}molecule^{-1}s^{-1}, (McGillen et al., 2020)), it is not favorable to have it in a concentration where it will not be photolyzed readily and thus accumulate in large quantities, react with OH, and form products. This would eventually lead to less biacetyl consumption by OH radicals, which is the opposite of what is intended here, and an accelerated build-up of NO_2 and HNO_3, which can induce competing chemistry as well.

In addition to the reactions (R24), (R25) and (R26) described section 2.1. for the OH formation from methyl nitrite photolysis, the following reactions can occur:

$$CH_3O^\bullet + NO_2 \rightarrow CH_3ONO_2 \text{ (R33)}$$

$$NO_2 + OH \rightarrow HNO_3 \text{ (R34)}$$

$$NO_2 + HO_2^\bullet \rightarrow HOONO_2 \text{ (R35)}$$
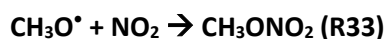
If too much NO_2 is formed, multiple side reactions can suppress OH production: the reaction (R33) consumes the $CH_3O^\bullet$ radical necessary to form the $HO_2^\bullet$ radical (reaction (R25) in section III-2.1.) that

generates OH radicals (reaction (R26) in section III-2.1.); the reaction (R34) which consumes OH radicals; the reaction (R35) which consumes $HO_2^{\bullet}$ which should react with NO to form the OH radicals from (reaction (R26) in section III-2.1.). These reactions, thus, reduce the rate of the decay measured. To avoid the contribution of these side reactions and favor the formation of OH radicals through (R24), (R25) and (R26) reactions, it would be possible to replace purified air with pure O_2; such experiments are too expensive if conducted in the 7300L chamber since these experiments require a constant flow of 5L min^{-1}.

Lastly, it is not possible to increase the light intensity in the chamber since all the lamps in the CSA were already used at their highest intensities. Therefore, the photolysis of the precursor reaches a limit in its efficiency to produce the OH radicals. Also, it was not possible to increase CH_3ONO since it scavenges OH radicals.

III-2.1.2.2. <u>LARKIN</u>

The LARKIN set-up described in section III-1.2. was employed to measure the kinetics of the reaction of biacetyl + OH. However, by using the LARKIN set-up, it was possible to improve some conditions that were not adjustable in the chamber. First, it is possible to use O_2 as a bath gas instead of purified air. Second, the use of a laser enables higher photon flux through the reactor, allowing methyl nitrite to be photolyzed more efficiently.

The experiments were conducted at various temperatures between 243 and 403K and pressures of 760±20 Torr. Known rate coefficients were measured in the set-up and they agreed with the literature values (furans + OH, see section III-3.2.). The rate coefficient was determined using the relative-rate method, with 2-nitropropane as a reference compound, with a rate coefficient of k_{2NP}(T=240–400K)=2.2×10^{-12}exp(-646/T) cm^{3}molecule^{-1}s^{-1} and k_{2NP} (T=298K)=(2.50±0.63)×10^{-13} cm^{3}molecule^{-1}s^{-1}, (McGillen et al., 2020). The bath gases used were purified air or O_2. Some measured temporal profiles are presented (see Figure III-35) for various temperature. The linearity was ensured for all the experiments, which suggests adherence to the second-order conditions.
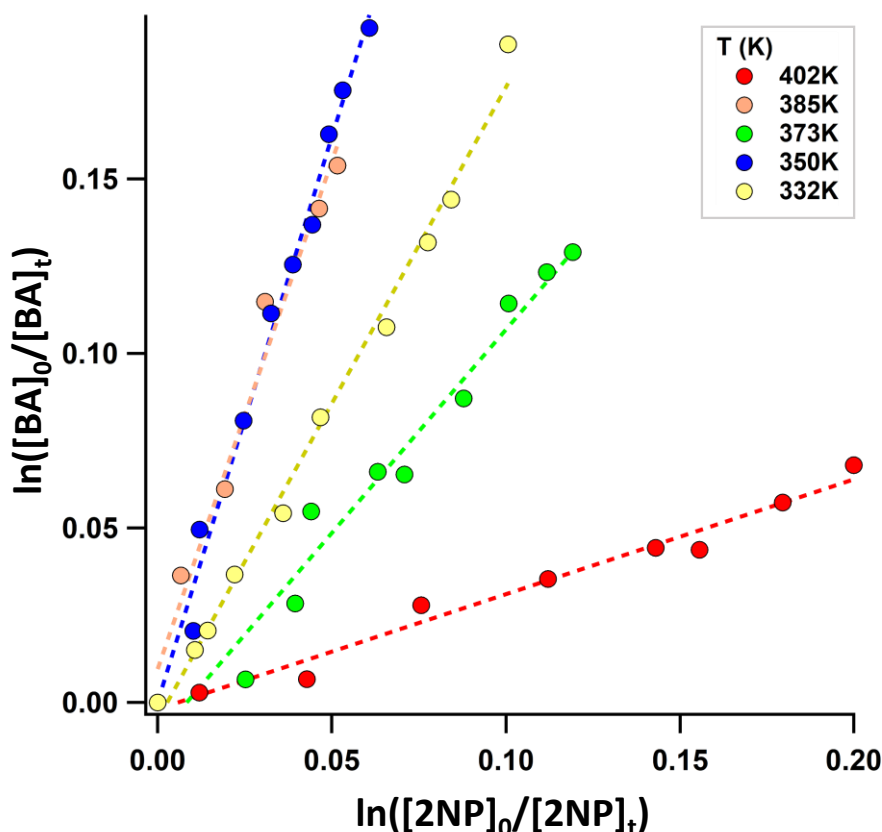
<u>Figure III-35</u> : First-order plot of the biacetyl consumption as a function of the reference compound (e.g., 2-nitropropane). The linearity observed at various temperature ensures the validity of the second-order assumption (see Eq. III-17).

The background wall-loss/photolysis rate of biacetyl, $k_{photolysis}$, was found to be relatively important, representing between 18 to 62% of the reaction rate and varied slightly between experiments (see Figure III-36). The correction for this contribution was applied as the averaged value of the photolysis rate (Figure III-36) since no notable tendency has been observed as function of temperature. No effect of the choice of the bath gas was observed on the wall-loss/photolysis rate, $k_{photolysis}$ (see purple/orange dots).

The cell was carefully cleaned with clean bath-gas and pumping as described in the experimental sections, and the gas was heated up to facilitate the removal of impurities on the walls. It could be possible that some impurities would outgas from the walls and react in the cell or impact the heterogeneous chemistry on the walls. However, no specific difference was observed in the value of $k_{photolysis}$ before and after these cleaning test. Thus, the scattering in $k_{photolysis}$ was not attributed to the contribution of such impurities.
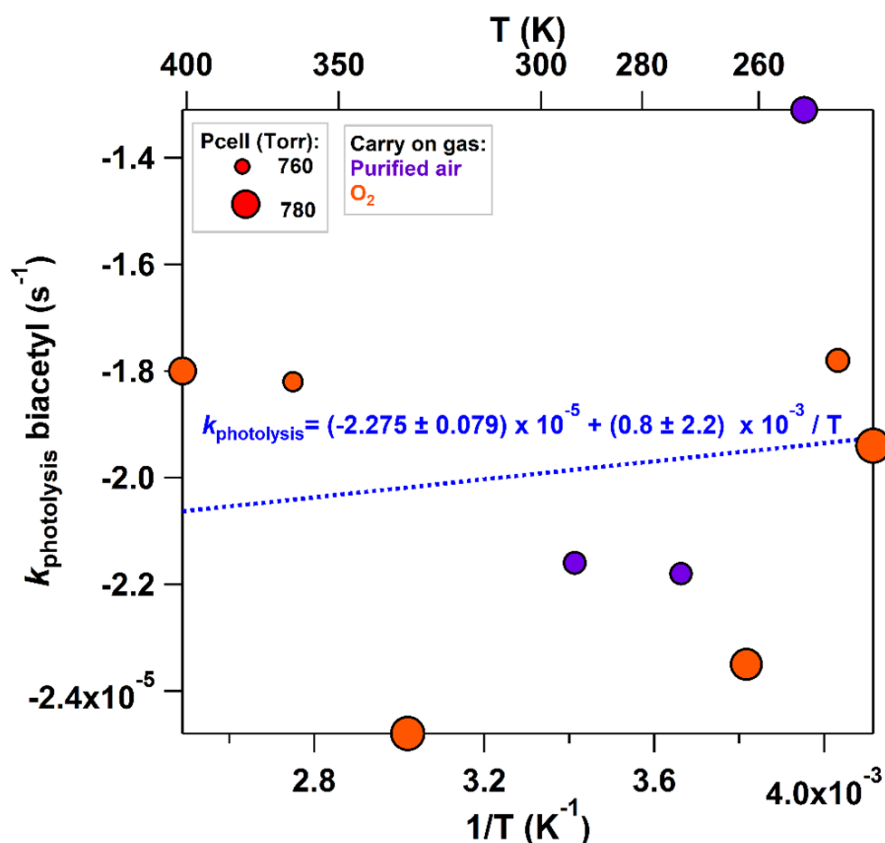
<u>Figure III-36 :</u> Wall-loss/photolysis rate, $k_{photolysis}$, as a function of the temperature, with different bath gases. Pressure in the cell was around 770±10 Torr.

The temperature-dependent rate coefficients were derived by correcting the measurements for wall-loss contribution and photolysis when occurring, and the second-order decays allowed to retrieve the rate coefficient of the reaction of biacetyl with OH, $k_{BA,LARKIN}$ (Table III-8 and Figure III-37). The measured values are presented in an Arrhenius plot in Figure III-37, together with the available literature data, from (Dagaut et al., 1988), (Darnall et al., 1979) and our measurements using DF/MS. It is observed that the values measured in LARKIN are in good agreement with the measurements of (Dagaut et al., 1988) and (Darnall et al., 1979) within the uncertainties, and in good agreement with the DF/MS measurements up to ~270K. The DF/MS Arrhenius relationship seems to be slightly lower than those measured in LARKIN. The k value measured at room temperature using the CSA is also in agreement with (Dagaut et al., 1988) and (Darnall et al., 1979). It is possible that the reaction of OH + biacetyl is pressure dependent similar to OH + HNO₃ reaction or OH + acetone, as suggested by non-Arrhenius behavior observed at low temperatures in Figure III-32 and Figure III-37 from the DF/MS measurements. This has been discussed in the section about DF/MS results. This could be due to the formation of a pre-reactive complex. Also, these differences could be due to multiple channels in the reaction that change experimental conditions (i.e., pressure). It is possible in the LARKIN set-up that the photolysis beam was very narrow with a large photon flux in a small volume leading to secondary reactions.

Table III-8 : Experimental conditions, including temperature in K and pressure $P_{tot}=770\pm10$ Torr for each experiment, together with temperature dependent rate coefficients, k_{BA}, cm^3 molecule^{-1} s^{-1}, with statistical uncertainties, and background loss rate (wall-loss/photolysis), $k_{photolysis}$, in s^{-1}.

T_{cell} ($\pm$1K)	$k_{BA} \pm unc(k_{BA})$ ($\times10^{-13}$ cm^3 molecule^{-1} s^{-1})	$k_{photolysis}$ (s^{-1})
273.4	2.09 ± 0.54	2.18×10^{-5}
243.3	1.55 ± 0.40	1.94×10^{-5}
248.1	1.58 ± 0.40	1.78×10^{-5}
253.0	1.69 ± 0.44	1.31×10^{-5}
253.0	1.60 ± 0.44	1.31×10^{-5}
262.1	1.85 ± 0.48	2.35×10^{-5}
294.0	2.56 ± 0.71	2.16×10^{-5}
312.9	2.87 ± 0.74	
332.5	2.93 ± 0.77	2.46×10^{-5}
350.5	3.31 ± 0.91	
363.6		1.82×10^{-5}
373.0	3.64 ± 0.94	
385.0	4.10 ± 1.07	
402.5	4.10 ± 1.15	1.80×10^{-5}
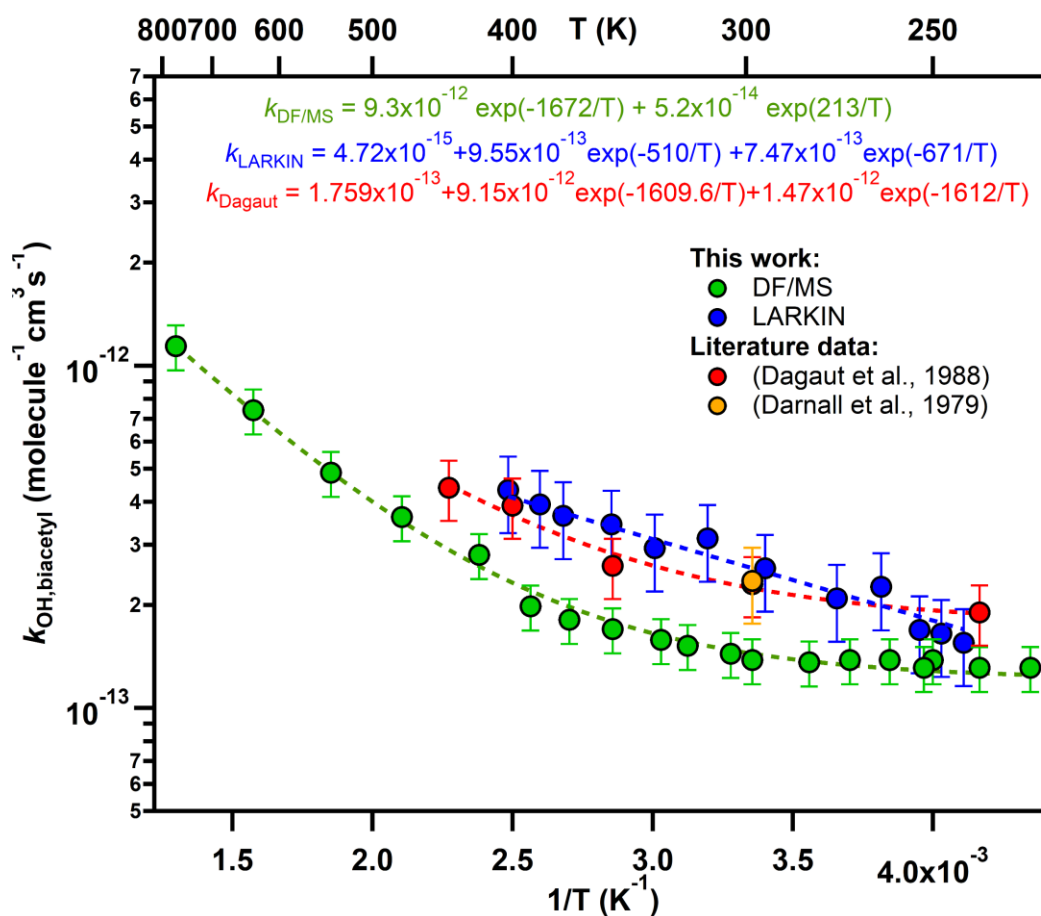
Figure III-37 : Arrhenius plot of the rate coefficients of OH + biacetyl as a function of inverse temperature, for a range of 212–740K and various pressure, measured in LARKIN, together with those measure in DF/MS, and literature data from (Dagaut et al., 1988) and (Darnall et al., 1979).

III-2.1.3.   **Discussion**

The behavior of biacetyl towards light absorption is discussed in several papers (Darnall et al., 1979; Horowitz et al., 2001; Link et al., 2021; Rajakumar et al., 2008, 2007; Turro et al., 1969). As discussed in the section of biacetyl + OH measurements in the PLP–LIF set-up, biacetyl photolyzes under UV-visible radiation to produce an energized acetyl radical which further reacts with O_2 to form OH and other products. The peroxyacetyl radical formed can also stabilize and react with NO_2 to form PAN. It is also known that hot $CH_3C(O)$ dissociates to give $CH_3 + CO$ (Somnitz et al., 2009, 2005). Further work is required to identify and quantify the other possible products that could be formed during this reaction (e.g., could it form $CH_3C(O)$-$C(O) + CH_3$ or $C_2H_6 + 2 CO$?).

From our experimental results, it has been observed that biacetyl is photolyzed up to 365 nm, but it has not been possible to identify $CH_3CO^\bullet$ in the relative-rate measurements, since it will be quickly converted to $CH_3C(O)O^\bullet_2$ and that radical will react further. There are also minor channels that produce OH. The $CH_3CO^\bullet$ radicals will be short-lived and form subsequent products. These radicals are also not detectable with the present instrumentation, but could be measured using cavity ring-down spectroscopy at wavelengths between 490 and 660 nm, for example, as in the previous work of (Rajakumar et al., 2008). On the other hand, it has been observed that biacetyl photolyzes at 248nm from the PLP–LIF measurements, and forms OH radicals.

Regarding the reaction with OH radicals, based on the literature, the mechanism (Figure III-39) by which OH radicals abstract hydrogen from biacetyl has been proposed by (Calvert et al., 2002), based on the analogy with glyoxal, and the fate of the radical formed has been obtained based on the study of (Christensen et al., 1998). O_2 rapidly adds to the radical to form a peroxy radical, further reacting with NO to produce an alkoxy radical, which decomposes to form CH_2O, CO and the $CH_3CO^\bullet$ radical (Christensen et al., 1998). However, further work could be useful to investigate further the mechanistic pathways through which biacetyl can react in the atmosphere.
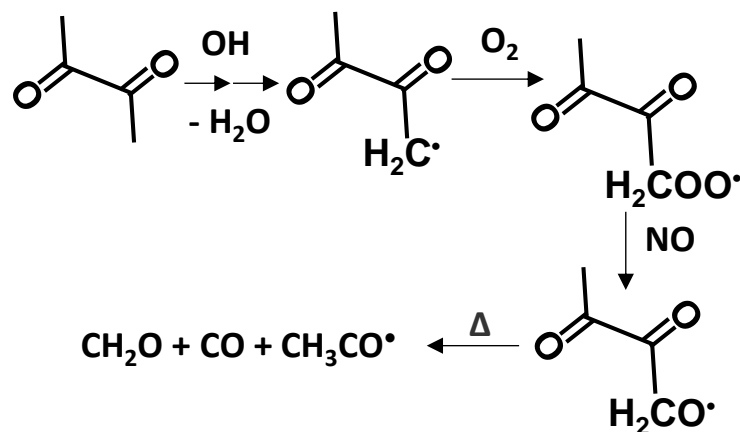
Figure III-38 : Mechanism of the reaction of OH + biacetyl, based on the work of (Calvert et al., 2002) and (Christensen et al., 1998), and analogy with the mechanism of acetone towards OH radical (Smith et al., 2002; Talukdar et al., 2003).

The experiments conducted to measure the rate coefficients of the reaction of OH + biacetyl have pointed out the difficulty that can sometimes be encountered in kinetics experiments (e.g., contribution of additional losses that cannot be corrected for adequately or avoided). The measurements in the PLP–LIF were challenging due to the photolysis of biacetyl under the present condition forming OH radical whose consumption is quantified. In this chamber, with the current configuration, it was hard to measure a rate coefficient of around 1×10^{-13} cm^3 molecule^{-1} s^{-1}. In the experiments in the CSA, it was also difficult to distinguish the contribution to the total loss from photolytic loss and OH induced loss. It was not possible to extend the duration of the experiment beyond a few hours depending on the reference compound used, due to the formation of products that make IR analysis more difficult and can induce secondary chemistry that can be significant. The values measured in the LARKIN set-up have been corrected for the photolysis process and potential radical interactions which was not negligible, however, the results agreed well with the literature data from Dagaut et al. (1988) and Darnall et al. (1979) especially at low temperatures. The measurements in the DF/MS set-up agreed with other reported data at low temperatures and start to differ at lower temperatures T>270K, however, this could be due to a pressure dependence of the reaction that displayed a non-Arrhenius behavior.

These measurements point out that this reaction still represents an interesting issue since its OH rate coefficient used in atmospheric models is still uncertain by a factor ~2 despite multiple determinations. This shows the importance of using multiple techniques to measure the rate coefficient of a reaction under various conditions. It would be useful to vary experimental conditions (e.g., pressure in LARKIN) in the techniques that were more challenging to study the kinetics of OH + biacetyl (e.g., here, CSA or LARKIN) in order to derive accurate measurements of the rate coefficients of that reaction. Also, the fluency should be varied in the LARKIN set-up to see the effect on the rate coefficients measured, and the beam should be expanded to minimize secondary reactions due to the narrow beam with high photon flux on a small volume. From this study, the DF/MS measurements seemed the most adapted and accurate, avoiding photolysis of biacetyl and subsequent issues with side chemistry, and competing contribution of these channels.

III-2.2. <u>Furans chemistry</u>

This work focused on studying the kinetics of furans and related compounds, that are found in large quantities in biomass burning plumes, but whose reactions with NO_3 have been less studied. In this section, new measurements of the rate constants of furans + NO_3 and pyrroles + NO_3 are presented, together with some furans + OH rate coefficients. Effect of substitution on the reactivity has been investigated and discussed for the reaction of furans with nitrate radicals.

III-2.2.1.   Furans + NO$_3$

In this section, the measurements of the room temperature rate coefficient of 16 BBVOCs, including a variety of 14 substituted furans and 2 pyrroles, have been measured using the relative-rate method in the CSA set-up (see experimental section). The data are presented together with literature values when available, in the Table III-9 and Figure III-40. Multiple reference compounds have been used to measure each reaction rate coefficient, and measurements were repeated at least 3 times to ensure an averaged value with minor uncertainties. The IR absorption bands of the VOCs under study, and of the reference compounds are presented in Appendices section App-III-5, together with the rate coefficient of the reference compound. The data analysis of the published data can be found in the associated paper (Newland et al., 2022; Zhou et al., 2017). The data presented here which are not presented in the published work (Newland et al., 2022) were analyzed by comparing both manual subtraction and automated subtraction using the ANIR software (https://data.eurochamp.org/anasoft/), usually confirmed by comparing the results from multiple bands, when possible.

The OH scavengers were not used in these experiments, but under the conditions employed (concentration of reactants and OH precursor), the contribution from the OH chemistry interference proved to be negligible using a box model simulation. Additionally, the contribution of the NO$_2$ chemistry has been found to be negligible compared to the reaction rate coefficient ($<2\times10^{-20}$ cm^3 molecule^{-1} s^{-1}) and can thus does not impact the measured rate coefficients values. Second-order plots are presented in Figure III-39 for the unpublished data and in Figure 2 of (Newland et al., 2022) for the published data, and the linearity indicates that the second-order assumption is verified and that no additional losses were encountered during the experiment.
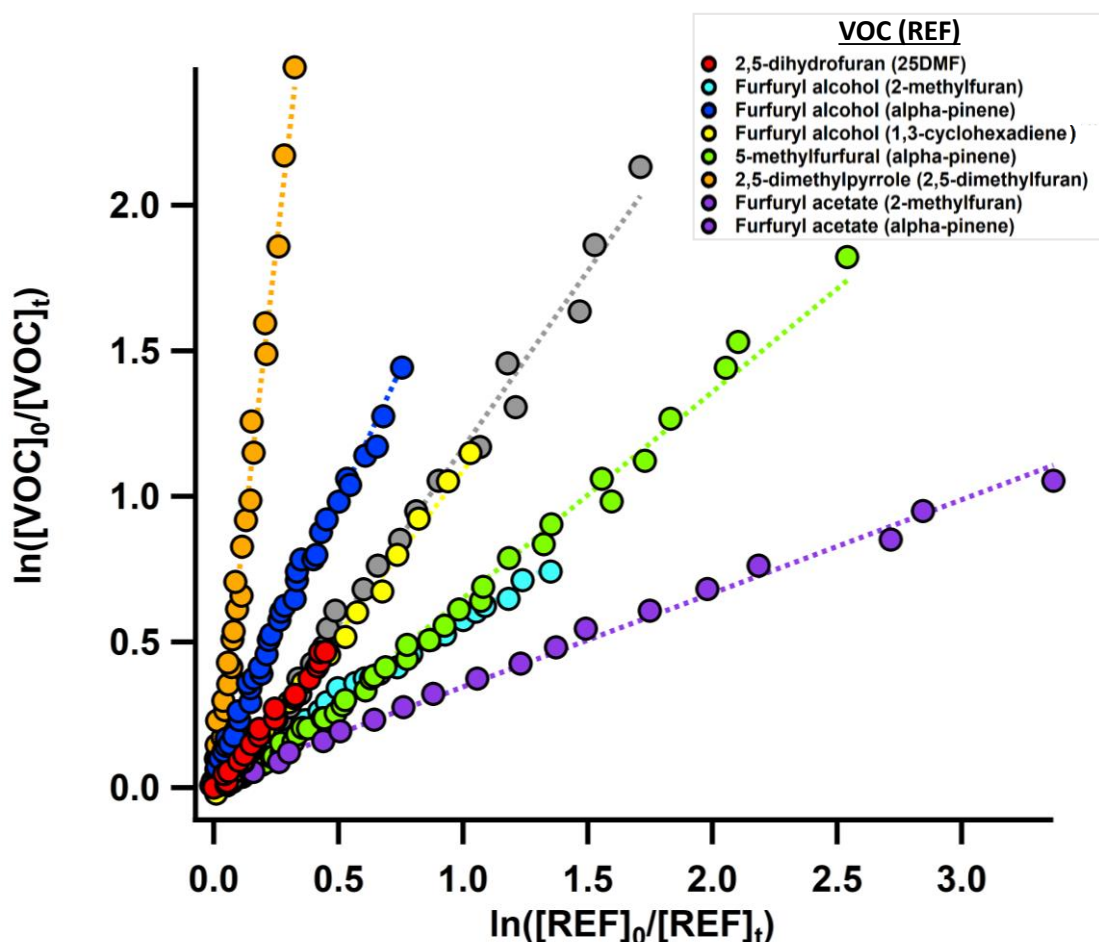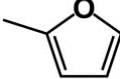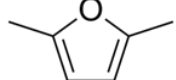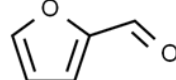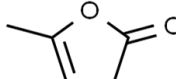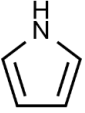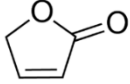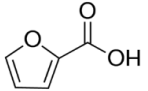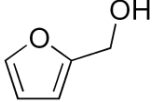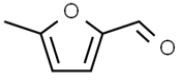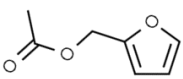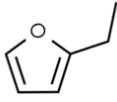
<u>Figure III-39</u> : Relative rate plots for 5 VOCs (2,5-dihjydrofuran, furfuryl alcohol, 5-methylfurfural, 2,5-dimethylpyrrole and furfuryl acetate) to some reference compounds (e.g., 2,5-dimethylfuran, 2-methylfuran, α-pinene, 1,3-cyclohexadiene) that where not published in the paper published (Newland et al., 2022). The linearity is ensured.

The NO_3 reaction rate coefficients have been derived for all the 16 compounds, as presented in the Table III-9 and Figure III-40. Uncertainties stated for the relative rate coefficients are usually <10% and mainly dominated by statistical errors. The experimental rate coefficients available in the literature for the selection of furans are presented in the Table III-9. The uncertainties on the rate coefficients were calculated as described in III-1.5. Our rate coefficients determined using different reference compounds agree well for all compounds, to within at worst 30%; often the agreement was much better. This shows that most of the experiments are reproducible. All the rate coefficients determined agree with literature data when available except for 2 compounds, 2,5-dimethylfuran and furfural, as further discussed below. Apart from 2,5-dimethyfuran and furfural, the values of the rate coefficient for the other VOC reported in this work are in good agreement with the literature data within 15%. This work reports, to our knowledge, the first measurements for the reaction rate coefficient of NO_3 with α-angelica lactone (5-methyl-2(3H)-Furanone), γ-crotonolactone (2(5H)-Furanone), 2,5-dimethylpyrrole, furfuryl alcohol, furfuryl acetate, 2,3-dihydrofuran, 2-ethylfuran, and 2,5-dihydrofuran. The first two rate coefficients have been published (Newland et al., 2022).

Table III-9 : NO₃ reaction rate coefficients for the 16 BBVOCs under study, including a variety 14 substituted furans and 2 pyrroles. The recommended values of the rate coefficient at room temperature for each reaction is a weighted averaged of all experiments done. The condition of each experiment is given (technique, reference compound used, source of NO₃ and number of repeats for each experiment). These data are reported for this work, with the data already published (Newland et al., 2022) and the new measurements (This work), together with literature data when available.

VOC	k_{NO3}[a]	Reference	Technique	Reference compound (repeats)	NO₃ source
Furan	$(1.45 \pm 0.15)\times10^{-12}$	This work	RR/CSA	cyclohexene (1)	N₂O₅
	$(1.55 \pm 0.16)\times10^{-12}$	This work	RR/CSA	α-pinene (1)	N₂O₅
	$(1.58 \pm 0.16)\times10^{-12}$	This work	RR/CSA	camphene (1)	N₂O₅
	$(1.49 \pm 0.15)\times10^{-12}$	This work	RR/CSA	α-angelicalactone (1)	N₂O₅
	$(1.45 \pm 0.23)\times10^{-12}$	**Recommendation This work**			
	$(1.5 \pm 0.2)\times10^{-12}$	**Atkinson et al. (1985)**	Chamber/RR	trans-2-butene[b]	N₂O₅
	$(0.998 \pm 0.062)\times10^{-12}$	**Kind et al. (1996)**	Flow reactor/RR	trans-2-butene	N₂O₅
	$(1.36 \pm 0.8)\times10^{-12}$	**Cabañas et al. (2004)**	Flow reactor/ absolute LIF[c]		HNO₃ + F
	$(1.51 \pm 0.38)\times10^{-12}$	**Recommendation (Al Ali et al., 2022)**	Chamber/RR	**See paper for individual runs**	N₂O₅
2-methylfuran	$(2.47 \pm 0.25)\times10^{-11}$	This work	RR/CSA	2-carene (2)	N₂O₅
	$(2.12 \pm 0.21)\times10^{-11}$	This work	RR/CSA	2,3-dimethyl-2-butene (2)	N₂O₅
	$(2.27 \pm 0.23)\times10^{-11}$	This work	RR/CSA	α-pinene (1)	N₂O₅
	$(1.89 \pm 0.19)\times10^{-11}$	This work	RR/CSA	pyrrole (1)	N₂O₅
	$(2.21 \pm 0.22)\times10^{-11}$	This work	RR/CSA	2,5-dimethylfuran[d] (2)	N₂O₅
	$(2.26 \pm 0.52)\times10^{-11}$	**Recommendation This work**			
	$(2.57 \pm 0.17)\times10^{-11}$	**Kind et al. (1996)**	Flow reactor RR	trans-2-butene	N₂O₅
	$(1.91 \pm 0.32)\times10^{-11}$	**Recommendation (Al Ali et al., 2022)**	Chamber/RR		N₂O₅
2,5-dimethylfuran	$(1.12 \pm 0.11)\times10^{-10}$	This work	RR/CSA	2-carene (1)	N₂O₅
	$(1.21 \pm 0.12)\times10^{-10}$	This work	RR/CSA	2,3-dimethyl-2-butene (1)	N₂O₅
	$(9.12 \pm 0.91)\times10^{-11}$	This work	RR/CSA	pyrrole (1)	N₂O₅
	$(9.06 \pm 0.90)\times10^{-11}$	This work	RR/CSA	2-methylfuran (1)	N₂O₅
	$(1.02 \pm 0.31)\times10^{-10}$	**Recommendation This work**			
DISAGREEMENT	**$(5.78 \pm 0.34)\times10^{-11}$**	**Kind et al. (1996)**	Flow reactor RR	trans-2-butene	N₂O₅
DISAGREEMENT	**$(5.82 \pm 1.21)\times10^{-11}$**	**Recommendation (Al Ali et al., 2022)**	Chamber/RR	**See paper for individual runs**	N₂O₅
Furfural	$(8.57 \pm 0.86)\times10^{-14}$	This work	RR/CSA	cyclohexene (1)	N₂O₅
	$(9.54 \pm 0.95)\times10^{-14}$	This work	RR/CSA	3-methyl-3-buten-1-ol (1)	N₂O₅
	$(8.37 \pm 0.84)\times10^{-14}$	This work	RR/CSA	furan (1)	N₂O₅
	$(9.50 \pm 0.95)\times10^{-14}$	This work	RR/CSA	camphene (1)	N₂O₅
	$(9.07 \pm 2.30)\times10^{-14}$	**Recommendation This work**	Small chamber/RR		N₂O₅
DISAGREEMENT	**$(1.20 \pm 0.28)\times10^{-12}$**	**Recommendation Colmenar et al. (2012)**	Small chamber/RR	2-methyl-2-butene, α-pinene	N₂O₅
α-Angelica lactone (5-methyl-2(3H)-Furanone)	$(2.89 \pm 0.29)\times10^{-12}$	This work	RR/CSA	α-pinene (1)	N₂O₅
	$(3.03 \pm 0.30)\times10^{-12}$	This work	RR/CSA	cyclohexene (1)	N₂O₅
	$(3.05 \pm 0.30)\times10^{-12}$	This work	RR/CSA	furan (2)	N₂O₅
	$(3.01 \pm 0.45)\times10^{-12}$	**Recommendation This work**			
Pyrrole	$(7.68 \pm 0.77)\times10^{-11}$	This work	RR/CSA	2-carene (1)	N₂O₅

Compound	Rate coefficient^a		Technique	Reference compound	Oxidant
Pyrrole	(7.07 ± 0.70)×10⁻¹¹	This work	RR/CSA	2,3-dimethyl-2-butene (2)	N_2O_5
	(6.58 ± 0.66)×10⁻¹¹	This work	RR/CSA	2,5-dimethylfuran^d (1)	N_2O_5
	(6.37 ± 0.64)×10⁻¹¹	This work	RR/CSA	2-methylfuran (2)	N_2O_5
	(6.94 ± 1.09)×10⁻¹¹	**Recommendation This work**			
	(4.6 ± 1.1)×10⁻¹¹	**Atkinson et al. (1985)**	Chamber/RR	2-methyl-2-butene	N_2O_5
	<1×10⁻¹⁰	**Cabañas et al. (2004)**	Flow reactor/ absolute LIF^c		HNO₃ + F
γ-crotonolactone (2(5H)-Furanone)	**<1.4×10⁻¹⁶**	**This work**	RR/CSA	cyclohexane (1)	N_2O_5
2-furoic acid	<1.45×10⁻¹²	This work	RR/CSA	furan	N_2O_5
2,5-dimethoxy-2,5-dihydrofuran	≪5×10⁻¹³	This work	RR/CSA	furan (1), 2,5-dimethylfuran (1), furfural (1), 2,5-dihydrofuran (1)	N_2O_5
2,5-dimethylpyrrole	(4.36 ± 1.09)×10⁻¹¹ (4.64 ± 1.19)×10⁻¹¹	This work	RR/CSA	2,5-dimethylfuran^d (2)	N_2O_5
	(4.50 ± 1.14)×10⁻¹¹	**Recommendation This work**			N_2O_5
Furfuryl alcohol	(1.05 ± 0.29)×10⁻¹¹	This work	RR/CSA	2-methylfuran (2)	N_2O_5
	(1.14 ± 0.29)×10⁻¹¹	This work	RR/CSA	α-pinene (1)	N_2O_5
	(1.29 ± 0.39)×10⁻¹¹	This work	RR/CSA	1,3-cyclohexadiene (2)	N_2O_5
	(1.01 ± 0.22)×10⁻¹¹	**Recommendation This work**			
5-methylfurfural	(4.42 ± 0.68) ×10⁻¹²	This work	RR/CSA	cyclohexene (1)	N_2O_5
	(4.39 ± 1.10) ×10⁻¹²	This work	RR/CSA	α-pinene (1)	N_2O_5
	(4.87 ± 0.78) ×10⁻¹² (4.17 ± 0.66) ×10⁻¹²	This work	RR/CSA	furan (2)	N_2O_5
	(4.46 ± 0.65)×10⁻¹²	**Recommendation This work**			
	(5.51±1.27)×10⁻¹²	**Colmenar et al. (2012)**	Small chamber/RR	2-methyl-2-butene	N_2O_5
Furfuryl acetate	(8.26 ± 1.67)×10⁻¹²	This work	RR/CSA	2-methylfuran (1)	N_2O_5
	(7.52 ± 1.88)×10⁻¹²	This work	RR/CSA	α-pinene (1)	N_2O_5
	(7.88±0.24)×10⁻¹²	**Recommendation This work**			
2,3-dihydrofuran	(6.13 ± 1.85)×10⁻¹¹	This work	RR/CSA	2,5-dimethylfuran^d (1)	N_2O_5
	(5.79 ± 1.45)×10⁻¹¹	This work	RR/CSA	α-pinene (1)	N_2O_5
	(5.96 ± 1.66)×10⁻¹¹	**Recommendation This work**			
2,5-dihydrofuran	(9.44 ± 0.40)×10⁻¹⁴	This work	RR/CSA	furfural^e (1)	N_2O_5
2-ethylfuran	(1.58 ± 0.32)×10⁻¹¹	This work	RR/CSA	2-methylfuran (1)	N_2O_5

^{a} Rate coefficient in cm³molecule⁻¹s⁻¹. ^{b} After correction to apply for reference. ^{c} LIF: Laser-induced fluorescence. ^{d} The rate coefficient used is that recommended from McGillen et al. (2020) database, 5.8×10⁻¹¹ cm³molec⁻¹s⁻¹. ^{e} The rate coefficient used is that from this work.
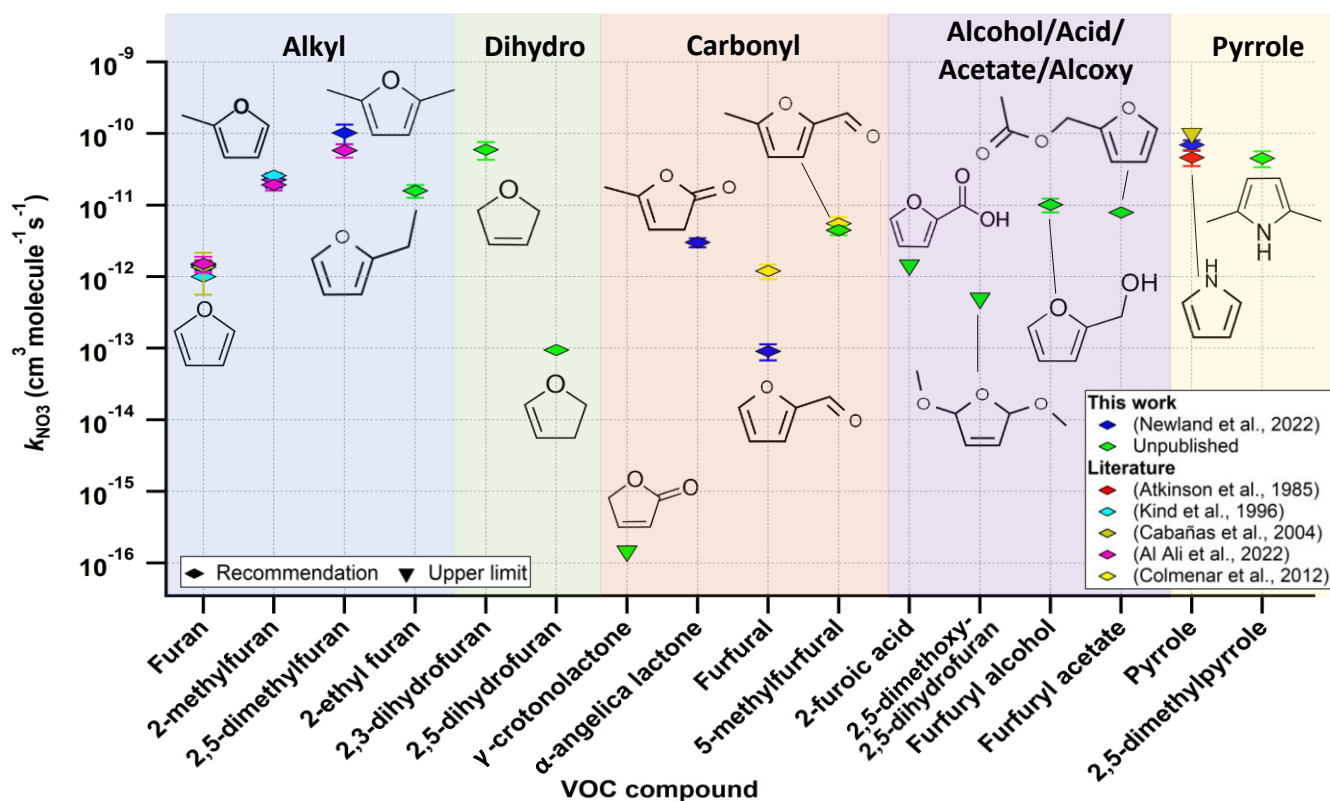
Figure III-40 : NO$_3$ reaction rate coefficients derived for the 16 BBVOCs measured in this work. Among the data, 7 rate coefficients have been published in (Newland et al., 2022) (dark blue horizontal diamond) and 9 rate coefficients are unpublished so far (green horizontal diamond). Rate coefficients and stated uncertainties are from Table III-7. Literature values are plotted, when available, and include the data presented in Table III-7 from: (Atkinson et al., 1985) in red, (Kind et al., 1996) in light blue, (Cabañas et al., 2004) in olive, (Al Ali et al., 2022) in pink, and (Colmenar et al., 2012) in yellow. When the values are upper limit for the rate coefficient, they are plotted as inverted triangles. The molecules are gathered by substitution types and functionalities present in the substituted furan, in the following order: alkyl (i.e., methyl, ethyl) (blue highlight), dihydrofuran (green highlight), carbonyl (orange highlight), other oxygenated groups (i.e., alcohol, acid, acetate and alkoxy) (purple highlight) and lastly the pyrroles (yellow highlight).

Discussion on the disagreements

Furan

The value measured for furan in this work is in good agreement with other reported data (Table III-9 and Figure III-40), and only disagrees slightly with the value reported from Kind et al. (1996).

2,5-dimethylfuran

The rate coefficient of 2,5-dimethylfuran measured from Kind et al. (1996), $k_{NO3,25DMF}$(Kind at al., 1996) = (5.78±0.34)×10^{-11} cm^{3}molecule^{-1}s^{-1}, and recommendation from (Al Ali et al., 2022), $k_{NO3,25DMF}$(Al Ali at al., 2022) = (5.82±1.21)×10^{-11} cm^{3}molecule^{-1}s^{-1}, do not agree with those measured in this work, $k_{NO3,25DMF}$(This work) = (1.02±0.31)×10^{-10} cm^{3}molecule^{-1}s^{-1}, by a factor of ~2. The reason of this disagreement is uncertain, and may be related to different surface effect, due to the difference in the flow reactor set-up compared

to the 7.3 m^3 chamber employed in this work. The relative rate measurements of Kind et al. (1996) were conducted in a low pressure (6.8–200 mbar) flow reactor. Concentrations were monitored using GC-FID. There is a disagreement of a factor ~2 between the rate coefficients of furan and 2,5-dimethylfuran reported in this work and those reported in Kind et al. (1996); however, the rate coefficients of 2-methylfuran are in good agreement between both studies which suggests that these discrepancies may not be attributed to systematic errors.

The reference 2,3-dimethyl-2-butene (23DM2B) was used in the three studies, but the value used for the reaction rate coefficient of 23DM2B with NO$_3$ is not the same: this work and Kind et al. (1996) used the recommended rate coefficient from McGillen et al. (2020) database $k_{23DM2B,1}$ = (5.69 ± 0.73)×10^{-11} cm^{3}molecule^{-1}s^{-1} (Atkinson, 1991) and (Al Ali et al., 2022) used a value of $k_{23DM2B,2}$ = (4.50 ± 0.40)×10^{-11} cm^{3}molecule^{-1}s^{-1} from (Lancar et al., 1991). When using the same value for the reference reaction that (Al Ali et al., 2022) used, the discrepancy is reduced ($k_{NO3,25DMF,2}$(This work – reevaluated) = (8.05±0.73)×10^{-11} cm^{3}molecule^{-1}s^{-1}). The rate coefficient determination still differs by a factor of 1.6, so, the choice of the reference reaction rate coefficient is not the complete explanation.

However, other references are used and the four rate coefficients determined using 4 references in this work are in fair agreement together, and this is also the case in the work of (Al Ali et al., 2022), which suggests that this is not the reason for the discrepancy. The relative rate plots are presented in the published paper (Newland et al., 2022), and the linearity is observed. The exact reasons for these discrepancies are thus unclear. The rate coefficients of this reaction must be studied in further work to refine the value of the rate coefficient. For the other analysis using 2,5-dimethylfuran as a reference, the rate coefficient recommended by (McGillen et al., 2020), $k_{NO3,25DMF}$ = 5.8×10^{-10} cm^{3}molecule^{-1}s^{-1}, is employed until a preferred value is recommended. It would be useful to measure the rate coefficients of 2,5-dimethylfuran using the same exact references as Kind et al. (1996) and Al Ali et al. (2022) in order to observe the differences.

Furfural

Similarly, the rate coefficient of the NO$_3$ reaction with furfural measured in this work is lower by more than an order of magnitude to that reported by (Colmenar et al., 2012) (see Figure III-41). This disagreement is not explained and could be due to some differences in the experimental conditions, such as chemistry on surfaces that are not well described. The reactivity of furans is governed by their substitution and it is clear from the Figure III-40 that NO$_3$ reactivity is influenced by the presence of electron supplying (e.g., –CH$_3$, –C$_2$H$_5$) groups. For example, the addition of a methyl group to the furan ring increases the NO$_3$ rate coefficient by a factor 16 (from 1.35×10^{-12} to 2.42×10^{-11} cm^{3}molecule^{-1}s^{-1}) and adding 2 methyl groups increases the rate coefficient by a factor 40 to 70 (respective to the value reported by Al Ali et al. (2022) or

that measured in this work). Methyl groups are very electron supplying groups and are thus expected to increase the reactivity towards the electrophilic addition of NO_3, as observed in this work. Because the –CHO substituent is a strongly electron withdrawing substituent attached to the furan ring, it would be expected to deactivate the ring towards the addition of NO_3 radicals and decrease the rate coefficient value (Kerdouci et al., 2014). This has been observed for other reactions of electrophilic addition with OH and O_3 (Jenkin et al., 2020; Kwok et al., 1995; McGillen et al., 2011). In order to have an estimation of the rate coefficient of the abstraction of the hydrogen attached to the aldehyde, it is possible to compare the rate coefficient of benzene since its ring is unreactive to the addition of NO_3 to that of benzaldehyde. The rate coefficient of NO_3 + benzene is $k_{NO3,benzene} = 3×10^{-17}$ $cm^3 molecule^{-1}s^{-1}$ (McGillen et al., 2020). The addition of an aldehyde group attached to the ring allows NO_3 to react via H-abstraction to the aldehyde hydrogen in benzaldehyde ($k_{NO3,benzaldehye}= 4×10^{-15}$ $cm^3 molecule^{-1}s^{-1}$, (McGillen et al., 2020). Thus, $k_{NO3,benzaldehye}$ can be approximated to be the rate coefficient of this process, assuming that the substitution effect between a furan and a benzene ring does not have a large impact upon the abstraction of the aldehydic hydrogen. It would consequently be expected that the rate coefficient of furfural is decreased significantly compared to that of furan due to the deactivating effect of –CHO group towards NO_3 addition, and that the additional H-abstraction pathway from the aldehyde group would not compensate for this effect by more than a value of about $k_{NO3,benzaldehye} = 4×10^{-15}$ $cm^3 molecule^{-1}s^{-1}$. It is noted that the procedure is different in our study and in that of Colmenar et al. (2012), especially for the injection of N_2O_5 which is continuous in our experiments on the contrary to (Colmenar et al., 2012) that injected all N_2O_5 at once at the start of the experiment. This could also lead to a different behavior of the secondary chemistry if N_2O_5 is in large concentrations in the chamber (e.g., accumulation of HNO_3, NO_2, N_2O_5), which is avoided when injecting in a continuous and controlled way N_2O_5 in order to avoid accumulation. The possibility that products of the reaction formed was an IR interference with the measurement of the VOC which would have reduced the loss thus resulting in a lower k value. However, this was ruled out since all the peaks were isolated and no product formation was observed on both the peaks of furfural and the reference used in each experiment. Despite these thoughts, the discrepancies between the available literature data are significant (factor 13) and it is thus necessary to conduct new experiments in order to determine the reasons of these differences and the correct value of the NO_3 rate coefficient of furfural.
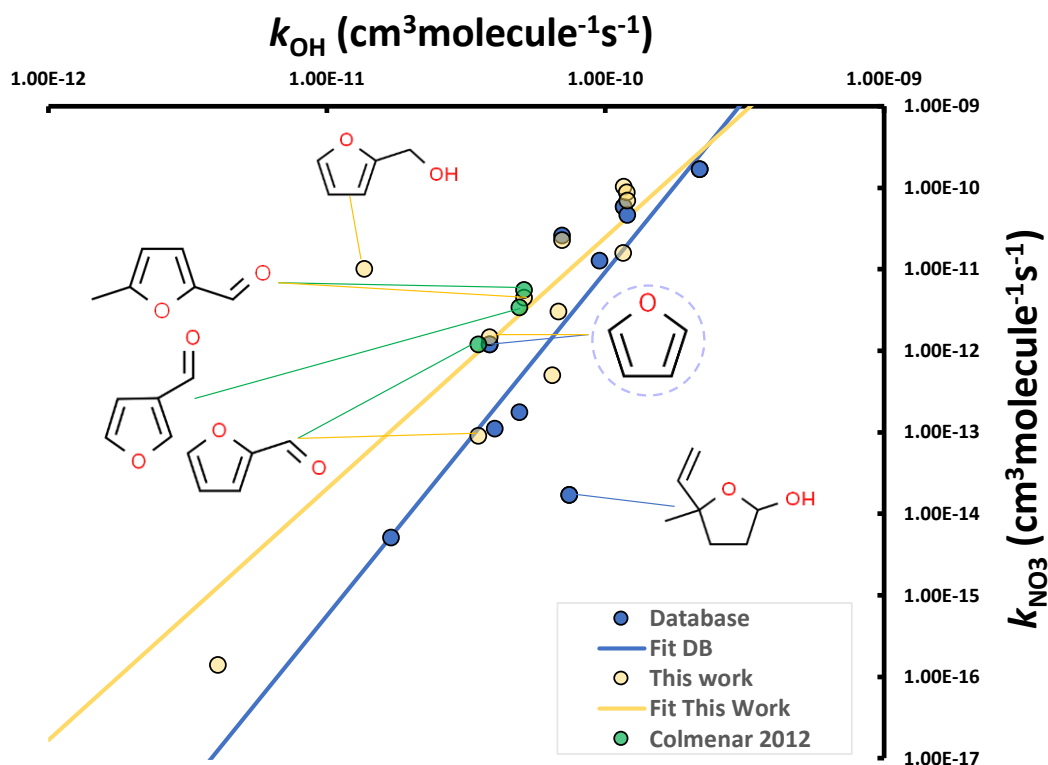
<u>Figure III-41</u> : Correlation between log(k_{OH}) and log(k_{NO3}) for the available furans measured in this work (noted "This work") and furan aldehydes measured in the work of Colmenar et al. (2012). The values of the furans provided in the database of McGillen et al. (2020) are also added as "DB". The fit of the available values from this work and the database are presented as a guide to show the trends in the data but not as a parametrization, since the data available does not include the exact same number and type of compounds.

Discussion on the substitution effect on the reactivity

Alkyl substitution

The presence of a methyl group increases the NO_3 rate coefficient of furan by approximately an order of magnitude, for example, for furan to 2-methylfuran to 2,5-dimethylfuran (Table III-9 and Figure III-40). Similarly, an activating effect from the methyl group can also be observed in the furanones, as 5-methyl-(3H)-furan-2-one displays a rate coefficient larger by 4 order of magnitude to that of (5H)-furan-2-one (Table III-9 and Figure III-40). Similarly, it can be observed that the addition of an ethyl group to furan also increases its rate coefficient, although by a factor smaller than a methyl group. It is also observed that the addition of a methyl group to the furfural increases the rate coefficient by a factor of 53 (k_{NO3}(furfural) = (9.07±2.30)× 10^{-14} cm^{3}molecule^{-1}s^{-}1 and k_{NO3}(5-methylfurfural) = (4.84±0.29)×10^{-12} cm^{3}molecule^{-1}s^{-1}). For α-angelicalactone, the rate coefficient measured in this work was k_{NO3}(α-angelicalactone)=(3.01±0.45)×10^{-12} cm^{3}molecule^{-1}s^{-1}). The rate coefficient of (3H)-furan-2-one (which corresponds to the same structure than α-angelicalactone but without the methyl substitution) has been measured to be 1.76 × 10^{-13} cm^3 molecule $^{-1}$ s^{-1} by (Berndt et al., 1997). Thus, in this case, also the reactivity is enhanced by the addition of methyl

substituent attached to the ring (factor of 17 higher). It is observed that the rate coefficient of pyrrole is not increased by the addition of 2 methyl groups, and this can be explained by the value of the rate coefficient NO_3 + pyrrole which is already very large and close to the collision limit, and thus, may not increase further. The trend in reactivity with alkyl substitution is consistent with what would be expected for an electrophilic addition and the known contributions of the substituents in electron donation capabilities.

Aldehyde

As discussed previously for the discrepancies in the determination of the rate coefficient of furfural, the formyl group substitution on an aromatic ring is expected to be strongly deactivating with respect to addition to that bond, as a result of the electron withdrawing mesomeric effect of the −C(O)H group (Kerdouci et al., 2014). This has been observed for analogous reactions with OH and O_3 (Jenkin et al., 2020; Kwok et al., 1995; McGillen et al., 2011). H-abstraction from the formyl group could occur, which would increase the total rate coefficient of the reaction by a typical value around $k_{abs}=10^{-14}$ cm^{3}molecule^{-1}s^{-1} (Kerdouci et al., 2014). The effect of the −C(O)H group on the electron density, which decreases the rate coefficient, outweighs the abstraction contribution, which increases the rate coefficient, and thus result in a lower reaction rate coefficient for furanaldehydes (k_{NO3}(furan)=(1.45±0.23)×10^{-12} cm^{3}molecule^{-1}s^{-1} = 16 × k_{NO3}(furfural)=(9.07±2.30)×10^{-14} cm^{3}molecule^{-1}s^{-1}). As discussed previously, the rate coefficient of 5-methylfurfural is larger than that of furan and furfural by a factor of 3 and 53 respectively, which suggests that the activating effect of the addition of a methyl group substituent compensates for the deactivating effect of the addition of the aldehyde substituent.

Aromaticity and conjugation

The pyrrole compound is more reactive than the furan compound, and this can be related to a difference in the level of aromaticity between the two structures, as discussed in (Wayne et al., 1991). Also, the dihydrofurans react very slightly slower than furan, within the uncertainties on the rate coefficient values. Dihydrofurans are not aromatic compounds and are thus expected to react as cycloalkenes. In the γ-crotonolactone ((5H)-furan-2-one) molecule, the C=C and C=O bonds are conjugated, which delocalizes the electrons of the π-orbital of the C=C bonds towards the C=O bond, and thus, reduce the reactivity towards addition to the C=C bond. This can also be observed in analogous acyclic compounds such as the conjugated ester methyl acrylate which has a rate coefficient slower by 2 orders of magnitude than that of the non-conjugated isomer vinyl acetate.

Low vapor pressure species

It is noted that the rate coefficient values for γ-crotonolactone, 2-furoic acid and 2,5-dimethoxy-2,5-dihydrofuran are only upper limits. It was experimentally challenging to study the kinetics of these compounds due to their very low vapor pressures (P_{vap} (γ-crotonolactone)=0.3±0.4 mmHg at 25°C , P_{vap} (2-furoic acid)= 0.0±0.5 mmHg at 25°C, and P_{vap}(2,5-dimethoxy-2,5-dihydrofuran) = 3.0±0.3 mmHg at 25°C (US EPA, 2015)). Different methods have been employed and tested to introduce 2-furoic acid in the chamber and nebulization has been the most promising one, using a proton-transfer-reaction time-of-flight mass spectrometer (PTR-ToF-MS) to identify the low concentration of 2-furoic acid introduced in the chamber. However, this requires further work to quantify the rate coefficients of this reaction and the upper value allows to compare to the reactivity of furan. 2-furoic acid is observed to be less reactive than furan from the experiments conducted. For the 2,5-dimethoxy-2,5-dihydrofuran compound, the addition of 2 methoxy group on each side of the furan ring decreases the reactivity relative to that of furan and 2,3-dihydrofuran.

Dihydrofurans

It is also observed that the rate coefficient of 2,5-dihydrofuran is slower than that of 2,3-dihydrofuran by more than 2 order of magnitude (factor 632). A possible reason for the deactivation of the furan ring towards NO_3 addition could be that steric effects would hinder the approach and addition of NO_3 to the double-bond of 2,5-dihydroufran due to its vicinity to the oxygen atom of the furan ring, compared to the isolated double-bond in 2,3-dihydrofuran.
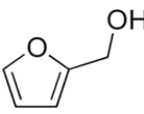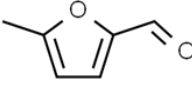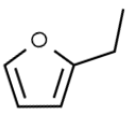
From this section, it can be concluded that NO_3 reactivity is sensitive to substitution effects. The effects of substitution on the NO_3 reactivity of furans can be significant and multiple, and they have the potential to compensate each other. Some disagreements have been found in the determination of the NO_3 rate coefficient of furfural (factor 13), and 2,5-dimethylfuran (factor ~2). New measurements are required to refine the study of these reactions since the reasons for these differences remain unclear. However, it is noted that in the literature database of VOC oxidation reactions, the NO_3 dataset possesses the most disagreement among the four major tropospheric oxidants (OH, Cl, NO_3, O_3). It has been discussed in Chapter I that measuring the rate coefficients of some compounds is particularly challenging (e.g., slow reactions, low volatility, etc.). The error bars in the experimental dataset are the largest, and this is related to secondary chemistry and effect to surface that still represents a challenge and remains not well understood.

III-2.2.2. **Furans + OH**

In order to evaluate the rate coefficients of the reaction of furans with OH radical, measurements were conducted in the LARKIN set-up. These results are presented in the Table III-10 and Figure III-42. As for the experiments of biacetyl + OH in LARKIN, these measurements have been conducted in O_2 to favor OH

radical formation and limit side reactions. The OH reaction rate coefficients with 2-ethylfuran and 2,3-dihydrofuran measured in this work is in good agreement with the literature data, within a factor of 1.3 and 0.7. This work presents the first measurements of the rate coefficient for furfuryl alcohol, and 5-methylfufural with OH. The IR absorption bands of the VOCs under study, and of the reference compounds are presented in Appendices section App-III-5, together with the rate coefficient of OH reactions with the reference compound.

Table III-10 : OH reaction rate coefficients for 5 furans under study, measured using the LARKIN set-up. The recommended values of the rate coefficient at room temperature for each reaction is a weighted averaged of all experiments done. The condition of each experiment is given (technique, reference compound used, source of NO_3 and number of repeats for each experiment). These data are reported for this work, together with literature data when available.

VOC	k_{OH}^a	Reference	Technique	Reference compound (repeats)	OH source
Furfuryl alcohol	$(1.67 \pm 0.44) \times 10^{-10}$	This work	LARKIN	MVK (1)	CH_3ONO
	$(1.25 \pm 0.32) \times 10^{-10}$ $(1.10 \pm 0.29) \times 10^{-10}$	This work	LARKIN	Cyclohexene (2)	CH_3ONO
	$(1.81 \pm 0.55) \times 10^{-10}$	This work	LARKIN	1-Methylcyclohexene (1)	CH_3ONO
	$(1.05 \pm 0.18) \times 10^{-10}$	This work	LARKIN	2,5-dimethylfuran (1)	CH_3ONO
	$(1.15 \pm 0.17) \times 10^{-10}$	This work	LARKIN	Isoprene (1)	CH_3ONO
	$(1.46 \pm 0.22) \times 10^{-10}$	**Recommendation This work**			
2,3-dihydrofuran	$(1.88 \pm 0.29) \times 10^{-10}$	This work	LARKIN	Isoprene (1)	CH_3ONO
	$(1.62 \pm 0.26) \times 10^{-10}$	This work	LARKIN	2,5-dimethylfuran (1)	CH_3ONO
	$(1.75 \pm 0.27) \times 10^{-10}$	**Recommendation This work**			
	$(1.2 \pm 0.28) \times 10^{-10}$	**Recommendation (McGillen et al., 2020)**			
5-methylfurfural	$(5.33 \pm 1.33) \times 10^{-11}$ $(5.27 \pm 1.32) \times 10^{-11}$	This work	LARKIN	cyclohexene (2)	CH_3ONO
	$(5.52 \pm 1.44) \times 10^{-11}$	This work	LARKIN	MVK (1)	CH_3ONO
	$(5.29 \pm 1.59) \times 10^{-11}$	This work	LARKIN	1-Methylcyclohexene (1)	CH_3ONO
	$(5.30 \pm 0.94) \times 10^{-11}$	**Recommendation This work**			
	$(5.10 \pm 0.48) \times 10^{-11}$	**Recommendation (McGillen et al., 2020)**			
2-ethylfuran	$(8.72 \pm 1.31) \times 10^{-11}$ $(8.62 \pm 1.30) \times 10^{-11}$	This work	LARKIN	Isoprene (2)	CH_3ONO
	$(8.62 \pm 1.73) \times 10^{-11}$	This work	LARKIN	TME (1)	CH_3ONO
	$(5.75 \pm 0.93) \times 10^{-11}$	This work	LARKIN	2,5-dimethylfuran (1)	CH_3ONO
	$(8.67 \pm 0.92) \times 10^{-11}$	**Recommendation This work**			
	$(1.16 \pm 0.41) \times 10^{-10}$	**Recommendation (McGillen et al., 2020)**			

^{a} Rate coefficient in cm^3 molecule^{-1} s^{-1}.
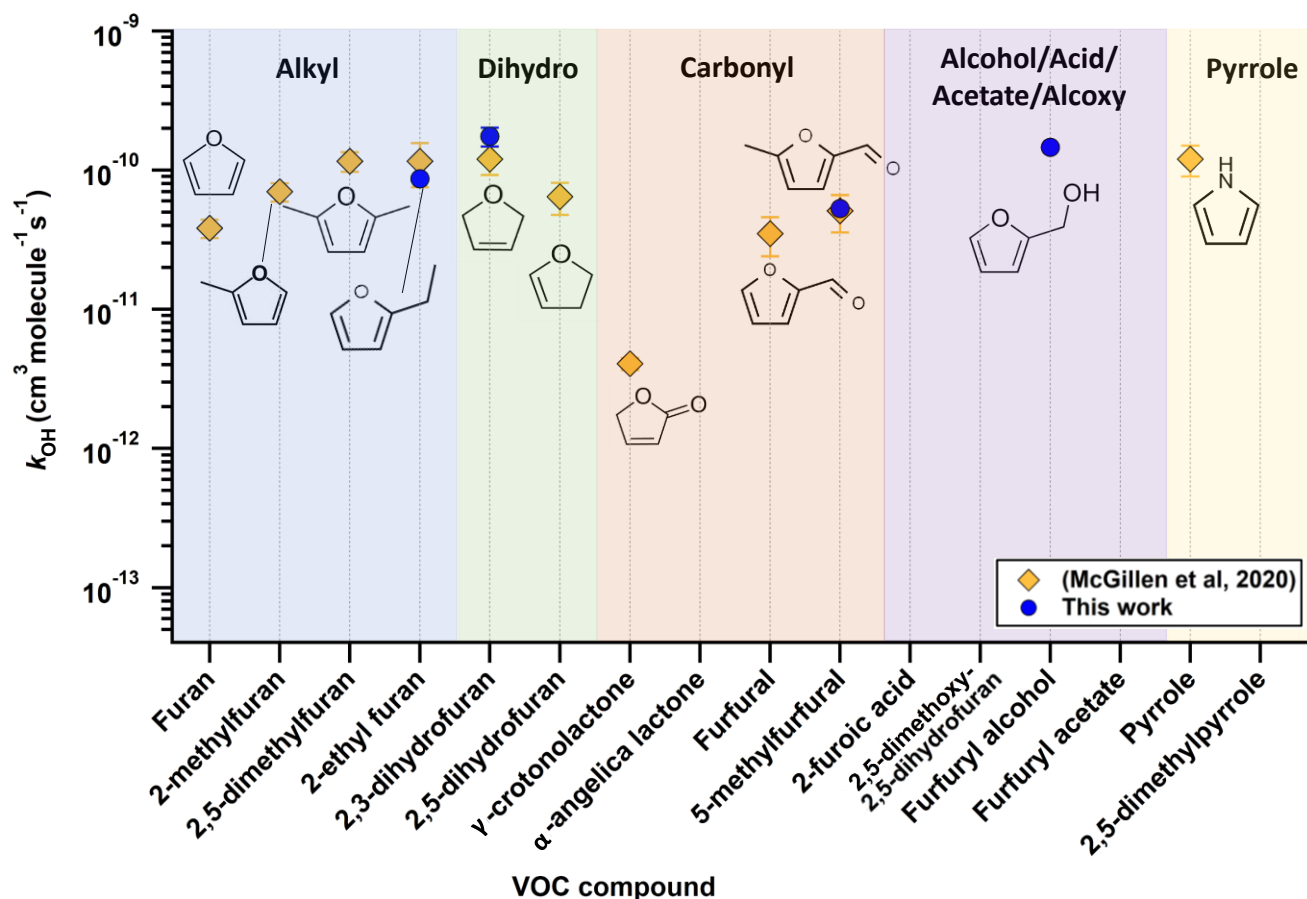
<u>Figure III-42</u> : OH reaction rate coefficients derived for the 4 furans measured in this work (blue circles), together with available literature data for 11 BBVOCs (yellow diamonds) taken from (McGillen et al., 2020) among the 16 species in the dataset studied for NO_3 reaction. Rate coefficients and stated uncertainties are from Table III-10. The molecules are gathered by substitution types and functionalities present in the substituted furan, in the following order: alkyl (i.e., methyl, ethyl) (blue highlight), dihydrofuran (green highlight), carbonyl (orange highlight), other oxygenated groups (i.e., alcohol, acid, acetate and alkoxy) (purple highlight) and lastly the pyrroles (yellow highlight).

Discussion on the substitution effect on the reactivity

In the Figure III-42, it can be observed that the addition of one or two alkyl substituents (methyl or ethyl) to furan increased the reactivity towards OH (blue panel "*Alkyl*"), which can be attributed to the activating effect of alkyl group attached to the double-bond and by the increased number of abstractable H atoms, which increased the value of the k_{abs} contributing to the overall rate coefficient. The reactivity of dihydrofurans is also higher than that of furan (Figure III-42, green panel "*Dihydro*"), which can be mostly attributed to the increased number of abstractable H atoms.

Concerning oxygenated substitution types, it is observed that γ-crotonolactone is less reactive than furan by a factor 9 and furfuryl alcohol by a factor 3. Conversely, furfural and 5-methylfurfural have a similar rate coefficient than that of furan, within a factor 1.1 and 0.7 respectively, which suggests that the C=O group when attached to the furan cycle deactivates the reactive double bond, while, the furfural compounds

166

remain similarly reactive compared to furan, which could be due to the electron delocalization within the cycle, contrary to the delocalization of electron on the C=O bond away from the reactive double bond in the cycle of β-crotonolactone.

Concerning carbonyl substituted compounds, furfural and 5-methylfurfural, the same observations that have been made for the NO_3 reaction are made here, but the effect is weaker. This highlights the fact that the substitution effect on the reactivity with OH is less strong than with NO_3. The presence of the –CHO group hinders the addition of OH to that specific reactive site, thus deactivating the double-bond reactivity with regards to the addition of OH. The reactivity of furfurals is thus usually half that of their alkyl substituted counterparts (Bierbach et al., 1995).

III-2.2.3.   Comparison of OH and NO_3 reactivities of furans

All the rate coefficients for the reaction of 16 BBVOCs with OH and NO_3 are gathered in the Figure III-43, with details in the caption. The mechanistic differences between OH and NO_3 reaction are discussed in Chapter I. The ratio between OH and NO_3 reactivity relative to that of furan for each compound is presented in the upper *y*-axis of the Figure III-43. The largest substitution effect is observed for NO_3 reaction for 2,5-dimethylfuran, with a rate coefficient ≈16 times larger than that of furan. The substitution effect appears to be milder on the OH reaction than on NO_3 (cf. red markers versus black markers in Figure III-43).

It can be observed that alkyl substitution (i.e., methyl and ethyl) enhances the reactivity towards both oxidants. The dihydrofurans have opposite behavior between NO_3 and OH reactions, while it increases OH reactivity, it decreases NO_3 reactivity, which could be attributed to the H-abstraction pathway contribution that plays a role in the OH reaction and not with NO_3 radicals. Concerning carbonyl substitution, the behavior is similar for both reactions, as discussed in the previous sections, except for furfuryl alcohol whose reactivity is increased compared to that of furan for NO_3 reaction and decreased for OH reaction. This shows the range of reactivities and the role of substitution for the furan compounds, which represent one group of compounds among the variety of species emitted from biomass burning.
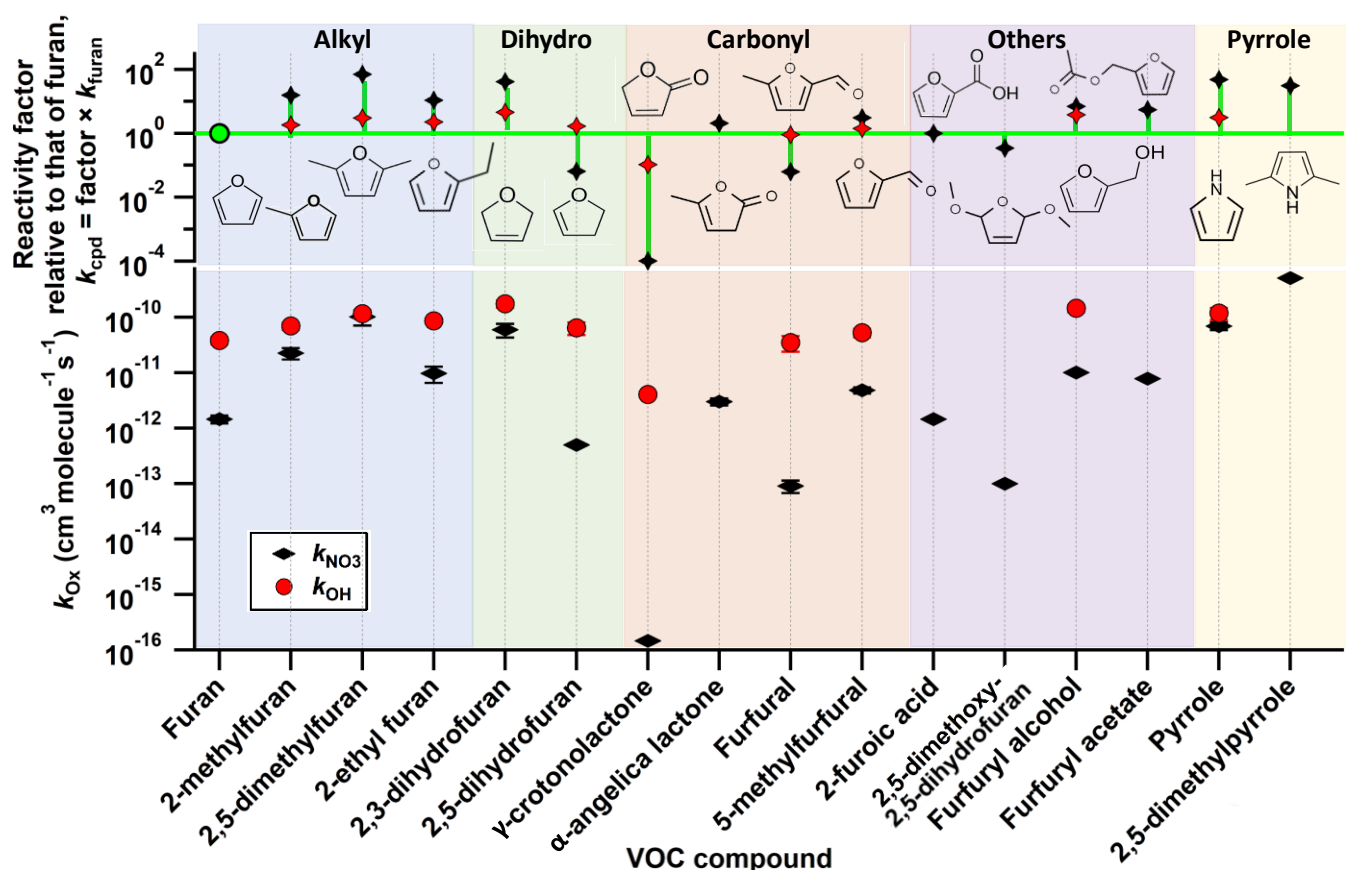
Figure III-43 : Rate coefficients derived for the 16 BBVOCs under study for the reaction with NO₃ (black horizontal diamonds), and OH (red circles), in lower y-axis, and ratios of the rate coefficients of each compound, k_{cpd}, relative to that of furan, k_{furan}, as k_{cpd} = ratio x k_{furan} for OH (red marker) and NO₃ (black marker), in upper y-axis. The values and uncertainties are those measured in this work, when available, from Table III-9 for NO₃ and Table III-10 for OH and, otherwise, taken from the literature recommendation from the database of (McGillen et al., 2020). The molecules are gathered by substitution types and functionalities present in the substituted furan, in the following order: alkyl (i.e., methyl, ethyl) (blue highlight), dihydrofuran (green highlight), carbonyl (orange highlight), other oxygenated groups (i.e., alcohol, acid, acetate and alkoxy) (purple highlight) and lastly the pyrroles (yellow highlight).

III-3. Atmospheric implications

III-3.1. Atmospheric loss of the BBVOCs under study

Caveat: In this section, the aim is to give an idea of the relative loss in the troposphere of OH and NO₃ for the BBVOCs studied, but the term tropospheric lifetime should be used with caution, as lifetime calculations are highly dependent on many conditions that may be hard to define (e.g., location, time, oxidant concentration in the air mass or its vicinity) and are based on many assumptions. Here, the compounds are short-lived compared to being well-mixed in the troposphere, so the comparison of lifetimes should be used as a measure of the relative contribution of different loss processes, but not as quantitative lifetimes.

Based on the reaction rate coefficients presented in the previous sections, the tropospheric lifetimes relative to each reaction, τ_{Ox}, was estimated using rough estimates of the daytime/nighttime concentrations of the OH and NO_3 radicals, when relevant, as follows:

$$\tau_{Ox}= 1/(k_{Ox} \times [Ox]) \text{ (Eq. III-21)}$$

The assumed concentrations are the averaged summertime midday OH concentrations of 5×10^6 molecule cm^{-3} (typical daily peak summertime concentrations of 1.5×10^6–1.5×10^7 molecule cm^{-3}), (Stone et al., 2012) and nighttime NO_3 concentrations of 2×10^8 molecule cm^{-3} (typical nighttime concentrations of 1×10^8 to $>1\times10^9$ molecule cm^{-3}) (Brown et al., 2012). The values are presented in Figure III-44. As mentioned in the caveat, the atmospheric lifetime should be regarded as an approximate value, as its actual loss will depend strongly on the time and location of its emission, mixing rates, and variations in the abundance of the OH and NO_3 radicals.
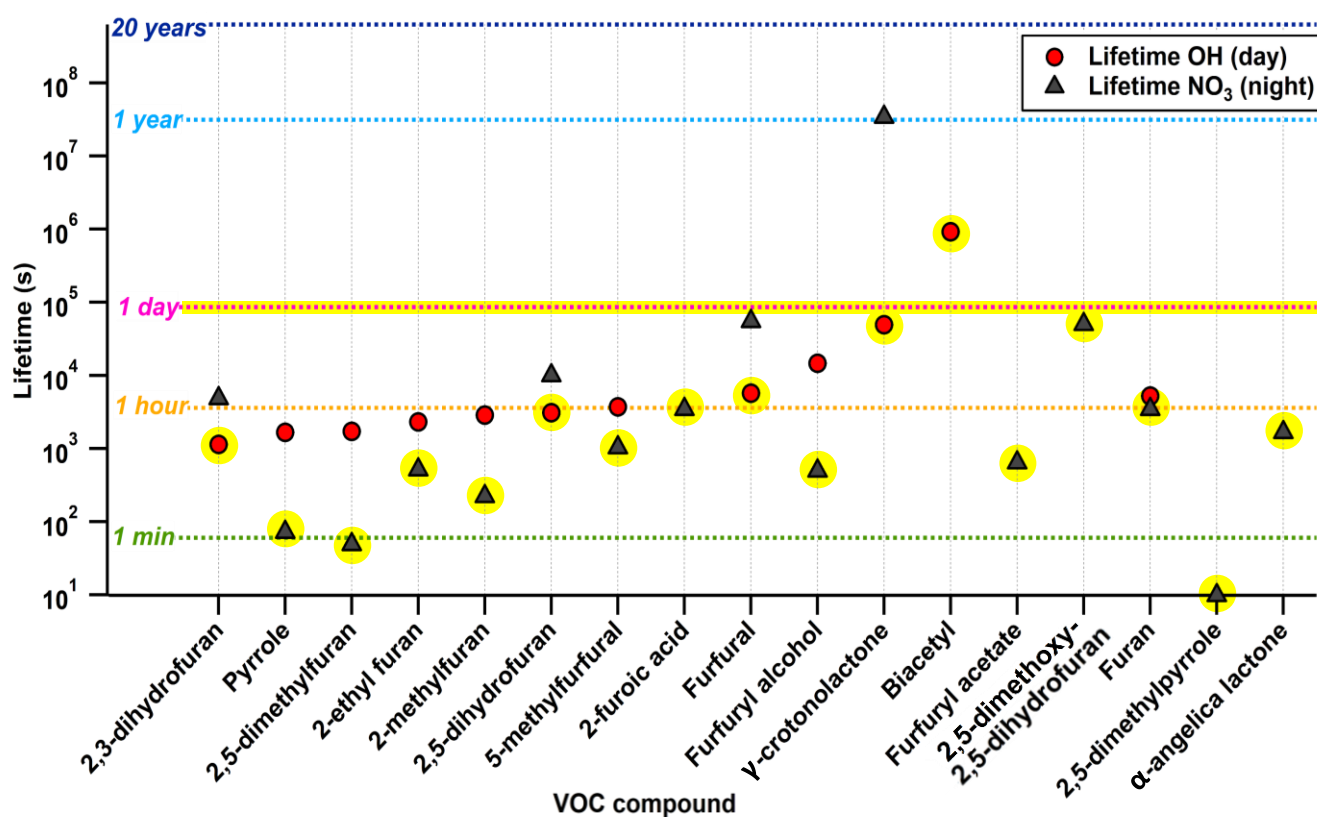
Figure III-44 : Atmospheric gas-phase lifetimes of the 17 BBVOCs reported in this study, including 14 furans, 2 pyrroles and biacetyl, assuming midday OH concentrations of 5×10^6 molecule cm^{-3}, and nighttime NO_3 concentrations of 2×10^8 molecule cm^{-3} The primary removal for each VOC (night and day) are highlighted in yellow for the furans, showing that all of them have short tropospheric lifetimes and are degraded within a day.

The concentrations of oxidants have a large spatial and temporal variability, dependent on the different sources and sinks, and the level of oxidant in biomass burning plumes is especially not well understood.

These values are thus an indication within the uncertainties on the oxidant concentrations and other factors and should be evaluated under specific conditions prior being used.

The studied furans are primarily removed during the day by reaction with OH and during nighttime by reaction with NO_3 (Figure III-44). Most of the BBVOCs under study will be removed from the troposphere within a day, by reaction with OH or NO_3, except for biacetyl. It is also possible that the reaction of O_3 which is thought to be insignificant for most furans but has been found to be an important removal for the loss of 2,5-dimethylfuran (Matsumoto, 2011). In an optically dark plume, the importance of NO_3 chemistry can in fact exceed that of OH, which requires daylight for the photochemical production of OH radicals. The reaction of biacetyl with OH is slow and result in a lifetime of ~11 days. It is likely that photolysis represents the primary removal of this di-ketone (Klotz et al., 2001).

Due to their short tropospheric lifetimes, these furans are not expected to survive for long periods in the plume. It is thus crucial to know the products that will be formed from their degradation initiated by OH and NO_3, and measure their lifetimes in order to assess their impact on atmospheric chemistry. There is a need for more field measurements of the concentration of oxidants in the biomass burning plumes, in order to better understand the chemistry related to wildfires.

Oxidation of furans by NO_3 is also of considerable importance for emissions resulting from domestic wood heating, a practice that is increasing in northern European cities (Chafe et al., 2015). This process is particularly important during the winter season, when daylight hours are shorter and water vapor abundance is lower, thus, diurnal peak of OH radicals in winter is generally an order of magnitude lower than that observed during the summer season, making NO_3 chemistry the dominant gas-phase oxidation process during this period.

III-3.2. <u>Atmospheric impact of the products of the OH and NO_3 initiated degradations</u>

As discussed in the previous section, the lifetimes of most furans and related BBVOCs under study is less than a day, which suggests that it is important to focus on the products they will form and their impact on atmospheric chemistry. From the OH and NO_3 degradation mechanisms described in the literature, products have been identified and their impacts are reported below. The mechanism of the reaction of furans and derivatives has been investigated in the literature in the presence and absence of NO_x as detailed in Appendices section App-III-6.1 with OH and App-III-6.2 with NO_3. The following discussion is based on the literature work on the degradation of furans initiated by OH (Aschmann et al., 2014; Bierbach et al., 1995; Davis et al., 2013; Gómez Alvarez et al., 2009; Hoang, 2021; Jiang et al., 2020; Tapia et al., 2011; Yuan et al., 2017) and NO_3 (Atkinson et al., 1985; Berndt et al., 1997; Bierbach et al., 1994; Colmenar et al., 2012; Huang et al., 2019; Joo et al., 2019; Tapia et al., 2011).

The initiation step by reaction with an oxidant (OH, NO_3, O_3 or Cl), is rapid as observed in the previous section. As summarized in the schematic Figure III-45, the main product of the mechanism of oxidation of furans are unsaturated 1,4-dicarbonyls, e.g., butenedial, resulting from the ring opening of the parent compound. These compounds will possess various functionalities depending on the oxidant initiating their degradation and the substitution of the parent furan compound (see R_1 and R_2 on Figure III-45). These 1,4-dicarbonyls may further be degraded into maleic anhydride, 3H-furan-2-one, and glyoxal (Bierbach et al., 1995). Other pathways retaining the ring of furan may occur, but they are usually minor compared to the ring opening products (see details in Appendices section App-III-6).

The yields of the products are dependent on (1) the presence of NO_x, which enhances the pathway that retains the ring rather than the ring cleavage that forms unsaturated dicarbonyls, (2) on the number of methyl substitution groups, as (Aschmann et al., 2014) observed that the yield of the 1,4-dicarbonyl products formed decreases with increasing number of methyl group substituents attached to the furan, and (3) on the position of the substituents, as the presence of an alkyl group attached to a carbon can hinder the OH addition onto this carbon and thus the yield of the associated product of this channel.
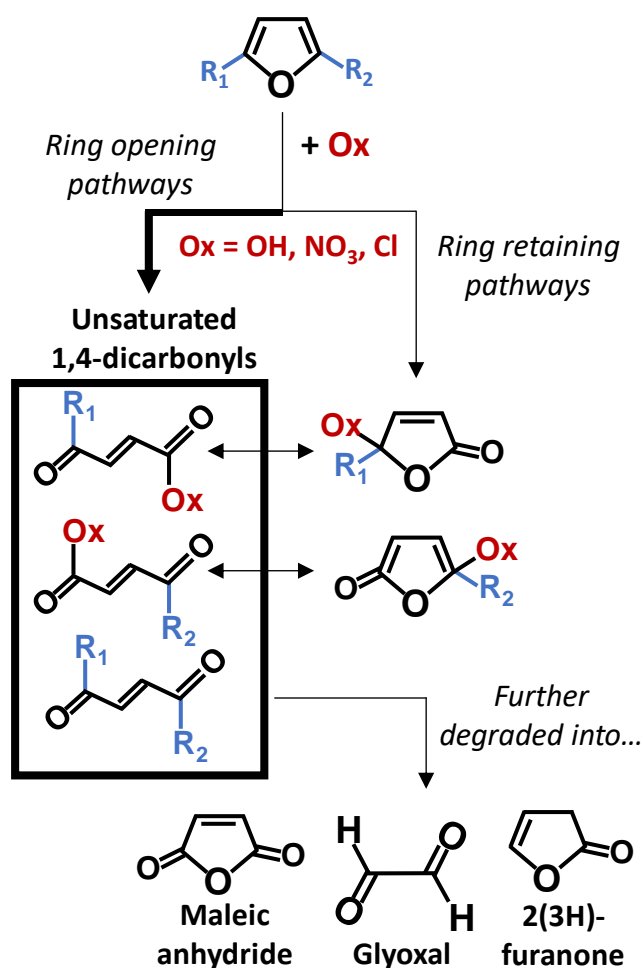
Figure III-45 : Schematic summarizing the products of the furan's degradation initiated by the reaction with an oxidant, such as OH, NO_3 or Cl, based on the literature studies provided in this section and in the Appendices section App-III-6. Ring opening are the

main pathways leading to formation unsaturated dicarbonyl that possess different functionalities depending on the oxidant or the parent compound. For example, NO$_3$ chemistry (Ox = NO$_3$) can lead to formation of organic nitrates. The unsaturated 1,4-dicarbonyls can be further degraded in various compounds that can further contribute to SOA formation.

Since furans react rapidly, within a day in most cases, and that their substitution affects the yield of the products formed and their functionalities, it is of crucial importance to describe the mechanism of the main removal of furans (OH and NO$_3$ reactions). Some work has been conducted on these compounds but there remain some unknowns. For example, the behavior of the 1,4-dicarbonyl in Figure III-45 if the R$_1$ substituent is an acid or a nitrate may be unclear. If R$_1$ is substituted with an oxygenated group, it is likely to decrease the vapor pressure of this product and increase its Henry's law constant, consequently favoring its partitioning into aerosols particles or in aqueous phase. This can be the focus of future work.

The products of the furan's oxidation are thought to contribute to SOA formation (e.g., 1,4-dicarbonyls, furanones (maleic anhydride, 2(3H)-furanone), glyoxal) (Carlton et al., 2007; Gómez Alvarez et al., 2009; Joo et al., 2019; Kodros et al., 2020; Strollo et al., 2013). For example, MA can be easily hydrolyzed and form maleic acid which can represent as source of SOA (Bunton et al., 1963; Lyman et al., 1990). Acylperoxy nitrates (Alvarado et al., 2010) and particle-phase organic nitrates (Boyd et al., 2015; Nah et al., 2016; Ng et al., 2017) formed during NO$_3$ + furans Ox = NO$_3$ in Figure III-45) is a NO$_x$ reservoir, which impacts O$_3$ formation (Alvarado et al., 2010; Joo et al., 2019). Maleic anhydride and 3H-furan-2-one are also toxic air pollutants (Grosjean, 1990a, 1990b). Maleic anhydride is also considered as a biomass burning tracer since it has been measured several times as a secondary organic gas formed in aging plumes (Bruns et al., 2017; Coggon et al., 2019; Hartikainen et al., 2018; Müller et al., 2016).

III-4.   Conclusions

In this chapter, new measurements focusing on biomass burning emissions have been carried out. Rate coefficients values are recommended for reaction of seven furan-type VOCs with NO$_3$ at 298 K and 760 Torr, based on a series of relative rate experiments. These new recommendations highlight the importance of NO$_3$ chemistry to the removal of furans and other similar VOCs under atmospheric conditions. The measured rate coefficients suggest that the reaction with NO$_3$ is the dominant nighttime sink for all of these furans, and reaction with OH is their primary removal process during the day, except for biacetyl. This work also extends the existing database of VOC + NO$_3$ reactions, providing reference values for future work.

New rate coefficient measurements were made for the reaction of 16 furan-type VOCs with NO$_3$ and 4 furans with OH under atmospheric conditions at 298 K and 760 Torr. These data are based on a comprehensive set of relative-rate experiments, shedding light on the critical role of NO$_3$ chemistry in the elimination of furans and similar VOCs from the atmosphere. The measured rate coefficients reveal that

for most furans studied in this research, as well as pyrrole and α-angelicalactone, the primary nighttime removal process is likely to be the reaction with NO_3. This emphasizes the significance of NO_3 as a crucial sink for furans in the atmosphere.

Concerning biacetyl, it has been found to be more challenging to measure its rate coefficient using different techniques, due to the contribution of photolysis at many wavelengths, many of which are experimentally used for producing the OH radicals. The DF/MS set-up appeared to be the most accurate and allows to determine the temperature-dependent rate coefficients of biacetyl + OH with good accuracy; however, these measurements are restricted to low pressures. Past experiments by Dagaut et al. (1988) agree with new measurements conducted using relative-rate method in LARKIN as a function of temperature. However, there are some differences in the determination of DF/MS and the literature data reported by Dagaut et al. (1988), Darnall et al. (1979), the CSA values and the LARKIN measurements at room temperature. The determinations of OH + biacetyl room temperature rate coefficient is still uncertain by a factor of 2. This could be due to the contribution of photolysis, and a potential effect of bath gas (e.g., O_2 which could impact the chemistry but is required to produce OH radicals in this set-up) in all the experiments but DF/MS. This could also be due to a pressure dependence of the reaction. Additionally, the PLP–LIF technique using H_2O_2 radical precursor as a source of OH was not adequate since it photolyzed biacetyl at 248 nm. Thus, this highlights the complexity of some reactions, and how challenging measurements can be in some set-ups.

This work contributes to the expansion of the existing database of BBVOCs reactions with OH and NO_3 providing essential reference values for future investigations in this field. The newly recommended rate coefficients offer insights into the fate of furans and related VOCs in the atmosphere, helping to better understand and model their behavior under various environmental conditions.

It has been shown that the lifetimes of the furans studied are short (<1day). These compounds will not significantly impact the chemistry of the troposphere. Hence, it is necessary to investigate the product formation from the OH- and NO_3-intitiated oxidation of furan derivatives, especially furfurals, and dihydrofurans. It is necessary to better quantify the yields of each product formed in order to better evaluate the contribution of furans to O_3 pollution and SOA formation. This could help the atmospheric chemical models to improve the representation of biomass burning chemistry and impact on air quality.

Despite the availability of various techniques, the study of emissions from biomass combustion remains a challenging task. These complexities necessitate the exploration of alternative approaches to gain a comprehensive understanding of the different types of emissions and their reactions. This work has highlighted the difficulties associated with experimental measurements of certain slow reactions, despite the availability of different experimental set-ups. This shows where estimation techniques can be useful as

complementary tool to estimate the kinetics when data are not yet available. Interestingly, the SAR approach described in Chapter II could be extended to other oxidants. However, it could not be applied to many VOCs emitted by biomass combustion and other natural sources without extensive workload, even though this can be the focus of further work. By considering a wider range of compounds and types of substitution, the predictive capabilities of existing SARs could be extended to give a more complete picture of biomass combustion emissions and their impact on the environment by being better described in atmospheric chemical models. This work underlines the need to study oxidation processes in addition to those by OH radicals, such as O_3, NO_3, etc. In addition, it reinforces the close relationship between substitution types and reactivity, as well as its complexity.

References

Adeniji, S.A., Kerr, J.A., Williams, M.R., 1981. Rate constants for ozone-alkene reactions under atmospheric conditions. Int. J. Chem. Kinet. 13, 209–217. https://doi.org/10.1002/kin.550130210

Akagi, S.K., Burling, I.R., Mendoza, A., Johnson, T.J., Cameron, M., Griffith, D.W.T., Paton-Walsh, C., Weise, D.R., Reardon, J., Yokelson, R.J., 2014. Field measurements of trace gases emitted by prescribed fires in southeastern US pine forests using an open-path FTIR system. Atmospheric Chemistry and Physics 14, 199–215. https://doi.org/10.5194/acp-14-199-2014

Akagi, S.K., Yokelson, R.J., Burling, I.R., Meinardi, S., Simpson, I., Blake, D.R., McMeeking, G.R., Sullivan, A., Lee, T., Kreidenweis, S., Urbanski, S., Reardon, J., Griffith, D.W.T., Johnson, T.J., Weise, D.R., 2013. Measurements of reactive trace gases and variable O_3 formation rates in some South Carolina biomass burning plumes. Atmospheric Chemistry and Physics 13, 1141–1165. https://doi.org/10.5194/acp-13-1141-2013

Akagi, S.K., Yokelson, R.J., Wiedinmyer, C., Alvarado, M.J., Reid, J.S., Karl, T., Crounse, J.D., Wennberg, P.O., 2011. Emission factors for open and domestic biomass burning for use in atmospheric models. Atmospheric Chemistry and Physics 11, 4039–4072.

Ali, E., Cramer, W., Carnicer, J., Georgopoulou, E., Hilmi, N.J.M., Cozannet, G.L., Lionello, P., 2022. Cross-Chapter Paper 4: Mediterranean Region. Climate Change 2022: Impacts, Adaptation and Vulnerability. Contribution of Working Group II to the Sixth Assessment Report of the Intergovernmental Panel on Climate Change. https://doi.org/10.1017/9781009325844.021.2233

Alvarado, A., Atkinson, R., Arey, J., 1996. Kinetics of the gas-phase reactions of NO3 radicals and O3 with 3-methylfuran and the OH radical yield from the O3 reaction. International journal of chemical kinetics 28, 905–909.

Alvarado, M.J., Logan, J.A., Mao, J., Apel, E., Riemer, D., Blake, D., Cohen, R.C., Min, K.-E., Perring, A.E., Browne, E.C., 2010. Nitrogen oxides and PAN in plumes from boreal fires during ARCTAS-B and their impact on ozone: an integrated analysis of aircraft and satellite observations. Atmospheric Chemistry and Physics 10, 9739–9760.

Alvarado, M.J., Lonsdale, C.R., Yokelson, R.J., Akagi, S.K., Coe, H., Craven, J.S., Fischer, E.V., McMeeking, G.R., Seinfeld, J.H., Soni, T., Taylor, J.W., Weise, D.R., Wold, C.E., 2015. Investigating the links between ozone and organic aerosol chemistry in a biomass burning plume from a prescribed fire in California chaparral. Atmospheric Chemistry and Physics 15, 6667–6688. https://doi.org/10.5194/acp-15-6667-2015

Alwe, H.D., Walavalkar, M.P., Sharma, A., Dhanya, S., Naik, P.D., 2014. Tropospheric oxidation of cyclic unsaturated ethers in the day-time: Comparison of the reactions with Cl, OH and O3 based on the determination of their rate coefficients at 298 K. Atmospheric Environment 82, 113–120.

Andersen, C., Nielsen, O.J., Østerstrøm, F.F., Ausmeel, S., Nilsson, E.J.K., Sulbaek Andersen, M.P., 2016. Atmospheric Chemistry of Tetrahydrofuran, 2-Methyltetrahydrofuran, and 2,5-

Dimethyltetrahydrofuran: Kinetics of Reactions with Chlorine Atoms, OD Radicals, and Ozone. J. Phys. Chem. A 120, 7320–7326. https://doi.org/10.1021/acs.jpca.6b06618

Andreae, M.O., 2019. Emission of trace gases and aerosols from biomass burning – an updated assessment. Atmospheric Chemistry and Physics 19, 8523–8546. https://doi.org/10.5194/acp-19-8523-2019

Andreae, M.O., Browell, E.V., Garstang, M., Gregory, G.L., Harriss, R.C., Hill, G.F., Jacob, D.J., Pereira, M.C., Sachse, G.W., Setzer, A.W., 1988. Biomass-burning emissions and associated haze layers over Amazonia. Journal of Geophysical Research: Atmospheres 93, 1509–1527.

Andreae, M.O., Merlet, P., 2001. Emission of trace gases and aerosols from biomass burning. Global Biogeochemical Cycles 15, 955–966. https://doi.org/10.1029/2000GB001382

Anglada, J.M., 2008. The Gas Phase HO-Initiated Oxidation of Furan: A Theoretical Investigation on the Reaction Mechanism. TOCPJ 1, 80–93. https://doi.org/10.2174/1874412500801010080

Arey, J., Obermeyer, G., Aschmann, S.M., Chattopadhyay, S., Cusick, R.D., Atkinson, R., 2009. Dicarbonyl Products of the OH Radical-Initiated Reaction of a Series of Aromatic Hydrocarbons. Environ. Sci. Technol. 43, 683–689. https://doi.org/10.1021/es8019098

Aschmann, S.M., Nishino, N., Arey, J., Atkinson, R., 2014. Products of the OH Radical-Initiated Reactions of Furan, 2-and 3-Methylfuran, and 2, 3-and 2, 5-Dimethylfuran in the Presence of NO. The Journal of Physical Chemistry A 118, 457–466.

Aschmann, S.M., Nishino, N., Arey, J., Atkinson, R., 2011. Kinetics of the Reactions of OH Radicals with 2- and 3-Methylfuran, 2,3- and 2,5-Dimethylfuran, and E- and Z-3-Hexene-2,5-dione, and Products of OH + 2,5-Dimethylfuran. Environ. Sci. Technol. 45, 1859–1865. https://doi.org/10.1021/es103207k

Atkinson, R., 1991. Kinetics and mechanisms of the gas-phase reactions of the NO3 radical with organic compounds. Journal of physical and chemical reference data 20, 459–507.

Atkinson, R., Arey, J., Tuazon, E.C., Aschmann, S.M., 1992. Gas-phase reactions of 1,4-benzodioxan, 2,3-dihydrobenzofuran, and 2,3-benzofuran with OH radicals and O3. Int. J. Chem. Kinet. 24, 345–358. https://doi.org/10.1002/kin.550240404

Atkinson, R., Aschmann, S.M., Carter, W.P.L., 1983. Kinetics of the reactions of O3 and OH radicals with furan and thiophene at 298 ± 2 K. International Journal of Chemical Kinetics 15, 51–61. https://doi.org/10.1002/kin.550150106

Atkinson, R., Aschmann, S.M., Tuazon, E.C., Arey, J., Zielinska, B., 1989. Formation of 3-methylfuran from the gas-phase reaction of OH radicals with isoprene and the rate constant for its reaction with the OH radical. International journal of chemical kinetics 21, 593–604.

Atkinson, R., Aschmann, S.M., Winer, A.M., Carter, W.P.L., 1985. Rate constants for the gas-phase reactions of nitrate radicals with furan, thiophene, and pyrrole at 295±1K and atmospheric pressure [WWW Document]. ACS Publications. https://doi.org/10.1021/es00131a010

Atkinson, R., Baulch, D.L., Cox, R.A., Crowley, J.N., Hampson, R.F., Hynes, R.G., Jenkin, M.E., Rossi, M.J., Troe, J., 2007. Evaluated kinetic and photochemical data for atmospheric chemistry: Volume III–gas phase reactions of inorganic halogens. Atmospheric Chemistry and Physics 7, 981–1191.

Atkinson, R., Carter, W.P., Winer, A.M., Pitts Jr, J.N., 1981. An experimental protocol for the determination of OH radical rate constants with organics using methyl nitrite photolysis as an OH radical source. Journal of the Air Pollution Control Association 31, 1090–1092.

Bedjanian, Y., 2019. Temperature-dependent rate constant for the reaction of hydroxyl radical with 3-hydroxy-3-methyl-2-butanone. The Journal of Physical Chemistry A 123, 10446–10453.

Bedjanian, Y., Le Bras, G., Poulet, G., 1999. Kinetic study of OH+ OH and OD+ OD reactions. The Journal of Physical Chemistry A 103, 7017–7025.

Bein, K.J., Zhao, Y., Johnston, M.V., Wexler, A.S., 2008. Interactions between boreal wildfire and urban emissions. Journal of Geophysical Research: Atmospheres 113. https://doi.org/10.1029/2007JD008910

Berndt, T., Böge, O., Rolle, W., 1997. Products of the gas-phase reactions of NO3 radicals with furan and tetramethylfuran. Environmental science & technology 31, 1157–1162.

Bierbach, A., Barnes, I., Becker, K.H., 1995. Product and kinetic study of the OH-initiated gas-phase oxidation of furan, 2-methylfuran and furanaldehydes at≈ 300 K. Atmospheric Environment 29, 2651–2660.

Bierbach, A., Barnes, I., Becker, K.H., 1992. Rate coefficients for the gas-phase reactions of hydroxyl radicals with furan, 2-methylfuran, 2-ethylfuran and 2, 5-dimethylfuran at 300\pm2 K. Atmospheric Environment. Part A. General Topics 26, 813–817.

Bierbach, A., Barnes, I., Becker, K.H., Wiesen, E., 1994. Atmospheric Chemistry of Unsaturated Carbonyls: Butenedial, 4-Oxo-2-pentenal, 3-Hexene-2,5-dione, Maleic Anhydride, 3H-Furan-2-one, and 5-Methyl-3H-furan-2-one. ACS Publications. https://doi.org/10.1021/es00053a028

Boyd, C.M., Sanchez, J., Xu, L., Eugene, A.J., Nah, T., Tuet, W.Y., Guzman, M.I., Ng, N.L., 2015. Secondary organic aerosol formation from the β-pinene+ NO 3 system: effect of humidity and peroxy radical fate. Atmospheric Chemistry and Physics 15, 7497–7522.

Brown, S.S., Stutz, J., 2012. Nighttime radical observations and chemistry. Chemical Society Reviews 41, 6405–6447.

Brown, S.S., Talukdar, R.K., Ravishankara, A.R., 1999. Reconsideration of the Rate Constant for the Reaction of Hydroxyl Radicals with Nitric Acid. J. Phys. Chem. A 103, 3031–3037. https://doi.org/10.1021/jp984721k

Bruns, E.A., Slowik, J.G., El Haddad, I., Kilic, D., Klein, F., Dommen, J., Temime-Roussel, B., Marchand, N., Baltensperger, U., Prévôt, A.S., 2017. Characterization of gas-phase organics using proton transfer reaction time-of-flight mass spectrometry: fresh and aged residential wood combustion emissions. Atmospheric Chemistry and Physics 17, 705–720.

Bunton, C.A., Fuller, N.A., Perry, S.G., Shiner, V.J., 1963. 542. The hydrolysis of carboxylic anhydrides. Part III. Reactions in initially neutral solution. Journal of the Chemical Society (Resumed) 2918–2926.

Cabañas, B., Baeza, M.T., Salgado, S., Martín, P., Taccone, R., Martínez, E., 2004. Oxidation of heterocycles in the atmosphere: Kinetic study of their reactions with NO3 radical. The Journal of Physical Chemistry A 108, 10818–10823.

Cabanas, B., Villanueva, F., Martin, P., Baeza, M., Salgado, S., Jimenez, E., 2005. Study of reaction processes of furan and some furan derivatives initiated by Cl atoms. Atmospheric Environment 39, 1935–1944. https://doi.org/10.1016/j.atmosenv.2004.12.013

Calogirou, A., Larsen, B.R., Kotzias, D., 1999. Gas-phase terpene oxidation products: a review. Atmospheric Environment 33, 1423–1439.

Calvert, J.G., Atkinson, R., Becker, K.H., Kamens, R.M., Seinfeld, J.H., Wallington, T.H., Yarwood, G., 2002. The mechanisms of atmospheric oxidation of the aromatic hydrocarbons.

Carlton, A.G., Turpin, B.J., Altieri, K.E., Seitzinger, S., Reff, A., Lim, H.-J., Ervens, B., 2007. Atmospheric oxalic acid and SOA production from glyoxal: Results of aqueous photooxidation experiments. Atmospheric Environment 41, 7588–7602.

Chafe, Z., Brauer, M., Héroux, M.-E., Klimont, Z., Lanki, T., Salonen, R.O., Smith, K.R., 2015. Residential heating with wood and coal: health impacts and policy options in Europe and North America.

Cheremisinoff, N.P., 2003. Industrial Solvents Handbook, Revised And Expanded. CRC Press.

Christensen, L.K., Sehested, J., Nielsen, O.J., Wallington, T.J., Guschin, A., Hurley, M.D., 1998. Kinetics and Mechanism of the Reactions of 2,3-Butadione with F and Cl Atoms, UV Absorption Spectra of CH 3 C(O)C(O)CH 2 · and CH 3 C(O)C(O)CH 2 O 2 · Radicals, and Atmospheric Fate of CH 3 C(O)C(O)CH 2 O· Radicals. J. Phys. Chem. A 102, 8913–8923. https://doi.org/10.1021/jp982431y

Ciccioli, P., Brancaleoni, E., Frattoni, M., Cecinato, A., Pinciarelli, L., 2001. Determination of volatile organic compounds (VOC) emitted from biomass burning of mediterranean vegetation species by GC-MS. Analytical Letters 34, 937–955. https://doi.org/10.1081/AL-100103604

Coggon, M.M., Lim, C.Y., Koss, A.R., Sekimoto, K., Yuan, B., Gilman, J.B., Hagan, D.H., Selimovic, V., Zarzana, K.J., Brown, S.S., 2019. OH chemistry of non-methane organic gases (NMOGs) emitted from laboratory and ambient biomass burning smoke: evaluating the influence of furans and oxygenated aromatics on ozone and secondary NMOG formation. Atmospheric Chemistry and Physics 19, 14875–14899.

Collard, F.-X., Blin, J., 2014. A review on pyrolysis of biomass constituents: Mechanisms and composition of the products obtained from the conversion of cellulose, hemicelluloses and lignin. Renewable and Sustainable Energy Reviews 38, 594–608. https://doi.org/10.1016/j.rser.2014.06.013

Colmenar, I., Cabañas, B., Martínez, E., Salgado, M.S., Martín, P., 2012. Atmospheric fate of a series of furanaldehydes by their NO3 reactions. Atmospheric Environment 54, 177–184. https://doi.org/10.1016/j.atmosenv.2012.02.087

Cox, R.A., 1975. Photolysis of gaseous nitrous acid: a technique for obtaining kinetic data on atmospheric photooxidation reactions. Int. J. Chem. Kinet.;(United States) 7.

Dagaut, P., Wallington, T.J., Liu, R., Kurylo, M.J., 1988. A kinetic investigation of the gas-phase reactions of hydroxyl radicals with cyclic ketones and diones: mechanistic insights. The Journal of Physical Chemistry 92, 4375–4377.

Darnall, K.R., Atkinson, R., Pitts, J.N., 1979. Observation of biacetyl from the reaction of OH radicals with o-xylene. Evidence for ring cleavage. Journal of Physical Chemistry 83, 1943–1946.

Davis, A.C., Sarathy, S.M., 2013. Computational Study of the Combustion and Atmospheric Decomposition of 2-Methylfuran. J. Phys. Chem. A 117, 7670–7685. https://doi.org/10.1021/jp403085u

Decker, Z.C.J., Robinson, M.A., Barsanti, K.C., Bourgeois, I., Coggon, M.M., DiGangi, J.P., Diskin, G.S., Flocke, F.M., Franchin, A., Fredrickson, C.D., Gkatzelis, G.I., Hall, S.R., Halliday, H., Holmes, C.D., Huey, L.G., Lee, Y.R., Lindaas, J., Middlebrook, A.M., Montzka, D.D., Moore, R., Neuman, J.A., Nowak, J.B., Palm, B.B., Peischl, J., Piel, F., Rickly, P.S., Rollins, A.W., Ryerson, T.B., Schwantes, R.H., Sekimoto, K., Thornhill, L., Thornton, J.A., Tyndall, G.S., Ullmann, K., Van Rooy, P., Veres, P.R., Warneke, C., Washenfelder, R.A., Weinheimer, A.J., Wiggins, E., Winstead, E., Wisthaler, A., Womack, C., Brown, S.S., 2021. Nighttime and daytime dark oxidation chemistry in wildfire plumes: an observation and model analysis of FIREX-AQ aircraft data. Atmospheric Chemistry and Physics 21, 16293–16317. https://doi.org/10.5194/acp-21-16293-2021

Eble, J., Bänsch, C., Olzmann, M., 2015. Kinetic Investigation of the Reactions of 2, 5-Dimethylfuran and 2-Methylfuran with Hydroxyl Radicals, in: Proceedings of the European Combustion Meeting, Budapest, Hungary.

El Othmani, H., Ren, Y., Bedjanian, Y., El Hajjaji, S., Tovar, C., Wiesen, P., Mellouki, A., McGillen, M.R., Daële, V., 2021. Gas-Phase Rate Coefficient of OH+ 1, 2-Epoxybutane Determined between 220 and 950 K. ACS Earth and Space Chemistry 5, 960–968.

Elwardany, A., Es-Sebbar, E., Khaled, F., Farooq, A., 2016. A chemical kinetic study of the reaction of hydroxyl with furans. Fuel 166, 245–252.

Forster, P., Ramaswamy, V., Artaxo, P., Berntsen, T., Betts, R., Fahey, D.W., Haywood, J., Lean, J., Lowe, D.C., Myhre, G., 2007. Changes in atmospheric constituents and in radiative forcing. Climate Change 2007: The Physical Science Basis. Contribution of Working Group I to the 4th Assessment Report of the Intergovernmental Panel on Climate Change.

Gilman, J.B., Lerner, B.M., Kuster, W.C., Goldan, P.D., Warneke, C., Veres, P.R., Roberts, J.M., de Gouw, J.A., Burling, I.R., Yokelson, R.J., 2015. Biomass burning emissions and potential air quality impacts of volatile organic compounds and other trace gases from fuels common in the US. Atmospheric Chemistry and Physics 15, 13915–13938. https://doi.org/10.5194/acp-15-13915-2015

Gkatzelis, G.I., Coggon, M.M., Stockwell, C.E., Hornbrook, R.S., Allen, H., Apel, E.C., Ball, K., Bela, M.M., Blake, D.R., Bourgeois, I., Brown, S.S., Campuzano-Jost, P., St. Clair, J.M., Crawford, J.H., Crounse, J.D., Day, D.A., DiGangi, J., Diskin, G., Fried, A., Gilman, J., Guo, H., Hair, J.W., Halliday, H.A., Hanisco, T.F., Hannun, R., Hills, A., Huey, G., Jimenez, J.L., Katich, J.M., Lamplugh, A., Lee, Y.R., Liao, J., Lindaas, J., McKeen, S.A., Mikoviny, T., Nault, B.A., Neuman, J.A., Nowak, J.B., Pagonis, D., Peischl, J., Perring, A.E., Piel, F., Rickly, P.S., Robinson, M.A., Rollins, A.W., Ryerson, T.B., Schueneman, M.K., Schwantes, R.H., Schwarz, J.P., Sekimoto, K., Selimovic, V., Shingler, T., Tanner, D.J., Tomsche, L., Vasquez, K., Veres, P.R., Washenfelder, R., Weibring, P., Wennberg, P.O., Wisthaler, A., Wolfe, G., Womack, C., Xu, L., Yokelson, R., Warneke, C., 2023. Parameterizations of US wildfire and prescribed fire emission ratios and emission factors based

on FIREX-AQ aircraft measurements (preprint). Gases/Field Measurements/Troposphere/ Chemistry (chemical composition and reactions). https://doi.org/10.5194/egusphere-2023-1439

Gómez Alvarez, E., Borrás, E., Viidanoja, J., Hjorth, J., 2009. Unsaturated dicarbonyl products from the OH-initiated photo-oxidation of furan, 2-methylfuran and 3-methylfuran. Atmospheric Environment 43, 1603–1612. https://doi.org/10.1016/j.atmosenv.2008.12.019

Greenberg, J.P., Friedli, H., Guenther, A.B., Hanson, D., Harley, P., Karl, T., 2006. Volatile organic emissions from the distillation and pyrolysis of vegetation. Atmospheric Chemistry and Physics 6, 81–91.

Greenberg, J.P., Zimmerman, P.R., Heidt, L., Pollock, W., 1984. Hydrocarbon and carbon monoxide emissions from biomass burning in Brazil. J. Geophys. Res. 89, 1350–1354. https://doi.org/10.1029/JD089iD01p01350

Grosjean, D., 1990a. Atmospheric Chemistry of Toxic Contaminants 1. Reaction Rates and Atmospheric Persistence. Journal of the Air & Waste Management Association 40, 1397–140. https://doi.org/10.1080/10473289.1990.10466792

Grosjean, D., 1990b. Atmospheric chemistry of toxic contaminants. 3. Unsaturated aliphatics: acrolein, acrylonitrile, maleic anhydride. Journal of the Air & Waste Management Association 40, 1664–1669.

Guenther, A., Hewitt, C.N., Erickson, D., Fall, R., Geron, C., Graedel, T., Harley, P., Klinger, L., Lerdau, M., McKay, W.A., 1995. A global model of natural volatile organic compound emissions. Journal of Geophysical Research: Atmospheres 100, 8873–8892.

Guenther, A., Karl, T., Harley, P., Wiedinmyer, C., Palmer, P.I., Geron, C., 2006. Estimates of global terrestrial isoprene emissions using MEGAN (Model of Emissions of Gases and Aerosols from Nature). Atmospheric Chemistry and Physics 6, 3181–3210.

Hartikainen, A., Yli-Pirilä, P., Tiitta, P., Leskinen, A., Kortelainen, M., Orasche, J., Schnelle-Kreis, J., Lehtinen, K.E.J., Zimmermann, R., Jokiniemi, J., Sippula, O., 2018. Volatile Organic Compounds from Logwood Combustion: Emissions and Transformation under Dark and Photochemical Aging Conditions in a Smog Chamber. Environ. Sci. Technol. 52, 4979–4988. https://doi.org/10.1021/acs.est.7b06269

Hatch, L.E., Luo, W., Pankow, J.F., Yokelson, R.J., Stockwell, C.E., Barsanti, K.C., 2015. Identification and quantification of gaseous organic compounds emitted from biomass burning using two-dimensional gas chromatography–time-of-flight mass spectrometry. Atmos. Chem. Phys. 15, 1865–1899. https://doi.org/10.5194/acp-15-1865-2015

Hatch, L.E., Yokelson, R.J., Stockwell, C.E., Veres, P.R., Simpson, I.J., Blake, D.R., Orlando, J.J., Barsanti, K.C., 2017. Multi-instrument comparison and compilation of non-methane organic gas emissions from biomass burning and implications for smoke-derived secondary organic aerosol precursors. Atmospheric Chemistry and Physics 17, 1471–1489.

Heintzenberg, J., 1989. Fine particles in the global troposphere A review. Tellus B 41B, 149–160. https://doi.org/10.1111/j.1600-0889.1989.tb00132.x

Hennigan, C.J., Miracolo, M.A., Engelhart, G.J., May, A.A., Presto, A.A., Lee, T., Sullivan, A.P., McMeeking, G.R., Coe, H., Wold, C.E., 2011. Chemical and physical transformations of organic aerosol from the photo-oxidation of open biomass burning emissions in an environmental chamber. Atmospheric Chemistry and Physics 11, 7669–7686.

Hoang, A.T., 2021. 2-Methylfuran (MF) as a potential biofuel: A thorough review on the production pathway from biomass, combustion progress, and application in engines. Renewable and Sustainable Energy Reviews 148, 111265.

Hobbs, P.V., Sinha, P., Yokelson, R.J., Christian, T.J., Blake, D.R., Gao, S., Kirchstetter, T.W., Novakov, T., Pilewskie, P., 2003. Evolution of gases and particles from a savanna fire in South Africa. Journal of Geophysical Research: Atmospheres 108. https://doi.org/10.1029/2002JD002352

Horowitz, A., Meller, R., Moortgat, G.K., 2001. The UV–VIS absorption cross sections of the α-dicarbonyl compounds: pyruvic acid, biacetyl and glyoxal. Journal of Photochemistry and Photobiology A: Chemistry 146, 19–27.

Huang, Z., Zhao, N., Ma, X., Xu, F., Zhang, Q., Zhuang, T., Wang, W., 2019. Theoretical study on the atmospheric oxidation reaction of 2-furanaldehyde initiated by NO3 radicals. Chemical Physics Letters 722, 50–57. https://doi.org/10.1016/j.cplett.2019.03.009

Illmann, N., Gibilisco, R.G., Bejan, I.G., Patroescu-Klotz, I., Wiesen, P., 2021. Atmospheric oxidation of α,β-unsaturated ketones: kinetics and mechanism of the OH radical reaction. Atmospheric Chemistry and Physics 21, 13667–13686. https://doi.org/10.5194/acp-21-13667-2021

IPCC, 2022. Climate Change 2022: Impacts, Adaptation and Vulnerability. Summary for Policymakers.

Jaffe, D.A., Wigder, N.L., 2012. Ozone production from wildfires: A critical review. Atmospheric Environment 51, 1–10.

Jenkin, M.E., Valorso, R., Aumont, B., Newland, M.J., Rickard, A.R., 2020. Estimation of rate coefficients for the reactions of O3 with unsaturated organic compounds for use in automated mechanism construction. Atmos. Chem. Phys. 20, 12921–12937. https://doi.org/10.5194/acp-20-12921-2020

Jiang, J., Carter, W.P.L., Cocker, D.R., Barsanti, K.C., 2020. Development and Evaluation of a Detailed Mechanism for Gas-Phase Atmospheric Reactions of Furans. ACS Earth Space Chem. 4, 1254–1268. https://doi.org/10.1021/acsearthspacechem.0c00058

Jiang, X., Tsona, N.T., Jia, L., Liu, S., Xu, Y., Du, L., 2018. Secondary organic aerosol formation from photooxidation of furan: effects of NOx level and humidity. Atmospheric Chemistry and Physics Discussions 1–27. https://doi.org/10.5194/acp-2018-477

Johnston, H.S., Graham, R., 1974. Photochemistry of NOx and HNOx Compounds. Can. J. Chem. 52, 1415–1423. https://doi.org/10.1139/v74-214

Joo, T., Rivera-Rios, J.C., Takeuchi, M., Alvarado, M.J., Ng, N.L., 2019. Secondary organic aerosol formation from reaction of 3-methylfuran with nitrate radicals. ACS Earth and Space Chemistry 3, 922–934.

Kaufman, F., 1984. Kinetics of elementary radical reactions in the gas phase. The Journal of Physical Chemistry 88, 4909–4917.

Kerdouci, J., Picquet-Varrault, B., Doussin, J.-F., 2014. Structure–activity relationship for the gas-phase reactions of NO3 radical with organic compounds: Update and extension to aldehydes. Atmospheric Environment 84, 363–372. https://doi.org/10.1016/j.atmosenv.2013.11.024

Kind, I., Berndt, T., Böge, O., Rolle, W., 1996. Gas-phase rate constants for the reaction of NO3 radicals with furan and methyl-substituted furans. Chemical Physics Letters 256, 679–683. https://doi.org/10.1016/0009-2614(96)00513-1

Klotz, B., Graedler, F., Sorensen, S., Barnes, I., Becker, K.-H., 2001. A kinetic study of the atmospheric photolysis of α-dicarbonyls. Int J Chem Kinet 33, 9–20. https://doi.org/10.1002/1097-4601(20010101)33:1<9::AID-KIN2>3.0.CO;2-V

Kodros, J.K., Papanastasiou, D.K., Paglione, M., Masiol, M., Squizzato, S., Florou, K., Skyllakou, K., Kaltsonoudis, C., Nenes, A., Pandis, S.N., 2020. Rapid dark aging of biomass burning as an overlooked source of oxidized organic aerosol. Proceedings of the National Academy of Sciences 117, 33028–33033.

Koss, A.R., Sekimoto, K., Gilman, J.B., Selimovic, V., Coggon, M.M., Zarzana, K.J., Yuan, B., Lerner, B.M., Brown, S.S., Jimenez, J.L., Krechmer, J., Roberts, J.M., Warneke, C., Yokelson, R.J., de Gouw, J., 2018. Non-methane organic gas emissions from biomass burning: identification, quantification, and emission factors from PTR-ToF during the FIREX 2016 laboratory experiment. Atmospheric Chemistry and Physics 18, 3299–3319. https://doi.org/10.5194/acp-18-3299-2018

Kwok, E.S.C., Atkinson, R., 1995. Estimation of hydroxyl radical reaction rate constants for gas-phase organic compounds using a structure-reactivity relationship: An update. Atmospheric Environment 29, 1685–1695.

Lancar, I.T., Daele, V., Le Bras, G., Poulet, G., 1991. Étude de la réactivité des radicaux NO3 avec le diméthyl-2, 3 butène-2, le butadiène-1, 3 et le diméthyl-2, 3 butadiène-1, 3. Journal de chimie physique 88, 1777–1792.

Lee, J.H., Tang, I.N., 1982. Absolute rate constants for the hydroxyl radical reactions with ethane, furan, and thiophene at room temperature. The Journal of Chemical Physics 77, 4459–4463. https://doi.org/10.1063/1.444367

Liljegren, J.A., Stevens, P.S., 2013. Measurements of the Kinetics of the Reaction of OH Radicals with 3-Methylfuran at Low Pressure. Int J of Chemical Kinetics 45, 787–794. https://doi.org/10.1002/kin.20814

Link, M.F., Farmer, D.K., Berg, T., Flocke, F., Ravishankara, A.R., 2021. Measuring Photodissociation Product Quantum Yields Using Chemical Ionization Mass Spectrometry: A Case Study with Ketones. J. Phys. Chem. A 125, 6836–6844. https://doi.org/10.1021/acs.jpca.1c03140

Lipari, Frank., Dasch, J.M., Scruggs, W.F., 1984. Aldehyde emissions from wood-burning fireplaces. Environ. Sci. Technol. 18, 326–330. https://doi.org/10.1021/es00123a007

Liu, D., Nyord, T., Rong, L., Feilberg, A., 2018. Real-time quantification of emissions of volatile organic compounds from land spreading of pig slurry measured by PTR-MS and wind tunnels. Science of The Total Environment 639, 1079–1087.

Liu, X., Huey, L.G., Yokelson, R.J., Selimovic, V., Simpson, I.J., Müller, M., Jimenez, J.L., Campuzano-Jost, P., Beyersdorf, A.J., Blake, D.R., Butterfield, Z., Choi, Y., Crounse, J.D., Day, D.A., Diskin, G.S., Dubey, M.K., Fortner, E., Hanisco, T.F., Hu, W., King, L.E., Kleinman, L., Meinardi, S., Mikoviny, T., Onasch, T.B., Palm, B.B., Peischl, J., Pollack, I.B., Ryerson, T.B., Sachse, G.W., Sedlacek, A.J., Shilling, J.E., Springston, S., St. Clair, J.M., Tanner, D.J., Teng, A.P., Wennberg, P.O., Wisthaler, A., Wolfe, G.M., 2017. Airborne measurements of western U.S. wildfire emissions: Comparison with prescribed burning and air quality implications. Journal of Geophysical Research: Atmospheres 122, 6108–6129. https://doi.org/10.1002/2016JD026315

Liu, X., Zhang, Y., Huey, L.G., Yokelson, R.J., Wang, Y., Jimenez, J.L., Campuzano-Jost, P., Beyersdorf, A.J., Blake, D.R., Choi, Y., St. Clair, J.M., Crounse, J.D., Day, D.A., Diskin, G.S., Fried, A., Hall, S.R., Hanisco, T.F., King, L.E., Meinardi, S., Mikoviny, T., Palm, B.B., Peischl, J., Perring, A.E., Pollack, I.B., Ryerson, T.B., Sachse, G., Schwarz, J.P., Simpson, I.J., Tanner, D.J., Thornhill, K.L., Ullmann, K., Weber, R.J., Wennberg, P.O., Wisthaler, A., Wolfe, G.M., Ziemba, L.D., 2016. Agricultural fires in the southeastern U.S. during SEAC4RS: Emissions of trace gases and particles and evolution of ozone, reactive nitrogen, and organic aerosol. Journal of Geophysical Research: Atmospheres 121, 7383–7414. https://doi.org/10.1002/2016JD025040

Lu, Q., Yang, X., Dong, C., Zhang, Z., Zhang, X., Zhu, X., 2011. Influence of pyrolysis temperature and time on the cellulose fast pyrolysis products: Analytical Py-GC/MS study. Journal of Analytical and Applied Pyrolysis 92, 430–438. https://doi.org/10.1016/j.jaap.2011.08.006

Lyman, W.J., Reehl, W.F., Rosenblatt, D.H., 1990. Handbook of chemical property estimation methods.

Mason, S.A., Field, R.J., Yokelson, R.J., Kochivar, M.A., Tinsley, M.R., Ward, D.E., Hao, W.M., 2001. Complex effects arising in smoke plume simulations due to inclusion of direct emissions of oxygenated organic species from biomass combustion. Journal of Geophysical Research: Atmospheres 106, 12527–12539. https://doi.org/10.1029/2001JD900003

Matsumoto, J., 2011. Kinetics of the Reactions of Ozone with 2,5-Dimethylfuran and Its Atmospheric Implications. Chem. Lett. 40, 582–583. https://doi.org/10.1246/cl.2011.582

Mauzerall, D.L., Logan, J.A., Jacob, D.J., Anderson, B.E., Blake, D.R., Bradshaw, J.D., Heikes, B., Sachse, G.W., Singh, H., Talbot, B., 1998. Photochemistry in biomass burning plumes and implications for tropospheric ozone over the tropical South Atlantic. J. Geophys. Res. 103, 8401–8423. https://doi.org/10.1029/97JD02612

McGillen, M.R., Archibald, A.T., Carey, T., Leather, K.E., Shallcross, D.E., Wenger, J.C., Percival, C.J., 2011. Structure–activity relationship (SAR) for the prediction of gas-phase ozonolysis rate coefficients: an extension towards heteroatomic unsaturated species. Phys. Chem. Chem. Phys. 13, 2842–2849. https://doi.org/10.1039/C0CP01732A

McGillen, M.R., Carter, W.P.L., Mellouki, A., Orlando, J.J., Picquet-Varrault, B., Wallington, T.J., 2020. Database for the kinetics of the gas-phase atmospheric reactions of organic compounds. Earth System Science Data 12, 1203–1216. https://doi.org/10.5194/essd-12-1203-2020

Morin, J., Romanias, M.N., Bedjanian, Y., 2015. Experimental study of the reactions of OH radicals with propane, n-pentane, and n-heptane over a wide temperature range. International Journal of Chemical Kinetics 47, 629–637.

Morris, G.A., Hersey, S., Thompson, A.M., Pawson, S., Nielsen, J.E., Colarco, P.R., McMillan, W.W., Stohl, A., Turquety, S., Warner, J., Johnson, B.J., Kucsera, T.L., Larko, D.E., Oltmans, S.J., Witte, J.C., 2006. Alaskan and Canadian forest fires exacerbate ozone pollution over Houston, Texas, on 19 and 20 July 2004. Journal of Geophysical Research: Atmospheres 111. https://doi.org/10.1029/2006JD007090

Mouat, A.P., Paton-Walsh, C., Simmons, J.B., Ramirez-Gamboa, J., Griffith, D.W., Kaiser, J., 2021. Emission factors of long-lived volatile organic compounds from the 2019–2020 Australian wildfires during the COALA campaign. Atmospheric chemistry and physics discussion.

Mouat, A.P., Paton-Walsh, C., Simmons, J.B., Ramirez-Gamboa, J., Griffith, D.W.T., Kaiser, J., 2022. Measurement report: Observations of long-lived volatile organic compounds from the 2019–2020 Australian wildfires during the COALA campaign. Atmospheric Chemistry and Physics 22, 11033–11047. https://doi.org/10.5194/acp-22-11033-2022

Müller, M., Anderson, B.E., Beyersdorf, A.J., Crawford, J.H., Diskin, G.S., Eichler, P., Fried, A., Keutsch, F.N., Mikoviny, T., Thornhill, K.L., Walega, J.G., Weinheimer, A.J., Yang, M., Yokelson, R.J., Wisthaler, A., 2016. In situ measurements and modeling of reactive trace gases in a small biomass burning plume. Atmospheric Chemistry and Physics 16, 3813–3824. https://doi.org/10.5194/acp-16-3813-2016

Nah, T., Sanchez, J., Boyd, C.M., Ng, N.L., 2016. Photochemical Aging of α-pinene and β-pinene Secondary Organic Aerosol formed from Nitrate Radical Oxidation. Environ. Sci. Technol. 50, 222–231. https://doi.org/10.1021/acs.est.5b04594

Newland, M.J., Ren, Y., McGillen, M.R., Michelat, L., Daële, V., Mellouki, A., 2022. NO 3 chemistry of wildfire emissions: A kinetic study of the gas-phase reactions of furans with the NO 3 radical. Atmospheric Chemistry and Physics 22, 1761–1772.

Ng, N.L., Brown, S.S., Archibald, A.T., Atlas, E., Cohen, R.C., Crowley, J.N., Day, D.A., Donahue, N.M., Fry, J.L., Fuchs, H., Griffin, R.J., Guzman, M.I., Herrmann, H., Hodzic, A., Iinuma, Y., Jimenez, J.L., Kiendler-Scharr, A., Lee, B.H., Luecken, D.J., Mao, J., McLaren, R., Mutzel, A., Osthoff, H.D., Ouyang, B., Picquet-Varrault, B., Platt, U., Pye, H.O.T., Rudich, Y., Schwantes, R.H., Shiraiwa, M., Stutz, J., Thornton, J.A., Tilgner, A., Williams, B.J., Zaveri, R.A., 2017. Nitrate radicals and biogenic volatile organic compounds: oxidation, mechanisms, and organic aerosol. Atmos Chem Phys 17, 2103–2162. https://doi.org/10.5194/acp-17-2103-2017

Obermeyer, G., Aschmann, S.M., Atkinson, R., Arey, J., 2009. Carbonyl atmospheric reaction products of aromatic hydrocarbons in ambient air. Atmospheric Environment 43, 3736–3744.

Oltmans, S.J., Lefohn, A.S., Harris, J.M., Tarasick, D.W., Thompson, A.M., Wernli, H., Johnson, B.J., Novelli, P.C., Montzka, S.A., Ray, J.D., 2010. Enhanced ozone over western North America from biomass burning in Eurasia during April 2008 as seen in surface and profile observations. Atmospheric Environment 44, 4497–4509.

Paine, J.B., Pithawalla, Y.B., Naworal, J.D., 2008. Carbohydrate pyrolysis mechanisms from isotopic labeling: Part 4. The pyrolysis of d-glucose: The formation of furans. Journal of Analytical and Applied Pyrolysis 83, 37–63. https://doi.org/10.1016/j.jaap.2008.05.008

Patwardhan, P.R., Satrio, J.A., Brown, R.C., Shanks, B.H., 2009. Product distribution from fast pyrolysis of glucose-based carbohydrates. Journal of Analytical and Applied Pyrolysis 86, 323–330. https://doi.org/10.1016/j.jaap.2009.08.007

Paulson, S.E., Flagan, R.C., Seinfeld, J.H., 1992. Atmospheric photooxidation of isoprene part I: The hydroxyl radical and ground state atomic oxygen reactions. International Journal of Chemical Kinetics 24, 79–101.

Pfister, G.G., Wiedinmyer, C., Emmons, L.K., 2008. Impacts of the fall 2007 California wildfires on surface ozone: Integrating local observations with global model simulations. Geophysical Research Letters 35. https://doi.org/10.1029/2008GL034747

Rajakumar, B., Flad, J.E., Gierczak, T., Ravishankara, A.R., Burkholder, J.B., 2007. Visible Absorption Spectrum of the CH 3 CO Radical. J. Phys. Chem. A 111, 8950–8958. https://doi.org/10.1021/jp073339h

Rajakumar, B., Gierczak, T., Flad, J.E., Ravishankara, A.R., Burkholder, J.B., 2008. The CH3CO quantum yield in the 248nm photolysis of acetone, methyl ethyl ketone, and biacetyl. Journal of Photochemistry and Photobiology A: Chemistry 199, 336–344. https://doi.org/10.1016/j.jphotochem.2008.06.015

Real, E., Law, K.S., Weinzierl, B., Fiebig, M., Petzold, A., Wild, O., Methven, J., Arnold, S., Stohl, A., Huntrieser, H., Roiger, A., Schlager, H., Stewart, D., Avery, M., Sachse, G., Browell, E., Ferrare, R., Blake, D., 2007. Processes influencing ozone levels in Alaskan forest fire plumes during long-range transport over the North Atlantic. Journal of Geophysical Research: Atmospheres 112. https://doi.org/10.1029/2006JD007576

Reid, J.S., Hobbs, P.V., Ferek, R.J., Blake, D.R., Martins, J.V., Dunlap, M.R., Liousse, C., 1998. Physical, chemical, and optical properties of regional hazes dominated by smoke in Brazil. J. Geophys. Res. 103, 32059–32080. https://doi.org/10.1029/98JD00458

Ren, Y., Grosselin, B., Daële, V., Mellouki, A., 2017. Investigation of the reaction of ozone with isoprene, methacrolein and methyl vinyl ketone using the HELIOS chamber. Faraday Discussions 200, 289–311.

Rogge, W.F., Hildemann, L.M., Mazurek, M.A., Cass, G.R., Simoneit, B.R.T., 1991. Sources of fine organic aerosol. 1. Charbroilers and meat cooking operations. Environ. Sci. Technol. 25, 1112–1125. https://doi.org/10.1021/es00018a015

Rosenfeld, D., 1999. TRMM observed first direct evidence of smoke from forest fires inhibiting rainfall. Geophys. Res. Lett. 26, 3105–3108. https://doi.org/10.1029/1999GL006066

Singh, H.B., Cai, C., Kaduwela, A., Weinheimer, A., Wisthaler, A., 2012. Interactions of fire emissions and urban pollution over California: Ozone formation and air quality simulations. Atmospheric Environment 56, 45–51.

Smith, I.W.M., Ravishankara, A.R., 2002. Role of Hydrogen-Bonded Intermediates in the Bimolecular Reactions of the Hydroxyl Radical. J. Phys. Chem. A 106, 4798–4807.

Somnitz, H., Fida, M., Ufer, T., Zellner, R., 2005. Pressure dependence for the CO quantum yield in the photolysis of acetone at 248 nm: A combined experimental and theoretical study. Physical Chemistry Chemical Physics 7, 3342–3352.

Somnitz, H., Ufer, T., Zellner, R., 2009. Acetone photolysis at 248 nm revisited: pressure dependence of the CO and CO 2 quantum yields. Physical Chemistry Chemical Physics 11, 8522–8531.

Stockwell, C.E., Veres, P.R., Williams, J., Yokelson, R.J., 2015. Characterization of biomass burning emissions from cooking fires, peat, crop residue, and other fuels with high-resolution proton-transfer-reaction time-of-flight mass spectrometry. Atmospheric Chemistry and Physics 15, 845–865.

Stone, D., Whalley, L.K., Heard, D.E., 2012. Tropospheric OH and HO 2 radicals: field measurements and model comparisons. Chemical Society Reviews 41, 6348–6404.

Strollo, C.M., Ziemann, P.J., 2013. Products and mechanism of secondary organic aerosol formation from the reaction of 3-methylfuran with OH radicals in the presence of NOx. Atmospheric Environment 77, 534–543.

Su, M.-C., Kumaran, S.S., Lim, K.P., Michael, J.V., Wagner, A.F., Harding, L.B., Fang, D.-C., 2002. Rate constants, 1100≤ T≤ 2000 K, for H+ NO2→ OH+ NO using two shock tube techniques: Comparison of theory to experiment. The Journal of Physical Chemistry A 106, 8261–8270.

Sudo, K., Akimoto, H., 2007. Global source attribution of tropospheric ozone: Long-range transport from various source regions. J. Geophys. Res. 112, D12302. https://doi.org/10.1029/2006JD007992

Talukdar, R.K., Gierczak, T., McCabe, D.C., Ravishankara, A.R., 2003. Reaction of Hydroxyl Radical with Acetone. 2. Products and Reaction Mechanism. J. Phys. Chem. A 107, 5021–5032.

Tapia, A., Villanueva, F., Salgado, M.S., Cabañas, B., Martínez, E., Martín, P., 2011. Atmospheric degradation of 3-methylfuran: kinetic and products study. Atmospheric Chemistry and Physics 11, 3227–3241.

Tuazon, E.C., Atkinson, R., 1990. A product study of the gas-phase reaction of Isoprene with the OH radical in the presence of NOx. Int. J. Chem. Kinet. 22, 1221–1236. https://doi.org/10.1002/kin.550221202

Tuazon, E.C., Atkinson, R., Winer, A.M., Pitts, J.N., 1984. A study of the atmospheric reactions of 1, 3-dichloropropene and other selected organochlorine compounds. Archives of Environmental Contamination and Toxicology 13, 691–700.

Turro, N.J., Engel, R., 1969. Quenching of biacetyl fluorescence and phosphorescence. Journal of the American Chemical Society 91, 7113–7121.

US EPA, O., 2015. EPI Suite^{TM}-Estimation Program Interface [WWW Document]. URL https://www.epa.gov/tsca-screening-tools/epi-suitetm-estimation-program-interface (accessed 7.6.22).

Villanueva, F., Barnes, I., Monedero, E., Salgado, S., Gómez, M.V., Martin, P., 2007. Primary product distribution from the Cl-atom initiated atmospheric degradation of furan: Environmental implications. Atmospheric Environment 41, 8796–8810.

Wayne, R.P., Barnes, I., Biggs, P., Burrows, J.P., Canosa-Mas, C.E., Hjorth, J., Bras, G.L., Moortgat, G.K., Perner, D., Poulet, G., Restelli, G., Sidebottom, H., 1991. The nitrate radical: Physics, chemistry, and the atmosphere. Atmospheric Environment. Part A. General Topics 25, 1–203. https://doi.org/10.1016/0960-1686(91)90192-A

Whelan, C.A., Eble, J., Mir, Z.S., Blitz, M.A., Seakins, P.W., Olzmann, M., Stone, D., 2020. Kinetics of the Reactions of Hydroxyl Radicals with Furan and Its Alkylated Derivatives 2-Methyl Furan and 2,5-Dimethyl Furan. J. Phys. Chem. A 124, 7416–7426. https://doi.org/10.1021/acs.jpca.0c06321

Wine, P.H., Thompson, R.J., 1984. Kinetics of OH reactions with furan, thiophene, and tetrahydrothiophene. International journal of chemical kinetics 16, 867–878.

Yokelson, R.J., Christian, T.J., Karl, T.G., Guenther, A., 2008. The tropical forest and fire emissions experiment: laboratory fire measurements and synthesis of campaign data. Atmospheric Chemistry and Physics 8, 3509–3527.

Yokelson, R.J., Crounse, J.D., DeCarlo, P.F., Karl, T., Urbanski, S., Atlas, E., Campos, T., Shinozuka, Y., Kapustin, V., Clarke, A.D., Weinheimer, A., Knapp, D.J., Montzka, D.D., Holloway, J., Weibring, P., Flocke, F., Zheng, W., Toohey, D., Wennberg, P.O., Wiedinmyer, C., Mauldin, L., Fried, A., Richter, D., Walega, J., Jimenez, J.L., Adachi, K., Buseck, P.R., Hall, S.R., Shetter, R., 2009. Emissions from biomass burning in the Yucatan. Atmospheric Chemistry and Physics 9, 5785–5812. https://doi.org/10.5194/acp-9-5785-2009

Yuan, Y., Zhao, X., Wang, S., Wang, L., 2017. Atmospheric Oxidation of Furan and Methyl-Substituted Furans Initiated by Hydroxyl Radicals. J. Phys. Chem. A 121, 9306–9319. https://doi.org/10.1021/acs.jpca.7b09741

Zhang, W., Du, B., Mu, L., Feng, C., 2008a. Computational study on the mechanism for the reaction of OH with 2-methylfuran. Journal of Molecular Structure: THEOCHEM 851, 353–357. https://doi.org/10.1016/j.theochem.2007.11.010

Zhang, W., Du, B., Mu, L., Feng, C., 2008b. Mechanism for the gas-phase reaction between OH and 3-methylfuran: A theoretical study. Int. J. Quantum Chem. 108, 1232–1238. https://doi.org/10.1002/qua.21617

Zhou, L., Ravishankara, A.R., Brown, S.S., Idir, M., Zarzana, K.J., Daële, V., Mellouki, A., 2017. Kinetics of the Reactions of NO3 Radical with Methacrylate Esters. J. Phys. Chem. A 121, 4464–4474. https://doi.org/10.1021/acs.jpca.7b02332

Appendices : Chapter III

App-III-1. Discharge-flow reactor
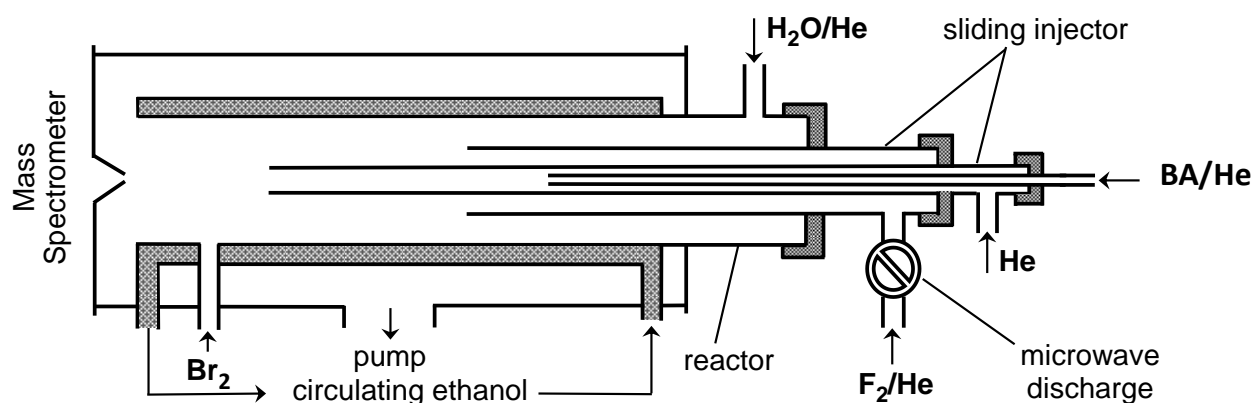
Figure App-III-1 : Diagram of the low temperature flow reactor: configuration used in the measurements of $k_{BA,DFMS}$ using reaction F+H_2O as a source of OH radicals.
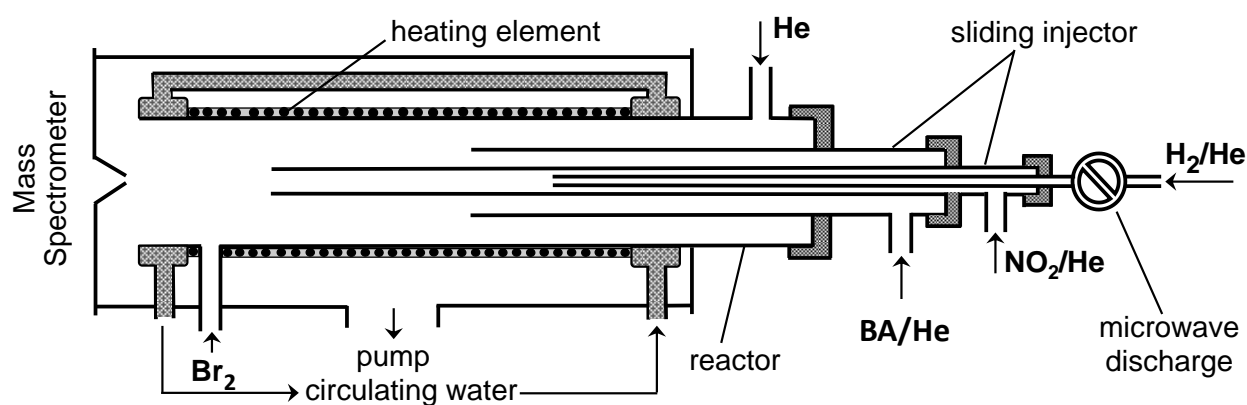
Figure App-III-2 : Diagram of the high temperature flow reactor: configuration used in the measurements of $k_{BA,DFMS}$ using H+NO_2 reaction as a source of OH radicals.
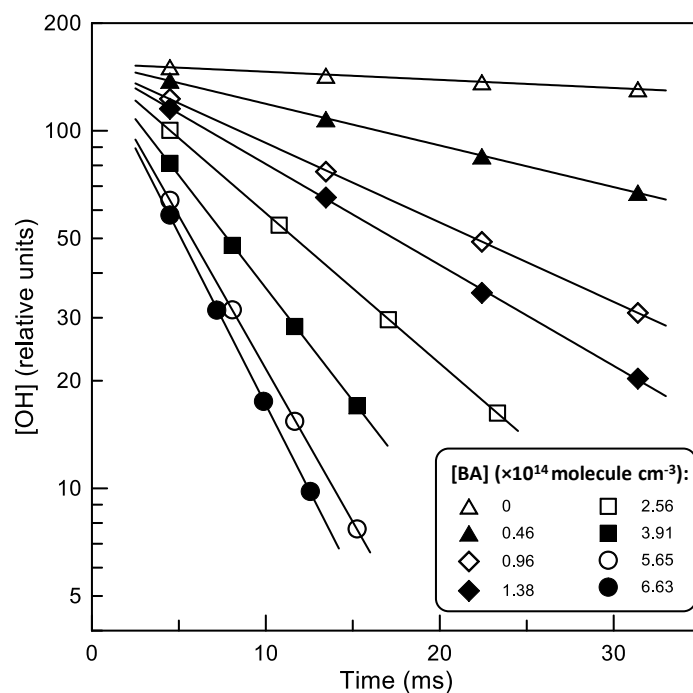
Figure App-III-3 : Examples of temporal profiles of OH radicals observed at T = 475 K using the DF/MS apparatus.

App-III-2. CSA relative rate measurements – biacetyl + OH

Table App-III-1 : Experimental conditions and rate coefficient determination for the OH reaction relative-rate measurements in the CSA for biacetyl with two references, acetone and methyl formate. Literature data from (Dagaut et al., 1988).

				Experimental conditions		Compounds concentrations		
Date	Technique	Reference	Product subtraction	P (Torr)	T (°C)	P_{SF6}[b]	[ref][c]	[BA][d]
26/04/2021		Acetone	-	760±10	21.8	1.114	4.814	4.652
27/04/2021		Acetone	-	760±10	22.5	0.96	4.478	4.814
29/04/2021		Methyl formate	-	760±10	21.9	1.13	4.26	6.61
29/04/2021		Methyl formate	Formic acid, AFA[g]	760±10	21.9	1.130	4.260	6.610
(Dagaut et al., 1988)	FP-RF[f]	-	-	25–50	298	-	-	(2–454)×10³ molecule cm⁻³
(Darnall et al., 1979)	FP-RF[f]	-	-	25–50[h]	298K			0.065 ppm

	Dilution/photolysis/additional losses			Reaction with OH			
Date	$k_{dilution,SF6}$[e]	$k_{d,ref}$[e] dark–photolysis	$k_{d,BA}$[e] dark–photolysis	k_{ref}[a]	k_{ref}[e]	k_{BA}[e]	k_{BA}[a]
26/04/2021	3.44×10⁻⁵	(1.87–2.21)	(1.09–2.34)	1.83	3.43	5.55	1.93
27/04/2021	5.13×10⁻⁵	(5.14–5.84)	(4.22–6.64)	1.83	3.92	4.09	2.49
29/04/2021	2.96×10⁻⁵	(1.67–1.71)	(1.55–2.63)	1.76	1.43	2.04	2.08
29/04/2021	2.96×10⁻⁵	(1.67–1.71)	(1.55–2.63)	1.76	2.34	1.28	1.84
(Dagaut et al., 1988)	-	-	-	-	-	-	2.3±0.2
(Darnall et al., 1979)	-	-	-	-	-	-	2.4±0.3

[a] Reaction rate coefficients are at room temperature, in ×10⁻¹³ cm³molecule⁻¹s⁻¹. [b] All pressures are in Torr. [c] [ref] refers to the concentration of the reference compound (see column Reference), in ppmv. [d] [BA] refers to the concentration of biacetyl in ppmv unless other specified. [e] $k_{dilution,SF6}$: dilution rate, $k_{d,ref}$ and $k_{d,BA}$ loss rates for the ref and BA, where dark is dilution under dark condition and photolysis with the illumination at 365nm; all rates are in ×10⁻⁵ s⁻¹. [f] FP-RF: Flash photolysis – resonance fluorescence. [g] AFA: Acetic formic anhydride [h] No value is provided in the original paper, but they refer to previous work where they describe the set-up and employ it at pressures between 25 to 50 Torr. Thus, this is a reasonable range for these experiments.

App-III-3. UV absorption cross-section

In order to characterize the UV-Vis absorption of biacetyl, attempts have been made to develop a set-up to measure the UV-Vis absorption spectrum. However, the results presented here are only preliminary since the spectrometer was not performing at its optimum and was sent to repair until this data. The measurements of the UV absorption of a biacetyl mixture (mixing ratio of 2.99% in He) at room temperature (T=298±5K) for 6–10 different pressures, with the associated concentrations ranging from 6.9×10¹⁵ to 2.58×10¹⁷ molecule cm⁻³, as illustrated in the Figure App-III-7.

The absorption cell is 1 m long, with quartz windows (transparent to UV) on each side, see Figure App-III-4. A pump and pressure gauges were attached to the cell in order to control the total pressure inside the cell. A deuterium lamp provided a uniform light within the cell for a spectrum within 180 to 900 nm, although the continuous part of its spectrum lies in the wavelength range of 190–370 nm. These results are preliminary, and thus, no efforts were made on changing the optical filter to avoid second-order absorption occurring at wavelength >400nm.

Light was collected by a spectrometer at the other end of the cell, optically aligned with the deuterium light beam. The spectrometer (300mm focal length) possesses 3 gratings: 1800 lines/mm, 1200 lines/mm, and 600 lines/mm allowing to browse the spectrum and measure over the 200–900 nm range, each being blazed at a specific wavelength of 500nm, 300nm and 500nm respectively. The spectrometer was employed using the software WINSPEC, and data were collected on a computer. Calibration lamps of Zn, Hg, and Cd were used to calibrate the spectrometer within the range 214–509nm, with the strong lines of Cd at 214.4, 508.5nm, and other lines within this range for all the three calibration lamps.
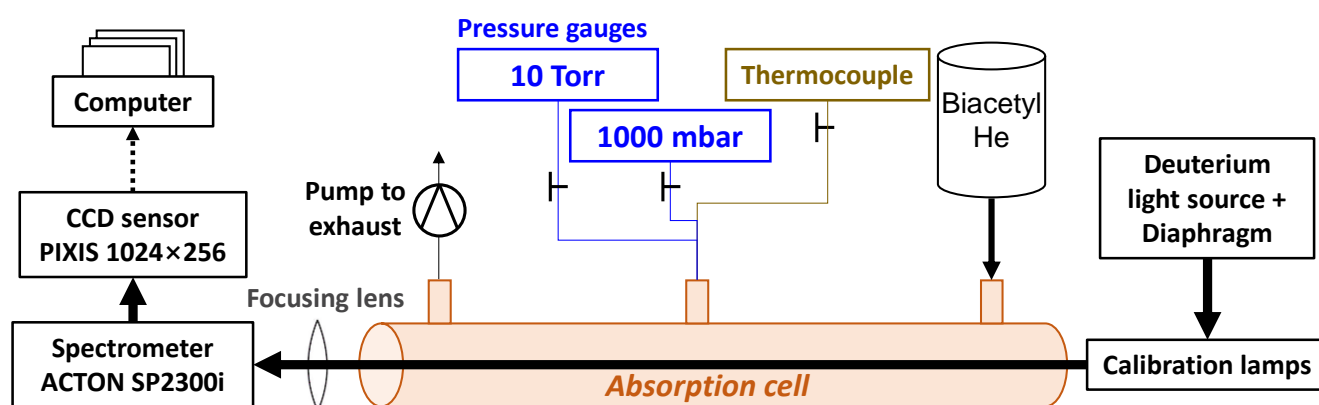
Figure App-III-4 : Schematic of the UV-Vis absorption set-up.

Two runs have been conducted to measure the absorption for the wavelength range from 180–540nm, and the absorption cross-sections have been calculated using a linear regression of the Beer Lambert's law, as presented in the Figure App-III-5 and Figure App-III-6 for a spectrum center on 280nm. The cross-sections have been averaged over the two runs of data when available, and a smoothing function has been applied to the averaged value 1 to 2 times. The resulting UV absorption spectrum are presented in log scale (Figure App-III-7), together with literature data from (Horowitz et al., 2001). The absorption cross-sections on the experimental wavelength employed in the atmospheric simulation chamber are as follows: σ_{254nm}= 3.8×10^{-20} cm^2 molecule^{-1} and σ_{365nm}= 1.2×10^{-20} cm^2 molecule$^{-1.}$
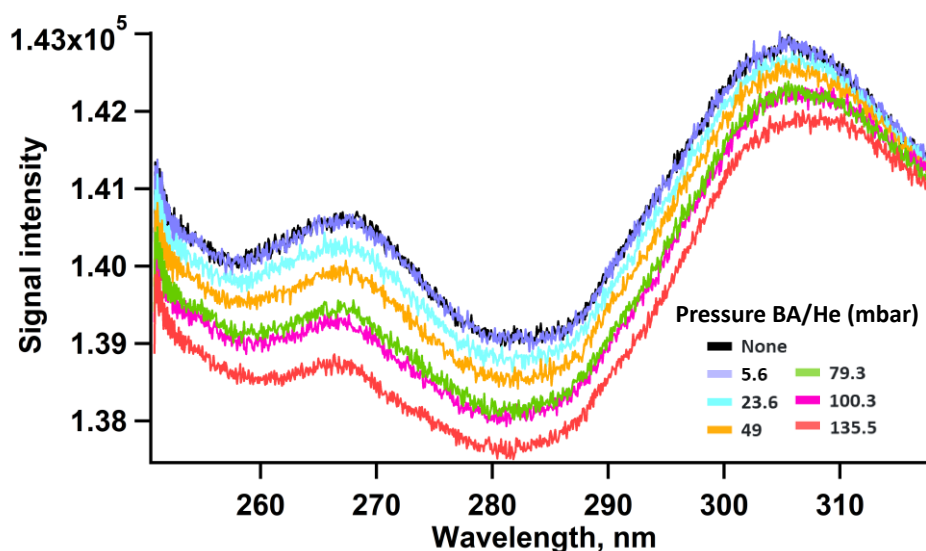
Figure App-III-5: Absorption spectrum between 245 and 315 nm, measured for a mixture of biacetyl (2.99% in He) at different pressure (mbar) ranging from 5.6 to 135.5 mbar. The pressure "None" represents the vacuum, other values are the total pressure in the UV-Vis absorption cell of the mixture of biacetyl (2.99% in He). It can be observed that the signal intensity decreases with increasing concentration of biacetyl in the cell, which is consistent with the fact that biacetyl is absorbing the UV radiation.
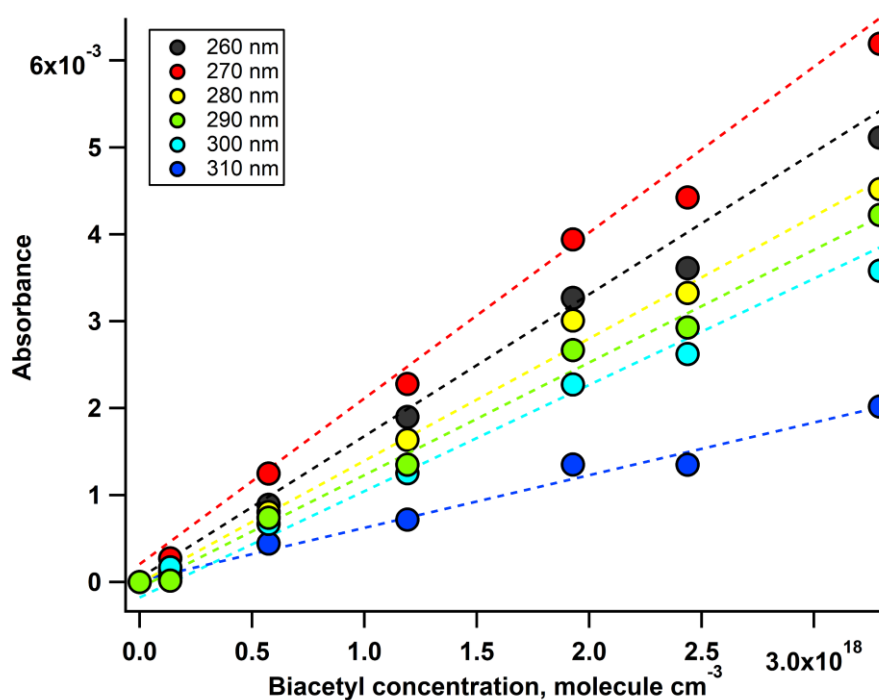
Figure App-III-6 : Beer-Lamber plots of the intensity signal measured in the experiment presented in Figure App-III-5, plotted for 6 wavelengths ranging from 260 to 310 nm. Absorbance is calculated as $A=-\log(I/I_0)$ where I is the intensity of the signal at various concentration of biacetyl and I_0 the initial signal with no biacetyl injected. As it is observed in Figure App-III-5, the signal has some variability, hence, the value used for the absorbance at each wavelength value λ is the average of the values in the range λ ± 0.5 nm. The linearity of the Beer-Lambert law for the concentration range under study is ensured for all wavelength.
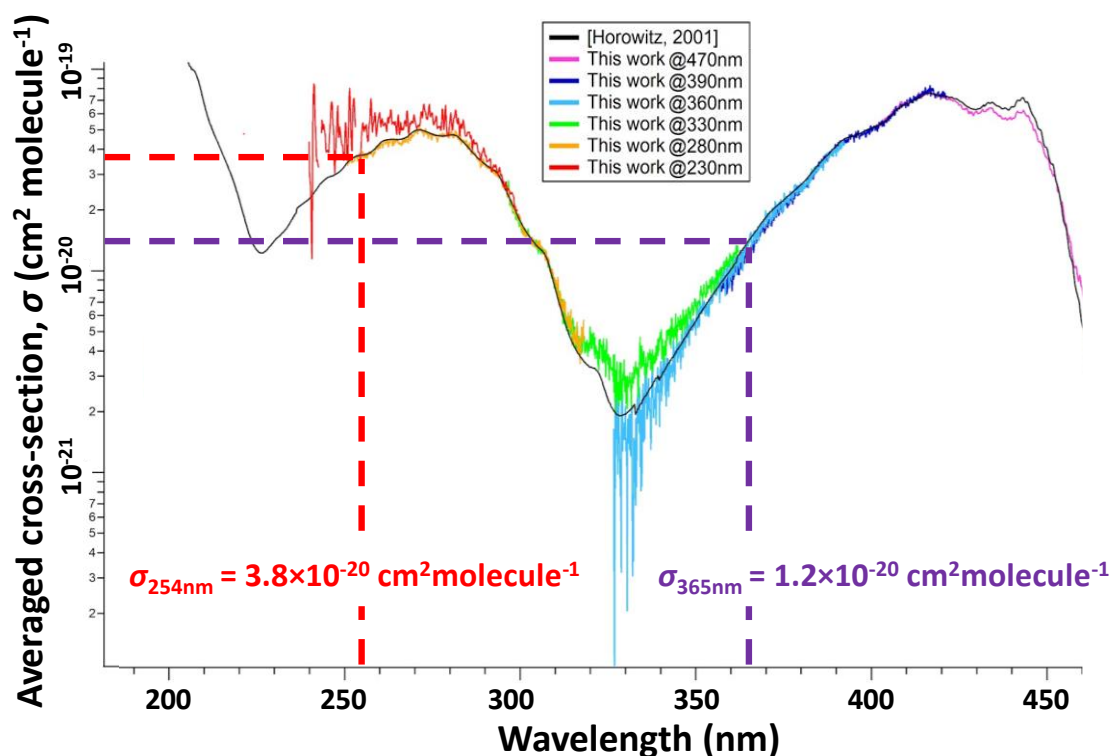
<u>Figure App-III-7</u>: Smoothed averaged of the absorption cross-sections (logarithmic scale) of biacetyl (2.99% in He) measured at room temperature (T=298±5K). Literature data from (Horowitz et al., 2001) are presented, and are in good agreement with new measurements reported.

App-III-4. PLP–LIF measurements of biacetyl photolysis and induced •OH radical fluorescence at 248nm

The UV absorption cross-sections of biacetyl have been determined, as presented in Appendices section App-III-3. The PLP–LIF set-up described in Chapter II, section III-2.1., and in published work, (Michelat et al., 2022), was employed to measure the rate coefficients of the OH reaction of 2,3-butanedione (biacetyl). While attempting to measure the rate of the reaction of biacetyl with OH radicals in the PLP–LIF apparatus, it appeared that biacetyl produces OH radicals under the 248 nm illumination from the KrF excimer laser, the *photolysis laser* hereafter. The OH radicals were excited using the Nd:YAG-pumped frequency-doubled dye laser at 282 nm, referred to as *probe laser*, and their fluorescence was detected at 308nm. Thus, if biacetyl photolyzed and forms OH radicals in addition to the OH precursor, it was challenging to measure its absolute OH rate coefficients in the PLP–LIF set-up.

The production of OH in the photolysis of biacetyl was investigated in this section by ensuring that the signal measured correspond to OH radical fluorescence, and not to background light scattering or impurities in the cell. The production and loss rates of OH radicals from biacetyl photolysis under various conditions have been estimated, and some mechanistic insights on the photolysis of biacetyl under these conditions have been derived. It could be possible to test other photolyte and different photolysis

wavelength to investigate these processes further. Also, it could be possible to run the experiment using $O(^1D)$ or ^{18}OH that cannot be produced by biacetyl. These were not tested since these represent preliminary experiments; however, it can be further investigated in future work.
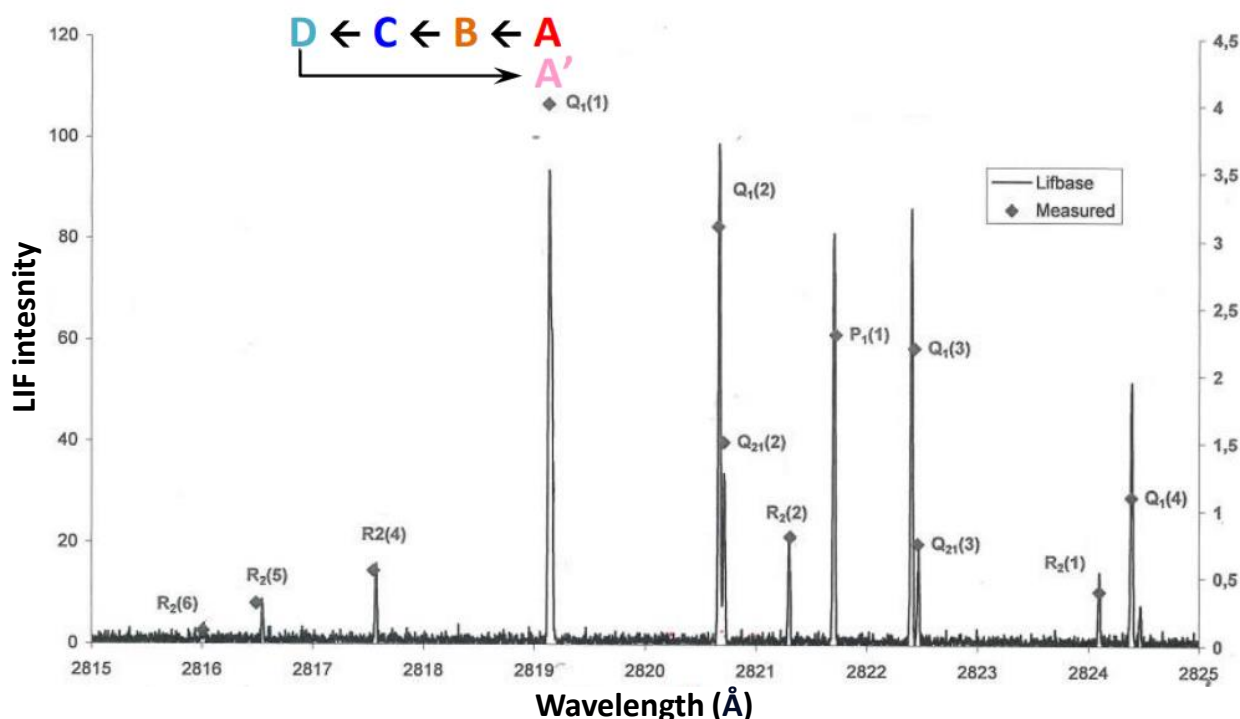
Figure App-III-8: Spectrum of the OH fluorescence intensity as a function of wavelength under set-up conditions. LIFBASE software was employed to simulate the LIF intensity under the conditions: T=300K, P=100Torr, gaussian line shape, thermalized system.

OH absorption spectrum with fluorescence (LIF) intensity

First, to ensure that biacetyl was producing OH radicals in the PLP–LIF set-up (Chapter II, section 2.1., (Michelat et al., 2022)), experiments have been conducted without introducing any OH precursor, but only by adding biacetyl and bath gas (helium) inside the cell. The spectrum of OH fluorescence is presented in Figure App-III-8. The output signal (Figure App-III-9) measured by the PMT in the PLP–LIF set-up containing biacetyl and helium was observed at various wavelengths of the probe laser which correspond to specific parts of the OH fluorescence spectrum: on the $Q_1(1)$ line (282.289 nm, and 282.282 nm), on the $R_2(4)$ line (282.132 nm), and offline (282.125 nm, and 282.277 nm). The $Q_1(1)$ line was chosen for the measurements of the OH rate coefficients because it is one of the most intense bands of the spectrum, and it is isolated from other bands (see Figure App-III-8).

Experimentally, the probe laser's crystal position was tuned to adjust the wavelength of the YAG output. Normally, absolute rate coefficient measurements were conducted on the line $Q_1(1)$ as it is the more intense and isolated one. It was thus possible to navigate throughout different wavelength and to observe

190

whether or not OH radicals were present, by measuring their fluorescence on typical lines (e.g., $Q_1(1)$, $R_2(4)$).

In the experiments without OH precursor, it was observed that when the wavelength of the YAG output is off an OH line, the intensity of the OH fluorescence signal goes to zero, as no absorption and emission occurred, as shown in the Figure App-III-9. When the lasers were tuned on an OH line, a fluorescence signal was detected, as would be observed if OH precursor was introduced in the cell. This was tested for multiple lines, and the OH absorption spectrum was identified by comparison with that in Figure App-III-8. Thus, it can be concluded that OH radicals were formed in these experiments.
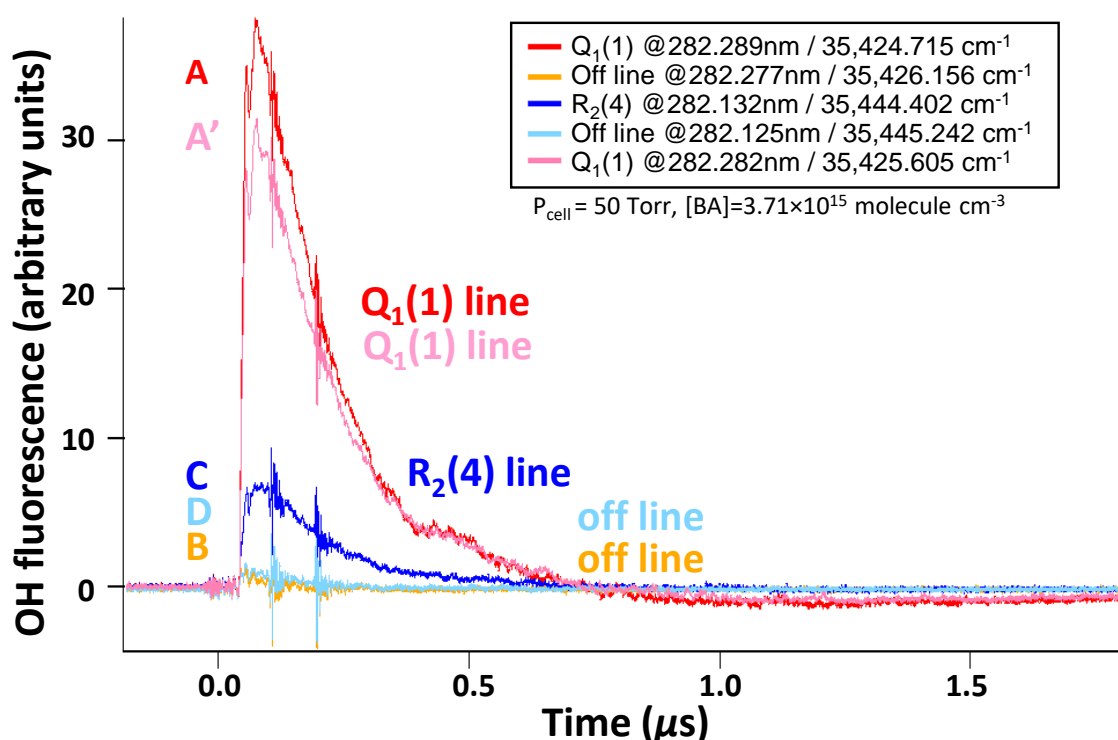
Figure App-III-9: OH fluorescence signal measured at the oscilloscope, at the delay time where the OH concentration was maximum (3600μs, see above) and at various YAG excitation wavelength. All experiments were conducted at a total pressure in the cell of P_{cell}=50Torr and at a biacetyl concentration of [BA]=3.71×10^{15} molecule cm^{-3}. The line chosen to excite the OH radials during the kinetics experiments in the PLP–LIF experiments is the $Q_1(1)$ line, since the output signal is at higher intensity and the line is isolated from the other fluorescence lines of the OH spectrum (Figure App-III-8). The ringing in the signal was not removed (e.g., by changing to a lower capacitance cable or changing the resistor) since these are preliminary results. This can be done in further work.

Background signal of photolysis and probe lasers

In order to ensure that these OH radicals were produced from biacetyl photolysis and not from other sources in the cell, the background signal was measured with the probe laser (Nd:YAG, 282nm) and/or the photolysis laser (Excimer, 248 nm) triggering in the cell without any compound added, i.e., before the experiment after a night of pumping. It is observed that under the vacuum condition (P_{void} ~ 2 Torr, blue and green plots, Figure App-III-10) and after flushing the system several times, i.e., flowing some He and

pumping, (P$_{cell}$ ~ 100 Torr, red/orange/green plots, Figure App-III-10), no LIF signal is measured. For comparison, a usual OH fluorescence decay from biacetyl has been plotted in gray, in Figure App-III-10, highlighting the fact that OH is produced from photolysis of biacetyl due to the photolysis laser which is then detected by the probe laser via OH fluorescence.

These measurements were conducted multiple times and the same signals were measured and were consequently reproducible. Hence, we can ensure that the fluorescence signal observed from biacetyl was not coming from a background light artefact (e.g., scattering) or any impurities fluorescence. It is thus concluded that these OH radicals were formed from the photolysis of biacetyl at 248 nm and that the probe laser was generating their fluorescence at 282nm as observed in these measurements.
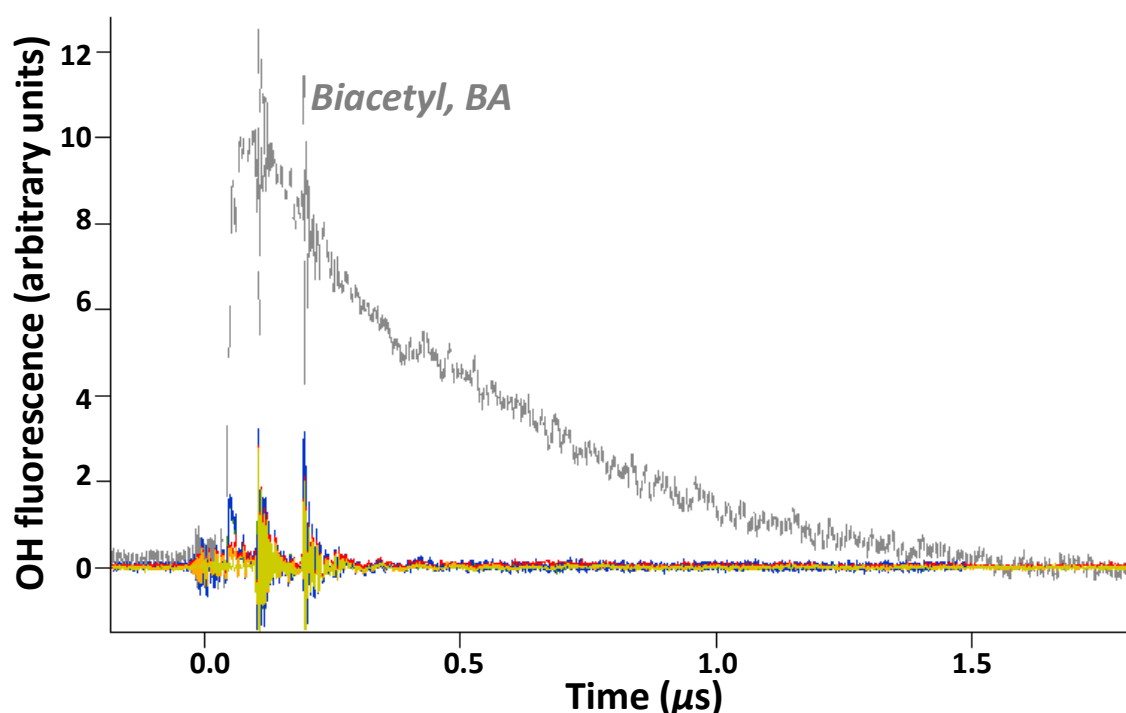
Figure App-III-10 : OH fluorescence signal measured at the oscilloscope, with the probe laser (YAG) and/or the photolysis laser (Excimer) triggering without any compound injected. The gray signal is with biacetyl in the cell at a concentration of 3.4×10^{14} molecule cm^{-3}), in 50 Torr of He. The blue and green ones were taken in the cell at vacuum after a night of pumping and the others (red, orange, olive) were taken after flushing the cell with some Helium. Temperature is maintained at T=25.5±0.5°C for all the experiments. It is observed that fluorescence of OH is measured only when biacetyl is present in the cell with both photolysis and probe laser triggering.

OH signal from biacetyl photolysis at various pressures and time delays

The common OH temporal profile from biacetyl photolysis is presented in Figure App-III-11, and is well described by a biexponential function with a maximum observed at a delay which is correlated with pressure and concentration of biacetyl in the cell (τ_{max}(37Torr)=2563μs and τ_{max}(50Torr)=2958 μs). The PMT signal, S$_t$, was measured at different delay times (200–12400μs), as identified by the colored markers on

the Figure App-III-11, and the associated plots measured by the oscilloscope (300 Hz) for the OH fluorescence are presented for different total pressures in the Figure App-III-12. It can be observed that OH radical was produced and consequently consumed.
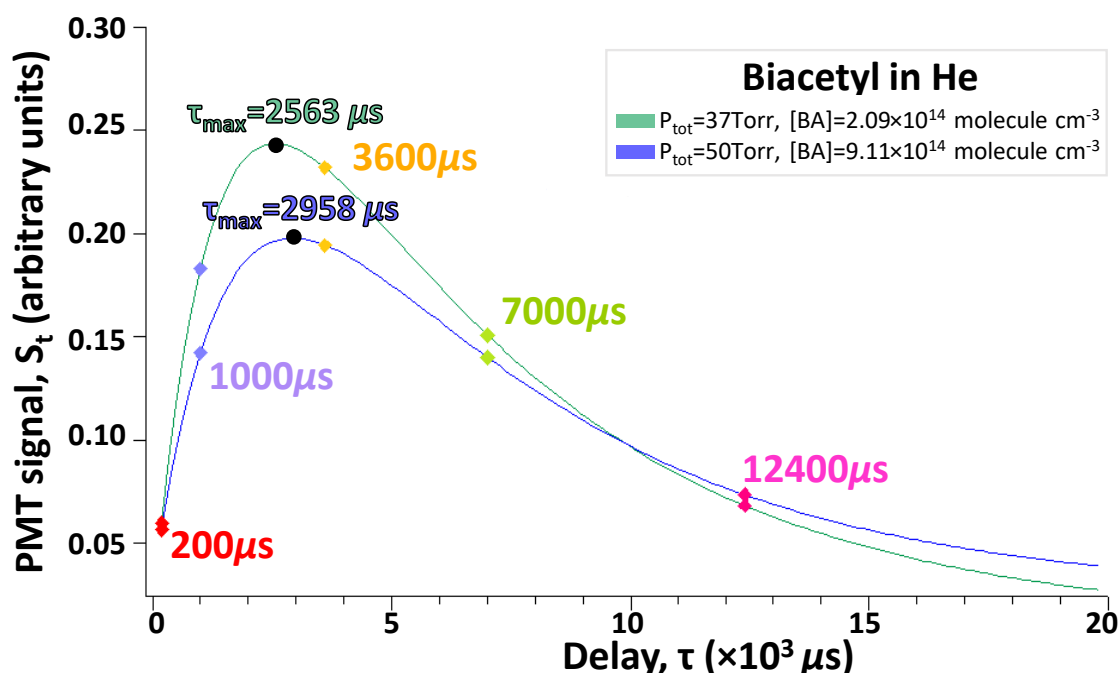
Figure App-III-11: Example of OH fluorescence decays for different total pressure and biacetyl concentration conditions. Data points at which OH signal was taken are shown with the red markers. Maximum of the decay is identified with a black point and value is written.
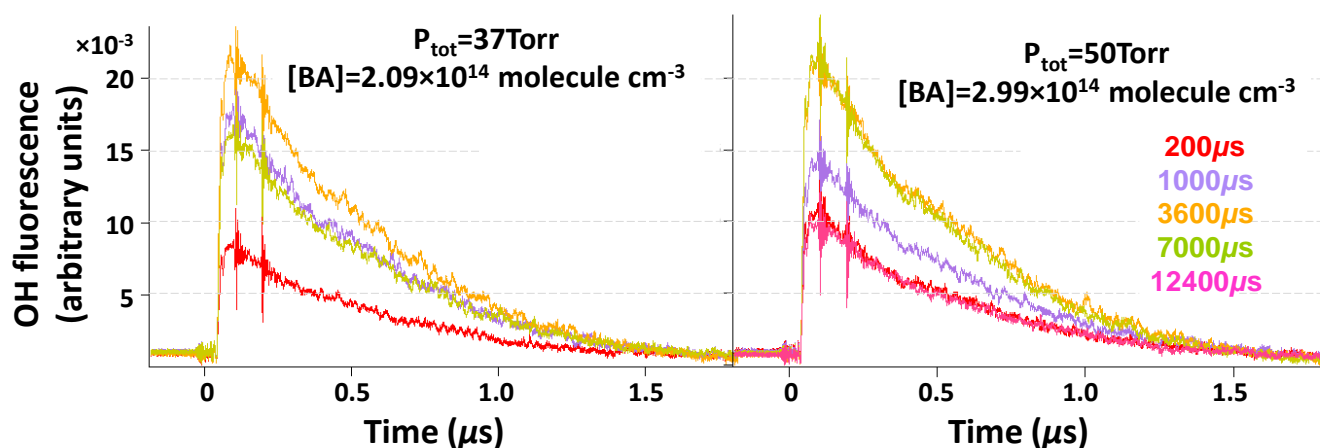
Figure App-III-12 : OH fluorescence signal measured at the oscilloscope, at various delay times, and for different total pressure in the cell from 37 (left) to 50 Torr (right). The same exact concentration of biacetyl between experiments could not be reach in the cell due to pressure equilibrium; hence, the concentration is mentioned for every measurement.

Retrieving OH rise and loss rates from biacetyl photolysis

Measurements of the absolute rate coefficients of OH + biacetyl in the LIF cell has been conducted and the temporal profiles of the OH fluorescence has been measured, as shown in the Figure App-III-13. It is apparent that biacetyl was both a source and a sink of OH radicals. These decays were measured in the

absence of OH precursor and presence of biacetyl only, which shows that they were produced and consumed both by photolysis of biacetyl and reaction with biacetyl (Figure App-III-13).
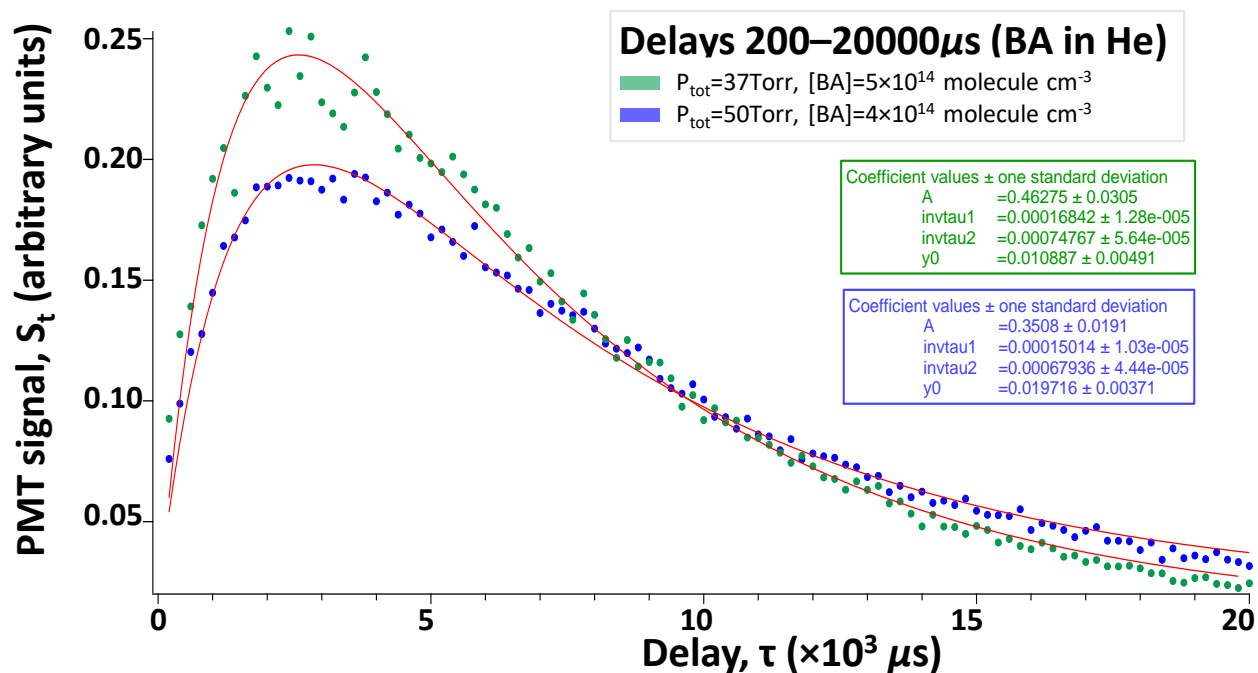
Figure App-III-13: Temporal profiles of the OH signal, measured at the PMT, S_t, at various pressures, 37 Torr in green (higher signal), 50 Torr in blue (middle signal), and 100 Torr purple (lower signal), and at a maximum concentration of biacetyl obtained under the experimental conditions associated. The values of the fits are presented in the colored box. The delay range has been varied from 100-10000 μs (a) to 200-20000 μs (b).

The fit of the OH temporal profiles is a biexponential function as follows:

$$S_{OH}(t) = y_0 + A [(\exp(-k'_1 t) - \exp(-k'_2 t)] \qquad \text{(Eq. App-III-1)}$$

where $S_{OH}(t)$ is fluorescence signal measured at time t, proportional to the total OH radical concentration, A is a constant, and k'_1 and k'_2 are either the pseudo-first-order rate coefficients for the loss or for the formation of the OH radical (Figure App-III-13). The parameters calculated under various pressure conditions for signal measured with different delay ranges is presented Table App-III-2.

Table App-III-2 : Parameters of the biexponential fit as described in (Eq. App-III-1) under various conditions.

Delay range		100-10000 μs			200-20000 μs	
[biacetyl] (molecule cm^{-3})	9×10^{14}	4×10^{14}	2×10^{14}	5×10^{14}	4×10^{14}
P_{cell} (Torr)	37	50	100 [a]	37	50
A	0.85 ± 0.21	0.75 ± 0.41	0.95 ± 61.3	0.46 ± 0.03	0.35 ± 0.02
k'_1 (μs^{-1})	$(2.97 \pm 0.36) \times 10^{-4}$	$(2.47 \pm 0.44) \times 10^{-4}$	$(3.35 \pm 8.69) \times 10^{-4}$	$(1.68 \pm 0.13) \times 10^{-4}$	$(1.50 \pm 0.10) \times 10^{-4}$
k'_2 (μs^{-1})	$(6.66 \pm 0.76) \times 10^{-4}$	$(4.47 \pm 0.75) \times 10^{-4}$	$(3.63 \pm 9.36) \times 10^{-4}$	$(7.48 \pm 0.56) \times 10^{-4}$	$(6.79 \pm 0.44) \times 10^{-4}$
y_0	0.068 ± 0.006	0.068 ± 0.004	0.022 ± 0.002	0.011 ± 0.005	0.020 ± 0.003

[a] The system was low in biacetyl for the measurement at 100 Torr. This is the reason why the decay is almost flat, which gives unprecise results for the fit (error ≈ value) and that there is no second measurement (200-20000μs).

The production and loss rates can be obtained by fitting with a double exponential function. However, in order to determine which of the two pseudo-first-order rate coefficient k'_1 and k'_2 is the production rate coefficient, it would be required to conduct new measurements (Figure App-III-14). For example, by measuring the decays using O_2 as a bath gas, it could be possible to determine which rate coefficient has been affected (since O_2 will favor the production of OH) and associate it to the production rate coefficient.
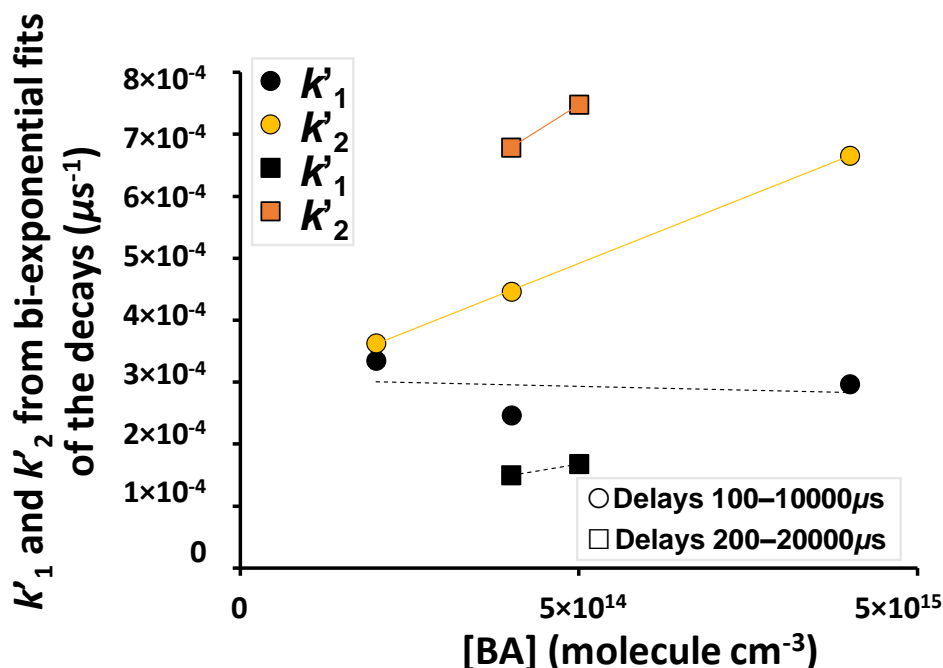
Figure App-III-14: Rise and fall time constants as a function of biacetyl measured at various delays (square and circles). It is observed that k'_2 is increasing with increasing concentration of biacetyl. However, k'_1 behavior is less clear, and could be opposite when measured at various delays. For shorter delays, it seems to decrease with concentration with concentration, and for longer delays, it seems to increase with concentration. Identifying each processes requires further measurements.

The mechanism by which biacetyl photolyzes is not well described, and a suggested mechanism is proposed in Figure App-III-15, based on the work of (Blitz et al., 2002; Link et al., 2021; Plum et al., 1983; Rajakumar et al., 2008). The photolysis of biacetyl at wavelength λ<470 nm has been observed to be a dominant atmospheric loss for biacetyl, that occurs via the cleavage of the central C–C bond to form two acetyl radicals, (Klotz et al., 2001; Plum et al., 1983; Profeta et al., 2011), as follows:

$$CH_3C(O)C(O)CH_3 + h\nu \rightarrow 2\ CH_3CO^\bullet \qquad (R36)$$
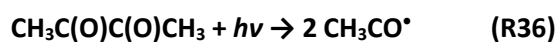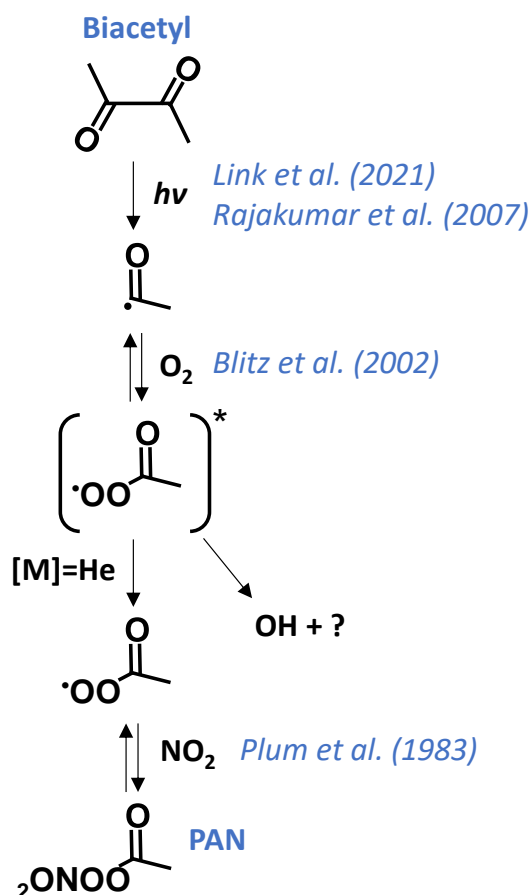
Figure App-III-15: Suggestion of the mechanistic pathways initiated by the 248nm-photolysis of biacetyl in the LIF cell (Blitz et al., 2002; Link et al., 2021; Plum et al., 1983; Rajakumar et al., 2008).

Chamber experiments to evaluate the photolysis rate of biacetyl under similar conditions (biacetyl-air under UV–Vis light filtered >300nm) have been conducted by (Plum et al., 1983) and conditions (biacetyl-air under natural sunlight) by (Klotz et al., 2001). (Plum et al., 1983) observed that the photodissociation of biacetyl and other α-dicarbonyls occurs from the absorption band in the range 340-470nm and that fluorescence or relaxation to the ground state is significantly competing with the photodecomposition in this region of the spectrum. The formation of acetyl radicals (R36) from the photodissociation of biacetyl in a NO_x-air mixture was observed through formation of PAN (see Figure App-III-15) in the study of (Plum et al., 1983) and similarly in the study of (Illmann et al., 2021) conducted with irradiation of 360 nm UV light, and O_2/NO_x conditions. From the work of Blitz et al. (2002) and other cited in the previous work, it is showed that the acetyl radical reacts with O_2 to produce OH radical. The acetyl radical forms an energized peroxyacetyl which may either be stabilized by the bath gas (He) or dissociate to form the hydroxy radical (Figure App-III-15). During the experiments conducted in the PLP–LIF, no O_2 was introduced (bath gas is helium) however, it is always hard to get rid of O_2 completely as a contaminant from ambient air. It is expected that even at low concentrations of contamination O_2 can react with acetyl to produce OH in the present experiments. It can be concluded that further work is required to determine the various rise and

loss rate coefficients of the biacetyl + OH reaction in PLP–LIF. This work represents preliminary results and highlights the challenges of the kinetic study conducted in this set-up. Further work would be necessary: (1) studying the kinetics in excess of O_2 would allow the OH production to be faster and measure the rise rate coefficient, (2) quantifying the OH produced from a photolyte with that from biacetyl, (3) quantify the OH (2Σ) quenching rate coefficient by biacetyl.

App-III-5. Furans rate coefficients

Table App-III-3: IR absorption bands of the reference compounds used in the study, together with their recommended rate coefficients taken from the database of McGillen et al. (2020).

$k_{NO3}{}^{a}$	$k_{OH}{}^{a}$	Compound
$(5.70 \pm 1.71) \times 10^{-11}$	$(1.10 \pm 0.22) \times 10^{-10}$	2,3-dimethyl-2-butene
$(2.0 \pm 0.3) \times 10^{-11}$	-	2-carene
$(6.20 \pm 1.55) \times 10^{-12}$	-	α-pinene
$(6.60 \pm 1.65) \times 10^{-13}$	-	camphene
$(5.60 \pm 0.84) \times 10^{-13}$	$(6.77 \pm 1.69) \times 10^{-11}$	cyclohexene
$(2.60 \pm 0.78) \times 10^{-13}$	-	3-methyl-3-buten-1-ol
$(1.35 \pm 0.20) \times 10^{-16}$	-	cyclohexane
$(4.62 \pm 1.16) \times 10^{-11}$	$(1.20 \pm 0.30) \times 10^{-10}$	1,3-cyclohexadiene
$(1.80 \pm 1.44) \times 10^{-10}$	$(3.50 \pm 0.70) \times 10^{-10}$	α-terpinene
$(9.42 \pm 3.29) \times 10^{-12}$	$(8.69 \pm 1.74) \times 10^{-11}$	2-methyl-2-butene
$(6.50 \pm 2.60) \times 10^{-13}$	$(1.00 \pm 0.05) \times 10^{-10}$	isoprene
$(1.30 \pm 0.39) \times 10^{-16}$	$(2.00 \pm 0.52) \times 10^{-11}$	methyl vinyl ketone (MVK)
$(9.31 \pm 2.79) \times 10^{-12}$	$(9.40 \pm 2.82) \times 10^{-11}$	1-Methylcyclohexene
-	$(1.05 \pm 0.21) \times 10^{-12}$	methyl ethyl ketone (MEK)
$(5.80 \pm 4.06) \times 10^{-11}$	$(1.16 \pm 1.86) \times 10^{-11}$	2,5-dimethylfuran

[a] All the literature reference rate coefficients are the recommendation from (McGillen et al., 2020), in cm^3 molecule^{-1} s^{-1}.

Table App-III-4 : IR absorption bands of the VOCs under study, with bold ones being those used for the spectrum analysis.

Compound	Main absorption bands (cm^{-1})							
furan	995	744						
2-methylfuran	792	726	1151	2965				
2,5-dimethylfuran	777	2938	2961					
furfural	756	1720						
α-angelicalactone	731	939	1100	1834				
pyrrole	724	1017	3531	718–722				
γ -crotonolactone	1098	805	866	1045	1812	2885	2945	
2-furoic acid	769-757	769-757		3484-3522	769-757	1169-1198		
2,5-dimethoxy-2,5-dihydrofuran	1111-1177							
2,5-dimethylpyrrole	775-783			1201-1247	996-1040	775-783		
Furfuryl alcohol	1202-1264							
5-methylfufural	757-708	2934-2968						
Furfuryl acetate	998-991	998-991	998-991	740-748				

2,3-dihydrofuran	2967-3015							
2 ethyl furan	3073-3033							
2,3-dimethyl-2-butene	2878	2930	3005					
2-carene	2874	2928	3009					
α-pinene	2971	2998	3035	789	2847	2893	2925	2931
camphene	2967	2972	2986	882	2881	3075		
cyclohexene	2934	744	919	1140	2892	2943	3033	3036
3-methyl-3-buten-1-ol	1065	896	903	2886	2948	2981	3084	
cyclohexane	2862	2933						
1,3-cyclohexadiene	722-757	722-740	1017-1036					
α-terpinene	2921-2935							
2,3-dimethyl-2-butene	2878	2930	3005					
2-carene	2874	2928	3009					
α-pinene	2971	2998	3035	789	2847	2893	2925	2931

App-III-6. Mechanism of furans oxidation

App-III-6.1. Furans + OH oxidation

The mechanism of the reaction of OH radicals with furans and derivatives has been investigated in the literature in the presence and absence of NO_x, based on the literature work of (Aschmann et al., 2014; Bierbach et al., 1995; Davis et al., 2013; Gómez Alvarez et al., 2009; Hoang, 2021; Jiang et al., 2020; Tapia et al., 2011; Yuan et al., 2017). It follows the similar pathways of addition and H-abstraction as described in Chapter I. It is noted that elevated NO_x levels have been observed in biomass burning air masses (Andreae et al., 1988) and it is thus relevant to understand the chemistry of furan oxidation under such conditions.
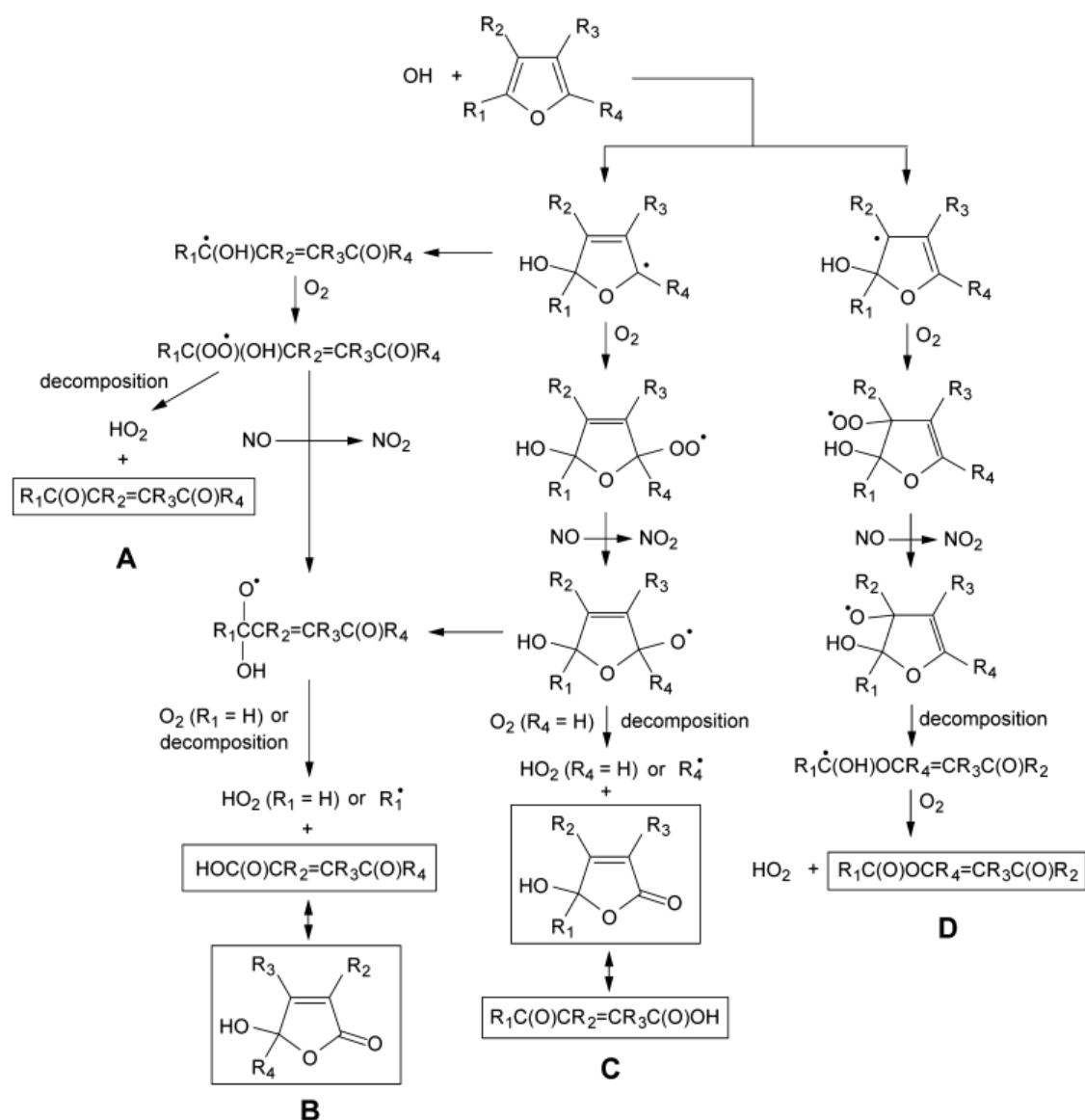
Figure App-III-16: Scheme 1 taken from (Aschmann et al., 2014) illustrating the different pathways of the OH-initiated oxidation of substituted furans under NO_x conditions. (A) is the dominant pathway in the absence of NO_x, and forms 1,4-dicarbonyls. Additional pathways (B), (C) and (D) occur in the presence of NO and lead to the formation of other compounds such as unsaturated carbonyl-acids, hydroxy furanone, and unsaturated carbonyl-ester in the case of 2,5-dimethylfuran (Aschmann et al., 2014).

Furan and alkyl substituted furans

The OH radical mechanism occur via OH addition to one of the double-bonds of the furan ring (Bierbach et al., 1995). The addition at the C-2 (or C-5) position is favored due to resonance-stabilization effects of the furan-OH adduct formed (see Appendices-III-5) (Aschmann et al., 2014; Bierbach et al., 1995). However, (Cabanas et al., 2005) suggested that in the case of certain alkyl substituted furans, e.g., 2-methylfuran or 3-methylfuran, the attack of the oxidant (OH or Cl) could be sterically hindered on the carbon onto which the substituent is attached, e.g., C-2 and C-3 respectively.

As illustrated Figure App-III-17, for the reaction of 2-methylfuran, the attack of OH (or Cl atom) on the positions C-3 and C-4 results in adducts with 2 resonant structures, while the attack on C-5 leads to an intermediate stabilized by three resonant structures, thus, it is the most feasible position attack. The attack on C-2 is sterically hindered due to the presence of the methyl group substituent (Bierbach et al., 1992; Cabanas et al., 2005). For the reaction of 3-methylfuran, two possible sites of attack are C-2 and C-5, each of which has 3 resonant structures (Bierbach et al., 1992; Cabanas et al., 2005).
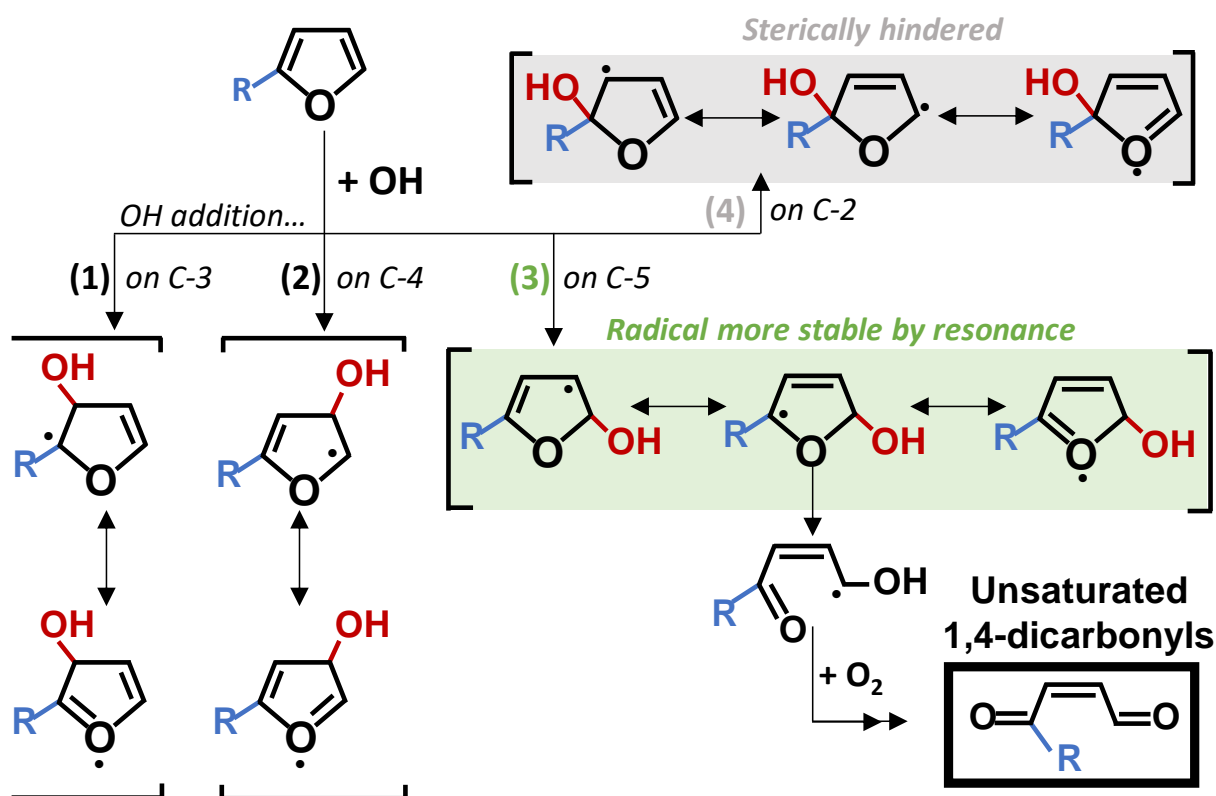
Figure App-III-17: Pathways for the attack of OH to furan (R=H) or an alkyl substituted furan, e.g., 2-methylfuran (R=CH$_3$), updated from (Bierbach et al., 1995), and the resulting intermediates formed in each case, with their resonant structures. Pathways (1) and (2), and pathways (3) and (4) are identical for furan (Bierbach et al., 1992; Cabanas et al., 2005). The most favorable pathways are those with more resonant structures that stabilize the intermediate (e.g., (3) is more stable by resonance than (1) or (2) for furan or 2-methylfuran) and without steric hindrance on the reactive site due to the presence of a substituent group (e.g., (4) for 2-methylfuran). The radical formed after ring cleavage can then follow the pathways presented in Figure App-III-16 in the presence or absence of NO$_x$.

The resulting furan adduct formed in each case can be resonance stabilized and further undergo electrophilic ring opening processes and reaction with O$_2$, forming a peroxy radical that further decompose to form butenedial (Figure App-III-18 and pathway (1) in Figure App-III-16). Butenedial can be further degraded and form maleic anhydride, 3H-furan-2-one, and glyoxal. (Bierbach et al., 1995) Butenedial could also fragment into smaller molecules (Liu et al., 1999) or phototautomerize (Newland et al., 2019).
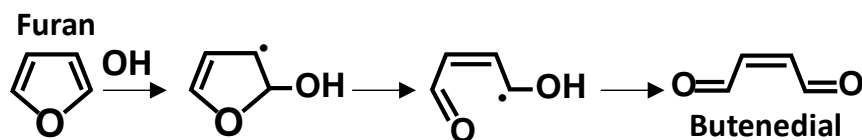
Figure App-III-18: Mechanism of the OH-initiated degradation of furan, derived from the product study and mechanism from (Bierbach et al., 1995).

In the presence of NOₓ, (Aschmann et al., 2014) observed that additional pathways can occur instead of ring cleavage of the resonance stabilized adduct. Similarly to the atmospheric oxidation described in Chapter I, O_2 can add to the radical adduct forming a peroxy radical, $RO_2^\bullet$, being further reduced by NO into an alkoxy radical, $RO^\bullet$, that will either decompose or undergo ring cleavage (pathways (B), (C) and (D) in Scheme 1 in the work of (Aschmann et al., 2014) in Figure App-III-16) to form unsaturated carbonyl-acids, hydroxy furanones, and unsaturated carbonyl esters depending on the substitutions of the parent compound (see Scheme 1 in the work of (Aschmann et al., 2014) in Figure App-III-16). Pathway (B) can also occur via reduction of the peroxy radical formed from the ring cleavage of the stabilized furan-OH adduct.
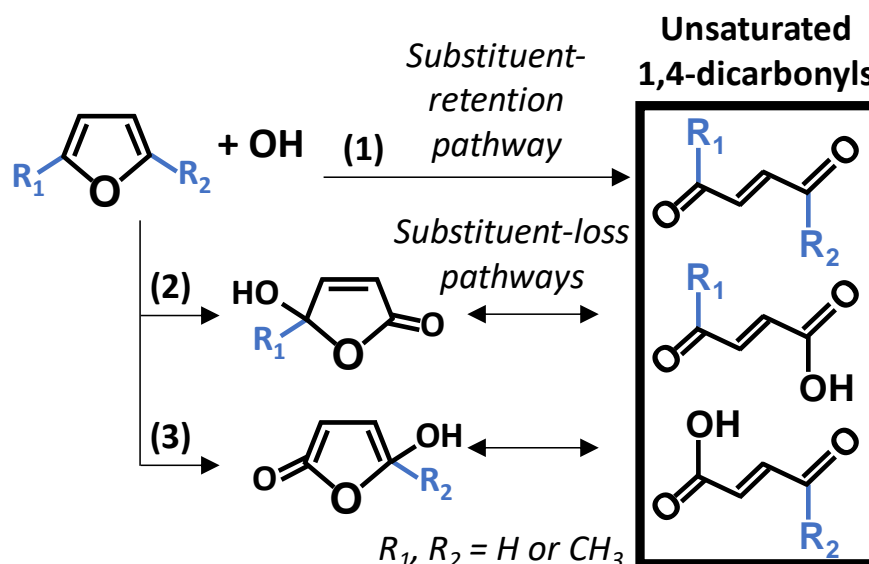
Figure App-III-19: Simplified pathways for the OH reaction of alkyl substituted furans. Pathway (1), which is more detailed in Figure App-III-16, occurs both in the presence and absence of NOₓ, (Bierbach et al., 1995) while in the presence of NOₓ, additional pathways (2) and (3) can occur (Aschmann et al., 2014; Gómez Alvarez et al., 2009; Tapia et al., 2011). Detailed pathways are presented in the Scheme 1 of the work of (Aschmann et al., 2014).

In both presence or absence of NOₓ, the main product of the mechanism are unsaturated 1,4-dicarbonyls (Figure App-III-19), such as butenedial for furan (e.g., dominant product observed in the studies of (Aschmann et al., 2014; Bierbach et al., 1995; Gómez Alvarez et al., 2009) in presence or absence of NO) and the corresponding dicarbonyl that retained the substitutions from the parent compound for alkyl substituted furans (e.g., major product of 2-methylfuran + OH observed by (Bierbach et al., 1992) was 4-oxo-2-penenal) (Bierbach et al., 1995, 1992). The 1,4-butenedial formed during the OH-initiated oxidation

of furan is primarily in the *E*-configuration, with a yield of 76% for the *E*- and 24% for the *Z*-isomer (Gómez Alvarez et al., 2009).

In presence of NOₓ, the products of the OH-initiated degradation of furan, 2- and 3-methylfuran are unsaturated 1,4-dicarbonyls are formed, together with unsaturated carbonyl-acids, hydroxy furanones (Aschmann et al., 2014; Gómez Alvarez et al., 2009; Tapia et al., 2011). The same products are observed in addition to unsaturated carbonyl-ester in the case of the reaction of OH + 2,5-dimethylfuran (Aschmann et al., 2014). The yield of the 1,4-dicarbonyls formed decreases with increasing number of methyl group substituents attached to the furan (Aschmann et al., 2014).

Furfurals and dihydrofurans

For furfurals, the product studies are sparse (Bierbach et al., 1995) and the OH mechanism is expected to include an additional H-abstraction pathway from the –CHO group compared to that of furan. For other substituted furans, no product study has been conducted to the best of our knowledge.

App-III-6.2. Mechanism of NO₃ + furans oxidation

The NO₃-intitiated degradation of furans follows a similar mechanism than that initiated by OH (Figure App-III-20). (Berndt et al., 1997) observed that the mechanism of NO₃ + furan and NO₃ + tetramethylfuran occurs via the formation of an adduct going through two pathways in competition: (1) forming cis-butenedial and (2) forming 3H-furan-2-one (see Figure App-III-20). For the reaction of furan, NO₃ attacks in 2-position predominantly (Marino, 1971) forming a resonance stabilized radical (see Figure App-III-20). In the pathway (1), NO₂ is lost, and the molecule rearranges to form cis-butenedial. In the pathway (2), a 1,2-H shift occurs to form 3H-furan-2-one, which is a process of 1,3-diradicals (Freidlina et al., 1974). The NO₂ group is eliminated and the diradical formed is stabilized after intramolecular H-transfer to 3H-furan-2-one (Bierbach et al., 1994). There is a possibility discussed by (Bierbach et al., 1994) that 3H-furan-2-one would be formed from intramolecular rearrangement of *cis*-butenedial initiated by VIS irradiation.

Butenedial is the major product of the NO₃ oxidation of furan, with a molar yield of 77%, together with 3H-furanone formed with a yield of around 19% (Berndt et al., 1997). An increasing yield of 3H-furan-2-one with increasing O₂ has been observed by (Berndt et al., 1997) but the reasons why remain unclear. This strengthens the need for more product studies on the oxidation of furans. Similar to OH, the alkyl substituted furan would form the substituted analog to the products of the furan oxidation (Berndt et al., 1997).
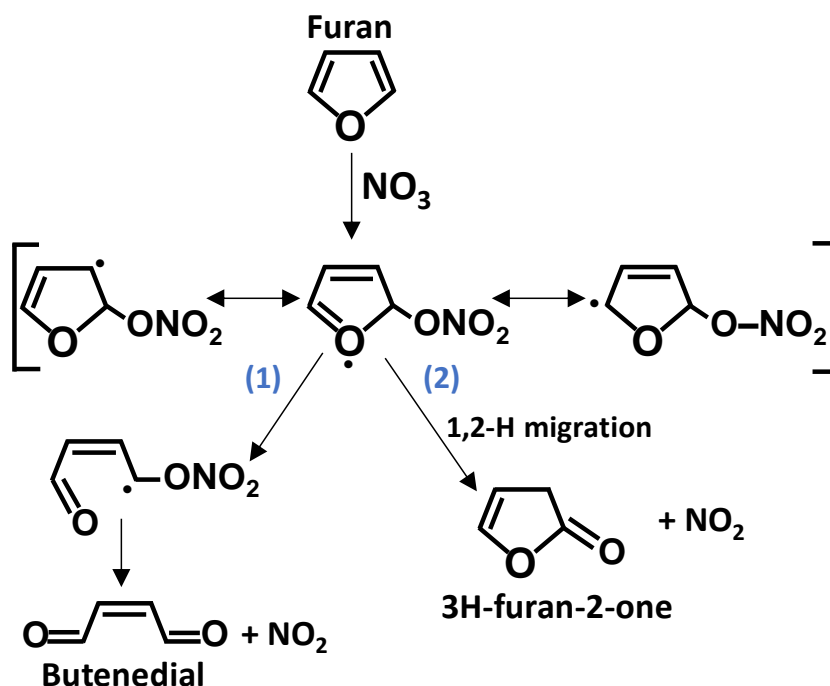
<u>Figure App-III-20:</u> Mechanism of the NO_3-initiated degradation of furan, derived from the product study and mechanism from (Berndt et al., 1997). The mechanism is similar to that of OH, with main products being 1,4-dicarbonyl (e.g., butenedial for furan + NO_3 reaction) and dihydroxy furanones.

Furfurals and dihydrofurans

No end product studies have been carried out on the NO_3 reaction of furfurals and dihydrofurans, except one theoretical study from (Huang et al., 2019) predicts nitrate esters and furanones as the main products of the reaction of 2-furanaldehyde with NO_3. It is expected that the mechanism of the NO_3 + furfurals reaction is similar to that of furan.

References

Andreae, M.O., Browell, E.V., Garstang, M., Gregory, G.L., Harriss, R.C., Hill, G.F., Jacob, D.J., Pereira, M.C., Sachse, G.W., Setzer, A.W., 1988. Biomass-burning emissions and associated haze layers over Amazonia. Journal of Geophysical Research: Atmospheres 93, 1509–1527.

Aschmann, S.M., Nishino, N., Arey, J., Atkinson, R., 2014. Products of the OH Radical-Initiated Reactions of Furan, 2-and 3-Methylfuran, and 2, 3-and 2, 5-Dimethylfuran in the Presence of NO. The Journal of Physical Chemistry A 118, 457–466.

Berndt, T., Böge, O., Rolle, W., 1997. Products of the gas-phase reactions of NO3 radicals with furan and tetramethylfuran. Environmental science & technology 31, 1157–1162.

Bierbach, A., Barnes, I., Becker, K.H., 1995. Product and kinetic study of the OH-initiated gas-phase oxidation of furan, 2-methylfuran and furanaldehydes at≈ 300 K. Atmospheric Environment 29, 2651–2660.

Bierbach, A., Barnes, I., Becker, K.H., 1992. Rate coefficients for the gas-phase reactions of hydroxyl radicals with furan, 2-methylfuran, 2-ethylfuran and 2, 5-dimethylfuran at 300±2 K. Atmospheric Environment. Part A. General Topics 26, 813–817.

Bierbach, A., Barnes, I., Becker, K.H., Wiesen, E., 1994. Atmospheric Chemistry of Unsaturated Carbonyls: Butenedial, 4-Oxo-2-pentenal, 3-Hexene-2,5-dione, Maleic Anhydride, 3H-Furan-2-one, and 5-Methyl-3H-furan-2-one. ACS Publications. https://doi.org/10.1021/es00053a028

Blitz, M.A., Heard, D.E., Pilling, M.J., 2002. OH formation from CH3CO+O2: a convenient experimental marker for the acetyl radical. Chemical Physics Letters 365, 374–379. https://doi.org/10.1016/S0009-2614(02)01484-7

Cabanas, B., Villanueva, F., Martin, P., Baeza, M., Salgado, S., Jimenez, E., 2005. Study of reaction processes of furan and some furan derivatives initiated by Cl atoms. Atmospheric Environment 39, 1935–1944. https://doi.org/10.1016/j.atmosenv.2004.12.013

Dagaut, P., Wallington, T.J., Liu, R., Kurylo, M.J., 1988. A kinetic investigation of the gas-phase reactions of hydroxyl radicals with cyclic ketones and diones: mechanistic insights. The Journal of Physical Chemistry 92, 4375–4377.

Davis, A.C., Sarathy, S.M., 2013. Computational Study of the Combustion and Atmospheric Decomposition of 2-Methylfuran. J. Phys. Chem. A 117, 7670–7685. https://doi.org/10.1021/jp403085u

Freidlina, R.K., Terent'ev, A.B., 1974. Rearrangements of Biradicals With Migration of an Alkyl Group or Hydrogen. Russian Chemical Reviews 43, 129.

Gómez Alvarez, E., Borrás, E., Viidanoja, J., Hjorth, J., 2009. Unsaturated dicarbonyl products from the OH-initiated photo-oxidation of furan, 2-methylfuran and 3-methylfuran. Atmospheric Environment 43, 1603–1612. https://doi.org/10.1016/j.atmosenv.2008.12.019

Hoang, A.T., 2021. 2-Methylfuran (MF) as a potential biofuel: A thorough review on the production pathway from biomass, combustion progress, and application in engines. Renewable and Sustainable Energy Reviews 148, 111265.

Horowitz, A., Meller, R., Moortgat, G.K., 2001. The UV–VIS absorption cross sections of the α-dicarbonyl compounds: pyruvic acid, biacetyl and glyoxal. Journal of Photochemistry and Photobiology A: Chemistry 146, 19–27.

Huang, Z., Zhao, N., Ma, X., Xu, F., Zhang, Q., Zhuang, T., Wang, W., 2019. Theoretical study on the atmospheric oxidation reaction of 2-furanaldehyde initiated by NO3 radicals. Chemical Physics Letters 722, 50–57. https://doi.org/10.1016/j.cplett.2019.03.009

Illmann, N., Gibilisco, R.G., Bejan, I.G., Patroescu-Klotz, I., Wiesen, P., 2021. Atmospheric oxidation of α,β-unsaturated ketones: kinetics and mechanism of the OH radical reaction. Atmospheric Chemistry and Physics 21, 13667–13686. https://doi.org/10.5194/acp-21-13667-2021

Jiang, J., Carter, W.P.L., Cocker, D.R., Barsanti, K.C., 2020. Development and Evaluation of a Detailed Mechanism for Gas-Phase Atmospheric Reactions of Furans. ACS Earth Space Chem. 4, 1254–1268. https://doi.org/10.1021/acsearthspacechem.0c00058

Klotz, B., Graedler, F., Sorensen, S., Barnes, I., Becker, K.-H., 2001. A kinetic study of the atmospheric photolysis of ?-dicarbonyls. Int J Chem Kinet 33, 9–20. https://doi.org/10.1002/1097-4601(20010101)33:1<9::AID-KIN2>3.0.CO;2-V

Link, M.F., Farmer, D.K., Berg, T., Flocke, F., Ravishankara, A.R., 2021. Measuring Photodissociation Product Quantum Yields Using Chemical Ionization Mass Spectrometry: A Case Study with Ketones. J. Phys. Chem. A 125, 6836–6844. https://doi.org/10.1021/acs.jpca.1c03140

Liu, X., Jeffries, H.E., Sexton, K.G., 1999. Atmospheric Photochemical Degradation of 1,4-Unsaturated Dicarbonyls. Environ. Sci. Technol. 33, 4212–4220. https://doi.org/10.1021/es990469y

Marino, G., 1971. Electrophilic substitutions of five-membered rings, in: Advances in Heterocyclic Chemistry. Elsevier, pp. 235–314.

Michelat, L., Mellouki, A., Ravishankara, A.R., El Othmani, H., Papadimitriou, V.C., Daële, V., McGillen, M.R., 2022. Temperature-Dependent Structure–Activity Relationship of OH + Haloalkene Rate Coefficients under Atmospheric Conditions and Supporting Measurements. ACS Earth Space Chem. 6, 3101–3114. https://doi.org/10.1021/acsearthspacechem.2c00296

Newland, M.J., Rea, G.J., Thüner, L.P., Henderson, A.P., Golding, B.T., Rickard, A.R., Barnes, I., Wenger, J., 2019. Photochemistry of 2-butenedial and 4-oxo-2-pentenal under atmospheric boundary layer conditions. Physical Chemistry Chemical Physics 21, 1160–1171.

Newland, M.J., Ren, Y., McGillen, M.R., Michelat, L., Daële, V., Mellouki, A., 2022. NO₃ chemistry of wildfire emissions: A kinetic study of the gas-phase reactions of furans with the NO 3 radical. Atmospheric Chemistry and Physics 22, 1761–1772.

Plum, C.N., Sanhueza, Eugenio., Atkinson, Roger., Carter, W.P.L., Pitts, J.N., 1983. Hydroxyl radical rate constants and photolysis rates of α-dicarbonyls. Environ. Sci. Technol. 17, 479–484. https://doi.org/10.1021/es00114a008

Profeta, L.T.M., Sams, R.L., Johnson, T.J., Williams, S.D., 2011. Quantitative Infrared Intensity Studies of Vapor-Phase Glyoxal, Methylglyoxal, and 2,3-Butanedione (Diacetyl) with Vibrational Assignments. J. Phys. Chem. A 115, 9886–9900. https://doi.org/10.1021/jp204532x

Rajakumar, B., Gierczak, T., Flad, J.E., Ravishankara, A.R., Burkholder, J.B., 2008. The CH3CO quantum yield in the 248nm photolysis of acetone, methyl ethyl ketone, and biacetyl. Journal of Photochemistry and Photobiology A: Chemistry 199, 336–344. https://doi.org/10.1016/j.jphotochem.2008.06.015

Tapia, A., Villanueva, F., Salgado, M.S., Cabañas, B., Martínez, E., Martín, P., 2011. Atmospheric degradation of 3-methylfuran: kinetic and products study. Atmospheric Chemistry and Physics 11, 3227–3241.

Yuan, Y., Zhao, X., Wang, S., Wang, L., 2017. Atmospheric Oxidation of Furan and Methyl-Substituted Furans Initiated by Hydroxyl Radicals. J. Phys. Chem. A 121, 9306–9319. https://doi.org/10.1021/acs.jpca.7b09741

Chapter IV :

Development of a general estimation technique to predict the rate coefficients for the addition of the major tropospheric oxidants to various UVOCs

Summary of the chapter IV

The Chapter IV focuses on the development and application of a new tool for predicting the rate coefficients of the oxidation of various types of volatile organic compounds (UVOCs) by different atmospheric oxidants. In the introduction and in the first section, the different SAR approaches used in the atmospheric chemistry community are presented, and the limitations of these methods are highlighted. Limitations include the need for a more comprehensive prediction tool that can be extrapolated to new multifunctional species.

The new parametrization developed in this work is presented in detail in the first section. This method uses *a priori* information describing electronic and steric properties of each molecule, obtained using theoretical calculation-based method, such as quantum chemical theory (DFT) or semi-empirical tools (PM6), and correlates them to the reactivity, for a large range of CHNOPSX atoms containing unsaturated VOCs. It applies to the four major tropospheric oxidants, OH, Cl, NO_3, and O_3, and is built in as an automated tool (so-called KINESTEASY) easy-to-use, and rapid.

The performance of this SAR is compared to that of the method from Chapter I, as well as existing methods, under the condition that they are automated or that data could be obtained for an extended set of reactions. The coverage and automation of each technique is compared and discussed. The performance for each oxidation reaction is discussed at room temperature.

This new tool extends its application scope to various substitution types, and thus can be adequate for use on a large number of compounds as input into atmospheric models. The general utility of the developed tool is combined with an open-source availability allowing contribution for improvements by any user. The accessibility of the tool to the modeling community, its facilitated use and running are of importance in situations where models lack experimental data.

The application of this tool is tested on a database of atmospherically relevant oxidation products, generated from the oxidation of α-pinene, *n*-decane, and toluene using the GECKO-A mechanism (Isaacman-VanWertz and Aumont, 2021). The reaction rate coefficients for the thousands of oxidation products of these three VOCs are predicted using the KINESTEASY tool, and total lifetimes are estimated as an indication of the tropospheric loss. In order to evaluate their impact on air quality, their photochemical ozone creation potential, $POCP_E$ (Jenkin et al., 2017) are calculated and vapor pressures are estimated using Epi Suite (US EPA, 2015). They are all contributing to O_3 pollution, except benzaldehydes, and to SOA formation. The need and usefulness for estimation techniques such as the tool developed in this chapter is strengthened.

Résumé du chapitre IV

Le chapitre IV se concentre sur le développement et l'application d'un nouvel outil pour prédire les coefficients de vitesses de l'oxydation de divers types de composés organiques volatils (COVs) insaturés par différents oxydants atmosphériques. Dans l'introduction et dans la première section, les différentes approches SAR utilisées dans la communauté de la chimie atmosphérique sont présentées, et les limites de ces méthodes sont soulignées. Ces limites incluent la nécessité d'un outil de prédiction plus complet qui puisse être extrapolé à de nouvelles espèces multifonctionnelles.

La nouvelle paramétrisation développée dans ce travail est présentée en détail dans la première section. Cette méthode utilise des informations *a priori* décrivant les propriétés électroniques et stériques de chaque molécule, obtenues à l'aide de méthodes de calcul théorique, telles que la théorie chimique quantique (DFT) ou des outils semi-empiriques (PM6), et les met en corrélation avec la réactivité, pour une large gamme d'atomes CHNOPSX contenant des COVs insaturés. Il s'applique aux quatre principaux oxydants troposphériques, OH, Cl, NO_3 et O_3, et est intégré en tant qu'outil automatisé (que nous appelons KINESTEASY) facile à utiliser et rapide. Les performances de cette SAR sont comparées à celles de la méthode du chapitre I, ainsi qu'à celles des méthodes existantes, à condition qu'elles soient automatisées ou que des données puissent être obtenues pour l'ensemble des composés étudiés. La couverture et l'automatisation de chaque technique sont comparées et discutées. Les performances de chaque réaction d'oxydation sont examinées à température ambiante. Ce nouvel outil étend son champ d'application à divers types de substitution, et peut donc être utilisé pour un grand nombre de composés en tant que données d'entrée dans les modèles atmosphériques. L'utilité générale de l'outil développé est combinée avec une disponibilité de source ouverte pour les modèles, permettant à tout utilisateur de contribuer aux améliorations. L'accessibilité de l'outil à la communauté des modélisateurs, son utilisation et son fonctionnement facilités sont importants dans les situations où les modèles manquent de données expérimentales.

L'application de cet outil est testée sur une base de données de produits d'oxydation pertinents pour l'atmosphère, générés à partir de l'oxydation de l'α-pinène, du *n*-décane et du toluène en utilisant le mécanisme GECKO-A (Isaacman-VanWertz et Aumont, 2021). Les coefficients de vitesse de réaction pour les milliers de produits d'oxydation de ces trois COVs sont prédits à l'aide de l'outil KINESTEASY, et les durées de vie totales sont estimées comme indication de la perte troposphérique. Afin d'évaluer leur impact sur la qualité de l'air, leur potentiel de création d'ozone photochimique, $POCP_E$ (Jenkin et al., 2017) est calculé et les pressions de vapeur sont estimées à l'aide d'EPI Suite (US EPA, 2015). Ils contribuent tous à la pollution par l'O_3, à l'exception des benzaldéhydes, et à la formation d'aérosols organiques secondaires. La nécessité et l'utilité de techniques d'estimation telles que l'outil développé dans ce chapitre sont renforcées.

Introduction

As discussed previously, measuring the reaction rate coefficients of the various and numerous unsaturated organic compounds found in the atmosphere can represent a challenge (see Chapter I and III). This requires some predictive techniques in order to derive rapid estimates to input in atmospheric chemical models. The electrophilic addition of tropospheric oxidant to UVOCs is a major initiation pathway of their atmospheric degradation (see Chapter I). At room temperature, the past SAR presented in Chapter II performs generally well to predict the electrophilic addition reaction rate coefficients of CHX alkenes with OH, Cl, NO_3 and O_3 but is limited to a subset of CHX alkenes and would require substantial work to extend it to apply to alkenes with more substitution types (Michelat et al., 2022). Additionally, this SAR relies strongly on the availability of experimental data and is using only purely fitting parameters, that do not contain much physico-chemical and mechanistic information. As observed in the previous chapter III, the volatile organic species that are present in the atmosphere are more varied than the CHX alkenes, and can contain a variety of substitution types (e.g., O, N, S and P substituents) and structures (e.g., furans and pyrroles) that are not covered by this SAR.

This motivates the development of a new tool to predict these electrophilic addition reactions for a comprehensive panel of UVOCs as those encountered in atmospheric chemical mechanisms. In this Chapter, a new SAR approach has been built in order to include the reaction of the 4 main tropospheric oxidants (OH, Cl, O_3, and NO_3) with a larger variety of alkenes and polyalkenes, including CHNOPSX substitution types, with X=F, Cl, Br, I. To predict these electrophilic addition reactions, the existing SARs are generally based on the group-additivity approach based on the original work of (Kwok and Atkinson, 1995) and its most recent updates, the perturbation frontier molecular-orbital (PFMO) or the diagonal-substitution patterns approach from Tokuhashi et al. (2021) and updates from (Michelat et al., 2022).

The **group-additivity approach** of (Kwok and Atkinson, 1995), described in Chapter II, section II-3.1.1. (Atkinson, 1997, 1988, 1987, 1986; Kwok and Atkinson, 1995) which uses the group contribution method, by dividing a molecule into its substituents and bonds and their bonded substituents, and distinguishes them by type of atom and functionality. Fitting factors are created for each group of substitution/functionality and optimized in order to correlate with kinetic data from measurements. Individual rate coefficient for the components is summed to equal the total rate coefficient for the reaction of electrophilic addition of OH with CHNOPSX compounds, where X=F, Cl, Br, I. More details can be found in the original work of Atkinson and co-workers (Atkinson, 1997, 1988, 1987, 1986; Kwok and Atkinson, 1995). This method has been implemented in an automated tool, EPI (Estimation Programs Interface) Suite, that is easy to use, rapid and computer-time efficient. Its interface can easily be used in batch-mode (Meylan and Howard, 1993). EPI Suite provides k_{O3} for addition and k_{OH} rate coefficients for the electrophilic

addition and H-abstraction pathways, among other values. The workflow of the automated tool is presented in Figure IV-46.

The updates of the SAR of Kwok and Atkinson are derived for reaction with OH, NO$_3$ and O$_3$, many of which are gathered in the Generator for Explicit Chemistry and Kinetics of Organics in the Atmosphere (**GECKO-A**) software package mechanism (http://geckoa.lisa.u-pec.fr/), (Aumont et al., 2005) and are continuously updated as part of the MAGNIFY project for mechanism development (http://www.lisa.u-pec.fr/fr/20-projets/projets/1234-magnify). For UVOCs reactions, GECKO-A predicts k_{OH} + CHON alkenes and aromatics (Aumont et al., 2005; Jenkin et al., 2018; Kwok and Atkinson, 1995), k_{NO3} and k_{O3} + CHON alkenes and polyalkenes (Aumont et al., 2005; Carter, 2000, 2021; Jenkin et al., 2020, 1997; Kerdouci et al., 2014, 2010), but not k_{Cl}. More details on these updated SARs can be found in the work of the authors, but are not detailed here since they are not available in an automated way to date.
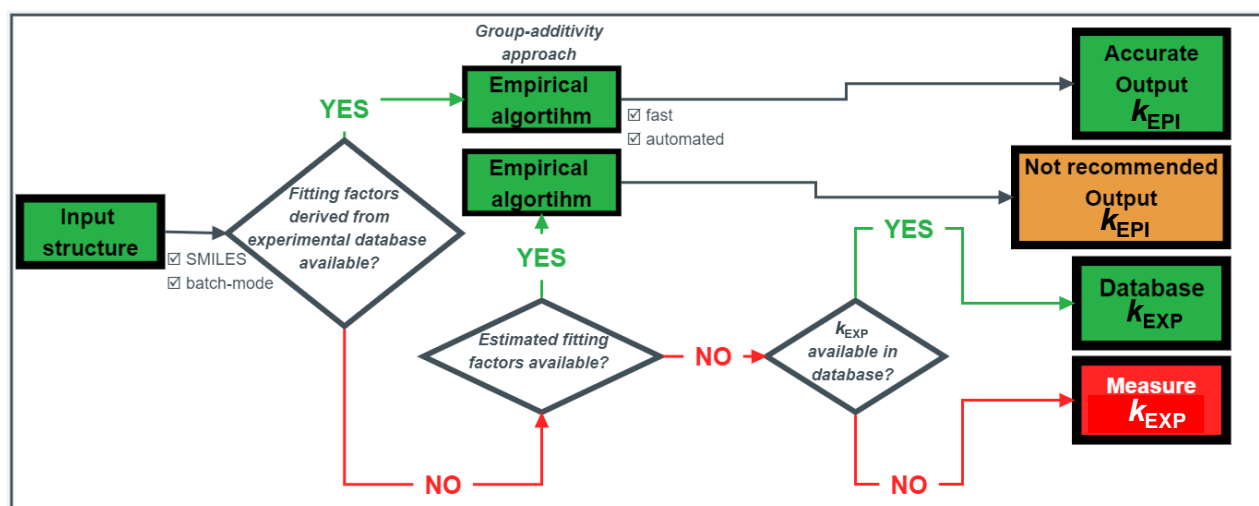
Figure IV-46 : Workflow for the EPI Suite tool (Meylan and Howard, 1993). Red cells are time and/or workload limiting steps, while green cells are automated and/or rapid steps. Steps in orange are rapid steps that rely on estimated adjustment factors and therefore render a non-recommended value for the rate coefficient studied, as indicated by the authors in the EPI Suite software manual (US EPA, 2015).

The **perturbation frontier molecular-orbital** (PFMO) method (King et al., 1999a, 1999b) correlates a molecular property of the compound, the orbital energies, to the total reactivity (King et al., 1999a, 1999b; Pfrang et al., 2007, 2006a, 2006c, 2006b, 2006b). The PFMO calculates the HOMO–LUMO/HOMO–SOMO gap (i.e., energy differences between the HOMO, *highest*, LUMO, *lowest*, or SOMO, *singly occupied molecular orbitals*) as a source of a priori information on the electronic structure of the molecule, and derive fitting factors by optimizing the prediction against experimental rate coefficients. However, PFMO relies on the validity of the linearity of the relationship between ln(k) and the orbital energy gaps or E$_{HOMO}$, which is generally applied to limited ranges of functionality and E$_{HOMO}$ (e.g., King et al., 1999a). This method focuses on the impact of a single electronic parameter on the reactivity, excluding any contribution of

additional electronic or steric effects, which may play an important role in electrophilic addition mechanisms. No automated software is currently available to the best of our knowledge.

The **diagonal-substitution patterns approach** that was presented in Chapter II, section II-2.1.2 and II-2.2 that applies to the oxidation of CHX alkenes (Michelat et al., 2022; Tokuhashi et al., 2021). At room temperature, this method provides OH, Cl, NO_3 and O_3 addition rate coefficients to CHX and was successfully extended to temperature dependence estimations for reactions of OH and NO_3. This method relies on experimental data on diagonal substitution patterns to derive its substituents factors, and on the availability of k(T) data to derive its Arrhenius parameters. However, there is a wide variety of structures and types of substitution within the class of BBVOCs compounds undergoing electrophilic addition, which can sometimes present an experimental challenge to investigate, as discussed in Chapter III. The SAR presented in Chapter II (Michelat et al., 2022) applies only to alkenes and CHX rings, with X=F, Cl, Br, thus excluding a wide variety of important BBVOCs (e.g., furans, oxygenates, nitrates). It is consequently necessary to extend its applicability to a wider range of functionalities. The workflow is presented in the Figure IV-47.
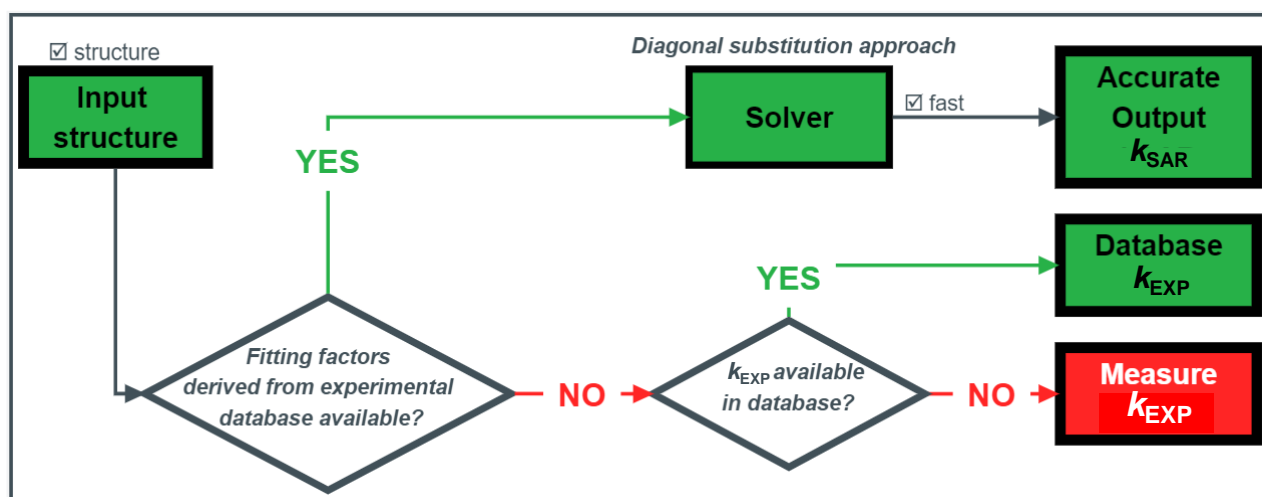
Figure IV-47 : Workflow for the SAR from (Michelat et al., 2022). Red cells are time and/or workload limiting steps, while green cells are automated and/or rapid steps.

The Figure IV-46 and Figure IV-47 highlight one key limitation of the method of Atkinson and co-workers (Atkinson, 1988, 1987, 1986; Kerdouci et al., 2014; Kwok and Atkinson, 1995) and our recent method based on diagonal substitution patterns (Michelat et al., 2022; Tokuhashi et al., 2021): they require extensive experimental data to derive fitting factors used to predict the addition rate coefficients. The predictive ability is good when sufficient kinetic data is provided to represent a class of compound. However, this is one of the limitations of current SARs. The predictions of well-studied class of compounds (e.g., alkyl substituted alkenes, some oxygenates) are accurate since the SARs are constrained with a large and

accurate dataset. However, there is a need to provide estimates for the less studied classes of compounds (e.g., low vapor pressure, less reactive, nitrates, highly oxidized, reactions with understudied oxidants such as NO_3, O_3 or Cl). This is where the SARs in Figure IV-46 and Figure IV-47 may be lacking data. As a result, these SARs may not be able to provide an estimate or provide it with large uncertainties since the fitting procedure is purely mathematical. As a result, the fitting factors may therefore not contain the information needed to predict the reactivity of compounds against which it has not been constrained. Hence, the extrapolation and application to new compounds understudied or with less accurate kinetic data may be less accurate and reliable, even though these SARs predicts well-trained classes of compounds with an excellent accuracy. As discussed above for PFMO, the fitting factors can be a representation of electronic effects, but may exclude some additional steric or electronic parameters.

The above-mentioned fitting factors are significantly dependent on the availability and accuracy of experimental data, and have no physico-chemical meaning. This is why there is a need for a new SAR method that is using physico-chemical properties of the structure of the studied VOC in order to input some *a priori* information in the optimization of the fitting factors. Also, there is the need to rely less on experimental data, which could be solved by using theoretical calculations.

However, as discussed in Chapter I, the electrophilic addition reaction is considered to be influenced by several factors including electron density, electron delocalization, and steric effects on the UVOC undergoing the addition (Calvert et al., 2000; Vereecken et al., 2018). It is noted that Cl is an atom while the others are radicals or a molecule with much larger sizes and dipole moments that will also influence the interactions. Thus, an attempt is made in this new parametrization to describe both the electronic and steric effects (i.e., steric hindrance, steric strain and steric repulsion) that would impact the electrophilic addition reaction of UVOCs.

To obtain new parameters based on physico-chemical properties, orbital energies and steric descriptors are calculated using a computationally efficient semi-empirical method, PM6, and benchmarked against density functional theory (DFT) calculations. It is noted that even if the absolute accuracy in energetics is not all that accurate, DFT calculations will represent the relative trends amongst the molecules. These parameters are combined in a multivariate linear regression that estimates site-specific rate coefficients, k_{addCi}, that are then summed on all carbon addition sites C_i to obtain the total addition rate coefficient, k_{add}. The H-abstraction reaction rate coefficient, k_{abs}, is estimated when relevant using prediction techniques described in the main text, and summed with addition rate coefficient provides the total reaction rate coefficient of the molecule, k_{pred}.

Since these calculated data are a source of *a priori* information in our predictions, this parametrization aims to be less dependent on well-trained structures in the SAR training set, and, hopefully, less affected by inaccurate data or poorly constrained substitution factors. The scope of the application of the method is then extended to any type of substitution within CHONPSX unsaturated compounds, under the assumption that the electronic structure of their constituent atoms is adequately described by our computational method. This covers a large variety of organic compounds that are encountered in the atmospheric field. As mentioned above for the other SARs presented, the classes of compound covered is generally limited to specific species or reactions. They do not cover the whole range of substitution types. Extending these approaches to more complex substitutions, such as highly oxidized molecules that are poorly constrained by available kinetic data, can be challenging and may be less reliable if using methodologies that are not yet as generalized. Additionally, the class of compounds with fewer predictions, such as furans, oxygenates, pyrroles, nitrates, sulphur- and phosphorus-containing species can be of importance in the atmosphere. Yet, data for atmospheric models are lacking. It is intended that better calculations of energies and other properties would enhance this approach in the future.

Tools described in this chapter aims to provide an approach that applies to a broad spectrum of compounds of interest to atmospheric chemistry. To enhance the generality of the approach, the correlations are derived from a diverse and comprehensive kinetic dataset to minimize the potential inaccuracies that may arise from extrapolating the SAR beyond its training set. This tool is built using physical principles, and trained with a large variety of input data. Therefore, it is suggested that they can be robust tools in estimating rate coefficient of UVOCs encountered in atmospheric chemical models.

In this work, the method developed is different than previous SARs described above for two reasons: (1) the energetics of the molecule under study are calculated using DFT or semi-empirical tools (PM6), and (2) the buried volume (%Vbur) variable is employed as a new concept assumed to be a measure of the steric effects. The source of *a priori* information input in this method is coming from DFT that directly calculates the properties of a molecule and provides a reliable tool for quantifying the electronic properties of a panel of different molecules. This method has two advantages compared to other SARs: (1) it relies on physical insights and not only on mathematical fittings, (2) it aims to extend the predictive ability to any molecule and radical that could undergo electrophilic addition, aiming to be a universal tool. However, it is noted that observations are still required to tie down the calculations, and this SAR is not completely independent on measurements since experimental kinetic data is required to anchor it. This raises the following questions. Is it possible to reduce the amount of experimental data needed to optimize the SAR parameters? How well does it compare with previous approaches?

Apart from EPI Suite, (US EPA, 2015) no automated software is provided to the scientific community for the SARs applicable to extensive lists of molecules. In this chapter, these challenges on the coverage of SARs, their automation and ease of use are addressed by providing a user-friendly, rapid, and automated tool to predict rate coefficients of CHNOPSX compounds oxidation. Our goal is to provide a tool accessible for all users, regardless of their expertise in kinetics or computational chemistry. The current version of this SAR is specifically optimized for room temperature rate coefficients of the electrophilic addition reactions of CHNOPSX unsaturated volatile organic compounds with OH, Cl, NO_3 and O_3 oxidants.

The parametrization of our SAR is based on *a priori* information on the molecular properties of the UVOC that are correlated to the rate coefficient data. The parametrization is optimized using experimental data from a comprehensive database for the reactions with each oxidant (McGillen et al. 2020). The tool employs automated and efficient quantum chemical calculations to derive variables that describe physical and mechanistic aspects. This approach differs in its principle from existing SARs, and is intended to complement existing methodologies for rate coefficient estimation, thereby assisting efforts in atmospheric chemical modeling.

IV-1.   SAR approaches

In this section, a new parametrization based on a multivariate linear regression from calculated variables accounting for electronic and steric effects has been developed. It applies to a variety of compounds, is fully automated, and gives site-specific kinetic data. The molecular properties inputted in the parametrization are calculated for each molecule using two different quantum chemical calculation methods, density-functional theory (DFT) or semi-empirical tools (PM6) and these two tools are described in the following sections IV-1.1.1 for DFT and IV-1.1.2 for PM6. In the section Results and discussion IV-2, the performance of each method will be discussed and compared to other existing methods mentioned in the Introduction of this chapter.

IV-1.1.   Theoretical calculation-based methods

The SAR method based on quantum chemistry in this work aims to provide a tool similar to EPI Suite by being efficient, easy to use and broadly applicable. As outlined in the chapter I, electrophilic addition reactions are influenced by several parameters, including electron density and steric effects, which are aimed to be parameterized in this SAR.

The E_{HOMO} of the π orbital involved in the reaction was calculated to quantify the effect of electron density, which allowed the derivation of a site-specific parameterization. However, for conjugated system undergoing electron delocalization, a parameterization representing the combination of these orbitals

from E_{HOMO}(molecule) and the number of conjugated bonds was derived, as explained in section IV-1.1.3. The buried volume, %Vbur, was calculated to describe steric effects, since it represents the percentage of the total volume of a sphere of specific radius, $r_{\%Vbur}$, in Angström, centered on an atom (C_i or C_j) occupied by the substituents (see Figure IV-48). The greater the buried volume, the more the electrophile encounters difficulty in approaching the reactive site, thereby reducing the reactivity on that side of the double bond. It can be observed in Figure IV-48 that the distribution of the %Vbur of $r_{\%Vbur}$=6Å and $r_{\%Vbur}$=3.5 Å is spread out over a narrow range of values (%Vbur from 6% to 37%) and is gaussian, similar to the buried volumes of radius 3.5 Å, except that the latter vary over a larger range (%Vbur from 29% to 86%), which makes it more selective between different species. The distribution of the %Vbur of $r_{\%Vbur}$ 2.5Å (%Vbur from 62% to 88%), but displays an almost bimodal distribution, which distinguish more strongly between species with smaller or larger alkyl group (cf. Figure App-IV-1 where tetrachloroethene, compound 2, is in the group of larger values while ethene, compound 1, or (4E)-1,4-hexadiene, compound 2, are part of the smallest values). The choice of a larger buried volume radius allows a better distinction of longer chain compounds, for which steric effects may be more important in O_3 and NO_3 reaction (cf. compound 3 and compound 4 getting more distinguished when using $r_{\%Vbur}$ of Å compared to 2.5Å and 3.5Å in Figure App-IV-1). Chemical intuition can help in selecting the %Vbur.

To parameterize the non-bonded repulsion between a substituent and an approaching electrophile, Pauling electronegativities are used, with higher values corresponding to greater repulsive effects. The molecular geometries, steric descriptors and orbital energies used in this work were calculated with two different computational methods, DFT (IV-1.1.1) and the less expensive semi-empirical PM6 method (IV-1.1.2). The parameterization is detailed in the section IV-1.1.3.
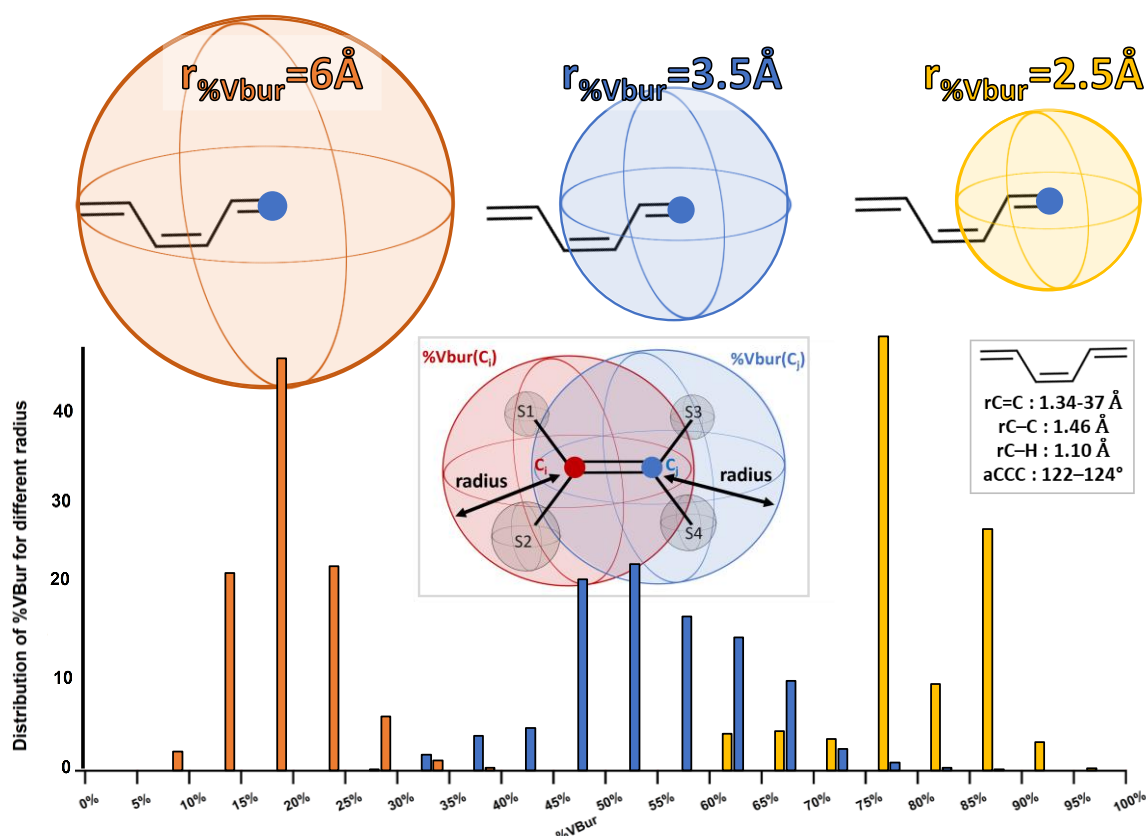
<u>Figure IV-48 :</u> Statistical distribution of buried volumes, %Vbur, for radius of 2.5, 3.5 or 6 Angströms. Inset (middle): Diagram of buried volume (%Vbur) centered on C_i (red) or C_j (blue). The radius varies according to the oxidant and the data set described. The larger $r_{\%Vbur}$, the more %Vbur is expected to describe the steric hindrance effect due to the crowding of substituents attached to the double bond, whether a single atom or a group of chained atoms. Inset (right-hand bottom): Bond lengths for the example molecule, (Z)-hexa-1,3,5-triene, are taken from the CCCBDB database (accessible at https://cccbdb.nist.gov/expgeom2x.asp?casno=2612466) (Johnson, 2022). These are assumptions on the buried volume variable and the choice of the $r_{\%Vbur}$ remains an arbitrary choice.

IV-1.1.1. <u>DFT calculations*</u>

The theoretical calculations I conducted in this chapter were carried out at Colorado State University, Fort Collins, USA, in collaboration with the Computational Chemistry research group headed by Prof. R. Paton, as part of my three-month visit to CSU.

In this work, density functional theory (DFT) level calculations are performed using the ωb97xd functional and the def2-TZVP basis set to study the electronic properties of a selected set of compounds (Chai and Head-Gordon 2008; Weigend and Ahlrichs 2005). The Gaussian 2016 software package is used to carry out the calculations, which enables the optimization of the molecule geometry and the calculation of a variety of electronic properties, including orbital energies, and steric descriptors (Frisch et al., 2016). Since the dataset contains halogenated species, the def2-TZVP basis set was used as it contains diffuse functions that

are useful to describe the electronic properties for molecules with extended π-systems or heavy atoms (Weigend and Ahlrichs 2005).

The computational chemistry auxiliary programs CREST, xTB and CENSO were used for conformer sampling, enabling efficient generation of conformer sets (Grimme et al., 2021, 2017; Pracht et al., 2020). After optimizing geometry and frequencies using the Gaussian package, the lowest-energy conformer has been selected and natural bond orbital (NBO) calculations performed, to obtain the π-orbital energy, E_{HOMO}, for a selection of monoalkenes. The buried volumes were calculated with a radius of 3.5Å using the DFT-based python package DBSTEP (Luchini et al., 2022). Different values of $r_{\%Vbur}$ in the range 2–6Å were tested and the value of $r_{\%Vbur}$=3.5Å has been selected since it provided the most optimized parametrization for the class of CHX compounds under study.

The results were compared with experimental data for a collection of 160 substituted alkenes. Additionally, energies were compared to those calculated from other levels of theory (PWPB95-D4/def2-QVPPD) as well as the DLPNO-CCSD(T1)/CBS(2,3/def2) coupled cluster method for 1,1,1,4,4,4-hexafluoro-trans-2-butene, all of which showed good agreement (Chai and Head-Gordon 2008; Riplinger et al. 2013). The combination of the ωB97X-D functional and the def2-TZVP basis set provides accurate results for the chemical systems studied, and this level of theory has not been upgraded to a cost-effective method, as this was beyond the scope and needs of this study. DFT approaches are widely used due to their good performance and computational efficiency, but their use for large sets of compounds remains computationally expensive, requires access to supercomputers and increases the workload due to non-automated computational steps (see the multiple red boxes in Figure IV-49).
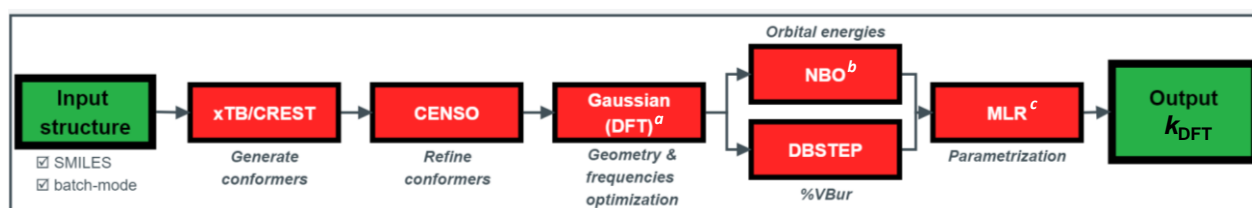
Figure IV-49 : Workflow for the DFT-based tool with red cells being time and/or workload limiting steps, and green cells being automated and/or rapid steps. [a] Density Functional Theory [b] Natural Bond Orbital [c] Multivariate linear regression

IV-1.1.2.   PM6 calculations

To reduce computational costs, the semi-empirical PM6 method available in the MOPAC2016 program was used to perform analogous calculations (Stewart, 2007). Although the PM6 method is not as accurate as more advanced quantum mechanical methods, it can be useful to rapidly screen a large number of compounds, or to study systems that are too large or complex for more precise methods. To do this, semi-empirical methods combine experimental data or *ab initio* calculations if no data are available, to quickly

calculate a variety of properties. The semi-empirical PM6 method uses parameterizations based on simplified Hartree-Fock calculations, which means that empirical corrections (i.e., derived from experimental data) are applied to Hartree-Fock theory in an aim of improving the performance of the calculations, as well as additional approximations (see (Stewart, 2007)). PM6 is a re-parameterization of the Neglect of Differential Diatomic Overlap (NDDO) method. NDDO is an integral approximation which neglects all two-electron integrals involving two-center charge distributions (i.e., this is a Zero Differential Overlap (ZDO) method). In PM6, modifications affecting the way the definition of the core-core interaction are applied. See more details on PM6 and NDDO in the work of the authors (Stewart, 2007).

The 3D coordinates are generated from the SMILES input list using the Open Babel package (O'Boyle et al., 2011) and its integrated fragment-based coordinate generation framework (Yoshikawa et Hutchison 2019). The optimized geometry coordinates and orbital energies are calculated using MOPAC2016 with the following commands: "AUX LARGE CHARGE=0 SINGLET PM6 SUPER LOCAL". More details on the keywords are available on the MOPAC website (http://openmopac.net/manual/allkeys.html). The RDKit Python library is used to identify the unsaturated carbon-carbon bond(s) present in the molecules, as well as their respective atomic indices, and the script retrieves the orbital energies corresponding to the highest occupied π-molecular orbital energies, E_{HOMO}(π-orbital), of the double bond of interest, and of the whole molecule, E_{HOMO}(molecule), from the output files of the MOPAC2016 calculations. The buried volume calculations are carried out using the python package MORFEUS (https://github.com/digital-chemistry-laboratory/morfeus). All these steps are automated in the final script (KINESTEASY-tool.zip).

The main advantage of MOPAC2016 is its complete automation, that was implemented in the form of a Python program here (see the green boxes which are automated steps in a python script, Figure IV-50). The calculation process is fast (a few seconds for 100 small molecules <C_{10} on an ordinary desktop computer with CPU=2.40GHz), and even if speeds are reduced for larger molecules with a higher number of electrons (a few minutes in some cases), it requires significantly less computation time than the DFT calculations for the same molecule (computational time of minutes (small molecule) to several hours (large molecules) using a large cluster (8 processors, memory 16GB with 2GB/core)).

As shown in the Figure IV-51 comparing calculated E_{HOMO}(molecule) and %Vbur values using DFT and PM6, the less computationally expensive approach correlates well with DFT values (R^2=0.84 and 0.79 respectively). The greatest difference in E_{HOMO} calculation is up to 2.27 eV, for fluoroethene, and PM6 values tend to be lower than DFT values on average. The E_{HOMO} value calculated for fluoroethene are -10.8068 eV using PM6 and -8.53485 eV using DFT, and the CCCBDB database lists values calculated between -10.3 and -10.5 eV using coupled cluster theory with different basis sets (https://cccbdb.nist.gov/) (Johnson, 2022). This result is closer to the PM6 value. Some other main outliers in the E_{HOMO} calculations have been

compared to the values calculated with higher level of theory (coupled clusters) when available and it appears that they are generally in better agreement with PM6 values. This suggests that the discrepancies do not come from the level of theory. Also, these results suggest that PM6 is robust and provides sufficiently accurate values for the purposes of this study, given that the use of a higher level of theory or specific methods for each compound is beyond the scope of this work. The DBSTEP and MORFEUS calculations of the buried volumes are in good general agreement, as shown in Figure IV-51a. The outliers can be attributed, in both %Vbur and E_{HOMO} correlation between PM6 and DFT, to the geometry optimization that varies from one method to another. Any systematic differences are being accounted for in the fitting coefficients that have been optimized for each oxidant parametrization.
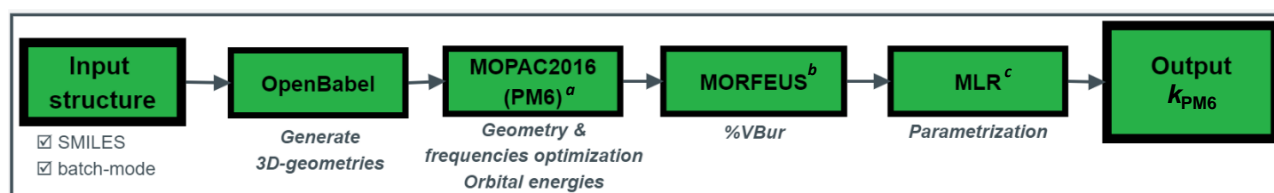
Figure IV-50 : Workflow for the PM6-based tool with green boxes being the rapid and automated steps combined in one unique Python script. The PM6 calculations are faster than those from DFT (see workflow in Figure IV-49). [a] Parametric method (PM6) using experimental and ab initio data [b] Python package [c] Multivariate linear regression
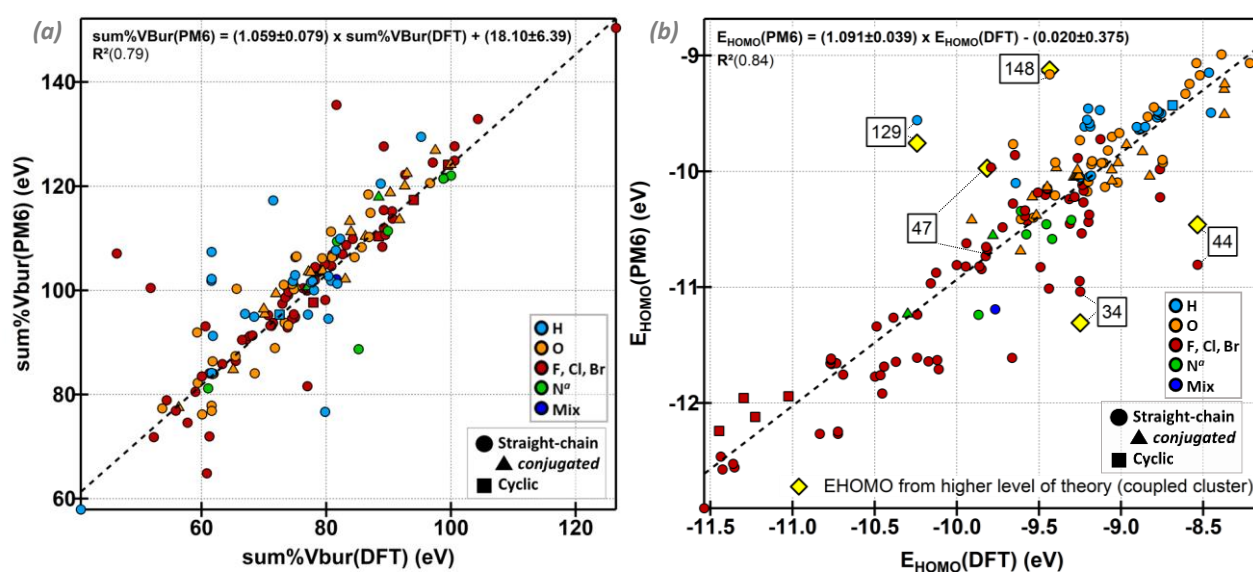
Figure IV-51 : Panel (a): The highest occupied molecular orbital energy (E_{HOMO}) from DFT- and PM6-calculations, in eV. Panel (b): the sum of the buried volumes on carbon C_i (%Vbur(C_i)) and C_j (%Vbur(C_j)) of the same double-bond x, in %, from DFT- and PM6-calculations. The substitution types are C_nX_m where n is no limited, and m=2n+1 and X includes H, O, F, Cl, Br, I, N, or a mix of these. Some major outliers for which coupled cluster calculations of the E_{HOMO} were available on the CCCBDB database (https://cccbdb.nist.gov/, (Johnson, 2022)) are identified on the panel (b), and the associated value is plotted in a yellow diamond. The structures and level of theory/basis set chosen are as follows: (34) 1,1-difluoroethylene, C=C(F)F, CCSD(T)/6-31G*; (44) vinyl fluoride, C=CF, CCSD(T)=FULL/def2TZVPP; (47) ethene, C=C, CCSD(T)=FULL/6-31G*; (129) 1-butene, C=CCC, CCSD(T)=FULL/def2TZVPP; (148) ethoxyethene, C=COCC, CCD/6-31G*. For each compound the value obtained from the higher

level of theory available in the database was chosen. It is observed that coupled cluster calculations are in better agreement with PM6 values than with DFT values for the outliers. This suggests that the outliers are not due to the level of calculations.

IV-1.1.3.   Parametrization

The predictions of the rate coefficients in this work are parametrized by a multivariate linear regression (MLR). This MLR is a function of the electronic and steric parameters calculated for each carbon site where the addition of the oxidant occurs, as illustrated in Figure IV-54. The reaction rate coefficient for the carbon site C_i is calculated from the orbital energy of the reactive π-orbital in which C_i is involved with another carbon C_j, $E_{HOMO}(C_iC_j)$, the buried volume centered on carbon C_i, %Vbur(C_i), and additional parameters accounting for electron delocalization in the system and the structure of the molecule.

The predicted total rate coefficient for the reaction of an oxidant with an UVOC, k_{pred}, is defined as:

$$k_{pred} = k_{add} + k_{abs} \text{ (Eq. IV-22)}$$

where k_{abs} is the H-abstraction rate coefficient and k_{add} is the predicted total addition rate coefficient. The methods to estimate k_{abs} and k_{add} are described below in sections IV-1.1.3.1 and IV-1.1.3.2.

IV-1.1.3.1. Estimation of the H-abstraction rate coefficient, k_{abs}

The EPI Suite tool is used to estimate the H-abstraction rate coefficient for OH, $k_{abs,OH}$, without modification. No estimation techniques provide automated H-abstraction rate coefficients for Cl reactions, but since it can represent a significant contribution to the total reaction rate coefficient, it was estimated in this work based on the OH-Cl correlation method for alkanes reactivity (Wallington et al., 1988). To do so, the natural logarithm of the rate coefficients for OH, $k_{abs,OH}$, are correlated to those of Cl, $k_{abs,Cl}$, for a dataset of alkanes (see Table App-IV-1 And Table App-IV-2 in Appendices section App-IV-1.2) for which only abstraction occurs (see Figure IV-52).

Longer chain alkanes (>C_6) and cyclic alkanes appears to reach a plateau in the correlation Figure IV-52, which corresponds to the collision limit of the H-abstraction pathway by Cl. To avoid overestimating the $k_{abs,Cl}$ rate coefficient (see Appendices section App-IV-1.2), a limit was set to the OH rate coefficient of 3.1×10^{-12} cm^3 molecule^{-1} s^{-1} which is the lowest value of the plateau. This value corresponds to a value for the rate coefficient of the H-abstraction by Cl of $k_{abs,Cl,lim} = 2.3 \times 10^{-10}$ cm^{3}molecule^{-1}s^{-1}. Then $k_{abs,Cl}$ can be estimated in our algorithm using the $k_{abs,OH}$ from EPI Suite and the equation on Figure IV-52, as follows:

$$k_{abs,Cl} = \exp(1.82 \times \ln k_{abs,OH} + 26.05) \text{ (Eq. IV-23)}$$

$$\text{If } k_{abs,OH} > k_{abs,OH,lim} = 3.1 \times 10^{-12} \text{ cm}^3 \text{ molecule}^{-1} \text{ s}^{-1}$$

$$\text{Then, } k_{abs,Cl} = k_{abs,Cl,lim} = 2.3 \times 10^{-10} \text{ cm}^3 \text{ molecule}^{-1} \text{ s}^{-1}$$

where $k_{abs,OH,lim}$ and $k_{abs,Cl,lim}$ are the exponential of the natural logarithm values of $\ln k_{abs,OH,lim}$ = -26.5 and $\ln k_{abs,Cl,lim}$ = -22.2, the limiting values of the plateau of the correlation in Figure IV-52.
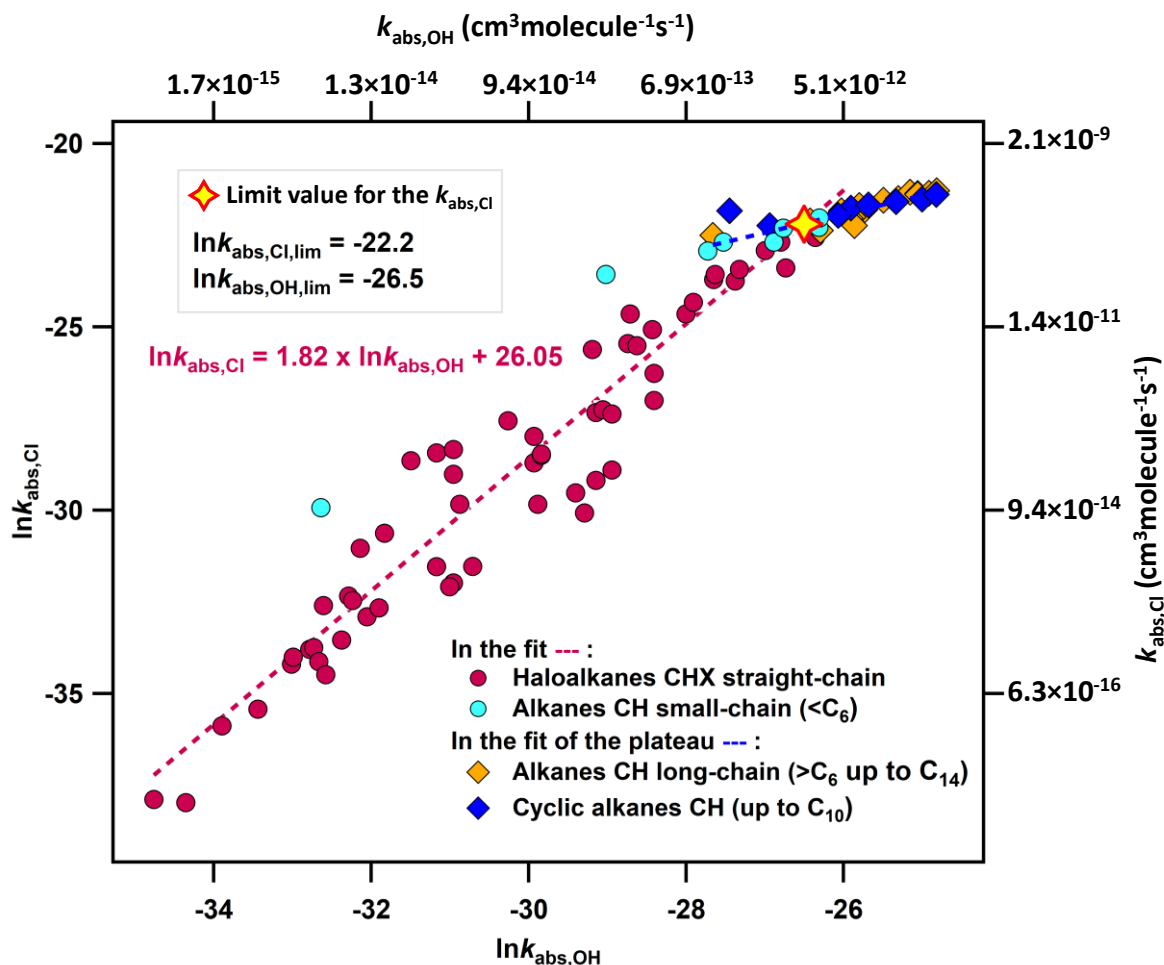
Figure IV-52 : Correlation OH-Cl for the H-abstraction reaction of a selection of alkanes (McGillen et al. 2020). The plateau is associated with the collision limit reached for the Cl reaction and potential effect of other processes than H-abstraction for longer-chain alkanes and cyclic alkanes. It is observed that these compounds are not following the same OH-Cl correlation compared to the other haloalkanes. These are not included in the fit of the OH-Cl correlation used in this chapter.

As with the Cl reaction, no automated tool provides H abstraction rate coefficients for the NO_3 reaction, however, abstraction is thought to be important only for hydrogen bonded to aldehydes, with weak C-H bond (Ren et al., 2021). Hence, a simple estimation technique was developed to estimate the total abstraction rate for the whole molecule, $k_{abs,NO3}$, by counting the number of aldehydic hydrogen atom, $N_{ald,H}$, and multiplying by an optimized base rate coefficient value $k_{abs,H}$=1.18×10^{-15} cm³molecule^{-1}s^{-1} per H abstracted by NO_3:

$$k_{abs,NO3} = N_{ald,H} \times k_{abs,H} \text{ (Eq. IV-24)}$$

IV-1.1.3.2. Estimation of the total addition rate coefficient, k_{add}

The predicted total addition rate coefficient, k_{add}, is calculated as:

$$k_{add} = \sum_{x=1}^{n} (k_{Ci,x} + k_{Cj,x}) \quad \textbf{(Eq. IV-25)}$$

with n being the number of $C_i=C_j$ double-bonds in the molecule, and $k_{Ci,x}$ or $k_{Cj,x}$ the site-specific electrophilic addition rate coefficient to the carbon C_i or C_j of the xth double-bond (Figure IV-54), defined as follows for atom C_i assuming that the contributions are mostly multiplicative:

$k_{Ci,x} = \exp[a \times E_{HOMO}(C_i=C_j) + b \times \%Vbur(C_i) + c \times (X_{Pauling(Ci)} + d) \times \%Vbur(C_i) + e] \times F_{structure}$ **for bond x (Eq. IV-26)**

where a, b, c, d, and e are optimized coefficients, $E_{HOMO}(C_i=C_j)$ the highest-occupied molecular orbital energy of the π-orbital of the $C_i=C_j$ double-bond, $\%Vbur(C_i)$ the buried volume centered on the carbon C_i, $X_{Pauling(Ci)}$ the sum of the Pauling electronegativities of the two atoms, S_1 and S_2, directly attached to the carbon C_i, and $F_{structure}$ the multiplication of structural factors. The choice of the buried volume $r_{\%Vbur}$ is arbitrary but has been chosen for each oxidant and dataset by selecting the $r_{\%Vbur}$ value that provided an MLR optimization with the most accurate predictions (Figure IV-48).

This approach essentially depends on energetics for the addition reaction and potential steric effects. To account for the conjugation effect on the π-orbital electron distribution, the $E_{HOMO}(C_i=C_j)$ is defined as follows:

If molecule is conjugated: $\quad E_{HOMO}(C_i=C_j) = (a_{conj} \times (N_{conj}-1) + b_{conj}) \times E_{HOMO}(molecule)$ **(Eq. IV-27)**

If not: $\quad E_{HOMO}(C_i=C_j) = E_{HOMO}(\text{π-orbital}(C_i=C_j))$ **(Eq. IV-28)**

where N_{conj} is the number of double-bonds that are part of the conjugated system, and a_{conj} and b_{conj} are optimized coefficients.

The steric repulsion of the oxidant by the substituents attached to the reactive double-bond was accounted for by the factor $X_{Pauling(Ci)}$, defined as the sum of the $X_{Pauling(Ci)}$ of each atom attached to C_i, so that it will results in $X_{Pauling(S1)} + X_{Pauling(S2)}$ for the example of C_i (see Figure IV-54).

The multiplication of the structural factors, $F_{structure}$, is defined by:

$$F_{structure} = F_{cyclic} \times F_{furan} \times F_{pyridine} \times F_{benzenoid} \times F_{cumulated} \quad \textbf{(Eq. IV-29)}$$

If a molecule contains a specific structure (e.g., a benzenoid cycle), $F_{structure}$ appends the optimized value of the corresponding factor (e.g., $F_{benzenoid}$), otherwise, the factor is equal to 1. Compounds identified as "cumulated" include only those molecules that possess a cumulative C=C=C bond. The optimized structural factors F_{furan}, $F_{pyridine}$, $F_{benzenoid}$ and $F_{cumulated}$ are constants optimized from the fit of the predicted rate coefficients of the addition reaction against the experimental rate coefficients (Table IV-11). For the cyclic structures, a variety of behavior is observed depending on the substitution types. For example, the rate coefficients, k_{OH} in $cm^3molecule^{-1}s^{-1}$, for CHO cycloalkenes as cyclopentene ($k_{OH} = 6.70\times10^{-11}$), 4-methyl-3-cyclohexene-1-one ($k_{OH} = 1.1\times10^{-10}$), azulene ($k_{OH} = 2.73\times10^{-10}$) or α-terpinene ($k_{OH}=3.50\times10^{-10}$) are very

reactive compounds, with $|E_{HOMO}|<11$ eV, while some very less reactive compounds such as CX highly halogenated cycloalkenes, such as 3,3,4,4-tetrafluorocyclobutene ($k_{OH} = 1.08\times10^{-13}$), or perfluorocyclobutene ($k_{OH} = 5.20\times10^{-14}$), tend to have a bigger absolute $|E_{HOMO}|>11$ eV, as shown in Figure IV-53. The same trend is observed when correlating $\ln k_{OH}$ with E_{HOMO} from DFT calculations. A single constant could not describe that variation adequately, hence, the cycle effect is parametrized, F_{cyclic}, as a function of the orbital energy of the molecule, E_{HOMO}, as follows:

$$F_{cyclic} = a_{cyclic}\times|E_{HOMO}(molecule)|+b_{cyclic} \text{ (Eq. IV-30)}$$

where a_{cyclic} and b_{cyclic} are optimized coefficients.
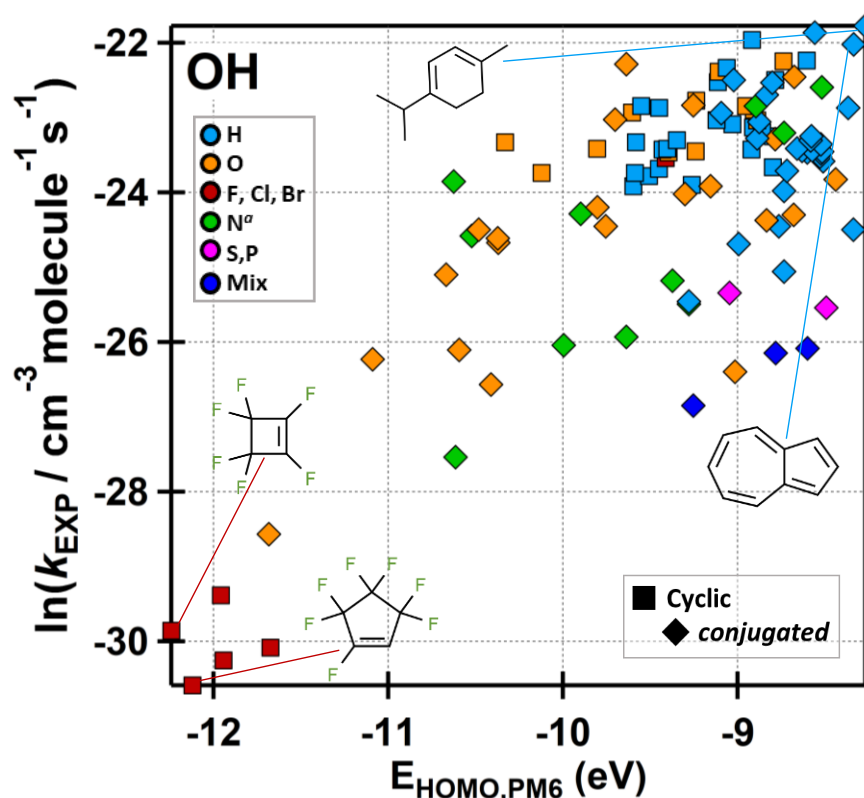
Figure IV-53 : Logarithm of the experimental rate coefficient of the OH reaction with all the cyclic UVOCs present in the kinetic database available, (McGillen et al. 2020) as a function of the calculated E_{HOMO} value of the molecule using PM6 method. The substitution types are C_nX_m where n has no limitation, and m=2n+1 and includes atoms H, O, F, Cl, Br, I, N, S, P or a mix of these atoms. There is an approximate correlation (as E_{HOMO} increases, the rate coefficient k_{EXP} increases), but there is a lot of variability, probably due to other factors such as steric hindrance or complex formation. It is possible that some of these rate coefficients are also affected by the experimental conditions (for example, presence of O_2).

For each oxidant, the coefficients were optimized (see values in Table IV-11) by reducing the relative ratio between the measured, k_{EXP}, and the predicted rate coefficients, k_{Ox}, of the database under study for each case, using a generalized reduced gradient non-linear solver method.

Table IV-11 : Optimized value of the coefficients of the MLR parametrization) for each oxidant studied. The coefficients values are rounded to 1×10^{-5} for a, 1×10^{-4} for b, c, d, a_{conj} and b_{conj}, 1×10^{-2} for e, 1×10^{-3} for a_{cyclic}, b_{cyclic}, F_{furans}, $F_{pyridines}$, $F_{cumulated}$, and $F_{benzenoids}$.

Rounding errors were found to be <0.2%, and are therefore considered to be of minor importance. The significant figures are given to reproduce the fitting of experimental data but are not carrying physical meaning by themselves. The signs and magnitude of these factors are relative to various variables and should not be attributed to a physical meaning of the factor by itself. This parametrization includes multiple parameters to take into account and thus, these fitting factors are so far considered purely mathematical.

Oxidant	a	b	e	a_{cyclic}	b_{cyclic}	F_{furans}	$F_{pyridines}$	$F_{cumulated}$	$F_{benzenoids}$	c	d	a_{conj}	b_{conj}
OH	1.75000	-0.0132	-4.93	-0.036	1.080	0.354	0.066	0.417	0.078	0.0031	4.0685	0.0028	1.0726
Cl	0.82983	-0.0226	-12.46	0.156	-0.484	0.412	0.001	1.966	0.150	0.0013	2.5095	-0.0002	1.0635
NO_3	2.10847	0.0556	-11.49	12.924	-127.140	128.695	0.042	0.219	0.307	0.0475	1.4331	0.0398	1.1611
O_3	0.98000	-0.0208	-21.15	0.131	0.125	1.563	0.620	0.116	1.000	-0.0603	6.5410	0.0263	2.1470

IV-1.1.3.3. Working example and flow diagram

A working example (Figure IV-54) and a flow diagram of the parametrization are presented in this section (Figure IV-55). In Figure IV-54, the reactive C=C double-bond structure is presented, with defined C_i and C_j reactive carbon sites, where i<j, and associated substituents S_{1-4}. The order of the numbering of the substituents (for C_{i-j} and S_{1-4}) is defined by the canonical atom order, as applied in the Python package RDKit and presented in the examples 1 and 2 by the red numbering. The atom indices will be defined the order by which the double-bonds will be numbered, and their respective substituents. For example, in the example 1, the unique double-bond in the molecule is the bond $x=1$, the C_i reactive site is centered on C_3 (i<j and 3<4) and its substituents are in order $S_1=C_2$ and $S_2=N_6$, and the C_j carbon is the atom C_4 with substituents $S_3=C_5$ and $S_4=H_{15}$ (Figure IV-54). In the case of the example 2, the molecule contains two double-bonds, indexed in numerical order, with $x=1$ being the bond $C_0=C_1$ and $x=2$ the bond $C_2=C_3$. The substituents are defined following the same procedure described before, see the Figure IV-54. Then, for each C_i or C_j reactive site of each bond x the variables used in the parametrization defined in sections IV-1.1.3.1 and IV-1.1.3.2 can be calculated, and allows to derive the site-specific rate coefficients using (Eq. IV-27), following the procedure represented in Figure IV-55 and detailed below.

C=C bond x in molecule:	
S_{1-4} = C, H, F, Cl, Br, N, O, S or P	

Ex.1 — bond $x=1$: $C_i, S_1, S_2: C_3, C_2, N_6$; $C_j, S_3, S_4: C_4, C_5, H_{15}$

$E_{HOMO}(C_3=C_4)$
%Vbur(C_3)
$X_{C3} = X_{C2} + X_{N6}$ → $k_{C3,1}$
%Vbur(C_4)
$X_{C4} = X_{C5} + X_{H15}$ → $k_{C4,1}$

Ex.2 — bond $x=1$: $C_i, S_1, S_2: C_0, H_8, H_9$; $C_j, S_3, S_4: C_1, C_2, Cl_7$

$E_{HOMO}(C_0=C_1)$
%Vbur(C_0)
$X_{C0} = X_{H8} + X_{H9}$ → $k_{C0,1}$
%Vbur(C_1)
$X_{C1} = X_{C2} + X_{Cl7}$ → $k_{C1,1}$

bond $x=2$: $C_i, S_1, S_2: C_2, C_1, Cl_6$; $C_j, S_3, S_4: C_3, Cl_4, Cl_5$

$E_{HOMO}(C_2=C_3)$
%Vbur(C_2)
$X_{C2} = X_{C1} + X_{Cl6}$ → $k_{C2,2}$
%Vbur(C_3)
$X_{C3} = X_{Cl3} + X_{Cl4}$ → $k_{C3,2}$

(Eq. IV-26)
(Fig. IV-55)

*Molecule atom indices are obtained from RDKit Python library, that uses the canonical atom order, and i<j for each bond x. Pauling enelctronegativities are noted: $X_{Ci} = X_{Pauling(Ci)}$

Figure IV-54 : Working examples for an alkene as example 1 and a dialkene as example 2, including the definition of the double-bond and substituents under study in a molecule, and variables used in the equations in section IV-1.1.3.2. However, these steps are automated in the KINESTEASY tool.

Starting from the structure of the molecule, the $F_{structure}$ factors will be defined as the multiplication of any F-factor that corresponds to the molecule structure (see flow diagram, purple pathway to $F_{structure}$, Figure IV-55). For example, if the molecule is a furan, then $F_{structure}=F_{furan}$. If the molecule contains both a cycle and an additional benzenoid cycle, then $F_{structure}=F_{cyclic}×F_{benzenoid}$. If the molecule has none of the structure listed, then $F_{structure}=1$.

Starting again from the structure of the molecule, for each double-bond x and its carbons C_i and C_j, the orbital energy (see light-blue pathway to "$E_{HOMO}(C_i=C_j)$", Figure IV-55), and the Pauling electronegativity term (see red pathway to "$X(C_i/C_j)$", Figure IV-55) are calculated. Additionally, for each of these sites, the values of the buried volume are calculated using the $r_{\%Vbur}$ corresponding to the reaction under study (see green pathway to "%Vbur(C_i/C_j)", Figure IV-55).

For the molecule, depending on the reaction under study (OH, Cl, NO_3 or O_3) and the number of H-atom present in the molecule, the values of the H-abstraction rate coefficient, k_{abs}, are calculated, if not 0, following the procedure described in section IV-1.1.3.1 (see dark-blue pathway to "k_{abs}", Figure IV-55). Finally, all the variables are combined to calculate the site-specific addition rate coefficient using (Eq. IV-27) as presented in section IV-1.1.3.2 and summed for all the reactive sites to obtain the total addition rate coefficient k_{add} as defined in (Eq. IV-26), and summed to the abstraction rate coefficient, k_{abs}, to obtain the total reaction rate coefficient, k_{pred}, using (Eq. IV-23).
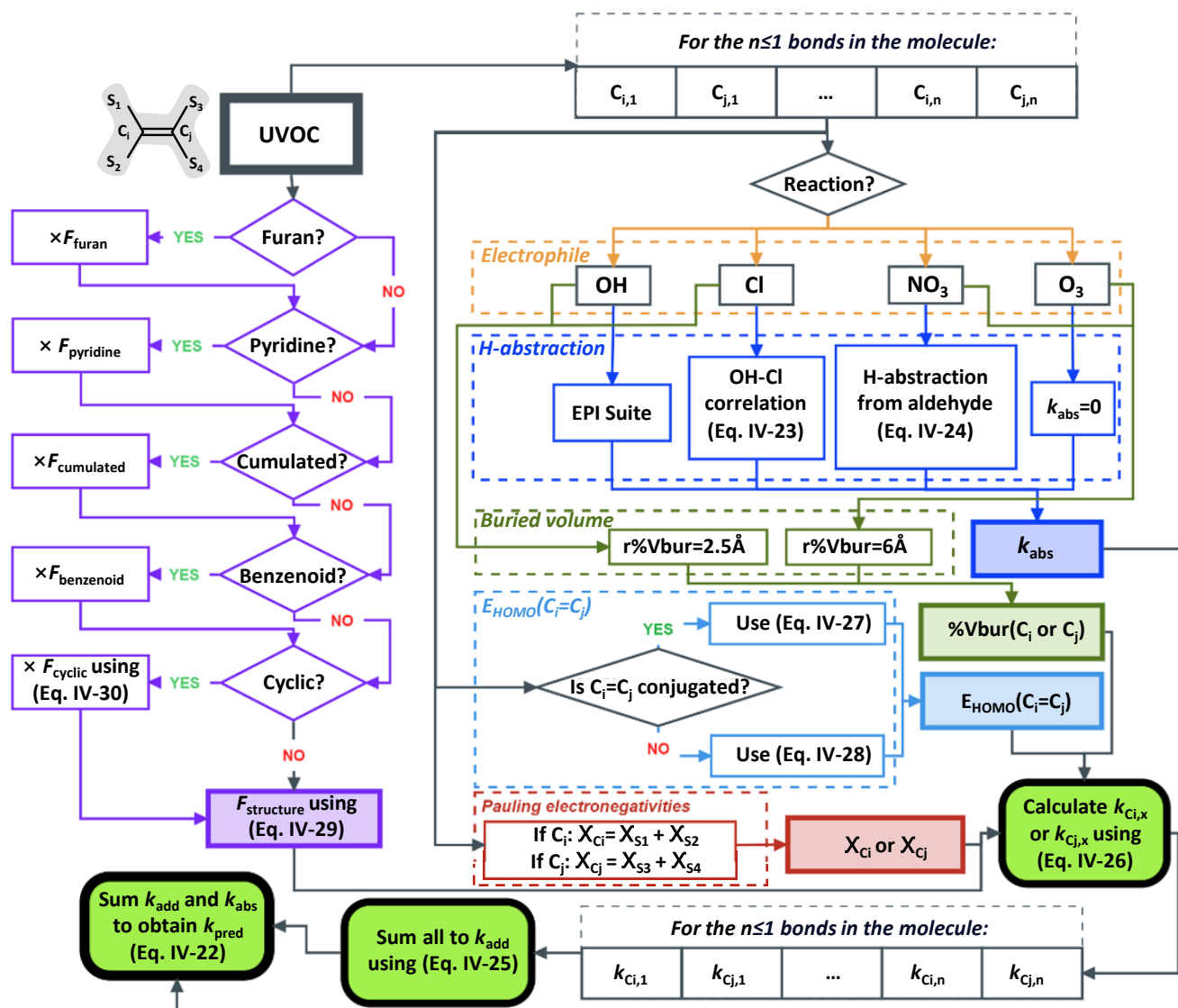
Figure IV-55 : Flow diagram of the KINESTEASY tool, with variables and equations presented in section IV-1.1.3.

IV-1.1.3.4. Available kinetic data

All kinetic data available at room temperature for unsaturated compounds from the most comprehensive reviewed database at the time of writing are gathered in Table IV-12 and Figure IV-56 (McGillen et al. 2020). The compounds are enumerated into two categories for each reaction: (1) chain types, or (2) substituents. To maximize the generality of this method, the entire database was included in the correlation analyses. From the Figure IV-56, it appears that some types of UVOCs are well studied (more k_{298} data for this class of UVOCs) while other are less studied (less k_{298} data for this class of UVOCs). For example, the majority of the compounds in the database are oxygenated or alkyl substituted UVOCs while smaller fractions are for example N-containing or S,P-containing UVOCs. Regarding the structures, most kinetic data are on straight-chain compounds or benzenoids, and very few data are provided on furans, pyridines or other types of cyclic compounds (apart from benzenoids). The Figure IV-56 also shows the lack of kinetic data on other

electrophile (Cl, NO_3 and O_3) compared to OH, as already mentioned in previous chapters. This points out the need for new kinetic data such as those provided in Chapter III, on NO_3 + furans reactions that are significantly less studied compared to the reactions of straight-chain alkenes with OH for example (see Figure IV-56).

Table IV-12 : Enumeration of all the kinetic data available, k_{Ox}, for compounds classified by their type of chain and their type of substitutions, and for the reaction with OH, NO_3, O_3, and Cl.

(1) Chain type	k_{OH}	k_{O3}	k_{NO3}	k_{Cl}	(2) Substituents	k_{OH}	k_{O3}	k_{NO3}	k_{Cl}
Straight-chain	215	146	108	107	H	159	127	109	63
Cyclic	41	51	45	14	N	58	11	5	13
Linear (conjugated)	82	71	42	43	O	212	119	127	95
Cyclic (conjugated)	65	16	20	16	F, Cl, Br	98	31	27	50
Pyridine	15	1	0	1	S, P	4	1	2	0
Cumulated	4	1	0	1	Mix	39	0	0	15
Furan	9	3	10	8					
Benzenoid	139	0	45	46					
Total	570	289	270	236	Total	570	289	270	236
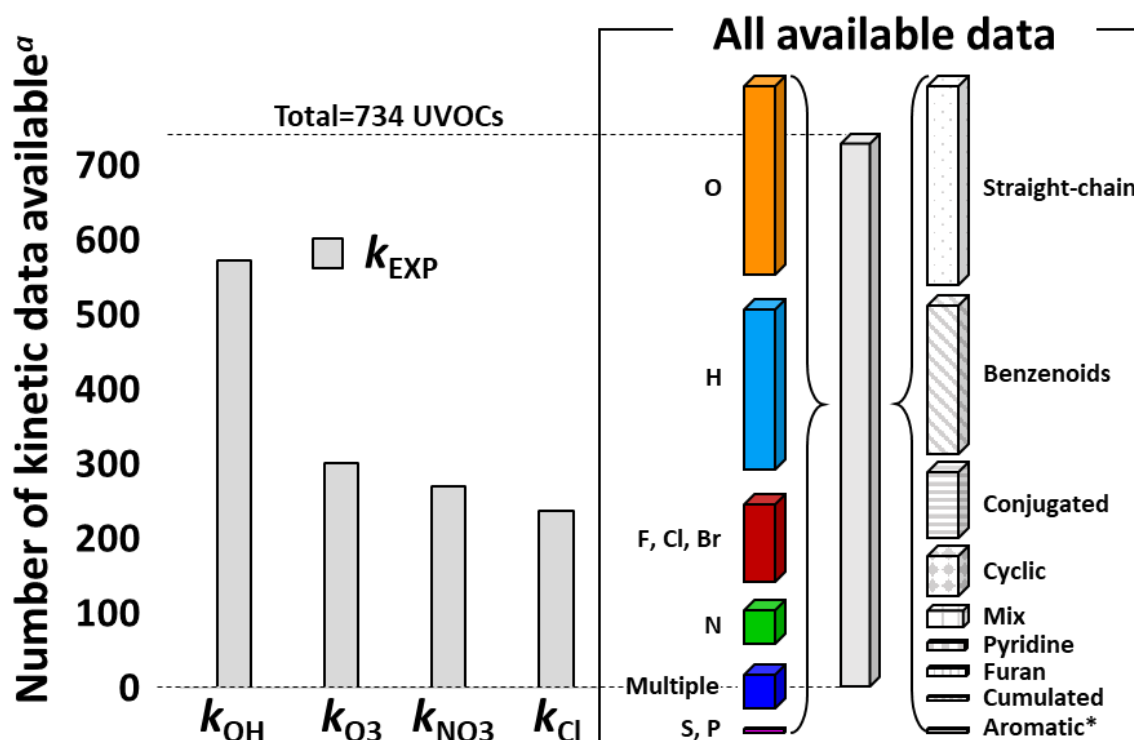
Figure IV-56 : All literature data available, numbered according to their structure type or their substituents. [a] Taken from (McGillen et al., 2020). *Aromatics are not including the aromatic structure that have their own classification, i.e., benzenoids, pyridine, or furan, but only other molecules that contain aromatic rings which do not fall in one of these categories. The right-hand side is presenting the percentage of each type and structure of the compounds composing the available database (in total 734 UVOCs), among which the k_{OH} of 570 UVOCs, the k_{O3} of 289 UVOCs, the k_{NO3} of 270 UVOCs and the k_{Cl} of 236 UVOCs are provided (left-hand side). All the UVOCs enumerated in this figure are implemented in the parametrization of this work.

IV-2. <u>Results and discussion</u>

The performance of the PM6-based method, implemented in the automated KINESTEASY tool, of the SAR presented in the previous sections is evaluated by comparing its predictions (PM6 method, k_{PM6}) with that of the non-automated DFT-based method (DFT method, k_{DFT}) and those of various existing methods that are automated or whose predictions can be easily calculated (extension of Michelat et al. (2022) SAR, k_{SAR}, EPI Suite, k_{EPI}, and GECKO-A, k_{GECKO}). This section is divided into three subsections:

(1) The haloalkenes dataset, CHX, where X=F, Cl, Br, to which the SAR of (Michelat et al., 2022) applies. This subset includes 77 alkenes, for which PM6, DFT and EPI Suite could also be applied.

(2) An extended dataset, CHONX, where X=F, Cl, Br, composed of the haloalkene dataset with additional compounds containing O and N substitutions, in order to compare PM6, DFT, and EPI Suite with GECKO estimations, since GECKO does not include any halogenated compounds,

(3) The entire literature database available for unsaturated organics, CHNOPSX, where X=F, Cl, Br, I, including polyalkenes compounds, to which the automated methods EPI Suite, GECKO and PM6 were applied, see Table IV-12.

In the following sections, the performance of the new methods using DFT and PM6 will be compared to the experimental data and to the other existing methods when possible. The key points that will be assessed in the following subsections are: (1) the ability of each method to predict accurately experimental data, (2) the universality of the method (percentage of coverage of the dataset studied), and (3) the extent of automation of the approach.

To assess the accuracy of each of the techniques, the mean unsigned error (MUE) is defined as the average absolute deviation between the of the ratios of the maximum over the minimum between the predicted, k_{pred}, and the experimental, k_{EXP}, rate coefficients. It was calculated as MUE= $\frac{1}{n} \times \sum_{i=1}^{n}$ |MAX($k_{EXP,I}$, $k_{pred,i}$)/MIN($k_{EXP,I}$, $k_{pred,i}$)| for a dataset of n rate coefficients. The performance of each technique is also assessed in a concise way by using the % of k_{pred} values within the dataset that agree within a factor of 2 with k_{EXP}. The % of factor 2 agreement is a good measure of the accuracy of the k_{pred} compared to measurements. However, it does not take into account the general correlation between a large variety of compounds. The MUE gives an estimation of the general correlation performance, with the average ratio within which predicted values are over- or underestimated compared to measurements, and can be combined to the % factor of 2 for this purpose.

IV-2.1. <u>OH reaction</u>

IV-2.1.1. <u>Haloalkenes dataset (CHX)</u>

Initially, the new approaches were applied to the OH reaction with a small dataset of haloalkenes, CHX alkenes, where X=F, Cl, Br, taken from the database of McGillen et al., 2020 for which different predictive tools exist, and upon which our new SAR was benchmarked. The dataset of 77 haloalkenes on which our previous work (Michelat et al., 2022) focused was used in this section, and compared with the predictions of the EPI Suite predictive tool (Michelat et al., 2022), and a comparison was made between the predictions of the EPI Suite predictive tool (k_{EPI}), the SAR of Michelat et al. (2022) (k_{SAR}), and the methods of the current work, using calculated values from DFT (k_{DFT}) and PM6 (k_{PM6}). The predicted rate coefficients are presented in Figure IV-57. Since GECKO-A has not been applied to halogenated species, this estimation method could not be included in the comparison.

The EPI Suite technique was used to estimate the total rate coefficient of this dataset. This method can be applied to 100% of the haloalkene dataset. From Figure IV-57, it is apparent that while there is a reliable performance of this technique towards alkenes (k_{EPI} predictions differ from k_{EXP} by a factor 1.14 at most), there are larger estimation errors (k_{EPI} predictions differ from k_{EXP} by a factor >358 at most) for the majority of haloalkenes. This method predicts 42% of the haloalkene dataset to within a factor of 2, with an MUE of 28.4 (Table IV-13 in section IV-2.1.3).

Next, the SAR of Michelat et al. (2022) was used to estimate the addition rate coefficient, which, for this selection of compounds is approximately equal to the total rate coefficient. This method was applied to 100% of this dataset. Figure IV-57 shows the generally excellent performance of this SAR, with 89% of estimates predicted within a factor of 2, with an MUE of 1.49 (Table IV-13 in section IV-2.1.3).

Next, the DFT approach of this work was used to estimate total rate coefficients for 100% of the haloalkene dataset. Contrary to the EPI Suite estimates, this approach is less reliable for the regular alkenes, but produces better estimates for haloalkenes. This method predicts 56% of this dataset to within a factor of 2 (see Figure IV-57), with an MUE of 2.66 (Table IV-13 in section IV-2.1.3).

Finally, the PM6 approach of this approach was used to estimate total rate coefficients for 100% of the haloalkene dataset. In this case, there is no clear difference in accuracy between the predictions of the different classes of compounds in this dataset, where 64% of predictions are within a factor of 2 and an MUE of 2.49 (Table IV-13 in section IV-2.1.3), with the biggest outlier being the (E)-1,3-dichloropropene (see Figure IV-57).

Comparing these four methods suggests that the SAR method of Michelat et al. provides the best parameterization of the haloalkene dataset. The k_{SAR} predictions are better than the EPI Suite estimations, k_{EPI} for the haloalkenes which can be explained by the difference in the principles of this SAR compared to the group-additivity approach of Kwok and Atkinson (1995). In this SAR (see Chapter II), the effect of the substitutions across the double-bond are not treated as separate groups but are combined in diagonal

substitution groups. This seems to better capture the effect that halogenated substituents can have on the double-bonds regarding the addition of the oxidants under study (OH, Cl, NO_3 and O_3). This can be interpreted in terms of electron density, which is affected by the electron withdrawing effect of halogens that can distort and lessen the π electron cloud away from the double-bond. It is sensitive to the position of the substituent attached to the double-bond and their symmetries, which seems better described with the diagonal substitution method presented in this SAR (Chapter II, (Michelat et al., 2022)). It is also generally superior to the estimates of the EPI suite tool, which may It is also noted that the factors to predict k_{EPI} may have been optimized on an older and less complete experimental dataset. The k_{EPI} estimates for the subset of regular alkenes in this dataset are better predicted by the EPI suite. It is notable that the estimations of the SAR of Michelat et al. (2022), k_{SAR}, require a large number of fitting factors (24 in total). However, EPI Suite requires a much larger number of fitting parameters (at least 36 in total for the addition reaction of OH, from Table 4–7 from the original work of Kwok and Atkinson (1995)) (Kwok and Atkinson 1995)).

The predictions of the DFT and PM6 approaches, k_{DFT} and k_{PM6}, agree with the experimental rate coefficients, k_{EXP}, with 64% and 56% of k_{DFT} and k_{PM6} within a factor of 2 of agreement with k_{EXP}, and MUEs of 2.66 and 2.49 respectively (Table IV-13 in section IV-2.1.3). However, k_{DFT} and $k_{PM6}$are less precise than k_{SAR}, but these estimates are made using a much smaller number of fitting parameters (13 in total for DFT/PM6). Therefore, this performance is considered to be promising and suggest that the method can be extrapolated beyond the boundaries of the haloalkene dataset with less risk of overfitting. Since there are fewer fitting factors used in the parametrization, it is suggested that the SAR is more general and can include more compounds without needing extensive amount of data to derive multiple specific fitting factors that could be required for these new compounds.

The approaches using DFT and PM6 are in general good agreement with k_{EXP}, which indicates that the least computationally expensive method does not reduce accuracy (56% and 64% for the DFT and PM6 methods are predicted with a factor of 2 agreement with measurements, Table IV-13 in section IV-2.1.3). Interestingly, despite a slightly reduced accuracy in k_{PM6} for the more reactive compounds, the accuracy of the PM6 approach is better than that of DFT (Table IV-13 in section IV-2.1.3), which may indicate that the calculations of the electronic and steric parameters from this method are more robust for this class of compounds, as observed in Figure IV-51 with the example of the outliers' calculations. The general correlation is largely improved in the PM6 model compared to DFT, which indicates that the PM6 calculations are adequate for describing this range of compounds. For the parametrization of this dataset, a radius of $r_{\%Vbur}$=3.5Å was used after trying various values (in the range of 2.5Å and 6Å) since it appeared to be the more adapted to optimize the MLR for the halogenated compounds, which represents most of the compounds of this dataset. PM6 estimates are also found to be generally more accurate than EPI Suite.

Nevertheless, the SAR of Michelat et al. (2022) is found to be the superior estimation technique in this comparison.
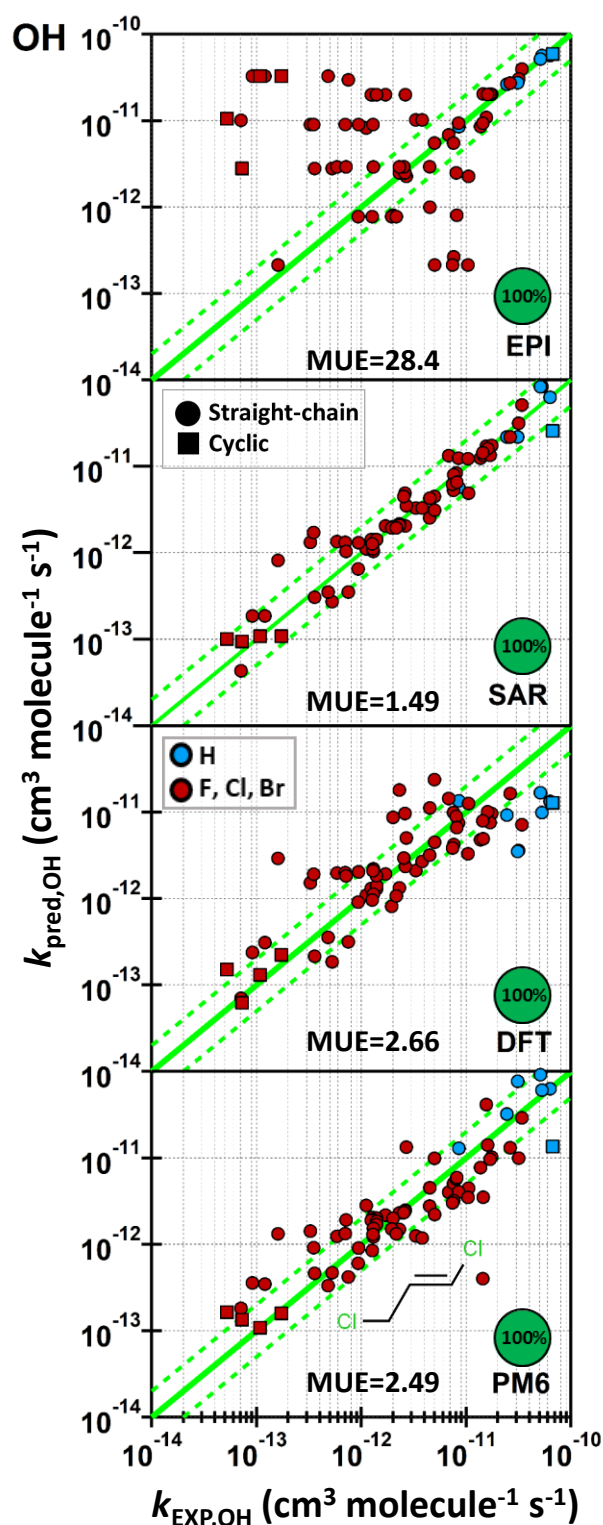
Figure IV-57 : Predictions of k_{OH} using 4 methods, i.e., EPI SUITE, SAR of (Michelat et al., 2022), DFT and PM6 tools, for a dataset of 72 haloalkenes, as selected in the work of (Michelat et al., 2022). The dataset includes straight-chain, and cyclic unsaturated compounds with substitution types C_nX_m where n has no limitation, but reaches 14 in our current dataset, and m=2n+1 and includes H, F, Cl, Br, or a mix of these atoms. For this dataset, $r_{\%Vbur}=3.5\text{Å}$ was used since it is the most adapted for this list. The pie chart represents the percentage of the whole k_{EXP} dataset for which the associated technique can provide an estimate.

IV-2.1.2.   Extended dataset (CHONX)

Following the haloalkene dataset, available prediction methods were applied to a more varied dataset of 160 unsaturated compounds including functionalities and chain-types that are more representative of atmospheric species, such as straight-chain (conjugated or not) and cyclic, together with substituents including H, O, F, Cl, Br, N, or a mixture of these atoms, which includes a variety of functionalities: alcohols, aldehydes, ketones, esters, ethers, (peroxy)nitrates, and isocyanate.

Since the SAR of Michelat et al. (2022) is difficult to extend beyond the halogenated monoenes at present, it cannot be applied to the extended dataset, or any of the subsequent datasets of this study. The EPI Suite technique was used to estimate the total rate coefficient of this dataset. This method can be applied to 100% of the extended dataset. From Figure IV-58, it is apparent that the performance for the CHON substitution types is similar to that of alkenes, and better than for the majority of haloalkenes. This method predicts 53% of the extended dataset to within a factor of 2, with an MUE of 21.19.

GECKO-A was used to estimate the total rate coefficient. This method was applied to 26% of this dataset. Figure IV-58 shows the generally excellent performance of this SAR, with 100% of estimates predicted within a factor of 2, with an MUE of 1.13 (Table IV-13 in section IV-2.1.3).

The DFT approach of this work was used to estimate total rate coefficients for 100% of the extended dataset. DFT was observed to be less reliable for the CHON alkenes (light blue/orange/green/blue, see Figure IV-58), while performing more reliably for the haloalkenes (red, see Figure IV-58). This method predicts 58% of this dataset to within a factor of 2, with an MUE of 2.54 (Table IV-13 in section IV-2.1.3).

Finally, the PM6 approach was used to estimate total rate coefficients for 100% of the extended dataset. In this case, 61% of predictions are within a factor of 2 (see Figure IV-58), with an MUE of 2.55 (Table IV-13 in section IV-2.1.3). The bigger outlier is, as for the haloalkene dataset, (E)-1,3-dichloropropene ; yet, it was not excluded from the dataset when optimizing the coefficients. When including these compounds, no major change was observed to the general fit.

The comparison of these four methods suggests that the DFT method provides the best overall parameterization of the extended dataset, while it is noted, for the subset to which it can be applied, that estimations from GECKO-A are significantly more reliable. The predictions from DFT and PM6 are in general good agreement, with an MUE of 2.10 between k_{PM6} and k_{DFT}, and the worse ratio between them being a factor 16 for (E)-1,3-dichloropropene which is the outlier in the PM6 estimations. The PM6 method does well in comparison with GECKO-A and DFT methods, but takes much less computer time. This indicates that the rapidity of the PM6 method does not come at the cost of accuracy in the predictions. It is thus possible to extend our dataset to all available kinetic data in order to assess the general performance of the PM6

tool. For this dataset, a value of $r_{\%Vbur}=3.5\text{Å}$ was used as for the previous dataset, since it appeared to be the most adapted for predicting rate coefficient of halogenated compounds which represents the majority of this extended list.
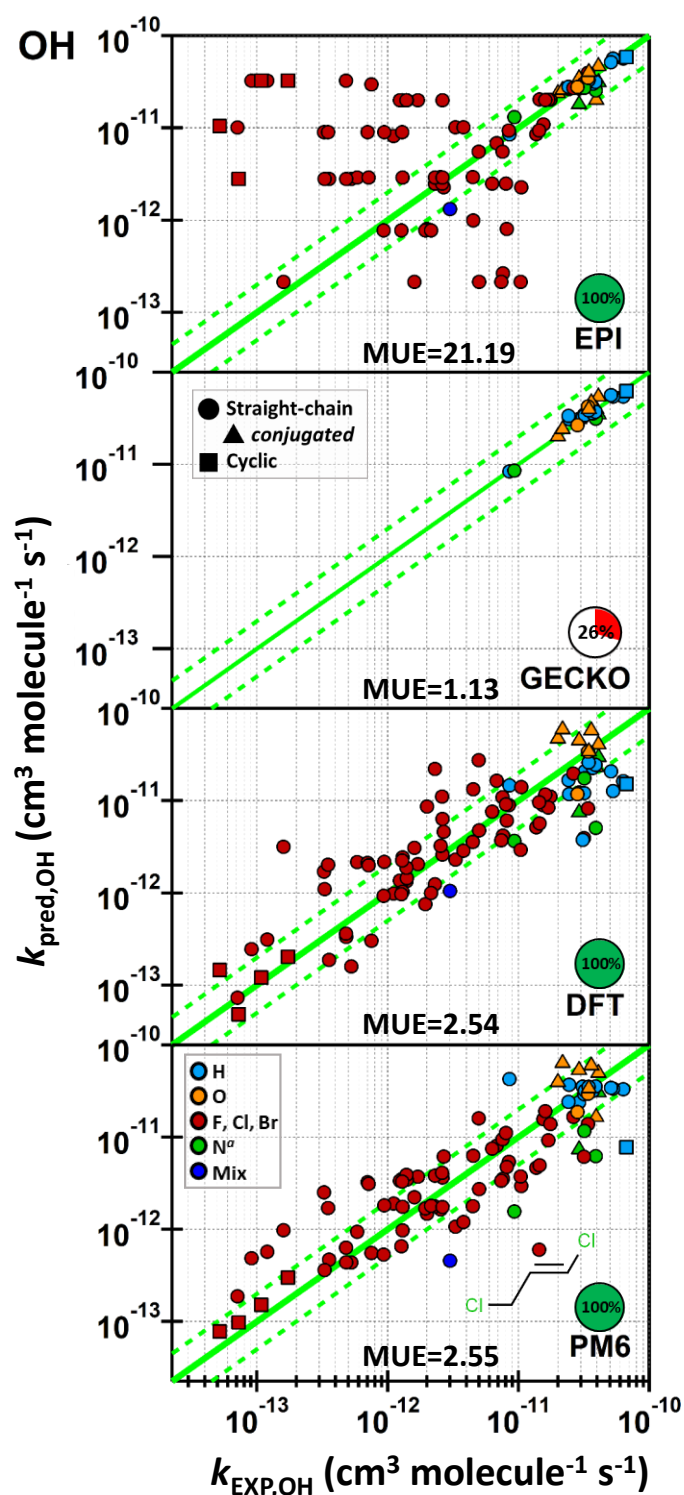
<u>Figure IV-58 :</u> Predictions of k_{OH} using 3 methods, i.e., EPI SUITE, GECKO-A, DFT and PM6 tools, for an extended dataset of 160 unsaturated compounds. The dataset includes straight-chain, cyclic, aromatics, benzenoids, conjugated, cumulated, furan, pyridine, or a combination of these structures, together with substitution types C_nX_m where n has no limitation, and m=2n+1 and

includes H, O, F, Cl, Br, N, or a mix of these atoms. For this dataset, $r_{\%Vbur}=3.5\text{Å}$ was used since it is the most adapted for this list. The pie chart represents the percentage of the whole k_{EXP} dataset for which the associated technique can provide an estimate.

IV-2.1.3. <u>All literature data available (CHNOPSX)</u>

To extend to more species of atmospheric importance and to investigate the applicability of these methods, the PM6 tool together with EPI Suite and GECKO-A were applied to the entire literature database available for the OH reaction. This dataset is composed of 570 unsaturated compounds, and a variety of structure types, including straight-chain (conjugated or not), cyclic (conjugated or not), benzenoids, cumulated, furan, pyridine, together with substitution types including H, O, F, Cl, Br, I, N, S, P or a mix of these atoms, which includes the variety of functionalities already measured, as can be found in the database of McGillen et al. (2020) (McGillen et al. 2020).

As before, since the SAR of Michelat et al. (2022) is currently difficult to extend to other structures and functionalities with substantial work, it has not been applied to this literature dataset. Similarly, given that no clear advantage to using the computationally expensive DFT over the efficient PM6 has been found in the previous comparisons, the DFT calculations were excluded from this comparison in the interest of computational time.

The EPI Suite technique was used to estimate the total rate coefficient of this dataset. This method can be applied to 100% of the literature dataset and predicts 74% of the dataset to within a factor of 2 (see Figure IV-59), with an MUE of 6.78 (Table IV-13 in section IV-2.1.3).

GECKO-A was used to estimate the total rate coefficient. This method was applied to 57% of this dataset, since it gives no estimations for halogenated, some oxygenated (e.g., peroxynitrates and some ketones) and some aromatics (e.g., some benzenoids). From Figure IV-59, shows the generally excellent performance of GECKO-A, with 90% of estimates predicted within a factor of 2, with an MUE of 1.62 (Table IV-13 in section IV-2.1.3).

Finally, the PM6 approach was used to estimate total rate coefficients for 100% of this dataset. In this case, there is no clear difference between prediction accuracy and the various classes of compound in this dataset, where 56% of predictions are within a factor of 2 (see Figure IV-59), with an MUE of 2.82 (Table IV-13 in section IV-2.1.3).

From Figure IV-59, it is apparent that no single technique is capable of yielding accurate estimates for all species contained within this dataset. For the limited range of compounds to which they can be applied, the SARs contained within GECKO-A provide the best estimates of the available data (90% of k_{GECKO} are within a factor of 2 of agreement with k_{EXP}, (Table IV-13). However, the overall coverage is low (57%) compared with the PM6 method of the present work and EPI Suite, both of which provide 100% coverage.

One reason for this is that the generality of the latter two methods leads to estimation errors. An example of this is seen when comparing the fidelity with which haloalkenes are predicted by PM6 in section IV-2.1.1, as opposed to the less accurate estimations that are made when the correlation is trained on the full dataset. This may indicate that there are still some important controls on the reactivity of these species that have yet to be adequately parameterized. Therefore, given the penalty that is incurred from increased coverage, it is important to consider whether it is useful for SARs to have a broader applicability. In an atmospheric chemical regime, one argument against this would be that most of the trace organic carbon in the atmosphere will contain CHON, therefore, this should be the focus of any predictive technique. However, when the types of functionalities in the CHON compounds that are present within the kinetic dataset are considered, it becomes clear that there is a considerable mismatch between chemical functionalities that are formed in the atmosphere versus those that are available for training SARs (McGillen et al., 2020). However, the aim for a universal tool is inherently tied to a loss of accuracy compared to other methods that are specific to each subset but less general. Therefore, whereas an SAR may be well trained on relatively uncommon functional groups such as ethers and alcohols, the reactivity of compounds with nitrate, carboxylic acid or peroxidic substitutions remains largely unknown. As a result, there is an advantage to having a more general SAR that has been trained on as many functionality types as possible, in that it is trained on correlations of the entire dataset and is therefore less affected by the absence of training data on individual functionalities and structure types. Furthermore, it is also useful to consider the possible advantages of a technique such as the PM6 approach of this study compared with more conventional group-additivity methodologies. In our case, the PM6 correlations are supported by *a priori* quantum chemical information. Because of this, so long as the PM6 method can provide useful information about a molecular structure, there will always be a basis for making an estimate. In contrast, a more general SAR such as EPI Suite, when confronted with an unknown substitution pattern, will provide estimates based upon a default substitution parameter which contains no specific information on the actual substitution in question (see orange box in workflow diagram Figure IV-46).
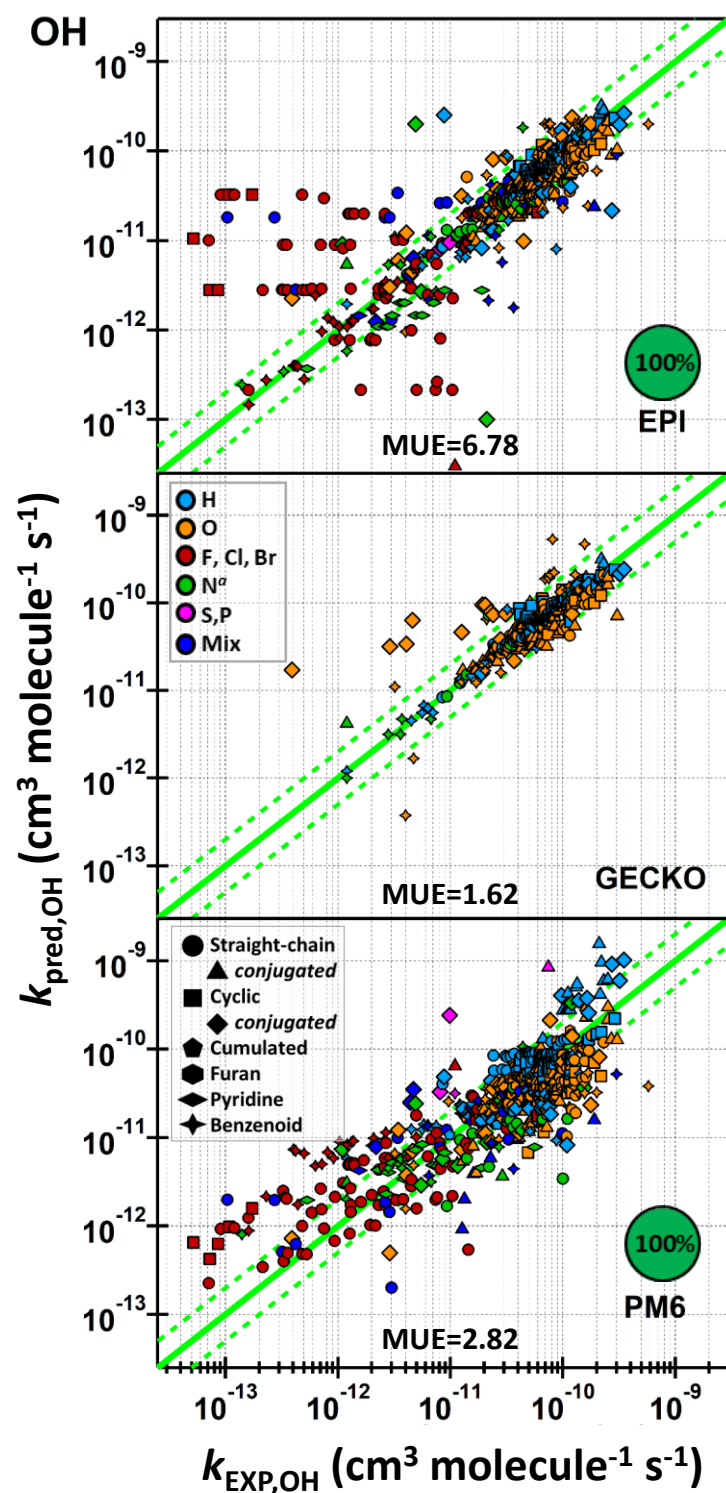
Figure IV-59 : Predictions of k_{OH} using 3 methods, i.e., EPI SUITE, GECKO-A and PM6 tools, for all the 570 compounds for which literature data were available. EPI SUITE and PM6 were able to retrieve predictions for all compounds, while GECKO-A only estimates 327 compounds within the whole dataset, excluding for example halogenated compounds and some oxygenates. The dataset includes straight-chain, cyclic, aromatic (excluding benzenoids), conjugated, cumulated, furan, pyridine, or a combination of these structures, together with substitution types C_nX_m where n has no limitation, and m=2n+1 and includes H, O, F, Cl, Br, I, N, S, P or a mix of these atoms. For this dataset, $r_{\%Vbur}$=2.5Å was used since it is the most adapted for this list. The pie chart represents the percentage of the whole k_{EXP} dataset for which the associated technique can provide an estimate.

Table IV-13 : Summary table of the OH predicted data using EPI Suite, SAR from Michelat et al. and its extension, DFT and PM6 approaches, together with the percentage of k_{pred} data within a factor of 2 of agreement with k_{EXP} / total number of data k_{pred} predicted by the method, percentage of coverage within the whole dataset of k_{EXP} and automation if available, and ^{a} MUE, the mean unsigned error, as defined in the text. The color scales are relative to the range of values in the column. The greener, the better the 3 key points (i.e., the prediction accuracy, the coverage and the automation), with red being the opposite.

oxidant	technique	dataset	% coverage	% within factor of 2	automated	MUE^a	Figure index
OH	EPI Suite	haloalkenes	100	42	Yes	28.4	
	GECKO-A		0	NA	NA	NA	
	SAR		100	89	No	1.49	IV-57
	DFT		100	56	No	2.66	
	PM6		100	64	Yes	2.49	
	EPI Suite	extended	100	53	Yes	21.19	
	GECKO-A		26	100	Yes*	1.13	
	SAR		0	NA	NA	NA	IV-58
	DFT		100	58	No	2.54	
	PM6		100	61	Yes	2.55	
	EPI Suite	all	100	74	Yes	6.78	
	GECKO-A		57	90	Yes*	1.62	
	SAR		0	NA	NA	NA	IV-59
	DFT		0	NA	NA	NA	
	PM6		100	56	Yes	2.82	

IV-2.2.   Extension to other oxidants: Cl, NO$_3$ and O$_3$

In this section, the relative performances of the various estimation techniques towards other oxidants are compared. In order not to present all the associated figures in the body of this chapter in a tedious manner, the results of these analyses are summarized in Table IV-13 for the OH reaction (see previous section IV-2.1 for more details). The details of these analyses are provided in section App-IV-2.1 in Appendices for Cl reaction and summarized in section IV-2.2.1. The details for the NO$_3$ and O$_3$ reactions are respectively provided in section App-IV-2.2 and App-IV-2.3 in Appendices and respectively summarized in section IV-2.2.2 and section IV-2.2.3.

IV-2.2.1.   Cl reaction

The Cl reaction with UVOCs was investigated. All the figures for the 3 datasets are presented in Appendices section App-IV-2.1 and are summarized in the Table IV-14. To the best of our knowledge, no existing methods with which to compare predictions are available. In this work, the extension of the SAR of Michelat et al. (2022), detailed in Chapter II, has been applied to the Cl reaction of the haloalkenes dataset, as well as both the DFT and PM6 tools. The SAR provides k_{pred} in excellent agreement with the measurements (98% of the k_{pred} agreeing within a factor 2 with k_{EXP} and an MUE of 1.13, Table IV-14). However, as with the OH dataset, this SAR approach is limited to the haloalkenes dataset at present and has yet to be automated. The DFT method also provides satisfactory results for both the haloalkenes and extended datasets, but was

not automated. In contrast, the PM6 method shows generally superior performance over DFT for the haloalkenes and extended datasets and was therefore applied to the full kinetic dataset of 236 UVOCs. In general, the SAR performance is slightly better than that for OH (89% of the k_{pred} agreeing within a factor 2 with k_{EXP} and an MUE of 1.49, Table IV-14), which may indicate that the underlying reaction mechanisms are less complex or are more easily parameterized. In the latter case, it is noted that the range of rate coefficients exhibited by the experimental Cl dataset is smaller ($k_{EXP,min}$=1.85×10^{-13} cm^3 molecule^{-1} s^{-1}, $k_{EXP,max}$=7.55×10^{-10} cm^3 molecule^{-1} s^{-1}), which is inherently less challenging for correlation-based methods.

Table IV-14 : Summary of the Cl predicted data using SAR from Michelat et al. and its extension, DFT and PM6 approaches, together with the percentage of k_{pred} data within a factor of 2 of agreement with k_{EXP} / total number of data k_{pred} predicted by the method, percentage of coverage within the whole dataset of k_{EXP} and automation if available, and [a] MUE, the mean unsigned error, as defined in the text. The color scales are relative to the range of values in the column. The greener, the better the 3 key points (i.e., the prediction accuracy, the coverage and the automation), with red being the opposite.

oxidant	technique	dataset	% coverage	% within factor of 2	automated	MUE[a]	Figure index
Cl	EPI Suite	haloalkenes	0	NA	NA	NA	App-IV-3
	GECKO-A		0	NA	NA	NA	
	SAR		100	98	No	1.13	
	DFT		100	89	No	1.52	
	PM6		100	86	Yes	1.44	
	EPI Suite	extended	0	NA	NA	NA	App-IV-4
	GECKO-A		0	NA	NA	NA	
	SAR		0	NA	NA	NA	
	DFT		100	89	No	1.48	
	PM6		100	87	Yes	1.42	
	EPI Suite	all	0	NA	NA	NA	App-IV-5
	GECKO-A		0	NA	NA	NA	
	SAR		0	NA	NA	NA	
	DFT		0	NA	NA	NA	
	PM6		100	79	Yes	2.13	

IV-2.2.2.   NO₃ reaction

The DFT and PM6 methods from this chapter were extended to apply to the NO$_3$ reaction. All the figures for the 3 datasets are presented in Appendices section App-IV-2.2 and are summarized in the Table IV-15. In this case, the GECKO-A mechanism provides estimates for a limited subset, which covered 75% of the extended dataset and 56% of the literature database available (270 UVOCs), excluding all the halogenated compounds, the aromatics and some oxygenates. The correlation is in excellent agreement with experiments (78% of the k_{pred} agreeing within a factor 2 with k_{EXP} and an MUE of 5, Table IV-15) but the coverage is significantly reduced compared to PM6, with 56% of coverage compared to 100% of coverage for PM6 for the whole literature dataset. The extension of the SAR of Michelat et al. (2022), detailed in Chapter II, was applied to NO$_3$ for the haloalkenes dataset, and it provides k_{pred} in excellent agreement with measurements (92% of the k_{pred} agreeing within a factor 2 with k_{EXP} and an MUE of 1.36, Table IV-15), but

it remains limited to CHX alkenes. The DFT and PM6 methods did not performed well to predict the haloalkenes dataset and its extension (% factor 2 of agreement with k_{EXP} of 33% and MUE of 10±0.6, Table IV-15), despite a good performance for OH and Cl reactions (see Table IV-13 and Table IV-14). Since DFT is not automated, PM6 was applied to the literature database available and its overall accuracy remains in poor agreement with the measurements (see Table IV-15). This can be explained by the large range of reactivities encountered for the NO_3 reaction (9 order of magnitude from 4.20×10^{-18} to 1.22×10^{-9} $cm^3 molecule^{-1}s^{-1}$) compared to the reactions of OH (5 order of magnitude from 3.00×10^{-14} to 1.55×10^{-9} $cm^3 molecule^{-1}s^{-1}$) and Cl (3 order of magnitude from 1.85×10^{-13} to 7.55×10^{-10} $cm^3 molecule^{-1}s^{-1}$), which can be a challenge for correlation that includes all the data, whereas adjusting a small range of values can be easier. Additionally, it is possible that mechanistic differences between these reactions are not well described in the parametrization, which result in larger uncertainties in the predictions (see Figure App-IV-8). EPI Suite does not predict k_{NO3}, hence, PM6 is the only tool that can be applied to any types of compounds in an automated way. GECKO-A provides better estimates, but remains limited to fewer species (CHON). The NO_3 reactions are not well predicted compared to those with the other reactants.

Table IV-15 : Summary of the NO_3 predicted data using GECKO-A, SAR from Michelat et al. and its extension, DFT and PM6 approaches, together with the percentage of k_{pred} data within a factor of 2 of agreement with k_{EXP} / total number of data k_{pred} predicted by the method, percentage of coverage within the whole dataset of k_{EXP} and automation if available, and ^{a} MUE, the mean unsigned error, as defined in the text. * Automated in the GECKO-A mechanism, but not available for any user. The color scales are relative to the range of values in the column. The greener, the better the 3 key points (i.e., the prediction accuracy, the coverage and the automation), with red being the opposite.

oxidant	technique	dataset	% coverage	% within factor of 2	automated	MUE^a	Figure index
NO_3	EPI Suite	haloalkenes	0	NA	NA	NA	App-IV-6
	GECKO-A		0	NA	NA	NA	
	SAR		100	92	No	1.36	
	DFT		100	33	No	10.25	
	PM6		100	33	Yes	10.59	
	EPI Suite	extended	0	NA	NA	NA	App-IV-7
	GECKO-A		75	85	Yes*	1.8	
	SAR		0	NA	NA	NA	
	DFT		100	25	No	11.39	
	PM6		100	14	Yes	16.02	
	EPI Suite	all	0	NA	NA	NA	App-IV-8
	GECKO-A		56	78	Yes*	5	
	SAR		0	NA	NA	NA	
	DFT		0	NA	NA	NA	
	PM6		100	22	Yes	43.34	

IV-2.2.3. O_3 reaction

Finally, each available method was applied to the O_3 reaction. All the figures for the 3 datasets are presented in Appendices section App-IV-2.3 and are summarized in the Table IV-16. For the haloalkenes

dataset, the extension of the SAR of Michelat et al. (2022) provides the best estimates (74% of the k_{pred} agreeing within a factor 2 with k_{EXP} and an MUE of 1.74, Table IV-16), while EPI Suite, DFT and PM6 give estimates with a similar performance. For EPI Suite, 39% of estimates within a factor of 2 of k_{EXP}, and those of DFT and PM6 are of 23% and 26% respectively (Table IV-16). However, the MUE of k_{EPI} is 21.23, which is higher than that of DFT and PM6, which suggest large uncertainties in the estimates within the dataset. When extending to more varied dataset, the GECKO-A method provides estimates in excellent agreement with the experiments, however, it still does not apply to the whole range of compounds (83% of the whole literature database, Table IV-16). Interestingly, the DFT and PM6 approaches are apparently not well suited to the ozonolysis mechanism. This may indicate that there are other important components to the ozonolysis, such as the fact that O_3 is adding to both carbons in the double-bond of the UVOC, thus forming an ozonide, contrary to the OH, Cl and NO_3 mechanisms where the addition occurs on one side of the double-bond (Leather et al., 2010; McGillen et al., 2011, 2008). In contrast to the other oxidants, EPI Suite provides generally superior estimates for the O_3 dataset.

Table IV-16 : Summary of the O_3 predicted data using EPI Suite, GECKO-A, SAR from Michelat et al. and its extension, DFT and PM6 approaches, together with the percentage of k_{pred} data within a factor of 2 of agreement with k_{EXP} / total number of data k_{pred} predicted by the method, percentage of coverage within the whole dataset of k_{EXP} and automation if available, and ^{a} MUE, the mean unsigned error, as defined in the text. * Automated in the GECKO-A mechanism, but not available for any user. The color scales are relative to the range of values in the column. The greener, the better the 3 key points (i.e., the prediction accuracy, the coverage and the automation), with red being the opposite.

oxidant	technique	dataset	% coverage	% within factor of 2	automated	MUE^a	Figure index
O_3	EPI Suite	haloalkenes	100	39	Yes	21.23	
	GECKO-A		0	NA	NA	NA	
	SAR		100	74	No	1.74	App-IV-9
	DFT		100	23	No	15.18	
	PM6		100	26	Yes	12.22	
	EPI Suite	extended	100	53	Yes	11.45	
	GECKO-A		70	86	Yes*	1.82	
	SAR		0	NA	NA	NA	App-IV-10
	DFT		100	27	No	16.19	
	PM6		100	26	Yes	14.5	
	EPI Suite	all	98	49	Yes	10.99	
	GECKO-A		83	75	Yes*	10.63	
	SAR		0	NA	NA	NA	App-IV-11
	DFT		0	NA	NA	NA	
	PM6		100	29	Yes	13.78	

IV-2.2.4.   Comparison of the techniques

By comparing various SAR techniques applied to different datasets, it is apparent that no single technique is superior. There are several criteria to gauge SAR performance, including the coverage and estimation accuracy. For example, while the SAR technique of Michelat et al. (2022) has a very good performance for

haloalkenes in the OH, Cl,NO$_3$ and O$_3$ datasets, it cannot be extended to other substitution types without extensive future work. Similarly, the SARs contained within GECKO-A are capable of making more accurate estimates of a limited subset of CHON compounds of the available kinetic dataset. Again, without substantial efforts to extend their domains of applicability, these SARs will continue to have poor coverage for the range of compounds emitted to and formed within the atmosphere. Broader, more applicable SARs demonstrate both strengths and weaknesses. The predictions of EPI Suite are generally reliable for simpler, monofunctional compounds, but are poorer for more complex structures and halogenated compounds. Furthermore, EPI Suite has no capacity for estimating the atmospherically important reactions of Cl and NO$_3$. Conversely, the PM6 method of the present study makes estimates for each of the four oxidants considered, and performs comparatively well for the haloalkenes, and is the only automated method for making estimates of Cl reactions at present. However, it has notable weakness in NO$_3$ and O$_3$ predictions in its current form.

The high coverage of the EPI Suite method comes from its algorithm design, which allows it to make predictions using default substitution factors, even when the behavior of a substituent is largely unknown. The advantage of this is that it will always produce an estimate, with the concomitant disadvantage being that this estimate is not based strictly upon the structure in question and may therefore be misleading. The PM6 approach that is presented in this chapter attempts to circumvent this problem through the use of *a priori* information from PM6 and accompanying calculations. As noted above, the performance for some datasets is good, and is worse for others. The reasons for this are likely to relate to the degree to which the descriptors chosen are capable of parameterizing each reaction type. Clearly there is a current need to improve upon the atmospherically important NO$_3$ and O$_3$ predictions. For this reason, this chapter's tool is available as an open source and free script that will allow for future upgrades as prediction techniques continue to develop and contribution from the community.

It is noted that the reactions of UVOCs with O$_3$ are different than those with OH and NO$_3$, since the molecule adds to both carbons of the double-bond of the UVOC. Similarly, Cl is an atom with no dipole moment on the contrary to OH and NO$_3$. Since Cl predictions are in good agreement with the experimental data, it is possible that the dipole moment does not make a significant difference in this parametrization of the addition reaction. Even though all of these are electrophilic addition reactions (along with H-abstraction), they are not similar and the simplistic approach of using E$_{HOMO}$ and buried volume may not be applicable due to these differences.

IV-3. General use of the KINESTEASY software tool

The program developed in this work outputs a report for each species which includes total rate coefficient for all the oxidant, and site-specific rate coefficients, as illustrated with an example in Figure IV-60, and provided for all the 727 compounds for which kinetics with at least one of the four atmospheric oxidants considered was available in the database of (McGillen et al., 2020) in the Appendices (*Kinetics_total.csv*, *Kinetics_site_speicfic.csv*, and *KINETICS_reports_results_all_database.pdf*)

This tool is designed to be accessible by the whole community and does not require familiarity with Python or programming in general. It is therefore fully automated in one python script *Main_KINESTEASY_tool.py*, that can be easily run by double-clicking on it or by opening it in an IDE like Spyder. Different outputs can be obtained, either total rate coefficients as *.csv*, either site-specific rate coefficients with more details on the parameters used as *.csv*, or a full report as pdf. The script requires the following packages: obabel, rdkit, reportlab (for the pdf report only) and MOPAC2016 and EPI Suite (for $k_{abs,OH}$ estimations) installed on the computer. Simple instructions for each are provided in the READ_ME.txt, and the Python libraries cited above can be automatically imported by double-clicking on the batch file *install_dependencies.bat* provided. This software is intended for use by those working in atmospheric modelling, industry and policy, each of whom may need to screen large chemical databases quickly and easily.

Electrophilic addition to 2,4-dibromodiphenyl ether
(BrC1=CC=C(OC2=CC=CC=C2)C(Br)=C1)

(1) Molecule structures with preferred reactive site highlighted for reaction with OH, O3, Cl,and NO3

Molecule structure with preferred reactive site(s) highlighted for all addition reactions

kOH Preferred site: [6]

kO3 Preferred site: [1, 2, 3, 4, 6, 7, 8, 9, 10, 11, 12, 14]

kCl Preferred site: [8, 9, 10]

kNO3 Preferred site: [4]

(2) All kinetics data

Carbon index (i)	kOH(Ci)	kCl(Ci)	kO3(Ci)	kNO3(Ci)
1	6.14e-12	2.62e-11	0.00e+00	9.01e-19
2	5.61e-12	2.86e-11	0.00e+00	2.71e-19
3	5.39e-12	2.78e-11	0.00e+00	3.73e-19
4	6.85e-12	2.57e-11	0.00e+00	5.94e-18
6	6.91e-12	2.59e-11	0.00e+00	3.83e-18
7	5.65e-12	2.87e-11	0.00e+00	2.21e-19
8	5.73e-12	2.90e-11	0.00e+00	1.61e-19
9	5.73e-12	2.90e-11	0.00e+00	1.52e-19
10	5.73e-12	2.90e-11	0.00e+00	1.91e-19
11	5.40e-12	2.78e-11	0.00e+00	2.85e-19
12	6.13e-12	2.62e-11	0.00e+00	1.43e-18
14	5.49e-12	2.81e-11	0.00e+00	2.44e-19
Total rate	**kOH**	**kCl**	**kO3**	**kNO3**
Calculated	7.08e-11	3.32e-10	0.00e+00	1.40e-17
Experimental	nan	nan	nan	nan

All rate coefficients are in units of cm3molecule-1s-1.

Total and site-specific kinetic data k_{pred} and k_{EXP} data for all oxidants

Molecule structure and atom indexes

Figure IV-60 : Example sheet of the output of the code, deriving overview on the reactivity of UVOCs with the four major atmospheric oxidants, with comparison with experimental data, and site-specific reactivities.

IV-4. Atmospheric implications

In this section, the ability of the KINESTEASY tool presented in this Chapter to estimate complex datasets in an automated way is tested and compared to the other automated and EPI Suite tool. This has been performed on a dataset atmospherically relevant, in order to assess their atmospheric implications. An assessment of the impact of organic compounds, and their oxidation products on air pollution is presented. In this section, the reaction rate coefficients are estimated using the KINESTEASY tool, and the rest of the

work is essentially done using a parameterized model to estimate these impacts. The central focus is placed on understanding the degradation process of three key compounds: α-pinene, toluene and *n*-decane. As these compounds undergo oxidation, they give rise to a complex mixture of products. In the paper of (Isaacman-VanWertz and Aumont, 2021), the GECKO-A mechanism (https://geckoa.lisa.u-pec.fr/, (Aumont et al., 2005)) was applied under the average continental atmospheric conditions. A large number, 182,000, of atmospherically relevant species were included in the bow model run by (Isaacman-VanWertz and Aumont, 2021), , two third of which are nitrate species. It is noted that GECKO-A, as other large mechanisms, does not include many reaction pathways that are assumed to be minor, although they could potentially be important when cumulated (Aumont et al., 2005; Isaacman-VanWertz and Aumont, 2021). Thus, this list of compounds is not exhaustive and may be subject to changes.

The oxidation of α-pinene, *n*-decane and toluene were examined. These compounds were chosen based on different factors. First, they represent the oxidation of cyclic alkene, saturated alkane, and aromatic compounds, respectively. Second, the oxidation mechanism of α-pinene is comparatively well-studied, which makes it a good test molecule in order to derive oxidation products from its atmospheric oxidation processes (Valorso et al., 2011). Third, it has one of the largest emissions of all natural volatile organic compounds in the atmosphere, and represents a major emission from forested areas. Conversely, toluene is a major emission that has both natural and anthropogenic sources, including forest wildfires, vegetation, and organic matter breakdown in soils, as well as industrial processes, or transportation emissions (Ng et al., 2007). Lastly, *n*-decane is an alkane, also largely emitted from fossil fuel sources (Aschmann et al., 2001). Because of their various chemical structures and source terms, these three compounds are used as representatives of the range of organic molecules that are emitted into the atmosphere.

The most relevant oxidation products are selected for the three oxidation mechanisms, which results in 38,594 compounds (Isaacman-VanWertz and Aumont, 2021). The KINESTEASY tool has initially been applied to all the unsaturated VOCs present in the initial dataset, which rendered 14,446 rate coefficients with the four oxidants. Their contribution to tropospheric O_3 pollution, a critical aspect of air quality regulation, has been investigated using the estimated photochemical ozone creation potential, $POCP_E$ (Jenkin et al., 2017). Then, among the 38,594 relevant structures selected in the original work of (Isaacman-VanWertz and Aumont, 2021) and associated to each degradation pathway, vapor pressures have been estimated in order to evaluate their contribution to SOA formation.

The objective is to understand the atmospheric implications of these compounds and their degradation products by estimating their lifetimes in the presence of the four primary atmospheric oxidants, using the tool presented in Chapter IV. Depending on their reactivity towards tropospheric oxidants, as well as their other potential removal pathways, UVOCs can persist in the atmosphere and be transported away from

their source. They can have various impacts on air quality by contributing to tropospheric ozone pollution or participating in the formation of secondary organic aerosols, the latter of which can have adverse health impacts (see Chapter I).

Estimating the room temperature and temperature dependence of large databases

Among the rate coefficients predicted for the 14,446 structures, only 18 k_{OH}, 12 k_{Cl}, 15 k_{O3}, and 15 k_{NO3} have been measured experimentally. All k_{OH} are predicted by EPI Suite, and only 132 reactions are not predicted for k_{O3}. No estimations are provided for k_{Cl} and k_{NO3}. Therefore, the new tool presented in Chapter IV offers the possibility to expand significantly the ability to obtain estimates of the rate coefficients of many compounds for the 4 tropospheric oxidants to input into atmospheric models. Using the method described in Chapter II, it is possible to estimate values of E_a/R and A-factors of the Arrhenius dependence of all the compounds for OH and NO$_3$. For conciseness, since this dataset is composed of >14,000 structures, these are not reported in this section. However, these can be obtained by applying the equations of the associated reaction presented in Chapter II and using the prediction of the room temperature rate coefficient obtained using the code from Chapter IV.

Tropospheric losses

Caveat: *As discussed in the Chapter III, the concept of lifetime is strongly dependent on various parameters and is used in this section as a measure of the relative loss of the compounds towards the oxidation by the 4 main tropospheric oxidants. The lifetimes provided are only rough estimates.*

The estimated lifetimes of these compounds are presented for each oxidant in the Figure IV-63. The lifetimes were derived with regards to the four tropospheric oxidants using (Eq. III-22) in section III-3.1 and the following concentration of each oxidant, i.e., the averaged summertime midday OH concentrations of 5×10^6 molecule cm^{-3} was chosen, (Stone et al., 2012) the mixing ratio of O$_3$ of 7×10^{11} molecule cm^{-3} was used, (Monks et al., 2009) nighttime NO$_3$ concentrations of 2×10^8 molecule cm^{-3} was selected, (Brown and Stutz, 2012) and daytime peak concentrations of atomic chlorine of 1×10^4 atoms cm^{-3} was applied (Wingenter et al., 1996). However, it is noted that the time, location, mixing and conditions of the emission are likely to affect these values significantly, as warned in the caveat (Brioude et al., 2010; Wuebbles et al., 2001).

$$1/\tau_{tot} = 1/\tau_{OH,day}$$
$$+ 1/\tau_{Cl,day}$$
$$+ 1/\tau_{O3,day}$$
$$+ 1/\tau_{NO3,night}$$
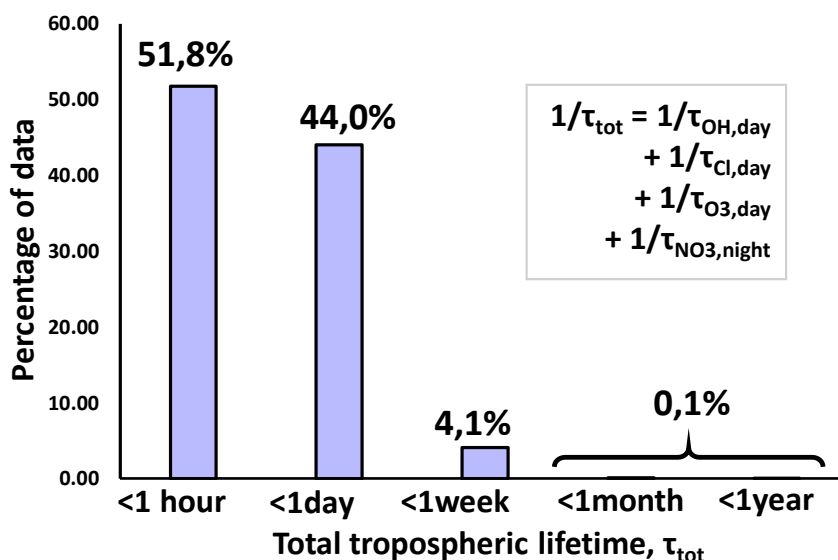
Figure IV-61 : Total tropospheric lifetimes of 14,446 unsaturated VOCs derived from the oxidation of α-pinene, toluene and *n*-decane for their reactions with OH, Cl, and O_3 during the day and NO_3 during the night estimated using the tool presented in Chapter IV of this thesis. The SMILES of the oxidation products are obtained from the GECKO-A mechanism application published by (Isaacman-VanWertz and Aumont, 2021). The main removal is by reaction with OH during the day and with NO_3 at night.

From the results, it was observed that the major removal during day-time is by reaction with OH and during nighttime by reaction with NO_3. As presented in Figure IV-61, most of the compounds are degraded within a day (~96%). These compounds are short-lived, and are consequently not well-mixed in the troposphere. Thus, they can have a significant impact on regional air quality. The primary removals of these UVOCs are by reaction with OH during the day and with NO_3 at night. The removal from NO_3 during the day is not considered since NO_3 is rapidly photolyzed, and the removal of OH, Cl and O_3 during the night are not considered since they are expected to be less important or similar to their daytime contribution due to lower concentrations. Also, concentration of oxidants is a challenging value to obtain, as mentioned in the caveat, and these lifetimes are just an indication of the time for tropospheric loss, but remain a rough estimate.

It is noted that the contribution of Cl chemistry is very minor, which is explained by the fact that the concentration is 500 times lower for Cl atoms compared to that of OH radicals, which leads to longer lifetimes towards Cl initiated loss. For O_3, the opposite is observed, the concentration is more than 5 orders of magnitude higher than that of OH radicals, but the rate coefficients are mostly smaller, making the reaction negligible for most compounds. Therefore, OH is the primary removal of these species in general.

These observations highlight the advantage of tools such as that proposed in Chapter IV which can apply to any UVOC found in the atmosphere. Despite being less accurate for some compounds, the extension to a larger coverage is useful in this case and shows the advantage of having estimates for more structures,

despite the cost of an increase in scatter. This would allow structures to have at least some estimate attached to their reactivity as opposed to no estimate at all.

POCP$_E$ parameters definitions and values

In order to assess the contribution of these compounds to tropospheric O_3 production, the estimated value of the photochemical ozone creation potential (POCP$_E$) has been calculated from the expression developed by (Jenkin et al., 2017) as follows:

$$POCP_E = (A \times \gamma_S \times R \times S \times F) + P + R_{O3} - Q \quad \text{(Eq. IV-31)}$$

where A, γ_S, R, and S are core parameters applicable to all VOCs, and F, P, R_{O3} and Q are parameters specific to certain types of compounds, as described below. A is a multiplication factor only. The parameter γ_S is related to the reactivity of the VOC based on its structure and defined as follows:

$$\gamma_S = (n_B/6) \times (28.05/M) \quad \text{(Eq. IV-32)}$$

where n_B is the number of oxidizable bonds in the VOC molecule (i.e., C–C, C=C, C–H, C#C) and M its molecular mass, with 6 and 28.05 being the number of oxidizable bonds and molecular mass of ethene which is the reference VOC. The parameter R is linked to the VOC reactivity with and defined by:

$$R = 1 - (B \times \gamma_R + 1)^{-1} \quad \text{(Eq. IV-33)}$$

where γ_R is calculated using:

$$\gamma_R = (k_{OH}/k_{OH}°) \times (6/n_B) \quad \text{(Eq. IV-34)}$$

where k_{OH} is the OH reaction rate coefficient of the studied VOC, and $k_{OH}°$ that of the reference compound, ethene, 8.52×10^{-12} cm^3 molecule^{-1} s^{-1} (McGillen et al., 2020) at room temperature and atmospheric pressure. These rate coefficients are estimated using the tool presented in Chapter IV. The S parameter is correlated with the size of the VOC as follows:

$$S = (1 - \alpha) \times \exp (- C \times n_C{}^\beta) + \alpha \quad \text{(Eq. IV-35)}$$

where n_C, the total number of carbons in the molecule. When n_c increases, as the size of the VOC increases, the value of S decreases in order to represent the effect of larger VOC acting as a sink of NO$_x$ and radicals through organic nitrate formation, ultimately reducing the amount of O_3 formed.

The parameter F is used to represent the impact of less reactive carbonyl product formation. A less reactive product is defined as a product whose OH reaction rate coefficient is less than 2×10^{-12} cm^3 molecule^{-1} s^{-1}. In this study, due to the large number of compounds generated from the oxidation mechanism, and the lack of information on their oxidation chemistry, the value of F was set to 1 by default.

Finally, the R_{O3} parameter accounts for the production of free radicals due to the reaction of VOCs with ozone. As with the F parameter, there is a lack of data, because of a lack of data, the value of R_{O3} was set to 0 by default. However, sensitivity tests were conducted, since the value of the yields of OH radicals, ϕ_{OH}, used in the definition of R_{O3} ranges between 0 and 1. For different molecules (e.g., propyne), it was observed that adding the ϕ_{OH} minimal (0) or maximal value (1) leads to less than 3% difference in the resulting $POCP_E$ value, indicating that the R_{O3} factor is not of major importance in the present dataset. All the parameter values have been optimized in the former work of (Jenkin et al., 2017) and given for a single-day USA urban conditions and multi-day north-west European conditions in Table IV-17.

Table IV-17 : Parameters used to calculate the $POCP_E$ of this dataset under two specific conditions: Multi-days North-West European conditions and single-day USA urban conditions. All the different cases for each molecule type are specified, and these are implemented in a python script to derive the parameters necessary for the calculation of $POCP_E$ using the equations (Eq. IV-32 – Eq. IV-36). These parameters are taken from (Jenkin et al., 2017).

	Parameters / Types of compounds	Multi-days North-West European conditions	Single-day USA urban conditions
A	aliphatic, benzaldehydes, styrenes	100	154
	*Aromatics**	*A=66+215×(1-exp(-0.35×N))*	*A=25+514×(1-exp(-0.65×N))*
	aromatic, 0 alkyl	66	25
	aromatic, 1 alkyl	130	320
	aromatic, 2 alkyl	173	427
	aromatic, 3 alkyl	206	509
	aromatic, 4 alkyl	228	544
	aromatic, 5 alkyl	244	562
	aromatic, 6 alkyl	255	572
B	all	4	1
α	all	0.56	0.37
C	all	0.0038	0.0041
β	all	2.7	2.7
D	aliphatic	0.38	0.25
ε	aliphatic	0.16	0.18
P	aldehyde/ketone (exception for acetone and a,b-unsaturated carbonyls)	14	10
	α-dicarbonyls	67	124
	acetone and a,b-unsaturated carbonyls	0	
	cycloketones	0	0
E	alkenes/unsaturated oxygenates	20.9	22
λ	alkenes/unsaturated oxygenates	0.043	0.15
Q	benzaldehydes/styrenes	74	80
	hydroxyarenes	41	-

* N is the number of alkyl substituents.

In this work, the parametrization was built in a python script so that it could be applied to the list of the >14,000 compounds derived from the oxidation mechanism of α-pinene, toluene, and *n*-decane. Both USA and EU conditions have been applied to this dataset, and compared below in Figure IV-62. $POCP_E$ provides a ranking of the ability of a VOC to produce ozone and thus its contribution to tropospheric ozone pollution. It can be observed from Figure IV-62 that most of the compounds produce tropospheric ozone, although a small percentage <10% reduces tropospheric ozone levels. The difference in behavior between USA and EU locations are minor.

All the compounds result in tropospheric O_3 production ($POCP_E>0$) and can affect air quality regionally. They are all UVOCs that can react with OH through the photochemical $NMVOCs/NO_x/O_3$ cycle presented in Chapter I (Figure I-2). Only benzaldehydes and benzene rings substituted with oxygenated groups are responsible for the reduction in O_3 ($POCP_E<0$), while other alkyl substituted benzenes, such as toluene, are producing O_3. These results are consistent with those reported by Jenkin et al. (2017). Benzene rings are not reactive towards O_3. The reason for this is that the H-abstraction of a phenolic hydrogen in the benzaldehydes by OH or NO_3 will form a β-hydroxyphenoxy/o-semiquinone radical, which further react with NO_2 to form nitrophenols and nitrocatechols. Thus, the loss of NO_2 and OH results in a reduction of O_3 formation.
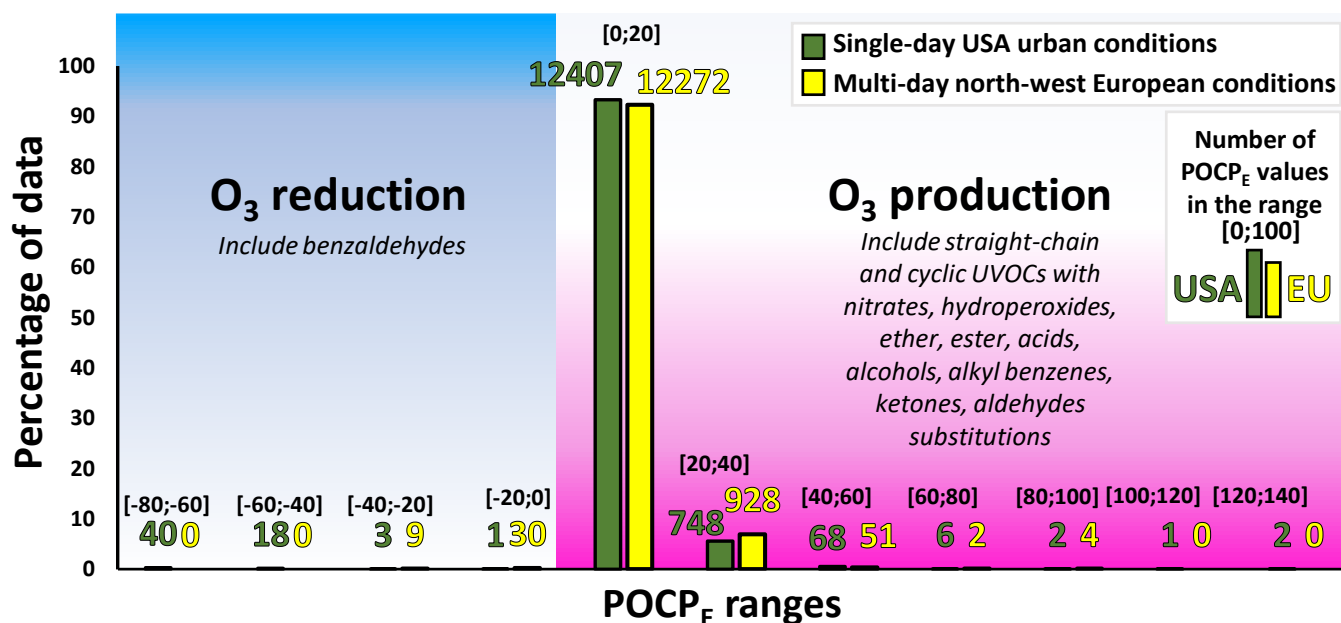
Figure IV-62 : $POCP_E$ of 14,446 unsaturated VOCs derived from the oxidation of α-pinene, toluene and estimated using the method of (Jenkin et al., 2017). The SMILES of the oxidation products are obtained from the GECKO-A mechanism application published by (Isaacman-VanWertz and Aumont, 2021), and the properties of each molecule is *calculated* using a python script built in this chapter.

Vapor pressure and secondary organic aerosols formation, SOAs

The vapor pressure P_{vap} is thermodynamic property that quantifies the equilibrium gas-particle partitioning of a compound. Organic compounds with a sufficiently low vapor pressure are expected to condense onto existing particles or to form new particles, (Hallquist et al., 2009) while compound with higher vapor pressure remain in the gas-phase. In Figure IV-63, the $\log_{10}$ of the estimated vapor pressure in atm, $\log_{10}(P_{vap})$, of the products of the oxidation of α-pinene (red), toluene (black) and *n*-decane (yellow) are presented as a function of the O:C ratios of the compounds. The P_{vap} are estimated using the MPBPWIN module of EPI Suite (US EPA, 2015). MPBPWIN uses three estimation methods (Antoine, Modified Grain, and the Mackay methods), and select the most adequate estimation tool value or an average of multiple depending on the properties of the VOC (see manual of EPI Suite (US EPA, 2015)). It must be noted that the estimation of P_{vap} remain challenging and that these values are used as estimates for discussion. The vapor pressure of sulfuric acid and acetone are displayed as indicator of lower vapor pressure compounds (around sulfuric acid, $P_{vap} = 3.2895×10^{-8}$ atm at 25°C (Roedel, 1979), purple line) which are likely to condense in aerosol phase (approximately low/extremely low volatility compounds), and higher vapor pressure compounds (similar to acetone, $P_{vap}=0.453$ atm at 25°C (Felsing and Durban, 1926), blue line) which readily converts to gas-phase without converting to liquid phase under atmospheric conditions (Finlayson-Pitts and Pitts, 1999; Hallquist et al., 2009). Here, most oxidation products are likely to condense on aerosols or form new aerosols, with the maximum of data for all distribution below the purple line (right-hand side distribution in Figure IV-63).

The O:C ratios indicates the degree of oxidation in the molecule. It is observed that higher O:C ratios are correlated with increasing likelihood to condense onto aerosols or forming new aerosols, for the oxidation products of the three species studied (Figure IV-63). Hence, highly oxidized products of the oxidation of VOCs are likely to contribute to SOA formation when emitted or formed in the atmosphere, as expected. It seems that a larger fraction of toluene oxidation products tends to be highly oxidized compared to α-pinene and *n*-decane. Most of the *n*-decane products have a O:C ratio below 1.5, while most of the toluene products have a O:C ratio above 1.5. Most of the α-pinene products have a O:C ratio below 2. The reasons for these can be due to the structure of the parent compound and mechanistic differences. Toluene is an alkyl substituted benzene, α-pinene is a cycloalkene and *n*-decane is an alkane. The carbon-chain of *n*-decane ($C_{10}H_{22}$) is long and it undergo H-abstraction with following oxidation in presence of O_2 and NO_x. α-pinene ($C_{10}H_{16}$) can undergo H-abstraction or addition of the tropospheric oxidants, and toluene (C_7H_8) can undergo H-abstraction or addition of the tropospheric oxidants except O_3 addition (see mechanisms in Chapter I). Thus, the ratio of oxygen atoms to carbon atom will be smaller in longer-chain compounds compared to smaller-chain compounds for most products that did not undergo decomposition. Also, the mechanistic differences can lead to different oxidation state (see carbonyl products from OH-oxidation in

Figure I-3 of Chapter I which is more oxidized than analogous carbonyl product from Cl-oxidation in Figure I-8 in Chapter I).

Among the 10,009 oxidation products of α-pinene, 77% contain nitrates, 23% are cyclic compounds, 99.98% are oxygenated, 0.01% (87 UVOCs) are unsaturated, and none are aromatics. Among the 7,738 oxidation products of *n*-decane, 73% contain nitrates, <0.01% (32 UVOCs) are unsaturated, 99.88% are oxygenated, and there are no cyclic compounds and no aromatics. Among the 21,128 oxidation products of toluene, 69%contain nitrates, 42% are cyclic compounds, 99.99% are oxygenated, 9% (1,828 UVOCs) are unsaturated and 0.03% (6 UVOCs) are aromatics. It is observed that toluene oxidation results in more various compounds some of which are unsaturated and aromatic compounds. All these various classes are spread out over the range of vapor pressures and O:C ratios without distinction. Only the aromatics from toluene oxidation have all an estimated vapor pressure of $\log_{10}(P_{vap})$ = -9.70 and an O:C ratio of 1. Among the types of compounds mentioned, none seems to contribute more significantly than another to the formation of SOAs. This example of three oxidation mechanisms highlights the diversity and large number of compounds that can be formed in the atmosphere, as discussed in Chapter I.
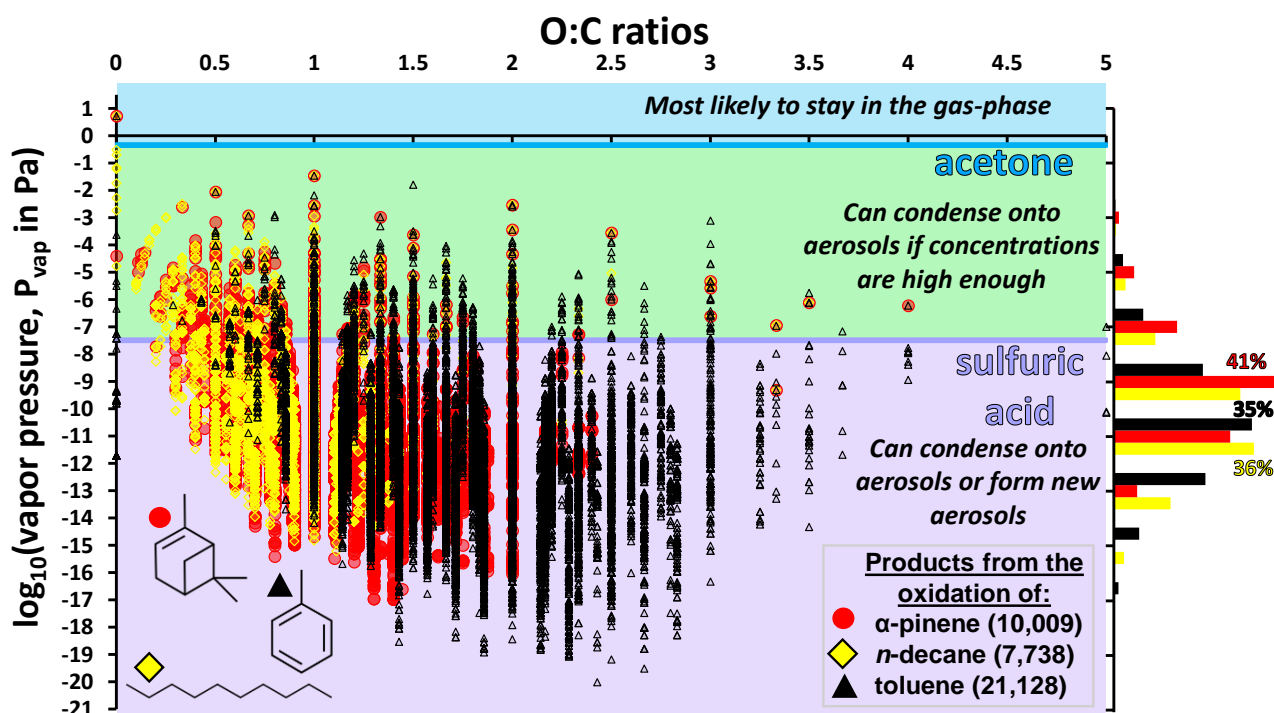
Figure IV-63 : Logarithm (base 10) of the estimated vapor pressure in atm, $\log_{10}(P_{vap})$, of the products of the oxidation of α-pinene (red), toluene (black) and *n*-decane (yellow) as a function of O:C ratios. The number of oxidation products are indicated in the parenthesis. The O:C ratios are the ratio between oxygen and carbon atoms in the compounds. The vapor pressures are estimated using the MPBPWIN module (US EPA, 2015). Right-hand side : Distribution of the $\log_{10}(P_{vap})$ for each list of products, with maximum of the frequency of data being indicated in percentage (α-pinene: red, toluene: black, and *n*-decane: yellow). The $\log_{10}(P_{vap})$ of acetone and sulfuric acid are displayed as indicators of the ability to condense onto aerosols or to form new aerosols. Most of the compounds are likely to participate in SOA formation.

IV-5. __Conclusions__

There is a potentially vast number of unsaturated volatile organic compounds encountered in the atmosphere either through direct emission or through secondary production. Because of their high reactivity towards various oxidants (e.g., OH, NO_3, O_3 and Cl), and the time and expense required for making new experimental kinetic measurements, it is necessary to find ways of estimating these data.

A new and fully automated technique for estimating site-specific reactivity of the UVOC compounds for each oxidant is presented in this chapter. The only input required for this software tool is a list of compounds rendered in the commonly used SMILES line notation. This method builds upon earlier free-energy relationships using the PFMO method, and employs other readily calculable parameters such as buried volume to augment these relationships. It is found that the computationally efficient PM6 method works as well or better than a more expensive DFT approach, allowing us to make predictions from *a priori* information about each target molecule. The potential advantage of this technique is that it can be extrapolated to less studied structures which have no directly representative data in the SAR training set.

This method is found to work better for reactions with OH, and also Cl (where it is the only automated estimation approach known). However, other approaches available in the literature possess their own advantages, especially for the reactions of NO_3 and O_3. The SAR method of Michelat et al. (2022) also demonstrates good performance for limited subsets of data, which suggests that further extensions of this methodology may be useful. In the absence of data, it may be preferable to provide an estimate even with uncertainties, as discussed by (Vereecken et al., 2018). This is the reason for developing this tool. It provides such estimates for a wide variety of compounds, without excluding any complex molecules, e.g., very long chain, multiple double bonds, highly oxidized and highly functionalized polycyclic structures.

In summary, in its first iteration, it is suggested that the KINESTEASY tool shows promise in predicting a highly diverse range of chemical structures, which is intended to be of use to the atmospheric chemistry community, which may be looking for easy and efficient way to obtain the kinetic data of long and various lists of chemical structures. This has been tested for the oxidation products of three VOCs largely emitted from natural and anthropogenic sources, α-pinene, *n*-decane, and toluene, representative of cyclic alkene, saturated alkane, and aromatic oxidation mechanism, respectively. Using the GECKO-A mechanism (Isaacman-VanWertz and Aumont, 2021). The most relevant oxidation products, as selected by (Isaacman-VanWertz and Aumont, 2021), represent thousands of compounds including a variety of oxygenated and nitrated alkanes, alkenes (if the parent compound is unsaturated), and aromatics (if the parent compound is an aromatic). All of these oxidation products are mostly degraded by OH during daytime and NO_3 during nighttime. Also, they all contribute to O_3 production, except for benzaldehydes, and are affecting regional air quality. They also contribute to SOA formation for the majority of these compounds, and thus could

affect public health. It would be interesting to complete this work by coupling these results with epidemiologic softwares, such as the VEGA tool (https://www.vegahub.eu/portfolio-types/vega-software/), to evaluate the public health impact of these compounds. This also shows the usefulness of having different estimation tools that allows a rapid screening of large databases of compounds in order to assess their impact on the atmosphere.

References

Aschmann, S.M., Arey, J., Atkinson, R., 2001. Atmospheric chemistry of three C10 alkanes. The Journal of Physical Chemistry A 105, 7598–7606.

Atkinson, R., 1986. Kinetics and mechanisms of the gas-phase reactions of the hydroxyl radical with organic compounds under atmospheric conditions. Chem. Rev. 86, 69–201.

Atkinson, R., 1987. A structure-activity relationship for the estimation of rate constants for the gas-phase reactions of OH radicals with organic compounds. Int. J. Chem. Kinet. 19, 799–828.

Atkinson, R., 1988. Estimation of gas-phase hydroxyl radical rate constants for organic chemicals. Environ Toxicol Chem 7, 435–442.

Atkinson, R., 1997. Gas-Phase Tropospheric Chemistry of Volatile Organic Compounds: 1. Alkanes and Alkenes. Journal of Physical and Chemical Reference Data 26, 215–290.

Aumont, B., Szopa, S., Madronich, S., 2005. Modelling the evolution of organic carbon during its gas-phase tropospheric oxidation: development of an explicit model based on a self generating approach. Atmospheric Chemistry and Physics 5, 2497–2517.

Brioude, J., Portmann, R.W., Daniel, J.S., Cooper, O.R., Frost, G.J., Rosenlof, K.H., Granier, C., Ravishankara, A., Montzka, S.A., Stohl, A., 2010. Variations in ozone depletion potentials of very short-lived substances with season and emission region. Geophysical Research Letters 37.

Brown, S.S., Stutz, J., 2012. Nighttime radical observations and chemistry. Chemical Society Reviews 41, 6405–6447.

Calvert, J.G., Atkinson, R., Kerr, J.A., Madronich, S., Moortgat, G.K., Wallington, T.J., Yarwood, J.G., 2000. The Mechanisms of Atmospheric Oxidation of the Alkenes, New York Oxford. ed. Oxford University Press.

Carter, W.P., 2000. Documentation of the SAPRC-99 chemical mechanism for VOC reactivity assessment. Contract 92, 95–308.

Carter, W.P.L., 2021. Estimation of Rate Constants for Reactions of Organic Compounds under Atmospheric Conditions. Atmosphere 12, 1250.

Chai, J.-D., Head-Gordon, M., 2008. Long-range corrected hybrid density functionals with damped atom–atom dispersion corrections. Physical Chemistry Chemical Physics 10, 6615–6620.

Felsing, W.A., Durban, S.A., 1926. The vapor pressures, densities, and some derived quantities for acetone. Journal of the American Chemical Society 48, 2885–2893.

Finlayson-Pitts, B.J., Pitts, J.N., 1999. Chemistry of the Upper and Lower Atmosphere: Theory, Experiments, and Applications. Elsevier Science.

Frisch, M.J., Trucks, G.W., Schlegel, H.B., Scuseria, G.E., Robb, M.A., Cheeseman, J.R., Scalmani, G., Barone, V., Petersson, G.A., Nakatsuji, H., Li, X., Caricato, M., Marenich, A.V., Bloino, J., Janesko, B.G., Gomperts, R., Mennucci, B., Hratchian, H.P., Ortiz, J.V., Izmaylov, A.F., Sonnenberg, J.L., Williams-Young, D., Ding, F., Lipparini, F., Egidi, F., Goings, J., Peng, B., Petrone, A., Henderson, T., Ranasinghe, D., Zakrzewski, V.G., Gao, J., Rega, N., Zheng, G., Liang, W., Hada, M., Ehara, M., Toyota, K., Fukuda, R., Hasegawa, J., Ishida, M., Nakajima, T., Honda, Y., Kitao, O., Nakai, H., Vreven, T., Throssell, K., Montgomery, J.A., Jr., Peralta, J.E., Ogliaro, F., Bearpark, M.J., Heyd, J.J., Brothers, E.N., Kudin, K.N., Staroverov, V.N., Keith, T.A., Kobayashi, R., Normand, J., Raghavachari, K., Rendell, A.P., Burant, J.C., Iyengar, S.S., Tomasi, J., Cossi, M., Millam, J.M., Klene, M., Adamo,

C., Cammi, R., Ochterski, J.W., Martin, R.L., Morokuma, K., Farkas, O., Foresman, J.B., Fox, D.J., 2016. Gaussian~16 Revision C.01.

Grimme, S., Bannwarth, C., Shushkov, P., 2017. A robust and accurate tight-binding quantum chemical method for structures, vibrational frequencies, and noncovalent interactions of large molecular systems parametrized for all spd-block elements (Z= 1–86). Journal of chemical theory and computation 13, 1989–2009.

Grimme, S., Bohle, F., Hansen, A., Pracht, P., Spicher, S., Stahn, M., 2021. Efficient quantum chemical calculation of structure ensembles and free energies for nonrigid molecules. The Journal of Physical Chemistry A 125, 4039–4054.

Hallquist, M., Wenger, J.C., Baltensperger, U., Rudich, Y., Simpson, D., Claeys, M., Dommen, J., Donahue, N.M., George, C., Goldstein, A.H., 2009. The formation, properties and impact of secondary organic aerosol: current and emerging issues. Atmospheric chemistry and physics 9, 5155–5236.

Isaacman-VanWertz, G., Aumont, B., 2021. Impact of organic molecular structure on the estimation of atmospherically relevant physicochemical parameters. Atmospheric Chemistry and Physics 21, 6541–6563.

Jenkin, M.E., Derwent, R.G., Wallington, T.J., 2017. Photochemical ozone creation potentials for volatile organic compounds: Rationalization and estimation. Atmospheric Environment 163, 128–137.

Jenkin, M.E., Saunders, S.M., Pilling, M.J., 1997. The tropospheric degradation of volatile organic compounds: a protocol for mechanism development. Atmospheric Environment 31, 81–104.

Jenkin, M.E., Valorso, R., Aumont, B., Newland, M.J., Rickard, A.R., 2020. Estimation of rate coefficients for the reactions of O3 with unsaturated organic compounds for use in automated mechanism construction. Atmos. Chem. Phys. 20, 12921–12937.

Jenkin, M.E., Valorso, R., Aumont, B., Rickard, A.R., Wallington, T.J., 2018. Estimation of rate coefficients and branching ratios for gas-phase reactions of OH with aliphatic organic compounds for use in automated mechanism construction. Atmos. Chem. Phys. 18, 9297–9328.

Johnson, R., 2022. Computational Chemistry Comparison and Benchmark Database, NIST Standard Reference Database 101.

Kerdouci, J., Picquet‐Varrault, B., Doussin, J., 2010. Prediction of Rate Constants for Gas-Phase Reactions of Nitrate Radical with Organic Compounds: A New Structure–Activity Relationship. ChemPhysChem 11, 3909–3920.

Kerdouci, J., Picquet-Varrault, B., Doussin, J.-F., 2014. Structure–activity relationship for the gas-phase reactions of NO3 radical with organic compounds: Update and extension to aldehydes. Atmospheric Environment 84, 363–372.

King, M.D., Canosa-Mas, C.E., Wayne, R.P., 1999a. Frontier molecular orbital correlations for predicting rate constants between alkenes and the tropospheric oxidants NO3, OH and O3. Phys. Chem. Chem. Phys. 1, 2231–2238.

King, M.D., Canosa-Mas, C.E., Wayne, R.P., 1999b. A structure–activity relationship (SAR) for predicting rate constants for the reaction of NO3, OH and O3 with monoalkenes and conjugated dienes. Phys. Chem. Chem. Phys. 1, 2239–2246.

Kwok, E.S.C., Atkinson, R., 1995. Estimation of hydroxyl radical reaction rate constants for gas-phase organic compounds using a structure-reactivity relationship: An update. Atmospheric Environment 29, 1685–1695.

Leather, K.E., McGillen, M.R., Percival, C.J., 2010. Temperature-dependent ozonolysis kinetics of selected alkenes in the gas phase: an experimental and structure–activity relationship (SAR) study. Phys. Chem. Chem. Phys. 12, 2935.

Luchini, G., Patterson, T., Paton, R.S., 2022. DBSTEP: DFT Based Steric Parameters.

McGillen, M.R., Archibald, A.T., Carey, T., Leather, K.E., Shallcross, D.E., Wenger, J.C., Percival, C.J., 2011. Structure–activity relationship (SAR) for the prediction of gas-phase ozonolysis rate coefficients: an extension towards heteroatomic unsaturated species. Phys. Chem. Chem. Phys. 13, 2842–2849.

McGillen, M.R., Carey, T.J., Archibald, A.T., Wenger, J.C., Shallcross, D.E., Percival, C.J., 2008. Structure–activity relationship (SAR) for the gas-phase ozonolysis of aliphatic alkenes and dialkenes. Phys. Chem. Chem. Phys. 10, 1757.

McGillen, M.R., Carter, W.P.L., Mellouki, A., Orlando, J.J., Picquet-Varrault, B., Wallington, T.J., 2020. Database for the kinetics of the gas-phase atmospheric reactions of organic compounds. Earth System Science Data 12, 1203–1216.

Meylan, W.M., Howard, P.H., 1993. Computer estimation of the Atmospheric gas-phase reaction rate of organic compounds with hydroxyl radicals and ozone. Chemosphere 26, 2293–2299.

Michelat, L., Mellouki, A., Ravishankara, A.R., El Othmani, H., Papadimitriou, V.C., Daële, V., McGillen, M.R., 2022. Temperature-Dependent Structure–Activity Relationship of OH + Haloalkene Rate Coefficients under Atmospheric Conditions and Supporting Measurements. ACS Earth Space Chem. 6, 3101–3114.

Monks, P.S., Granier, C., Fuzzi, S., Stohl, A., Williams, M.L., Akimoto, H., Amann, M., Baklanov, A., Baltensperger, U., Bey, I., 2009. Atmospheric composition change–global and regional air quality. Atmospheric environment 43, 5268–5350.

Ng, N.L., Kroll, J.H., Chan, A.W.H., Chhabra, P.S., Flagan, R.C., Seinfeld, J.H., 2007. Secondary organic aerosol formation from m-xylene, toluene, and benzene. Atmospheric Chemistry and Physics 7, 3909–3922.

O'Boyle, N.M., Banck, M., James, C.A., Morley, C., Vandermeersch, T., Hutchison, G.R., 2011. Open Babel: An open chemical toolbox. Journal of Cheminformatics 3, 33.

Pedretti, A., Mazzolari, A., Gervasoni, S., Fumagalli, L., Vistoli, G., 2021. The VEGA suite of programs: An versatile platform for cheminformatics and drug design projects. Bioinformatics 37, 1174–1175.

Pfrang, C., King, M.D., Canosa-Mas, C.E., Flugge, M., Wayne, R.P., 2007. Gas-phase rate coefficients for the reactions of NO3, OH and O3 with α,β-unsaturated esters and ketones: Structure–activity relations (SARs). Atmospheric Environment 41, 1792–1802.

Pfrang, C., King, M.D., Canosa-Mas, C.E., Wayne, R.P., 2006a. Correlations for gas-phase reactions of NO3, OH and O3 with alkenes: An update. Atmospheric Environment 40, 1170–1179.

Pfrang, C., King, M.D., Canosa-Mas, C.E., Wayne, R.P., 2006b. Structure–activity relations (SARs) for gas-phase reactions of NO3, OH and O3 with alkenes: An update. Atmospheric Environment 40, 1180–1186.

Pfrang, C., Tooze, C., Nalty, A., Canosa-Mas, C.E., Wayne, R.P., 2006c. Reactions of NO3 with the man-made emissions 2-methylpent-2-ene, (Z)-3-methylpent-2-ene, ethyl vinyl ether, and the stress-induced plant emission ethyl vinyl ketone. Atmospheric Environment 40, 786–792.

Pracht, P., Bohle, F., Grimme, S., 2020. Automated exploration of the low-energy chemical space with fast quantum chemical methods. Physical Chemistry Chemical Physics 22, 7169–7192.

Ren, Y., Zhou, L., Mellouki, A., Daële, V., Idir, M., Brown, S.S., Ruscic, B., Paton, R.S., McGillen, M.R., Ravishankara, A.R., 2021. Reactions of NO$_3$ with aromatic aldehydes: gas-phase kinetics and insights into the mechanism of the reaction. Atmospheric Chemistry and Physics 21, 13537–13551.

Riplinger, C., Sandhoefer, B., Hansen, A., Neese, F., 2013. Natural triple excitations in local coupled cluster calculations with pair natural orbitals. The Journal of chemical physics 139, 134101.

Roedel, W., 1979. Measurement of sulfuric acid saturation vapor pressure; Implications for aerosol formation by heteromolecular nucleation. Journal of Aerosol Science 10, 375–386.

Stewart, J.J.P., 2007. Optimization of parameters for semiempirical methods V: Modification of NDDO approximations and application to 70 elements. J Mol Model 13, 1173–1213.

Stone, D., Whalley, L.K., Heard, D.E., 2012. Tropospheric OH and HO 2 radicals: field measurements and model comparisons. Chemical Society Reviews 41, 6348–6404.

Tokuhashi, K., Takizawa, K., Kondo, S., 2021. Rate constants for reactions of OH radicals with (Z)-CF3CCl=CHCl, CHF2CF=CF2, (E)-CF3CH=CHF, (Z)-CF3CH=CHF, CH3CF=CH2, and CH2FCH=CH2. Atmospheric Environment 255, 118428.

US EPA, O., 2015. EPI Suite[TM]-Estimation Program Interface [WWW Document]. URL https://www.epa.gov/tsca-screening-tools/epi-suitetm-estimation-program-interface (accessed 7.6.22).

Valorso, R., Aumont, B., Camredon, M., Raventos-Duran, T., Mouchel-Vallon, C., Ng, N.L., Seinfeld, J.H., Lee-Taylor, J., Madronich, S., 2011. Explicit modelling of SOA formation from α-pinene photooxidation: sensitivity to vapour pressure estimation. Atmospheric Chemistry and Physics 11, 6895–6910.

Vereecken, L., Aumont, B., Barnes, I., Bozzelli, J.W., Goldman, M.J., Green, W.H., Madronich, S., Mcgillen, M.R., Mellouki, A., Orlando, J.J., Picquet-Varrault, B., Rickard, A.R., Stockwell, W.R., Wallington, T.J., Carter, W.P.L., 2018. Perspective on Mechanism Development and Structure-Activity Relationships for Gas-Phase Atmospheric Chemistry: Perspective On Gas-Phase Atmospheric Chemical Kinetic Mechanism. Int. J. Chem. Kinet. 50, 435–469.

Wallington, T.J., Dagaut, P., Kurylo, M.J., 1988. Correlation between gas-phase and solution-phase reactivities of hydroxyl radicals towards saturated organic compounds. J. Phys. Chem. 92, 5024–5028.

Weigend, F., Ahlrichs, R., 2005. Balanced basis sets of split valence, triple zeta valence and quadruple zeta valence quality for H to Rn: Design and assessment of accuracy. Physical Chemistry Chemical Physics 7, 3297–3305.

Wuebbles, D.J., Patten, K.O., Johnson, M.T., Kotamarthi, R., 2001. New methodology for Ozone Depletion Potentials of short-lived compounds: n-Propyl bromide as an example. Journal of Geophysical Research: Atmospheres 106, 14551–14571.

Appendices : Chapter IV

App-IV-1. Additional information on the parametrization

App-IV-1.1. Buried volumes
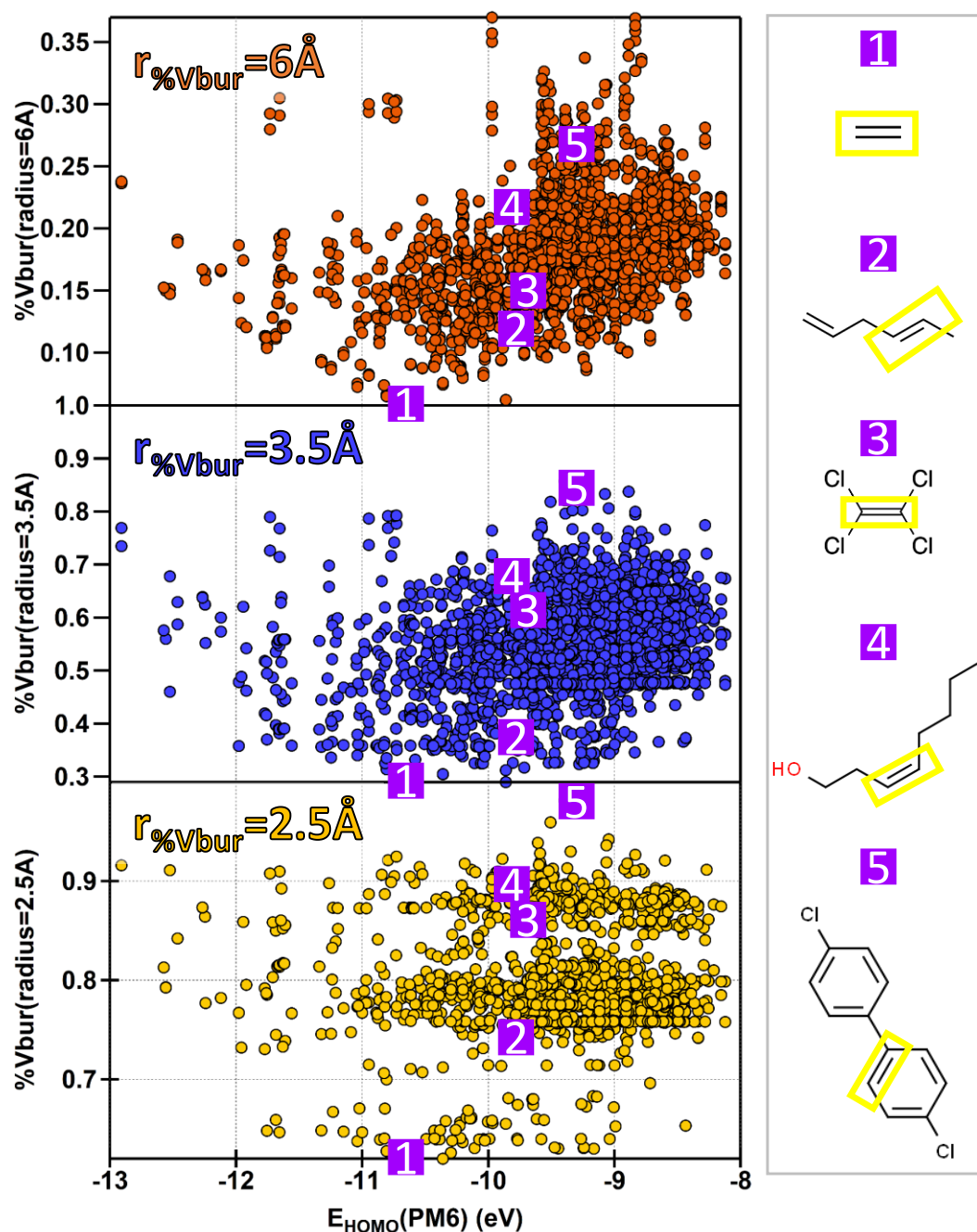
<u>Figure App-IV-1</u> : Buried volumes for different $r_{\%Vbur}$ (2.5, 3.5, and 6Å) as a function of E_{HOMO} calculated using PM6. Example molecules are located on each of the panels and were chosen for their structure (short/long chain, alkyl substituted or chlorinated) to assess the bulkiness of the substituents attached to the olefinic bond. Additionally, these molecules have a similar E_{HOMO}, which allows us to assess the impact of the different values of buried volumes since the other main variable of the multivariate linear regression (E_{HOMO}) will be approximately constant. From the simplest UVOC, ethene (compound 1), to tetrachloroethene (compound 2) substituted with bulky chlorine atoms, and longer chain alkenes and benzenoids. These plots highlight how larger $r_{\%Vbur}$ can distinguish longer chain alkenes, while smaller $r_{\%Vbur}$ includes mostly the alkyl groups and close neighbors (e.g., difference of values for compounds 3 and 4 that are very similar for $r_{\%Vbur}$ 2.5Å and 3.5Å and starts to be distinct for $r_{\%Vbur}$ 6Å). We chose the $r_{\%Vbur}$ accordingly, for O_3 and NO_3 a larger $r_{\%Vbur}$ is more adapted, while for OH and Cl a smaller $r_{\%Vbur}$ is better. This highlights the

relative importance of the steric effects in each reaction, and the impact of direct neighbors or of the whole chain (e.g., 1,3-cycloaddition mechanism). The buried volumes distribution for a $r_{\%Vbur}$ of 2.5Å appears to be bimodal, and we think it is due to geometric reasons since the sphere will include mostly closest neighbors that have not many possibilities.

App-IV-1.2. Estimation of the H-abstraction rate coefficient for Cl

Table App-IV-1 : All rate coefficients included in the correlation of the OH-Cl abstraction rate coefficients, as described in section IV-2.1.3.1.

CHX alkanes	CCl	CC(Br)C	FC(Br)F	CH small chain
FC(CC(Cl)(Cl)F)(F)F	FCCl	CCCCl	FCF	C
ClC(C(F)(F)F)Br	CC(F)(F)F	CCCBr	CCBr	CC
FC(C(F)(F)F)F	CI	CCCCCCBr	CCl	CCC
CC(Cl)(F)F	ClCCl	CCCCCCl	FCC(F)F	CCCC
FCC(F)(F)F	FCCF	CCCCCBr	CF	CC(C)C
FC(C1(F)CCC1(F)F)(F)F	ClC(Cl)Cl	CCC(Cl)C	FC(Cl)Cl	CC(C)(C)C
CC(Cl)(Cl)F	ClCBr	CCCCBr	CBr	CCC(C)C
FC(C(F)F)F	BrCBr	CC(I)C	CCCl	CCCCC
FCC(C(F)(F)F)(F)F	ClC(Br)Cl	CCCl	CC(F)F	CCCCCC
FC(CC(F)(F)F)F	ClCC(Cl)Cl	CCCCCl	ClCCCl	CCCC(C)C
CC(CC(F)(F)F)(F)F	CCF	FC(Cl)F	BrC(Br)Br	CCC(CC)C
FC(C(F)(F)F)Cl	ClC(Br)Br	CC(Cl)(Cl)Cl	BrCCBr	CC(C(C)C)C
ClC(C(F)(F)F)Cl	ClCC(Cl)C	ClCC(F)(F)F	CC(Cl)Cl	
FC(C(Cl)(F)F)Cl	CC(Cl)C	ClCC(CCl)Cl	CC(Cl)(C)C	

Table App-IV-2 : All rate coefficients not included in the correlation of the OH-Cl abstraction rate coefficients, as described in section IV-2.1.3.1.

CHX cycle	CH long-chain	CCCCCCCCCCCCCC
CC1CCCC1	CCCCCCC	CC(C(C)(C)C)(C)C
C1CCCC1	CCCCC(C)C	CC(CC(C)(C)C)C
C1CCCCC1	CCCCCCCC	CC(C(C)(C)C)C
C1CCC1	CCCCCCCCC	CC(CC(C)C)C
CCC1CCCC1	CCCCCCCCCC	
C1CCCCCC1	CCCCCCCCCC	
C1CCCCCCC1	CCCCCCCCCCCC	
C1CCCCCCCC1	CCCCCCCCCCCCC	

Limit of the H-abstraction rate coefficient for Cl:

Apart from the collision limit, the value of the $k_{Cl,abs,lim}$ has been optimized regarding the results obtained in the MLR. Initially, the value was set at $k_{OH,abs,lim}$ = 5.1×10^{-12} cm^{3}molecule^{-1}s^{-1} leading to a limit in Cl H-abstraction rate coefficient of $k_{Cl,abs,lim}$ = 5.36×10^{-10} cm^{3}molecule^{-1}s^{-1}. The limit value is associated to the

plateau (reaching the collision limit of the H-abstraction process) but also to the limitation of the MLR optimization. The values $k_{Cl,abs}$ are estimated from the values predicted by EPI Suite for $k_{OH,abs}$. When fixing the limiting value of $k_{OH,abs,lim}$ to the middle part of the plateau (5.1×10^{-12} cm³molecule⁻¹s⁻¹) this resulted in values of $k_{Cl,abs}$ that were too high which was inhibiting the other MLR parameters of k_{add} to adjust accurately since they add to compensate for an increased contribution of k_{abs} to the total reaction rate $k_{pred} = k_{add}+ k_{abs}$. All the compounds were well predicted except oxygenated that were overpredicted (Figure App-IV-2, panel (b)). This could not converge because the k_{abs} value was too big. So, the limiting value in $k_{Cl,abs,lim}$ was decreased to the actual value (bottom of the plateau, $k_{Cl,abs,lim} = 3.1\times10^{-12}$ cm³molecule⁻¹s⁻¹) where the main trend of CHX and the plateau are intersecting, and then, it can be observed that the MLR could be optimized without overestimating any class of compounds (Figure App-IV-2, panel (b)).

(a) Limit value $k_{OH,abs,lim}$ at 5.1×10^{-12} **(b) Limit value $k_{OH,abs,lim}$ at 3.1×10^{-12}**
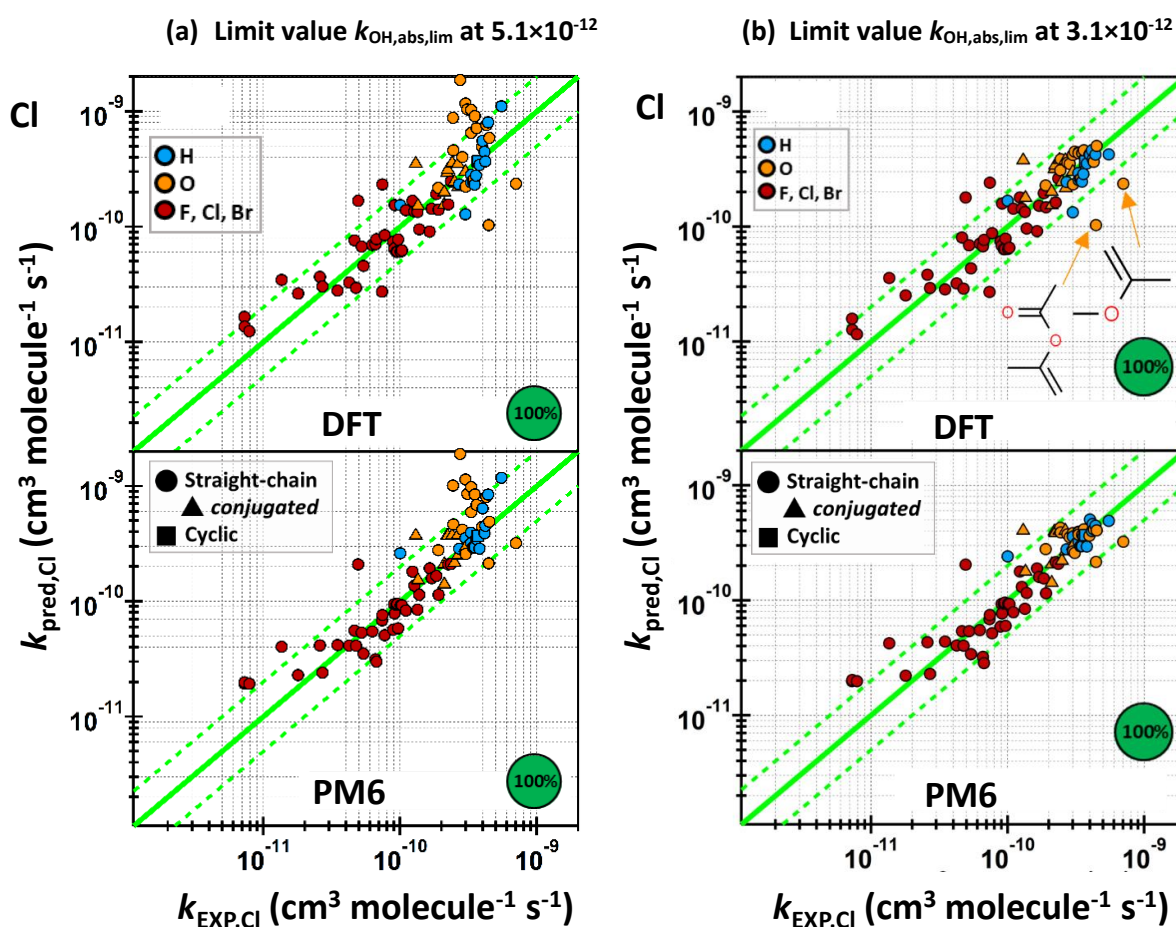
Figure App-IV-2 : MLR optimization for the Cl reaction with the extended dataset with using two different limit values for $k_{abs,OH}$ and $k_{abs,Cl}$: (a) $k_{OH,abs,lim}$ at 5.1×10^{-12} and thus $k_{Cl,abs,lim}$ at 5.4×10^{-10}; (b) $k_{OH,abs,lim}$ at 3.1×10^{-12} and thus $k_{Cl,abs,lim}$ at 1.8×10^{-10}.

App-IV-2. Additional results and discussion

App-IV-2.1. Cl reaction

App-IV-2.1.1. Haloalkenes dataset (CHX)

The SAR from Michelat et al. (2022) was extended to predict Cl rate coefficients, and it provided estimates in excellent agreement with experiments (Panel SAR, Figure App-IV-3). Overall, when comparing k_{PM6} with k_{SAR} from the extension made of the SAR of (Michelat et al., 2022), it appears that the k_{SAR} are more accurate with 100% being between a factor 2 of agreement with experimental data (Figure App-IV-3). It is thus a reliable tool for predicting Cl addition rate coefficient for haloalkenes compounds. However, the DFT and PM6 methods are agreeing well with experiments and show a good general agreement within the range of compounds. The predictions of PM6 appears to be more accurate than that of DFT, despite a computationally cheaper calculation of the variables. The DFT and PM6 method have the ability to be extended to include more substitution types, on the contrary to the SAR of Michelat et al. All the results on the performance for this reaction are presented in Table IV-14.
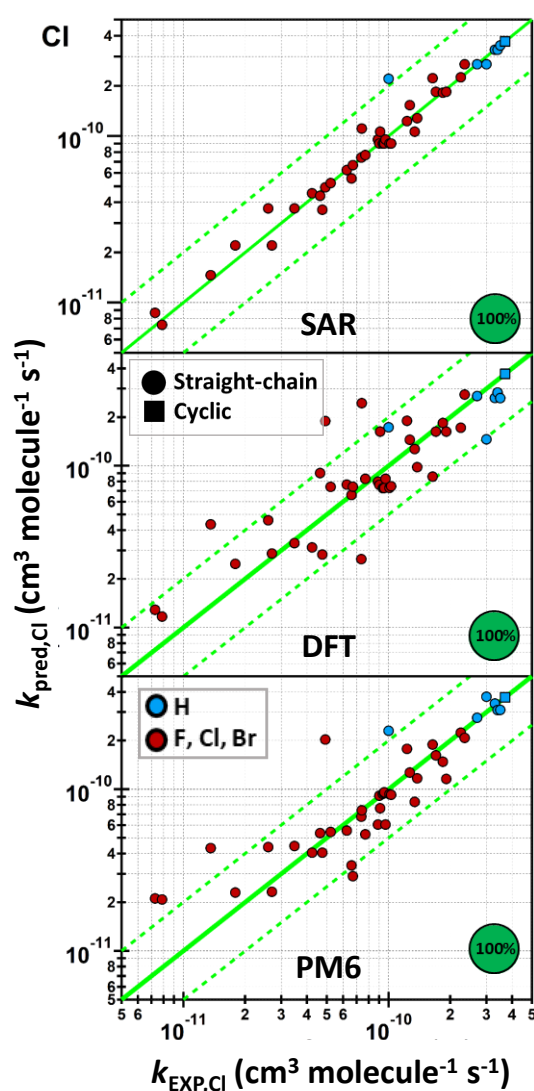
<u>Figure App-IV-3</u> : Predictions of k_{Cl} using 3 methods, i.e. SAR, DFT and PM6 tools, for all the 77 compounds of the haloalkenes dataset. For this dataset, a $r_{\%Vbur}$ of 3.5Å for buried volume has been selected since it is the most adapted for halogenated compounds which represents the majority of this list. The substitution types are C_nX_m where n has no limitation, and m=2n+1 and

includes H, F, Cl, Br, or a mix of these atoms. The pie chart represents the percentage of the whole k_{EXP} dataset for which the associated technique can provide an estimate.

App-IV-2.1.2. Extended dataset (CHONX)

Then, the DFT and PM6 tools were applied to the extended dataset, including more functional groups. The predictions of DFT are in very good agreement with the experiments, among tall the various class of compounds, with less than 89% and 87% of the k_{DFT} and k_{PM6} predictions respectively are agreeing within a factor 2 with k_{EXP} (Figure App-IV-4). The PM6 predictions did improve the estimate of some outliers of the DFT method, for example, the two oxygenates that were underpredicted using DFT (Figure App-IV-4). All the results on the performance for this reaction are presented in Table IV-14.
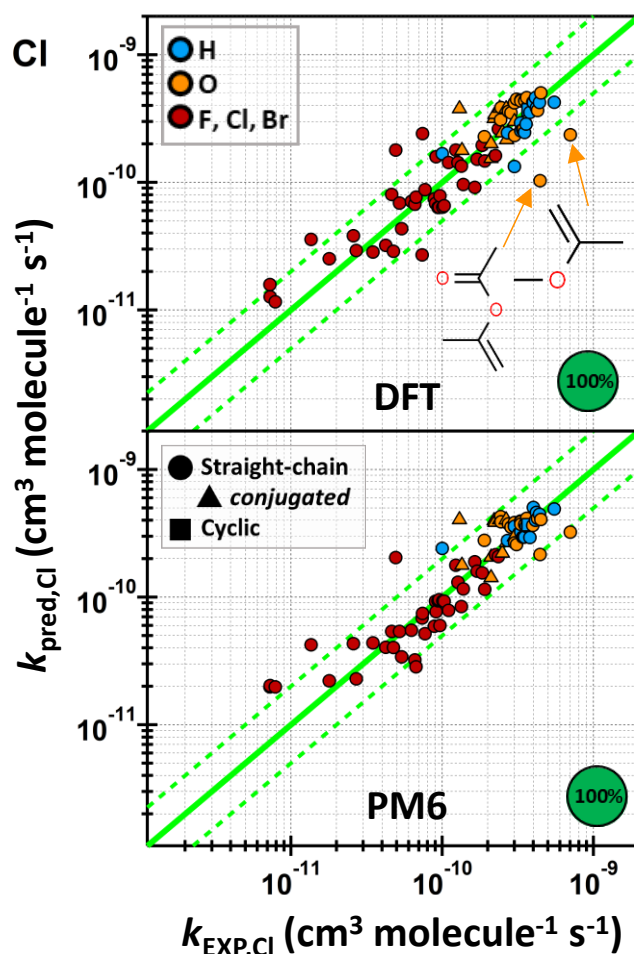
Figure App-IV-4 : Predictions of k_{Cl} using 2 methods, i.e., DFT and PM6 tools, for the extended database including CHOFClBrON species. For this dataset, a $r_{\%Vbur}$ of 3.5Å for buried volume was used since it is the most adapted for halogenated compounds which represents the majority of this list. The substitution types are C_nX_m where n has no limitation, and m=2n+1 and includes H, O, F, Cl, Br, or a mix of these atoms. The pie chart represents the percentage of the whole k_{EXP} dataset for which the associated technique can provide an estimate.

App-IV-2.1.3. All literature data available (CHNOPSX)

In this section, the estimation of the rate coefficients for the Cl reaction for the 236 species with kinetic data available (Figure App-IV-5). The H-abstraction rate coefficient of Cl was predicted using (Eq. IV-24). The performance of the PM6 tool for the Cl reaction is good, since 79% of the compounds are predicted within a factor of 2 compared to measurements. Additionally, PM6 method predicts rate coefficient for any types of CHNOPSX compounds without excluding any substitution types or chain, within the available dataset. It is a great improvement since no other automated estimation techniques is predicting k_{Cl} for UVOCs to the best of our knowledge. For that reason, no intercomparison between models was possible. The pyridine is the only pyridine in the dataset, which explains why it is perfectly since $F_{pyridine}$ factor was trained only for this compound. This highlights the problem of too many fitting factors, which can over-fit certain classes of compounds and give perfect predictions for them but lack precision when applied to molecules outside this restricted range.
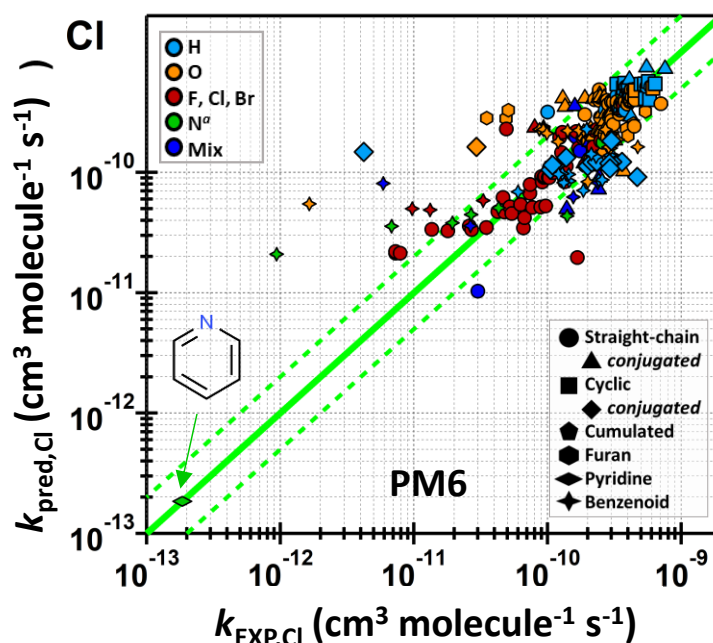
<u>Figure App-IV-5</u> : PM6 tool predictions for $k_{298,Cl}$, in cm³ molecule⁻¹ s⁻¹, of 236 unsaturated compounds for which literature data are available. The dataset includes straight-chain, cyclic, aromatics, conjugated, cumulated, furan, pyridine, or a combination of these structures, together with substitution types including C_nX_m where n has no limitation, and m=2n+1 and includes H, O, F, Cl, Br, I, N, or a mix of these atoms. For this dataset, $r_{\%Vbur}$ =2.5Å since it is the most adapted for this list. The pie chart represents the percentage of the whole k_{EXP} dataset for which the associated technique can provide an estimate.

App-IV-2.2. NO₃ reaction

App-IV-2.2.1. Haloalkenes dataset (CHX)

In order to compare the methods, the SAR of Michelat et al. (2022) was extended to NO₃ and it provides accurate estimates for the haloalkenes dataset (Panel SAR, Figure App-IV-6). However, it appears that both DFT and PM6 predictions have large uncertainties, which may be due to the $r_{\%Vbur}$ set at 3.5Å. By investigating this issue further using the PM6 tool, it was observed that a $r_{\%Vbur}$ of 6Å was more adapted for

describing NO_3 reactivity, probably due to an increased contribution from steric effects that are better described with a larger $r_{\%Vbur}$. Since DFT provides similar performance to PM6, there was no need to improve the DFT method and we only focused on the computationally cheap PM6 approach, in the interest of time. All the results on the performance for this reaction are presented in Table IV-15.
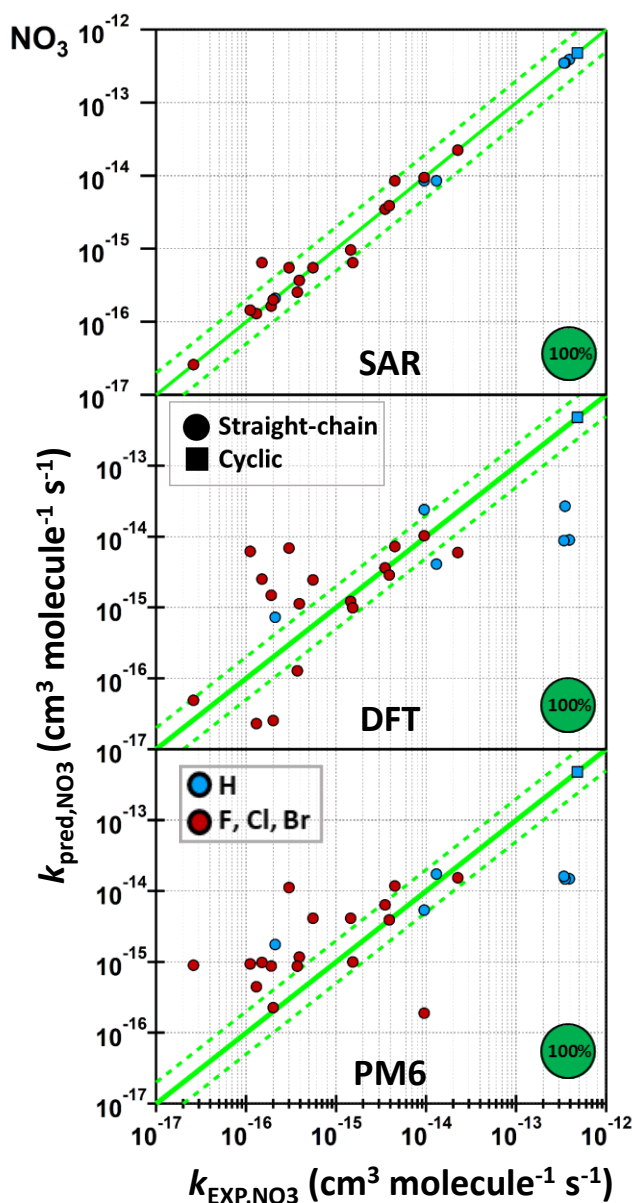
Figure App-IV-6 : Predictions of k_{NO3} for the haloalkenes dataset using 3 methods, i.e., SAR, DFT and PM6 tools. We use for this dataset, $r_{\%Vbur}=3.5$Å since it is the most adapted for halogenated compounds which represents the majority of this list. The substitution types are C_nX_m where n has no limitation, and m=2n+1 and includes H, F, Cl, Br, or a mix of these atoms. The pie chart represents the percentage of the whole k_{EXP} dataset for which the associated technique can provide an estimate.

App-IV-2.2.2. Extended dataset (CHONX)

Then, the DFT and PM6 methods were extended to more substitution types, and k_{GECKO}, k_{DFT} and k_{PM6} were compared. It is observed that GECKO-A predictions are in excellent agreement with the experimental values, but the method covers a smaller range of compounds compared to the other approaches (Figure

App-IV-7). On the other hand, the DFT and PM6 tools seem to lack a parameter to adequately describe the NO$_3$ reactivity can be seen by the two trends in the subgroups of compounds. However, the trends in the subgroups are not scattered, and it is possible, as discussed in the previous section, that modifying the r$_{\%Vbur}$ will improve the predictive ability of this algorithm. DFT performance seems to be better than that of DFT for more reactive compounds, which could come from the difference in buried volumes between both calculation methods (Figure App-IV-7). All the results on the performance for this reaction are presented in Table IV-15. Including the H-abstraction rate is not optimizing the prediction of the more reactive compounds for this dataset.
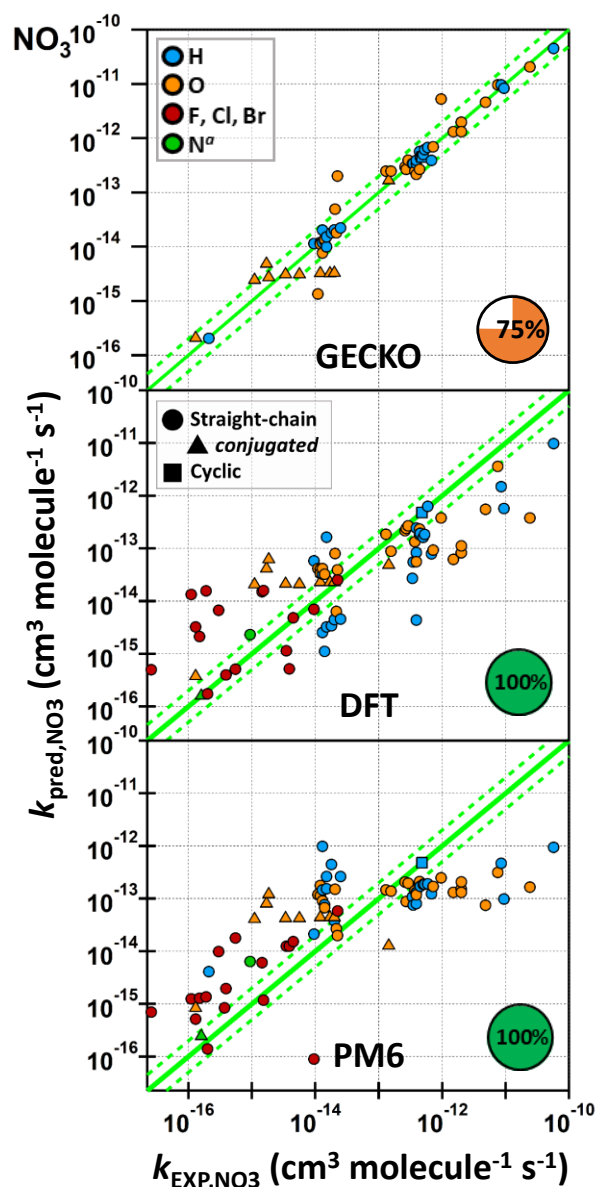
Figure App-IV-7 : Predictions of k_{NO3} using 3 methods, i.e., GECKO, DFT and PM6 tools, for the extended database including CHONX species. GECKO-A does not include halogenated species and some CHON species, which does not cover the whole dataset of this section. For this dataset, r$_{\%Vbur}$=3.5Å is used since it is the most adapted for halogenated compounds which represents the majority of this list. The substitution types are C$_n$X$_m$ where n has no limitation, and m=2n+1 and includes H, O, F, Cl, Br, N or a mix of these

atoms. The pie chart represents the percentage of the whole k_{EXP} dataset for which the associated technique can provide an estimate.

App-IV-2.2.3. All literature data available (CHNOPSX)

In this section, the estimation of the rate coefficients for the NO₃ reaction for the 270 compounds with experimental data available are presented (Figure App-IV-8). GECKO-A provides no estimate for aromatic compounds, the mechanism prefers measured data for this class of compound. Additionally, GECKO-A is predicting 64% of the species in this dataset and the excluded correspond to aromatics, halogenated, some nitrated and some oxygenated compounds, which are important atmospheric types of compounds. The PM6 tool is more general in this sense. Benzenoids are not well predicted in our correlation, and require further work before recommending the predicted values from this work. However, when including more compounds, similarly to Cl, a slight improvement of the description of the whole dataset can be observed, probably due to the fact that it contains more functionalities and data. Underestimation can still be observed for the oxygenated species, despite the fact that the rate coefficient H-abstraction of aldehydic hydrogens has been considered. It is likely that another important process is not well described using our algorithm for the reaction of NO₃ + CO unsaturated organic compounds, and this will require further investigation. Results on the performance can be found in Table IV-15.
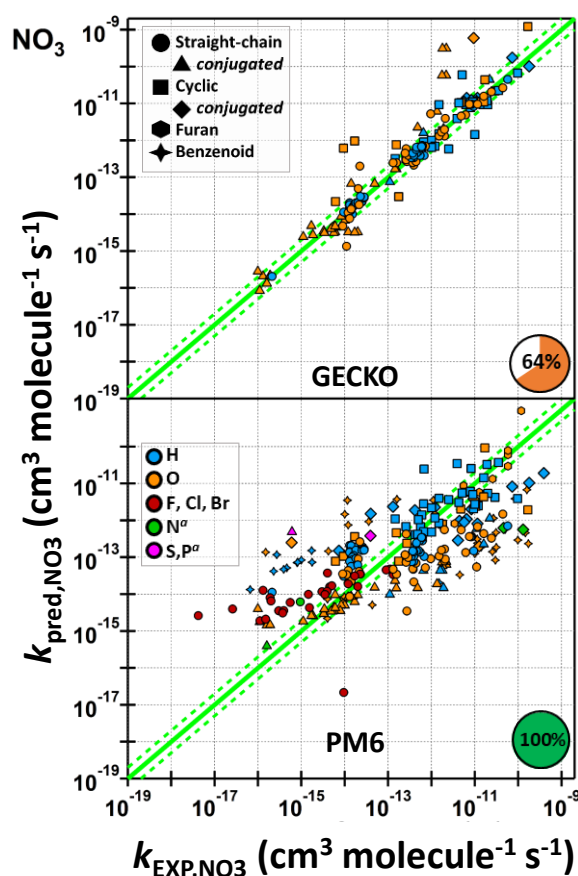
Figure App-IV-8 : PM6 tool predictions for $k_{298,NO3}$ from GECKO-A and PM6 tools of 270 unsaturated compounds for which literature data are available, while PM6 was able to retrieve predictions for all compounds, GECKO-A only estimates 173 compounds within

266

the whole dataset, excluding for example halogenated compounds and some oxygenates. The dataset includes straight-chain, cyclic, aromatics, conjugated, furan, or a combination of these structures, together with substitution types C_nX_m where n has no limitation, and m=2n+1 and includes H, O, F, Cl, Br, I, N, S, P or a mix of these atoms. For this dataset, $r_{\%Vbur}=6Å$ is used since it is the most adapted for this list. NO_3 abstraction of aldehydic hydrogen atoms is included in the predictions. The pie chart represents the percentage of the whole k_{EXP} dataset for which the associated technique can provide an estimate.

App-IV-2.3. O$_3$ reaction

App-IV-2.3.1. Haloalkenes dataset (CHX)

In the case of O_3, the mechanism is more complicated, and can occur through 1,3-cycloaddition or epoxidation, and the importance of steric hindrance and steric strain is more complex for different types of compounds compared to OH or Cl additions (McGillen et al., 2011, 2008) Hence, the orbital energies defined in section IV-1.11.3.2. are all calculated using $E_{HOMO}(C_i\text{-}C_j)$ = $E_{HOMO}(\pi\text{-orbital}(C_i\text{-}C_j))$ for O_3, as it improves the general performance of the SAR and could be explained by this difference in mechanism. The k_{SAR} predictions are in excellent agreement with the literature (Figure App-IV-9), but it is noted that most of F-factors are overfitted since they are trained on one unique value (see Table II-4). All the results on the performance for this reaction are presented in Table IV-16.
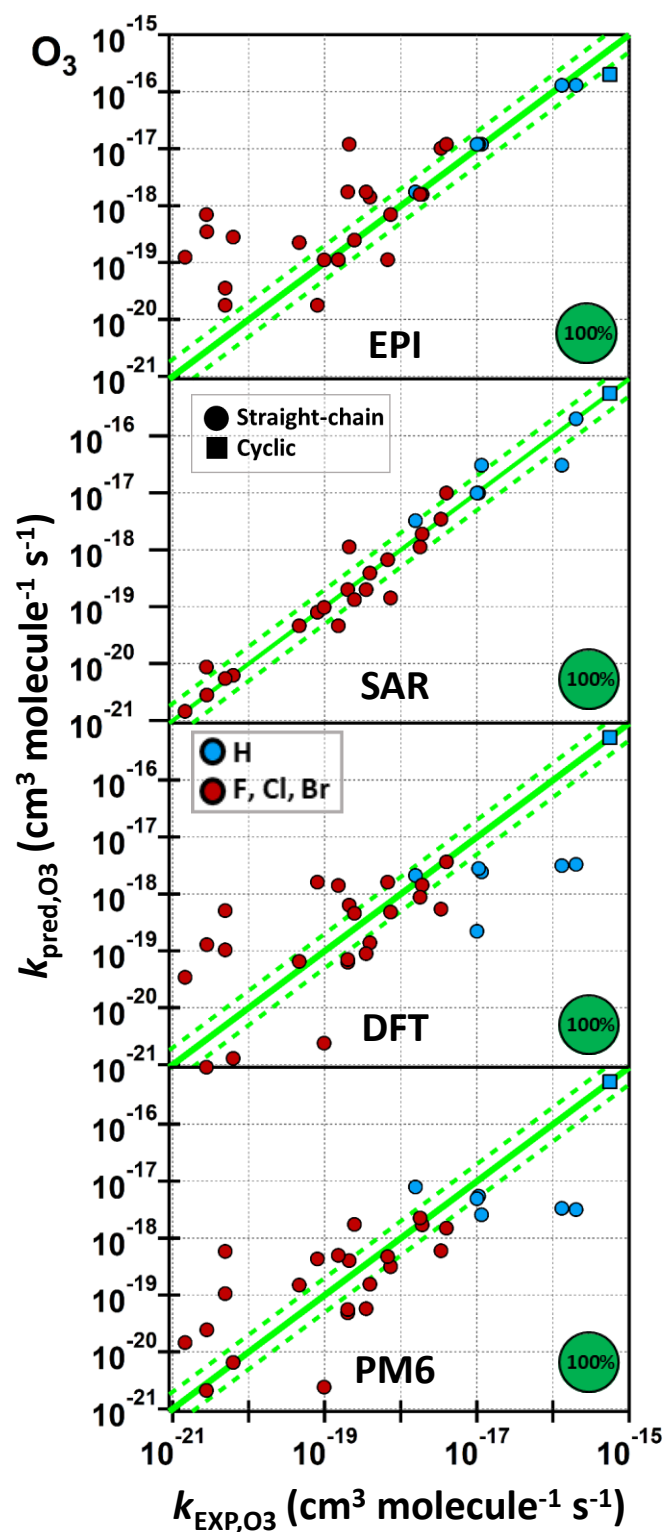
<u>Figure App-IV-9</u> : Predictions of the dataset of 77 haloalkenes, using EPI Suite, the updated version of the SAR of Michelat et al. (2022) for O_3 reaction, DFT and PM6 tools, compared to measurements. For this dataset, $r_{\%Vbur}=3.5$Å is used since it is the most adapted for halogenated compounds which represents the majority of this list. The substitution types are C_nX_m where n has no limitation, and m=2n+1 and includes H, F, Cl, Br or a mix of these atoms. The pie chart represents the percentage of the whole k_{EXP} dataset for which the associated technique can provide an estimate.

App-IV-2.3.2. Extended dataset (CHONX)

When looking at the predictions for the extended dataset, it seems that some factors for the O₃ reaction are not well represented in this parametrization (Figure App-IV-10). Further work is required. Some improvement is observed for DFT and PM6, within a similar range of accuracy than EPI Suite, but it still needs some improvement. GECKO-A predictions are the most accurate, but does not cover the whole dataset (70% predicted). All the results of the performance for this reaction are presented in Table IV-16.
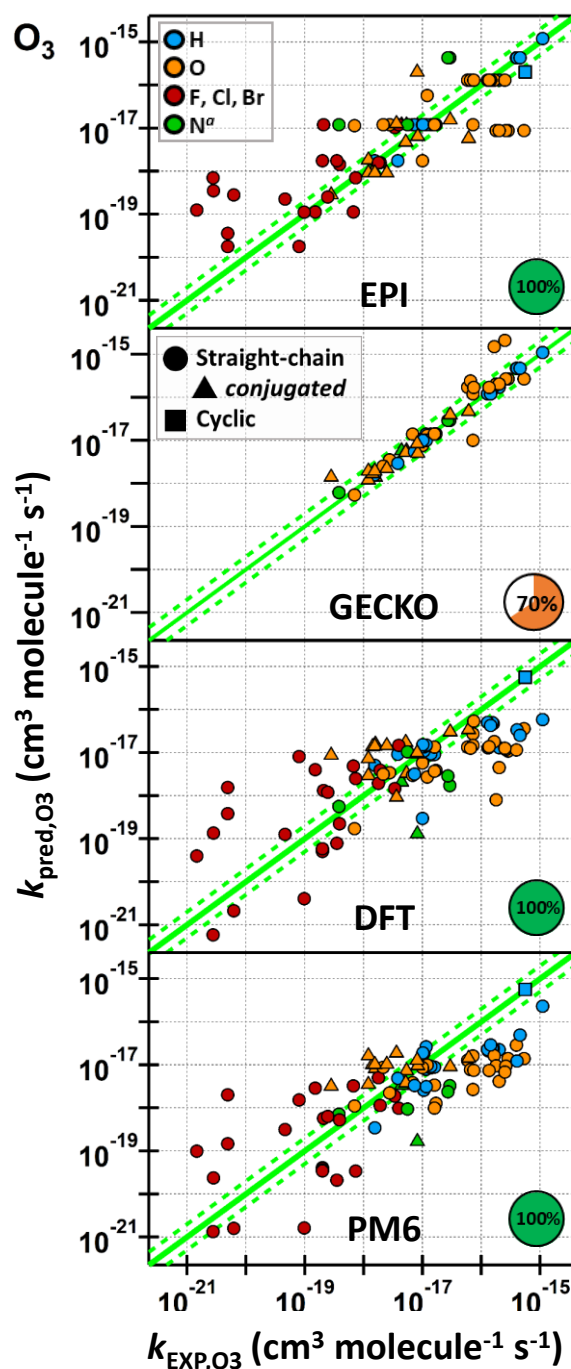
<u>Figure App-IV-10</u> : Predictions of k_{O3} using 4 methods, i.e., EPI Suite, SAR, DFT and PM6 tools, for the extended database including CHONX species. For this dataset, $r_{\%Vbur}$=3.5Å is used since it is the most adapted for halogenated compounds which represents the

majority of this list. The substitution types are C_nX_m where n has no limitation, and m=2n+1 and includes H, O, F, Cl, Br, N, or a mix of these atoms. The pie chart represents the percentage of the whole k_{EXP} dataset for which the associated technique can provide an estimate.

App-IV-2.3.3. All literature data available (CHNOPSX)

In this section we present the estimation of the rate coefficients for the O_3 reaction for the 289 compounds with experimental data available (Figure App-IV-11). The predictions from EPI Suite cover 98% of the k_{O3} literature data, k_{GECKO} covers 83%, while PM6 estimates the rate of the whole dataset. All the results on the performance for this reaction is presented in Table IV-16.

The PM6 method applied for O_3 is slightly different than that of other oxidants since it uses the E_{HOMO} of the whole molecule only, with the correction for conjugated system applied to all molecules without distinction. This has been showed after different trials to improve the MLR predictions. The exact reason for this is not completely identified, however, it is expected to be due to the specific mechanism of O_3 addition (see Chapter I), the interaction between the UVOC and the ozone molecule is forming a delocalized system of electron which is well described in our method via the delocalization term. Hence, treating these molecules as subject to electron delocalization is a better description. Ozone is adding to both carbons of the double-bond to form an ozonide, contrary to OH or NO_3 radicals' mechanisms. Also, benzenoids compounds included are those with an additional double-bond apart from those in the benzenoids cycle that were excluded since they are unreactive towards O_3 addition.

Overall, the k_{PM6} predictions are in general agreement and stronger correlation compared to EPI Suite which displays critical degeneracy in the estimates, with large factor of over and under estimation (Figure App-IV-11). The correlation of k_{GECKO} is good, despite the lack of estimation for a part of the compounds, especially less reactive ones, and these compounds represent the less studied atmospheric species of potential interest, for which estimations may be useful due to the lack of data. Hence, PM6 tool is making a step towards better predictive ability in this sense. Yet, from the trend in the correlation it seems that a parameter is still missing in our parametrization. Despite our effort, no adequate representation was found and this is related to the complexity of the ozonolysis mechanism. This will be investigated in further work, and these results are presented for discussion without being recommended for use.

The percentage of the whole literature dataset predicted within a factor of 2 of agreement with k_{EXP} is of 29% for k_{PM6}, 49% for k_{EPI} and 75% for k_{GECKO}. Yet, GECKO-A does not predict all the types of compounds present in the database. Over the 289 species with available kinetic data, 17% does not have any estimation, which includes halogenated, S-containing, some specific features like nitryle or N=C=O features, some cycles with nitrate substitutions, some substituted furans, some ketones and aldehydes, and some

conjugated compounds. EPI Suite estimates 98% of the compounds, excluding a few compounds like 2,5-dimethylfuran, 3-methylfuran, which are all not estimated in GECKO-A as well.

These compounds which are of importance for atmospheric chemistry, since they are measured in high concentration in biomass burning plumes and should be adequately described in atmospheric models. Estimations are provided for these rate coefficients that EPI Suite does not predict, and the associated k_{PM6} agree with the experimental measurements within a factor 6, except for 1-benzofuran that is underestimated by a factor of 13. It represents a great improvement, since it fills the gap where no data was available to feed the models, and within a satisfying order of magnitude of accuracy.

However, improvement can be made to improve the description for O_3 reactivity using PM6. Indeed, large uncertainty remain in the predictions, as a large fraction of compounds remains overestimated by, at most, a factor of 4×10^2, for (Z)-1,2-Dichloroethene (Figure App-IV-11). However, this compound and others with the largest error in the predictions are not estimated by GECKO-A at all, so, it is by comparison a good starting point for improving our ability to predict these compounds (Figure App-IV-11).

By comparison, the worst overestimation of k_{EPI} is up to a factor of 6×10^2, for 1-(Cedr-8-en-9-yl)ethanone. This illustrates how this SAR can start to fail for larger and more complex molecules. For this compound, GECKO provides no estimate, which shows how limited this SAR is by the time of writing. The worst prediction from GECKO is more than 1×10^3 lower than the measured value for butadiene, while k_{EPI} and k_{PM6} are within a factor 22 of agreement. The overall excellent agreement of GECKO with experiments may be the result of an accurate fit of the experimental data of simple molecules, while coming at the expense of not extending them to more complex compound, excluding a variety of species, and leading to an overfit of the known data at the expense of not being able to predict the unknown species.
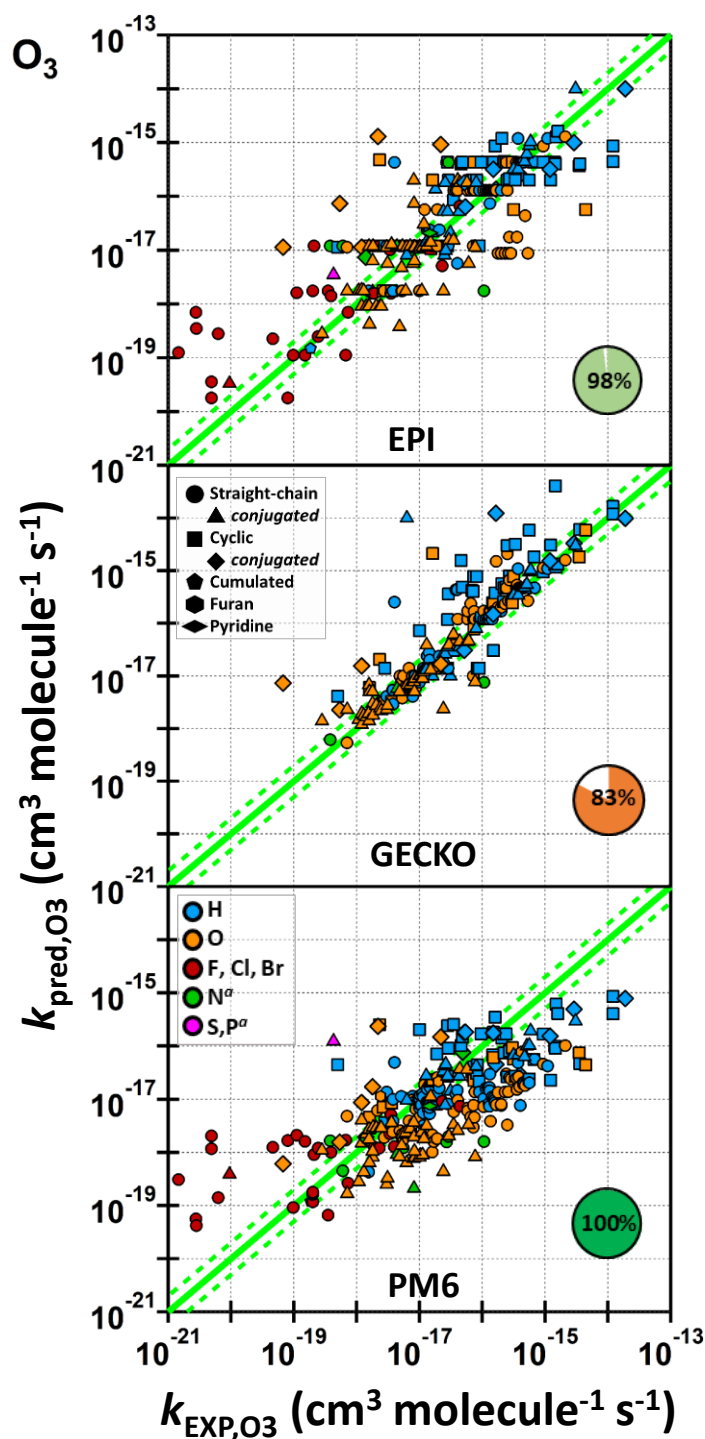
Figure App-IV-11: PM6 tool predictions for $k_{298,O3}$ from EPI Suite, GECKO-A and PM6 tools of 289 unsaturated compounds for which literature data are available, while PM6 was able to retrieve predictions for all compounds, GECKO-A only estimates 241 compounds and EPI Suite 284 compounds within the whole dataset, excluding for example halogenated compounds and some oxygenates. The dataset includes straight-chain, cyclic, aromatics, conjugated, furan, pyridine or a combination of these structures, together with substitution types C_nX_m where n has no limitation, and m=2n+1 and includes H, O, F, Cl, Br, I, N, S, P or a mix of these atoms. The pie chart represents the percentage of the whole k_{EXP} dataset for which the associated technique can provide an estimate. For this dataset, $r_{\%Vbur}=3.5Å$ is used since it is the most adapted for halogenated compounds which represents the majority of this list

References

McGillen, M.R., Archibald, A.T., Carey, T., Leather, K.E., Shallcross, D.E., Wenger, J.C., Percival, C.J., 2011. Structure–activity relationship (SAR) for the prediction of gas-phase ozonolysis rate coefficients: an extension towards heteroatomic unsaturated species. Phys. Chem. Chem. Phys. 13, 2842–2849.

McGillen, M.R., Carey, T.J., Archibald, A.T., Wenger, J.C., Shallcross, D.E., Percival, C.J., 2008. Structure–activity relationship (SAR) for the gas-phase ozonolysis of aliphatic alkenes and dialkenes. Phys. Chem. Chem. Phys. 10, 1757.

Michelat, L., Mellouki, A., Ravishankara, A.R., El Othmani, H., Papadimitriou, V.C., Daële, V., McGillen, M.R., 2022. Temperature-Dependent Structure–Activity Relationship of OH + Haloalkene Rate Coefficients under Atmospheric Conditions and Supporting Measurements. ACS Earth Space Chem. 6, 3101–3114.

Conclusion and perspectives

Conclusion and perspectives

This work was carried out to answer key questions concerning atmospheric chemistry, particularly the chemistry of gases emitted by anthropogenic activity, natural processes, and biomass burning. One of the main questions was to elucidate the reaction rate coefficients of these reactions by combining different experimental techniques to augment the reaction rate coefficients database used for atmospheric chemistry models and improve our knowledge of the reactivity of poorly studied gases.

New experimental measurements of the reaction rate coefficients of unsaturated VOCs with two important tropospheric oxidants, OH and NO_3, have been conducted by combining different techniques. Both absolute and relative rate methods have been used. Absolute rate coefficients for OH reactions have been measured using pulsed-laser photolysis–laser-induced fluorescence (PLP–LIF) and discharge flow reactor (DFR). Relative-rate coefficients have been measured using an atmospheric simulation chamber (CSA) and a Long Axis Reactor for KINetic studies (LARKIN). These experiments have focused on two classes of compounds: (1) industrial species, and (2) biomass-burning-related species.

The industrial species include two hydrofluoroolefins, 3,3,3-trifluoropropene, and 1,1,3,3-tetrafluoropropene, which are used as new replacements for high global-warming potential hydrofluorocarbons and are thus largely manufactured and emitted into the atmosphere. The determination of the temperature-dependent rate coefficients for the reaction of OH with 3,3,3-trifluoropropene (212–367 K) using PLP–LIF was in good agreement with the literature-reported data (Andersen et al., 2005; González et al., 2015; Orkin et al., 1997; Tokuhashi et al., 2018a). The temperature-dependent rate coefficients determined in this work for the reaction of OH with 1,1,3,3-tetrafluoropropene (T = 223–373 K) were the first reported value to the best of our knowledge. These two reaction rate coefficients display a negative dependence, which is more negative for OH + 1,1,3,3-tetrafluoropropene than for OH + 3,3,3-trifluoropropene. This can be attributed to the difference in the substitution across the double-bond, which can affect the reactivity towards the electrophilic addition of OH. These results have been published in (Michelat et al., 2022).

Biacetyl is emitted from biomass burning and other industrial processes (e.g., as a flavoring in food or e-cigarettes) and is thus important for atmospheric chemistry. The OH temperature-dependent rate coefficient of the OH + biacetyl reaction has been determined using DFR and LARKIN, and the room temperature rate coefficient has been determined using CSA with some uncertainties. The challenges associated with these experiments have been discussed. Especially, the measurements of OH + biacetyl rate coefficient using PLP–LIF were hampered due to the photolysis of biacetyl at 248 nm laser pulse used to produce OH radicals. Also, the relative-rate measurements in the CSA experiments were difficult under our experimental conditions due to a total loss of biacetyl close to that from dilution and photolysis.

However, the LARKIN determinations (273–403 K, P=760 Torr) are close to the literature-reported data at room temperature (Dagaut et al., 1988; Darnall et al., 1979). The DFR reaction rate coefficient values (230–770K, P=2–8 Torr) are lower than those from LARKIN and reported data at room temperature. They also display a non-Arrhenius behavior at lower temperatures. These results suggest a pressure dependence of the reaction and the potential role of a hydrogen-bonded complex, similar to the reaction of OH + acetone (Smith et al., 2002; Talukdar et al., 2003). The primary removal of biacetyl in the troposphere is expected to be via its photolysis.

Furans are biomass-burning compounds emitted into the atmosphere in large concentrations (Andreae, 2019; Decker et al., 2021, 2019). The rate coefficients of a series of furans with atmospheric oxidants have been studied. A special focus has been placed on their nighttime chemistry for multiple reasons: (1) nighttime chemistry of biomass burning emissions is generally less well understood than daytime OH chemistry, (2) it is a major removal for furans and related species emitted in large quantities from wildfires, and (3) there are in general a lack of data for NO_3 rate coefficients compared to that of OH. Room temperature reaction rate coefficients for NO_3 with 14 furans and two pyrroles, in addition to the OH room temperature rate coefficient for four furans, have been measured. Among these reported data, 10 of these rate coefficients are the first determination reported to the best of our knowledge. The reported data generally agree with the literature, except for 2,5-dimethylfuran and furfural, which should be the focus of further work. Thanks to these new measurements on roughly twenty species of industrial VOCs or those emitted by forest fires, it has been possible to establish links between the structure and reactivity of these species. The trend observed in NO_3 and OH reactivities is consistent with expectations of electrophilic addition reactions and the known contributions of electron-donating substituents. Furans are highly reactive with the nitrate radical, which will be their primary removal process at night, except for 2,5-dimethylfuran, whose reaction with O_3 is a significant loss (Matsumoto, 2011). Part of these results have been published in (Newland et al., 2022).

Accurate measurements of the reaction rate coefficients are necessary to feed the available kinetic database, used as input for atmospheric models, and to develop predictive methods such as structure-activity relationships (SARs). SARs can parametrize the reactivity in a very simplified way which allows them to make predictions easily. This is useful since it provides rapid estimates that may be employed by atmospheric modelers as well as industry and policy-makers who need to screen large databases easily. Also, since it is not always possible to perform all the experiments that would be required, due to the large amount of data remaining to be measured or due to experimental challenges, it is useful to have a first approximation of the reactivity to guide the laboratory approach. It is possible using SARs to predict the rate coefficients of a large number of compounds and thus identify those that may need to be studied for multiple reasons: (1) they are outliers in the correlation with experimental data, (2) they have a specific

reactivity that could lead to adverse effects on air quality or climate, (3) they have functional groups or structures that are poorly represented in the database, and measuring their rate coefficients can make a significant contribution to improving the description of the class of compounds to which they belong in predictive tools.

From the study of the halogenated alkenes, a trend in the reactivity of these halogenated olefins was observed, with cyclic or perhalogenated compounds tending to have lower reactivity and positive temperature dependence, in contrast to alkenes and compounds substituted with fewer halogenated groups. Based on this observation, it was possible to develop a tool for estimating the rate coefficients of reactions of a variety of haloalkenes, CHX with X=F, Cl, Br, with OH, at room temperature and as a function of temperature (Michelat et al., 2022). Following the success of the method, due to a large number of data and a good understanding of the reaction with the OH radical, an extension was made to the oxidants Cl, NO_3, and O_3. The latter have fewer kinetic data, particularly as a function of temperature, and therefore represent a preliminary trial, which could be improved as new rate coefficient values and mechanistic information become available. The temperature-dependent predictions for the Cl reaction were not satisfactory. These are due to the lack of data for Cl and the absence of an energy barrier in the reaction. This can be because Cl is an atom without dipole moment, contrary to its counterparts under study (OH, NO_3, and O_3). Also, the predictions for O_3 are not as accurate as those of OH and NO_3. This can be due to some mechanistic differences between ozonolysis and OH and NO_3 addition reactions. Ozone is added to both carbons of the double-bond to form an ozonide, while OH and NO_3 are added to one of the carbons of the double-bond. These differences may result in that the OH reactivity-based SAR towards addition to haloalkenes does not apply to O_3 addition. However, for OH and NO_3, the predictions were in excellent agreement with the experimental temperature-dependent rate coefficients. Predicting the Arrhenius parameters requires only estimating the reaction rate at room temperature, and this work represents the first formulation of this type for halogenated unsaturated compounds.

It is noted that a SAR can only be as good as its training set, and it is thus useful to develop new methods that are less tied to experimental data. There is a need for some more information, such as electronic and steric properties that can be calculated using quantum chemistry, to extend SAR approaches towards many different classes of molecules, especially those that are less well studied and thus poorly constrained from the experimental database available. Atmospheric models include a variety of molecule types and functional groups that must be covered by SARs. As mentioned in the introduction, tropospheric chemistry involves a diversity of reactions with atmospheric oxidants and various unsaturated VOCs.

The above reasoning motivated the development of another estimation tool (the so-called KINESTEASY tool) that could be applied to a variety of compounds based on *a priori* information on the structure of the

molecule. Most SARs use only pure fitting parameters, without physical meaning or without incorporating molecule-specific properties into the optimization. This can limit extrapolation to compounds, structures, and substitutions that are poorly represented in the available kinetic database. Thus, a tool applying to a diversity of alkenes and polyalkenes, including aromatics, cyclic, benzenoids, furans, and pyridines, has been developed for various CHNOPSX substitutions with X=F, Cl, Br, I, for reactions with OH, Cl, NO_3, and O_3. This tool is intended to be used for large databases of atmospheric interest. As such, it has several advantages: it is fully automated, it applies to the four main oxidation processes in the troposphere, it provides total and reaction site-specific kinetic data, and it relies on the properties of the electronic and steric structures of the compounds of interest calculated using quantum or semi-empirical chemistry tools. This easy-to-use tool complements the previous SAR, which is limited in terms of the number of compounds included and reactions studied.

Using the KINESTEASY tool, it was possible to estimate the reaction rate coefficients of a very large data set, such as all the compounds formed during the oxidation of three major VOCs, α-pinene, toluene, and *n*-decane, using the GECKO-A mechanism (Isaacman-VanWertz and Aumont, 2021). The oxidation of these three compounds rendered 14,446 species. It should be noted that these three species are emitted into or produced in large quantities in the troposphere. Yet they and their reaction products represent a small subset of the VOCs emitted naturally and anthropogenically. Application of the tool is easy and relatively fast, with only the semi-empirical calculations (PM6) performed using the MOPAC software; these calculations are limited by the computing power (in the worst case, >1 day for +14,000 species on a personal computer). Combining this tool with other models made it possible to assess the impact on air quality. Most of these compounds contribute to tropospheric ozone formation and can condense to form secondary organic aerosols or be hydrolyzed. The outputs of the tool built in this thesis can be easily included in other models and render other properties and impacts of these molecules. For example, this tool could be coupled with the VEGA software (https://www.vegahub.eu/portfolio-types/vega-software/) to assess various health impacts of these molecules (i.e., carcinogenic, mutagenic, and irritating properties for eyes and skin, absorption by the human body, or rapid metabolism).

In conclusion, the aim to address some of the multifaceted challenges posed by atmospheric chemistry and air pollution has been achieved using a variety of approaches, including laboratory measurements, estimation tools, and theoretical calculations. This work highlights the need to combine different approaches, to test the limits and strengths of existing methods and fill in any remaining gaps. It also highlights the value of interdisciplinary research in describing and understanding a broader picture of the challenges facing scientists as a community. As stated in the introduction, "what molecules are today is a reflection of what they have been," as Hubert Reeves said. This work aims to help understand and predict the chemical processes that make the atmosphere what it is today. The tool developed and the new

measurements are intended to contribute to developing future environmental and climate-friendly policies and feed into atmospheric chemical models.

Perspectives:

SAR developed on haloalkenes + OH (Michelat et al., 2022), the KINESTEASY tool, and possible extensions

From the work on developing new SARs, the need for temperature-dependent kinetic data for Cl, NO_3, and O_3 reactions is pointed out. The available data was very limited compared to those for OH reactions, which is a challenge for estimation techniques. Having new data could constrain the estimation methods and thus allow the prediction of these values for more types of compounds, and with more reliability- a possible focus for future work. Also, the SAR built in this thesis and presented in Chapter II can be further automated to expand its application to other substituent types and test its validity. This could be useful since the principles of this SAR differ from most estimation techniques available, the latter of which are built upon the group contribution method of Atkinson and coworkers (Kwok and Atkinson, 1995). The KINESTEASY tool developed in Chapter IV should be improved by optimizing its efficiency. Also, it would be interesting to couple it with the recently published work (McGillen et al., 2024) on the electrotopological approach to estimate the H-abstraction rate coefficient of a selection of alkanes. This work could be extended to alkenes. Since it is fully automated in a Python script, it could be incorporated into the KINESTEASY tool to make a unique tool that provides addition and abstraction rate coefficients. It would also be interesting to use the outputs of these SARs in atmospheric models and observe the impacts on air quality and climate from new compounds for which no estimation was available previously. For example, the estimations of haloalkenes reactivity from EPI Suite have large uncertainties and GECKO-A is not predicting those. So, it could be interesting to see the improvement when using the new predictions from this work's SARs.

Furans' chemistry

From the work conducted on furans, it appears that there is a need for product studies concerning the nighttime oxidation of furans to identify the products formed and quantify the branching ratios of each pathway. This includes reactions with NO_3 and O_3. Furthermore, to facilitate the reduction of mechanisms in atmospheric chemistry models and to aid the implementation and development of new estimation techniques, it is essential to know the mechanisms and provide accurate data on the different reactions for various species and substitutions. This should be the focus of further work.

Biacetyl chemistry

The experimental study of biacetyl presented multiple challenges. It was observed that the photolysis of biacetyl in the PLP–LIF set-up and the CSA, as well as the formation of OH radicals, were making the measurement of the OH reaction rate coefficient difficult. This should be further investigated. For example,

absolute measurements could be conducted in the PLP–LIF using O_2 as a bath gas, using isotopically labeled OH (e.g., $O(^1D)$ or ^{18}OH), and quantifying the quenching of OH by biacetyl. The results obtained from DF/MS and in the LARKIN set-up showed that there is still a factor of 2 of uncertainty in the value of the rate coefficient of biacetyl at room temperature. There is a need to refine these values by investigating the potential pressure dependence of this reaction, as suggested by the non-Arrhenius behavior observed for the reaction. This should be the focus of future work.

References

Andersen, M.S., Nielsen, O.J., Toft, A., Nakayama, T., Matsumi, Y., Waterland, R.L., Buck, R.C., Hurley, M.D., Wallington, T.J., 2005. Atmospheric chemistry of CxF2x+ 1CHCH2 (x= 1, 2, 4, 6, and 8): Kinetics of gas-phase reactions with Cl atoms, OH radicals, and O3. Journal of Photochemistry and Photobiology A: Chemistry 176, 124–128.

Andreae, M.O., 2019. Emission of trace gases and aerosols from biomass burning – an updated assessment. Atmospheric Chem. Phys. 19, 8523–8546. https://doi.org/10.5194/acp-19-8523-2019

Aumont, B., Szopa, S., Madronich, S., 2005. Modeling the evolution of organic carbon during its gas-phase tropospheric oxidation: development of an explicit model based on a self-generating approach. Atmospheric Chem. Phys. 5, 2497–2517. https://doi.org/10.5194/acp-5-2497-2005

Dagaut, P., Wallington, T.J., Liu, R., Kurylo, M.J., 1988. A kinetic investigation of the gas-phase reactions of hydroxyl radicals with cyclic ketones and diones: mechanistic insights. The Journal of Physical Chemistry 92, 4375–4377.

Darnall, K.R., Atkinson, R., Pitts, J.N., 1979. Observation of biacetyl from the reaction of OH radicals with o-xylene. Evidence for ring cleavage. Journal of Physical Chemistry 83, 1943–1946.

Decker, Z.C.J., Robinson, M.A., Barsanti, K.C., Bourgeois, I., Coggon, M.M., DiGangi, J.P., Diskin, G.S., Flocke, F.M., Franchin, A., Fredrickson, C.D., Gkatzelis, G.I., Hall, S.R., Halliday, H., Holmes, C.D., Huey, L.G., Lee, Y.R., Lindaas, J., Middlebrook, A.M., Montzka, D.D., Moore, R., Neuman, J.A., Nowak, J.B., Palm, B.B., Peischl, J., Piel, F., Rickly, P.S., Rollins, A.W., Ryerson, T.B., Schwantes, R.H., Sekimoto, K., Thornhill, L., Thornton, J.A., Tyndall, G.S., Ullmann, K., Van Rooy, P., Veres, P.R., Warneke, C., Washenfelder, R.A., Weinheimer, A.J., Wiggins, E., Winstead, E., Wisthaler, A., Womack, C., Brown, S.S., 2021. Nighttime and daytime dark oxidation chemistry in wildfire plumes: an observation and model analysis of FIREX-AQ aircraft data. Atmospheric Chem. Phys. 21, 16293–16317. https://doi.org/10.5194/acp-21-16293-2021

Decker, Z.C.J., Zarzana, K.J., Coggon, M., Min, K.-E., Pollack, I., Ryerson, T.B., Peischl, J., Edwards, P., Dubé, W.P., Markovic, M.Z., Roberts, J.M., Veres, P.R., Graus, M., Warneke, C., de Gouw, J., Hatch, L.E., Barsanti, K.C., Brown, S.S., 2019. Nighttime Chemical Transformation in Biomass Burning Plumes: A Box Model Analysis Initialized with Aircraft Observations. Environ. Sci. Technol. 53, 2529–2538. https://doi.org/10.1021/acs.est.8b05359

González, S., Jiménez, E., Ballesteros, B., Martínez, E., Albaladejo, J., 2015. Hydroxyl radical reaction rate coefficients as a function of temperature and IR absorption cross sections for CF3CH=CH2 (HFO-1243zf), potential replacement of CF3CH2F (HFC-134a). Environ Sci Pollut Res 22, 4793–4805. https://doi.org/10.1007/s11356-014-3426-2

Isaacman-VanWertz, G., Aumont, B., 2021. Impact of organic molecular structure on the estimation of atmospherically relevant physicochemical parameters. Atmospheric Chemistry and Physics 21, 6541–6563.

Kwok, E.S.C., Atkinson, R., 1995. Estimation of hydroxyl radical reaction rate constants for gas-phase organic compounds using a structure-reactivity relationship: An update. Atmospheric Environment 29, 1685–1695.

Matsumoto, J., 2011. Kinetics of the Reactions of Ozone with 2,5-Dimethylfuran and Its Atmospheric Implications. Chem. Lett. 40, 582–583. https://doi.org/10.1246/cl.2011.582

McGillen, M.R., Michelat, L., Orlando, J.J. and Carter, W.P., 2024. The use of the electrotopological state as a basis for predicting hydrogen abstraction rate coefficients: a proof of principle for the reactions of alkanes and haloalkanes with OH. Environmental Science: Atmospheres. DOI:10.1039/D3EA00147D

Michelat, L., Mellouki, A., Ravishankara, A.R., El Othmani, H., Papadimitriou, V.C., Daële, V., McGillen, M.R., 2022. Temperature-Dependent Structure–Activity Relationship of OH + Haloalkene Rate Coefficients under Atmospheric Conditions and Supporting Measurements. ACS Earth Space Chem. 6, 3101–3114.

Newland, M.J., Ren, Y., McGillen, M.R., Michelat, L., Daële, V., Mellouki, A., 2022. NO 3 chemistry of wildfire emissions: A kinetic study of the gas-phase reactions of furans with the NO3 radical. Atmospheric Chemistry and Physics 22, 1761–1772.

Orkin, V.L., Huie, R.E., Kurylo, M.J., 1997. Rate constants for the reactions of OH with HFC-245cb (CH3CF2CF3) and some fluoroalkenes (CH2=CHCF3, CH2=CFCF3, CF2=CFCF3, and CF2=CF2). The Journal of Physical Chemistry A 101, 9118–9124.

Smith, I.W.M., Ravishankara, A.R., 2002. Role of Hydrogen-Bonded Intermediates in the Bimolecular Reactions of the Hydroxyl Radical. J. Phys. Chem. A 106, 4798–4807.

Talukdar, R.K., Gierczak, T., McCabe, D.C., Ravishankara, A.R., 2003. Reaction of Hydroxyl Radical with Acetone. 2. Products and Reaction Mechanism. J. Phys. Chem. A 107, 5021–5032.

Tokuhashi, K., Takizawa, K., Kondo, S., 2018a. Rate constants for the reactions of OH radicals with CF3CX=Y2 (X= H, F, CF3, Y= H, F, Cl). Environmental Science and Pollution Research 25, 15204–15215.

US EPA, O., 2015. EPI Suite^{TM}-Estimation Program Interface [WWW Document]. URL https://www.epa.gov/tsca-screening-tools/epi-suitetm-estimation-program-interface (accessed 7.6.22).

Conclusions et perspectives

Ce travail a été réalisé pour répondre à des questions clés concernant la chimie atmosphérique, en particulier la chimie des gaz émis par l'activité anthropogénique, les processus naturels et la combustion de la biomasse. L'une des principales questions était d'élucider les coefficients de vitesse de ces réactions en combinant différentes techniques expérimentales afin d'enrichir la base de données des coefficients de vitesse de réaction utilisée pour les modèles de chimie atmosphérique et d'améliorer notre connaissance de la réactivité des gaz peu étudiés.

De nouvelles mesures expérimentales des coefficients de vitesse de réaction des COVs insaturés avec deux oxydants troposphériques importants, OH et NO_3, ont été réalisées en combinant différentes techniques. Des méthodes de vitesses absolues et relatives ont été utilisées pour déterminer les coefficients de vitesse de réaction des COVs insaturés. Les coefficients de vitesse absolus pour les réactions OH ont été mesurés à l'aide de la photolyse laser pulsée et de la fluorescence induite par laser (PLP–LIF) et du réacteur à flux de décharge (DFR). Les coefficients de vitesse relatifs ont été mesurés à l'aide d'une chambre de simulation atmosphérique (CSA) et d'un réacteur à axe long pour les études cinétiques (LARKIN). Ces expériences se sont concentrées sur deux classes de composés : (1) les espèces industrielles et (2) les espèces liées à la combustion de la biomasse.

Les espèces industrielles comprennent deux hydrofluorooléfines, le 3,3,3-trifluoropropène et le 1,1,3,3-tétrafluoropropène, qui sont utilisées comme nouveaux remplaçants des hydrofluorocarbures au potentiel de réchauffement global et sont donc largement produites et émises dans l'atmosphère. La détermination des coefficients de vitesse dépendant de la température pour la réaction de OH avec le 3,3,3-trifluoropropène (212–367 K) à l'aide du PLP–LIF était en bon accord avec les données rapportées dans la littérature (Andersen et al., 2005; González et al., 2015; Orkin et al., 1997; Tokuhashi et al., 2018a). Les coefficients de vitesse dépendant de la température déterminés dans ce travail pour la réaction de OH avec le 1,1,3,3-tetrafluoropropène (T = 223–373 K) sont les premières valeurs rapportées à notre connaissance. Les coefficients de vitesse de ces deux réactions présentent une dépendance négative à la température, qui est plus négative pour OH + 1,1,3,3-tetrafluoropropène que pour OH + 3,3,3-trifluoropropène. Ceci peut être attribué à la différence de substitution à travers la double liaison qui peut jouer un rôle dans la réactivité vis-à-vis de l'addition électrophile de OH. Ces résultats ont été publiés dans (Michelat et al., 2022).

Le biacétyle est émis par la combustion de la biomasse et d'autres processus industriels (par exemple, en tant qu'arôme dans les aliments ou les e-cigarettes) et est donc important pour la chimie atmosphérique. Les coefficients de vitesse de la réaction OH + biacétyle dépendant de la température de l'OH a été déterminé en utilisant DFR et LARKIN, et le coefficient de vitesse à température ambiante a été déterminé

en utilisant la CSA avec quelques incertitudes. Les défis associés à ces expériences ont été discutés. En particulier, les mesures du coefficient de vitesse OH + biacétyle à l'aide du PLP–LIF ont été entravées par la photolyse du biacétyle à l'impulsion laser de 248 nm utilisée pour produire des radicaux OH.

De même, les mesures des coefficients de vitesse relatif dans les expériences CSA étaient difficiles dans nos conditions expérimentales en raison d'une perte totale de biacétyle proche de celle résultant de la dilution et de la photolyse. Cependant, les déterminations de LARKIN (273–403 K, P=760 Torr) sont proches des données rapportées dans la littérature à température ambiante (Dagaut et al., 1988; Darnall et al., 1979). Les valeurs des coefficients de vitesse de la réaction DFR (230–770 K, P=2–8 Torr) sont inférieures à celles de LARKIN et aux données rapportées à température ambiante. Elles affichent aussi un comportement non-Arrhénius à plus basse températures. Ces résultats suggèrent que la réaction dépend de la pression et que le rôle potentiel d'un complexe à liaison hydrogène formé est similaire à la réaction OH + acétone (Smith et al., 2002; Talukdar et al., 2003). L'élimination primaire du biacétyle dans la troposphère devrait se faire par photolyse.

Les furanes sont des composés issus de la combustion de la biomasse qui sont émis en grandes concentrations dans l'atmosphère (Andreae, 2019; Decker et al., 2021, 2019). Les coefficients de vitesse d'une série de furanes avec les oxydants atmosphériques ont été étudiés. Une attention particulière a été accordée à leur chimie nocturne pour plusieurs raisons : (1) la chimie nocturne des émissions issues de la combustion de la biomasse est généralement moins bien comprise que la chimie diurne des OH, (2) il s'agit d'une élimination majeure pour les furanes et les espèces apparentées émises en grandes quantités par les feux de forêt, et (3) il y a en général un manque de données pour les coefficients de vitesses du NO_3 par rapport à celle de l'OH. Les coefficients de vitesse de réaction à température ambiante pour NO_3 avec 14 furannes et deux pyrroles, en plus du coefficient de vitesse à température ambiante de OH pour quatre furannes, ont été mesurés. Parmi les données rapportées, 10 de ces coefficients de vitesse sont les premières déterminations rapportées à notre connaissance. Les données rapportées sont généralement en bon accord avec la littérature, sauf pour le 2,5-diméthylfurane et le furfural, qui devraient faire l'objet de travaux ultérieurs. Grâce à ces nouvelles mesures sur une vingtaine d'espèces de COVs insaturés industriels ou émis par les feux de forêts, il a été possible d'établir des liens entre la structure et la réactivité de ces espèces. La tendance observée pour les réactivités NO_3 et OH est cohérente avec les attentes de réactions d'addition électrophile, et avec les contributions connues des substituants donneurs d'électrons. Les furanes sont très réactifs avec le radical nitrate, qui sera leur principal processus d'élimination pendant la nuit, à l'exception du 2,5-diméthylfurane dont la réaction avec O_3 est une perte importante (Matsumoto, 2011). Une partie de ces résultats a été publiée dans (Newland et al., 2022).

Des mesures précises des coefficients de vitesse des réactions sont nécessaires pour alimenter la base de données cinétiques disponible, utilisée comme entrée pour les modèles atmosphériques, et pour développer des méthodes prédictives telles que les relations structure-activité (SARs). Les SARs peuvent paramétrer la réactivité d'une manière très simplifiée, ce qui leur permet de faire des prédictions facilement. Cette méthode est utile car elle fournit des estimations rapides qui peuvent être utilisées par les modélisateurs atmosphériques ainsi qu'aux industriels et aux décideurs politiques qui ont besoin d'évaluer facilement les vitesses de réactions de grandes bases de données. En outre, comme il n'est pas toujours possible de réaliser toutes les expériences nécessaires, en raison de la grande quantité de données restant à mesurer ou de difficultés expérimentales, il est utile de disposer d'une première approximation de la réactivité pour guider l'approche en laboratoire. Il est possible d'utiliser les SARs pour prédire les coefficients de vitesses d'un grand nombre de composés et d'identifier ainsi ceux qui pourraient devoir être étudiés pour de multiples raisons: (1) ils sont aberrants dans la corrélation avec les données expérimentales, (2) ils ont une réactivité spécifique qui pourrait avoir des effets néfastes sur la qualité de l'air ou le climat, (3) ils ont des groupes fonctionnels ou des structures qui sont mal représentés dans la base de données, et la mesure de leur cinétique peut contribuer de manière significative à l'amélioration de la description de la classe de composés à laquelle ils appartiennent dans les outils prédictifs.

L'étude des alcènes halogénés a permis d'observer une tendance dans la réactivité de ces oléfines halogénées, les composés cycliques ou perhalogénés ayant tendance à avoir une réactivité plus faible et une dépendance positive à la température, contrairement aux alcènes et aux composés substitués par moins de groupes halogénés. Sur la base de cette observation, il a été possible de développer un outil permettant d'estimer la coefficients de vitesse des réactions d'une variété d'haloalcènes, CHX avec X=F, Cl, Br, avec OH, à température ambiante et en fonction de la température (Michelat et al., 2022). Suite au succès de la méthode, dû à un grand nombre de données et à une bonne compréhension de la réaction avec le radical OH, une extension a été faite aux oxydants Cl, NO_3, et O_3. Ces derniers disposent de moins de données cinétiques, en particulier en fonction de la température, et représentent donc un essai préliminaire, qui sera amélioré au fur et à mesure que de nouvelles valeurs de coefficients de vitesse et des informations mécanistiques seront disponibles. Les prévisions en fonction de la température pour la réaction Cl n'étaient pas satisfaisantes. Elles sont dues au manque de données pour le Cl et à l'absence de barrière énergétique dans la réaction. Cela peut être dû que Cl est un atome sans moment dipolaire, contrairement à ses homologues étudiés (OH, NO_3 et O_3). De même, les prédictions pour O_3 ne sont pas aussi précises que celles de OH et NO_3. Cela peut s'expliquer par certaines différences mécaniques entre l'ozonolyse et les réactions d'addition de OH et de NO_3. L'ozone est ajouté aux deux carbones de la double liaison pour former un ozonide, alors que OH et NO_3 sont ajoutés à l'un des carbones de la double liaison. Ces différences peuvent avoir pour conséquence que la SAR fondée sur la réactivité de OH pour l'addition

aux haloalcènes ne s'applique pas à l'addition de O_3. Cependant, pour OH et NO_3, les prédictions étaient en excellent accord avec les coefficients de vitesse expérimentaux dépendant de la température. La prédiction des paramètres d'Arrhénius ne nécessite qu'une estimation de la vitesse de réaction à température ambiante, et ce travail représente la première formulation de ce type pour les composés insaturés halogénés.

Il convient de noter que la qualité d'une SAR dépend de son ensemble d'apprentissage et qu'il est donc utile de développer de nouvelles méthodes qui sont moins liées aux données expérimentales. Il est nécessaire de disposer de plus d'informations, telles que les propriétés électroniques et stériques qui peuvent être calculées à l'aide de la chimie quantique, afin d'étendre les approches SARs à un grand nombre de classes de molécules différentes, en particulier celles qui sont moins bien étudiées et donc mal contraintes à partir de la base de données expérimentale disponible. Les modèles atmosphériques comprennent une variété de types de molécules et de groupes fonctionnels qui doivent être couverts par les SARs. Comme mentionné dans l'introduction, la chimie de la troposphère implique une diversité de réactions avec les oxydants atmosphériques et divers COVs insaturés.

Le raisonnement ci-dessus a motivé le développement d'un autre outil d'estimation (appelé KINESTEASY) qui pourrait être appliqué à une variété de composés sur la base d'informations a priori sur la structure de la molécule. La plupart des SARs utilisent uniquement des paramètres d'ajustement purs, sans signification physique ou sans incorporer les propriétés spécifiques de la molécule dans l'optimisation, ce qui peut limiter l'extrapolation aux composés, structures et substitutions qui sont mal représentés dans la base de données cinétiques disponible. Ainsi, un outil s'appliquant à une diversité d'alcènes et de polyalcènes, y compris les aromatiques, les cycliques, les benzénoïdes, les furannes et les pyridines, a été développé pour diverses substitutions CHNOPSX avec X=F, Cl, Br, I, pour des réactions avec OH, Cl, NO_3, et O_3. Cet outil est destiné à être utilisé pour de grandes bases de données d'intérêt atmosphérique. En tant que tel, il présente plusieurs avantages : il est entièrement automatisé, il s'applique aux quatre principaux processus d'oxydation dans la troposphère, il fournit des données cinétiques totales et spécifiques au site de réaction, et il s'appuie sur les propriétés des structures électroniques et stériques des composés d'intérêt calculées à l'aide d'outils de chimie quantique ou semi-empirique. Cet outil facile à utiliser complète la SAR précédente, qui est limitée en termes de nombre de composés inclus et de réactions étudiées.

L'outil KINESTEASY a permis d'estimer les coefficients de vitesse de réaction d'un très grand ensemble de données, comme l'ensemble des composés formés lors de l'oxydation de trois COVs majeurs, l'α-pinène, le toluène et le n-décane, en utilisant le mécanisme GECKO-A (Isaacman-VanWertz et Aumont, 2021). L'oxydation de ces trois composés a rendu 14 446 espèces. Il est à noter que ces trois espèces sont émises ou produites en grande quantité dans la troposphère. Pourtant, elles et leurs produits de réaction ne

représentent qu'un petit sous-ensemble des COVs émis naturellement et anthropiquement. L'application de l'outil est facile et relativement rapide, seuls les calculs semi-empiriques (PM6) étant effectués à l'aide du logiciel MOPAC; ces calculs sont limités par la puissance de calcul (dans le pire des cas, >1 jour pour +14 000 espèces sur un ordinateur personnel). La combinaison de cet outil avec d'autres modèles a permis d'évaluer l'impact sur la qualité de l'air. La plupart de ces composés contribuent à la formation d'ozone troposphérique et peuvent se condenser pour former des aérosols organiques secondaires ou être hydrolysés. Les résultats de l'outil construit dans cette thèse peuvent être facilement inclus dans d'autres modèles et rendre d'autres propriétés et impacts de ces molécules. Par exemple, cet outil pourrait être couplé au logiciel VEGA (https://www.vegahub.eu/portfolio-types/vega-software/) pour évaluer les différents impacts sanitaires de ces molécules (c'est-à-dire les propriétés cancérigènes, mutagènes et irritantes pour les yeux et la peau, l'absorption par le corps humain, ou les effets rapides de l'exposition à l'ozone).

En conclusion, notre objectif de relever certains des défis à multiples facettes posés par la chimie atmosphérique et la pollution de l'air a été atteint en utilisant une variété d'approches, y compris des mesures en laboratoire, des outils d'estimation et des calculs théoriques. Ce travail met en évidence la nécessité de combiner différentes approches, de tester les limites et les forces des méthodes existantes et de combler les lacunes restantes. Cela souligne aussi la valeur de la recherche interdisciplinaire dans la description et la compréhension d'une image plus large des défis auxquels les scientifiques sont confrontés en tant que communauté. Comme indiqué dans l'introduction, "ce que sont les molécules aujourd'hui est le reflet de ce qu'elles ont été", comme l'a dit Hubert Reeves. Ce travail vise à aider à comprendre et à prédire les processus chimiques qui font de notre atmosphère ce qu'elle est aujourd'hui. L'outil développé et les nouvelles mesures doivent contribuer à l'élaboration des futures politiques environnementales et climatiques et alimenter les modèles chimiques atmosphériques.

Perspectives :

SAR développée sur les haloalcènes + OH (Michelat et al., 2022), l'outil KINESTEASY, et extensions possibles

Le travail sur le développement de nouvelles SARs a mis en évidence le besoin de données cinétiques en fonction de la température pour les réactions de Cl, NO_3, et O_3. Les données disponibles sont très limitées par rapport à celles de réaction avec OH, ce qui constitue un défi pour les techniques d'estimation. L'obtention de nouvelles données pourrait contraindre les méthodes d'estimation et permettre ainsi de prédire ces valeurs pour un plus grand nombre de types de composés et avec une plus grande fiabilité. Cela pourrait être l'objet de travaux futurs. En outre, la SAR construite dans cette thèse et présenté au chapitre II sera davantage automatisée afin d'étendre son application à d'autres types de substituants et de tester sa validité. Cela pourrait être utile car les principes de cette SAR diffèrent de la plupart des techniques

d'estimation disponibles, ces dernières étant basées sur la méthode de contribution de groupe d'Atkinson et de ses collègues (Kwok et Atkinson, 1995). L'outil KINESTEASY développé au chapitre IV devrait être encore amélioré en optimisant son efficacité. Il serait également intéressant de le coupler avec le travail récemment publié (McGillen et al., 2024). L'utilisation de l'état électrotopologique comme base pour prédire les coefficients de vitesse d'abstraction de l'hydrogène. Les auteurs ont utilisé l'approche électrotopologique pour estimer le coefficient de vitesse d'abstraction de l'hydrogène d'une sélection d'alcanes. Ce travail pourrait être étendu aux alcènes et, puisqu'il est entièrement automatisé dans un script Python, pourrait être incorporé dans l'outil KINESTEASY en un seul outil qui fournit des coefficients de vitesses de réaction d'addition et d'abstraction. Il serait également intéressant d'utiliser les résultats de ces SARs dans les modèles atmosphériques et d'observer les impacts sur la qualité de l'air et le climat des nouveaux composés pour lesquels aucune estimation n'était disponible auparavant. Par exemple, les estimations de la réactivité des haloalcènes à partir de la suite EPI ont de grandes incertitudes, et GECKO-A ne les prédit pas, il serait donc intéressant de voir l'amélioration en utilisant les nouvelles prédictions de nos SARs.

Chimie des furanes

Les travaux menés sur les furannes montrent qu'il est nécessaire de réaliser des études de produits concernant l'oxydation nocturne des furannes afin d'identifier les produits formés et de quantifier les coefficients de vitesses de chaque voie. Ceci inclut les réactions avec NO_3 et O_3. En outre, pour faciliter la réduction des mécanismes dans les modèles de chimie atmosphérique et pour aider à la mise en œuvre et au développement de nouvelles techniques d'estimation, il est essentiel de connaître les mécanismes et de fournir des données précises sur les différentes réactions pour diverses espèces et substitutions. Ce point devrait faire l'objet d'un travail plus approfondi.

Chimie du biacétyle

L'étude expérimentale du biacétyle a présenté de nombreux défis. Il a été observé que la photolyse du biacétyle dans l'installation PLP–LIF et la CSA, ainsi que la formation de radicaux OH, rendaient difficile la mesure du coefficient de vitesse de la réaction OH. Cette question devrait être étudiée de manière plus approfondie. Par exemple, des mesures absolues pourraient être effectuées dans le PLP–LIF en utilisant de l'O_2 comme gaz inerte, en utilisant des radicaux OH isotopiquement identifiés (c'est-à-dire ^{18}OH ou $O(^1D)$) et en quantifiant l'extinction de l'OH par le biacétyle. Les résultats obtenus par DF/MS et dans l'installation LARKIN a montré qu'il existe encore un facteur d'incertitude de 2 dans la valeur du coefficient de vitesse du biacétyle à température ambiante. Il est nécessaire d'affiner ces valeurs en étudiant la dépendance potentielle de cette réaction par rapport à la pression, comme le suggère le comportement non-Arrhénien observé pour la réaction. Cette question devrait faire l'objet de travaux futurs.

List of figures

List of tables

Remerciements

« Nous devons croire que nous sommes doués pour quelque chose et que cette chose, à n'importe quel prix, doit être atteinte. »

Marie Curie (1867–1934), scientifique, Prix Nobel

Je tiens à présenter toute ma gratitude et ma reconnaissance à mes directeurs de thèse, qui m'ont accompagné tout au long de cette thèse, m'ont transmis leurs savoirs, et m'ont guidé vers l'accomplissement de cette thèse du mieux possible, Max, Wahid, Ravi. Le temps investi afin de me permettre de réaliser cette thèse, d'apprendre, de comprendre, et de m'améliorer est précieux et j'en suis extrêmement reconnaissante. L'inspiration et la réflexion qu'ils m'ont transmises par leur expérience, leurs connaissances et leur raisonnement constituent une richesse scientifique qui me sera utile et chère à jamais. Je tiens à les remercier particulièrement pour le temps qu'ils m'ont consacré, ce qui est une denrée rare pour des chercheurs dévoués comme eux.

Je tiens également à sincèrement remercier mes rapporteurs, Pr. Bénédicte PICQUET-VARRAULT, et Pr. John WENGER, d'avoir accepté d'évaluer cette thèse, et pour le temps et le travail qu'ils y ont consacré. Je tiens également à remercier vivement mes examinateurs et les membres du jury pour le temps et l'attention qu'ils ont accordés à mon travail, le Pr. Anne MONOD, Pr. Bernard AUMONT, Alexandre KUKUI, mes rapporteurs et mes directeurs de thèse.

Je remercie tous les membres du groupe et du laboratoire qui m'ont également beaucoup aidée, appris et accompagnée, notamment Yuri, Yangang, Mahmoud, Rodrigo, Véro, Fanny, Pengcheng, Romain,

Je remercie les membres du *Paton Research Group* qui m'ont accompagnée et beaucoup appris en peu de temps sur un domaine relativement nouveau pour moi durant mon séjour aux États-Unis,

Je tiens à remercier plus personnellement et à dédier ce travail à toutes les personnes qui m'accompagnent au quotidien, et m'ont toujours apporté du soutien durant ces 3 années dédiées à ma thèse, malgré les épreuves personnelles à surmonter : ma soeur, mes parents, mes grands-parents, ma famille, pour qui la reconnaissance est immense et sans qui je ne serais pas qui je suis et n'aurait pas eu l'occasion de faire ce travail,

à mon groupe si unique d'amis qui m'ont toujours soutenu, comme le noyau d'un atome, et avec qui les interactions scientifiques ont toujours été stimulantes et passionnantes, Natacha, Pierrot, Vico, Baptiste, Maxence, Théo, Benoît,

à mes ami(e)s très chèr(e)s et celles.eux qui ont été présent(e)s tout au long de ces années, de près ou de loin, Sarah, Camille, Léa, Maud, Alban, David, Mattieu, Jojo, Mélina, à Pascale et Phiphi qui m'ont accueilli pendant quelques temps durant la première année comme dans une seconde famille,

à ceux qui nous manquent, à mamie, à papy, à tata Marie, à Nicole, à Guillaume, à Nisette,

et à Hubert Reeves (1932–2023) qui m'a transmis la passion pour la science de l'infiniment petit.

Acknowledgements

« We must believe that we are gifted for something, and that this thing, at whatever cost, must be attained. »

Marie Curie (1867–1934), scientifique, Prix Nobel

I would like to express my gratitude and appreciation to my thesis supervisors, who have accompanied me throughout this thesis, passed on their knowledge to me, and guided me towards the completion of this thesis in the best possible way, Max, Wahid, Ravi. The time invested to enable me to complete this thesis, to learn, understand and improve is precious and I am extremely grateful. The inspiration and reflection they have passed on to me through their experience, knowledge and reasoning constitute a scientific wealth that will be useful and dear to me forever. A precious thanks for the time they devoted to me, which is a rare good for dedicated researchers like them.

I would also like to sincerely thank my rapporteurs, Pr. Bénédicte PICQUET-VARRAULT, and Pr. John WENGER, for agreeing to evaluate this thesis, and for the time and work they devoted to it. I also want to deeply thank my examinators and jury members for the time and consideration they allowed to my work, Pr. Anne MONOD, Pr. Bernard AUMONT, Alexandre KUKUI, my rapporteurs and my thesis supervisors.

I would also like to thank all the members of the group and the laboratory who have helped, learned and accompanied me, in particular Yuri, Yangang, Mahmoud, Rodrigo, Benoît, Véro, Fanny, Pengcheng and Romain, I would like to thank the members of the Paton Research Group, who accompanied me and taught me a lot in a short space of time in a field that was relatively new to me during my stay in the United States,

More personally, I would like to thank and dedicate this work to all the people who have been with me on a daily basis, and have always given me support during these 3 years dedicated to my thesis, despite the personal difficulties to be overcome: my sister, my parents, my grandparents, my family, without whom I wouldn't be who I am and wouldn't have had the opportunity to do this work,

to my special group of friends who have always supported me, like the nucleus of an atom, and with whom scientific interactions have always been stimulating and fascinating, Natacha, Maxence, Théo, Vico, Pierrot, Baptiste, Benoît,

to my friends and those who have been with me throughout these years and supported me from near and far, Sarah, Camille, Léa, Maud, Alban, David, Mattieu, Jojo, Mélina, to Pascale and Phiphi who welcomed me for some time during the first year like a second family,

to those that we miss, to Grandma, Grandpa, Auntie Marie, Nicole, Guillaume, Nisette,

and to Hubert Reeves (1932-2023), who passed on to me his passion for the science of the infinitely small.

Lisa MICHELAT

Mesure et prévision de la cinétique d'oxydation atmosphérique des composés organiques volatils non saturés, en mettant l'accent sur la combustion de la biomasse et les espèces industrielles.

Résumé

La pollution de l'air est une des premières causes de mortalité dans le monde, et constitue un enjeu majeur pour la santé publique, associé au changement climatique. Ces deux problèmes majeurs sont directement liés à la composition chimique de l'atmosphère. Afin d'évaluer la contribution des activités humaines sur cette composition chimique, il est nécessaire d'étudier l'évolution des espèces chimiques une fois émis dans l'atmosphère, en identifiant les réactions par lesquels elles sont dégradées, les produits formés ainsi que les vitesses de ces procédés. Parmi les gaz émis industriellement et naturellement, une grande majorité sont des composés organiques volatiles insaturés, qui réagissent particulièrement vite avec les oxydants troposphériques responsables de l'initiation de leur dégradation. Cependant, ces gaz sont présents dans l'atmosphère en quantités extrêmement variées, et il est donc très difficile de mesurer toutes ces constantes de vitesse de réaction expérimentalement , ce qui motive la nécessité de développer des techniques d'estimation, telles que les relations structure-activité (SARs), afin de fournir des données aux modèles atmosphériques, lorsque ces derniers ne disposent pas de données expérimentales.

Ma thèse porte sur la cinétique de l'oxydation des composés organiques volatils (COVs) insaturés en phase gazeuse dans l'atmosphère, dans le but de développer un outil automatisé basé sur les SARs qui peut prédire le coefficient de vitesse d'une grande variété d'alcènes substitués, sans avoir recours à des calculs informatiques coûteux. Pour ce faire, j'ai effectué des travaux expérimentaux afin de mesurer des coefficients de vitesses de réactions d'un certain nombre de COV, en fonction de la température, dans des chambres de simulation atmosphériques et des réacteurs couplés à des techniques spectroscopiques. J'ai combiné les résultats obtenus à des calculs de chimie quantique théoriques, afin de développer une SAR permettant d'estimer ces coefficients de vitesses de réactions. Ces méthodes utilisent des calculs de théorie de la fonctionnelle de la densité (DFT), très précis mais coûteux en termes de temps de travail et de calculs, que nous avons pu substituer par des outils semi-empiriques rapides et informatiquement peu coûteux, optimisant grandement l'efficacité et l'applicabilité de l'outil. J'ai ensuite écrit un code Python à source ouverte pour en faire un outil automatisé, rapide et simple d'utilisation, qui est efficace pour l'usage général des physico-chimistes de l'atmosphère.

Cet outil peut prédire les constantes de vitesses de réaction d'addition électrophile des oxydants atmosphérique OH, Cl, O_3 et NO_3 à des composés insaturés sur la base d'une nouvelle méthodologie. Comparée à d'autres techniques, elle nécessite moins de paramètres d'ajustement, est plus générale et, puisqu'elle est basée sur des informations calculées a priori, possède un meilleur potentiel d'extrapolation à de nouveaux composés. Plus précisément, la prédiction de nouveaux composés repose uniquement sur le calcul de leurs propriétés chimiques à l'aide de notre logiciel, et moins sur les données expérimentales existantes.

Par conséquent, il peut être étendu avec succès pour prédire des réactions qui restent moins connues ou difficiles à mesurer en laboratoire, telles que l'oxydation nocturne des COVs issus de la combustion de la biomasse (par exemple, l'oxydation de furanes et de pyrroles initiée par réaction avec NO_3). Ces résultats peuvent être facilement utilisés comme données d'entrée pour les modèles chimiques atmosphériques, et par les industries et les décideurs politiques pour éviter les émissions persistantes dans l'atmosphère.

Mots clés : Feux de biomasse, Composés organiques volatiles insaturés, Cinétique, Relation structure à activité (SAR), Oxydation, Furanes

Measuring and predicting the atmospheric oxidation kinetics of unsaturated volatile organic compounds, with a focus on biomass burning and industrial species.

Summary

Air pollution is one of the main causes of mortality and is a major public health issue in conjunction with climate change. These two major challenges are directly linked to atmospheric chemical composition. In order to assess the contribution of human activities on chemical composition, it is necessary to study the chemistry of these gases once emitted into the atmosphere, identifying the reactions by which they are destroyed, the products thus formed and the reaction rates of these processes. Among the gases emitted both industrially and naturally, many are unsaturated volatile organic compounds , which in general react rapidly with the tropospheric oxidants that initiate their degradation. However, these gases are present in an extremely large quantity and variety in the atmosphere, and it is very difficult to measure the values of that many reactions experimentally , which necessitates the development of estimation techniques, in order to provide data for atmospheric models, when no experimental data is available.

My thesis focuses on the kinetics of gas-phase oxidation of unsaturated volatile organic compounds (UVOCs) in the atmosphere, with the aim of developing an automated SAR-based tool that can predict the rate coefficient of a wide variety of substituted alkenes, without the need for costly computer calculations. To achieve this, I carried out experimental work to measure reaction rate coefficients, as a function of temperature, in atmospheric simulation chambers and using other spectroscopic techniques. I have combined these with theoretical quantum chemical calculations, to develop a SAR for estimating these reaction rate coefficients. These methods use density functional theory (DFT) calculations, which are highly accurate but costly in terms of time and computations, which we were able to substitute with fast and computationally inexpensive semi-empirical tools, greatly optimizing the efficiency and the applicability of the tool. I then wrote an open-source Python code to turn it into an automated, fast and easy-to-use tool, which is effective for general use by atmospheric chemists.

This tool can predict the rate coefficients of electrophilic addition of OH, Cl, O_3 and NO_3 to unsaturated VOCs based on a new methodology. Compared with other techniques, it requires fewer fitting parameters, is more general and, since it is based on a priori calculated information, has better potential for extrapolation to new species. More specifically, the prediction of new compounds relies solely on the calculation of their chemical properties using our software, and not solely on existing experimental data.

Consequently, it can be successfully extended to predict reactions that remain less well-known or difficult to measure in the laboratory, such as the nighttime oxidation of VOCs from biomass combustion (e.g., the oxidation of furans and pyrroles by NO_3). These results can be easily used as input data for atmospheric chemical models, and by industry and policymakers to avoid the emission of persistent species into the atmosphere.

Keywords : Biomass burning, Unsaturated Volatile Organic Compounds, Kinetics, Structure Activity Relationship (SAR), Oxidation, Furans

ICARE-CNRS ORLEANS

✉ 3E avenue de la recherche scientifique, CNRS, Délégation régionale, 45071 Orléans cedex 2